



SAKARYA ÜNİVERSİTESİ

FEN BİLİMLERİ ENSTİTÜSÜ DERGİSİ

Sakarya University Journal of Science (SAUJS)



SAKARYA
ÜNİVERSİTESİ

e-issn: 2147-835X

Volume: 28

Issue: 3

June 2024

VOLUME: 28 ISSUE: 3
E-ISSN 2147-835X

June 2024
<https://dergipark.org.tr/tr/pub/saufenbilder>

SAKARYA UNIVERSITY JOURNAL OF SCIENCE



SAKARYA
ÜNİVERSİTESİ

The Owner on Behalf of Sakarya University

Prof. Dr. Hamza Al
Sakarya University, Sakarya-Türkiye

Publishing Manager

Hüseyin Özkan Toplan
Department of Metallurgical and Materials Engineering
Sakarya University, Sakarya-Türkiye
toplano@sakarya.edu.tr

Editor in Chief

Ömer Tamer
Department of Physics
Sakarya University, Sakarya-Türkiye
omertamer@sakarya.edu.tr

Associate Editors

İhsan Hakan Selvi
Department of Information Systems Engineering
Sakarya University, Sakarya-Türkiye
ihselvi@sakarya.edu.tr

Editorial Board

Asude Ateş
Department of Environmental Sciences and
Engineering
Sakarya University
Sakarya - Türkiye
aates@sakarya.edu.tr

Bahadır Respect
Department of Nuclear Physics
Ankara University
Ankara - Türkiye
bsaygi@ankara.edu.tr

Berrin Denizhan
Department of Industrial Engineering
Sakarya University
Sakarya - Türkiye
denizhan@sakarya.edu.tr

Hüseyin Aksoy
Department of Biology
Sakarya University
Sakarya - Türkiye
haksoy@sakarya.edu.tr

Mehmet Uysal
Department of Metallurgical and
Materials Engineering
Sakarya University
Sakarya - Türkiye
mehmetu@sakarya.edu.tr

Muhammed Fatih Adak
Department of Computer Science and Engineering
Sakarya University
Sakarya - Türkiye
fatihadak@sakarya.edu.tr

Muhammet Hilmi Nişancı
Department of Electrical and Electronics Engineering
Sakarya University
Sakarya - Türkiye
nisanci@sakarya.edu.tr

Mustafa Gülfen
Department Analytical Chemistry
Sakarya University
Sakarya - Türkiye
mgulfen@sakarya.edu.tr

Osman Sönmez
Department of Civil Engineering
Sakarya University
Sakarya - Türkiye
osonmez@sakarya.edu.tr

Serap Coşansu
Department of Food Engineering
Sakarya University
Sakarya - Türkiye
scosansu@sakarya.edu.tr

Tahsin Turgay
Department of Architecture
Sakarya University
Sakarya - Türkiye
turgay@sakarya.edu.tr

Ufuk Durmaz
Department of Mechanical Engineering
Sakarya University
Sakarya - Türkiye
udurmaz@sakarya.edu.tr

Section Editor (Civil Engineering)

Elif Ağcakoca
Department of Civil Engineering
Sakarya University
Sakarya - Türkiye
elifd@sakarya.edu.tr

Faruk Fırat Çalım
Department of Civil Engineering
Adana Alparslan Türkeş
Science and Technology University
Adana - Türkiye
ffcalim@atu.edu.tr

Issa Al-Harthy
Department of Civil and Architectural Engineering
Sultan Qaboos University
Oman
aissa@squ.edu.om

Jamal Khatib
Department of Civil Engineering
University of Wolverhampton
United Kingdom
jmkhatib@wlv.ac.uk

Khalifa Al-Jabri
Department of Civil and Architectural Engineering
Sultan Qaboos University
Oman
aljabri@squ.edu.om

Hakan Alp
Department of Geophysical Engineering
İstanbul University-Cerrahpaşa
İstanbul - Türkiye
hakanalp@iuc.edu.tr

Tuba Tatar
Department of Civil Engineering
Sakarya University
Sakarya - Türkiye
ttatar@sakarya.edu.tr

Gökhan Dok
Department of Civil Engineering
Sakarya University of Applied Sciences
Sakarya - Türkiye
gokhandok@subu.edu.tr

Section Editor (Chemistry)

Can Serkan Keskin
Department of Chemistry
Sakarya University
Sakarya - Türkiye
ckeskin@sakarya.edu.tr

Gražyna Simha Martynková
Department of Chemistry Education Vsb-Technical
University of Ostrava
Czech Republic
grazyna.simha@vsb.cz

Murat Tuna
Department of Chemistry
Sakarya University
Sakarya - Türkiye
tuna@sakarya.edu.tr

Aligholi Niaie
Department Chemical Engineering
University of Tabriz
Iran
aniaei@tabrizu.ac.ir

Nahit Gencer
Department of Biochemistry
Balıkesir University
Sakarya - Türkiye
ngencer@balikesir.edu.tr

Section Editor (Biology)

Cansu Akbulut
Department of Biology
Sakarya University
Sakarya - Türkiye
cansua@sakarya.edu.tr

Luis Materon
Department of Biology
University of Texas Rio Grande Valley
USA
luis.materon@utrgv.edu

Nazan Deniz Yön Ertuğ
Department of Biology
Sakarya University
Sakarya - Türkiye
nkoc@sakarya.edu.tr

Nihan Akıncı Kenanoğlu
Department of Biology
Çanakkale Onsekiz Mart University
Çanakkale - Türkiye
nakinci@comu.edu.tr

Oğuz Kurt
Department of Biology
Manisa Celal Bayar University
Manisa - Türkiye
oguz.kurt@cbu.edu.tr

Sezgi Somuncu
Department of Biology
Sakarya University
Sakarya - Türkiye
sezgisomuncu@sakarya.edu.tr

Sezen Toksoy Köseođlu
Department of Biology
Sakarya University
Sakarya - Türkiye
sezentoksoy@sakarya.edu.tr

Section Editor (Mathematics)

Murat Güzeltepe
Department of Mathematics
Sakarya University
Sakarya - Türkiye
mguzeltepe@sakarya.edu.tr

Murat Sarduvan
Department of Mathematics
Sakarya University
Sakarya - Türkiye
msarduvan@sakarya.edu.tr

Ali Demir
Department of Mathematics
Kocaeli University
Kocaeli - Türkiye
ademir@kocaeli.edu.tr

Luan Hoang
Department of Mathematics
Texas Tech University
USA
luan.hoang@ttu.edu

Selma Özçađ
Department of Mathematics
Hacettepe University
Ankara - Türkiye
sozcag@hacettepe.edu.tr

Necati Olgun
Department of Mathematics
Gaziantep University
Gaziantep - Türkiye
olgun@gantep.edu.tr

Section Editor (Computer Science and Engineering)

Fahrettin Horasan
Computer Science and Engineering
Kırıkkale University
Kırıkkale - Türkiye
fhorasan@kku.edu.tr

Kevser Ovaz Akpınar
Computer Science and Engineering
Rochester Dubai Institute of Technology
Dubai
kxocad1@rit.edu

Muhammed Maruf Öztürk
Computer Science and Engineering
Süleyman Demirel University
Isparta - Türkiye
muhammedozturk@sdu.edu.tr

Mustafa Akpınar
Computer Science and Engineering
High Tech Collages
United Arab Emirates
mustafakpınar@gmail.com

Section Editor (Physics)

Ceren Tayran
Department Physics
Gazi University
Ankara - Türkiye
c.tayran@gazi.edu.tr

Grzegorz Jaworski
Department Physics
University of Warsaw
Poland
grzegorz.jaworski@pwr.edu.pl

Section Editor (Industrial Engineering)

Feyza Gürbüz
Department Industrial Engineering
Erciyes University
Kayseri - Türkiye
feyza@erciyes.edu.tr

Caner Erden
Department Industrial Engineering
Sakarya University of Applied Sciences
Sakarya - Türkiye
cerden@subu.edu.tr

Hatice Esen
Department Industrial Engineering
Kocaeli University
Kocaeli - Türkiye
hatice.eris@kocaeli.edu.tr

Mehmet Emin Aydın
Department Industrial Engineering
University of The West of England Bristol
England
mehmet.aydin@uwe.ac.uk,

Barış Yüce
Department Industrial Engineering
University of Exeter
United Kingdom
b.yuce@exeter.ac.uk

Benjamin Durakovic
Department Industrial Engineering
International University of Sarajevo
Bosnia and Herzegovina
bdurakovic@ius.edu.ba

Section Editor (Mechanical Engineering)

Elif Eker Kahveci
Department of Mechanical Engineering
Sakarya University
Sakarya - Türkiye
eeker@sakarya.edu.tr

Erman Aslan
Department of Mechanical Engineering
Kocaeli University
Kocaeli - Türkiye
erman.aslan@kocaeli.edu.tr

Mohammad Sukri Bin Mustapa
Department of Mechanical Engineering
University Tun Hussein Onn Malaysia
Malaysia
sukri@uthm.edu.my

Raja Mazuir Bin Raja Ahsan Shah
Department of Mechanical Engineering
Coventry University
United Kingdom
ac9217@coventry.ac.uk

Seong Jin Park
Department of Mechanical Engineering
Pohang University of Science and Technology
Korea
sjpark87@postech.ac.kr

Abderrahmane Benbrik
Department of Mechanical Engineering
M'hamed Bougara University
Egypt
abderrahmane.benbrik@univ-boumerdes.dz

Ali Cemal Benim
Department of Mechanical Engineering
Düsseldorf University of Applied Sciences
Germany
alicemal@prof-benim.com

Herman Nied
Department of Mechanical Engineering
Lehigh University
USA
hfn2@lehigh.edu

Shi-Chune Yao
Department of Mechanical Engineering
Carnegie Mellon University
USA
sy0d@andrew.cmu.edu

Tauseef Aized
Department of Mechanical Engineering
Uet Lahore
Pakistan
tauseef.aized@uet.edu.pk

Section Editor (Environmental Sciences and Engineering)

Ece Ümmü Deveci
Department of Environmental Sciences and
Engineering
Niğde Omer Halisdemir University
Niğde - TÜRKİYE
eudeveci@ohu.edu.tr

Senay Çetin Doğruparmak
Department of Environmental Engineering
Kocaeli University
Kocaeli - Türkiye
senayc@kocaeli.edu.tr

Section Editor (Food Science)

Aslı Uçar
Department of Food Sciences
Ankara University
Ankara - Türkiye
aucar@ankara.edu.tr

Edgar Perez Esteve
Department of Food Sciences
Polytechnic University of Valencia
Spain
edpees@upv.es

Syed Abbas
Department of Cereal Technology, Food Microbiology
Curtin University
Australia
s.abbas@curtin.edu.au

Section Editor

(Electrical and Electronics Engineering)

Abdullah Oğuz Kızılcay
Department of Electrical and Electronics Engineering
Zonguldak Bülent Ecevit University
Zonguldak - Türkiye
oguzkizilcay@yyu.edu.tr

İbrahim Bahadır Başığit
Department of Electrical and Electronics Engineering
Isparta University of Applied Sciences
Isparta - Türkiye
bahadirbasyigit@isparta.edu.tr

Francesco De Paulis
Department of Electrical and Electronics Engineering
L'Aquila University
Italy
francesco.depaulis@univaq.it

Mesut Baran
Department of Electrical and Electronics Engineering
North Carolina State University
USA
baran@ncsu.edu

Ozan Erdinç
Department of Electrical and Electronics Engineering
Yıldız Technical University
İstanbul - Türkiye
oerdinc@yildiz.edu.tr

Rıfki Terzioğlu
Department of Electrical and Electronics Engineering
Bolu Abant İzzet Baysal University
Bolu - Türkiye
rifkiterzioğlu@ibu.edu.tr

Section Editor (Architecture)

İsmail Hakkı Demir
Department of Architecture
Sakarya University
Sarkaya - Türkiye
idemir@sakarya.edu.tr

Section Editor (Materials Science)

Miraç Alaf
Department Metallurgical and Materials Engineering
Bilecik Şeyh Edebali University
Bilecik - Türkiye
mirac.alaf@bilecik.edu.tr

Kamaruzzaman Sopian
Department Metallurgical and Materials Engineering
Universiti Kebangsaan
Malaysia
ksopian@ukm.edu.my

English Language Editor

Seçkin Arı
Department of Computer Engineering
Sakarya University, Sakarya-Türkiye
ari@sakarya.edu.tr

Editorial Assistant

Evrım Yüksel
Department of Environmental Engineering
Institute of Sciences, Sakarya University
Sakarya-Türkiye
eyuksel@sakarya.edu.tr

Statistical Editor

Önder Gökmen Yıldız
Department of Mathematics
Bilecik Şeyh Edebali University, Bilecik-Türkiye
ogokmen.yildiz@bilecik.edu.tr

Managing Editor

Hüseyin Yasin Uzunok
Department of Physics
Sakarya University, Sakarya-Türkiye
hyuzunok@sakarya.edu.tr

Technical Editor

Hatice Vural
Department of Electrical and Electronics Engineering
Amasya University, Amasya-Türkiye
hatice.vural@amasya.edu.tr

Layout Editor

Mehmet Emin Çolak
Scientific Journals Coordinatorship
Sakarya University
Sakarya-Türkiye
mehmetcolak@sakarya.edu.tr

Yakup Beriş
Scientific Journals Coordinatorship
Sakarya University
Sakarya-Türkiye
yakupberis@sakarya.edu.tr

Indexing



Contents

Research Article

- 1 Experimental Study on Engineering Properties of Recycled Olivine Aggregate Filled CF Reinforced Electrically Conductive Mortars
Heydar Dehghanpour, Fatih Doğan, Serkan Subaşı, Muhammed Maraşlı 452-465
- 2 An Approach for Modelling Accidental Eccentricity Effects in Symmetrical Frame Buildings Exhibiting Semi-Rigid Diaphragm Behavior
Melih Sürmeli 466-479
- 3 Investigation of Usability of Sepiolite as a Pozzolan in Production of High Performance Cementitious Composites
Rasim Cem Saka, Serkan Subaşı 480-495
- 4 A Research on Architects' Comfort Conditions in Working Environments
Yiğit Can Yardımcı 496-504
- 5 Investigation of Biofilm Production and Determination of Antibiotic Resistance Profile of Staphylococcus aureus Isolated from Ground Beef and Meatballs
Tuğba Sarı, Ceren Baskan 505-516
- 6 Comparative Analysis of Machine Learning Models for Android Malware Detection
Selma Bulut, Adem Korkmaz 517-530
- 7 Design of Sulfur Resistant Cobalt Catalysts by Boron Promotion: Atomic Scale Insights
Ali Can Kızılkaya 531-541
- 8 Theoretical Analysis and Simulation of SiO₂ and ZrO₂ Based Antireflective Coatings to Improve Crystalline Silicon Solar Cell Efficiency
İmran Kanmaz 542-549
- 9 Investigation of the Effect of High-Frequency Induction Sintering on Phase Structure and Microstructure of SiC Reinforced Aluminum Matrix Composites
Muhterem Koç, Mehmet Sadrettin Zeybek 550-557
- 10 First-principles Calculations of TlCdF₃ Compound under Pressure
Belgin Koçak, Yasemin Çiftci 558-566
- 11 The Role of Water on the Oxidation Process of Graphene Oxide Structures
Kürşat Kanbur, Işıl Birlık, Fatih Sargın, Funda Ak, Azem Ahmet Türk 567-578
- 12 Vancomycin-Loaded Gel Ocular Drug Delivery System for Treatment of Endophthalmitis
Ebru Erdal 579-588
- 13 Beta Vulgaris L. Extract: pH Effect on Total Phenolic Content and Antioxidant Properties
Rama Alkayarı, Zuhul Şahin, Fatih Sonmez, Mustafa Küçükislamoğlu 589-593
- 14 Preparation of Hybrid Films Containing Chitosan, Starch, Ascorbic Acid, and Different Metal Ions for Release of Doxorubicin
Ümran Duru Kamacı 594-601
- 15 Pigment Production From Bacteria Isolated From Whey
Sude Çardak, İlke Karakaş, Nurcihan Hacıoğlu Doğru 602-609
- 16 A Detailed Comparison of Two New Heuristic Algorithms Based on Gazelles Behavior
Emine Baş 610-633

17	Solid Waste Analysis and Improvement Studies in Local Governments (Cayırova Municipality Example) <i>Kader Duran, Berna Kırıl Mert</i>	634-645
18	Experimental Study on Springback Properties of 6061 Aluminum in V-Bending <i>Ahmed Ozan Örnekcı, Seçil Ekşi</i>	646-653
19	Investigation of Alkali Activated Ferrochromium Slag Composites Including Waste Marble Powder <i>Merve Koç Keskinılınç, Servet Yıldız, Şule Sekin Eronat, Mehmet Emiroğlu</i>	654-667
20	Investigation of Modifying Alloying Elements in High-Pressure Injection Casting Eutectic Al-Si Alloys <i>Alpaslan Kılıçarslan, Hatem Akbulut</i>	668-684

Experimental Study on Engineering Properties of Recycled Olivine Aggregate Filled CF Reinforced Electrically Conductive Mortars

Heydar Dehghanpour^{1*}, Fatih Doğan², Serkan Subaşı³, Muhammed Maraşlı⁴

¹Istanbul Aydın University, Faculty of Engineering, Department of Civil Engineering, İstanbul, Türkiye, haydardehgan@aydin.edu.tr

²Munzur University, Rare Earth Elements Application and Research Center (MUNTEAM), Tunceli, Türkiye, fatihdogan@munzur.edu.tr

³Duzce University, Faculty of Engineering, Department of Civil Engineering, Düzce, Türkiye, serkansubasi@duzce.edu.tr

⁴Fibrobeton Company, R&D Center, Düzce, Türkiye, muhammed@fibrobeton.com.tr

*Corresponding Author

ARTICLE INFO

ABSTRACT

Keywords:

Cementitious mortars

Olivine

Carbon fiber

Resistivity

Damping ratio



Article History:

Received: 04.08.2022

Accepted: 25.12.2023

Online Available: 06.06.2024

Electrically conductive concretes produced for different purposes were introduced years ago and since then, intensive scientific research has been going on. Studies in the literature have generally been carried out on conventional concretes with electrical conductivity for floor applications. The current study investigates carbon fiber reinforced mortars filled with fine olivine aggregate. Fine aggregate filled mortars are generally produced for building facade applications. Within the scope of the study, the mechanical, electrical, dynamic and microstructural properties of cementitious mortars containing 0.5%, 0.75% and 1.0% carbon fiber and 100% recycled olivine aggregate were investigated. The purpose of performing dynamic resonance tests was to investigate the effect of carbon fiber on damping ratio. 28-Day compressive, flexural, dynamic resonance, ultrasonic pulse velocity (UPV), Leeb hardness and dry density tests of conductive mortar samples obtained from four different mixtures were performed. In addition, 2, 14, 28, 90 and 180 days electrical conductivity tests were carried out to determine their resistivity in different time intervals. The purpose of performing dynamic resonance tests was to investigate the effect of carbon fiber on damping ratio. While a significant positive effect of CF on electrical conductivity and damping ratio was observed, a negligible decrease in mechanical results was observed. Calcium silicate hydrate (C-S-H) structure formed by hydration using olivine filler in the cement mixture confirmed the binding formations.

1. Introduction

It has been known that the electrical conductivity of cement-based mortars, which are insulating in the dry state and semiconductor in the wet state, shows low performance. However, when voltage is applied to concrete, which has electrical conductivity, it resists electric current [1, 2]. Different studies have been carried out to determine the conductivity of cement mortars and concrete. It has been tried to increase the conductivity of the concrete by adding different conductive additives to the cement mortar [3].

Electrically conductive concrete could be produced by adding conductive materials such as carbon nanotubes, graphene, carbon black, and carbon fiber to cement-based mixtures. Conductive materials provide both structural and electrical use possibilities due to their excellent electrical conductivity and superior mechanical properties [4].

It was stated that the distribution of graphene and carbon fiber in the cement mortar affects the electrical and mechanical properties of the material [5]. On the other hand, it has been

reported that carbon fiber, which is not homogeneously dispersed in the cement matrix, has a negative effect on the compressive strength and flexural strength of the material [6]. It has been stated that carbon nanotube [7] and graphene [8] as conductive additives added to concrete mix are important factors in reducing concrete material resistance.

Ma et al. [9] emphasized that the possible increase in electrical resistance due to insufficient dispersion of graphene in the cement matrix can be overcome by making carbon dispersion more effective. Bi et al. [10] used silicium dioxide (SiO₂) to improve the dispersion of carbon nanotubes in the cement mixture. However, they stated that due to the high cost of these conductive components, it limits their widespread use in construction. Also, it was stated that the distribution and size of the filling material in the cement matrix were at least as important as the conductivity of the material used to increase the conductivity of the concrete [11].

It was stated that low-cost fiber conductive components of different structures could improve the electrical conductivity of conductive concrete [12]. Among the conductive additives, carbon fiber has been preferred in the production of conductive cement mortars, which are superior in terms of both mechanical and physical properties. In addition, it was stated that the distribution of carbon fiber added to the concrete mortar in the mixture and the mixing method are important factors affecting the conductivity of the concrete mortar [13].

Wen and Chunk [12] reported that the use of 50% carbon fiber and 50% carbon black contributes to the resistance of the material in electrically conductive concrete. In addition, they stated that the use of conductive aggregates instead of sand and aggregate contributed significantly to the conductivity of concrete. He et al. [14] reported that 0.6% by volume of carbon fiber and 30% by volume of conductive aggregate should be added to Portland cement to obtain under of 3.5 Ω .cm electrical resistivity. Similarly, in the study of conductive mortar containing swcnt and steel fiber, it was stated in the literature that the electrical resistance decreased up to 500 cm. Ω [15].

Also, it could be used for heating and defrosting by putting carbon fiber in an electrically conductive cement mortar. However, as thermal stress may occur on the concrete road with this application, the structure is damaged and thermal stability decreases. Therefore, electrically conductive cement mortar application could be realized by reducing the thermal stress between layers [16]. Vilaplana et al. [17] reported that conductive concrete exhibited an electrical resistance of 97.86 Ω cm with carbon fiber reinforcement in the range of 0.29% - 0.58% by volume in the concrete mix, and this resistance was lower than that of portland concrete.

On the other hand, cement has been widely used as a binder in the construction industry. However, during cement production, there is both high energy consumption and significant carbon dioxide (CO₂) emissions into the atmosphere. Instead of cement alkali activated binder materials such as kaolin, metakaolin, and fly ash are recommended [18]. The CO₂ emission value of olivine was measured as 9 Mtons of CO₂ per year-1 after approximately 25 years of use [19]. The use of recycled and reusable materials instead of aggregate and sand used in cement mortars may benefit from reducing concrete waste. It has been stated that olivine cement mortar can provide low density and less mechanical resistance by affecting both physical and mechanical properties. Thus, it will be able to contribute to building materials in terms of sustainability [20]. To ensure sustainable concrete production, it is expected that using olivine as a binder in cement mortar will be more suitable both in terms of environment and economy.

Papayianni et al. [21] aimed to develop shotcrete mixtures with olivine aggregates that can act as a protective coating in case of high temperature exposure such as fire in a tunnel. They used olivine aggregate instead of limestone aggregate in shotcrete mixes. The results showed that replacing limestone with olivine was superior in strength at all strain temperatures of concrete; This proves that the use of olivine-based shotcrete enables the production of fire resistant shotcrete at temperatures up to 850°C. There has been limited research on the compressive

strength of concrete materials based on olivine minerals.

The mechanical properties of the concrete obtained by using olivine mineral instead of aggregate and sand in cement mortar were tested. In addition, scanning electron microscopy-energy distribution spectrometry (SEM-EDS) was used to examine the effect of olivine in concrete structure on microstructure and porosity. In this study, a new type of conductive concrete was designed by using olivine as aggregate, and carbon fiber as conductive material. The engineering properties of the conductive concrete material were investigated by changing the carbon fiber ratio.

2. Material and Methods

2.1. Material properties

100% olivine aggregate was used as the filling material in all mixtures. The specific gravity of olivine aggregate used was 3.24. CEM II-42.5 R white cement, which is preferred in facade cladding, was used as binder. As a pozzolanic additive material, calcined kaolin was preferred in equal proportions in all mixtures. The particle size ranges of olivine, cement, and calcined kaolin were compared in figure 1. 12 mm long, 7.2 μm diameter, and 0.00155 electrically resistant, CF has been used as conductivity enhancing fiber. Polycarboxylate based superplasticizer was used to ensure adequate workability in all mixtures.

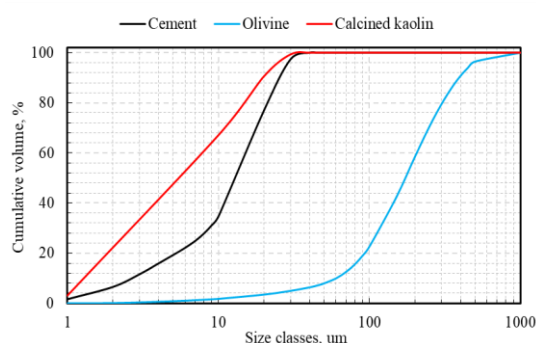


Figure 1. Grain size analysis curves of cement and filling materials

Details of materials used in electrically conductive mortars are given in Table 1. olivine filled pure mix is a normal primix mortar consisting of filler, binder, pozzolanic, water, and plasticizer, and is defined as the matrix for

other mixtures. In the primix mixture, all dry ingredients are put into the mixer, mixed for 90 seconds, then plasticizer is added together with water and mixed for 90 seconds again, then placed in molds. In carbon fiber mixtures, after all the components came together and the matrix was ready, the fibers were added and mixed with a mixer for 90 seconds.

Table 1. Component ratios in electrically conductive mortars

No	1	2
Code	OLV	OLV-0.50CF
Olivine (g)	1350	1341
Cement (g)	500	500
Calcined kaolin (g)	50	50
Su (g)	220	220
CF (g)	0	9
Superplasticizer (g)	6	7.5
No	3	4
Code	OLV-0.75CF	OLV-1.0CF
Olivine (g)	1337	1333
Cement (g)	500	500
Calcined kaolin (g)	50	50
Su (g)	220	220
CF (g)	13	17
Superplasticizer (g)	8.5	10

2.2. Test methods

The electrical resistivity of the 40x40x160 mm mortar samples produced were obtained by the two-point uniaxial measurement method, which is frequently preferred in studies such as [1, 11]. The electrical resistivity of an object is a measure of its opposition to the electrical conductivity [3]. The potential difference applied in all resistivity measurements was 30 V. Longitudinal resonance frequency testing was performed for samples according to ASTM C215 standard [22] in this. The sample was fastened in the midpoint between two supports and oscillation was applied from one end of the sample with a spherical impact pull, while the impact response from the other end was measured with an accelerometer. Using the data obtained by the accelerometer, different equivalent resonance frequency diagrams are drawn for each sample. Based on the longitudinal resonance frequency, damping ratio of mortars is calculated. Schematic images of resistivity and dynamic resonance test methods are shown in Figure 2.

The method used in this study is based on the half-power bandwidth method [23, 24]. The schematic experimental setup view of resonance

and resistivity tests are shown in Figure 1. UPV tests were performed according to ASTM C597 [25]. The ASTM A956 standard [26] was used to determine the Leeb hardness of the produced samples. Flexural and compressive strength tests were carried out in accordance with the TS EN 196-1 standard [27] on three 40 x 40 x 160 mm prismatic samples obtained from each mixture.

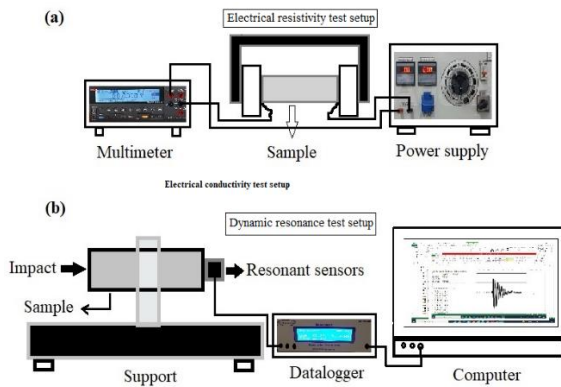


Figure 2. (a) Two-point uniaxial electrical resistivity measurement test setup, (b) Dynamic resonance test setup

Scanning Electron Microscope (SEM) (Hitachi VP-SEM SU1510) was used to examine the microstructure of powder samples and prepared concrete samples and to analyze structures at the sample interface after mechanical testing. X-ray diffraction (XRD) analysis technique was used for phase identification of crystal materials. The crystal phases of the pure olivine mixture sample and the 0.75% CF added sample were determined, together with the analysis of cement powder, calcined kaolin and olivine sand added to the cement mixture. Powder samples and crystal phase characterizations of the prepared samples were performed with RIKAGU Smart Lab X-ray diffractometer. $K\alpha$ Cu at a wavelength of 1.54 nm was used as the X-ray source, and scanning was performed in the range of 10° to 90° .

3. Results and Discussion

3.1. Mechanical test results

The flexural and compressive test results of the mortar samples produced within the scope of the study are compared and summarized in figure 3. When compressive and flexural strengths are compared, a harmonious parallel relationship is observed between them. The linear relationship between them is shown in figure 4. The linear

relationship between compressive strength and flexural strength can prove that the mixture is homogeneous and that the fibers are evenly distributed. Campos et al. [28] proved that there is a negative relationship between the air content of normal strength concrete and its compressive and flexural strengths. According to their research, a significance test on fresh field properties revealed that air content is the most important fresh field property affecting compressive and flexural strengths. These researchers have reported its direct usability in models that relate air content, compressive strength and flexural strengths.

Considering the effect of CF on compressive strength, it was observed that the strength of the sample containing 0.5% CF increased by 2.63% compared to the strength of the pure OLV sample. However, the compressive strength of the mixtures with 0.75% and 1% CF added decreased by %3.53 and %7.40, respectively. In the flexural strength results, 0.50% and 0.75% CF had a positive effect of %13.23 and %1.61, respectively, while a negative effect of 4.84% of 1% CF was observed. This behavior of carbon fiber in cementitious materials has also been proven in the literature and it has been reported that the reason is due to the voids formed in the mixture [3].

The reason for the voids formed in the mixture is that the carbon fibers used in high doses clump in the mixture and workability problems are experienced. It has been proven that the addition of CF at higher dosages improves the flexural strength compared to the compressive strength when compared with other studies in the literature [29]. In order to prevent crack formation and propagation in bending, the optimum fiber ratio is different according to the condition of the element subjected to compressive load.

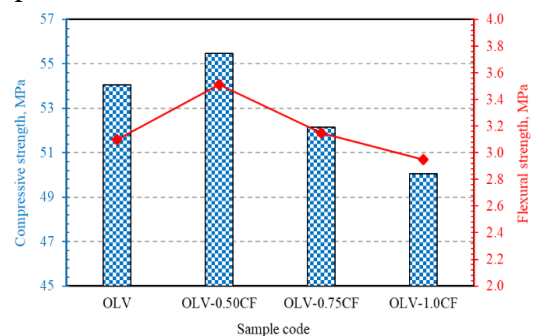


Figure 3. Compressive and flexural test results

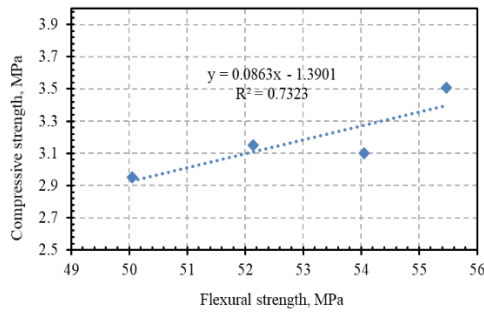


Figure 4. Relationship between compressive and flexural strengths

3.2. Non-destructive test results

In this section, the properties of the products obtained within the scope of the study were examined by applying some non-destructive testing methods. For electrical resistivity measurement, the electrical current values of 2, 14, 28, 90 and 180 days of samples produced from 4 different mixtures were read. The resistivity results obtained are summarized in figure 5. Considering the effect of CF in the samples, it was observed that the resistivity values decreased significantly with the addition of fiber and increasing its ratio. When the age effect is examined, the resistivity values of the samples increased rapidly in the first ages, while the conductivity loss rate decreased in the later ages.

One of the reasons for the decrease in the conductivity value depending on time is the drying of the water in the mixture in any way. Some of this water can be consumed for the formation of CSH products and some by evaporation. Another reason for the decrease in conductivity over time is the development of CSH products and the obstruction of the electrical current path by wrapping around the conductive fibers. This behavior may appear less in conventional concretes because the fine minerals content is not as high as in the current study, so there is less chance of passive layer formation around the fibers over time.

Resistivity values of OLV, OLV-CF0.5, OLV-CF0.75 and OLV-CF1.0 samples increased by 13, 3.7, 2.1 and 1.9, respectively, in the 2-180 day range. Here, the increase in the carbon fiber ratio seems to decrease the age effect on the resistivity. However, the 180-day resistivity values of these samples were obtained as 39921.29, 391.40, 205.33 and 101.43 Ω .cm, respectively. These

values were confirmed by comparison with the literature [3, 30].

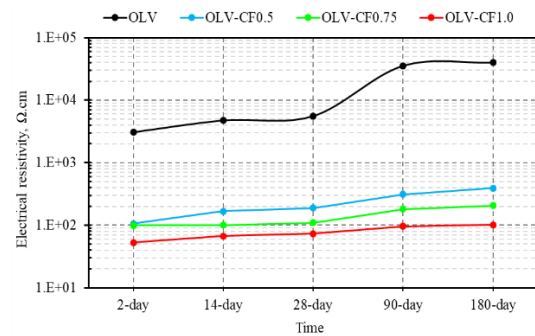


Figure 5. Resistivity results of specimens

The frequency-amplitude curves of the 28-day prismatic samples obtained from 4 different mixtures were drawn after the resonance test and compared in figure 6. Building elements produced from cementitious materials are exposed not only to mechanical but also to dynamic loads throughout their service life [31]. Therefore, it is important to examine the dynamic properties, especially the damping ratio, of these materials containing different additives and fibers. The damping ratio is one of the main parameters representing the vibration dampening property of materials [32]. According to the resonance test information in the literature, it is known that narrow and steep Frequency-Amplitude curves have less damping property of the relevant material, and wide and low curves have higher damping properties [33].

When the test results in this study are compared and the damping ratio values in figure 7 are compared, similar behavior in the literature can be achieved. Considering the damping ratio values, it was observed that the values of all three CF added mixtures increased compared to the pure OLV mixture. The damping ratio values of 0.5%, 0.75% and 0.1% CF added mixtures increased by 15.61%, 26.16% and 14.27%, respectively, compared to the pure mixture. However, the damping rate of the mixture with 1.0% CF added decreased by 9.42% compared to the 0.75% CF added. In the literature, it has been reported that the damping ratio increases when the amount and length of synthetic fibers increase up to a certain interval [32, 34]. The [15] study proves that the use of fiber above its optimum ratio can result in a reduction in damping ratio.

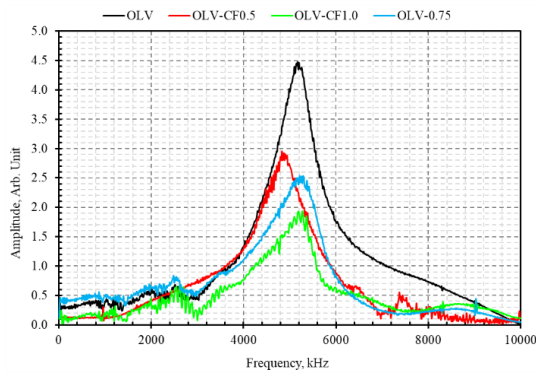


Figure 6. Amplitude-frequency curves of conductive mortar specimens

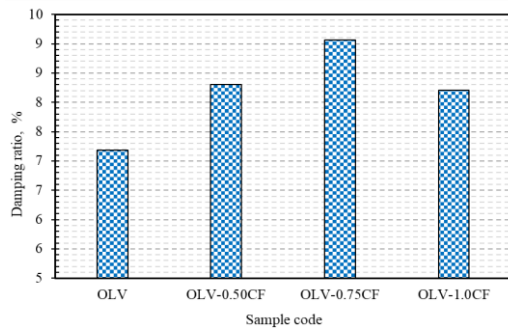


Figure 7. Damping ratios of specimens

UPV and density test results of electrically conductive mortar samples obtained from four different mixtures are shown in figure 8. When the results were compared, it was observed that there was a very strong linear relationship between them. The UPV values of 0.5%, 0.75% and 0.1% CF added mixtures decreased by 11.17%, 17.08% and 26.46%, respectively, compared to the pure mixture. Considering the density test results, the values of the same mixtures decreased by 4.60%, 6.69% and 11.30%, respectively. UPV test is a method that gives information about the internal structure defects of materials.

Also, UPV method, known as a non-destructive method, is a technique used to determine the estimated compressive strength of building materials. UPV refers to the time it takes for the ultrasonic pulse to travel a certain distance through a material, usually in concrete and mortar specimens. As the rate of defects such as voids increases in cementitious materials, the ultrasonic sound velocity decreases, and on the contrary, the sound velocity increases with a decrease in the void ratio [35, 36]. This situation is also understood in figure 8 as the density values are parallel to the UPV values. In figure 9, the correlation coefficient of the linear

relationship was calculated as 0.9965. However, this correlation is valid between 0-1% CF ratio, different relationships can be observed at different rates. UPV results also had a direct parallel relationship with compressive, flexural, resistivity and Leeb hardness test results. However, like all these test results, the UPV values also had an inverse relationship with the damping ratio.

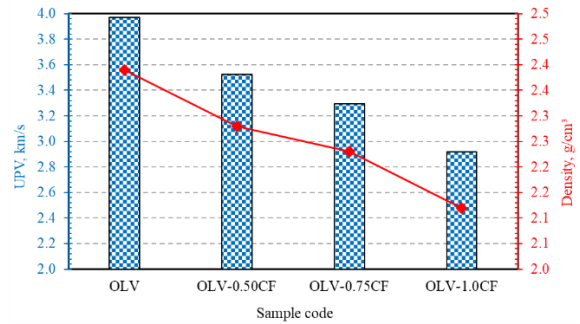


Figure 8. UPV and density values

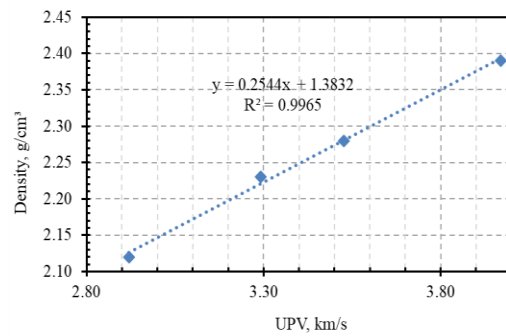


Figure 9. Relationships between UPV and density test results

Schmidt hammer test is generally applied to obtain information about the surface hardness of cementitious materials. In addition, as a more practical method, the application of the Leeb hardness test has been seen in a few studies. The Leeb hardness test method is a method developed for metal materials, but some researchers have also used it in the measurement of cementitious materials. In a study in the literature, the Leeb hardness value for a conventional concrete was obtained between 362-405 HL. Leeb hardness values measured for mortar samples vary between 560 and 542 HL. Gomez-Heras et al. [37] stated that the finer the grain size, the higher the Leeb hardness. This situation is directly related to the filling of fine-grained minerals into micro and macro pores [38]. Therefore, in this study, it can be proven to be true that the Leeb hardness is higher compared to conventional

concretes, since the aggregate particle size is less than 1 mm. Since there has been no hardness research about olivine filled mortars, it is impossible to compare the obtained hardness values with the literature.

Considering the Lebb hardness results summarized in figure 10, it was observed that the hardness values decreased with the addition of CF and increasing its ratio. The negative effect of CF on hardness may be related to the resulting porosity. The low diameter of the CF may reduce the workability of the mixtures and settling problems may occur. This leads to a decrease in some physical and mechanical properties of the composite material. A similar behavior is observed when the hardness results are compared with the compressive and flexural strength results. Comparing OLV-CF0.5, OLV-CF0.75 and OLV-CF1.0 mixtures with pure OLV mixture, Leeb hardness was observed to decrease by -1.25%, -1.61% and -3.21%, respectively.

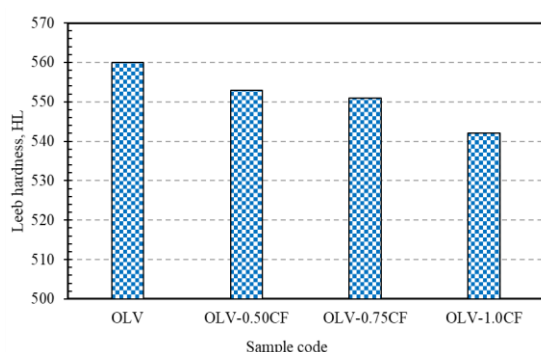


Figure 10. Leeb hardness test results

3.3. Microstructure analysis results

SEM images of cement powder, calcined kaolin powder, olivine sand, and CF are shown in figure 11. Calcined kaolin produces dehydroxylation and does not cause any change in the nested particle structure [39]. On the other hand, it is seen that the gap between the calcined kaolin particles in the cement matrix increases. This could be attributed to the increase in the surface area of the particles. In the micrograph of olivine sand, an irregular shape was seen in figure 11 (c). It could be observed that replacing the normal silica sand material with olivine sand will affect the chemical composition of the fractions in the concrete mix. The surface morphology of CF analyzed by SEM is shown in figure 11 (d). CFs with a highly

smooth surface have an average diameter of about $7.2 \mu\text{m}$ and an average length of 12 mm.

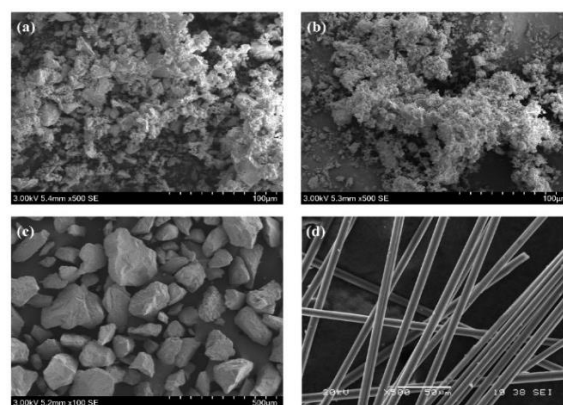


Figure 11. SEM images of cement powder (a), calcined kaolin powder (b), carbon fiber (c) and olivine sand (d) used in mixtures

Figure 12 shows XRD patterns of cement powder, calcined kaolin, and olivine sand. The peak intensities in the powder samples allow the determination of specific phase groups in the compositions. In addition, the peak intensities provide information about the residue mixtures. Crystalline phases at low peak densities contain phases that are difficult to identify. Calcite, C2S, and C3S phases were detected in the cement powder material. The cement mortar produced using fine and natural sea sand was allowed to absorb water completely. The intense peaks in the X-ray diffractogram are C2S and C3S. As stated by Jaya et al. [40], C2S (Ca_2SiO_4) and C3S (Ca_3SiO_5) crystal phases, which show the hydraulic properties of cement, participate in the hydration reaction that strengthens the cement structure.

On the other hand, quartz, kaolinite, olivine, forsterite, and portlandite (calcium hydroxide) phases detected in XRD diffractograms of powder samples indicate hydration reaction products. Behnamfard et al. [41] associated the presence of quartz in the composition of kaolin powder with an increase in SiO_2 content. A large amount of olivine was observed in the XRD crystal phase analysis of olivine sand. Thus, it is expected that olivine sand, which is used instead of aggregate in the cement mixture, will form a dense structure in the matrix.

SEM images of pure olivine-filled cement mortar at 500, 2000, and 5000 magnifications, respectively, after 28 days of curing are given in

figure 13 The microstructure of the olivine-filled cementitious mortar generally shows homogeneously dispersed hydration products. In figure 13 (a), C-S-H structures were formed. It is seen that the olivine-filled cement mortar has a dense crystalline structure at the micro level (figure 13 (b)). It could be noted that magnesium hydrated silicates form crystal structures. In the high magnification SEM image of the olivine filled cement mortar, needle-like structure of ettringite was observed in the olivine filled mortar mixture.

Also, it could be emphasized that the olivine filler contributes to the strength performance of the concrete sample by affecting the microstructure. Moreover, partial agglomerations are seen in the microstructure of olivine sand, which is used instead of aggregate in the cement mixture by growing small particles. It could be defined as particles that have not completed their chemical reaction in the cement matrix [42]. The size of the scattered agglomerated particles seen in figure 13 (b) ranges. It is seen that micro-scale particles are formed by the transformation of small-sized particles into large particles with Ostwald repining [43].

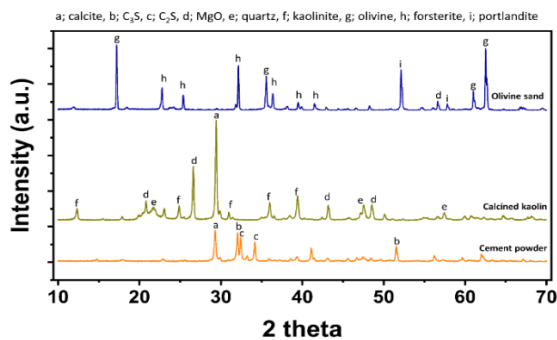


Figure 12. XRD results of cement powder (a), calcined kaolin powder (b) and olivine sand (c) used in mixes

In contrast, the olivine filler in the cement matrix appears to reduce the level of voids in the microstructure. Thus, it could be concluded that the formation of air bubbles in the hardened cement mixture is prevented and the voids decreases. Reduced voids in the matrix structure contribute to the increase in strength and are compatible with the above-mentioned compressive strength and flexural strength results. As a result, the use of olivine sand as aggregate instead of silica sand in the cement

mixture could be associated with the binding property of olivine. In addition, considering the UPV test results of the conductive concrete samples, the higher UPV value of the OLV sample compared to the other samples could be attributed to the compact structure in the microstructure. The presence of only cement mortar components and the absence of conductive additive particles in the micrographic structure seen in figure 13 (c) could be explained by the low electrical resistance of the OLV sample mentioned above. The absence of conductive particles in the mixture increased the insulation of the cement mortar and aggregate in the structure and caused a decrease in the electrical resistance.

The 500, 2000, and 5000 magnification SEM images of the 0.75% CF reinforced OLV-0.75CF sample, which provided the optimum conditions among the test samples containing three different ratios of CF to the cement mixture, were shown in figure 14. As it is known, micro cracks damage the structure of the concrete, negatively affect the strength of the material, and reduce the durability of the structures [44]. It has been seen that the CFs in the cement matrix are effective in the porous structure of the concrete and there is a partially regular distribution. Since the non-homogeneous distribution of CFs in the cement matrix could not contribute to the crack resistance, it caused a decrease in the strength of the concrete sample. Guo et al. [45] reported that the mechanical behavior of concrete with a CF content of 1.4% decreased.

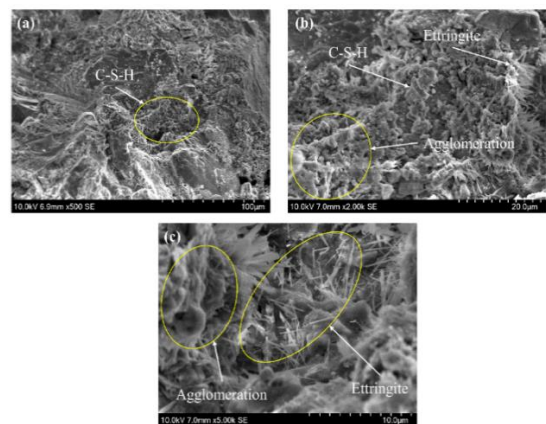


Figure 13. SEM images of 28-day pure olivine filled mixture; (a) 500 magnification, (b) 2000 magnification and (c) 5000 magnification

Figure 14 (a) shows CFs, it could be concluded that the increased CF content in the cement matrix significantly affects the voids [46]. The CFs seen in figure 14 (a) and (b) have prevented the formation of large-scale cracks in the concrete. Thus, it could be said that CFs resist the stresses caused by high pressure, prevent crack propagation, and contribute to the mechanical strength of concrete. Also, In figure 14 (a) and (b), the hydration products adhering to the CF show that the CFs in the matrix are bonded with the cement mortar. CFs forming a bond between the aggregate and the cement matrix prevented crack propagation, which caused a decrease in mechanical strength based on the applied stresses. On the other hand, figure 14 (c) shows the cracked region between the aggregate and the cement matrix.

During the mechanical test applied to the concrete, it is understood that the concrete could not show enough resistance to the loaded pressure and ruptures started. This cracked structure is indicated as the weak zone and is associated with a decrease in material strength (Mehta, P.K., Monteiro, P.J.M., 2014. Concrete: Microstructure, Properties, and Materials, 4 ed. McGraw-Hill, Nova York). It could be concluded that CFs randomly distributed in the cement matrix contribute partially to the concrete strength, and the Leeb hardness value decreases with the formation of brittle structures. In addition, it is seen that CFs adhere strongly to the cement matrix and generally do not break, resisting the pressure applied to the sample. It could be concluded that the CFs remain intact within the matrix, even if the concrete is physically fractured by the applied pressure.

Figure 14 (c) shows ettringite structures concentrated in C-S-H formed by hydration. It has been reported that needle-like ettringite structures affect the porosity. In addition, it is stated that C-S-H formations in the structure support the increase in strength in concrete [47]. The high rate of ettringite in the structure affects the formation of cracks in the matrix. Thus, low crack formation at the OLV-0.75CF sample interface may be associated with increased resistance to compressive stress.

Moreover, the content of conductive CFs in the cement matrix allows current to flow between the particles in the mixture. This could be attributed to the increase in the electrical resistance of the OLV-0.75CF sample compared to the above-mentioned electrical resistance test results. Also, it can be stated that the conductive network structure formed by CFs in the cement matrix is stable. Furthermore, the short distance between the unevenly distributed CFs in the matrix contributed to the conductivity of the cement mortar by forming a network between the aggregate and the cement. As stated by Chen et al. [48], a conductive network can be created by reducing the distance between conductive fiber particles.

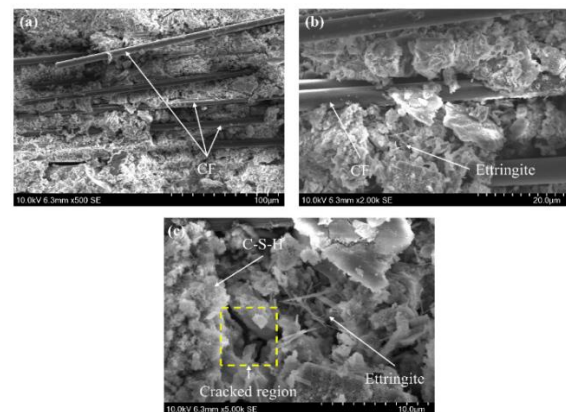


Figure 14. SEM images of 28-day olivine filled, 0.75% CF reinforced mixture; (a) 500 magnification, (b) 2000 magnification and (c) 5000 magnification

The contribution of CFs dispersed in the matrix to the desired electrical conductivity is related to controlling the CF content in the mixture. Thus, a balance is established between both the mechanical properties and the electrical conductivity properties of CF. On the other hand, it can be stated that the effect of the olivine filler used as aggregate in the mixture on the conductivity of CF is low.

Figure 15 shows the XRD models of the olivine-sand-filled mortar sample (OLV) and olivine-filled (OLV-0.75CF) sample containing 0.75% CF, used instead of aggregate in the cement mixture. Olivine sand in the cement mixture resulted in the formation of forsterite crystal phase because of the hydration reaction with magnesium. The C-S-H phase in the phase analysis of the OLV sample shows the crystalline

phase product formed by the hydration reaction. Thus, it is confirmed that mixtures with binding properties are formed with a hydration period of 28 days. On the other hand, ettringite peaks were formed depending on the CF content in the XRD model of the OLV-0.75CF sample. Also, C-S-H (calcium silicate hydrate) hydration products were detected. In addition to these, a carbon peak was detected, proving that CF added as a reinforcement component in the cement mixture is in the cement matrix. All the XRD phases appear to be in crystalline form. Ramkumar et al. [49] attributed the presence of hydration products to the effect of secondary hydration and filler material in cements containing carbon. It can be associated with the olivine filling in the conductive concrete mix.

In addition, it could be stated that CFs with high surface area accelerate the hydration process with other particles in the matrix, and as a result, contribute to the strength of the concrete [50]. Nambiar and Ramamurthy reported that the compressive strength increased with the decrease of the spaces between cells in the cement matrix. Thus, the ineffectiveness of CFs added to the cement matrix in filling the micropores can be explained by the relatively low compressive strength value mentioned above. In addition, although the strength of the cement matrix was increased with CFs, it was understood that the effect on the compressive strength of the concrete material was limited. The very weak calcite peak can be explained by the formation of a layer on the surface of the CFs by the cement particles during the hydration reaction.

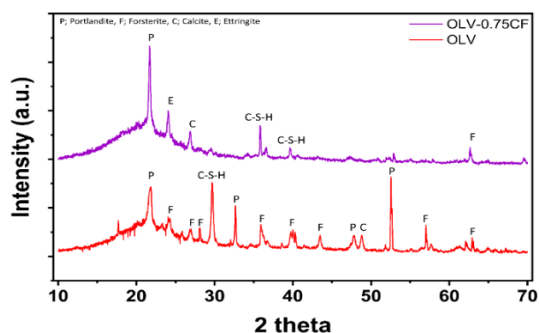


Figure 15. XRD results of 28-day pure and 0.75% CF reinforced mixture

4. Conclusion

In this study, the effects of olivine sand, which is used instead of aggregate, and CFs, which are used as additive components, on the strength properties and electrical resistance of the concrete sample are explained by experimental studies. According to the electrical resistivity results, while the wet effect was more pronounced in the insulator sample, the resistivity values of the conductive mortars containing CF changed less over time. The lowest resistivity value was measured for the mixture containing 1% CF. Carbon fiber also had a significant positive effect on the damping ratio. The sample showing the highest damping rate was 0.75%.

It has been understood that 28 days of hydration provides an increase in compressive strength and flexural strength. When the CF content was 0.75%, the compressive and flexural strength effects of CF on conductive concrete increased significantly. However, 0.75% CF content increased fiber agglomeration and caused a decrease in the strength of the concrete sample. CFs in the cement mixture prevented crack growth and improved the mechanical properties of the conductive concrete. It was observed that the compressive strength and flexural strength of the cement mixture decreased relatively with the increase in CF content. Thus, it is concluded that the effect of CF on compressive strength, flexural strength, and Leeb hardness is limited.

SEM analysis results of OLV-0.75CF sample show that CFs contribute to the mechanical properties of cement mortar by preventing crack formation. In addition, the low distance between the CFs observed in the SEM images contributed to the reduction of the electrical resistance of the concrete.

It was observed that CFs strengthened the bond between the cement matrix/CF by filling the voids in the voids structures of the cement matrix. However, OLV-0.75CF sample with optimum content in electrical resistance test results obtained higher conductivity compared to other samples. C-S-H structure formed by hydration using olivine filler in the cement mixture confirmed the binding formations. It is

understood that olivine filler and CF additive can be compatible with conductive concrete. It could be said that the ettringite peak seen in the XRD analysis results reduces the contribution of CF, which increases the strength of the cement matrix. As a result, the increase in the mechanical properties of the olivine-filled cement mortar was more pronounced compared to the CF-added conductive concrete. The contribution of 0.75% CF content in the cement mortar to the mechanical properties of the concrete was lower than the electrical resistance effect of the sample. On the other hand, CFs form a stable conductive network structure between the cement mortar and the aggregate, significantly reducing the electrical resistance. It could be said that the CF content in the conductive concrete mixture contributes to both the mechanical and electrical properties of the concrete.

Article Information Form

Acknowledgments

Thanks to Fibrobeton Company for their support. We also thank Eti Krom Inc. for their support of olivine materials.

Funding

This study was carried out within the scope of the project coded STB-072161 of Fibrobeton R&D Center.

Authors' Contribution

The authors contributed equally to the study.

The Declaration of Conflict of Interest/ Common Interest

No conflict of interest or common interest has been declared by the authors.

The Declaration of Ethics Committee Approval

This study does not require ethics committee permission or any special permission.

The Declaration of Research and Publication Ethics

The authors of the paper declare that they comply with the scientific, ethical and quotation rules of SAUJS in all processes of the paper and that they do not make any falsification on the data collected. In addition, they declare that Sakarya University Journal of Science and its editorial

board have no responsibility for any ethical violations that may be encountered, and that this study has not been evaluated in any academic publication environment other than Sakarya University Journal of Science.

Copyright Statement

Authors own the copyright of their work published in the journal and their work is published under the CC BY-NC 4.0 license.

References

- [1] H. Dehghanpour, K. Yilmaz, "Heat behavior of electrically conductive concretes with and without rebar reinforcement", *Materials science medziagotyra journal*. 26, 471–476, 2020
- [2] H. Dehghanpour, K. Yilmaz, "The relationship between resistances measured by two-probe, Wenner probe and C1760-12 ASTM methods in electrically conductive concretes", *SN applied sciences*. 2, 10, 2020.
- [3] H. Dehghanpour, K. Yilmaz, M. Ipek, "Evaluation of recycled nano carbon black and waste erosion wires in electrically conductive concretes", *Construction and building materials*. 221, pp.109–121, 2019.
- [4] C. A. Espinoza-Moreno, M. Rodriguez-Rodriguez, M. J. Pellegrini-Cervantes, C. P. Barrios-Durstewitz, R. E. Núñez-Jaquez, H. J. Peinado-Guevara, M. Chinchillas-Chinchillas, G. Fajardo-San-Miguel, "Electrical percolation and fluidity of conductive recycled mortar cement: graphite powder: recycled sand with addition of industrial waste carbon fiber", *Carbon letters journal*. 31, pp. 707–720, 2021.
- [5] M. Haghgoo, R. Ansari, M. K. Hassanzadeh-Aghdam, "Prediction of electrical conductivity of carbon fiber-carbon nanotube-reinforced polymer hybrid composites", *Composites part b engineering*. 167, pp.728–735, 2019.

- [6] J. Wei, Q. Zhang, L. Zhao, L. Hao, Z. Nie, “Effect of moisture on the thermoelectric properties in expanded graphite/carbon fiber cement composites”, *Ceramic international journal*. 43, pp. 10763–10769, 2017.
- [7] M. Saafi, K. Andrew, P. L. Tang, D. McGhon, S. Taylor, M. Rahman, S. Yang, X. Zhou, “Multifunctional properties of carbon nanotube/fly ash geopolymeric nanocomposites”, *Construction and building materials*. 49, pp.46–55, 2013.
- [8] M. Saafi, L. Tang, J. Fung, M. Rahman, F. Sillars, J. Liggat, X. Zhou, “Graphene/fly ash geopolymeric composites as self-sensing structural materials”, *Smart materials and structures*. 23, 065006, 2014.
- [9] Y. Ma, W. Liu, J. Hu, J. Fu, Z. Zhang, H. Wang, “Optimization on the piezoresistivity of alkali-activated fly ash/slag mortar by using conductive aggregates and carbon fibers”, *Cement and concrete composites*. 114, 103735, 2020.
- [10] S. Bi, M. Liu, J. Shen, X. M. Hu, L. Zhang, Ultrahigh “Self-Sensing Performance of Geopolymer Nanocomposites via Unique Interface Engineering”, *ACS applied materials and interfaces*. 9, pp. 12851–12858, 2017.
- [11] A. S. El-Dieb, M. A. El-Ghareeb, M. A. H. Abdel-Rahman, E. S. A. Nasr, “Multifunctional electrically conductive concrete using different fillers”, *Journal of building engineering*. 15, pp.61–69, 2018.
- [12] S. Wen, D. D. L. Chung, “Partial replacement of carbon fiber by carbon black in multifunctional cement–matrix composites”, *Carbon*. 45, pp. 505–513, 2007.
- [13] H. Dehghanpour, K. Yilmaz, F. Afshari, M. Ipek, “Electrically conductive concrete: A laboratory-based investigation and numerical analysis approach”, *Construction and building materials*. 260 119948, 2020.
- [14] Y. He, L. Lu, S. Jin, S. Hu, “Conductive aggregate prepared using graphite and clay and its use in conductive mortar”, *Construction and building materials*. 53, pp.131–137,2014.
- [15] H. Dehghanpour, F. Doğan, S. Subaşı, M. Maraşlı, “Effects of single-walled carbon nanotubes and steel fiber on recycled ferrochrome filled electrical conductive mortars”, *Journal of sustainable construction materials and technologies*. 2022.
- [16] R. Hai, “Effect of Carbon Fiber Gradient Distribution on Heat Property of Electrically Conductive Cement Mortar”, *Advanced materials research*. 415–417, 1474–1477, 2011.
- [17] J. Vilaplana, F. Baeza, O. Galao, E. Zornoza, P. Garcés, “Self-Sensing Properties of Alkali Activated Blast Furnace Slag (BFS) Composites Reinforced with Carbon Fibers”, *Materials (Basel)*. 6, pp. 4776–4786, 2013.
- [18] M. H. Fasihnikoutalab, A. Asadi, C. Unluer, B.K. Huat, R.J. Ball, S. Pourakbar, “Utilization of Alkali-Activated Olivine in Soil Stabilization and the Effect of Carbonation on Unconfined Compressive Strength and Microstructure”, *Journal of materials in civil engineering*. 29, 2017.
- [19] F. Montserrat, P. Renforth, J. Hartmann, M. Leermakers, P. Knops, F.J.R. Meysman, “Olivine Dissolution in Seawater: Implications for CO₂ Sequestration through Enhanced Weathering in Coastal Environments”, *Environmental science & technology*. 51, pp. 3960–3972, 2017.
- [20] C. Fan, R. Huang, H. Hwang, S. J. Chao, “Properties of concrete incorporating fine recycled aggregates from crushed concrete wastes”, *Construction and building materials*. 112, pp.708–715, 2016.
- [21] I. Papayianni, M. Papachristoforou, V. Patsiou, V. Petrohilou, “Development of

- fire resistant shotcrete with olivine aggregates, Assessment”, Upgrading and refurbishment of infrastructures. 114–115, 2013.
- [22] ASTM C215, “Standard Test Method for Fundamental Transverse”, Longitudinal, and torsional resonant frequencies of concrete specimens, American society for testing and materials, 2019.
- [23] V. M. Malhotra, N. J. Carino, “Nondestructive Testing Of Concrete”, ASTM International, 100 Barr Harbor Drive, West Conshohocken, 2004.
- [24] S. Bedr, N. Mezouar, L. Verrucci, G. Lanzo, “Investigation on shear modulus and damping ratio of Algiers marls under cyclic and dynamic loading conditions”, 2473–2493, 2019.
- [25] ASTM C597, “Standard test method for pulse velocity through concrete”, American society for testing and materials. 2009.
- [26] ASTM A956, “Standard Test Method for Leeb Hardness Testing of Steel Products”, American society for testing and materials. 2006.
- [27] TS EN 196-1, “Methods of testing cement–Part 1: Determination of strength”, Turkish Stand. 2005.
- [28] R. Campos, M. M. M. Larrain, M. Zaman, V. Pozadas, “Relationships between compressive and flexural strengths of concrete based on fresh field properties”, International journal of pavement research and technology. 14, pp 161–167 2021.
- [29] F. Doğan, H. Dehghanpour, S. Subaşı, M. Maraşlı, “Characterization of carbon fiber reinforced conductive mortars filled with recycled ferrochrome slag aggregates”, Journal of sustainable construction materials and technologies. 7, pp. 145–157, 2022.
- [30] J. Wu, J. Liu, F. Yang, “Three-phase composite conductive concrete for pavement deicing”, Construction and building materials. 75, pp. 129–135, 2015.
- [31] J. X. Lin, Y. Song, Z. H. Xie, Y. C. Guo, B. Yuan, J. J. Zeng, X. Wei, Static and dynamic mechanical behavior of engineered cementitious composites with PP and PVA fibers”, Journal of building engineering. 29, 101097, 2020.
- [32] A. Noushini, B. Samali, K. Vessalas, “Effect of polyvinyl alcohol (PVA) fibre on dynamic and material properties of fibre reinforced concrete”, Construction and building materials. 49, pp.374–383, 2013.
- [33] J. Tian, C. Fan, T. Zhang, Y. Zhou, “Rock breaking mechanism in percussive drilling with the effect of high-frequency torsional vibration”, Energy sources, part a: recovery, utilization and environmental effects. 0, 1–15,2019.
- [34] K. G. R. T. Reddy, D. Arul Prakash, “Dynamic analysis on steel fibre concrete beams”, International journal of civil engineering and technology. 7, pp. 179–184, 2016.
- [35] F. Sahin, M. Uysal, O. Canpolat, T. Cosgun, H. Dehghanpour, “The effect of polyvinyl fibers on metakaolin-based geopolymer mortars with different aggregate filling”, Construction and building materials. 300, 124257, 2021.
- [36] A. Kabirova, M. Uysal, M. Hüsem, Y. Aygörmmez, H. Dehghanpour, S. Pul, O. Canpolat, “Physical and mechanical properties of metakaolin-based geopolymer mortars containing various waste powders”, European journal of environmental and civil engineering. 1–20, 2022
- [37] M. Gomez-Heras, D. Benavente, C. Pla, J. Martinez-Martinez, R. Fort, V. Brotons, “Ultrasonic pulse velocity as a way of improving uniaxial compressive strength estimations from Leeb hardness

- measurements”, *Construction and building materials*. 261, 119996, 2020.
- [38] H. Dehghanpour, S. Subasi, S. Guntepe, M. Emiroglu, M. Marasli, “Investigation of fracture mechanics, physical and dynamic properties of UHPCs containing PVA”, glass and steel fibers, *Construction and building materials*. 328, 127079, 2022.
- [39] Y. M. Liew, H. Kamarudin, A. M. Mustafa Al Bakri, M. Luqman, I. Khairul Nizar, C.M. Ruzaidi, C. Y. Heah, “Processing and characterization of calcined kaolin cement powder”, *Construction and building materials*. 30, 794–802, 2012.
- [40] R. P. Jaya, M. I. M. Yusak, M. R. Hainin, N. Mashros, M. N. M. Warid, M. I. Ali, M. H. W. Ibrahim, “Physical and chemical properties of cement with nano black rice husk ash”, *Nanoscience and nanotechnology: nano-SciTech*, p. 020024, 2019.
- [41] A. Behnamfard, K. Chegini, R. Alaei, F. Veglio, “The effect of thermal and acid treatment of kaolin on its ability for cyanide removal from aqueous solutions”, *Environmental earth sciences*. 78, 408, 2019.
- [42] Y. M. Liew, H. Kamarudin, A.M. Mustafa Al Bakri, M. Bnhussain, M. Luqman, I. Khairul Nizar, C. M. Ruzaidi, C. Y. Heah, “Optimization of solids-to-liquid and alkali activator ratios of calcined kaolin geopolymeric powder”, *Construction and building materials*. 37, pp.440–451, 2012.
- [43] O. Mardiana, Haryadi, “Production and Application of Olivine Nano-Silica in Concrete”, *IOP conference series: materials science and engineering*. 204, 012008, 2017.
- [44] F. de Souza Abreu, C. C. Ribeiro, J. D. Da Silva Pinto, T.M. Nsumbu, V.T.L. Buono, “Influence of adding discontinuous and dispersed carbon fiber waste on concrete performance”, *Journal of cleaner production*. 273, 122920, 2020.
- [45] Z. Guo, C. Zhuang, Z. Li, Y. Chen, “Mechanical properties of carbon fiber reinforced concrete (CFRC) after exposure to high temperatures”, *Composite structures*. 256, 113072, 2021.
- [46] M. Safiuddin, M. Yakhlaf, K. A. Soudki, “Key mechanical properties and microstructure of carbon fibre reinforced self-consolidating concrete”, *Construction and building materials*. 164, pp. 477–488, 2018.
- [47] H. Dehghanpour, F. Doğan, K. Yılmaz, “Development of CNT–CF–Al₂O₃-CMC gel-based cementitious repair composite”, *Journal of building engineering*. 45, 103474, 2022.
- [48] M. Chen, P. Gao, F. Geng, L. Zhang, H. Liu, “Mechanical and smart properties of carbon fiber and graphite conductive concrete for internal damage monitoring of structure”, *Construction and building materials*. 142, pp. 320–327, 2017.
- [49] V. R. Ramkumar, G. Murali, N.P. Asrani, K. Karthikeyan, “Development of a novel low carbon cementitious two stage layered fibrous concrete with superior impact strength”, *Journal of building engineering*. 25, 100841, 2019.
- [50] Y. Bai, B. Xie, H. Li, R. Tian, Q. Zhang, “Mechanical properties and electromagnetic absorption characteristics of foam Cement-based absorbing materials”, *Construction and building materials*. 330, 127221, 2022.

An Approach for Modelling Accidental Eccentricity Effects in Symmetrical Frame Buildings Exhibiting Semi-Rigid Diaphragm Behavior

Melih Sürmeli 

Bursa Technical University, Faculty of Engineering and Natural Sciences, Department of Civil Engineering, Bursa, Türkiye, melih.surmeli@btu.edu.tr

ARTICLE INFO

ABSTRACT

Keywords:

Accidental eccentricity
Semi-rigid diaphragm
Flexible diaphragm
Precast building
RC building



Article History:

Received: 28.11.2022
Accepted: 18.03.2024
Online Available: 06.06.2024

The accidental eccentricity effect is specified, in earthquake codes, to account for the possible uncertainties in the mass and stiffness distribution of the structural system and the effect of the torsional component of the earthquake ground motion on the building. Türkiye Building Earthquake Code (TBEC-2018) considers the additional eccentricity effect only for the cases where rigid diaphragm behavior is provided in the slabs. However, in buildings with A2 and A3 irregularities or flexible diaphragms including insufficient strength and stiffness, the in-plane deformations and stresses on diaphragms may change the behavior of buildings under earthquake loads. In this study, a practical approach to be used in the equivalent earthquake load method was proposed to apply the accidental eccentricity effect on symmetrical frame buildings with semi-rigid diaphragms. The approach is based on distributing the total accidental torsion to the nodes as fictitious forces. Two numerical examples were presented. The first is a single-story precast industrial-type RC building, where the calculation steps of the procedure explained in detail. The building was modeled with both semi-rigid and rigid diaphragm assumptions, and a comparison of two modeling assumptions under accidental torsion was presented. Torsional irregularity factors obtained from building modeled by semi-rigid diaphragm assumption provided greater values with respect to those modeled by rigid diaphragm. This shows the significance of considering accidental eccentricity for semi-rigid diaphragms. The second numerical example, which is a RC concrete building, was used to validate the proposed methodology via finite element model (FEM) built-in algorithm. The obtained displacement demands by using the proposed methodology were very close to FEM results as a reference for the real solution. It is concluded from this study that the proposed methodology is reliable and can be used for modeling accidental eccentricity effects on symmetrical-plan buildings with semi-rigid diaphragms.

1. Introduction

In addition to carrying vertical loads, another important task of flooring and roofing systems is to transfer the inertia forces to the foundation safely under horizontal loads. In this context, the degree of flexibility of the diaphragms plays an important role. ASCE 7.16 [1] Chapter 12.3.1 classifies diaphragms as rigid and flexible. If horizontal loads are distributed to vertical elements in proportion to their relative stiffness under earthquake loads and the in-plane deformation of the diaphragm is negligible, the

diaphragm is classified as rigid. Both inherent and accidental torsion should be included in the analysis model in the case of a rigid diaphragm. Therefore, the flexural stiffness of all vertical elements for two orthogonal earthquake directions, and beams' flexural stiffnesses with respect to diaphragm plane should be found in the mathematical model. The greater horizontal stiffness of the rigid diaphragm results in smaller period values than the flexible diaphragm, leading to larger earthquake forces being transferred to vertical elements.

In accordance with ASCE 7.16, flexible diaphragm is defined based on two criteria. The first one is classified as prescriptive criteria, which is not applicable to RC precast buildings directly. The latter criteria, referred as calculated criteria, is expressed such that in-plane deflection under lateral load is more than two times the average story drift of the adjoining vertical elements. Figure 1 illustrates the deflections of flexible diaphragm. Deflection δ_{MDD} is the mid-span deflection of the flexible diaphragm and δ_{ADVE} is the average deflection of vertical elements.

Therefore, the flexible diaphragm condition can be defined as $\delta_{MDD}/\delta_{ADVE} > 2$. The lateral loads are distributed to the supporting vertical elements via the beams reflecting in-plane stiffness of flexible diaphragm. Hence, the distribution of horizontal forces to vertical elements is independent of their relative stiffness. Instead, the inertia forces are proportional to masses corresponding to tributary areas of each vertical element. Therefore, a two-dimensional beam model with supporting vertical elements can be sufficient to analyze the flexible diaphragm under horizontal loads for single-story buildings, and the vertical elements are designed based on the tributary masses assigned. For multi-story buildings, each frame may be modeled independently, with seismic masses assigned to tributary area. Such type of behavior of flexible diaphragms prevents the efficient transmission of torsional forces to vertical elements.

In fact, the diaphragms behave neither rigid nor flexible, the behavior is between two cases, in other words, semi-rigidly. Related to this subject, ASCE 7-16 Section 12.3.1 states that the stiffness of the diaphragm should be included in the model. In certain circumstances such as the buildings having plan irregularities etc., TBDY-2018 necessitates modeling the buildings with both rigid and semi-rigid diaphragms. For the model with a rigid diaphragm, the accidental eccentricity effects are taken into consideration. This modeling assumption is mostly used for the design of vertical elements. While, semi-rigid modeling assumption without considering accidental eccentricity is used to determine design forces for all structural elements, and slabs are designed according to this. The

envelope of the two modeling assumptions then is selected as the final design case. As a more realistic approach, the building may be modeled with semi-rigid diaphragm considering accidental eccentricity effects. Thus, both flexibility of the diaphragm and the flexibility of vertical elements are taken into account including accidental and inherent torsion in the design. In this context, the stiffness of the roof and slab members should be carefully modeled. ASCE 7.16 C12.8.4.2 states that accidental torsional moment can be defined as the summation of nodal moments or forces through the diaphragm.

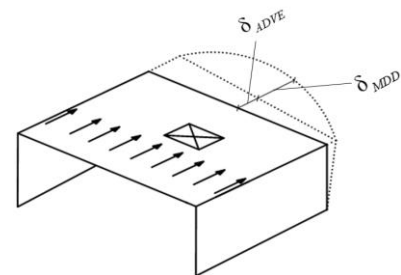


Figure 1. Flexible diaphragm [1]

Several researches about the flexibility of horizontal diaphragms have been conducted in recent years [2-13]. In general, the degree of flexibility of diaphragms have been investigated via nonlinear time history analysis for buildings with rigid perimeter shear walls or vertical trusses. It has been found as a common result that the fundamental periods of the buildings considering flexible diaphragms are greater than those modeled by rigid diaphragms. This can result from a smaller base shear value if one design the building with the rigid diaphragm. The degree of flexibility increases as the depth-to-length ratio of diaphragm increases.

Mortazawi and Humar [2], Humar and Popovski [3] investigated the effects of flexibility on the ductility demand and internal forces in the diaphragm. They concluded that flexibility caused a significant increase in the ductility demand on the lateral load-resisting system, particularly when the diaphragm is designed to remain elastic. Also, a significant increase in bending moment at mid-span and shear force at the quarter span of diaphragm were observed. Sadashiva et al. [4, 5] showed that the diaphragm flexibility mostly affects single-story structures, and reported that an increase in the number of

stories decreases the diaphragm flexibility. Shake table tests were performed by Tremblay et al. [6] to investigate the behavior of low-rise steel buildings with flexible roof diaphragms including metal roof deck diaphragms. Shrestha [7] conducted a study to investigate the flexibility and ductility characteristics of steel deck roof diaphragms and to incorporate this information into the design of single-story steel buildings.

The numerical analysis was performed by Opensees using trusses for metal roof decks. Farrow and Fleischman [8, 9] investigated the expected seismic demands for precast concrete parking structure diaphragms and proposed seismic design guidelines for long-span precast diaphragms. The strength, stiffness, and ductility of the double tee diaphragms for the cases of topped and pre-topped were investigated. Fleischman et al. [10, 11] conducted research projects about precast concrete diaphragms to establish underlying design philosophy and planned analytical/ experimental activities. Ju and Lin [12] analyzed a total of 520 buildings including rectangular, U-shaped and T-shaped buildings with and without shear walls. The buildings were modeled by both rigid-floor and flexible-floor assumptions. They concluded that the rigid diaphragm assumption was sufficient for buildings without shear walls based on response-spectrum analyses. Whereas, they achieved a large difference between rigid-floor and flexible-floor assumptions for the buildings with shear walls.

Tena-Colunga et al. [13] studied a different type of floor systems such as two-way ribbed RC slabs, beam and block, steel decks and waffle RC flat slabs to investigate the potential flexibility of diaphragm by assessing different plan aspect ratios of the buildings and stiffness of floor systems. They concluded that for office buildings, particularly floor spans greater than 10 m, semi-rigid, semi-flexible or flexible behavior can be observed in floor diaphragms based on performed linear finite element analyses. Torsional effects on the buildings under earthquake loads are classified as inherent and accidental torsion. Inherent torsion occurs when center of mass (CM) and center of rigidity (CR) do not coincide. While accidental torsion is indirectly considered in earthquake codes by

shifting the CM with a constant ratio of floor plan dimensions or applying a torsional moment at the CM corresponding to seismic force multiply by accidental eccentricity. The causes of accidental torsion may be explained as i) the difference between the real and design mass distributions, ii. the variations of the center of rigidity because of unpredictable mechanical properties in seismic force-resisting system, iii. Un-symmetrical yielding of the components of seismic force-resisting system, iv. Torsional ground motion [14].

Fahjan et al. [15] and Xuanhua et al. [16] proposed alternative procedures to account for accidental torsion for response spectrum analysis. Akyürek [17] also recommended a design eccentricity formula including frequency ratio (torsional frequency/ translational frequency) and effective rotational radius. Basu et al. [14], Basu and Giri [18] proposed a method to account for accidental eccentricity via torsional ground motion as a product of accidental eccentricity and translational ground motions.

There are very few studies including accidental eccentricity in semi-rigid diaphragms. Fang [19] investigated the seismic behavior of steel structures with semi-rigid diaphragms. In his study, the distribution of diaphragm forces was assumed as triangular.

In this study, a simple procedure was proposed to account for accidental eccentricity for symmetrical plan framed buildings with a semi-rigid diaphragm to be used in equivalent earthquake load method. The total accidental torsion was defined as the summation of the moment created by fictitious nodal forces which were calculated by multiplying nodal mass with the distance between CM of diaphragm and node coordinate. A single story precast concrete building (RC) consisting of cantilever-type columns tied with pinned connections to roof girders was used as the first numerical example to evaluate the proposed method. The roof consists of corrugated sandwich panels with polyurethane foam core. The poor diaphragm behavior of these buildings was widely reported as one of the main causes of damage and partial collapse [20-28]. A truss model proposed by

Yüksel et al [29] was used for in-plane behavior of the roof panels. The roof was also modeled as the rigid diaphragm and the responses under accidental torsion are compared. As a second numerical example, single story RC building was chosen for the verification of proposed procedure.

2. Proposed Procedure

According to Turkish Building Earthquake Code (TBEC 2018) [30], accidental eccentricity to be used in equivalent seismic load method can be considered as an additional torsional moment applied to CM of the floor diaphragms. These torsional moments are shown in Figure 2 as $M_{ii}^{(X)}$ and $M_{ii}^{(Y)}$ for the loading directions X and Y, respectively.

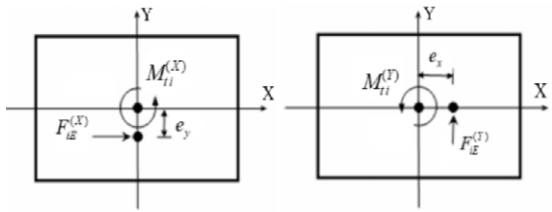


Figure 2. The consideration of accidental eccentricity for equivalent seismic load method

Where, $F_{iE}^{(X)}$ and $F_{iE}^{(Y)}$ are the equivalent seismic loads at i^{th} story for X and Y directions, e_x and e_y are corresponding accidental eccentricities, respectively. Then one can calculate the equivalent torsional moments due to accidental eccentricities as:

$$M_{ii}^{(X)} = F_{iE}^{(X)} e_y \quad M_{ii}^{(Y)} = F_{iE}^{(Y)} e_x \quad (1)$$

Consideration of accidental eccentricity as equivalent torsional moments can be applied only when rigid diaphragm assumption is valid. The proposed procedure herein uses the same total torsional moments $M_{ii}^{(X)}$ and $M_{ii}^{(Y)}$. However, the procedure distributes total moments to the frame nodes as fictitious forces based on their tributary mass and rotational inertia. Therefore, accidental eccentricity for semi-rigid diaphragms could be taken into account.

The moment of inertia of a point mass is calculated as the square of the mass times the perpendicular distance to the rotation axis of the

joint, $I_0 = m r^2$. From this point of view, each nodal mass may oppose to rotational inertia forces mass times the perpendicular distance ($f = m r$). Instead of using distance r , accidental torsional moments on the floors may be considered separately for X and Y directional frames. Eq. 2 is given to define this:

$$m_{ij}^{(X)} = f_{ij}^{(X)} Y_j \quad m_{ij}^{(Y)} = f_{ij}^{(Y)} X_j \quad (2)$$

Where, $m_{ij}^{(X)}$ and $m_{ij}^{(Y)}$ are the torsional moments calculated by multiplying fictitious nodal forces $f_{ij}^{(X)}$ and $f_{ij}^{(Y)}$ with Y_j and X_j joint coordinates with respect to CM, respectively. These fictitious forces are calculated in the following equations:

$$f_{ij}^{(X)} = \beta^{(X)} m_j Y_j \quad f_{ij}^{(Y)} = \beta^{(Y)} m_j X_j \quad (3)$$

Where, m_j is j^{th} node mass, $\beta^{(X)}$ and $\beta^{(Y)}$ are factors calculated from total accidental torsional moments $M_{ii}^{(X)}$ and $M_{ii}^{(Y)}$. The factors are calculated as follows:

$$M_{ii}^{(X)} = \sum_{j=1}^N m_{ij}^{(X)} = \sum_{j=1}^N f_{ij}^{(X)} Y_j = \sum_{j=1}^N \beta^{(X)} m_j Y_j^2 \quad (4)$$

$$\beta^{(X)} = \frac{M_{ii}^{(X)}}{\sum_{j=1}^N m_j Y_j^2}$$

$$M_{ii}^{(Y)} = \sum_{j=1}^N m_{ij}^{(Y)} = \sum_{j=1}^N f_{ij}^{(Y)} X_j = \sum_{j=1}^N \beta^{(Y)} m_j X_j^2 \quad (5)$$

$$\beta^{(Y)} = \frac{M_{ii}^{(Y)}}{\sum_{j=1}^N m_j X_j^2}$$

The idealization of a total accidental moment for Y directional seismic load in terms of fictitious nodal forces is shown in Figure 3.

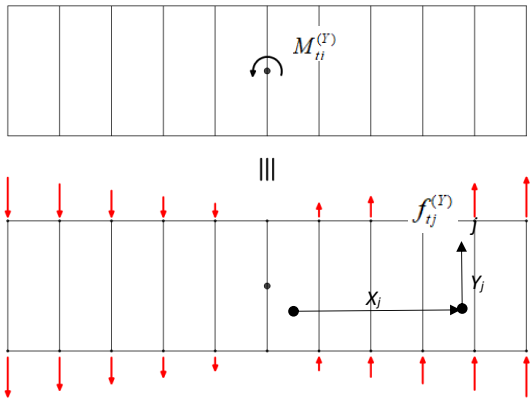


Figure 3. Idealization of torsional moment due to accidental eccentricity

3. Numerical Examples

Single-story precast RC building and single-story RC building were chosen as numerical examples. The step-by-step application of the proposed procedure was presented in the precast example. The RC building example was utilized in order to validate the proposed procedure with SAP2000 program.

3.1. Single-story precast industrial building

A single-story precast industrial building was used to implement the proposed methodology. The front elevation and roof plan are shown in Figure 4 and Figure 5, respectively. The seismic load-resisting system of the building consists of cantilever type columns tied with pinned connections to roof girders. The building plan dimensions are 20×80 m consisting of 1 bay with 20 m length in the X direction and ten bay with 8 m length in the Y direction. The clear length of the columns is 8 m.

The purlins were located at 1.93 m intervals on non-prismatic roof girders. Both of the connections of the roof girder to columns, gutter beams to columns and purlins to roof girders were pinned. The cross-sectional dimensions of the roof girder, purlin, gutter beam, column and RC panel are illustrated in Figure 6. The four sides of the building were covered by RC concrete panels whose connections to the gutter beam are roller and to the ground fixed. Therefore, the panels did not transfer their weight to the structure. However, half of their seismic mass assumed was found at the roof level.

The finite element model (FEM) of the building was created by SAP2000 [31] program and the perspective view is shown in Figure 7. All of the structural members were modeled as frame members. The connections of gutter beams and purlins to roof girders and roof girders to column's gussets were defined as pinned. The roof was covered by corrugated sandwich panels with polyurethane foam core. Truss members were used to model in-plane behavior of the roof panels [29].

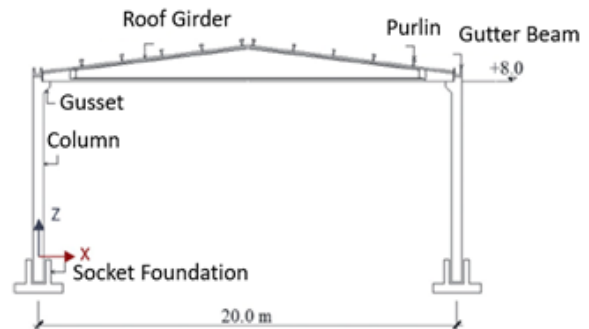


Figure 4. The elevation view of the precast building

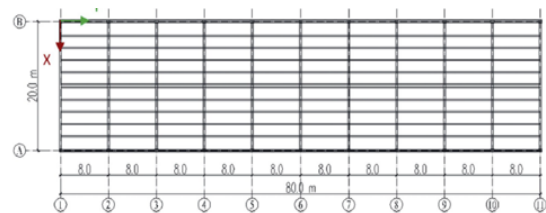


Figure 5. The plan of the precast building

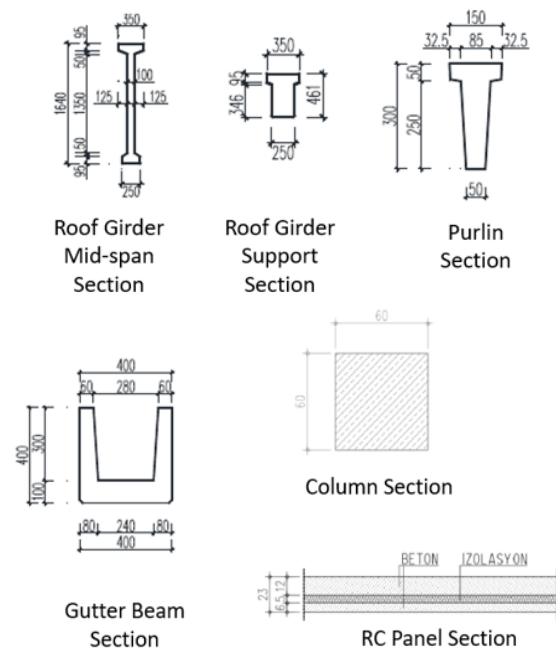


Figure 6. The cross-sectional dimensions of structural elements

3.1.1. Definition of roof diaphragm

The effective stiffness of the truss members was calculated from the following equation [29]:

$$k_{0.01} = \frac{(EA)_e}{L_p} = \frac{\alpha \times \gamma \times (\pi \times D) \times (t_1 + t_2) \times f_y \times n}{0.02 \times L} \quad (6)$$

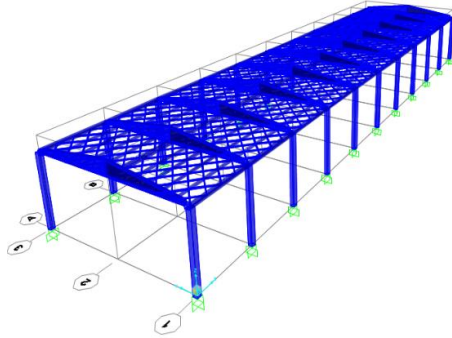


Figure 7. Perspective view of numerical example

Where, L_p is the length of the truss member, α is the effective area of fasteners and is neglected in this study and taken α value of 1, γ is direction factor (safety factor to account for loading direction and experimental uncertainties, the recommended value is 0.67), D is diameter of fasteners, t_1 and t_2 are bottom and top sheet thicknesses, f_y is the yield strength of the sheets, n is number of fasteners per meter, and L is span length of the sandwich panel (the distance between purlins).

The truss members were arranged at 2 m intervals in the Y direction. From geometry, L_p is equal to 2.779 m and corresponding truss angle (θ) was then calculated as 46.02° . The fastener parameters are $D=4$ mm, $t_1 = t_2=0.4$ mm, $n =5.5$ and $f_y =255$ MPa. The parameter γ was taken as 0.67. From the above equation, effective stiffness of truss member is calculated as $(EA)_e =765225$ MPa. Also, the design capacity of the panels is given by:

$$F_{\max} = 0.02 \times (EA)_e \times \cos \theta = 10.6 \text{ kN} \quad (7)$$

3.1.2. Loads and joint masses

The loads applied to building are as follows:

- i) *Facade* : 4.50kN/m²
(only involved in mass calculation)
- ii) *Roof covering* : 0.12 kN/m²

- iii) *Snow loading* : 0.75 kN/m²
- iv) *Purlin* : 4.88 kN
(one piece of 8m)
- v) *Gutter Beam* : 16.40 kN
(one piece of 8m)
- vi) *Roof Beam* : 83.00 kN
(one piece of 19.4 m)

In accordance with TBEC-2018, the masses were calculated from the seismic weight combination of $w_j = w_{G,j} + 0.3w_{S,j}$. Where, w_j is j^{th} node seismic weight, $w_{G,j}$ and $w_{S,j}$ are the dead and snow load participation, respectively. Seismic mass for j^{th} node then calculated as $m_j = w_j / g$. The nodal masses were determined as 29.45 kNs²/m and 26.01 kNs²/m at inner and outer nodes, respectively. The total mass of the building was calculated as 634.14 kNs²/m.

3.1.3. Modal analysis

Modal analysis was performed and mode shapes and modal participation mass ratios were calculated. Modal participation mass ratios are listed in Table 1 and the first three vibrational mode shapes are shown in Figure 8-10.

Table 1. Modal participation mass ratios

Mod No	Period (sec)	U _X	U _Y	θ_z
1	0.892	0.000	0.941	0.000
2	0.891	0.997	0.000	0.000
3	0.877	0.000	0.000	0.882

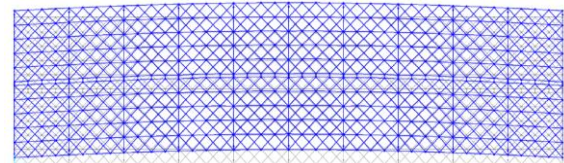


Figure 8. First mode shape, dominant mode in Y direction

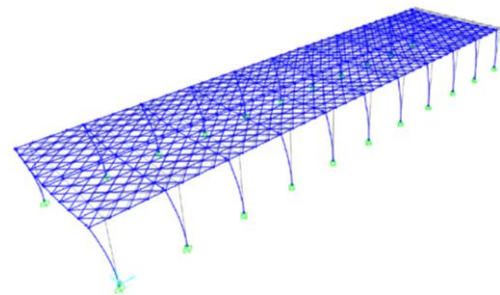


Figure 9. Second mode shape, dominant mode in X direction

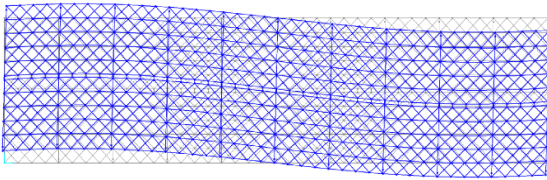


Figure 10. Third Mode Shape, dominant mode in torsional direction

3.1.4. Implementation of equivalent earthquake load method

The building is assumed to be located at latitude 40.871923 and longitude 29.38123 on Z3 local site class. Based on coordinates and soil class, in accordance with TBEC-2018, short period map spectral acceleration coefficient is $S_S=1.082$, map spectral acceleration coefficient for 1.0 sec is $S_1=0.302$ and corresponding design acceleration coefficients are $S_{DS}=1.298$ and $S_{D1}=0.453$. The elastic design acceleration spectrum then is drawn in Figure 11.

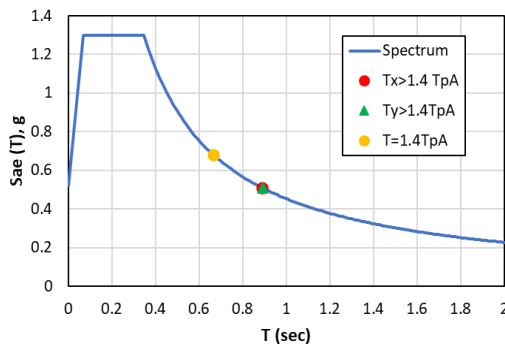


Figure 11. Elastic acceleration design spectrum

Empirical dominant natural vibration period was calculated by following Eq. 8:

$$T_{pA} = C_t H_N^{3/4} = 0.1 \times 8^{3/4} = 0.476 \text{ sec} \quad (8)$$

TBEC-2018 does not allow a natural period value greater than $1.4T_{pA} = 0.666 \text{ sec}$. Therefore, equivalent seismic forces should be determined using the empirical period value. The spectral acceleration corresponding to X, Y directional dominant periods together with $1.4T_{pA}$ is also depicted in Figure 11.

The building is classified as single-story building in which seismic loads are fully resisted by columns with hinged upper connections and corresponding seismic behavior factor $R=3.0$ and

overstrength factor $D=2.0$. As an industrial building, the importance factor was taken as 1.0. Earthquake load reduction factor (R_a) was calculated by the following formula for $T > T_B$:

$$R_a = \frac{R}{I} = \frac{3}{1} = 3 \quad (9)$$

Total seismic base shear was determined from Eq. 10:

$$V_{tE}^{(X)} = m_t S_{ar} (T_p^{(X)}) \geq 0.04 m_t I S_{DS} g \quad (10)$$

Where, $S_{ar} (T_p^{(X)})$ is reduced design spectral acceleration in terms of g and calculated as:

$$S_{ar} (T_p^{(X)}) = \frac{S_{ae} (T_p^{(X)})}{R_a (T_p^{(X)})} \quad (11)$$

Since, semi-rigid diaphragm is assigned to roof plane, equivalent seismic force should be distributed through diaphragm. Herein, the forces were distributed to column top nodes. As a single-story building, the base shear is equal to total of equivalent seismic force. The distribution of equivalent seismic forces to joints were calculated by Eq. 12:

$$f_{jE}^{(X)} = \frac{f_{tE}^{(X)}}{m_i} m_j \quad f_{jE}^{(Y)} = \frac{f_{tE}^{(Y)}}{m_i} m_j \quad (12)$$

The base shear and the equivalent earthquake load for inner and outer nodes are given in Table 2.

Table 2. Base shears and equivalent nodal earthquake forces

$V_{tE}^{(X)} = V_{tE}^{(Y)}$ (kN)	$V_{tE_{min}}^{(X)} = V_{tE_{min}}^{(Y)}$ (kN)	$f_{jE}^{(X)} = f_{jE}^{(Y)}$ (kN)	
		Inner Nodes	Outer Nodes
1410.5	323.1	65.5	57.9

The implementation of equivalent earthquake loads for X and Y directions are shown in Figure 12 and Figure 13, respectively.

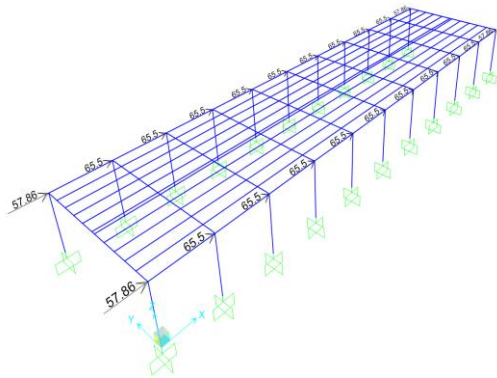


Figure 12. Implementation of equivalent seismic forces for X direction

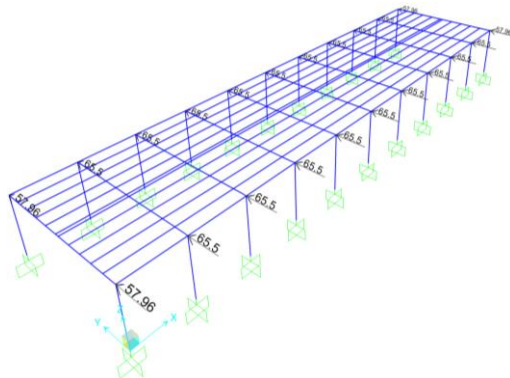


Figure 13. Implementation of equivalent seismic forces for Y direction

3.1.5. Assessment of flexible diaphragm condition

In order to assess the flexible diaphragm condition, the building is opposed to Y directional equivalent seismic forces. The deflected shape including the displacements values at mid-span and corner is shown in Figure 14.

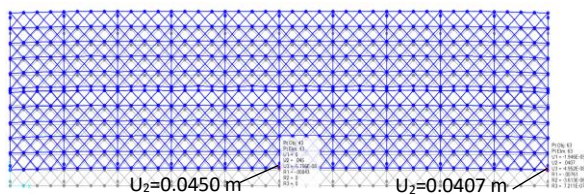


Figure 14. Deflected shape under Y Direction Equivalent Seismic Forces

Since the ratio $\delta_{MDD} / \delta_{ADVE} = 0.045 / 0.0407 = 1.106 < 2$ the roof can be classified as semi-rigid diaphragm.

3.1.6. Implementation of accidental torsion in terms of fictitious forces

In accordance with TBEC-2018, the accidental eccentricities were taken as 5% of the plan

dimensions. The total accidental torsional moments were calculated from Eq. 1 as $M_{ii}^{(X)} = 1410.5$ kNm and $M_{ii}^{(Y)} = 5642.0$ kNm. These moments were distributed to nodes as equivalent fictitious forces $f_{ij}^{(X)}$ and $f_{ij}^{(Y)}$. The calculation of the parameters $\beta^{(X)}$ and $\beta^{(Y)}$ using the equations 4 and 5 and corresponding fictitious forces determined from Eq. 3. are listed in Table 3 and Table 4. Implementation of fictitious forces to numerical model for X and Y directions are illustrated in Figure 15 and Figure 16, respectively.

Table 3. Calculation of fictitious forces to account for accidental eccentricity in the X direction

Joint No	m_j	Y_j	$\beta^{(X)} m_j Y_j^2$	$f_{ij}^{(X)}$
(j)	(kNs ² /m)	(m)	(kNs ² m)	(kN)
1	26.01	-10	2601.3	5.79
2	29.45	-10	2944.8	6.55
3	29.45	-10	2944.8	6.55
4	29.45	-10	2944.8	6.55
5	29.45	-10	2944.8	6.55
6	29.45	-10	2944.8	6.55
7	29.45	-10	2944.8	6.55
8	29.45	-10	2944.8	6.55
9	29.45	-10	2944.8	6.55
10	29.45	-10	2944.8	6.55
11	26.01	-10	2601.3	5.79
12	26.01	10	2601.3	-5.79
13	29.45	10	2944.8	-6.55
14	29.45	10	2944.8	-6.55
15	29.45	10	2944.8	-6.55
16	29.45	10	2944.8	-6.55
17	29.45	10	2944.8	-6.55
18	29.45	10	2944.8	-6.55
19	29.45	10	2944.8	-6.55
20	29.45	10	2944.8	-6.55
21	29.45	10	2944.8	-6.55
22	26.01	10	2601.3	-5.79
$\Sigma =$			63412.2	
$\beta^{(X)} =$			0.022243	

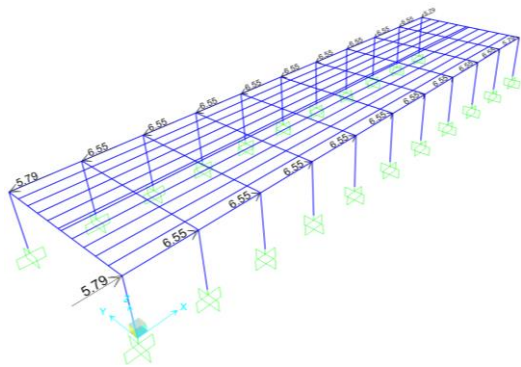


Figure 15. Implementation of accidental torsion in terms of fictitious forces in the X direction

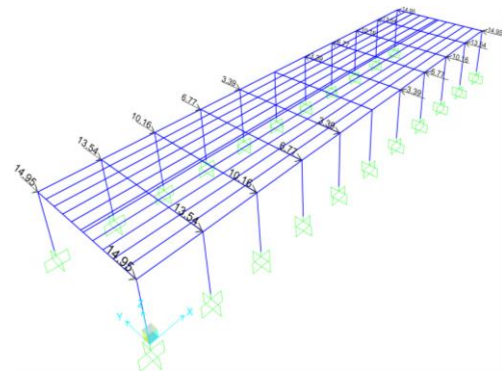


Figure 16. Implementation of accidental torsion in terms of fictitious forces in the Y direction

Table 4. Calculation of fictitious forces to account for accidental eccentricity in the Y direction

Joint No	m_j	X_j	$\beta^{(Y)}m_jX_j^2$	$f_{i_j}^{(Y)}$
(j)	(kNs ² /m)	(m)	(kNs ² m)	(kN)
1	26.01	-40	41620.3	-14.95
2	29.45	-32	30155.2	-13.54
3	29.45	-24	16962.3	-10.16
4	29.45	-16	7538.8	-6.77
5	29.45	-8	1884.7	-3.39
6	29.45	0	0.0	0.00
7	29.45	8	1884.7	3.39
8	29.45	16	7538.8	6.77
9	29.45	24	16962.3	10.16
10	29.45	32	30155.2	13.54
11	26.01	40	41620.3	14.95
12	26.01	-40	41620.3	-14.95
13	29.45	-32	30155.2	-13.54
14	29.45	-24	16962.3	-10.16
15	29.45	-16	7538.8	-6.77
16	29.45	-8	1884.7	-3.39
17	29.45	0	0.0	0.00
18	29.45	8	1884.7	3.39
19	29.45	16	7538.8	6.77
20	29.45	24	16962.3	10.16
21	29.45	32	30155.2	13.54
22	26.01	40	41620.3	14.95
$\Sigma=$			392645.0	
$\beta^{(Y)}=$			0.014369	

3.1.7. Deformed shapes under combined forces

Equivalent earthquake forces and fictitious forces due to accidental torsion are combined as depicted for two cases: i. Positive X directional forces and counter-clockwise torsional direction ii. Positive Y directional forces and counter-clockwise torsional direction. These loading are shown in Figure 17.

Under combined forces +EXP and +EYP, the deformed shapes are drawn in Figures 18 and 19, respectively.

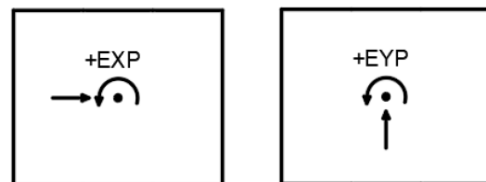


Figure 17. Combination of equivalent earthquake forces with accidental torsion

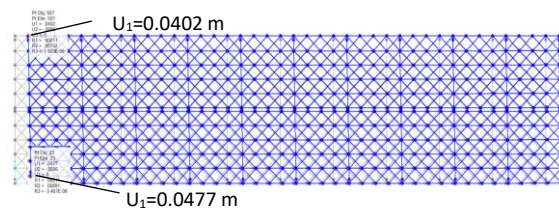


Figure 18. The deformed shape under loading +EXP (semi-rigid diaphragm)

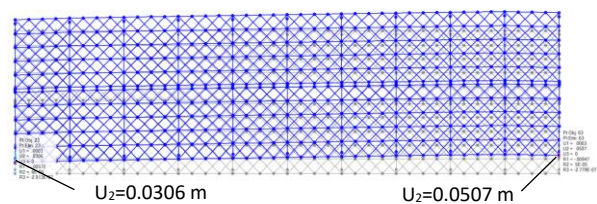


Figure 19. The deformed shape under loading +EYP (semi-rigid diaphragm)

3.1.8. Modeling of the building with rigid diaphragm

The structure was also modeled with rigid diaphragm (Figure 20). Equivalent seismic forces and accidental moments were applied to the master joint located on CM of diaphragm for X and Y directions. Since the connections of the columns to the main girder and gutter beams are pinned, the free vibration periods are the same as the building modeling by a semi-rigid diaphragm. Hence, the loads applied are the same for both models. The deflected shapes under +EXP and +EYP loading are shown in Figure 21 and Figure 22, respectively.

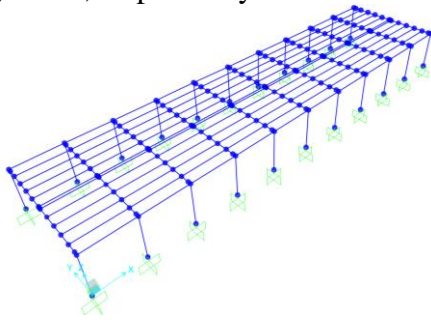


Figure 20. The numerical model with rigid diaphragm

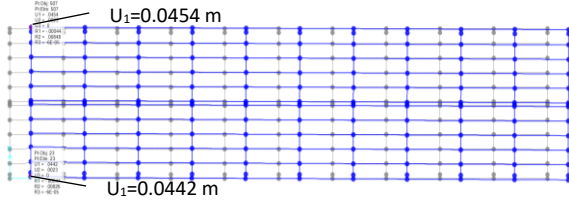


Figure 21. Deformed Shape under loading +EXP (rigid diaphragm assumption)

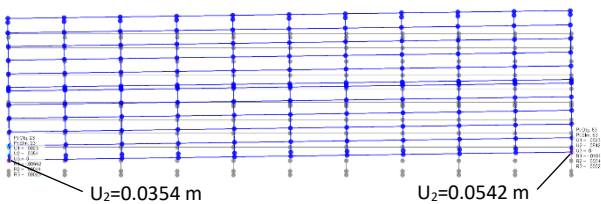


Figure 22. Deformed Shape under loading +EYP (rigid diaphragm assumption)

3.1.9. Comparison of rigid and semi-rigid diaphragm assumptions in terms of displacements

The maximum and minimum reduced drifts (Δ_{\max}) and (Δ_{\min}) were calculated for the two types of diaphragm modeling approaches and given in Table 4 and Table 5. In addition, the torsional irregularity coefficients (η_{bi}) for rigid

and semi rigid diaphragm cases can be found in Table 5 and Table 6 for X and Y direction, respectively. According to TBEC-2018, η_{bi} is calculated from the following equation.

$$\eta_{bi} = \frac{\Delta_{i\max}}{\Delta_{iave}} \quad \Delta_{iave} = \frac{\Delta_{i\max} + \Delta_{i\min}}{2} \quad (11)$$

Table 5. Comparison of the displacements obtained from rigid and semi-rigid diaphragm modeling approaches for X direction

Diaphragm Type	X Direction		
	Δ_{\max} (m)	Δ_{\min} (m)	η_{bi}
Semi-rigid	0.0477	0.0402	1.085
Rigid	0.0454	0.0442	1.013

Table 6. Comparison of the displacements obtained from rigid and semi-rigid diaphragm modeling approaches for Y direction

Diaphragm Type	Y Direction		
	Δ_{\max} (m)	Δ_{\min} (m)	η_{bi}
Semi-rigid	0.0507	0.0306	1.247
Rigid	0.0542	0.0354	1.210

3.2. Single story reinforced concrete building

3.2.1. The geometry of the building

Second numerical example is single story RC building (Figure 23). The bay widths in X direction were equally spaced as 8 m and the bay width in Y direction was 10m. The column cross-sectional dimensions were selected as 50×150 cm and 50×50 cm at the corner and inner columns, respectively to increase the diaphragm flexibility of the building. Also, the slabs were divided into 1.0m x 1.0m meshes to account for mass distribution. The cross-sectional dimension of beam was 30×60 cm. The building height was 8 m and the slab thickness was 25 cm. Column, beam and slab weights were automatically calculated by the program. Effective rigidity values were assigned for columns, beams and slabs' cross sections in accordance with TBEC-2018.

3.2.2. The loads, seismic masses, earthquake design parameters

Covering and live loads were taken as 2 kN/m² and 5 kN/m², respectively. The same spectral parameters with numerical example 1 were used in equivalent earthquake load method. The definitions in TBDY-2018, total mass and base shear values for Y direction are listed in Table 7. Since the diaphragm flexibility effects are significant for Y direction, the analysis results are only be discussed for Y direction. Semi-rigid diaphragm was assigned to the nodes at 8 m level. Mass values were calculated automatically for each joint based on their tributary areas in FEM. The program converts the seismic weight calculated from g+nq loading to joint masses. Then equivalent seismic story forces were contributed to the joints proportional to their masses.

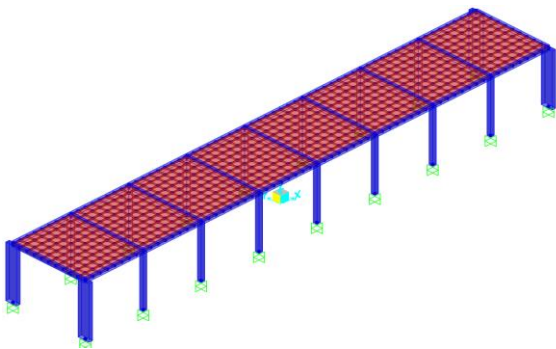


Figure 23. Perspective view of RC Building

Table 7. Parameters to be used in the equivalent seismic load method

Parameter	Value
Building Importance Factor (I)	1
Building Occupancy Class (BKS)	3
Earthquake Design Class (DTS)	1
Building Height Class (BYS)	7
Building Behavior Factor (R)	8
Overstrength Factor (D)	3.0
Total Seismic Mass (m_t)	772.8 kNs ² /m
Vibration period in Y direction	0.662 sn
Base Shear Force in Y Direction	647.05 kN

3.2.3. Assessment of flexible diaphragm condition

The equivalent seismic force method without accidental eccentricity was implemented to the building in Y direction to check for flexible

diaphragm condition (Figure 24). The mid-span and corner displacements are depicted in a deformed shape in Figure 24. Since $\delta_{MDD}/\delta_{ADVE}=0.0105/0.0067=1.567$ was between 1 and 2, diaphragm can be classified as semi-rigid.

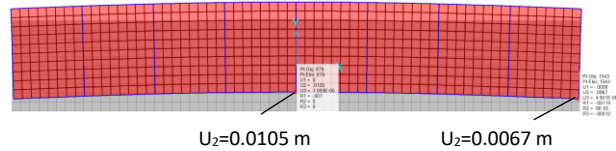


Figure 24. Deflected Shape under Y Direction Equivalent Seismic Forces

3.2.4. Verification of proposed methodology

The accidental eccentricity effects were evaluated using two different ways in order to verify the proposed methodology. The first way was to use automated algorithm in FEM which automatically distributes accidental eccentricity effects to nodes. The second way was using the proposed methodology. As applied in Example 1, the total accidental torsion was contributed to nodal fictive forces proportional to joint masses and coordinates. Figure 25 depicts the implementation of the proposed procedure for Y direction and the deflected shape for +EYP loading is shown in Figure 26.

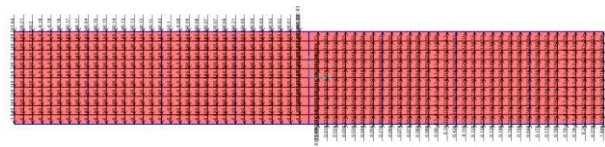


Figure 25. Implementation of accidental torsion in terms of fictitious forces in Y direction

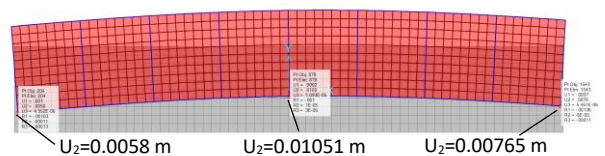


Figure 26. The deformed shape under loading +EYP (semi-rigid diaphragm)

The calculated reduced drift values obtained from FEM automated procedure and proposed methodology are listed in Table 8. The left and right corner displacements are Δ_{min} and Δ_{max} are given together with Δ_{MDD} . As it is seen, the results are very close to each other.

Table 8. Comparison of the displacements obtained from proposed and FEM automated procedures for Y direction

Procedure for accidental eccentricity	Y Direction		
	Δ_{\max} (m)	Δ_{MDD} (m)	Δ_{\min} (m)
Automated procedure built in FEM	0.00763	0.01051	0.00581
Proposed	0.00765	0.01051	0.00580

4. Conclusions

A simple numerical procedure was proposed to account for the accidental eccentricity effects on the symmetrical frame-type buildings having semi-rigid diaphragms. Two numerical examples, which are single-story RC precast building and single-story RC building, were implemented for the proposed procedure.

Single Story RC Precast Building

The building was modeled with semi-rigid and rigid diaphragm assumptions to investigate the behavior difference between the buildings. The following conclusions can be drawn from this case:

- 1) The maximum reduced displacement demands obtained from the building with semi-rigid diaphragm were 5.07% greater and 6.55% smaller than those obtained with rigid diaphragm assumptions, for X and Y directions, respectively.
- 2) Greater torsional irregularity factors were obtained of 7.11% and 3.06% from building with semi-rigid diaphragm for X and Y directions, respectively.
- 3) This shows the significance of considering accidental eccentricity effects on semi-rigid diaphragms to safely design the buildings.

Single-Story RC Building

Single-story RC building was chosen to verify the proposed procedure with FEM built-in algorithm. The building was modeled by semi-rigid diaphragm in the software. The proposed

and automated procedures were compared in terms of displacements obtained. The results were well correlated.

It is concluded from this study that the proposed methodology is reliable and can be used for modeling accidental eccentricity effects on symmetrical-plan buildings with semi-rigid diaphragms.

Article Information Form

Acknowledgments

The author would like to thank Prof. Dr. Ercan Yüksel for his contributions to the paper.

Funding

The author has not received any financial support for the research, authorship, or publication of this study.

The Declaration of Conflict of Interest/ Common Interest

No conflict of interest or common interest has been declared by the author.

The Declaration of Ethics Committee Approval

This study does not require ethics committee permission or any special permission.

The Declaration of Research and Publication Ethics

The author of the paper declares that they comply with the scientific, ethical and quotation rules of SAUJS in all processes of the paper and that they do not make any falsification on the data collected. In addition, they declare that Sakarya University Journal of Science and its editorial board have no responsibility for any ethical violations that may be encountered, and that this study has not been evaluated in any academic publication environment other than Sakarya University Journal of Science.

Copyright Statement

Authors own the copyright of their work published in the journal and their work is published under the CC BY-NC 4.0 license.

References

- [1] ASCE-7, "Minimum design loads for buildings and other structures. ASCE standard ASCE/SEI 7-16," American Society of Civil Engineering, ISBN 0-7844-7996-4, 2016.
- [2] P. Mortazavi, J. Humar, "Consideration of diaphragm flexibility in the seismic design of one-story buildings," *Engineering Structures*, vol. 127, pp. 748-758, 2016.
- [3] J. Humar, M. Popovski, "Seismic response of single-storey buildings with flexible diaphragm," *Canadian Journal of Civil Engineering*, vol. 40, pp. 875-886, 2013.
- [4] V. K. Sadashiva, G. A. MacRae, B. L. Deam, "A Mechanics Based Approach to Quantify Diaphragm Flexibility Effects," *Proceedings of the Ninth Pacific Conference on Earthquake Engineering Building an Earthquake-Resilient Society*, Auckland, New Zealand, 2011, pp. 114-121.
- [5] V. K. Sadashiva, G. A. MacRae, B. L. Deam, M. S. Spooner, "Quantifying the seismic response of structures with flexible diaphragms," *Earthquake Engineering and Structural Dynamics*, vol. 41, pp. 1365-1389, 2012.
- [6] R. Tremblay, T. Berair, A. Filiatrault, "Experimental Behaviour of Low-Rise Steel Buildings with Flexible Roof Diaphragms," *12th World Conference on Earthquake Engineering*, Auckland, New Zealand, 2000, pp. 2567-2575.
- [7] K. M. Shrestha, "Use of flexible and ductile roof diaphragms in the seismic design of single-storey steel buildings," *Doctor of Philosophy McGill University*, 2011.
- [8] K. T. Farrow, R. B. Fleischman, "Effect of Dimension and Detail on the Capacity of Precast Concrete Parking Structure Diaphragms," *PCI Journal*, vol. 48, no.5, pp. 46-61, 2003.
- [9] R. B. Fleischman, K. T. Farrow, "Seismic Design Recommendations for Precast Concrete Diaphragms in Long Floor Span Construction," *PCI Journal*, vol. 48, no.6, pp. 46-62, 2003.
- [10] R. B. Fleischman, C. J. Naito, J. Restrepo, R. Sause, S. K. Ghosh, "Seismic Design Methodology for Precast Concrete Diaphragms Part 1: Design Framework," *PCI Journal*, vol. 50, no.5, pp. 68-83, 2005.
- [11] R. B. Fleischman, S. K. Ghosh, C. J. Naito, G. Wan, J. Restrepo, M. Schoettler, R. Sause, L. Cao, "Seismic Design Methodology for Precast Concrete Diaphragms Part 2: Design Framework," *PCI Journal*, vol. 50, no. 6, pp. 14-31, 2005.
- [12] S. H. Ju, M.C. Lin, "Comparison of Building Analyses Assuming Rigid or Flexible Floors," *Journal of Structural Engineering*, vol. 125, no. 1, pp. 25-31, 1999.
- [13] A. Tena-Colunga, K. L. Chinchilla-Portillo, G. Juarez-Luna "Assessment of the diaphragm condition for floor systems used in urban buildings," *Engineering Structures*, vol. 93, pp. 70-84, 2015.
- [14] D. Basu, M. C. Constantinou, A. S. Whittaker, "An equivalent accidental eccentricity to account for the effects of torsional ground motion on structures," *Engineering Structures*, vol. 69, pp. 1-11, 2014.
- [15] Y. M. Fahjan, C. Tüzün, J. Kubin, "An Alternative Procedure for Accidental Eccentricity in Dynamic Modal Analyses of Buildings," *First European Conference on Earthquake Engineering and Seismology*, Genewa, Switzerland, 2006, pp. 1166-1174.
- [16] F. Xuanhua, Y. Jiacong, S. Shuli, C. Pu, "An alternative approach for computing seismic response with accidental eccentricity," *Earthquake Engineering and Engineering Vibration*, vol. 13, pp. 401-410, 2014.

- [17] O. Akyürek, "Tasarım eksatrikliği için alternatif bir öneri," *Journal of Polytechnic*, vol. 26, no. 2, pp. 609-623, 2023.
- [18] D. Basu, S. Giri, "Accidental eccentricity in multistory buildings due to torsional ground motion," *Bulletin of Earthquake Engineering*, vol. 13, pp. 3779-3808, 2015.
- [19] C. Fang, "The Seismic Behavior of Steel Structures with Semi-Rigid Diaphragms," Doctor of Philosophy Virginia Polytechnic Institute and State University, 2015.
- [20] Ş. Özden, H. Erdoğan, E. Akpınar, H. M. Atalay, "Performance of precast concrete structures in October 2011 Van earthquake, Türkiye," *Magazine of Concrete Research*, vol. 66, no. 11, pp. 543-552, 2014.
- [21] M. Fishinger, B. Zoubek, T. Isakovic, "Seismic Response of Precast Industrial Buildings," *Perspectives on European Earthquake Engineering and Seismology*, vol. 1, pp. 131-177, 2015.
- [22] A. Belleri, E. Brunesi, R. Nascimbene, M. Pagani, P. Riva, "Seismic Performance of Precast Industrial Facilities Following Major Earthquakes in the Italian Territory," *Journal of Performance of Constructed Facilities*, vol. 29, no. 5, pp. 1-10, 2014.
- [23] M. Saatçioğlu, D. Mitchell, R. Tinawi, N. J. Gardner, "The August 17, 1999, Kocaeli (Türkiye) earthquake - Damage to structures," *Canadian journal of Civil Engineering*, vol. 28, pp. 715-737, 2001.
- [24] M. H. Arslan, H. H. Korkmaz, F. G. Gülay, "Damage and failure pattern of prefabricated structures after major earthquakes in Türkiye and shortfalls of the Turkish Earthquake code," *Engineering Failure Analysis*, vol. 13, pp. 537-557, 2006.
- [25] J. K. Iverson, N. M. Hawkins, "Performance of precast/prestressed concrete building structures during the Northridge earthquake," *PCI Journal*, vol. 39, no. 2, pp.38-55, 1994.
- [26] J. K. Ghosh, N. Cleland, "Observations from the February 27, 2010, earthquake in Chile," *PCI Reconnaissance Team Report*, *PCI Journal*, vol. 57, no.1 pp. 52-75, 2012.
- [27] S. L. Wood, "Seismic rehabilitation of low-rise precast industrial buildings in Türkiye," In *Advances in Earthquake Engineering for Urban Risk Reduction*, Springer, Dordrecht, Netherlands, NATO science series IV, vol. 66, *Earth and Environmental Sciences*, 2003, pp. 167-177.
- [28] G. Toniolo, A. Colombo, "Precast concrete structures: the lessons learned from the L'Aquila earthquake," *Structural Concrete*, vol. 13, pp. 73-83, 2012.
- [29] E. Yüksel, A. Güllü, H. Özkaynak, C. Soydan, A. Khajehdehi, E. Şenol, A. M. Saghayesh, H. Saruhan, "Experimental investigation and pseudoelastic truss model for in-plane behavior of corrugated sandwich panels with polyurethane foam core," *Structures*, vol. 29, pp. 823-842, 2021.
- [30] TBEC-2018, "Turkish Building Earthquake Code," Turkish Disaster and Emergency Management Presidency, Türkiye- Lagal Gazette No:30364, Ankara, 2018.
- [31] CSI SAP2000 v22.2.0, "Integrated Software for Structural Analysis and Design," Computers and Structures Inc., Berkeley, California, 2020.

Investigation of Usability of Sepiolite as a Pozzolan in Production of High Performance Cementitious Composites

Rasim Cem Saka^{1*}, Serkan Subaşı²

¹Dokuz Eylül University, Faculty of Engineering, Department of Civil Engineering, İzmir, Türkiye, rasimcem.saka@deu.edu.tr

²Düzce University, Faculty of Engineering, Department of Civil Engineering, Düzce, Türkiye, serkansubasi@duzce.edu.tr

*Corresponding Author

ARTICLE INFO

ABSTRACT

Keywords:
Sepiolite
Pozzolanic activity
Calcination
Strength



Article History:
Received: 08.02.2023
Accepted: 09.02.2024
Online Available: 06.06.2024

The continuous growth of population and urbanization in the world significantly increases the demand for cement. In terms of sustainability, the cement industry needs to develop new and effective pozzolans with the appropriate recycling of alternative raw materials. It is also important to evaluate sepiolite, which has very limited resources in the world compared to other industrial minerals and whose economic deposits are limited to Spain and Türkiye. In this study, the usability of sepiolite as a pozzolan in cement and its effects on physical, mechanical and durability properties were investigated. First of all, the chemical and physical properties of sepiolite in Eskisehir region were investigated. Crude and ground sepiolite calcined at 500 °C, 700 °C and 900°C were substituted for CEM I 42.5 R class standard Portland cement at 5-10-15% and 20% ratios. The pozzolanic activities of produced sepiolite substituted cement were determined according to ASTM C-311. As a result, crude sepiolite retains more water than calcined sepiolite, thus negatively affecting the strength properties of the concrete. Additionally, sepiolite is considered suspicious (harmful-harmless) in terms of alkali silica reactivity except 10%-15%-20% crude sepiolite substitutions. Overall, It has been observed that sepiolite does not have sufficient pozzolanic properties in cementitious composites.

1. Introduction

The most important component of concrete production is undoubtedly cement. As a result of the high demand for concrete in the construction sector, the cement industry performs the most intensive production worldwide. Due to such intensive production, cement is among industrial productions that harm the environment. In recent years, the need for energy efficiency has prompted researchers to produce sustainable solutions within the cement industry [1]. The cement industry is faced with making more durable and sustainable production using less energy without sacrificing the mechanical

properties of the material to be produced. For this reason, blended cement production has been one of the most common developments compared to normal cement production [2]. Additives such as blast furnace slag, fly ash, silica fume and natural pozzolans are used in the production of blended cement because of having economic and technical advantages [3, 4]. Pozzolans reduce the participation rate of clinker to the cement, thus improving the economy of cement and some of its properties according to needs. In addition, pozzolan-added cements also make cement more environmentally friendly material [5-7].

Sepiolite is a clay mineral in the sepiolite-palygorskite group consisting of magnesium hydrosilicate. Sepiolite with fibrous structure is formed by the alignment of octahedral and tetrahedral oxide layers. In addition, there are channel spaces along the fiber [8]. According to Nagy-Bradley, the chemical formula of sepiolite clay is $\text{Si}_{12}\text{Mg}_9\text{O}_{30}\text{OH}_6(\text{OH}_2)_4 \cdot 6\text{H}_2\text{O}$ [9]. Sepiolite has a temperature sensitive structure. Zeolitic and adsorbed water molecules are lost as the temperature increases. In addition, when interacting with acids, its crystal structure may be partially destroyed. Temperature and acid effects make sepiolite changes its porosity and surface properties. Thus, it is possible to change the colloidal, catalytic and absorptive properties of their most important features. Spain produces almost all of the world's sedimentary sepiolite production. The highest quality meerschaum in the world is provided from the provinces of Eskisehir and Konya.

Kavas et al. added 3-5-10-15-20% and 30% sepiolite in addition to 5% gypsum to Portland cement clinker and tried to improve the properties of the mixture. Expansion tests, initial and final sets, bending and compressive strength tests were performed on the produced mixtures, and it was investigated at what rate the sepiolite substituted for cement improved these properties. As a result of the study, it was observed that 10% sepiolite substitution in concrete improved the mechanical properties of the mixtures and did not cause any negative effects on other properties [10].

In another study they carried out, the structural properties of cementitious mixtures containing sepiolite and the optimum mixing ratios were examined. Addition of 10% sepiolite improved the physical and mechanical properties of the mortar. Compared to the Portland cement mixture, the compressive strength values on the 2nd, 7th and 28th days, respectively, were found as 3.5-6.2% and 7.7% higher, and the flexural strength values were 12.7%-5.7% and 6.3% higher, respectively. According to SEM images, it was seen that the reason for this improvement was the formation of a network structure between the sepiolite fibrous structure and the cement matrix [11].

Fuente et al. demonstrated that it is possible to produce corrugated roofing from fiber concrete containing sepiolite [12, 13]. Andrejkovičová et al. prepared lime-based mortars with 10, 20% and 30% metakaolin and 5% fine sepiolite additives in order to facilitate the preparation of repair mortar in low humidity conditions. Mechanical properties and dynamic elastic modulus were examined after 28, 90 and 180 days of curing. It has been observed that as the amount of metakaolin increases in lime mortars, the mechanical strength after 90 days increases. The addition of sepiolite to blended air lime/air lime-metacaolin mixtures led to an improvement in compressive and bending strengths, especially in later wet curing, due to its microfibrillar morphology and adsorption properties. 5 wt% fine sepiolite and 20 wt% metakaolin appear to be an optimal mixture for air lime mortars. [14].

Martinez-Ramirez et al. studied the carbonation properties of lime mixture containing sepiolite and found that It was observed the mechanical properties of less than 5% sepiolite substituted mixtures did not change and the carbonation process in lime mortars slowed down due to the water absorption feature of sepiolite [15]. In the study carried out on physical and mechanical properties of sepiolite-substituted cementitious mortars, mortars were formed by substituting 0-10-20% and 30% Eskisehir region sepiolite by weight instead of CEM I 42.5R cement. The mechanical and physical properties of the produced sepiolite added mortars on the 7th, 28th and 56th days were examined. As a result, it was recommended that the sepiolite additive ratio should not exceed 10% of the cement. It has been stated that the use of sepiolite at higher rates is suitable only in the applications of non-bearing walls and leveling concretes [16].

With the widespread use of aerated concrete, which is one of the wall materials, researches have gained importance. For this purpose, Savaş et al. studied the effect of sepiolite clay replacement on the compressive strength and thermal properties of quartzite, which is used as the main raw material in the production of aerated concrete material [17]. In the study, it is planned to produce G2-04 class gas concrete, which is used as wall building material. Aerated concrete was produced by substituting 5-10-15-

20-25% of sepiolite obtained from Eskisehir Sivrihisar region instead of quartzite. After curing the samples at 60 °C for 4 hours, they were autoclaved at 180 °C under 11 bar pressure for 6,5 hours. Compressive strength and thermal conductivity values of the produced samples were determined. As a result, by increasing the sepiolite substitution ratio, the compressive strength values of the samples decreased, while an improvement in heat conduction was observed [17].

Pozzolans are silica and alumina materials that have little or no binding property on their own, but when finely grinded, they combine with CH in aqueous environments and gain binding property. Studies on sepiolite were also carried out to determine the pozzolanic activity properties. In a study, sepiolite was calcined at 370-570 and 830 °C, and the properties of cementitious mortars containing calcined and crude sepiolite were investigated by compressive strength and rheology tests after reaction at 40 °C for 2-7-28 and 91 days. As a result, it was seen that sepiolite is a very inactive pozzolanic material and its water requirement is high. From 370 °C to 570 °C, calcination does not increase significantly. It was observed that the most effective calcination temperature was 830 °C, which increased the compressive strength of the mortar by 84% compared to the compressive strength of the reference Portland cement (PC) mortar [18].

Pu et al. investigated the compressive-flexural strength and microstructure of metakaolin - fly ash geopolymer activated with sodium hydroxide and sodium silicate solutions containing 0-5-10-15-20% sepiolite by mass. While an increase was observed in the compressive strength values of the mixtures made by adding 10% sepiolite at the end of 7 days, a decrease was observed in the strength values due to the increase in sepiolite addition. Similarly, with the addition of sepiolite up to 10%, the curing-independent flexural strength was improved. Crack formations were observed in the sample with 20% sepiolite compared to samples containing 10% sepiolite [19].

In order to determine the effects of air entrainment on the pores of hardened mortars, the rheological properties of the cement mixture

foamed with air entrained aluminum powder were examined. As a result, it was observed that fly ash in Portland cement combined with metakaolin and sepiolite caused the highest expansion rate [20].

In addition to the studies on the effect of sepiolite in cementitious mixtures, it was wondered how it behaves with binders in polymer structure, and the effect of polyurethane and polyvinylalcohol addition on the rheological properties of sepiolite mixtures was investigated in a study. The results showed that the polymer molecules bind to the surface of the sepiolite and stabilize the viscosity properties at certain densities. In addition, it was observed that polyurethane polymer covers the sepiolite surface faster than polyvinylalcohol, but polyvinylalcohol coating has a smoother structure [21]. When the literature is examined, it is thought that sepiolites are suitable for use in the production of cementitious materials both as a filling material and because of their pozzolanic character.

In this study, the usability of ground sepiolite from Eskisehir region in cementitious mixtures was investigated. In this context, the pozzolanic activity characteristic of the sepiolite material was determined and the hydration properties of the mixtures produced by sepiolite substitution were revealed. The effect of sepiolite substitution on cement paste and mortar mixtures was investigated.

2. General Methods

2.1. Materials

2.1.1. Cement

In the study, CEM I 42.5 R standard Portland cement produced in accordance with TS EN 197-1 standard and supplied from Bolu Cement Factory was used. The physical and chemical analysis values of cement are given in Table 1.

Table 1. Physical and chemical analysis values of cement.

Components (%)	CEMI 42.5R	TS EN 197-1	
CaO	63.03		
Al ₂ O ₃	4.77	C+S≥50%	
SiO ₂	29.12	-	
Fe ₂ O ₃	4.37	-	
SO ₃	2.99	Lim .≤5%	
MgO	2.35	Lim .≤4%	
Na ₂ O	0.29	-	
Cl-	0.0141	-	
K ₂ O	0.49	Lim .≤0.10%	
LOI	1.30	Lim .≤5%	
Insoluble Residue	0.46	Lim .≤5%	
Physical Properties		TS EN 197-1	
Set (Min.)	Initial	125	min. 60
	Final	202	-
Density (g/cm ³)		3.17	-
		435	-
Blaine Fineness (cm ² /g)		9	-
Total Volume expansion (mm)		1.5	max . 10
% 45 µm sieve		2,5	-
Compressive Strength (N/mm ²)	2 days	27.5	min. 20
	7 days	45.7	-
	28 Days	56.8	max . 62.5 min. 42.5

2.1.2. Sepiolite

Sepiolite clay used in the study was obtained from Eskisehir region and was used in mixtures by calcining at 500°C, 700°C and 900°C temperatures as well as being used as crude. Sepiolite which was crude and calcined at 900°C, was substituted for the cement at the rates of 0%, 5%, 10%, 15% and 20%. The values of the chemical analysis results of the sepiolite are presented in Table 2.

Table 2. Chemical analysis values of crude sepiolite

Chemical Content Values of Crude Sepiolite (%)			
MgO	23.1	Fe ₂ O ₃	0.23
Al ₂ O ₃	0.45	Cr ₂ O ₃	0.001
SiO ₂	26.34	Na ₂ O	0.07
SO ₃	0.05	Mn ₂ O ₃	0.0023
K ₂ O	0.20	TiO ₂	0.05
CaO	14.59	other	35.75

2.1.3. CEN standard sand

CEN standard sand produced in different countries according to TS EN 196-1 is used to determine the strength value of cement [22]. The grain size distribution of natural silica sand with

a silicon dioxide content of at least 98% and preferably spherical grains should comply with Table 3.

Table 3. Grain size distribution of CEN sand

Sieve opening (mm)	% Remaining in cumulative sieve
2.00	0
1.60	7
1.00	33
0.50	67
0.16	87
0.08	99

In the study, CEN standard sand in form of 1350±5 g bags in accordance with TS EN 196-1 was used in the mortar mixture.

2.1.4. Water

In the study, Düzce Municipality drinking water was used as mixing water in production of the samples.

2.2. Method

2.2.1. Experiments on powder samples

2.2.1.1. Density

Experiment was carried out with Micromeritics Accupyc II 1340 branded gas pycnometer. The device is a fully automatic gas pycnometer system that measures according to the gas displacement principle. It is also called helium pycnometer in the literature. Density measurements of crude sepiolite and samples that were calcined for 3 hours at three different temperatures (500°C, 700°C, 900°C) were measured at least 5 times.

2.2.1.2. Laser particle size analysis

Grain size measurement is one of measurements needed in many industries and engineering fields such as sand, clay, ceramics, cement, food, cosmetics, paint and soil mechanics. Although there are different methods to determine the grain size, the basic principle of the laser diffraction method is based on the inverse relationship between the grain sizes and the refraction angles of the rays. In this method, laser beams are sent on the particles, and the rays that are refracted by hitting the particles and

reflected in the forward direction pass through a lens and fall on the detector. The rays coming on the detector are converted into grain size and dispersion percentage values with the help of computer.

In the study, calcination process was applied at 500 °C, 700 °C, 900 °C and laser grain size analysis of crude powder sepiolite samples was performed with Malvern Mastersizer 3000 branded device.

2.2.1.3. Thermal analysis

Thermogravimetry is used to determine the mass loss or increase in material as a function of time or temperature. The test sample is heated at a constant rate and the mass change is measured depending on the temperature. In general, the reactions that cause the mass of test samples to change; Oxidation reactions occur as decomposition or evaporation of a component.

A graph of mass versus time or temperature is called the TG curve. The change in the mass of the material due to temperature and the range of this change are an indicator of the thermal stability of the material. In this study, the thermal analysis experiment of crude sepiolite was carried out at Düzce University - Scientific and Technological Research Application and Research Center.

2.2.1.4. Chemical analysis

X-Ray Fluorescence Analysis (XRF) is performed to determine the chemical properties of a material. In this analysis, it is possible to determine the elements in the material and the oxide percentages of these elements.

In this study, chemical analyzes on crude, powdered sepiolite samples calcined at 500 °C, 700 °C and 900 °C were analyzed by Çimsa A.Ş.

2.2.1.5. FT-IR analysis

This analysis is used to determine the functional groups in the structure of the molecule. When infrared light interacts with the material, the chemical bonds are stretched, bent, and compressed. As a result, the functional groups in

the structure absorb IR light of a certain wavelength independently from the rest. Fourier transform infrared device named spectroscopy can be abbreviated as FT-IR. Analyzes of sepiolite were carried out with the Shimadzu IRPrestige 21 branded device in Düzce University - Scientific and Technological Research Application and Research Center.

2.2.1.6. Calcination

The process of heating a material below its melting point in order to remove volatile substances such as moisture and carbon dioxide is called calcination. It is one of the most common operations to make the ore useful after the grinding process. Lime and cement are also obtained by calcining some materials.

In this study, crude sepiolite was calcined in a Ref -San branded muffle furnace at 500°C, 700°C and 900°C temperatures for 3 hours.

2.2.1.7. SEM and EDS analysis

SEM images of the microstructures of the crude and calcined sepiolite samples at 900 °C were obtained with the FEI QuantaFeg 250 branded varying pressure device at Düzce University, Scientific and Technological Research Application and Research Center. EDS analyzes were performed using EDAX Apollo X branded device.

2.2.2. Experiments on paste samples

2.2.2.1. Consistency test

In this experiment, 5%, 10%, 15% and 20% calcined and crude sepiolite were substituted for the cement at 900°C, and the consistency test was carried out in accordance with TS EN 196-3 [23].

2.2.2.2. SEM and EDS analysis

In the experiment, a total of 9 paste samples were taken from 0%, 5%, 10%, 15%, 20% crude and calcined sepiolite substituted paste samples at 900°C, which were removed from the water cure after 28 days. SEM images of the samples were obtained with FEI QuantaFeg 250 brand

variable pressure device at Düzce University - Scientific and Technological Research Application and Research Center. EDS analyzes were performed using EDAX Apollo X branded device.

2.2.3. Experiments on mortar samples

2.2.3.1. Flow test

In the test performed according to the TS EN 459-2 standard, the flow diameter values of calcined and crude sepiolite substituted mortar samples at 0%, 5%, 10%, 15% and 20% were measured. The average of the measurements made with an accuracy of 1 mm was taken [24].

2.2.3.2. Alkali-silica reactivity by accelerated test method

According to ASTM C-1260-01 standard, the experiment was carried out by pouring mortar mixtures containing 0%, 5%, 10%, 15% and 20% substituted crude and calcined sepiolite into 2.5x2.5x28.5 cm molds [25]. After 24 hours, the samples removed from the molds were kept in distilled water at 80 °C for one day and reference measurements were taken. The size changes at the end of the 3rd, 7th and 14th days were measured in the solution prepared by using NaOH 40g in pellet form with 99% purity for 1 liter of distilled water.

2.2.3.3. Compressive strength test

Compressive strength test was carried out in accordance with TS EN 196-1 standard. The water ratios were determined so that the mixtures replaced with 5%, 10%, 15% and 20% crude and calcined sepiolite had the same flow diameter as the 0% reference mixture. Total of 12 samples with 50x50x50 mm dimensions were prepared to be tested on the 7th, 28th, 56th and 90th days. In the experiment, a cement pressure test device with a loading capacity of 30 tons and variable loading speed was used, and the compressive strengths of the mortar samples were calculated according to Equation 1.

$$f_c = \frac{P_{max}}{A_c} \text{ (MPa)} \quad (1)$$

Here;

A_c : Cross-sectional area of the sample (mm²)

f_c : Compressive strength (MPa)

P_{max} : The highest load reached at the time of fracture (N)

2.2.3.4. Pozzolanic activity test

Pozzolanic activity is defined as the extent to which materials with pozzolanic properties can react with hydrated lime and water, and gain binding.

In order for pozzolanic materials to show sufficient activity, they must be amorphous and fine-grained, contain sufficient silica, alumina and iron oxide. The pozzolanic activity is found by calculating the value called “strength activity index” according to the ASTM C-311 standard. The calculation of the index is given in Equation 2 [26].

$$\text{Strength activity index} = \left(\frac{A}{B}\right) * 100 \quad (2)$$

Here;

A= compressive strength of mortar samples containing pozzolan,

B= compressive strength of the control mortar samples without pozzolan.

3. Results and Discussion

3.1. Experiments on powder samples

3.1.1. Density

AccuPyc II 1340 fully automatic gas pycnometer measuring according to the gas displacement principle are given in Table 4.

Table 4. Densities of sepiolite samples calcined at different temperatures

Sample Name	Density (g/cm ³)
Crude Sepiolite	2.5319
Calcined at 500°C sepiolite	2.7044
Calcined at 700°C sepiolite	2.9603
Calcined at 900°C sepiolite	3.2546

When the table is examined, an increase in the density value was observed depending on the increase in calcination temperature. It was

observed that the density of the crude sepiolite was the lowest, while the sepiolite calcined at 900°C had the highest density value. After the calcining process, the density value of the sample increased by 29% at 900°C.

3.1.2. Laser particle size analysis results

Laser particle size analysis was performed on calcined and crude sepiolite samples. The results are given in Figure 1 comparatively.

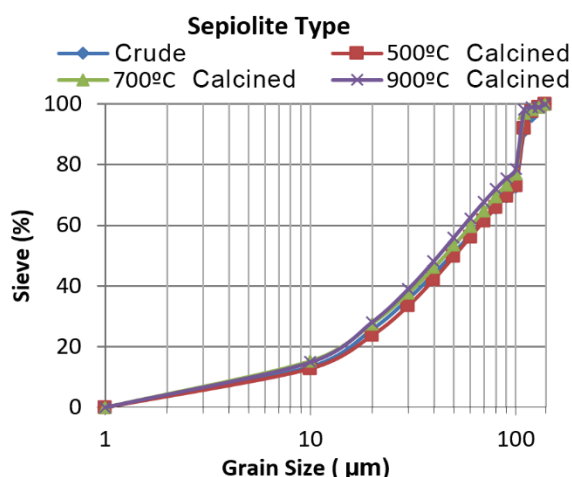


Figure 1. Laser particle size analysis results

The graph shows that the grain size distribution of the crude sepiolite is close to the sepiolite materials calcined at different temperatures. It was observed that the highest grain size of calcined and crude sepiolite was 130 micron meters. As a result, although the largest grain diameter of the sepiolite material decreased due to the increase in the calcined temperature during calcination, no significant difference was observed compared to the crude sepiolite sample.

3.1.3. Thermal analysis results

The thermal analysis values performed on the crude sepiolite sample are given in Figure 2.

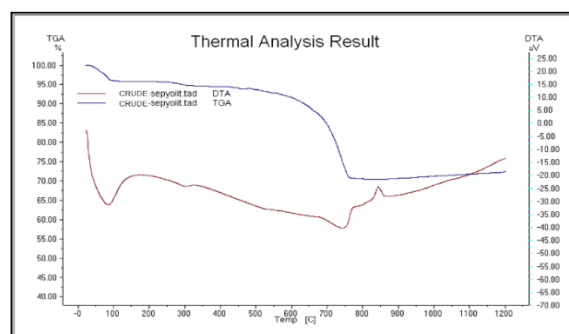


Figure 2. Thermal analysis results of crude sepiolite

While clear endothermic peaks were observed at 100 and 750°C temperatures from DTA curves, exothermic peaks were observed at 860°C. When the mass losses at different temperatures from the TG curve are examined, the dehydration of the chemical and physical water content between 0-200°C temperatures was in the order of 5%. Significant peaks showing the decarbonation of the carbonate phase were observed between 700-770°C. The mass loss in this section was determined to be around 15%. The total weight loss of sepiolite was 30% in the temperature range of 0-1200°C.

3.1.4. Chemical analysis results

The results of the chemical analysis are given in Table 5.

Table 5. Chemical analysis results of calcined sepiolites applied at different temperatures

Chemical Comp.	Sepiolite Type			
	Crude S.	Calcined S. at 500°C.	Calcined S. at 700°C.	Calcined S. at 900°C.
SiO ₂	26.34	29.01	42.07	40
Al ₂ O ₃	0.45	0.45	0.74	0.67
Fe ₂ O ₃	0.23	0.27	0.35	0.36
CaO	14.59	16.68	18.96	22.68
MgO	23.06	26.26	31.34	35.35
SO ₃	0.05	0.06	0.07	0.08
TiO ₂	0.05	0.05	0.07	0.07
Cr ₂ O ₃	0.001	0.001	0.0018	0.0017
Mn ₂ O ₃	0.0023	0.0026	0.0044	0.0045
other	35.75	27.3	6.6	0.5
Loss of Glow	36.9	31.1	4.31	1.40

When the chemical analysis values of the samples at different temperature values are examined, it is seen that all values increase with the increase in temperature, and the glow loss value of the crude sepiolite sample is 36.9%.

3.1.5. FTIR analysis results

FTIR analysis test with crude sepiolite is shown in Figure 3.

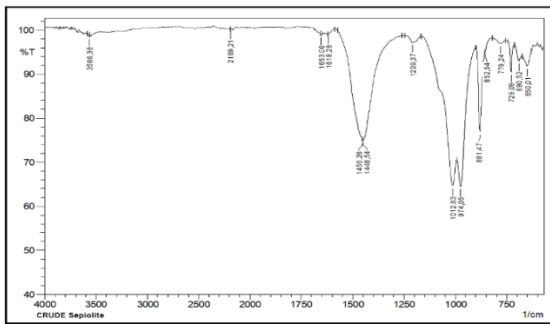


Figure 3. FTIR analysis graph of crude sepiolite

As a result of the FTIR analysis of the crude sepiolite material, open vibrations are observed at wave numbers of 650, 690, 729, 779, 881, 974, 1012, 1209, 1448, 1456, 1618, 1653 and 3566 cm^{-1} . Wave numbers of 729, 881, 1448 and 1456 cm^{-1} indicate the presence of dolomite in the structure. Si-O bonds in the lattice structure are seen as asymmetric and symmetrical vibrations at wave numbers of 650, 690, 974, 1012 and 1209 cm^{-1} . The water ions and molecules in its structure are in the form of OH stretching vibrations at wave numbers of 3566 cm^{-1} and H-O-H bending vibrations at wavenumbers of 1618 and 1653 cm^{-1} .

3.1.6. SEM and EDS analysis results

In the study, SEM images obtained from the samples are given in Figure 4 and EDS analysis values are given in Figure 5.

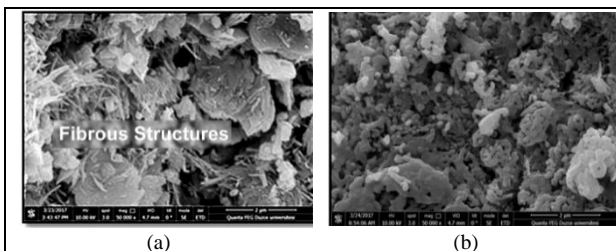


Figure 4. SEM analysis images a) Crude sepiolite
b) Sepiolite calcined at 900 °C

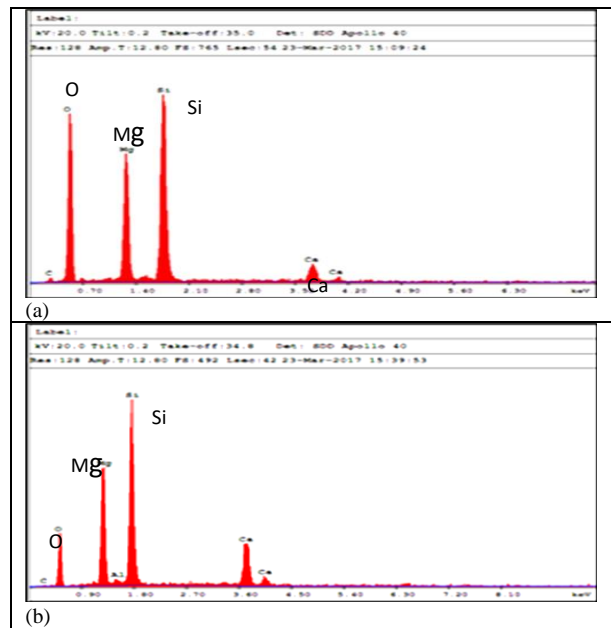


Figure 5. EDS analysis values a) Crude sepiolite b) Sepiolite calcined at 900°C

Fibrous structures of the crude sepiolite sample are seen. It is understood that the structure of the fiber structures changed after the calcination process and took an oval shape.

When the EDS results are examined, it is seen that the oxygen contained in the crude sepiolite is largely removed from the system after calcination process.

3.2. Experiments on paste samples

3.2.1. Consistency test results

The water requirement of paste mixtures containing different amounts of calcined and crude sepiolite was determined with the vicat instrument. The graph of the change in the W/B ratio depending on the amount of sepiolite is given in Figure 6, and the relationship between these values is given in Figure 7.

According to the results, it is seen that the water absorption value of the crude sepiolite is higher than the calcined sepiolite material, and the water demand increases with the increase of sepiolite content in the paste mixture. Compared to the control sample, the water requirement increased by 59% with the 20% crude sepiolite substitution, while the 20% calcined sepiolite substitution increased the water requirement of the mixture by 28%. From this, it is concluded

that the crude sepiolite material absorbs more water than the calcined sepiolite.

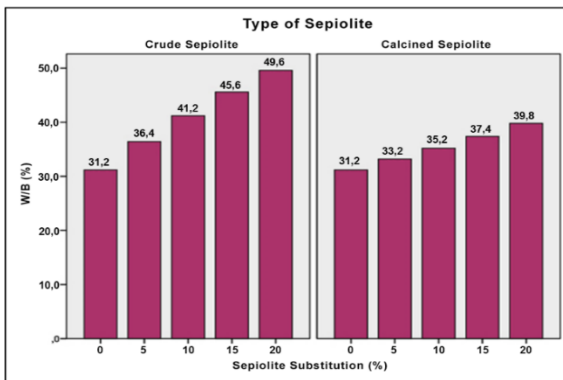


Figure 6. Graph of W/B ratios depending on the amount of sepiolite

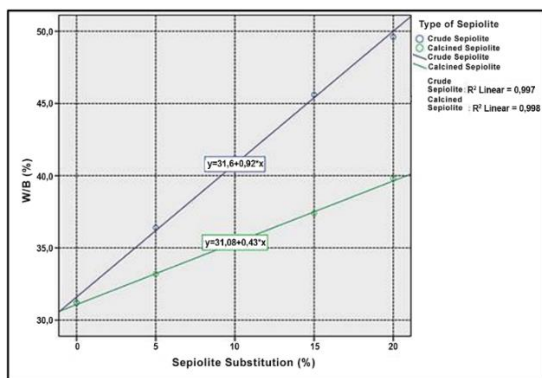


Figure 7. Graph of the relationship between sepiolite substitution rates and W/B value

3.2.2. SEM and EDS analysis results

CSH is a hydration product that gives strength to cement. As a result of the examinations carried out with the electron microscope, information about the structure of C-S-H can be obtained. These structures can generally be in two different states as fibrous and thin plates. With the increase of CSH products over time, boards and fibers develop and get into each other and increase the strength values of cement [27, 28]. In the study,

SEM and EDS analyzes of 0% control, 20% crude and 20% calcined substituted samples are given in Figure 8, Figure 9 and Figure 10.

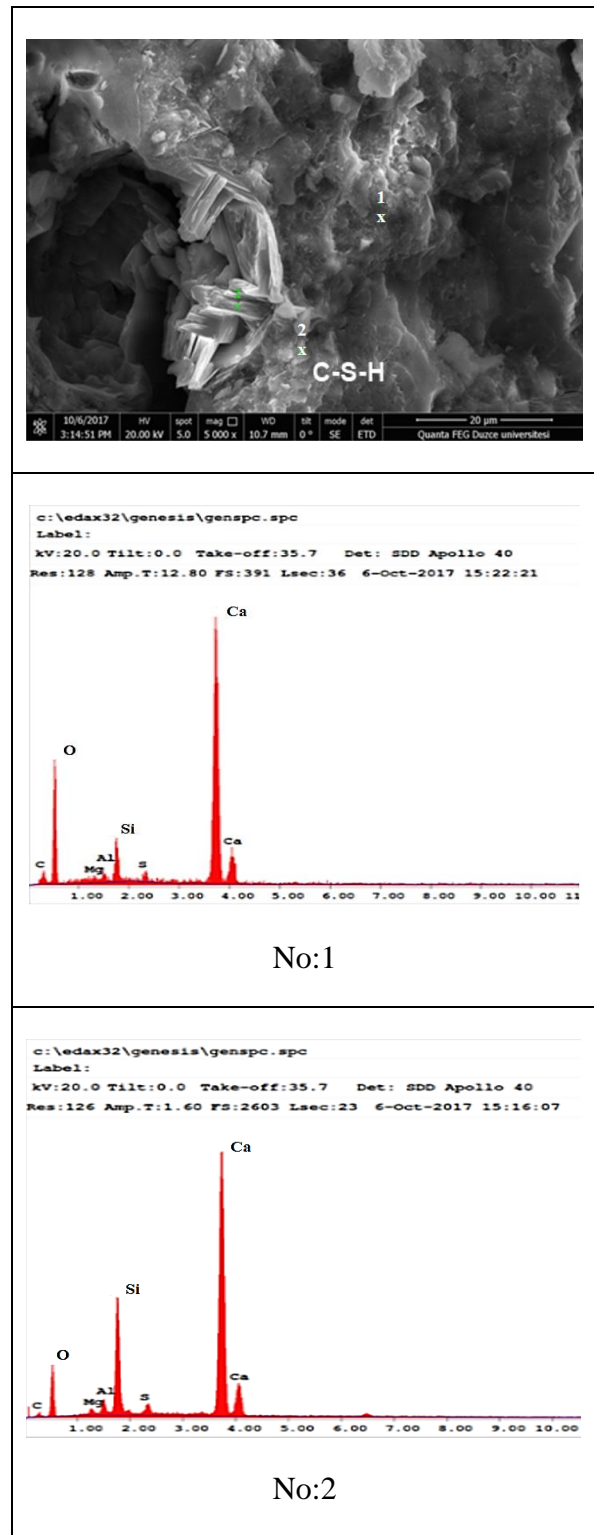


Figure 8. EDS analysis and SEM image of the control sample with 0% substitution

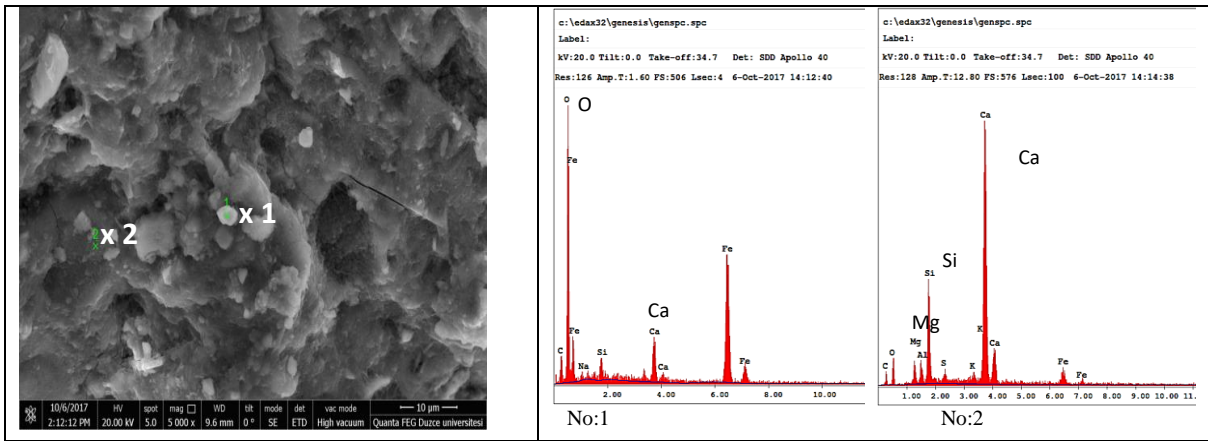


Figure 9. EDS analysis and SEM image of 20% crude sepiolite substituted sample

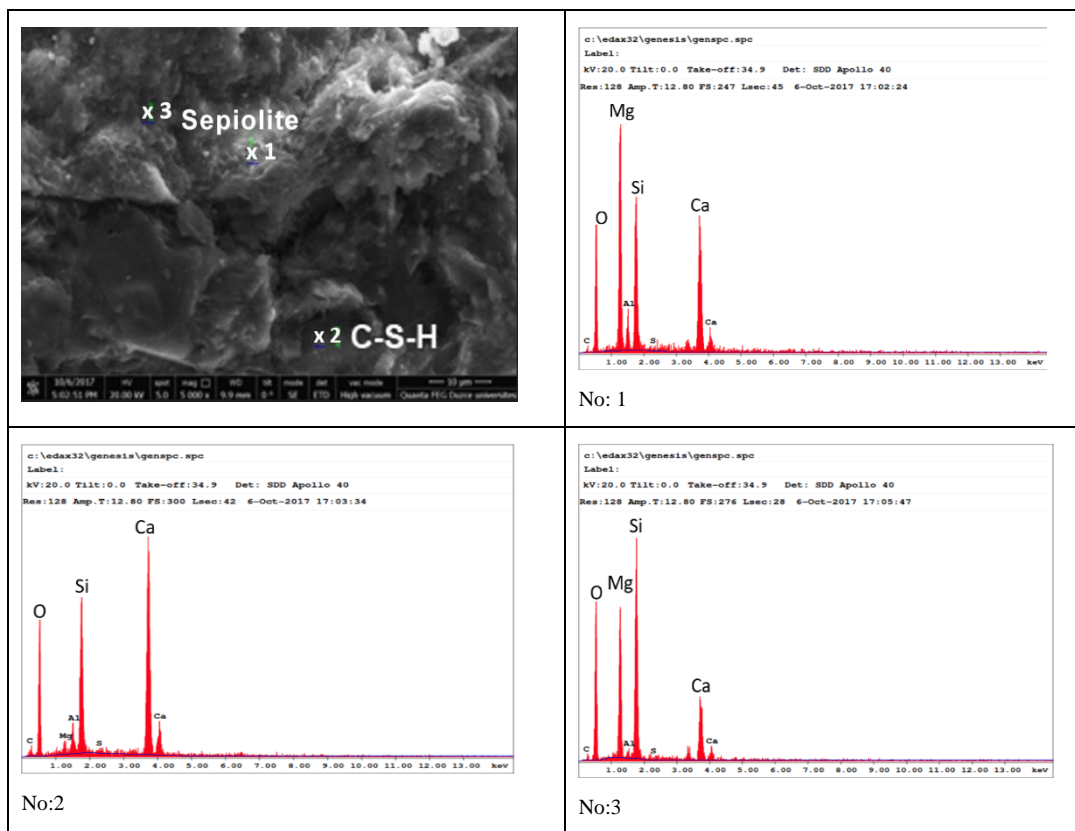


Figure 10. EDS analysis and SEM image of 20% calcined sepiolite substituted sample

When the SEM results were examined, hydrated phases such as CSH, CH and ettringite were determined in the structure. It has been observed that the adherence between the cement matrix and the sepiolite is weak, and as a result of this weakness, cracks are formed at the interface between the matrix and the sepiolite, thus adversely affecting the strength of the concrete. It is understood from the crack formation observed between the cement products and the crude sepiolite that the bond is weaker in crude sepiolite compared to calcined sepiolite.

When the EDS results are examined, Si, Ca, O, Al, Mg, S elements in the paste show similarity in all sepiolite substituted samples. In addition, it is seen that the Mg ratio in the sepiolite samples is high.

3.3. Experiments on mortar samples

3.3.1. Flow diameter results

The flow diameter of the sepiolite-free control mortar was determined in accordance with the standard, and water content determinations were

made to reach similar spreading diameters in the samples with different ratios of calcined and crude sepiolite substituted. The graphical representation of the W/B ratios depending on the sepiolite substitution ratio is given in Figure 11. When the results were evaluated, the increase in the sepiolite ratio in connection with the consistency test performed on the paste mixtures increased the water requirement of the mortar samples. When calcined and crude sepiolite were compared, it was observed that calcination of sepiolite resulted in a decrease in the water absorption of the samples.

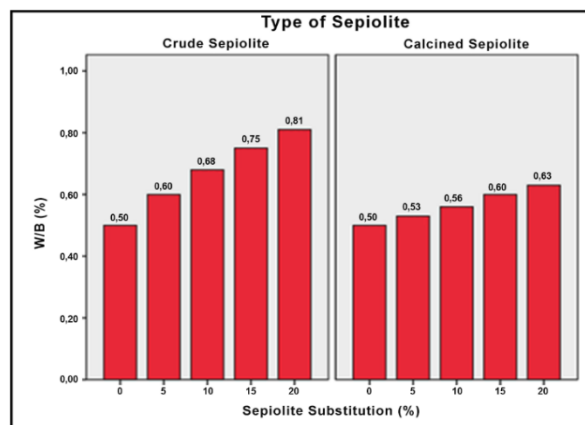


Figure 11. W/B values based on sepiolite substitution ratio

The highest water demand was observed in samples with 20% crude sepiolite replacement, an increase of 62% compared to the control. In samples with 20% calcined sepiolite replacement, the increase value was determined as 26%.

3.3.2. Alkali silica reactivity results by accelerated experiment method

Mortar samples containing different amounts of sepiolite were subjected to expansion test using the alkali silica method with accelerated mortar stick. The changes in sample lengths are given graphically in Figure 12.

Sepiolite substitution did not cause significant expansion on the mortar samples. This shows that although calcined and crude sepiolite have a high MgO ratio, there is no expansion feature in cementitious composite materials. While some more expansion was observed in mortar samples replaced with calcined sepiolite compared to samples replaced with crude sepiolite, the highest expansion value was observed in the

sample with 20% calcined sepiolite substituted at the rate of 0.16%. While there was no significant change in the expansion values of the samples on the 3rd and 7th days, nearly 4 times of expansion value was observed in the 14th day expansion values compared to the 3rd and 7th days.

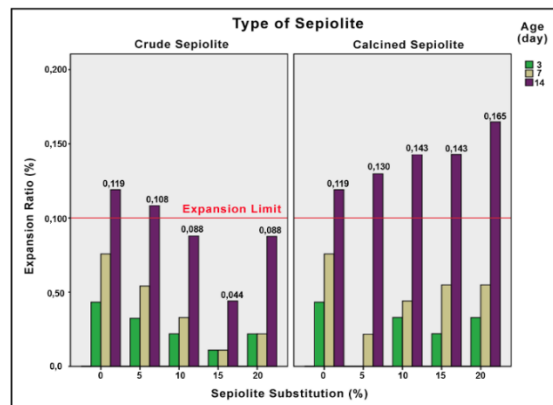


Figure 12. Expansion values depending on the sepiolite substitution ratio

It was observed that the expansion value caused by alkali silica reaction in samples was below 0.2% and it was determined that sepiolite was suspicious (harmful-harmless) in terms of alkali silica reactivity, except 10%-15%-20% crude sepiolite substitutions.

3.3.3. Compressive strength test results

According to TS EN 196-1, the graph of 7, 28, 56 and 90-day compressive strength tests based on the sepiolite replacement rate performed on the mortar samples produced is given in Figure 13.

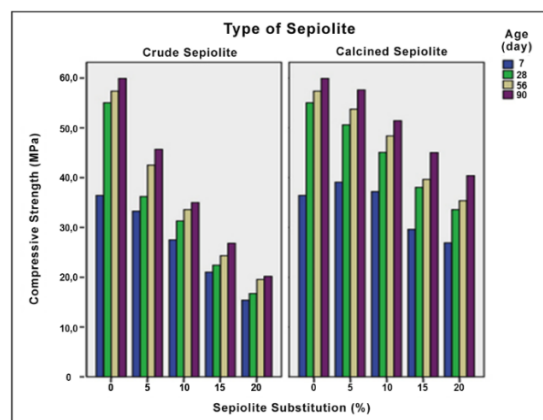


Figure 13. Compressive strength results of mortar samples

When compressive strength results were examined, it was seen that the compressive

strength results decreased as the sepiolite substitution increased. It was observed that compressive strength results of samples containing calcined sepiolite were higher than samples containing crude sepiolite. In addition, with 5% and 10% calcined sepiolite replacement, it is understood that the compressive strength value at early ages is higher than the compressive strength value of the control sample.

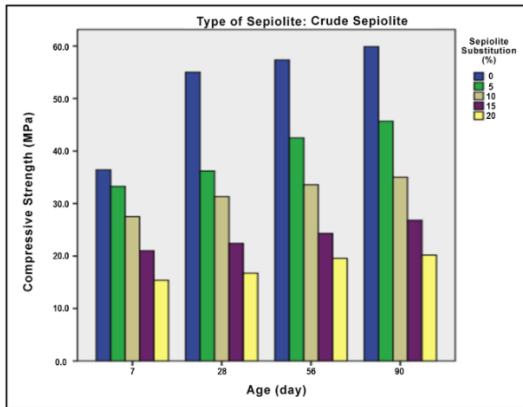


Figure 14. Results of compressive strength values of crude sepiolite substituted mortar samples at 0%,5%, 10%, 15% and 20% depending on the curing age of the sample

In addition, the graphical representation of the results of the compressive strength of the crude sepiolite substituted mortars at 0%, 5%, 10%, 15% and 20% depending on the sample age is given in Figure 14. The test results of the compressive strength values of the calcined sepiolite-replaced mortar samples are given graphically in Figure 15. According to results, as the sample curing time

increases, the compressive strength values of all mixtures increase. The samples reached their highest compressive strength after 90 curing days. In addition, as the crude sepiolite substitution rate is increased, the compressive strength values of the samples decrease, while the lowest compressive strength was observed in the samples with 20% crude sepiolite substitute, and the highest compressive strength value was observed in the control samples without sepiolite. After 28 days of curing, the highest increase in strength is in the control samples with 51%.

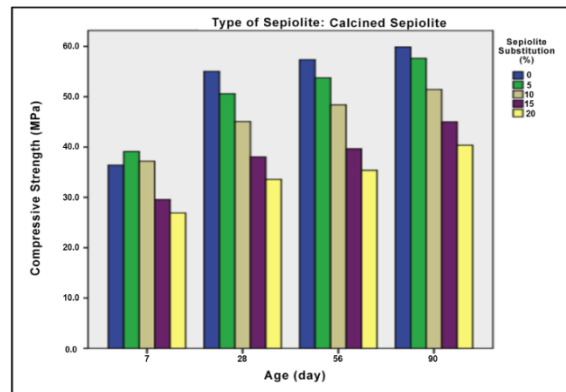


Figure 15. Test results of compressive strength values of samples with 0%, 5%, 10%, 15% and 20% crude sepiolite replacement depending on the sample curing time

When the early compressive strength results at the end of 7 days of curing of 5% and 10% calcined sepiolite-replaced samples were examined, it was observed that the strength values were higher than the control sample, and the compressive strength was lower at later ages than the control sample.

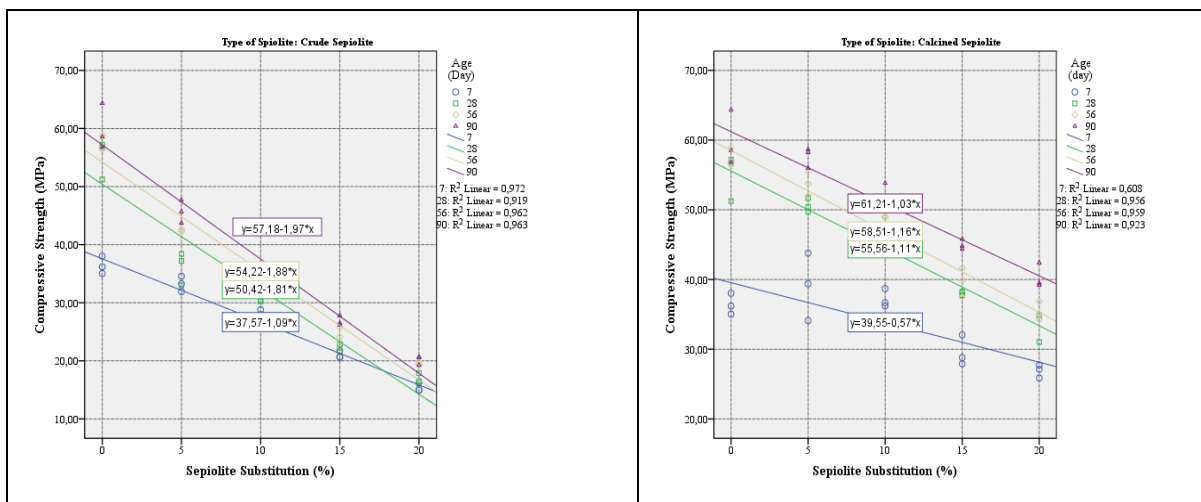


Figure 16. Graph of the relationship between sepiolite substitution rates and compressive strength results

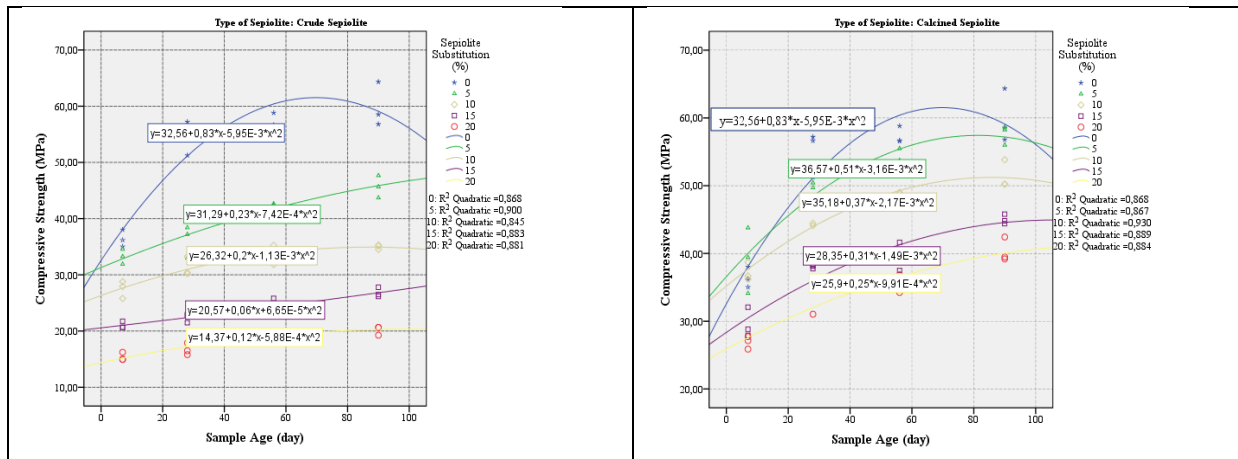


Figure 17. Graph of the relationship between sample curing age and compressive strength results

Regression analysis was performed to model the relationship between the substitution sepiolite ratio and the compressive strength results. It has been observed that there is a relationship between the amount of sepiolite substitution and the compressive strength, which can be explained by the first-order equation $Y=a+bX$. The relationship graph between the values and the explanatory model equations are shown in Figure 16, and the relationship graph between the compressive strength results and the sample age, which can be explained by the second-order equation $Y=a+bX+cX^2$, is shown in Figure 17.

3.3.4. Pozzolanic activity experiment results

The pozzolanic activity index was calculated based on the strength of the 20% calcined and crude sepiolite-substituted samples after 28 days of curing, according to the ASTM C-311 standard, and is given in Table 6. According to the table, it was observed that the pozzolanic activity index value of calcined and crude sepiolite was below 75% according to ASTM C-311 and did not show adequate pozzolanic properties.

Table 6. Pozzolanic activity index strength results.

	0% Sepiolite Control Sample	20% Crude Sepiolite Samples	Samples with 20% Calcined Sepiolite
28 G. Compressive Strength (Mpa)	55.03	16.73	33.57
Pozzolanic Activity Index	-	30.40	61.00

4. Conclusion

Density, chemical analysis, laser particle size analysis, FTIR analysis, thermal analysis, calcination process and SEM-EDS analyzes were performed on calcined and crude sepiolite samples to investigate the usability of ground sepiolite obtained from Eskisehir region in cement production. SEM-EDS analyzes and consistency test were performed on paste samples, and compressive strength, flow diameter determination, pozzolanic activity and alkali-silica reactivity tests were performed on mortar samples.

As a result of the data obtained from the test results and the statistical evaluations;

In powder samples;

- The density value increases with the calcination of the crude sepiolite, and the highest density is reached with the calcination applied at 900°C,
- crude sepiolite also has a fibrous structure, and after calcining, its fibrous structure deteriorates and turns into an oval shape [18].

In paste samples;

- Compared to the control mixture, 20% crude sepiolite substitute increased the water demand by 59%, while 20% calcined sepiolite by 28%. Crude sepiolite retains more water than calcined sepiolite. Studies in the literature confirm that the water demand of the

mixture increases with the increase in sepiolite content [29],

- The bond between the sepiolite and the matrix is weak, and as a result, cracks occur at the sepiolite interface, thus negatively affecting the strength properties of the concrete, the bond is weaker in crude sepiolite compared to calcined sepiolite,

In mortar samples;

- The water absorption values of the samples decreased by calcining the sepiolite, 20% of the crude sepiolite replacement increased the water requirement by 62% compared to the control mixture, and this increase was 26% in the samples with 20% calcined sepiolite replacement. Since the workability of the control mixture decreased with sepiolite substitution, the water content was increased [30].
- The expansion value of the samples can be considered suspicious (harmful-harmless) in terms of reactivity, as it remains between 0.2% and 0.1% after 14 days, except 10%-15%-20% crude sepiolite substitutions,
- Due to the increase in the sepiolite replacement ratio, the compressive strength values of the samples decrease in the early and advanced ages compared to control samples [31]. The increase in water demand with the increase in the substitution rate were effective in this decrease. The crude sepiolite substitution causes lower compressive strength compared to the calcined sepiolite substitute, and at the end of 90 curing days, a 62% decrease in the lowest compressive strength value is realized in the samples with 20% crude sepiolite replacement. The addition of more water to reach similar spreading diameters reduced the strength of mortar [32],

It has been determined that crude and calcined sepiolite substitutions in different proportions to cement do not show sufficient pozzolanic properties in cementitious composites. The study conducted by Wu et al. confirmed that the pozzolanic activity increased by calcining sepiolite [31].

Article Information Form

Funding

This article was supported by Düzce University Scientific Research Project numbered 2016.07.05.466.

Authors' Contribution

The authors contributed equally to the study.

The Declaration of Conflict of Interest/ Common Interest

No conflict of interest or common interest has been declared by the authors.

The Declaration of Ethics Committee Approval

This study does not require ethics committee permission or any special permission.

The Declaration of Research and Publication Ethics

The authors of the paper declare that they comply with the scientific, ethical and quotation rules of SAUJS in all processes of the paper and that they do not make any falsification on the data collected. In addition, they declare that Sakarya University Journal of Science and its editorial board have no responsibility for any ethical violations that may be encountered, and that this study has not been evaluated in any academic publication environment other than Sakarya University Journal of Science.

Copyright Statement

Authors own the copyright of their work published in the journal and their work is published under the CC BY-NC 4.0 license.

References

- [1] X. Gao, Y. Yang, H. Deng, "Utilization of beetmolasses as a grinding aid in blended cements," *Construction and Building Materials*, vol. 25, pp. 3782-3789, 2011.
- [2] R. Snellings, G. Mertens, Ö. Cizer, J. Elsen, "Early age hydration and pozzolanic reaction in natural zeolite blended cements: Reaction kinetics and products by in situsynchrotron X-ray powder diffraction,"

- Cement and Concrete Research, vol. 40, pp. 1704-1713, 2010.
- [3] H. Y. Aruntaş, M. Gürü, M. Dayı, İ. Tekin, "Utilization of waste marble dust as an additive in cement production," *Materials and Design*, vol. 31, no. 8, pp. 4039-4042, 2010.
- [4] O. S. Al-Amoudi, M. Maslehuddin, M. Ibrahim, M. Shameem, M. H. Al-Mehthel, "Performance of blended cement concrete prepared with constant workability," *Cement and Concrete Composites*, vol. 33, pp. 90-102, 2011.
- [5] İ. Ustabaş, Ş. Erdoğan, "Farklı öğütücü kolaylaştırıcı katkı çimentoların özelliklerinin kıyaslaması," in *Chemical Admixtures on Structures 4th Symposium*, Ankara, Türkiye, 2013.
- [6] C. Hosten, B. Fidan, "An industrial comparative study of cement clinker grinding systems regarding the specific energy consumption and cement properties," *Powder Technology*, vol. 221, pp. 183-188, 2012.
- [7] A. Atmaca, M. Kanoglu, "Reducing energy consumption of a rawmill in cement industry," *Energy*, vol. 42, no. 1, pp. 261-269, 2012.
- [8] M. A. V. Rodriguez, J. D. L. Gonzalez, M. A. Banares, "Acid activation of a spanish sepiolite, physico chemical karakterizatio, free silica content and surface area of the solids obtained," *Clay Minerals*, vol. 29, pp. 361-367, 1994.
- [9] C. E. Weaver, L. D. Pollard, "The chemistry of clay minerals," Elsevier Scientific Publishing Company, vol. 10, pp. 127, 1973.
- [10] T. Kavas, E. Sabah, "Sepiyolitli Takviyeli Çimento Üretiminde Kullanılabilirliğinin Araştırılması," in *4. Endüstriyel Hammaddeler Sempozyumu*, İzmir, Türkiye, 2001.
- [11] T. Kavas, E. Sabah, M. S. Çelik, "Structural properties of sepiolite-reinforced cement composite," *Cement and Concrete Research*, vol. 34, pp. 2135-2139, 2004.
- [12] E. Fuente, R. Jarabo, A. Moral, Á. Blanco, L. Izquierdo, C. Negro, "Effect of sepiolite on retention and drainage of suspensions of fiber-reinforced cement," *Construction and Building Materials*, vol. 24, no. 11, pp. 2117-2123, 2010.
- [13] E. Fuente, R. Jarabo, A. Moral, C. Negro, L. Izquierdo, "Effect of sepiolite on the behaviour of fibre cement suspensions in the manufacture of fibre-reinforced cement," in *11th Int. Inorganic-Bonded Fiber Composites Conference*, Madris, Spain, 2018.
- [14] S. Andrejkovičová, E. Ferraz, A. L. Velosa, A.S. Silva, F. Rocha, "Fine sepiolite addition to air lime-metakaolin mortars," *Clay Minerals*, vol. 46, pp. 621-635, 2011.
- [15] S. Martínez-Ramírez, F. Puertas, B.M.T. Varela, "Carbonation process and properties of a new lime mortar with added sepiolite," *Cement and Concrete Research*, vol. 25, no. 1, pp. 39-50, 1995.
- [16] A. Demir, "Sepiyolitli harçların mekanik ve fiziksel özelliklerinin incelenmesi," in *Ejovoc Special Issue 2nd International Multidisciplinary Eurasian Congress*, Odessa, Ukraine, 2016.
- [17] M. Savaş, İ. Demir, S. Güzelküçük, Ç.G. Şengül, H. Yaprak, "Thermal and Compressive Strength Properties of Sepiolite Substituted Autoclaved Aerated Concrete," *Journal of Polytechnic*, vol. 17, no. 1, pp. 43-47, 2014.
- [18] C. He, E. Makovicky, B. Osbæck, "Thermal treatment and pozzolanic activity of sepiolite," *Applied Clay Science*, vol. 10, pp. 337-349, 1996.

- [19] S. Pu, P. Duan, C. Yan, D. Ren, "Influence of sepiolite addition on mechanical strength and microstructure of flyash-metakaolin geopolymer paste," *Advanced Powder Technology*, vol. 27, pp. 2470-2477, 2016.
- [20] J. P. Melo, A. S. Aguilar, F. H. Olivares, "Rheological properties of aerated cement pastes with fly ash, metakaolin and sepiolite additions," *Construction and Building Materials*, vol. 65, pp. 566-573, 2014.
- [21] N. Alan, S. İşçi, "Surface modification of sepiolite particles with polyurethane," *Progress in Organic Coatings*, vol. 77, pp. 444-448, 2014.
- [22] TS EN 196-1, "Methods of testing cement - Part 1: Determination of strength," Ankara, 2002
- [23] TS EN 196-3, "Methods of testing cement-part 3: determination of setting time and soundness," Ankara, Türkiye, 2002.
- [24] TS EN 459-2, "Building lime - Part 2: Test methods," Ankara, Türkiye, 2003.
- [25] ASTM C-1260-01, "Standard Test Method for Potential Alkali Reactivity of Aggregates (Mortar-Bar Method)," USA, 2001
- [26] ASTM C-311, "Standard Test Methods for Sampling and Testing Fly Ash or Natural Pozzolans for Use in Portland-Cement Concrete," USA, 2004.
- [27] A. Bideci, A. H. Gültekin, H. Yıldırım, S. Oymael, Ö. Sallı Bideci, "Internal structure examination of light weight concrete produced with polymer-coated pumice aggregate," *Composites Part B: Engineering*, vol. 54, pp. 439-447, 2013.
- [28] F. A. Shaker, A. S. El-Dieb, M. M. Reda, "Durability of styrene-butadiene latex modified concrete," *Cement and Concrete Research*, vol. 27, pp. 711-720, 1997.
- [29] X. Chenxi, W. Caihui, L. Wenhao, S. Kaili, Z. Guangxing, S. Guowen, K. Lijuan, "Internal Curing Mechanism of Sepiolite in Cement Paste," *Journal of Wuhan University of Technology-Mater. Sci. Ed.*, pp. 857-864, 2023.
- [30] H. Doostkami, S. Formagini, P. Serna, M. R. Flores, "Effects of healing start time and duration on conventional and high-performance concretes incorporating SAP, crystalline admixture, and sepiolite: A comparative study," *Case Studies in Construction Materials*, vol. 20, 2024.
- [31] C. Wu, Z. Hong, B. Zhan, S. Cui, S. Kou, "Pozzolanic activity of calcinated low-grade natural sepiolite and its influence on the hydration of cement," *Construction and Building Materials*, vol. 309, 2021.
- [32] W. Chunran, K. Shicong, "Effects of high-calcium sepiolite on the rheological behaviour and mechanical strength of cement pastes and mortars," *Construction and Building Materials*, vol. 196, pp. 105-114, 2019.

A Research on Architects' Comfort Conditions in Working Enviroments

Yiğit Can Yardımcı 

Bursa Uludag University, Faculty of Architecture, Department of Architecture, Bursa, Türkiye,
yardimciyigitcan@gmail.com

ARTICLE INFO

ABSTRACT

Keywords:
Architects
Comfort conditions
Working environment



Article History:
Received: 07.04.2023
Accepted: 04.07.2023
Online Available: 06.06.2024

Architects have difficult working conditions due to the profession of architecture and they stay in the working environment during intensive working hours. For this reason, it is important to improve the comfort conditions in the working environment for architects to feel physically and psychologically better. The aim of this study is to evaluate the comfort conditions in the working environment of architects working in Bursa. In the literature, the number of studies examining the physical comfort conditions of architects in the work environment is limited. Therefore, this study is important in terms of explaining the comfort conditions of architects in their working environment. In this direction, 203 architects were reached and a questionnaire was used as a data collection method. The questionnaire consists of 2 stages. The first phase includes demographic characteristics and the second phases includes questions about comfort conditions. When the comfort conditions of the architects were examined; it was seen that they were satisfied with the sub-factors of artificial lighting, indoor temperature and natural ventilation adequacy, indoor air quality, absence of bad odors in the working environment, seat ergonomics, equipment adequacy. However, they feel uncomfortable with the several auditory comfort conditions in the work environment. When the correlation between demographic characteristics and comfort conditions in the working environment is examined, the correlation coefficients are in the range of 0-0.20, indicating that demographic characteristics have a very weak or no relationship with comfort conditions in the working environment.

1. Introduction

Comfort is the state of achieving the highest level of satisfaction with minimum effort in human conditions. Comfort conditions are the most important factor in ensuring a good quality of life for users. People living in developed countries spend 90% of their time indoors [1]. In order to be physically and mentally healthy and productive, it is essential to provide comfort conditions in indoor environments. There are certain conditions that must be met in indoor environments to ensure comfort conditions. These conditions are thermal, acoustic, visual, indoor air quality and ergonomics [2].

With appropriate environmental conditions, businesses can expect reduced absenteeism, illness allowances and economic benefit complaints. Especially in developed countries, employee costs are higher than building costs [3-6]. There are many studies that examine the physical comfort conditions of the working environment. Gonzales et al. examined the impact of spatial and aesthetic values of office buildings and their surroundings on user satisfaction [7]. Dorgan and Dorgan argued that indoor environmental quality is important because employees are in the office for long periods of time. They found that there is a relationship between the health and productivity of the occupants and the physical quality of the environments [8]. Sunstrom et al. investigated

the effect of environmental noise on employees' job satisfaction, job performance and environmental satisfaction. They found that user satisfaction decreases when ambient noise increases [9]. Leather et al [10] examined the effects of noise, air quality, temperature and lighting on employee psychology and work stress. Muhic and Butala investigated the effects of heating and air quality on users in an office building.

According to the results, the majority of the users expressed their dissatisfaction with the thermal environment and air quality. They observed that absenteeism was higher in offices with air conditioning [11]. According to Leaman's study, the productivity of users who are not satisfied with the air quality, lighting and noise conditions in offices is also affected [12]. Roelofsen concluded that the thermal environment and air quality are most effective on the productivity of office workers [13]. Whitley et al [14] found that office satisfaction is effective on the productivity of employees. They found a relationship between satisfaction with office conditions and job satisfaction and environmental control.

The profession of architecture is interdisciplinary with various business lines [15]. Architects have very difficult working conditions because of the structure of the architectural profession. Therefore, it is necessary to improve the comfort conditions in the working environment for architects to feel psychologically and physically well and to increase their productivity in the workplace. In this direction, a survey was conducted with 203 architects to measure the comfort conditions in the working environment of architects in Bursa. With this study, it is aimed to determine the comfort conditions of architects in their working environments [16].

2. Literature Review

2.1. Comfort conditions

Comfort can be defined as the feeling of well-being achieved by the possibilities of science and technology. For generations, human beings have made efforts to transform their environment into comfortable environments. However, with the developing environmental conditions and

technology, comfort expectations change periodically. There are certain factors to improve comfort conditions in the working environment. These factors are visual, auditory and thermal comfort, indoor air quality and ergonomic conditions [16-17].

2.1.1. Thermal comfort

Thermal comfort can be defined as a sense of psychological and physical comfort in terms of ambient conditions such as temperature, air flow rate and humidity. In order to sustain people's lives in a healthy way, body temperature must be kept at a normal temperature. There are various factors that determine the body's heat balance. These factors are environmental factors, personal factors and heat balance systems. While environmental factors need to be determined from outside, personal factors are determined by the individuals themselves. Environmental factors are temperature, humidity, air flow rate and air quality. Personal factors are body surface area, activity and clothing. Apart from these factors, there are parameters that are difficult to assess. These include national geographical location, body and active structure, age, gender, changes in thermal values, heart rhythm, menstrual cycle, colors used indoors, type of food consumed, air pressure and number of users [18].

There are many studies on thermal comfort. Lan [19] investigated the effects of thermal comfort changes on employees' job performance and emotions. It was observed that employee performance decreased when the environmental temperature was neutral. At high temperatures, participants felt uncomfortable and had to spend more effort to maintain their job performance with negative emotions. In their study, Bajc et al [20] emphasized the importance of proper ventilation during the winter season to achieve a healthy and productive working environment and optimal thermal comfort levels. Wargocki et al [21] found that in conditions of bad indoor environmental quality, employee performance can drop by 100% and cause absenteeism.

2.1.2. Visual comfort

Visual comfort is the provision of visual perception to the satisfaction of the individual. Visual comfort of the users is important in terms of physiological and psychological aspects by increasing the working efficiency, confidence and perception level of the individuals. In order to make visual comfort conditions appropriate in a workplace; first of all, the level of illumination in the environment must be sufficient. The fact that daylight is an unusable light source when it comes directly into the working environment and excessive brightness negatively affects the user's eye comfort.

For this reason, the way the light is received into the space is important. The user's psychological and visual needs are positively met with an appropriate lighting design. Research on users has shown that there are positive effects when sufficient natural lighting is provided in an office environment. These positive effects are; increase in the amount of production in the input, decrease in work accidents, decrease in fatigue-irritability, increase in working speed, decrease in lighting-

related costs and increase in academic success rate [2].

Studies have shown that designing for efficient daylighting is one of the most important approaches in high-performance modern buildings [22-23]. In order to get the most out of daylight individually, interior design should ensure the visual comfort of users [24].

2.1.3. Acoustic comfort

Acoustic comfort is defined as the state of being satisfied with the auditory conditions in the environment [1]. Environmental problems have emerged with social change. Noise is one of these problems [25]. Noise can be defined as physiologically undesirable, disturbing, unpleasant and physically irregular sounds [26]. The average acceptable outdoor noise value is determined by WHO as 55 dB(A) decibels. Above this threshold, depending on the function of the environment inside the building, machine and man-made noises occur. The indoor noise level limit values of commercial buildings are shown in Table 1 [27].

Table 1. Indoor noise level limit values of commercial buildings

Usage Area	Closed Window	Open Window	
	Leq (DBA)	Leq (DBA)	
Big Office	45	55	
Meeting rooms	35	45	
Computer rooms or large typewriters	50	60	
Game rooms	60	70	
Commercial buildings	Private office (hands-on)	45	55
	General office (account, writing departments)	50	60
	Business centers, shops, etc.	60	70
	Commercial storage	60	70
	Restaurants	45	55

Uncomfortable working environment conditions that occur when auditory comfort is not provided can lead to dissatisfaction with the overall workplace environment, loss of production and increased workplace work [28-30].

2.1.4. Indoor air quality

Indoor air quality is defined as air in which pollutants are not at the level of harmful combinations in the air in accordance with the rates determined according to ASHRAE 62-1989 and 2001 standards and 80% or more of the

people in the environment are satisfied with the air quality. The quality of the air that people need indoors varies according to the type of use, user density and duration of use. However, the rate of air exchange required depends on the use, outdoor air quality, location of the place, emission levels of harmful and malodorous materials that make up building components and furniture, and the ventilation system used in the building [31]. Among the studies on indoor air quality, Wargocki et al. [32] and Kosonen et al. [4] found that work performance improved with improved air quality.

2.1.5. Ergonomics

Ergonomics is a branch of science that examines the suitability of the working environment for individuals to be productive while working by complying with safety and health conditions at work. While ensuring the organization and design of the working environment according to the individual factor, human-machine-environment harmony is prioritized [33]. In 1949, the word "ergonomics" was first used in England and spread to countries in Europe. In the USA, the word "human engineering" was used as the equivalent of ergonomics [34]. Ergonomic design is a type of design that aims to increase the quality of the product and the efficiency of the work process in the environment formed by the work and the individual. Anthropometric design, one of the ergonomic design methods, is the most widely used method in the field of architecture as it is related to human dimensions and body [35].

In a review of ergonomics-related studies, Rivilis et al [36] found moderate evidence that ergonomic interventions can reduce the number of sick days, workers' compensation demands and musculoskeletal symptoms. Brewer et al [37]

found mixed evidence of the impact of office interventions on visual health and musculoskeletal symptoms among computer users.

3. Material and Method

Comfort conditions in the working environment are important for the organization and employees to feel physically and mentally comfortable. Therefore, this study aims to evaluate the impact of comfort conditions in the working environment on architects. Sample of this study consists of architects in different working environments in Bursa, Türkiye. For this study, questionnaire was used as a data collection tool. The questionnaire was applied online and the questionnaire form was created on Google Forms. On the basis of the number of architects working as architects in Bursa, the minimum sample size should be 177 participants. Accordingly, a total of 203 architects, 117 women and 86 men, were reached in Bursa. The sample size is appropriate for the validity and reliability of the study [16]. The evaluation criteria and score ranges of the answers are shown in Table 2.

Table 2. The evaluation criteria and score ranges of the answers

Likert Scale	Options	Ranges	Evaluation Criteria
5	Absolutely agree	4.20-5.00	very high level
4	I agree	3.40-4.19	high level
3	Undecided	2.60-3.39	medium level
2	I do not agree	1.80-2.59	low level
1	I strongly disagree	1.00-1.79	very low level

Table 3. Normality test on survey factors

	Kolmogorov-Smirnov ^a			Shapiro-Wilk		
	Stat.	df	Sig.	Stat.	df	Sig.
Internal satisfaction	.122	203	.003	.939	203	.009
External satisfaction	.126	203	.000	.951	203	.000
Overall satisfaction	.141	203	.000	.912	203	.000
Thermal comfort	.147	203	.000	.952	203	.000
Visual comfort	.225	203	.002	.893	203	.007
Auditory comfort	.146	203	.000	.952	203	.000
Indoor air quality	.182	203	.000	.912	203	.00
Ergonomics	.141	203	.000	.936	203	.000
Economic factors	.138	203	.0015	.942	203	.0027
Psycho-social factors	.108	203	.000	.957	203	.000
Organisational-managerial factors	.146	203	.000	.924	203	.000

Before analyzing the scales, reliability and normality distribution were examined and some tests were conducted. It was aimed to use the

correct analysis methods in the analysis of the data. Normality test, kurtosis and skewness coefficient values were used to analyze the

distribution of the data. For the normal distribution of the data, the sig. values of the Kolmogorov-Smirnov and Shapiro-Wilk tests should be > 0.05 , and the kurtosis and skewness coefficient values should be between -1.5 and $+1.5$ [38-39]. However, as a result of the normality tests, the p (asmp. Sig.) values of the scales are <0.05 . Skewness and kurtosis coefficients are not between -1.5 and $+1.5$. As a result of the findings, it was determined that the data distribution was not normal. The normality test is shown in Table 3 below.

SPSS 23.0 program was used to analyze the data obtained from the sample with the questionnaire. Analysis methods such as descriptive statistics, Spearman Correlation analysis and Mann Whitney U test were used to examine the impact of several factors on the samples.

4. Findings

The findings of the study show that architects are satisfied with the comfort conditions of the environment in which they work. In this study, Likert-type 5-point scale was used and overall comfort conditions value was found as 3.40 out of 5. This value is at a high level according to the criteria shown in Table 2. The values of "visual comfort", "indoor air quality" and "ergonomics" which consist of general comfort values were at a high level, while the values of "thermal comfort" and "acoustic comfort" were at a medium level. Figure 1 shows the average distribution of comfort conditions.

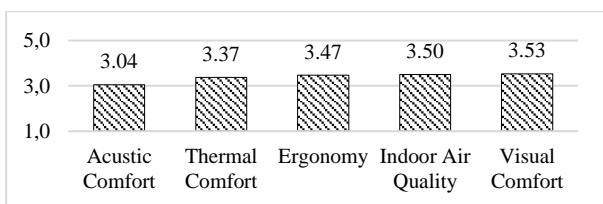


Figure 1. The average distribution of the levels of comfort conditions

When the comfort conditions sub-parameters were analyzed, it was seen that some values were higher than the average value. These values are "indoor temperature" (thermal comfort), "natural lighting" and "artificial lighting"(visual comfort), "indoor acoustics"(acoustic comfort), "indoor air quality", "natural ventilation" and "absence of bad odors"(indoor air quality), "seat

ergonomics", "equipment size" and "equipment adequacy" (ergonomics). These values are at a high level based on the evaluation criteria in Table 2. The frequencies and percentages of comfort conditions are shown in Table 4.

Table 4. Frequency and percentage of comfort conditions

Parameter		Measures				
		1	2	3	4	5
Indoor temperature	Freq.	0	22	14	160	6
	%	0	10.8	6.9	78.8	3
Indoor temperature caused by seasonal temperature changes	Freq	0	78	38	80	6
	%	0	38.4	18.7	39.4	3
Amount of humidity	Freq	0	31	77	92	2
	%	0	15.3	37.9	45.3	1
Natural lighting	Freq	1	34	37	123	7
	%	0.5	16.7	18.2	60.6	3.4
Artificial lighting elements	Freq	0	27	42	125	8
	%	0	13.3	20.7	61.6	3.9
Indoor acoustics	Freq.	1	34	50	113	4
	%	0.5	16.7	24.6	55.7	2
Mechanical systems' noise	Freq	3	133	30	33	3
	%	1.5	65.5	14.8	16.3	1.5
Outdoor noise	Freq	4	72	51	69	5
	%	2	35.5	25.1	34	2.5
Speech privacy	Freq	0	47	60	90	5
	%	0	23.2	29.6	44.3	2.5
Indoor air quality	Freq	1	26	51	120	4
	%	0.5	12.8	25.1	59.1	2
natural ventilation	Freq.	1	21	29	147	4
	%	0.5	10.3	14.3	72.4	2
Artificial ventilation	Freq.	1	33	55	111	2
	%	0.5	16.3	27.1	54.7	1
Absence of bad odor	Freq	2	26	58	110	6
	%	1	12.8	28.6	54.2	3
Seat ergonomy	Freq	3	33	37	124	5
	%	1.5	16.3	18.2	61.1	2.5
Computer at eye level	Freq	0	44	40	110	6
	%	0	21.7	19.7	54.2	3
equipment's size	Freq	1	28	39	128	6
	%	0.5	13.8	19.2	63.1	3
Equipment adequacy	Freq.	1	31	42	122	6
	%	0.5	15.3	20.7	60.1	3

When parameters of comfort conditions in the working environment were analyzed, it was found that some values were lower than the average value. These values are "seasonal indoor temperature" and "humidity" (thermal comfort), "outdoor noise" and "speech privacy" (acoustic comfort), "artificial ventilation" (indoor air quality) and "eye level" (ergonomics). These values are medium level according to the criteria in Table 2. The "mechanical system noise value"(acoustic comfort) is at low level. Average distributions of comfort conditions sub-parameters are shown in Figure 2.

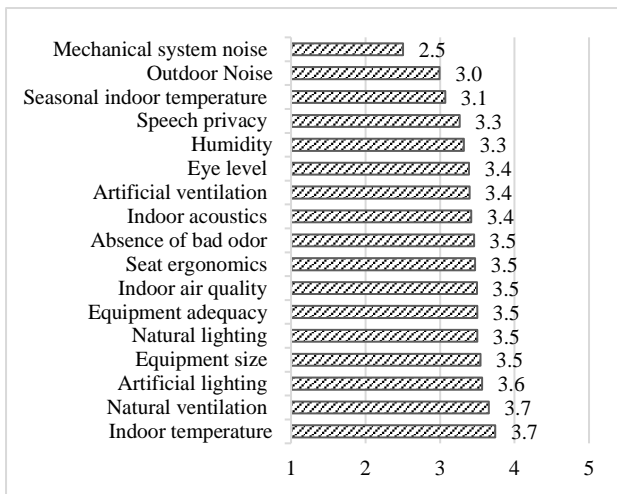


Figure 2. Average distributions of comfort conditions sub-parameters

Based on the findings, architects do not feel comfortable acoustically in the environment where they work. The fact that the acoustic comfort value is low in the research and the values of mechanical system noise and outdoor ambient noise, which are sub-factors of acoustic comfort, have the lowest values is evidence of this fact.

Thermal comfort parameters show that architects are at a medium level about thermal comfort in the working environment. Architects who were satisfied with the indoor temperature were undecided about the seasonal indoor temperature and humidity in their working environment. Especially the values of "seasonal indoor temperature" is remarkable with a value of 3.06 out of 5.

There was a statistically weak correlation between demographic variables (age, professional experience, type of organization, average working hours, working style, working order) and comfort parameters with values between 0-0.39. Thermal comfort level had the strongest statistical correlation with average working hours and the weakest statistical correlation with the number of employees. Auditory comfort level had the strongest statistical correlation with working organization and the weakest statistical correlation with working style. Table 5 shows the correlation analysis between comfort conditions and demographic characteristics.

Table 5. The correlation analysis between comfort conditions and demographic characteristics

Parameter	Avg. working hours	Working order	Working time (year)	Age	Pro. exp.	Way of working	Type of Organization
Thermal Comfort	0.228	-	-	-	-	-	-
Seasonal indoor temperature	0.185	-	-	-	-	-	-
Amount of humidity	-	-	-	-0.184	-0.165	-	-
Acoustic Comfort	-	0.209	-	-	-	-0.076	-
Mechanical system noise	-	0.175	-	-	-	-	0.208
Ergonomics	-	-	-	-	-	-0.172	-
Equipment size	-	0.162	-	-	-	-	-
Seating Ergonomics	-	0.181	-	-	-	-	-
Equipment adequacy	0.185	0.154	0.167	0.159	-	-0.187	-

(0.00) - (0.20)= Very weak relationship, (0.21) - (0.40)= Weak relationship, (0.41) - (0.59)= Medium relationship, (0.60) - (0.79)= High relationship, (0.80) - (1.00)= Very high relationship

5. Conclusion

Comfort conditions in the working environment can have positive or negative effects on employees. It is important for the organization and employees to feel physically and mentally comfortable. Companies can expect a reduction in absenteeism, illness permissions and economic benefit complaints when appropriate environmental conditions are provided. Therefore, this study aims to evaluate the impact

of comfort conditions on architects. In this study, architects' comfort conditions in the working environment are moderate or high, except for some acoustic comfort parameters.

Working equipment and physical working positions are important for architects, who spend most of the day sitting in front of a computer, to feel physically and mentally well. Everything such as posture, the chair they use, the position of the computer, the arrangement of other work

equipment affects the physical health and productivity of office architects who do not have much mobility during the day. In addition, it is seen that if the indoor air quality in the working environment is not good, fatigue will occur and productivity will decrease. In cases where thermal comfort, visual comfort and acoustic comfort conditions are low, physical and mental health problems of the users can also cause disruptions in their work. Therefore, improving comfort conditions in buildings will make users feel better and be more productive.

Article Information Form

Acknowledgments

The author would like to thank Prof. Dr. Yasemin Erbil for her contributions.

Funding

The author (s) has no received any financial support for the research, authorship or publication of this study.

The Declaration of Conflict of Interest/ Common Interest

No conflict of interest or common interest has been declared by the author.

The Declaration of Ethics Committee Approval

This study requires ethics committee permission or any special permission.

The Declaration of Research and Publication Ethics

The author of the paper declare that he comply with the scientific, ethical and quotation rules of SAUJS in all processes of the paper and that they do not make any falsification on the data collected. In addition, he declare that Sakarya University Journal of Science and its editorial board have no responsibility for any ethical violations that may be encountered, and that this study has not been evaluated in any academic publication environment other than Sakarya University Journal of Science.

Copyright Statement

Authors own the copyright of their work published in the journal and their work is published under the CC BY-NC 4.0 license.

References

- [1] Ş. F. Sezer, V. T. Arslan, A. Çahantimur, "Alışveriş merkezlerinde kullanıcı memnuniyetinin konfor koşulları açısından değerlendirilmesi: Bursa örneği," *Uludağ Üniversitesi Mühendislik-Mimarlık Fakültesi Dergisi*, vol. 19, no. 1, pp. 81-95, 2014.
- [2] N. Yüksel, "Günümüz kamu kurumlarında yapısal konfor koşullarının tespit edilmesine yönelik bir çalışma," *Uludağ Üniversitesi Mühendislik-Mimarlık Fakültesi Dergisi*, vol. 10, no. 2, pp. 21-31, 2005.
- [3] P. Wargoeki, "Productivity and health effects of high indoor air quality", *Encyclopedia of Environmental Health*, vol. 4, pp. 688–693, 2011.
- [4] R. Kosonen, F. Tan, "Assessment of productivity loss in air-conditioned buildings using pmv index", *Energy and Buildings*, vol. 36, pp. 987–993, 2014.
- [5] J. E. Woods, "Cost avoidance and productivity in owning and operating buildings", *Occupational Medicine*, vol. 4, no. 4, pp. 753-770, 1989.
- [6] M. Tarantini, G. Pernigotto, A. Gasparella, "A co-citation analysis on thermal comfort and productivity aspects in production and office buildings", *Buildings*, vol.7, no.2, 36, 2017.
- [7] M. S. R. Gonzalez, C. A. Fernandez, J. M. S. Cameselle, "Empirical validation of a model of user satisfaction with buildings and their environments as workplaces," *Journal of Environmental Psychology*, vol.17, pp. 69-74, 1997.
- [8] C.E. Dorgan, C.B, Dorgan, *Assessment of link between productivity and indoor air quality*, Second Edition, *Creating the Productive Workplace*, 2006.
- [9] E. Sundstrom, J. P. Town, R. W. Rice, D. P. Osborn, M. Brill, "Office noise,

- satisfaction and performance,” *Environment and Behaviour*, vol. 2, no. 6, pp. 195-222, 1994.
- [10] P. Leather, D. Beale, L. Sullivan, “Noise, psychosocial stress and their interaction in the workplace,” *Journal of Environmental Psychology*, vol. 23, pp. 213-222, 2003.
- [11] S. Muhic, V. Butala, “The influence of indoor environment in office buildings on their occupants: expected-unexpected,” *Building and Environment*, vol. 39, pp. 289-296, 2004.
- [12] A. Leaman, “Dissatisfaction and Office Productivity,” *Facilities*, vol. 13, no. 2, pp. 3-19, 1995.
- [13] P. Roelofsen, “The impact of office environments on employee performance: the design of the workplace as a strategy for productivity enhancement,” *Journal of Facilities Management*, vol. 1, no. 3, pp. 247-264, 2002.
- [14] T. D. R. Whitley, P. J. Makin, D. J. Dickson, “Job satisfaction and locus of control: impact on sick building syndrome and self-reported productivity,” 7th International Conference on Indoor Air Quality and Climate, Nagoya, Japan, 1996.
- [15] Ö. F. Bayraktarlı, A. Y. Topraklı, “A literature review for knowledge management maturity scale for architecture firms of Türkiye,” *Gazi University Journal of Science Part B: Art Humanities Design and Planning*, vol. 8 no. 1, pp. 543-552, 2020.
- [16] Y. C. Yardımcı, “Mimarların iş tatmini ve çalışma ortamındaki konfor koşulları ile verimlilik ilişkisinin incelenmesi,” M.S. thesis, Bursa Uludağ University, Türkiye, 2021.
- [17] Ş. Sirel, “Yapı fiziği konuları ders notları”, Yapı Fiziği Uzmanlık Enstitüsü, İstanbul, Jan 13, 2023. [Online]. Available: http://www.yfu.com/kitapciklar/yapi_fizigi_konulari_II.pdf.
- [18] Ashrae, “ASHRAE Handbook- HVAC Systemes and Equipment”, American Society of Heating Refrigerating and Air-Condition Engineers Inc, 2008.
- [19] L. Lan, Z. Lian, “Use of neurobehavioral tests to evaluate the effects of indoor environment quality on productivity”, *Building and Environment*, vol.44, no.11, pp. 2208-2217, 2009.
- [20] T. Bajc, M. Todorović, A. M. Papadopoulos, “Indoor environmental quality in non-residential buildings-experimental investigation” *Thermal Science*, vol. 20, pp. 1521-1529, 2016.
- [21] P. Wargocki, O. Seppänen, J. Andersson, D. Clements-Croome, K. Fitzner, S. O. Hanssen, “Indoor climate and productivity in offices”, *REHVA guidebook*, vol. 6, no. 10-14, 2006.
- [22] K. Panopoulos, A. M. Papadopoulos, “Smart facades for non-residential buildings: An Assessment”, *Advances In Building Energy Research*, vol.11, no:1, pp. 26-36, 2017.
- [23] M. M. Tahmasebi, S. Banihashemi, M. S. Hassanabadi, “Assessment of the variation impacts of window on energy consumption and carbon footprint.” *Procedia Engineering*, vol. 21, pp. 820-828, 2011.
- [24] J. Y. Garretón, R. G. Rodriguez, , A. Ruiz, A. E. Pattini, “Degree of eye opening: a new discomfort glare indicator”, *Building and Environment*, vol. 88, pp. 142-150, 2015.
- [25] H. Yılmaz, S. Özer, “Gürültü kirliliğinin peyzaj planlama yönünden değerlendirilmesi ve çözüm önerisi,” *Atatürk Üniversitesi Ziraat Fakültesi Dergisi*, vol. 28, no. 3, pp. 515-531, 1997.
- [26] A. Sarp, “Yapının iç çevresindeki gürültünün yapı biyolojisi açısından incelenmesi,” M.S. thesis, Yıldız Technical University, Türkiye, 2000.

- [27] E. İldeş, “Konfor koşullarının alışveriş merkezi çalışanları üzerindeki etkilerinin değerlendirilmesi; Edirne Erasta örneği,” M.S. thesis, Trakya University, Türkiye, 2019.
- [28] P. J. Lee, B. K. Lee, J. Y. Jeon, M. Zhang, J. Kang, “Impact of noise on self-rated job satisfaction and health in open-plan offices: A structural equation modelling approach”, *Ergonomics*, vol.59 no.2, pp. 222-234, 2016.
- [29] C. M. Mak, Y. P. Lui, “The effect of sound on office productivity”, *Building Services Engineering Research and Technology*, vol. 33, no. 3, pp. 339-345, 2012.
- [30] C. B. Danielsson, L. Bodin, C. Wulff, T. Theorell, “The relation between office type and workplace conflict: a gender and noise perspective”, *Journal of Environmental Psychology*, vol. 42, pp. 161-171, 2015.
- [31] E. B. Gökmeral, “Sürdürülebilir ve bütünleşik bina tasarım süreçlerinde iç mimarlık: ofis binalarında sürdürülebilirliğin bir tamamlayıcısı olarak iç mimarlık disiplininden yararlanmaya odaklı bir araştırma” M.S. Thesis, Mimar Sinan Fine Arts University, Türkiye, 2014.
- [32] P. Wargocki, D. P. Wyon, P. O. Fanger, “Productivity is affected by the air quality in offices” In *Proceedings of Healthy Buildings*, vol. 1 no. 1, pp. 635-40, 2000.
- [33] R. S. Bridger, “Introduction to ergonomics”, McGraw Hill Inc, New York: ABD, 1995.
- [34] K. Karl, K. Henrike, K. Kroemer, “Ergonomics: How to design for ease and efficiency,” Prentice Hall, 2000.
- [35] C. Toka, “İnsan-araç bağıntısında ergonomik tasarım ilkeleri,” İstanbul Devlet Güzel Sanatlar Akademisi Basımevi, İstanbul: Türkiye, 1978.
- [36] I. Rivilis, D. Van Eerd, K. Cullen, D. C. Cole, E. Irvin, J. Tyson, Q. Mahood, “Effectiveness of participatory ergonomic interventions on health outcomes: A systematic review”, *Applied ergonomics*, vol. 39 no. 3, pp. 342-358, 2008.
- [37] S. Brewer, D. V., Eerd, B. C. Amick Iii, E. Irvin, K. M. Daum, F. Gerr, D. Rempel, “Workplace interventions to prevent musculoskeletal and visual symptoms and disorders among computer users: A systematic review”, *Journal Of Occupational Rehabilitation*, vol. 16, pp. 317-350, 2006.
- [38] Y. Terzi, “SPSS ile İstatistiksel Veri Analizi”, OMÜ Fen Edebiyat Fakültesi, Samsun, Jan 2, 2023. [online]. <https://avys.omu.edu.tr/storage/app/public/yukselt/133061/%C4%B0PP2.pdf>
- [39] B.G. Tabachnick, L. S. Fidell, “Using multivariate statistics”, Pearson, Boston 2013.

Investigation of Biofilm Production and Determination of Antibiotic Resistance Profile of *Staphylococcus aureus* Isolated from Ground Beef and Meatballs

Tuğba Sarı¹ , Ceren Başkan^{2*} 

¹ Amasya University, Sciences Institute, Department of Biology, Amasya, Türkiye, tubiyus.6836@gmail.com

² Amasya University, Sabuncuoğlu Şerefeddin Health Services Vocational School, Amasya, Türkiye, ceren.yavuz@amasya.edu.tr

* Corresponding Author

ARTICLE INFO

ABSTRACT

Keywords:

Antibiotic resistance
Biofilm
Ground beef
Meatballs
S. aureus



Article History:

Received: 15.10.2023

Accepted: 13.03.2024

Online Available: 06.06.2024

Staphylococcus aureus (*S. aureus*) is bacterium that threatens public health because it causes infections and food intoxication. For this reason, within the scope of this study, it was aimed to determine the presence of *S. aureus*, antibiotic resistance profiles, and biofilm formation in ground beef and meatball samples consumed in Amasya. In the study, 60 meat samples purchased from Amasya were used as material. First, conventional culture technique and PCR testing were used for the isolation of *S. aureus*. Secondly, antibiotic resistance profiles of the *S. aureus* were analyzed by disc diffusion. Finally, biofilm production of the *S. aureus* was analyzed phenotypically by the microtiter plate method and genotypically by PCR. Through the study, we identified 58 *S. aureus* isolates that were confirmed phenotypically and genotypically. Disc diffusion results showed that all *S. aureus* were sensitive to imipenem and piperacillin-tazobactam, but resistant to methicillin 43.10% (25/58), erythromycin 41.37 % (24/58), penicillin 58.62% (34/58), gentamicin 10.34% (6/58), chloramphenicol 17.24% (10/58), tobramycin 6.89% (4/58), and levofloxacin 1.72% (1/58). Biofilm production was determined as 58.62% (34/58) in the microtiter plate. In the PCR analysis, the *icaA* or *icaD* gene of a total of 4 (6.89%) different isolates was evaluated as positive. As a result, the presence of antibiotic-resistant *S. aureus* in ground beef and meatballs and the production of biofilm by the bacteria pose a potential risk. Therefore, it is important for human health to take the necessary precautions to reduce the risk of *S. aureus* contamination during the processing, and transportation.

1. Introduction

Foodborne diseases, which the World Health Organization (WHO) defines as a disease caused by infectious pathogens or toxins thought to be caused by the consumption of contaminated food or water, are an important public health concern around the world [1]. Another important public health problem is that pathogens that gain resistance to antibiotics in foodborne infections transfer these resistance genes through horizontal gene transfer [2, 3]. Infections caused by antibiotic-resistant bacteria through foods spread rapidly in society, causing serious economic losses, and infections with high morbidity and mortality [4, 5]. Antibiotic resistance (AMR) is

increasing rapidly around the world through food. According to the latest data from underdeveloped and developed countries, it has been determined that approximately 10% of the population suffers from foodborne diseases [6-8].

S. aureus is a pathogen that plays a role in foodborne infections and intoxications. Staphylococcal food poisoning from food contaminated with enterotoxins of *S. aureus* is a common cause of gastroenteritis. Staphylococcal foodborne poisoning has a short incubation period and is characterized by symptoms such as weakness, vomiting, and diarrhea [9-12]. The human nose is the largest ecological reservoir of

S. aureus, an opportunistic pathogen involved in many life-threatening disease processes such as skin and soft tissue infections, toxic shock syndrome, sepsis, pneumonia, etc. [13, 14]. Most of the food contamination from *S. aureus* is through contact with food handlers who are carriers. Today, the presence of methicillin-resistant *S. aureus* in addition to many antibiotics reduces the treatment rate of food-borne intoxications. Products such as milk and meat, which we frequently consume in terms of health, are among the foods most frequently contaminated with *S. aureus* [15]. Contamination with raw meat can occur at many stages, from the cutting stage to distribution, storage, etc. the vegetative form *S. aureus* can die with proper cooking techniques. However, Staphylococcal enterotoxins are thermostable and therefore cannot be destroyed by thermal processes [16, 17].

The surface of foods with high protein content such as meat are environments where pathogenic microorganisms such as *S. aureus* can come together and form a biofilm by surrounding them with extracellular polymeric substance (EPS). This leads to cross-contamination, reduced shelf life of foods and the potential for foodborne illness. Bacterial biofilms cause problems in food sanitation because they are resistant to environmental stresses. In addition, biofilms that will form in various equipment used in the food industry cause surface corrosion and financial problems. Therefore, elucidating the structure for the removal and inhibition of *S. aureus* biofilms is an area of public health interest [18].

As a result of the literature review, the focus was on determining the antibiotic resistance profile and biofilm production of *S. aureus* isolates, which are mostly responsible for hospital-acquired infections [19-21]. In foods, there are studies to determine the prevalence and antibiotic resistance of *S. aureus*, which is generally isolated from dairy products, especially traditional cheese [22-24]. However, studies conducted to determine the prevalence and antibiotic resistance of *S. aureus* in meat samples in Turkey are limited. Among these, no studies were found to determine the biofilm production genotypically [15, 25]. For this reason, it is important to carry out studies on these issues to

prevent food infections caused by *S. aureus*. In the present study, the aim of this study is to determine the antibiotic resistance profiles of *S. aureus* isolates isolated from ground beef and meatball samples and to analyze their biofilm production phenotypically and genotypically.

2. Materials and Methods

2.1. Food samples

In this study, a total of 60 samples (30 ground beef, and 30 meatballs) were purchased from different butchers and supermarkets in Amasya between February and July 2022. The samples were brought to the biological activity laboratory of Amasya University by keeping the cold chain in line with aseptic techniques.

2.2. Isolation of *S. aureus*

The methods used in the isolation of *S. aureus* in the samples previously for the isolation of bacteria from foods were taken as reference [15, 26]. For this purpose, firstly, decimal dilutions (10^{-1} , 10^{-2} , 10^{-3}) of the samples were made with buffered peptone water (0.1%, Biolife, Milano, Italya-4122592), and then spread on Baird Parker Agar (BPA, Biolife, Milano, Italya-NL6209) containing with 5% egg yolk tellurite (Merck, Darmstadt, Germany-K95798185) using the spread plating technique. The plates incubated at 37 °C for 24-48 hours. Then, three or five colonies were selected from lecithinase positive, black, and bright colonies and inoculated on tryptic soy agar (TSA, Merck, Darmstadt, Germany-105458) for phenotypic (Gram stain, catalase test, growth on mannitol salt agar, and coagulase test) and genotypic identification.

2.3. Genotypic identification of isolates and PCR analysis of biofilm-encoding genes

DNA was isolated by boiling from overnight cultures formed by inoculating phenotypically confirmed isolates as *S. aureus* on TSA agar. A colony growing on TSA was taken and homogenized in 500 µl sterile distilled water. Then it was kept in a dry block heater at 95 °C for 15 minutes. Finally, it was centrifuged at 10,000 g for 5 minutes and the supernatant containing genomic DNA was taken into a clean

tube and kept at -20 °C for further studies [27]. For genotypic validation of isolated isolates, PCR was performed using primers of the genus specific (*Staphylococcus* spp.) 16S rRNA gene (756F:5' AACTCTGTTATTAGGGAAGAACA3' and 756R:5' CCACCTTCCTCCGGTTTGTACC 3') and the *nuc* gene (F: 5' GCGATTGATGGTGATACGGTT3' and R: 5' AGC CAA GCC TTG ACG AAC TAA AGC3') encoding the *S. aureus* specific thermonuclease enzyme [28, 29]. The *icaA* (F: 5' CCTAACTAACGAAAGGTAG3' and R: 5' AAGATATAGCGATAAGTGC3') and *icaD* (F: 5'AAACGTAAGAGAGGTGG3' and R: 5' GGCAATATGATCAAGATAC3') genes responsible for biofilm production of isolates, was determined by PCR [30]. After PCR, Amplicons were separated by molecular size by electrophoresis using 1% Agarose (biomax). After electrophoresis, it was visualized with a UV transilluminator.

2.4. Disc diffusion testing

The antibiotic resistance profile of isolates was performed by disc diffusion test according to CLSI criteria [31]. Overnight cultures of *S. aureus* isolates were set to 0.5 McFarland in sterile 0.9% NaCl and cultured on a Mueller-Hinton agar (MHA, Biolife, Milano, Italy-4017402500) surface. Commercially purchased antibiotic discs [levofloxacin (LEV; 5 µg, ASD04800), tobramycin (TOB; 10 µg, ASD09201), gentamicin (CN; 10 µg, ASD04405), imipenem (IPM; 10 µg, ASD04500), piperacillin-tazobactam (PTZ; 100/10) µg, ASD07620), penicillin (P; 10 µg, ASD07400), methicillin (ME, 5 µg, ASD05430), erythromycin (E; 15 µg, ASD03700) Bioanalyse Ltd., Turkey] were placed on MHA medium with a sterile forceps at appropriate intervals and incubated at 35 °C for 18 hours. The results were evaluated as susceptible, intermediate, and resistant. *S. aureus* ATCC 25923 was used as a reference.

2.5. Quantification of the biofilm production test

Biofilm production of isolates was determined quantitatively by the flat bottomed 96-well microtiter plate method. For this purpose,

overnight *S. aureus* cultures were brought to 0.5 McFarland in sterile 0.9% NaCl solution and diluted 1/50 rate. 150 µl of the prepared bacterial suspensions were inoculated into the wells of 96-well microtiter plates and incubated at 37°C for 24 hours. At the end of the incubation time, the broth was drained from the wells and washed three times with phosphate buffer. For fixation purposes, 99% methanol was added to the wells and kept at 25 °C for 15 minutes.

After this time, methanol was drained from the wells and dried. To stain the bacterial growth in the biofilm, 150 µL of 0.1% crystal violet was added to the wells and kept at 25 °C for 15 minutes. After incubation, the dye was drained from the wells and washed three times with distilled water so that the biofilm layer was not damaged. The wells were dried by inverting the plate. To dissolve the formed biofilm layer, 150 µL of ethanol-acetone (80:20) was added to the wells and allowed to stand for 15 minutes. Measurement was made in the microplate reader by adjusting the wavelength to 570 nm [22, 32].

3. Result

A total of 60 meat samples (30 meatballs, 30 ground beef) were analyzed in the study. Approximately 4 or 5 colonies with typical *Staphylococcus* sp. morphology (2-3 mm in diameter, black or gray in color, mostly opaque in appearance, convex, lecithinase positive) were selected on the agar.

From the isolates examined, 297 *Staphylococcus* spp. were isolated and 58 (19.52%, 32 meatball, 26 ground beef) of these isolates were determined to be *S. aureus* phenotypically (Gram staining, catalase, growth on mannitol salt agar, and coagulase test) and genotypically (16S rRNA, *nuc* genes). Photographs of the data from the phenotypic tests are shown in Figure 1. Lecithinase positive, black and shiny colonies were selected on Baird Parker agar, and as a result of phenotypic tests, Gram positive, coagulase and catalase positive, yellow colonies on mannitol salt agar were identified as *S. aureus*.

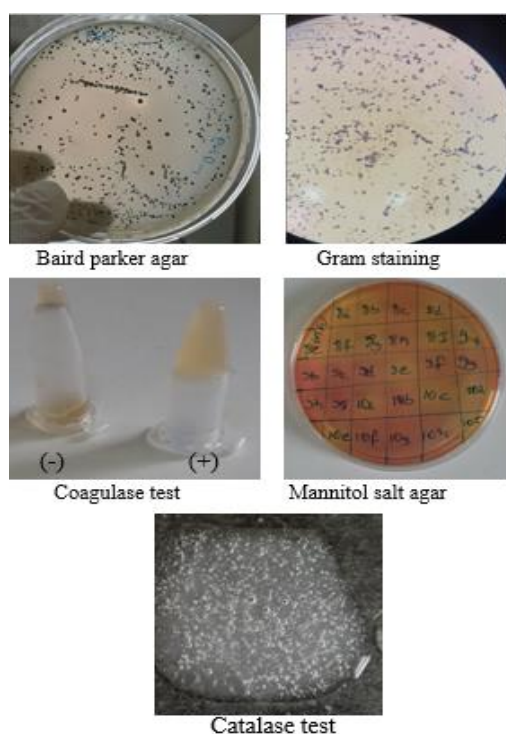


Figure 1. Phenotypic test results of *S. aureus*

From genotypic tests, the presence of the genus-specific 16S rRNA gene region and the species-specific *nuc* gene encoding the thermonuclease enzyme specific to these isolates was determined in 58 isolates. *S. aureus* strain was detected in all 58 isolates examined (Figure 2).

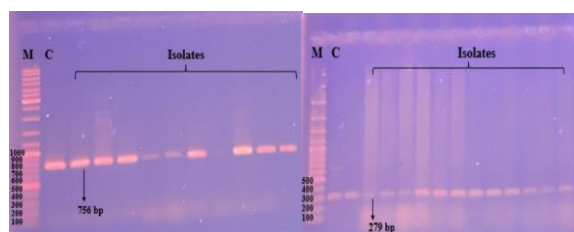


Figure 2. PCR results to confirm genotypic identification of *S. aureus* isolates. 16S rRNA (756 bp), *nuc* gene (279 bp), M: Marker (100 bp) C: Control, *S. aureus* ATCC 25923

As a result of the disc diffusion test, it was determined that at least one of the 58 isolates was resistant to the others except imipenem and piperacillin tazobactam antibiotics. Additionally, of the isolates, 34 (58.62%), 25 (43.10%), 24 (41.37%), 10 (17.24%), 6 (10.34%), 4 (6.89%), and 1 (1.72%) showed resistance (intermediate resistance or resistance) to penicillin, methicillin, erythromycin, chloramphenicol, gentamicin, tobramycin, and levofloxacin, respectively (Table 1).

Biofilm production of a total of 58 isolates was determined by 2 different methods. It was determined that 34 (58.62%) and 4 (6.89%) isolates formed biofilm using microtiter plate and genotypic (determination of *icaA* and *icaD* genes) methods, respectively. The biofilm production value of the isolate used as a reference in the microtiter plate test was read with a multiplate reader and the OD 0.7593 value was obtained. Afterwards, the OD values of the isolates were analyzed and the biofilm production of 34 (58.62%) isolates with a value higher than the positive control (>0.7593) was accepted as positive (Figure 3).

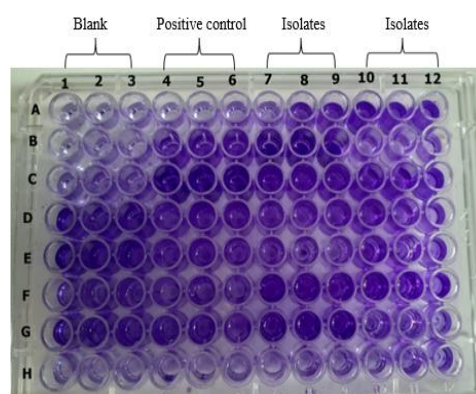


Figure 3. Biofilm formation of *S. aureus* in microtitration plate. It was repeated at least three times for each isolate.

Genotypically, it was determined that 2 isolates had the *icaA* gene and 3 isolates had the *icaD* gene. It was determined that there are 4 (6.89%) different isolates with at least one gene (*icaA* or *icaD*) (Figure 4).

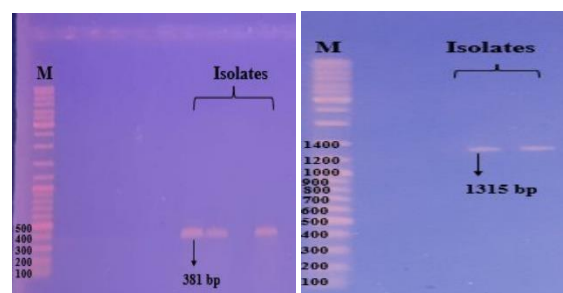


Figure 4. Biofilm production tests of *S. aureus* isolates. *icaD* gene (381 bp), *icaA* gene (1315 bp), M: Marker (100 bp)

Table 1. Antibiotic resistance profiles of *S. aureus* isolates

	<i>S. aureus</i> isolates (N=58)					
	R		I		S	
	n	%	n	%	n	%
C	10	17.24	-	-	48	82.75
CN	5	8.62	1	1.72	52	89.65
E	21	36.20	3	5.17	34	58.62
IPM	-	-	-	-	100	100
LEV	1	1.72	-	-	57	98.27
ME	3	5.17	22	37.93	33	56.89
P	34	58.62	-	-	24	41.37
TPZ	-	-	-	-	100	100
TOB	3	5.17	1	1.72	54	93.10

C: Chloramphenicol, CN: Gentamicin, E: Erythromycin, IPM: Imipenem, LEV: Levofloxacin, ME: Methicillin, P: Penicillin, TOB: Tobramycin, TPZ: Piperacillin-Tazobactam R: Resistant, I: Intermediate resistant, S: Sensitive.

4. Discussion

Meat, consumed throughout the world, is a rich source of many nutrients, especially protein and fat, which are essential for the human body [33]. However, its rich protein content provides a culture medium for the growth of microorganisms. Microbial contamination in meat can occur not only due to poor production practices, but also from food-producing animals, as well as food handlers who are carriers [34, 35]. Pathogens such as *Bacillus* spp., *Escherichia coli*, and *S. aureus* can cause contamination of meat. Among these pathogens, *S. aureus* is one of the pathogens that play a particularly important role in food-borne poisoning. However, its prevalence varies among different foods, animals, and countries [26, 35, 36].

In this study, 58/297 (19.52%) of the bacteria isolated from the ground beef and meatball samples examined bacteriologically were determined to be phenotypically and genotypically *S. aureus*. Previous studies conducted in different countries reported the percentage of positive *S. aureus* isolates in ground beef in Greece to be 26.31% [37], 36% in Iran [38], 26.22% in Iran [26], 16% in Egypt [7], 33.08% in Africa [35] 12.5% in Turkey [39], 21.23% in the Turkey [15]. Interestingly, in another study conducted in Turkey, they determined the prevalence of *S. aureus* obtained from meat and meatball to be as high as 96.2% and 89.1%, respectively [40]. When the study

results obtained from different countries or the same countries are examined, differences in the prevalence of *S. aureus* may be caused by people working in the food industry being carriers, not paying attention to hygiene rules during meat slaughter, and contamination during the transportation and storage of meat [35].

Today, the intensive and unconscious use of antibiotics has become a worldwide problem. Intensive use of antibiotics, especially on animals, causes antibiotic residues to form in animal foods and the proliferation of resistant bacteria. Antibiotic resistance genes found in antibiotic-resistant bacteria in foods can be transferred through the food chain. The spread of antibiotic-resistant bacteria causes foodborne infections that are difficult to treat [38, 41].

Intensive use of the antibiotic methicillin, especially in infections caused by *S. aureus*, has led to an increase in the number of methicillin-resistant *S. aureus*. This could lead to an antibiotic resistance crisis that could cause fatal infections worldwide. The presence of livestock-associated MRSA is a concern in cases of staphylococcal food poisoning [36]. Therefore, it is important to investigate the prevalence of *S. aureus* in foods and determine antibiotic resistance profiles to prevent foodborne infections. Studies in the literature have focused on certain groups of antibiotics to determine the antibiotic resistance of *S. aureus* isolates [36, 42, 43].

Unlike studies in the literature, in this study, the resistance profile of *S. aureus* against 9 different antibiotics (chloramphenicol, gentamicin, erythromycin, imipenem, levofloxacin, methicillin, penicillin, tobramycin, piperacillin-tazobactam) was determined. In this study, all *S. aureus* were sensitive to imipenem, a carbapenem antibiotic, and piperacillin tazobactam, a combination beta-lactamase inhibitor. In contrast, it was determined that the isolates showed the highest resistance (resistant or moderately resistant) to erythromycin, methicillin, and penicillin among the antibiotics used. High penicillin G resistance in *S. aureus* isolates isolated from meat samples has been reported in other studies conducted in Turkey as well as in studies conducted in countries around

the world such as Greece, Nigeria, Iran, China, and Italy [15, 25, 36-38, 44, 45]. A high rate of resistance has recently been detected in *S. aureus* isolates against macrolide group antibiotics [46]. In this study, erythromycin, a macrolide group antibiotic, was used and 24 of the isolates (41.37%) were found to be resistant. Hasanpour et al. determined that *S. aureus* isolates obtained from beef in Iran were 37.50% resistant to erythromycin.

Additionally, in the same study, it was reported that the isolates were resistant to 12 different antibiotics (ampicillin, ceftriaxone, amoxicillin-clavulanic acid, tetracycline, azithromycin, oxacillin, and penicillin) [47]. Another study conducted in Nigeria reported that *S. aureus* isolates had a 15.70% resistance rate to erythromycin [48]. According to CLSI criteria, cefoxitin antibiotic is preferred over oxacillin antibiotic in determining methicillin resistance due to more reproducible results. In our study, MRSA resistance of *S. aureus* isolates was not detected. However, the resistance profile of *S. aureus* isolates against the antibiotic methicillin was determined [49]. In this study, *S. aureus* isolates were found to be highly resistant to 25 (43.10% resistant or moderately resistant) methicillin antibiotics. The main reason for the difference observed between studies in the literature may be the difference in antibiotic groups used in the treatment of infections caused by *S. aureus*, especially in food-producing animals, in different geographical regions.

The ability of *S. aureus* to cause infection is increased by the ability of the bacterium to form biofilm, which is the extracellular matrix layer, an important virulence factor [50]. In the food industry, data on biofilm production of *S. aureus* isolates are limited. It is known that *S. aureus* isolates can form biofilms by spreading on foods of animal origin and equipment in the food slaughtering environment, such as slaughterhouses. It is known that after biofilm production, its resistance to various disinfectants and antibiotics increases and creates a basis for cross contamination [51].

Various phenotypic and genotypic methods are used to detect biofilm production, such as standard tube, Congo Red Agar, microtiter plate

methods and molecular validations [52, 53]. In this study, biofilm production was detected by the microtiter plate method, which is a phenotypic test, and the genotypic method. According to the OD values obtained according to the microtiter method, we found that 34 of 58 *S. aureus* isolates (58.62%) formed biofilms. In studies conducted in the literature, it was determined that biofilm production according to the microtiter method was 50%, 60% and 95.5% in *S. aureus* isolates originating from milk [54], chicken meat [55] and ground beef [37], respectively. Poly-N acetyl β 16 glucosamine (PNAG) surface polysaccharide, which is involved in intercellular adhesion of the biofilm layer and synthesized by proteins encoded by the intercellular adhesion operon (*icaADBC* genes), is an important structure. In this study, biofilm production of *S. aureus* isolates was analyzed by PCR targeting *icaA* and *icaD*. In PCR analysis, the presence of the *icaA* gene was detected in only 2 isolates and the *icaD* gene was detected in 3 isolates.

Various studies have stated that biofilm production is associated with the presence of *icaA* and *icaD* genes, especially for *S. aureus* isolates responsible for hospital-acquired infections or for *S. aureus* isolates isolated from daily milk and dairy products. There are very few studies on whether *S. aureus* isolates of meat origin genotypically produce biofilm. Therefore, the relationship between biofilm production and *ica* genes examined in the study can be evaluated in the light of data obtained from isolates other than ground beef and meatballs [30, 53, 56]. This is necessary because there is little data on these parameters for isolates originating from ground meat and meatballs. The results in this study were in contrast to Prenafeta et al. who reported that the *icaA* and *icaD* genes were positive in all isolates [54].

Vasudevan et al isolated 35 *S. aureus* from bovine mastitis. They reported that although a total of 24 of these isolates produced slime phenotypically, all of them had the *ica* locus [30]. Abbasi et al. determined that *S. aureus* isolates contained 65.38%, 57.69%, 50% and 42.30% of *icaD*, *icaA*, *icaB* and *icaC* genes, respectively [26]. Similar to our study, Avila-Novoa et al. reported that while biofilm production was

detected at a rate of 90.4% according to the microtiter plate method, the rate of isolates with *icaA* and *icaD* genes was much lower (4, 5.1%) [57]. These results show that *S. aureus* strains may have biofilm-forming capacities at different rates depending on the source from which they are isolated (human or food). In addition, other gene regions (*icaB* and *icaC*) need to be analyzed in order to obtain a clear result regarding genotypic biofilm production.

5. Conclusion

According to the findings of the current study, ground beef and meatball samples consumed in Amasya province of Turkey were found to be highly contaminated with *S. aureus*. As a result of the disc diffusion test, it was seen that some isolates were resistant to antibiotics. The possibility of other bacteria becoming resistant through mobile genetic elements as a result of widespread horizontal gene transfers between bacteria may be a concern for health and food safety.

The fact that more *S. aureus* isolates were obtained in meatball samples than in ground meat samples in the study reveals that hygiene rules are not taken into consideration, especially during the processing of food, and the possibility of contamination by carrier food handlers. Contamination caused by *S. aureus* can be reduced, especially by improving hygiene conditions. In addition, biofilm production of *S. aureus* isolates is a source of risk for the food industry. Therefore, in terms of public health, animal food samples should be examined at regular intervals for antibiotic resistance, and it is important to take the necessary sanitation and hygienic measures.

Article Information Form

Funding

The author (s) has no received any financial support for the research, authorship or publication of this study.

Authors' Contribution

The authors contributed equally to the study.

The Declaration of Conflict of Interest/ Common Interest

No conflict of interest or common interest has been declared by the authors.

The Declaration of Ethics Committee Approval

This study does not require ethics committee permission or any special permission.

The Declaration of Research and Publication Ethics

The authors of the paper declare that they comply with the scientific, ethical and quotation rules of SAUJS in all processes of the paper and that they do not make any falsification on the data collected. In addition, they declare that Sakarya University Journal of Science and its editorial board have no responsibility for any ethical violations that may be encountered, and that this study has not been evaluated in any academic publication environment other than Sakarya University Journal of Science.

Copyright Statement

Authors own the copyright of their work published in the journal and their work is published under the CC BY-NC 4.0 license.

References

- [1] S. Parvin, Y. Ali, S. Talukder, A. Nahar, E. H. Chowdhury, T. Rahman, T. Islam, "Prevalence and multidrug resistance pattern of methicillin resistant *S. aureus* isolated from frozen chicken meat in Bangladesh," *Microorganisms*, vol. 9, no. 3, pp. 636, 2021.
- [2] S. Karimi, H. Momtaz, "Molecular typing, phenotypic and genotypic assessment of antibiotic resistance and virulence factors amongst the *Staphylococcus aureus* bacteria isolated from raw chicken meat," *Molecular Genetics, Microbiology and Virology*, vol. 37, no. 4, pp. 226-241, 2022.
- [3] D. Bae, D. M. Macoy, W. Ahmad, S. Peseth, B. Kim, J. W. Chon, G. R. Ryu, G. H. Ban, S. A. Kim, H. J. Kang, J. S. Moon, M. G. Kim, "Distribution and characterization of antimicrobial resistant pathogens in a pig farm, slaughterhouse,

- meat processing plant, and in retail stores,” *Microorganisms*, vol. 10, no. 11, pp. 2252, 2022.
- [4] World Health Organization (2021), “Global Antimicrobial Resistance and Use Surveillance System (GLASS)”, Available at: <https://www.who.int/publications/item/9789240027336>.
- [5] Q. Tao, Q. Wu, Z. Zhang, J. Liu, C. Tian, Z. Huang, P. K. Malakar, Y. Pan, Y. Zhao, “Meta-analysis for the global prevalence of foodborne pathogens exhibiting antibiotic resistance and biofilm formation,” *Frontiers in Microbiology*, vol. 13, pp. 906490, 2022.
- [6] J. Kim, J. Ahn, “Emergence and spread of antibiotic-resistant foodborne pathogens from farm to table,” *Food Science and Biotechnology*, vol. 31, no. 12, pp.1481-1499, 2022.
- [7] V. K. Ahmed, I. M. Helal, M. M. Zaky, M. Abdulla, “Antimicrobial activity of *Actinomycetes* extracts against multidrug-resistant *Staphylococcus aureus* and *Salmonella* spp. isolated from meat,” *Alfarama Journal of Basic & Applied Sciences*, vol. 3, no. 2, pp. 283-299, 2022.
- [8] T. Asfaw, D. Genetu, D. Shenkute, T. Shenkutie, Y. E. Amare, B. Yitayew, “High levels of multidrug-resistant and beta-lactamase-producing bacteria in meat and meat contact surfaces, Debre Berhan Town, Ethiopia,” *Infection and Drug Resistance*, vol. 16, no. 1, pp. 1965-1977, 2023.
- [9] M. G. Basanisi, G. Nobili, G. La Bellaa, R. Russo, G. Spano, G. Normanno, G. La Salandraa, “Molecular characterization of *Staphylococcus aureus* isolated from sheep and goat cheeses in southern Italy,” *Small Ruminant Research*, vol. 135, pp. 17-19, 2016.
- [10] A. Fetsch, S. Joler, “*Staphylococcus aureus* as a foodborne pathogen,” *Current Clinical Microbiology Reports*, vol. 5, pp. 88–96, 2018.
- [11] M. Yousefi, M. Farshidi, M. A. Sani, L. Payahoo, “Investigation of the microbial quality and the occurrence of Shiga-like-toxin-producing *Escherichia coli* and methicillin resistant *Staphylococcus aureus* in traditional cheeses produced in northwest of Iran,” *Nutrition & Food Science*, vol. 3, pp. 407-417, 2018.
- [12] S. Gürbüz, Ç. Güngör, “Determination of some foodborne pathogens and residual nitrate and nitrite in traditional fermented sausages in Turkey,” *International Food Research Journal*, vol. 27, no. 1, pp. 39-46. 2020.
- [13] P. Visciano, F. Pomilio, R. Tofalo, L. Sacchini M. A Saletti, E. Tieri, M. Schirone, G. Suzzi, “Detection of methicillin resistant *Staphylococcus aureus* in dairy cow farms,” *Food Control*, vol. 46, pp. 532-538, 2014.
- [14] J. M. Kwiecinski, A. R. Horswill, “*Staphylococcus aureus* bloodstream infections: pathogenesis and regulatory mechanisms,” *Current Opinion in Microbiology*, vol. 53, pp. 51-60, 2020.
- [15] P. Şanlıbaba, “Prevalence, antibiotic resistance, and enterotoxin production of *Staphylococcus aureus* isolated from retail raw beef, sheep, and lamb meat in Turkey,” *Internatol Journal Food Microbiology*, vol. 361, pp. 109461, 2022.
- [16] W. Sankomkai, W. Boonyanugomol, K. Kraisriwattana, J. Nutchanon, K. Boonsam, S. Kaewbutra, W. Wongboot, “Characterisation of classical enterotoxins, virulence activity, and antibiotic susceptibility of isolated from Thai fermented pork sausages, clinical samples, and healthy carriers in northeastern Thailand,” *Journal of Veterinary Research*, vol. 64, no. 2, pp. 289-297, 2020.
- [17] G. K. Sivaraman, S. S. Grupta, S. Visnuvinayagam, T. Muthulakshmi, R.

- Elangovan, V. Perumal, G. Balasubramaniam, T. Lodha, A. Yadav, "Prevalence of *S. aureus* and/or MRSA from seafood products from Indian seafood products," *BMC Microbiology*, vol. 22, no. 1, pp. 233, 2022.
- [18] N. Guo, B. Xue, Y. Shen, T. Zhang, "Target-based screening for natural products against *Staphylococcus aureus* biofilms," *Critical reviews in Food Science and Nutrition*, vol. 63, no. 14, pp. 2216-2230, 2023.
- [19] M. T. Kashef, N. M. Saleh, N. H. Assar, M. A. Ramadan, "The antimicrobial activity of ciprofloxacin-loaded niosomes against ciprofloxacin-resistant and biofilm-forming *Staphylococcus aureus*," *Infection and Drug Resistance*, vol. 13, pp. 1619-1629, 2020.
- [20] S. Derakhshan, M. Navidinia, F. Haghi, "Antibiotic susceptibility of human associated *Staphylococcus aureus* and its relation to agr typing, virulence genes, and biofilm formation," *BMC Infectious Diseases*, vol. 21, pp. 627, 2021.
- [21] C. Wang, Y. Xiong, C. Bao, Y. Wei, Z. Wen, X. Cao, Z. Yu, X. Deng, G. Li, Q. Deng, "Antibacterial and anti-biofilm activity of radezolid against *Staphylococcus aureus* clinical isolates from China," *Frontiers in Microbiology*, vol. 14, pp. 1131178, 2023.
- [22] J. Gajewska, W. Chajęcka-Wierżchowska, "Biofilm formation ability and presence of adhesion genes among coagulase-negative and coagulase-positive *Staphylococci* isolates from raw cow's milk," *Pathogens*, vol. 9, no. 8, pp. 654, 2020.
- [23] J. Gajewska, W. C. Wierżchowska, A. Zaderowska, "Occurrence and characteristics of *Staphylococcus aureus* strains along the production chain of raw milk cheeses in Poland," *Molecules*, vol. 27, no. 19, pp. 6569, 2022.
- [24] D. Ashraf, R. A. Ombarak, A. Samir, A. B. Abdel-Salam, "Characterization of multidrug-resistant potential pathogens isolated from milk and some dairy products in Egypt," *Journal of Advanced Veterinary and Animal Research*, vol. 10, no. 2, pp. 275-283, 2023.
- [25] T. Cebeci, N. Gündoğan, "Enterotoxin production and antibiotic resistance profile of *Staphylococcus aureus* isolated from meat samples," *Hitit Medical Journal*, vol. 3, no. 2, pp. 13-19, 2021.
- [26] K. Abbasi, E. Tajbakhsh, H. Momtaz, "Antimicrobial resistance, virulence genes, and biofilm formation in *Staphylococcus aureus* strains isolated from meat and meat products," *Journal of food safety*, vol. 41, no. 2, pp. 1-10, 2021.
- [27] S. Yoon, Y. K. Park, T. S. Jung, S. B. Park, "Molecular typing, antibiotic resistance and enterotoxin gene profiles of *Staphylococcus aureus* isolated from humans in South Korea," *Microorganisms*, vol. 10, no. 3, pp. 642, 2022.
- [28] K. Zhang, J. Sarling, B. L. Chow, S. Elsayed, Z. Hussain, D. L. Church, D. B. Gregson, T. Louie, J. M. Conly, "New quadruplex PCR assay for detection of methicillin resistance and simultaneous discrimination of *S. aureus* from coagulase-negative *Staphylococci*," *Journal Clinical Microbiology*, vol. 42, no. 11, pp. 4947-4955, 2004.
- [29] J. A. McClure, J. M. Conly, V. Lau, S. Elsayed, T. Louie, W. Hutchins, K. Zhang, "Novel multiplex PCR assay for detection of the *Staphylococcal* virulence marker Panton-Valentine leukocidin genes and simultaneous discrimination of methicillin-susceptible from resistant *Staphylococci*," *Journal Clinical Microbiology*, vol. 44, no. 3, pp. 1141-1144, 2006.
- [30] P. Vasudevan, M. K. M. Nair, T. Annamalai, K. S. Venkitanarayanan, "Phenotypic and genotypic characterization of bovine mastitis isolates

- of *Staphylococcus aureus* for biofilm formation,” *Veterinary Microbiology*, vol. 92, no. 1-2, pp.179-185, 2003.
- [31] Clinical laboratory standart institute, (CLSI), “Performance Standards for antimicrobial susceptibility testing. Twentieth edition,” Informational Supplement M100-S22, Wayne, PA, 2012.
- [32] T. Saba, M. Sajid, A. A. Khan, R. Zahra, “Role of intracellular adhesion *icaAD* and *agr* genes in biofilm formation in clinical *S. aureus* isolates and assessment of two phenotypic methods,” *Pakistan Journal of Medical Science*, vol. 34, no. 3, pp. 633-637, 2018.
- [33] K. Kolodziejczak, A. Onopiuk, A. Szpicer, A. Poltorak, “Meat analogues in the perspective of recent scientific research: a review,” *Foods*, vol. 11, no. 1, pp. 105, 2022.
- [34] L. Grispoli, P. A. Popescu, M. Karama, V. Gullo, G. Poerio, E. Borgogni, P. Torlai, G. Chianese, A. G. Fermani, P. Sechi, B. Cenci-Goga, “Study on the growth and enterotoxin production by *Staphylococcus aureus* in canned meat before retorting,” *Toxins*, vol. 11, no. 5, pp. 291, 2019.
- [35] T. Thwala, E. Madoroba, A. Basson, P. Butaye, “Prevalence and characteristics of *Staphylococcus aureus* associated with meat and meat products in African countries: a review,” *Antibiotics*, vol. 10, no. 9, pp. 1108, 2021.
- [36] E. O. Igbinosa, A. Beshiru, I. H. Igbinosa, A. G. Ogofure, T. C. Ekundayo, A. I. Okoh, “Prevalence, multiple antibiotic resistance and virulence profile of methicillin resistant *Staphylococcus aureus* (MRSA) in retail poultry meat from Edo, Nigeria,” *Frontiers in Cellular and Infection Microbiology*, vol. 13, pp. 1122059, 2023.
- [37] D. Komodromos, C. Kotzamanidis, V. Giantzi, S. Pappa, A. Papa, A. Zdragas, A. Angelidis, D. Sergelidis, “Prevalence, infectious characteristics and genetic diversity of *Staphylococcus aureus* and methicillin-resistant *Staphylococcus aureus* (MRSA) in two raw-meat processing establishments in Northern Greece,” *Pathogens*, vol. 11, no. 11, pp. 1370, 2022.
- [38] M. Rajaei, M. H. Moosavy, S. N. Gharajalar, S. A. Khatibi, “Antibiotic resistance in the pathogenic foodborne bacteria isolated from raw kebab and hamburger: phenotypic and genotypic study,” *BMC Microbiology*, vol. 21, pp. 272, 2021.
- [39] E. Keyvan, H. Özdemir, “Sığır karkaslarında *Staphylococcus aureus*’un varlığı, enterotoksijenik özellikleri ve antimikrobiyal dirençliliği,” *Ankara Üniversitesi Veteriner Fakültesi Dergisi*, vol. 63, pp. 17-23, 2016.
- [40] N. Gündoğdu, A. Devren, “Protease and lipase activity of *Staphylococcus aureus* obtained from meat, chicken and meatball samples,” *Gazi University Journal of Science*, vol. 23, no. 4, pp. 381-384, 2010.
- [41] M. H. Chaia, T. A. M. Faiqa, S. M. Z. Ariffinb, Z. Suhailia, M. Z. Sukimana, M. F. Ghazali, “Prevalence of methicillin resistant *Staphylococcus aureus* in raw goat milks from selected farms in Terengganu, Malaysia,” *Tropical Animal Science Journal*, vol. 43, no. 1, pp. 64-69, 2020.
- [42] A. M. Edris, A. A. A. Maarouf, R. A. E. Amin, E. A. I. Bahbah, “Prevalence of *Staphylococci* in meat products with special reference to methicillin-resistant *Staphylococcus aureus* (MRSA) at Kaliobia Governorate,” *Benha Veterinary Medical Journal*, vol. 35, no. 2, pp. 364-374, 2018.
- [43] G. A. Ballash, A. L. Albers, D. F. Mollenkopf, E. Sechrist, R. J. Adams, T. E. Wittum, “Antimicrobial resistant bacteria recovered from retail ground meat products in the US include a *Raoultella*

- ornithinolytica* co-harboring *bla_{KPC-2}* and *bla_{NDM-5}*,” Scientific Reports, vol. 11, pp. 14041, 2021.
- [44] S. Wu, J. Huang, Q. Wu, J. Zhang, F. Zhang, X. Yang, H. Wu, H. Zeng, M. Chen, Y. Ding, J. Wang T. Lei, S. Zhang, L. Xue, “*Staphylococcus aureus* isolated from retail meat and meat products in China: incidence, antibiotic resistance and genetic diversity,” Frontiers in Microbiology, vol. 9, pp. 2767, 2018.
- [45] M. G. Basanisi, G. La Bella, G. Nobili, S. Tola, M. A. Cafiero, G. La Salandra, “Prevalence and characterization of methicillin-resistant *Staphylococcus aureus* (MRSA) isolates from retail meat in south Italy,” Italian Journal of Food Science, vol. 32, no. 2, pp. 410-419, 2020.
- [46] Z. T. Baghbaderani, A. Shakerian, E. Rahimi, “Phenotypic and genotypic assessment of antibiotic resistance of *Staphylococcus aureus* bacteria isolated from retail meat,” Infection and Drug Resistance, vol. 13, pp. 1339-1349, 2020.
- [47] D. A. Hasanpour, L. Khaji, S. M. Sakhaei, Z. Mashak, D. F. Safarpour, Y. Safaee, A. Hosseinzadeh, I. Alavi, E. Ghasem, F. M. Rabiei, “One-year prevalence of antimicrobial susceptibility pattern of methicillin-resistant *Staphylococcus aureus* recovered from raw meat,” Tropical Biomedicine, vol. 34, no. 2, pp. 396-404, 2017.
- [48] P. Fowoyo, S. Ogunbanwo, “Antimicrobial resistance in coagulase-negative *Staphylococci* from Nigerian traditional fermented foods,” Annals of Clinical Microbiology and Antimicrobial, vol. 16, no. 4, pp. 1-7, 2017.
- [49] A. Kılıç, E. Doğan, S. Kaya, M. Baysallar, “Yedi yıllık sürede klinik örneklerden izole edilen *Staphylococcus aureus* suşlarında *mecC* ve Panton-Valantine lökositin gen varlığının araştırılması,” Mikrobiyoloji Bülteni, vol. 49, no. 4, pp. 594-599, 2015.
- [50] R. Parastan, M. Kargara, K. Solhjooc, F. Kafilzadeh, “*Staphylococcus aureus* biofilms: structures, antibiotic resistance, inhibition, and vaccines,” Gene Reports, vol. 20, pp. 100739, 2020.
- [51] A. C. Silva-de-Jesus, R. G. Ferrari, P. Panzenhagen, C. A. ConteJunior, “*Staphylococcus aureus* biofilm: the role in disseminating antimicrobial resistance over the meat chain,” Microbiology, vol. 168, pp. 001245, 2022.
- [52] L. E. Alcaraz, S. E. Satorres, R. M. Lucero, O. N. P. Centorbi, “Species identification, slime production and oxacillin susceptibility in coagulase-negative staphylococci isolated from nosocomial specimens,” Brazilian Journal of Microbiology, vol. 34, no. 1, pp. 45-51, 2003.
- [53] A. Ciftci, A. Findik, E. E. Onuk, S. Savasan, “Detection of methicillin resistance and slime factor production of *Staphylococcus aureus* in bovine mastitis,” Brazilian Journal of Microbiology, vol. 40, no. 2, pp. 254-261, 2009.
- [54] A. Prenafeta, M. Sitjà, M. A. Holmes, G. K. Paterson, “Communication: Biofilm production characterization of *mecA* and *mecC* methicillin-resistant *Staphylococcus aureus* isolated from bovine milk in Great Britain,” Journal of Dairy Science, vol. 97, pp. 4838–4841, 2014.
- [55] A. E. M. A. Morshdy, A. E. Tharwat, A. M. A. Merwad, N. A. M. Abdallah, T. Saber, “Prevalence, phenotypic-genotypic resistance and biofilm formation of *Staphylococcus aureus* in chicken meat with reference to its public health hazard,” Veterinary Medicine and The One Health Concept, vol. 60, pp. 413–424, 2023.
- [56] M. E. A. Bissong, C. N. Ateba, “Genotypic and phenotypic evaluation of biofilm production and antimicrobial resistance in *Staphylococcus aureus* isolated from milk, NorthWest province, South Africa,” Antibiotics, vol. 9, pp. 156, 2020.

- [57] M. G. Avila-Novoa, M. Iñiguez-Moreno, O. A. Solís-Velazquez, J. P. Gonzalez-Gomez, P. J. Guerrero-Medina, M. Gutierrez-Lomel, “Biofilm Formation by *Staphylococcus aureus* isolated from Food Contact Surfaces in the Dairy Industry of Jalisco, Mexico,” *Journal of Food Quality*, vol. 2018, pp. 1746139, 2018.

Comparative Analysis of Machine Learning Models for Android Malware Detection

Selma Bulut^{1*}, Adem Korkmaz²

¹Kırklareli University, Technical Sciences Vocational School, Department of Computer Programming, Kırklareli, Türkiye, selma.bulut@klu.edu.tr

²Bandırma University, Gonen Vocational School, Department of Web Design and Coding, Balıkesir, Türkiye, ademkorkmaz@bandirma.edu.tr

*Corresponding Author

ARTICLE INFO

ABSTRACT

Keywords:

Android malware detection
Machine learning algorithms
Naticusdroid dataset
Comparative analysis
Data integrity

The rapid growth of Android devices has led to increased security concerns, especially from malicious software. This study extensively compares machine-learning algorithms for effective Android malware detection. Traditional models, such as random forest (RF) and support vector machines (SVM), alongside advanced approaches, such as convolutional neural networks (CNN) and XGBoost, were evaluated. Leveraging the NATICUSdroid dataset containing 29,332 records and 86 traces, the results highlight the superiority of RF with 97.1% and XGBoost with 97.2% accuracy. However, evolving malware and real-world unpredictability require a cautious interpretation. Promising as they are, our findings stress the need for continuous innovation in malware detection to ensure robust Android user security and data integrity.

Article History:

Received: 27.08.2023

Accepted: 15.03.2024

Online Available: 06.06.2024

1. Introduction

Mobile phones, which entered our lives in the 1990s, were initially produced for texting and talking; however, with the advent of evolving technology and mobile internet, they have allowed us to perform all sorts of tasks efficiently. People use smartphones for various activities, from shopping, reading newspapers, and banking transactions to communicating via social media. Therefore, smartphones have become an indispensable part of our lives.

In smartphones, one of the operating systems such as Android, IOS, Samsung, KaiOS, BlackBerryOS, Tizen, and Windows mobile can be found. By the end of 2022, with a 71.75% market share, Android has been recognized as the most widely used operating system. In 2023, it is

anticipated that there will be approximately 3.6 billion active Android smartphone users dispersed across 190 nations. Android has attained a 70.94% share of the global mobile operating system market, while Apple's iOS has secured a 28.33% share [1].

Google developed the Android operating system. It is the fastest-growing, open-source, and fully customizable mobile operating system software in smartphone operating systems. Android extends an open-source platform, offering unrestricted access and managerial control to Original Equipment Manufacturers (OEMs), encompassing entities such as Samsung, Xiaomi, Oppo, Vivo, Huawei, Motorola, and Google. Subsequently, these manufacturers have commercialized their devices at markedly economical price points, particularly when

contrasted with the average sale price of Apple iOS devices, quantified at 261 dollars in the fiscal year 2021. This situation reveals the fundamental reason for Android's success today. However, the Android operating system is preferred in smartphones, wearable devices, and smart TVs [2, 3].

With the increase in the number of smartphone applications downloaded and used through app stores (Google Play, App Store), security issues have emerged as a problem. Malware that we encounter on computers is now taking over our smartphones. Malicious software that permeates smartphones can precipitate a spectrum of harmful consequences, including unauthorized access to users' personal information, surveillance of user activities and geographical locations, unauthorized intrusion into social media accounts, penetration into banking accounts, dissemination of unauthorized messages, and diminution of memory and battery longevity [4]. The rapid increase in Android applications and being the most preferred operating system has made it a target for malicious software.

According to the Kaspersky Security Network, 4,948,522 mobile malicious software, adware, and risky software attacks were prevented in the first quarter of 2023. Advertising software is the most common threat to mobile devices, accounting for 34.8% of all detected threats [5]. In recent years, the Android operating system (AOS) has released several updates to address various security vulnerabilities [6].

The primary protection mechanism in the Android operating system is Google Play Protect, which identifies malicious software applications in the Google Play Store. However, there are many third-party app stores where malicious software applications can be downloaded. Another security element is a permission-based resource access system that prevents applications from unauthorized access to resources such as cameras, microphones, and internal file storage [7].

The AOS's Android Market Security Model operates similarly to the Linux security model. In this model, permissions granted to files are user-based. A user cannot read, modify, and execute

another user's file unless that user gives permission. When applications run, they must request permission from the user once during installation based on the resources they will use and the areas they will access. Permissions are defined within the AndroidManifest.xml file in the APK (Android application package) [4].

Table 1. Android Sensitive Permissions [8].

Sensitive	PERMISSION GROUP
Calendar	READ_CALENDAR, WRITE_CALENDAR
Camera	CAMERA
Contacts	READ_CONTACTS, WRITE_CONTACTS, GET_ACCOUNTS
Locations	ACCESS_FINE_LOCATION, ACCESS_COARSE
Microphone	RECORD_AUDIO
Phone	READ_PHONE_STATE, CALL_PHONE, READ_CALL_LOG, WRITE_CALL_LOG, ADD_VOICEMAIL, USE_SIP, PROCESS_OUTGOING_CALLS
Sensors	BODY_SENSORS
SMS	SEND_SMS, RECEIVE_SMS, READ_SMS, RECEIVE_WAP_PUSH, RECEIVE_MMS
Storage	READ_EXTERNAL_STORAGE, WRITE_EXTERNAL_STORAGE

Table 1 displays the list of these sensitive permissions. These permissions are divided into four protection levels: i) Normal, ii) Dangerous, iii) Signature, and iv) Signature|Privileged [9]. Permissions classified as 'Dangerous' are the most sensitive among these, as they manage users' personal information, and when used with malicious intent, they can jeopardize users' security and privacy. Therefore, user consent is sought for these permissions [7]. For instance, SEND_SMS permission is essential for communication and social media apps that allow text messages to be sent.

Malicious software can use this permission to communicate with their centers or send messages to premium numbers. This can lead to unexpected billing charges. While granting two permissions separately might be harmless, giving them simultaneously can significantly increase privacy and security risks. For example, while the INTERNET and READ SMS permissions are benign when taken separately, they can be used for an app that can read your text messages and send them to a third party [10].

Malicious software such as Trojans, ransomware, spyware, and worms exploit users unfamiliar with Android's permission system, jeopardizing their data. Hence, there is a need to educate users about Android permissions. In the AOS security model, the person installing the app must consciously grant these permissions. Third-generation app developers sometimes use these permissions either knowingly or unwittingly. The primary responsibility lies with the user, the person installing the app. One must decide if the requested permission is necessary for the application and grant permissions accordingly.

The principal objective of this study is to meticulously evaluate the efficacy of various machine learning algorithms in the context of Android permissions analysis, focusing on detecting potential security threats posed by malicious applications. Given the pervasive nature of mobile devices in daily life and the consequent escalation of security risks, the research endeavors to scrutinize and compare the predictive capabilities of a broad spectrum of models—including Convolutional Neural Networks (CNN), Artificial Neural Networks (ANN), Random Forest (RF), k-Nearest Neighbors (k-NN),

Support Vector Machines (SVM), CatBoostClassifier, and XGBoost. This comparative analysis aims to identify the most effective algorithms in terms of accuracy, F1 score, and computational efficiency and contribute to the development of robust, scalable solutions for enhancing the security of Android operating systems. Through a comprehensive assessment of the NATICUSdroid dataset, encompassing 29,332 records across 86 permissions, this study seeks to advance our understanding of how machine learning techniques can be leveraged to fortify defenses against the ever-evolving landscape of mobile malware threats, thereby providing invaluable insights for both academic research and practical applications in cybersecurity.

2. Related Work

Machine learning-based Android malicious software detection studies are categorized into static and dynamic analyses. The static analysis

includes notifications, permissions, API calls, and intents. It can be obtained without running the malicious software. On the other hand, dynamic analysis focuses on monitoring an application's activity, such as logcat errors, shared memory corruption, system calls, and processes [11]. Dynamic analysis can be obtained by running the malicious software. The most commonly used method is static analysis, but it lacks accuracy. Dynamic analysis is more effective but requires a virtual environment or an Android device [12]. Hybrid analysis combines static and dynamic features [13].

Various datasets for malicious software analysis have become available in recent years. Using these datasets, researchers have tried all supervised, unsupervised, and deep learning strategies to detect Android malicious software [14]. The datasets under scrutiny may encapsulate static attributes, such as Application Programming Interface (API) invocations, intentional actions, permission requests, and dynamic characteristics, including logcat error manifestations, shared memory allocations, and system call interactions. Studies conducted for this purpose have been examined.

Y. Zhou and X. Jiang [15] conducted a significant study examining the characterization and evolution of Android malicious software. This research investigated how specific permissions and behaviors could be used to detect malicious applications by analyzing malware behaviors. S. Y. Yerima and S. Khan [16] employed static attributes, encompassing permissions, intents, API invocations, and instantiation dates, extracted from benign and malicious software datasets furnished with date labels to scrutinize the efficacy of assorted machine-learning classifiers. They preferred machine learning methodologies such as NB, SVM, and RF.

A. Rahali, A. H. Lashkari, G. Kaur, L. Taheri, F. Gagnon, and F. Massicotte [17] proffered a methodology entailing an image-based deep neural network to systematically classify and characterize software exemplars, derived from a malware dataset that encompasses 12 paramount malware categories and 191 noteworthy malicious software entities.

J. Kim, Y. Ban, E. Ko, H. Cho, and J. H. Yi [18] propounded MAPAS, a malware detection system that furnishes elevated accuracy while enabling adaptable deployment of computational resources. MAPAS scrutinizes the behavioral attributes of malevolent applications by analyzing API call graphs, employing convolutional neural networks (CNN). The authors juxtaposed MAPAS with an alternative detection methodology, MaMaDroid, to evaluate its relative performance and efficacy. F. Giannakas, V. Kouliaridis, and G. Kambourakis [19] employed shallow and deep machine learning techniques to predict malicious software on the Android platform. This involved researching, optimizing, and evaluating the performance of 28 different machine learning algorithms, including a DNN model.

K. Liu, G. Zhang, X. Chen, Q. Liu, L. Peng, and L. Yurui [10] summarized the process of sample collection, data preprocessing, feature selection, machine learning models, algorithms, and evaluation of detection efficiency using machine learning. They also assessed future expectations for research based on machine learning detection of malicious Android software. C. D. Nguyen, N. H. Khoa, K. N. D. Doan, and N. T. Cam [20] instantiated machine learning and deep learning algorithms to categorize malware into respective families and categories, leveraging multiple datasets. The researchers conducted a comprehensive evaluation and elected appropriate methodologies, ensuring optimal alignment with each dataset.

C. Ding, N. Luktarhan, B. Lu, and W. Zhang [21] applied deep learning techniques, formulating a classification schema predicated upon permission and intent features discerned through static and network traffic attributes identified through dynamic analysis. S. Shi, S. Tian, B. Wang, T. Zhou, and G. Chen [13] introduced SFCGDroid, a malware detection method that uses precise function call graphs to identify malicious behaviors. SFCGDroid utilizes both static and dynamic features to identify malicious activities. The process achieved high accuracy and F1 scores on a broad dataset of Android software.

R. Islam, M. I. Sayed, S. Saha, M. J. Hossain, and M. A. Masud [11] executed a classification of Android malicious software, employing an optimal feature selection methodology in tandem with an ensemble machine learning approach, aiming to enhance the precision and reliability of the categorization process.

In the research conducted by M. N. U. R. Chowdhury, A. Haque, H. Soliman, M. S. Hossen, T. Fatima, I. Ahmed [22], an examination of various machine learning approaches—spanning supervised, unsupervised, and deep learning paradigms—utilized for Android malware detection was undertaken. Moreover, a comparative analysis of the performance of assorted Android malware detection methodologies was proffered, and the evaluative metrics employed to gauge their efficacy were explored in the discourse. Conclusively, the discourse also illuminated the detriments and challenges inherent to contemporary methodologies.

H. Rathore, S. Chari, N. Verma, S. K. Sahay, and M. Sewak [23] elucidate a comprehensive investigation predicated on data mining techniques for static malware detection. The authors proffer an exhaustive analysis of each phase inherent to data mining-based malware detection, including data aggregation, preprocessing, feature extraction, application of learning algorithms, and evaluative procedures, while also dialoguing upon the evolution of Android malware and extant detection techniques.

3. Material and Method

3.1. NATICUSdroid (Android Permissions) Dataset

The dataset is in binary format and describes the permissions each application may be using. Each row represents an app, and each column represents a specific Android permission. A '1' in a cell indicates that the corresponding application uses this permission, while a '0' does not. The data set contains 29332 records of 86 permissions on Android phones, such as android.permission.CAMERA, and android.permission.READ_CONTACTS [24].

Figure 1 shows the Android Permission Classification attribute data distribution.

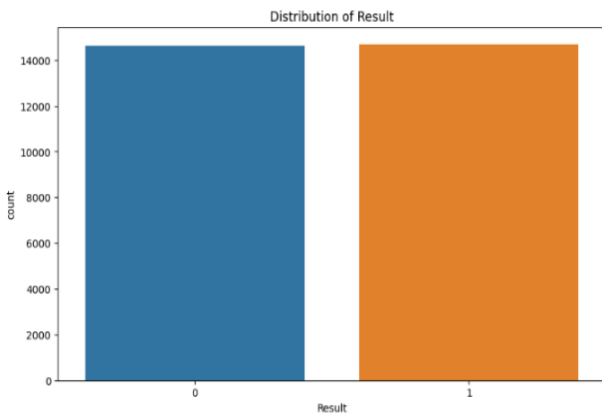


Figure 1. Android Permissions Classification attribute data distribution

3.2. Data analysis

Before initiating the study, an examination of the data for preprocessing purposes revealed that data balancing measures were deemed unnecessary due to the relatively even distribution of the Android Permission Classification attribute, which comprised 14,700 records for class 1 and 14,632 for class 0. Given the unconditional nature of the Android permission attributes, represented as 1 and 0, normalization procedures were not required. Furthermore, the dataset was found to be

complete, with no instances of missing or incomplete data. This thorough data assessment ensured the dataset was adequately prepared for the subsequent analysis without additional preprocessing steps such as balancing or normalization.

In the study, an extensive classification task was conducted utilizing a myriad of algorithms, including Convolutional Neural Networks (CNN), Artificial Neural Network (ANN), Random Forest (RF), k-nearest Neighbors (k-NN), Support Vector Machines (SVM), CatBoostClassifier, and XGBoost. Each algorithm, ranging from the spatial hierarchy-utilizing CNNs to the gradient-boosted precision of XGBoost, was rigorously trained and subsequently evaluated based on standard classification metrics like accuracy, F1 score, and AUC-ROC. A comprehensive comparative analysis spotlighted the superior performers, considering varied facets such as training duration, model interpretability, and predictive prowess. The culmination of the study offered invaluable insights, underscoring the most efficacious algorithms and proffering recommendations for practical deployments or prospective research avenues. The sequential process followed in the research study is shown in Figure 2.

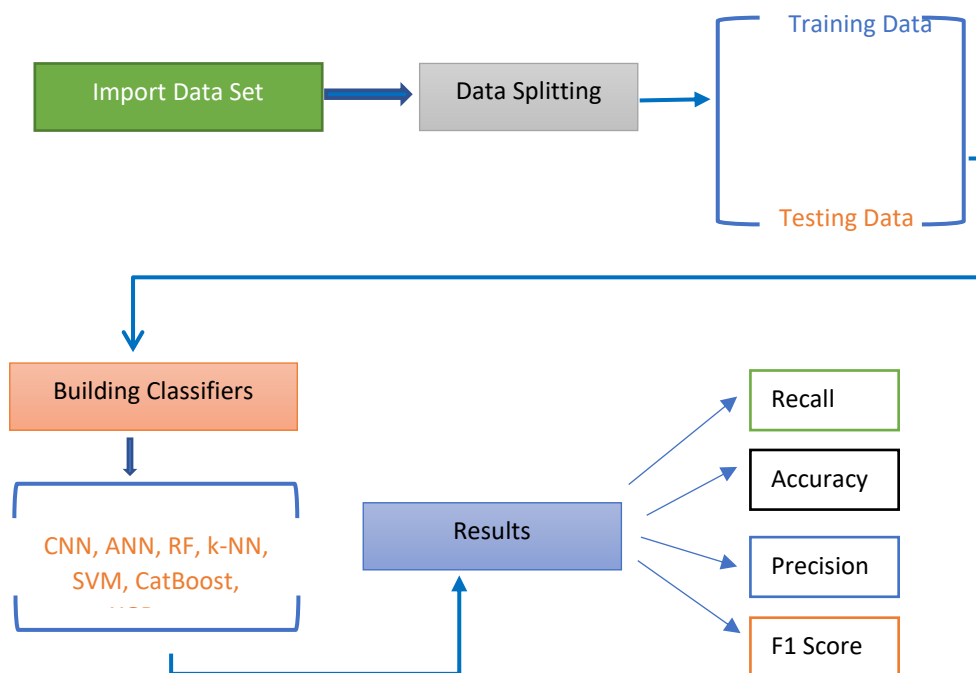


Figure 2. Research methodology steps

3.2.1. Artificial neural networks

Artificial Neural Networks (ANNs) represent a category of machine learning models conceptualized and developed by drawing inspiration from biological neural networks' architectural structure and functional dynamics. ANNs are composed of interlinked artificial neurons, which are systematically arranged in layers and responsible for processing and transmitting information via connections that are weighted and adjusted during the learning process [25]. The artificial neuron mimics a biological neuron's input, processing, and output properties. Figure 3 shows the results produced by the network: The net input obtained by multiplying the information entered into the network by its weights (W) is processed with the transfer function and taken from the output layer [26-28].

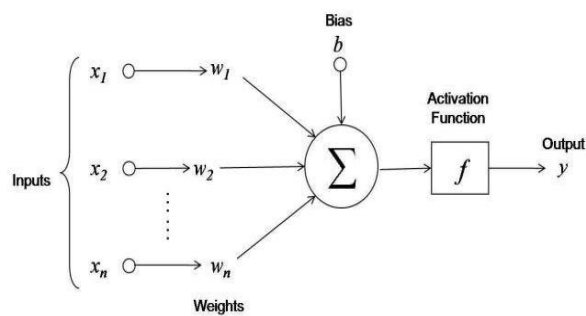


Figure 3. Artificial neuron network structure [29]

Classification with artificial neural networks (ANNs) involves training a neural network model to classify data into different classes or categories. ANNs have been ubiquitously utilized for classification endeavors, attributed to their capacity to decipher intricate patterns and interrelations within data. The network comprises an input layer, an intermediate hidden layer hosting ten neurons, a subsequent hidden layer furnished with five neurons, and an output layer endowed with a neuron count equivalent to the number of classes inherent in the classification task. About the activation functions, the hidden layers employ the Rectified Linear Unit (ReLU), whereas the sigmoid activation function is implemented in the output layer.

In case there is no linear relationship between the inputs and outputs of artificial neural networks,

Multilayer Perceptrons (Multilayer Perceptron) are used to learn. Therefore, this method was used in the study.

3.2.2. Convolutional neural networks (CNNs)

Convolutional Neural Networks (CNNs) are a specialized category of deep neural networks predominantly applied to computer vision tasks, designed explicitly to process grid-like topology data, such as images [30]. These networks use convolutional layers with filters or kernels that traverse the input data, producing a feature map that emphasizes critical features, making them particularly adept at identifying local patterns ranging from simple edges to complex image structures [31]. A significant component, the pooling layer, typically follows the convolutional layer, aiming to down-sample the spatial dimensions of the data, enhancing the model's robustness and reducing computational demands [32]. As one progresses more profoundly into a CNN, the architecture detects intricate structures, with the concluding fully connected layers classifying the discerned high-level features into categories. Their hierarchical design, enabling the adaptive learning of spatial hierarchies from input images, has solidified CNNs as a premier choice for numerous computer vision applications.

3.2.3. Random forest (RF)

The Random Forest (RF) algorithm efficiently amalgamates multiple randomized decision trees, producing results by averaging their predictions. Particularly powerful when variables outnumber observations, each tree within the RF is trained on a random data subset. Only a randomized subset of features is considered at every decision node, mitigating overfitting and enhancing generalization [33]. RF is a versatile supervised learning method suitable for classification and regression, building trees on random data samples, and finalizing predictions through a majority vote [34]. These decision trees recursively partition data based on specific criteria until a set stopping point, with tree splits determined by preset criteria [35].

3.2.4. K-Nearest neighbor (k-NN)

The K-nearest neighbor (KNN) algorithm is a supervised learning method predominantly used for classification. By measuring the similarity of data points to the nearest instances in the training set, KNN classifies them based on the most frequent class among its "K" neighbors. The effectiveness of KNN relies on several parameters, such as the choice of "K," distance metrics like Euclidean or Manhattan, and the normalization of data [36, 37]. Introduced by Fix and Hodges (1952), the algorithm's computational demands increase with larger datasets [38]. Normalizing training data is pivotal to its accuracy [39].

3.2.5. Support vector machines (SVM)

The Support Vector Machine (SVM) is a powerful supervised machine learning technique introduced by Vapnik et al. in 1997, rooted in statistical learning theory [40]. Designed for classification and regression tasks, SVMs excel in diverse applications such as learning, clustering, and density estimation. The algorithm is exceptionally versatile, addressing both binary and multi-class classification problems. The crux of SVM lies in identifying support vectors—the data points nearest to the class boundaries—and maximizing the distance between these vectors and the separating hyperplane. While various hyperplanes might separate the data, SVM chooses the one with the maximum distance from both classes, ensuring optimal and robust classification [41].

3.2.6. CatBoostClassifier

The CatBoostClassifier is a gradient-boosting algorithm designed to work effectively with categorical features. Developed by Yandex, a Russian search engine company, it utilizes a collection of decision trees to make predictions. A standout capability of the CatBoostClassifier is its ability to handle categorical features without needing one-hot or label encoding. It employs a technique called "ordered boosting," which considers the order of categories, enhancing the algorithm's performance [42].

3.2.7. XGBoost

XGBoost, for eXtreme Gradient Boosting, is a widely-used machine learning algorithm suitable for regression and classification tasks. It operates within a gradient-boosting framework, combining multiple weak predictive models, typically decision trees, to form a robust predictive model. XGBoost differentiates itself by building trees using numerous cores and organizing data to minimize search times. Such efficiency measures reduce model training times, improving performance [43, 44].

3.3. Model performance and evaluation

The TP, TN, FP, and FN Confusion matrix metrics provide values for correct or incorrect classification of packets in the firewall. These values were used to calculate precision, recall, f-measure, and accuracy metrics as follows [45]:

$$\text{Precision} = \frac{TP}{(TP+FP)} \tag{1}$$

$$\text{Recall} = \frac{TP}{(TP+FN)} \tag{2}$$

$$\text{F-measure} = \frac{(2 \times \text{precision} \times \text{recall})}{(\text{precision} + \text{recall})} \tag{3}$$

$$\text{Accuracy} = \frac{(TP+TN)}{(TP+TN+FP+FN)} \tag{4}$$

The Sigmoid and ReLU activation functions used in the artificial neural network are calculated as follows:

$$\text{Sigmoid} : f(a) = \frac{1}{1+e^{-a}} = \frac{e^a}{1+e^a} \tag{5}$$

$$\text{ReLU} : (0,a)=0, \text{if } a < 0; (0,a)=a, \text{if } a \geq 0 \tag{6}$$

Table 2 gives the confusion matrix table.

		Predict Class	
		Yes	No
Actual Class	Yes	TP	FN
	No	FP	TN

3.4. Limitations

This study, while comprehensive in its approach, acknowledges several limitations. Our analysis primarily relied on the NATICUSdroid dataset, which, despite its breadth, might not encapsulate the entire Android ecosystem's nuances. The range of algorithms employed, from conventional techniques like RF and SVM to advanced ones like CNN and ANN, leaves out potential hybrid models and other sophisticated methodologies. Our focus on 86 permissions as features might not capture the full spectrum of signals beneficial for malware detection, such as API calls or code patterns. Furthermore, the rapid evolution of malware techniques poses a challenge, suggesting that today's effective models might struggle with tomorrow's threats. Generalizing our promising results, especially

from the RF model, to real-world scenarios requires caution due to the inherent unpredictability of malware distribution in live environments. The "black box" nature of some models, intense learning ones, presents a transparency challenge, and a more granular comparative analysis among models could further enrich our insights. These recognized limitations pave the way for future research aiming for a more holistic view of malware detection.

4. Results

Our extensive analysis of Android permissions using various machine-learning algorithms observed notable distinctions in performance metrics across the models.

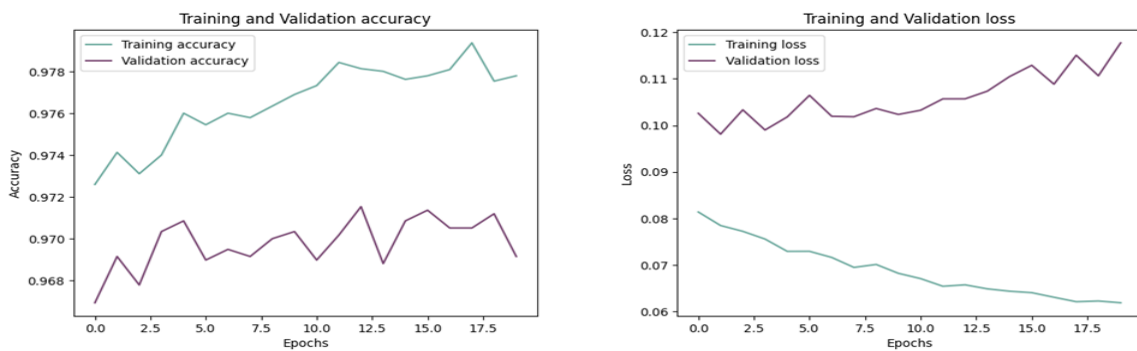


Figure 4. CNN Accuracy and loss of training and validation values

As seen in Figure 4, the 20-epoch CNN results show a model with stable performance but signs of overfitting. While the training accuracy increased slightly from 97.73% to 97.94% and the loss decreased, the validation metrics were less consistent. Validation loss rose from 0.1161 to 0.1307, and accuracy hovered in the 96-97%

range. This divergence between training and validation suggests the model is overfitting, excelling on training data but not generalizing effectively to new data. Implementing dropout layers, data augmentation, or regularization might be beneficial to improve performance.

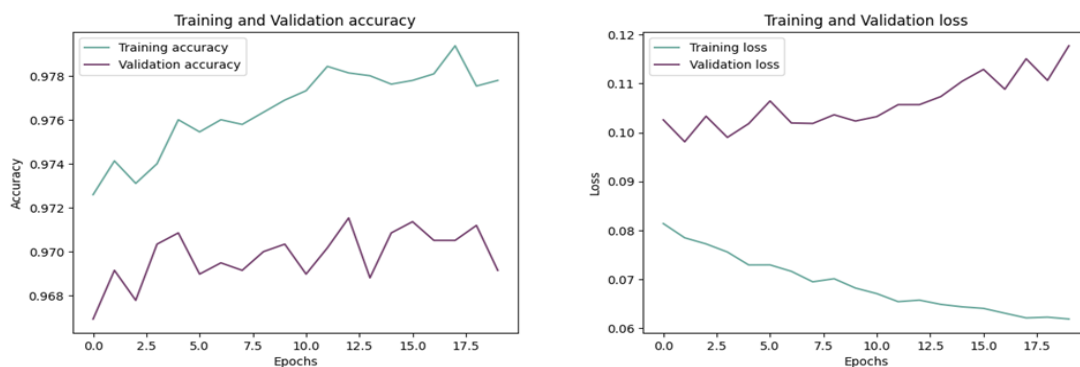


Figure 5. ANN Accuracy and loss of training and validation values

As seen in Figure 5, the results from the 20-epoch ANN algorithm display consistent model improvement. The training loss began at 0.2052 and decreased to 0.0824 by the end, while the training accuracy rose from 92.70% to 97.34%. Validation metrics also showed progress, with accuracy starting at 96.20% and finishing at 97.17%. However, after the 10th epoch, the

validation metrics slightly oscillated, hinting at possible overfitting. The closeness of the training and validation metrics suggests good model generalization, but future training beyond 20 epochs should be approached with caution to avoid overfitting. Regularization or dropout might be considered for enhanced robustness in extended training.

Table 3. Analysis results of the Confusion Matrix

		CNN	ANN	RF	k-NN	SVM	CatBoostClassifier	XGBoost	
		<i>Predicted</i>							
<i>Actual</i>	0	2849 95	2879 65	2876 68	2864 80	2800 156	2877 67	2874 70	
	1	100 2823	115 2808	100 2823	125 2798	116 2795	101 2822	90 2833	

The Confusion Matrix is a diagnostic tool for classification models, delineating the nuances of their predictive performance. Each algorithm in the confusion matrix in Table 3 reveals its strengths and potential areas for improvement. XGBoost distinctly emerges as the frontrunner, delivering a harmonious blend of high true positives and one of the lowest false positives, underscoring its adeptness at accurately distinguishing both classes. Conversely, the SVM exhibits a propensity for a higher rate of false negatives, indicating occasional oversights in identifying positive instances. The k-NN

algorithm, while proficient, sometimes misrepresents negative instances as positive, as denoted by its elevated false positive count. CatBoostClassifier and RF, both robust, closely trail XGBoost's commendable performance. Although slightly lagging behind the top trio of XGBoost, CatBoostClassifier, and RF, CNN and ANN still showcase admirable proficiency. Collectively, these results underscore the quintessential role of algorithm selection and optimization dictated by the dataset's inherent characteristics and distribution.

Table 4. Analysis results of the dataset

	CNN	ANN	RF	k-NN	SVM	CatBoostClassifier	XGBoost
Accuracy	0.966	0.969	0.971	0.952	0.953	0.971	0.972
F1 Score	0.966	0.969	0.971	0.961	0.953	0.971	0.972
Times	98sn	48sn	3sn	17sn	21sn	59sn	3sn

In the analysis presented in Table 4, seven classification algorithms are compared based on Accuracy, F1 Score, and running time, revealing nuanced insights into their performance. The XGBoost model achieves the highest accuracy and F1 score at 0.972, closely followed by the Random Forest and CatBoostClassifier models at 0.971. This suggests that ensemble methods, particularly those based on decision tree ensembles like XGBoost, Random Forest, and CatBoost, perform exceptionally well in

accuracy and maintain a balance between precision and recall, as reflected by the F1 scores.

CNN and ANN also show strong performance with accuracy and F1 scores above 0.96, indicating their capability to capture complex data patterns. However, they require significantly more computation time, with CNN being the most time-consuming at 98 seconds and ANN at 48 seconds. This highlights a trade-off between

performance and computational efficiency when employing deep learning models.

K-NN and SVM exhibit the lowest accuracy and F1 scores among the models, with k-NN at 0.952 and SVM at 0.953 for accuracy and a slightly better F1 score for k-NN at 0.961 than SVM's F1 score. Despite their lower performance metrics, k-NN and SVM are relatively more computationally efficient than CNN and ANN but less so than RF and XGBoost, which only require 3 seconds to compute, making them highly efficient choices with superior accuracy.

In summary, ensemble methods like XGBoost, Random Forest, and CatBoostClassifier offer an optimal blend of high accuracy, excellent F1 scores, and computational efficiency. In contrast, CNN and ANN, while powerful in model performance, demand significantly higher computation times, potentially limiting their applicability in scenarios where rapid model inference is critical. Meanwhile, traditional machine learning models like k-NN and SVM provide a decent balance between computational demand and model performance but do not match the superior metrics of ensemble methods.

Table 5. Previous similar studies and their results

Ref / Year	Dataset	Number of features	Applied models	Results-Accuracy
[6] / 2021	NATICUSdroid	29,000 benign	RF	97%
[13] / 2023	SFCGDroid	26,939 Android software datasets		98.22%
[17] / 2020	Didroid		Deep Learning	93.36%
[20] / 2023	Drebin CICMaldroid2020	Drebin: 204 features CICMaldroid:337 features	RF, ET, DNN, 1D-CNN	Drebin 1D-CNN and RF 99.6% CICMaldroid DNN 98.26%, 1D-CNN 98.2%
[46] / 2014	Drebin	123,453 applications and 5,560 malware samples	SVM	94%
[47] / 2022	CICMaldroid2020	17,341 samples	semi-supervised DNN	97.7%
[48] / 2021	CCCS-CIC-AndMal-2020	14 malware categories and 180 malware families	J48, NB, SVM, AB, LR, KNN, RF, MLP	Malware Category over 96 % Malware Family over 99%
[49] / 2019	TFDroid		SVM	93.7%
[18] / 2022	MaMaDroid MAPAS		CNN	MAPAS 91.27% MaMaDroid 84.99%
Our Study	NATICUSdroid	29332 records of 86 permissions	CNN, ANN, RF, k-NN, SVM, CatBoostClassifier, XGBoost	XGBoost 97.2% RF 97.1%

Table 5 reviews studies from 2014 to 2023 on malware detection across various datasets. Mathur et al. [6] worked on the NATICUSdroid dataset with 29,000 benign features, achieving a 97% accuracy using Random Forest (RF). Similarly, Shi et al. [13] reported a 98.22% accuracy and 98.20% F1 score from the SFCGDroid dataset with 26,939 Android software. On the Didroid dataset, Rahali et al. [17] used deep learning to reach 93.36% accuracy. A multi-model approach was taken by Nguyen et al. [20] on two datasets (Drebin and

CICMaldroid2020), with the highest accuracy being 99.6% on Drebin using 1D-CNN and RF. Arp et al. [46] also analyzed the Drebin dataset, achieving 94% accuracy using SVM. Employing a semi-supervised DNN on the CICMaldroid2020 dataset, Mahdavar et al. [47] reported a 97.7% accuracy. Fiky et al. [48] showcased a broad model application on the CCCS-CIC-AndMal-2020 dataset, with results surpassing 96% for malware category accuracy and over 99% for malware family accuracy. CNN models were applied by Kim et al. [18] on

the MaMaDroid and MAPAS datasets, obtaining accuracies of 84.99% and 91.27%, respectively. Lastly, a multi-algorithm study labeled "Our Study" was conducted on the NATICUSdroid dataset, wherein the RF model yielded an accuracy of 97.1%.

5. Conclusion and Discussion

The landscape of malware detection has undergone significant advancements, with studies spanning from 2014 to 2023 adopting various datasets and leveraging diverse machine learning and deep learning algorithms. Our comprehensive review of these studies showcases the consistent effort toward achieving higher accuracy rates and understanding the nuances of malware categorization and family detection.

Upon comparison, it is evident that Random Forest (RF) consistently performed well across different datasets, as noted in studies by Mathur et al. [6] and our own, registering accuracy rates of around 97%. However, Nguyen et al. [20] demonstrated that with a suitable dataset and model combination, particularly 1D-CNN on the Drebin dataset, accuracy could skyrocket to 99.6%. Such high-accuracy figures emphasize the potential of hybrid approaches, blending traditional machine-learning techniques with deep-learning structures.

However, it is also essential to acknowledge the robust results derived from singular models. The SVM, as utilized by Arp et al. [46] and Lou et al. [49], generated commendable results, highlighting the continued relevance of foundational machine learning methods amidst the surge of deep learning models. Kim et al. [18] focus on CNNs underscores the increasing reliance on deep learning for complex classification tasks, especially given the intricate nature of malware detection.

Our study's multi-algorithm approach to the NATICUSdroid dataset was insightful, revealing each model's strengths and limitations in the dataset's context. While XGBoost emerged as the top performer, it was enlightening to juxtapose

its results against algorithms like CNN, ANN, k-NN, SVM, CatBoostClassifier, and RF.

In conclusion, while the overarching goal across studies remains consistent—achieving higher accuracy in malware detection—the path to that end varies. It is essential to focus on the accuracy figures and consider factors like the false-positive rate, F1 score, and the intricacies of the dataset in use. As malware continues to evolve, so too must our methodologies, urging a blend of both foundational and avant-garde approaches to stay ahead in the ever-evolving cyber landscape.

Article Information Form

Funding

The authors has no received any financial support for the research, authorship or publication of this study.

Authors' Contribution

The authors contributed equally

The Declaration of Conflict of Interest/ Common Interest

No conflict of interest or common interest has been declared by the authors.

The Declaration of Ethics Committee Approval

This study does not require ethics committee permission or any special permission.

The Declaration of Research and Publication Ethics

The authors of the paper declare that they comply with the scientific, ethical and quotation rules of SAUJS in all processes of the paper and that they do not make any falsification on the data collected. In addition, they declare that Sakarya University Journal of Science and its editorial board have no responsibility for any ethical violations that may be encountered, and that this study has not been evaluated in any academic publication environment other than Sakarya University Journal of Science.

Copyright Statement

Authors own the copyright of their work published in the journal and their work is published under the CC BY-NC 4.0 license.

References

- [1] A. Turner. (2022, Jan 12). How many Android users are there? Global statistics. [Online]. Available: <https://www.bankmycell.com/blog/how-many-android-users-are-there>
- [2] Google. (2023, Aug 26). Wear OS by Google. [Online]. Available: <https://wearos.google.com>
- [3] Android. (2023, Aug 25). Android TV. [Online]. Available: <https://www.android.com/tv/>
- [4] S. Büyükgöze, "Mobil uygulama marketlerinin güvenlik modeli incelemeleri," Türkiye Bilişim Vakfı Bilgisayar Bilimleri ve Mühendisliği Dergisi, 12(1), pp.9-18. 2019.
- [5] A. Kivva, (2023, Jun 07). IT threat evolution Q1 2023. Mobile statistics. [Online]. Available: <https://securelist.com/it-threat-evolution-q1-2023-mobile-statistics/109893/>
- [6] A. Mathur, L. M. Podila, K. Kulkarni, Q. Niyaz, A. Y. Javaid, "NATICUSdroid: A malware detection framework for Android using native and custom permissions," Journal of Information Security and Applications, vol. 58, no. 102696, p. 102696, 2021.
- [7] A. Mathur, E. Ewoldt, Q. Niyaz, A. Javaid, X. Yang, "Permission-educator: App for educating users about android permissions," in Conf. Intelligent Human Computer Interaction, Cham: Springer International Publishing, 2022, pp.361–371.
- [8] K. Liu, G. Zhang, X. Chen, Q. Liu, L. Peng, L. Yurui, "Android malware detection based on sensitive patterns," Telecommunication Systems, vol. 82, no. 4, pp. 435–449, 2023.
- [9] Android Developers. (2023, Aug 26). Permissions on android. [Online]. Available: <https://developer.android.com/guide/topics/permissions/overview>.
- [10] E. Georgescu, (2020, Oct 16). The hidden dangers of Android permissions - description and mitigation. [Online]. Available: <https://heimdalsecurity.com/blog/android-permissions-full-guide/>.
- [11] R. Islam, M. I. Sayed, S. Saha, M. J. Hossain, M. A. Masud, "Android malware classification using optimum feature selection and ensemble machine learning," Internet of Things and Cyber-Physical Systems, vol. 3, pp. 100–111, 2023.
- [12] Q. Wu, X. Zhu, B. Liu, (2021). "A survey of android malware static detection technology based on machine learning," Mobile Information Systems, pp. 1-18, 2021.
- [13] S. Shi, S. Tian, B. Wang, T. Zhou, G. Chen, "SFCGDroid: android malware detection based on sensitive function call graph," International Journal of Information Security, pp.1-10, 2023.
- [14] L. Zhen, R. Wang, N. Japkowicz, D. Tang, W. Zhang, J. Zhao, "Research on unsupervised feature learning for Android malware detection based on Restricted Boltzmann Machines," Future Generation Computer Systems, Volume 120, pp.91-108, 2021.
- [15] Y. Zhou, X. Jiang, "Dissecting android malware: Characterization and evolution," in Conf. Security and Privacy, 2012, pp.95-109.
- [16] S. Y. Yerima, S. Khan, "Longitudinal performance analysis of machine learning based Android malware detectors," in Conf. Cyber Security and Protection of Digital Services (Cyber Security), 2019, pp.1-8.

- [17] A. Rahali, A. H. Lashkari, G. Kaur, L. Taheri, F. Gagnon, F. Massicotte, "DIDroid: Android malware classification and characterization using deep image learning," in Conf. Communication and Network Security, 2020, pp.70-82.
- [18] J. Kim, Y. Ban, E. Ko, H. Cho, J. H. Yi, "MAPAS: a practical deep learning-based android malware detection system," *International Journal of Information Security*, vol. 21, no. 4, pp. 725–738, 2022.
- [19] F. Giannakas, V. Kouliaridis, G. Kambourakis, "A closer look at machine learning effectiveness in Android malware detection," *Information (Basel)*, vol. 14, no. 1, p. 2, 2022.
- [20] C. D. Nguyen, N. H. Khoa, K. N. D. Doan, N. T. Cam, "Android Malware Category and Family Classification Using Static Analysis," in Conf. Information Networking (ICOIN), IEEE, 2023, pp. 162-167.
- [21] C. Ding, N. Luktarhan, B. Lu, W. Zhang, "A hybrid analysis-based approach to android malware family classification," *Entropy*, 23(8), 1009, 2021.
- [22] M. N. U. R. Chowdhury, A. Haque, H. Soliman, M. S. Hossen, T. Fatima, I. Ahmed, "Android malware Detection using Machine learning: A Review," arXiv preprint arXiv:2307.02412, 2023.
- [23] H. Rathore, S. Chari, N. Verma, S. K. Sahay, M. Sewak, "Android Malware Detection Based on Static Analysis and Data Mining Techniques: A Systematic Literature Review," in Conf. Broadband Communications, Networks and Systems Cham: Springer Nature Switzerland, 2023, pp. 51-71.
- [24] A. Mathur, NATICUSdroid (Android Permissions) Dataset. UCI Machine Learning Repository, 2022.
- [25] K. He, X. Zhang, S. Ren, J. Sun, "Deep residual learning for image recognition," in Conf. Computer Vision and Pattern Recognition (CVPR), 2016, pp.770-778.
- [26] E. Öztemel, *Yapay sinir ağları*, Papatya Yayıncılık, ISBN: 978-975-6797-39-6. Istanbul, Turkey, 2023.
- [27] S. Haykin, *Neural Networks and Learning Machines*, Pearson: Upper Saddle River, Neural Networks and Learning Machines, vol. 3, India, 2009.
- [28] E. Egrioglu, C. H. Aladag, U. Yolcu, V. R. Uslu, M. A. Basaran, "A new approach based on artificial neural networks for high order multivariate fuzzy time series," *Expert System with Applications*, vol. 36, no. 7, pp. 10589–10594, 2009.
- [29] U. Porwal, Z. Shi, S. Setlur, *Machine learning in handwritten Arabic text recognition*, In *Handbook of Statistics Vol. 31*, pp. 443-469, Elsevier, 2013.
- [30] Y. LeCun, L. Bottou, Y. Bengio, P. Haffner, "Gradient-based learning applied to document recognition.," *Proceedings of the IEEE*, 86(11), 1998, pp.2278-2324.
- [31] A. Krizhevsky, I. Sutskever, G. E. Hinton, "ImageNet classification with deep convolutional neural networks". In *Advances in neural information processing systems*, pp. 1097-1105, 2012.
- [32] D. Scherer, A. Müller, S. Behnke, "Evaluation of pooling operations in convolutional architectures for object recognition," in Conf. Artificial Neural Networks (ICANN), 2010, pp. 92-101.
- [33] L. Breiman, "Random forests," *Machine learning*, 45(1), pp.5-32, 2001.
- [34] S. J. Rigatti, "Random forests," *Journal of Insurance Medicine*, 47(1), 31-39, 2017.
- [35] M. Schonlau, R. Y. Zou, "The random forest algorithm for statistical learning," *The Stata Journal*, 20(1), pp.3-29, 2020.

- [36] S. B. Kotsiantis, I. Zaharakis, P. Pintelas, "Supervised machine learning: A review of classification techniques," *Emerging artificial intelligence applications in computer engineering*, 160(1), pp.3-24, 2007.
- [37] Ö. Tomak, *Derin Öğrenme Algoritmalarının EKG Aritmilerinin Sınıflandırılmasında Değerlendirilmesi*, Karadeniz Teknik Üniversitesi, Trabzon, 2018.
- [38] G. Bilgin, "Makine öğrenmesi algoritmaları kullanarak erken dönemde diyabet hastalığı riskinin araştırılması," *Journal of Intelligent Systems: Theory and Applications*, 4(1), pp.55-64, 2021.
- [39] O. Seveli, "Farklı Sınıflandırıcılar ve Yeniden Örnekleme Teknikleri Kullanılarak Kalp Hastalığı Teşhisine Yönelik Karşılaştırmalı Bir Çalışma," *Journal of Intelligent Systems: Theory and Applications*, 5(2), pp.92-105, 2022.
- [40] V. Vapnik, S. Golowich, A. Smola, "Support vector method for function approximation, regression estimation and signal processing," *Advances in neural information processing systems*, 9, pp.281-287, 1996.
- [41] S. R. Gunn, "Support vector machines for classification and regression", *ISIS technical report*, 14(1), pp.5-16, 1998.
- [42] B. Deekshitha, C. Aswitha, C. S. Sundar, A. K. Deepthi, "URL Based Phishing Website Detection by Using Gradient and Catboost Algorithms." *International Journal Research Applied Science and Engineering Technology*, 10(6), pp.3717-3722, 2022.
- [43] S. Ramraj, N. Uzir, R. Sunil, S. Banerjee, "Experimenting XGBoost algorithm for prediction and classification of different datasets," *International Journal of Control Theory and Applications*, 9(40), pp.651-662, 2016.
- [44] N. Memon, S. B. Patel, D. P. Patel, "Comparative analysis of artificial neural network and XGBoost algorithm for PolSAR image classification," in *Conf. Pattern Recognition and Machine Intelligence*, Cham: Springer International Publishing, 2019, pp.452-460.
- [45] A. Korkmaz, S. Büyükgöze, "Sahte Web Sitelerinin Sınıflandırma Algoritmaları İle Tespit Edilmesi," *Avrupa Bilim ve Teknoloji Dergisi*, (16), pp.826-833, 2019.
- [46] D. Arp, M. Spreitzenbarth, M. Hubner, H. Gascon, K. Rieck, "Drebin: Effective and explainable detection of android malware in your pocket," In *Conf Network and Distributed System Security Symposium (NDSS)*, Vol. 14, 2014, pp. 23-26.
- [47] S. MahdaviFar, D. Alhadidi, A. A. Ghorbani, "Effective and efficient hybrid android malware classification using pseudo-label stacked auto-encoder," *Journal of network and systems management*, 30, pp.1-34, 2022.
- [48] A. H. E. Fiky, A. E. Shenawy, M. A. Madkour, "Android malware category and family detection and identification using machine learning," *arXiv preprint arXiv:2107.01927*, 2021.
- [49] S. Lou, S. Cheng, J. Huang, F. Jiang, "TFDroid: Android malware detection by topics and sensitive data flows using machine learning techniques," in *Conf. information and computer technologies (ICICT) IEEE*, 2019, pp.30-36.

Design of Sulfur Resistant Cobalt Catalysts by Boron Promotion: Atomic Scale Insights

Ali Can Kızılkaya 

İzmir Institute of Technology, Faculty of Engineering, Department of Chemical Engineering, İzmir, Türkiye, alicankizilkaya@iyte.edu.tr

ARTICLE INFO

ABSTRACT

Keywords:

Boron
Cobalt
Sulfur
Catalysis
Density Functional Theory

The effect of boron promotion on atomic sulfur formation by hydrogen sulfide dissociation on Co(111), flat surfaces of cobalt nanoparticles, was investigated using Density Functional Theory calculations. The results show that on clean Co(111), hydrogen sulfide dissociation proceeds fast due to low activation barriers, yielding atomic sulfur on the cobalt surfaces. Boron promotion hinders the dissociation of hydrogen sulfide due to increased activation barriers. Furthermore, boron prevents the interaction of sulfur compounds with cobalt surface atoms, as these poisons bind on boron. The findings indicate that boron is an effective promoter that can be used to design sulfur resistant cobalt catalysts.

Article History:

Received: 31.08.2023

Accepted: 07.03.2024

Online Available: 06.06.2024

1. Introduction

Boron is a crucial element used in several industries ranging from materials and chemistry to defence, energy and medical industries. Türkiye is home to 73% of global boron reserves, based on estimates of Eti-Maden, the Turkish state-owned boron-focused mining company. Therefore, utilizing boron for both existing and novel purposes stands as a strategic choice for Türkiye that can boost its technological development. Boron has been historically utilized based on high-performance glass (mainly fibreglass) making, accounting for ~50% of the global boron consumption.

Among other major uses are the manufacture of plant nutrients in agriculture and also detergents in the chemical industry, but boron-based materials find minor uses in many industries including nuclear, metallurgical, textile, and cosmetic sectors [1]. Furthermore, renewed interest in boron due to its unique electronic and chemical properties [2] have resulted in R&D activities for boron utilization in novel areas.

Boron-based materials are researched as therapeutic agents in medical treatments [3], hydrogen storage materials [4], and as heterogeneous catalysts in thermo-, electro- and photo-chemical processes [5], among others.

Among the industries where boron is used, chemical industry is an important component, since it consumes significant amounts of energy, resulting in 19% of all industrial CO₂ emissions [6]. In chemical industry, one of the main current challenges is to make the sector more sustainable, for example via increasing energy efficiency and limiting the formation of waste and by-products. For this purpose, the most reasonable solution is the use of catalysts. Catalysts are used in more than 90% of all chemical processes, delivering significant sustainability benefits [7]. However, catalysts are usually made from rare and precious elements. Due to the growing needs and concerns to make the chemical industry more sustainable, an important area of research is to synthesize catalysts based on more abundant elements [8].

In line with this goal of sustainability, catalysts with components that are based on boron have recently been receiving increased attention in academia. A heterogeneous catalyst is made up of three essential components, an active phase, a high area support material and typically a promoter that can boost the activity, selectivity or stability of the catalyst. Boron-based materials were found to have important catalytic properties as active sites in heterogeneous catalysts. Different chemical phases of the boron based catalysts included nitrides, carbides, phosphides and oxides [5]. Boron carbides and phosphides were found to be efficient photocatalysts for water splitting. Carbon nanotubes and graphene that are used as electrocatalysts were found to have increased activity for oxygen reduction reaction (ORR) when coupled with elemental boron. Similarly 1D hexagonal boron nitride (h-BN) sheets also demonstrated high performance for the electrocatalytic OR reaction [5].

The utilization of h-BN sheets in thermal oxidative dehydrogenation of alkanes resulted in numerous studies investigating supported boron-based catalysts for this reaction. Among these, metallic and non-metallic borides and porous materials in the form of boron oxide and boron-phosphorus mixed oxides showed high propylene selectivities in the partial oxidation of propane [9]. Other publications revealed that different types of oxidic supports (such as alumina, magnesia, silica, etc.) can have varying effects on the boron-based active sites and optimization of the support could lead to improved selectivity or stability of the catalysts via boron-support interactions [10].

Boron has also been used as a promoter in several catalytic reactions with different effects. Among the most important examples are boron-doped carbon nanotubes for photocatalytic and electrocatalytic applications [11] and boron-doped iron [12] or cobalt based catalysts [13] for thermal catalytic Fischer-Tropsch Synthesis (FTS). Boron-doped graphene was used as an electrocatalyst with increased activity in fuel cell applications [14], boron doping was found to increase selectivity to ethanol on Cu(111) for carbon dioxide electroreduction [15]. For photocatalytic applications, boron-doped TiO₂ was found to be an effective catalyst for

antibiotic degradation [16]. In the area of thermal catalysis, boron was found to be an important promoter that can prevent the deactivation of iron or cobalt based Fischer-Tropsch Synthesis catalysts. On iron catalysts, an experimental study [12] indicated that boron promotion reduces the rate of deactivation, while in a later study [17] based on DFT modeling, it was found that boron reduces the deactivation rate by blocking the adsorption sites for carbon.

Boron promotion was also investigated for cobalt FTS catalysts. Tan et al. have presented [13] a detailed analysis of the boron promotion related to carbon deposition on cobalt FTS catalysts, based on a combined experimental and computational study. They performed Density Functional Theory (DFT) calculations on both flat and stepped cobalt surfaces to examine the structure of boron promoted cobalt catalysts. Supporting the computational model in this study, they indicated that atomic boron is stable at the hcp site on Co(111) surfaces. Furthermore, they indicated that boron atoms weaken carbon adsorption by withdrawing electronic charge from the cobalt surfaces.

Despite the promising results related to the effect of boron promotion on hindering deactivation by carbon deposition, its effects on sulfur poisoning were rarely investigated. In an experimental study, Li and Coville [18] analyzed the effect of boron on the sulfur poisoning of cobalt FTS catalysts. It was speculated that boron prevents sulfur poisoning via hindering the charge accumulation on cobalt atoms due to sulfur poisoning. However, as their study did not include data related to the chemical and electronic structure of sulfur and boron additives on the catalyst surface, they were unable to provide evidence for the boron promotion mechanism.

In a recent study [19], the potential of boron as a promoter to hinder sulfur poisoning was evaluated on other metal surfaces, including Pd, Pt, Rh and Ru, based on DFT modeling. Similar to this study, they also investigated H₂S dissociation on Pd(111) surface. It was concluded that on Pd surfaces boron can act as a promoter to prevent sulfur poisoning by

hindering H₂S dissociation and weakening the binding of atomic sulfur.

Based on the analysis of the literature, it is obvious that boron is used as a promoter to hinder deactivation by coke deposition on cobalt [13] and iron [12]. Furthermore, a recent study also indicated that it can prevent H₂S dissociation on palladium catalysts [19]. Therefore, it is of interest to analyze how H₂S dissociates on cobalt surfaces and how boron promotion affects its dissociation and the adsorption of dissociation products. Up to our knowledge, there are neither experimental nor computational investigations related to H₂S dissociation and how it is affected by boron promotion on the cobalt surfaces.

The aim of this study is to compare the adsorption and dissociation of hydrogen sulfide on clean vs boron promoted cobalt surfaces, in order to evaluate the potential of boron as a promoter for cobalt FTS catalysts to prevent sulfur poisoning. The adsorption of H₂S, its dissociation and the adsorption of dissociation products are investigated with state-of-the-art computational modeling based on DFT calculations. The results indicate that boron can act as an effective promoter for preventing the sulfur poisoning of FTS catalysts as it hinders the dissociation of H₂S and also prevents the interaction of H₂S and the dissociation products with cobalt surface atoms by acting as an adsorption site for sulfur species.

2. Computational Methods

Periodic Density Functional Calculations (DFT) were performed using the Vienna Ab-initio Simulation Package (VASP) [20, 21]. The exchange-correlation energy was calculated with the revised Perdew–Burke–Ernzerhof functional (revPBE) [22] including the non-local vdW–DF correlation [23–26]. The use of vdW–DF functional allows us to predict accurately model adsorption of molecules with low adsorption energies that bind on surfaces mainly via van der-Waals interactions such as H₂S. The surfaces were cut from a bulk fcc-Co structure with a lattice parameter of 3.56 Å, optimized with the vdW–DF functional. The calculated lattice parameter matches very well with the experimental value of 3.55 Å [27].

The electron-ion interaction was modeled by the projector-augmented wave (PAW) method [28]. Spin-polarized calculations were performed to account for the magnetic properties of cobalt with a plane wave cut-off energy of 400 eV. Surface terraces of face-centered-cubic (fcc) Co nanoparticles were modeled with 4 atomic layers-thick Co(111) slab models with a p(2x2) unit cell. The adsorption of H_xS (x=2,1,0) species in this unit cells corresponds to a coverage of 25% of the surface cobalt atoms with adsorbates, in other words, a surface coverage of 0.25 monolayer (ML).

The atoms at the bottom 2 layers half of the slabs in the z-direction were kept fixed at their pre-optimized positions, while all other atoms were allowed to relax during optimization calculations. The reciprocal space was sampled with a (5×5×1) k-points grid automatically generated using Monkhorst-Pack method [29]. A vacuum height of 15 Å was inserted between slabs to avoid coupling between successive slabs in the z-direction. Dipole corrections in z-direction were used for all optimizations. The structural models were optimized until all the forces acting on atoms are smaller than 0.02 eV/Å.

The binding (adsorption) energies (E_{ad}) of surface species (adsorbates) are calculated based on the formula:

$$E_{ad} = E_{slab_ad} - E_{slab} - E_{ad_vac} \quad (1)$$

where E_{slab_ad} represents the energy of the optimized system of adsorbate on the slab, E_{slab} represents the energy of the clean slab (without the adsorbate) and E_{ad_vac} represents the energy of the adsorbate molecule in a vacuum. The reaction energies (RE) were calculated after the optimization of initial states (IS) and final states (FS) of the reactions, based on the following formula:

$$RE = E_{FS} - E_{IS} \quad (2)$$

After initial and final states are calculated, the transition states were optimized by CI-NEB [30] method until the forces acting on the image with the highest energy are lower than 0.04 eV/Å. All transition states were further confirmed by

vibrational frequency analysis, which indicated a single imaginary vibrational frequency for them. During the vibrational frequency analysis, the atoms were displaced from their equilibrium positions by 0.015 Å. After the identification of TS structures, the activation barriers (E_a) are calculated based on the formula:

$$E_a = E_{TS} - E_{IS} \quad (3)$$

3. Results and Discussion

3.1. H₂S adsorption and dissociation on Co(111)

Sulfur poisoning on cobalt surfaces was previously ascribed to atomic sulfur species, based on experimental and computational surface science studies [31]. Therefore, adsorption of H₂S on Co(111) surface and its successive dissociation to atomic sulfur species is investigated. H₂S decomposition on metal surfaces occurs via stepwise dehydrogenation yielding first SH and then atomic S species. To calculate the activation barriers with DFT modeling, first, initial and final states for H₂S and SH dissociation reaction should be optimized.

Therefore, optimal adsorption configurations of H₂S, SH and S, i.e. H_xS (x=2,1,0), species on Co (111) surface are calculated. There are 4 different adsorption sites on Co(111), namely the 4-fold hollow (hcp) site, 3-fold hollow site (fcc), bridge site and the top site. These adsorption sites are shown in Figure 1, based on the adsorption of atomic sulfur in each site.

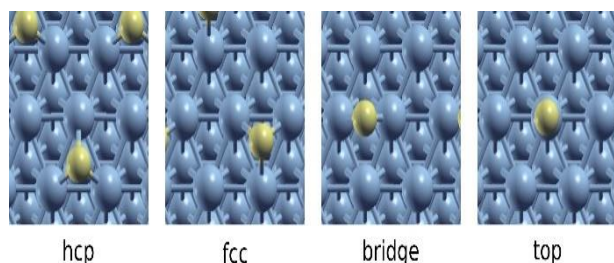


Figure 1. Different adsorption sites on Co(111), a) hcp, b) fcc, c) bridge and d) top (S atoms are shown to illustrate the adsorption sites clearly)

In order to identify the optimal adsorption configuration for the H_xS species, each adsorbate is optimized in all 4 different adsorption sites. Adsorption energies of H_xS species on different adsorption sites on Co(111) are listed in Table 1.

Table 1. The adsorption energies of H_xS species (kJ/mol) on different adsorption sites on Co(111) (NA indicates that adsorption of the indicated species is not possible on the specific site)

	hcp	fcc	bridge	top
H ₂ S	NA	NA	NA	-43
SH	-255	-258	NA	NA
S	-471	-493	NA	NA

The adsorption geometry with the minimum adsorption energy is the preferred, i.e., energetically the most stable, adsorption configuration, which indicates the experimentally observed adsorption site under identical surface structures and vacuum conditions. The preferred adsorption configurations of H₂S, SH and S species are shown in Figure 2.

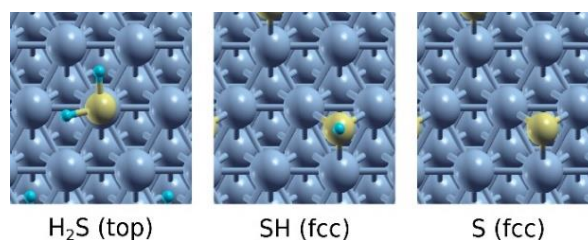


Figure 2. The preferred (most stable) adsorption sites and geometries of H_xS species on Co(111)

The results show that H₂S adsorption can only occur on the top sites, similar to what has been reported on several other transition metal surfaces [32]. For both SH and S species, adsorption occurs on the hollow sites, while adsorption at the fcc site is more stable for both species. A previous study has indicated that SH adsorption is most stable at the bridge sites while S adsorption occurs preferentially at the fcc sites on transition metals like Ni and Ru [32]. Our results indicate that S adsorption is similar on cobalt with other transition metals, while SH adsorption is different as it occurs on the fcc hollow sites, compared to the bridge sites on metals like Ni and Ru. The adsorption energies of SH and S species are calculated as -258 and -493 kJ/mol respectively, indicating that both of these species are strongly chemisorbed on Co(111) surface.

After the identification of the preferred adsorption sites for H_xS species, initial and final state configurations for reactions are optimized on Co(111). For the initial and final states that involve coadsorption of the species (such as the

final state of H₂S dissociation involving SH and H), all possible coadsorption configurations were investigated and the geometry with the minimum energy is used as the initial/final state of the reaction. Based on the optimized initial state (IS) and final state (FS) configurations, transition state (TS) geometries were obtained based on CI-NEB calculations. The IS, TS and FS structures for H₂S decomposition reactions are shown in Figure 3.

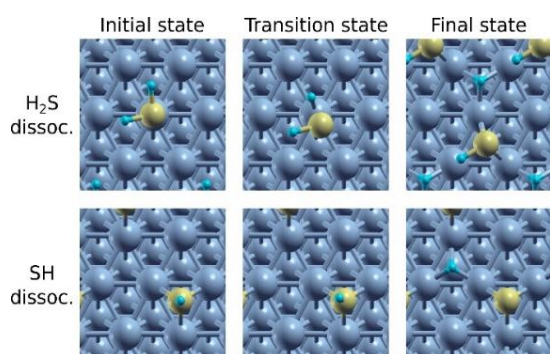


Figure 3. The IS, TS and FS structures for H₂S dissociation reactions on Co(111)

Based on the TS obtained for the reactions, activation barriers are obtained for the dissociation reactions. Similarly, the reaction energies are calculated based on the energy difference of the final state (FS) and initial state (IS). Based on the IS, TS and FS configurations shown in Figure 3, the kinetic parameters of H₂S dissociation to atomic S on Co(111) are calculated, as shown in Table 2.

Table 2. The activation barriers (E_a) and the reaction energies (RE) (kJ/mol) for H₂S and SH dissociation on Co(111)

	E_a	RE
H ₂ S → SH + H	33	-94
SH → S + H	7	-105

The data in Table 2 indicates that H₂S decomposition to HS and S have low barriers, which will result in fast dissociation of H₂S to atomic S under FTS reaction conditions. Our results are in line with the experimental findings that H₂S readily decomposes to atomic S on Co(0001) single crystal surfaces at low temperatures and that atomic S deposits were observed on Co(0001) surfaces after exposure of Co(0001) surface to FTS reactants of CO and H₂

in the presence of H₂S under applied pressure and temperature conditions [31].

3.2. H₂S adsorption and decomposition on boron covered Co(111)

Boron adsorption is investigated on all possible (hcp, fcc, bridge and top) adsorption sites of the Co(111) surface. Among these configurations, boron adsorption is only possible at the hcp and fcc hollow sites. Among these two sites, hcp is the most stable adsorption site with an E_{ad} of 492 kJ/mol and boron adsorption at the hcp site is 11 kJ/mol more stable compared to the adsorption at fcc site. These results are in line with the literature, where boron adsorption was reported to be most stable at the hcp site on Co(111) [13], [33]. Boron adsorbed at the most stable hcp site on the Co(111) surface is shown in Figure 4.

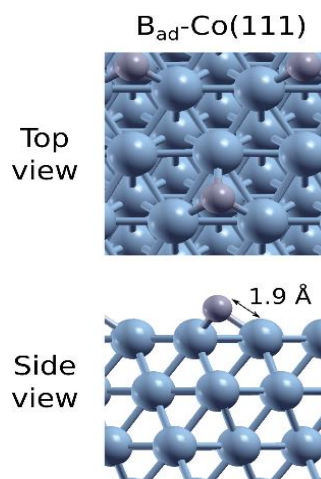


Figure 4. Top and side views of boron adsorbed at the most stable hcp site on Co(111)

Boron promotion results in the formation of adsorption sites on boron covered Co(111) [B-Co(111)] that are close to the boron atom, and sites that are far away from boron, as shown in Figure 5.

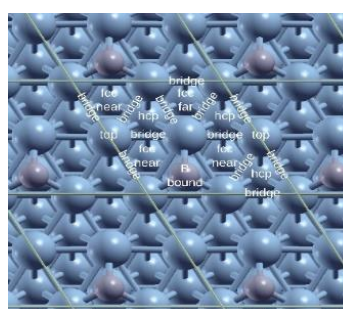


Figure 5. The adsorption sites on the B-Co(111) surface

Figure 5 shows that on B-Co(111), two different types of fcc sites are present, the ones that are near and far from B. There are single types of hcp, bridge and top sites, similar to the case of clean Co(111). Interestingly, H_xS species can also adsorb on boron atoms without interacting with the surface cobalt atoms, as shown in B-bound adsorption site on B-Co(111) in Figure 5. The adsorption of H_xS species were investigated in all adsorption sites shown on B-Co(111) and the results are shown in Table 3.

Table 3. The adsorption energies of H_xS species (kJ/mol) on different adsorption sites on B-Co(111)

	hcp	fcc-near	fcc-far	bridge	top	B-bound
H_2S	-29	NA	-29	NA	-29	-36
SH	NA	NA	-169	-235	NA	-329
S	NA	NA	-437	NA	NA	-482

On B-Co(111), most stable adsorption sites for H_xS adsorption are located where the species are B-bound, i.e. bonded to surface boron atoms. H_xS adsorption at sites that are away from B, where they interact only with Co atoms at the surface are found to have lower E_{ad} values. The preferred adsorption sites for H_xS species, bound to boron atoms on B-Co(111), are shown in Figure 6.

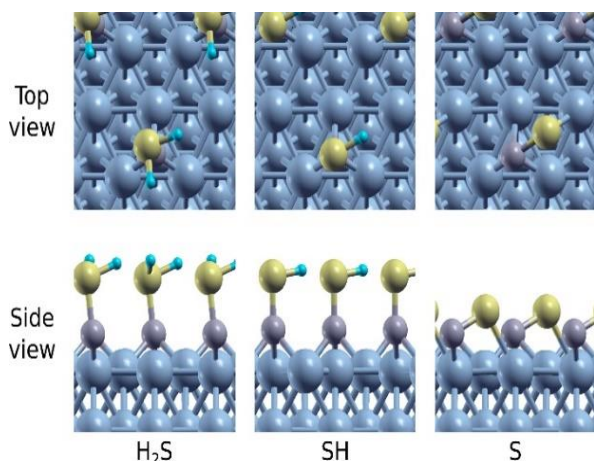


Figure 6. The preferred (most stable) adsorption sites and geometries for H_xS species on B-Co(111)

The results shown in Table 3 and Figure 6 allow to draw important conclusions related to the effect of boron on H_xS adsorption on Co(111). When Co(111) surface is covered with boron, the binding of H_2S , SH and S species are significantly stronger when they occur bound to B atoms, compared to their adsorption on cobalt atoms of B-Co(111) surface. To understand how boron effects the adsorption energies of H_xS with respect to the clean Co(111) surface, adsorption

energies of H_xS species are compared for both surfaces, as shown in Table 4.

Table 4. Comparison of adsorption energies of H_xS species (kJ/mol) on Co(111) vs B-Co(111) surfaces

	Co(111)	B-Co(111) [B-bound]	B-Co(111) [Co-bound]
H_2S	-43	-36	-29
SH	-258	-329	-235
S	-493	-482	-437

Table 4 shows that on the boron covered B-Co(111) surface, H_xS adsorption at sites that are away from boron, results in H_xS adsorption energies that are even lower compared to the ones on clean Co(111). Overall, these findings show that boron atoms will act as H_xS sinks on the Co(111) surface, i.e. H_xS species will bind preferentially on B atoms instead of surface cobalt atoms. As a result, boron promotion will hinder the adsorption of H_xS species on the metallic cobalt surface, resulting in significantly lower H_xS coverages on the catalyst surface. In order to understand how boron promotion effects H_2S dissociation to atomic S, IS, TS and FS configurations were optimized for H_2S and SH dissociation reactions, as shown in Figure 7.

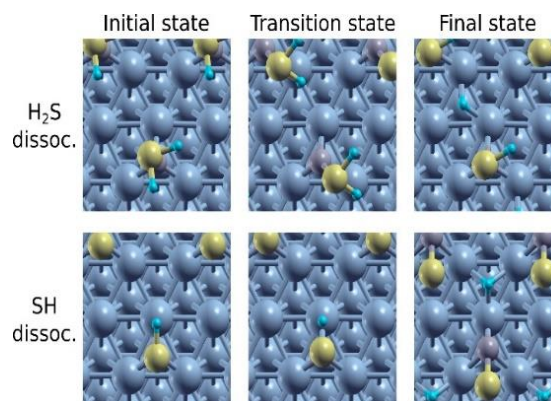


Figure 7. IS, TS and FS structures for H_2S and SH dissociation on B-Co(111)

Figure 7 indicates that the dissociation of H_2S yields SH species bound to boron, while the H atom is located on the cobalt surface. This shows that SH produced as a result of H_2S dissociation will be bound to boron atoms and not interact with cobalt atoms. Similarly, SH dissociation also produces S atoms that are bound to boron, having no interaction with cobalt atoms. Nevertheless, it is also important to investigate if the SH and S species that are produced as a result of dissociation reactions and bound to boron can migrate to their less stable adsorption sites where

they are bound to carbon atoms. Therefore, the kinetic parameters of both H_xS dissociation from the most stable B-bound adsorption sites and their migration to surface cobalt atoms and successive dissociation are investigated and summarized in Table 5.

Table 5. The activation barriers (E_a) and the reaction energies (RE) (kJ/mol) of H_xS dissociation and H_xS migration reactions on B-Co(111) surface

	E_a	RE
$H_2S_{B_bound} \rightarrow SH_{B_bound} + H$	7	-146
$H_2S_{Co_bound} \rightarrow SH_{fcc_far} + H$	NA	NA
$SH_{B_bound} \rightarrow S_{B_bound} + H$	74	-18
$SH_{B_bound} \rightarrow SH_{bridge}$	108	94
$S_{B_bound} \rightarrow S_{fcc_far}$	82	45

Table 5 shows a clear effect of boron promotion on Co(111) surface related to H_2S and SH dissociation. H_2S species can dissociate easily to SH with a very low barrier of 7 kJ/mol starting from their preferred B-bound configuration. However, this dissociation will yield SH species that are not interacting with cobalt atoms but instead bound to B atoms, pointing away from the surface. In order to produce SH species on the cobalt surface, the dissociation of H_2S bound to the cobalt surface atoms (i.e. away from B, located on top, fcc or hcp adsorption sites) have to occur. However, the results indicated that this pathway cannot occur, as during the dissociation process SH species get bonded to boron atoms and thus cannot reach the cobalt surface. Therefore, the results indicate that H_2S dissociation on B-Co(111) can only occur on boron atoms and not on the surface cobalt atoms.

SH that is produced as a result of H_2S dissociation is preferentially located on boron atoms. These B-bound SH species can either dissociate to B-bound atomic S or can migrate to the bridge adsorption sites where it is bonded to cobalt atoms. The comparison of kinetic parameters for these two competing pathways show that the dissociation of SH to B-bound atomic S is kinetically favored as it has a lower (74 kJ/mol) activation barrier compared to its

migration to bridge site with an activation barrier of 108 kJ/mol. These results show that SH dissociation will proceed on B-Co(111) surface to yield atomic S bonded to boron.

An important consideration related to atomic sulfur on B-Co(111) is related to its migration from the most stable B-bound adsorption site to the fcc_far adsorption sites where it interacts directly with surface cobalt atoms. The results showed that this migration is endothermic with a sizeable activation barrier of 82 kJ/mol. Therefore, the analysis also shows that atomic S that is produced on the B-Co(111) surface will remain bonded to boron atoms and therefore atomic boron will act as a sulfur sink that keeps the metallic cobalt atoms free from sulfur poisoning. In order to further clarify the promotional effect of boron on Co(111) related to sulfur poisoning, the kinetic parameters of H_2S dissociation is compared on clean Co(111) vs B-Co(111) in Table 6.

Table 6. The activation barriers (E_a) and reaction energies (RE) (kJ/mol) of H_2S and SH dissociation on Co(111) vs B-Co(111)

	Co(111)		B-Co(111) [B-bound]		B-Co(111) [Co-bound]	
	E_a	RE	E_a	RE	E_a	RE
$H_2S \rightarrow SH + H$	33	-94	7	-146	NA	NA
$SH \rightarrow S + H$	7	-105	74	-18	133	111

Table 6 indicates that on clean Co(111), H_2S dissociation to atomic S occurs rapidly due to low activation barriers of 33 kJ/mol and 7 kJ/mol of H_2S and SH dissociations, respectively. As a result of the dissociation, metallic cobalt atoms are covered with atomic S and therefore catalyst surface is poisoned and deactivated. The low activation barriers for dissociation explain why cobalt nanoparticles can easily get poisoned by even low concentrations of H_2S in the gas atmosphere.

On boron covered Co(111), the situation is remarkably different. H_2S adsorption occurs preferentially on the B atoms and not interacting with the cobalt atoms, while H_2S dissociation can occur easily on B atoms, with an even lower activation barrier than the clean Co(111) surface. However, H_2S dissociation cannot occur on the metallic cobalt surface. Furthermore, the dissociation product of SH will be located on

boron atoms with no effect on surface cobalt atoms, just like the case of H₂S adsorption. From this state of SH atoms adsorbed on boron, in order for atomic S to be formed on surface cobalt atoms, SH species has to first migrate to the surface cobalt atoms and dissociate, which is a highly endothermic reaction with a high overall activation barrier of 133 kJ/mol. Therefore, only atomic S bound to boron can form as a result of SH dissociation with an activation barrier of 74 kJ/mol. A comparison of SH dissociation on clean vs boron promoted Co(111) also shows that the activation barrier on B-Co(111) is 67 kJ/mol higher compared to the clean Co(111), which indicates that the rate of atomic S formation on boron promoted Co(111) will be significantly lower compared to the one on clean Co(111).

Overall, the findings in this study indicate that boron is an effective promoter for cobalt based FTS catalysts which can hinder deactivation by sulfur poisoning. The promotional effect of boron stems from the fact the sources of atomic S, the species that is responsible for catalyst poisoning, H₂S and SH species can only be adsorbed on boron atoms and not the surface cobalt atoms, on a cobalt surface that is promoted by boron. Furthermore, the formation of atomic S from SH is significantly slowed down due to an increase in the activation barrier for dissociation. Similar to H₂S and SH, atomic S species will prefer adsorption on boron atoms without being able to interact with surface cobalt atoms. Therefore, our study highlights important molecular scale insights about how boron promotion effectively suppresses the sulfur poisoning of the cobalt FTS catalysts. These findings can pave the way towards the design of more stable and poison-resistant heterogeneous catalysts based on fundamental understanding.

4. Conclusion

In order to investigate the potential of boron promotion in preventing sulfur poisoning of cobalt FTS catalysts, molecular modeling of H₂S decomposition based on periodic DFT was performed on clean and boron promoted Co(111) surfaces, atomically flat terraces, the most stable surface that is found in highest concentration on fcc-cobalt nanoparticles. The main conclusions of the study can be summarized as follows:

1) H₂S dissociation occurs on Co(111) via stepwise dissociation of H₂S to first SH and finally to atomic S species. On non-promoted, clean Co(111), both dissociation reactions are exothermic, with low activation barriers of 33 and 7 kJ/mol for H₂S and SH dissociation respectively. These results explain why cobalt catalysts are rapidly poisoned by sulfur at even low concentrations of gas phase H₂S.

2) On boron promoted Co(111), [B-Co(111)], the adsorption of H₂S, SH and S are all more stable on boron atoms compared to their adsorption on surface cobalt atoms. The adsorption energies of H_xS species on the cobalt atoms of B-Co(111) are significantly lower compared to the ones on clean Co(111). These results show that B atom act as sinks for H_xS species, clearing the cobalt surface atoms from the sulfur species.

3) On B-Co(111), H₂S dissociation can only occur with H₂S species bound to boron and produces SH species that are also B-bound. SH species that are adsorbed on boron atoms cannot migrate to surface cobalt atoms due to an high activation barrier of 108 kJ/mol. Instead, SH dissociation to atomic S on B-Co(111) also occurs on B-atoms, with a 67 kJ/mol higher activation barrier compared to the clean Co(111).

4) Boron can act as an effective promoter that hinders the deactivation of cobalt catalysts via sulfur poisoning, based on fundamental insights obtained by molecular modelling. This study demonstrates how fundamental understanding can be used to screen promoters for heterogeneous catalysts and therefore acts as a guide for future studies related to rational design of more stable solid catalysts.

Article Information Form

Funding

The author has not received any financial support for the research, authorship or publication of this study.

Authors' Contribution

The author contributed fully to the study.

The Declaration of Conflict of Interest/ Common Interest

No conflict of interest or common interest has been declared by the authors.

The Declaration of Ethics Committee Approval

This study does not require ethics committee permission or any special permission.

The Declaration of Research and Publication Ethics

The authors of the paper declare that they comply with the scientific, ethical and quotation rules of SAUJS in all processes of the paper and that they do not make any falsification on the data collected. In addition, they declare that Sakarya University Journal of Science and its editorial board have no responsibility for any ethical violations that may be encountered, and that this study has not been evaluated in any academic publication environment other than Sakarya University Journal of Science.

Copyright Statement

Authors own the copyright of their work published in the journal and their work is published under the CC BY-NC 4.0 license.

References

- [1] D. M. Schubert, "Borates in Industrial Use BT - Group 13 Chemistry III: Industrial Applications," H. W. Roesky, D. A. Atwood, Eds. Berlin, Heidelberg, Germany: Springer Berlin Heidelberg, 2003, pp. 1–40.
- [2] Z. Huang, S. Wang, R. D. Dewhurst, N. V. Ignatev, M. Finze, H. Braunschweig, "Boron: Its Role in Energy-Related Processes and Applications," *Angewandte Chemie- International Edition*, vol. 59, no. 23, pp. 8800–8816, 2020.
- [3] B. C. Das, P. Thapa, R. Karki, C. Schinke, S. Das, S. Kambhampati, S. K. Banerjee, P.V. Veldhuizen, A. Verma, L. M. Weiss, T. Evans, "Boron chemicals in diagnosis and therapeutics," *Future Medicinal Chemistry*, vol. 5, no. 6, pp. 653–676, 2013.
- [4] T. Umegaki, J. M. Yan, X. B. Zhang, H. Shioyama, N. Kuriyama, Q. Xu, "Boron- and nitrogen-based chemical hydrogen storage materials," *International Journal of Hydrogen Energy*, vol. 34, no. 5, pp. 2303–2311, 2009.
- [5] Y. Fang X. Wang, "Metal-Free Boron-Containing Heterogeneous Catalysts," *Angewandte Chemie - International Edition*, vol. 56, no. 49, pp. 15506–15518, 2017.
- [6] I. Eryazici, N. Ramesh, C. Villa, "Electrification of the chemical industry—materials innovations for a lower carbon future," *MRS Bulletin*, vol. 46, no. 12, pp. 1197–1204, Dec. 2021.
- [7] I. Chorkendorff J. W. Niemantsverdriet, *Concepts of Modern Catalysis and Kinetics*, 3rd Edition, Weinheim, Germany: Wiley-VCH Verlag, 2017, pp 1-21.
- [8] D. S. Su, J. Zhang, B. Frank, A. Thomas, X. Wang, J. Paraknowitsch, R. Schlögl, "Metal-Free Heterogeneous Catalysis for Sustainable Chemistry," *ChemSusChem*, vol. 3, no. 2, pp. 169–180, Feb. 2010.
- [9] X. Gao, M. Liu, Y. Huang, W. Xu, X. Zhou, S. Yao, "Dimensional Understanding of Boron-Based Catalysts for Oxidative Propane Dehydrogenation: Structure and Mechanism," *ACS Catalysis*, vol. 13, pp. 9667–9687, 2023.
- [10] W. D. Lu, B. Qiu, Z. K. Liu, F. Wu, A. H. Lu, "Supported boron-based catalysts for oxidative dehydrogenation of light alkanes to olefins," *Catalysis Science and Technology*, vol. 13, no. 6, pp. 1696–1707, 2023.
- [11] D. Jana, C. L. Sun, L. C. Chen, K. H. Chen, "Effect of chemical doping of boron and nitrogen on the electronic, optical, and electrochemical properties of carbon nanotubes," *Progress in Materials Science*, vol. 58, no. 5, pp. 565–635, 2013.

- [12] H. Wan, M. Qing, H. Wang, S. Liu, X. W. Liu, Y. Zhang, H. Gong, L. Li, W. Zhang, C. Song, X. D. Wen, Y. Yang, Y. W. Li, "Promotive effect of boron oxide on the iron-based catalysts for Fischer-Tropsch synthesis," *Fuel*, vol. 281, no. 1, pp. 118714–118723, 2020.
- [13] K. F. Tan, J. Chang, A. Borgna, M. Saeys, "Effect of boron promotion on the stability of cobalt Fischer-Tropsch catalysts," *Journal of Catalysis*, vol. 280, no. 1, pp. 50–59, 2011.
- [14] M. S. Yazıcı F. G. B. San, "Bor doplu CVD grafen üretimi ve yakıt pili performansı," *Journal of Boron*, vol. 4, no. 3, pp. 141–147, 2019.
- [15] J. S. Wang, G. C. Zhao, Y. Q. Qiu, C. G. Liu, "Strong Boron–Carbon Bonding Interaction Drives CO₂ Reduction to Ethanol over the Boron-Doped Cu(111) Surface: An Insight from the First-Principles Calculations," *Journal of Physical Chemistry C*, vol. 125, pp. 572–582, 2021.
- [16] E. B. Şimşek, "Doping of boron in TiO₂ catalyst: Enhanced photocatalytic degradation of antibiotic under visible light irradiation," *Journal of Boron*, vol. 2, no. 1, pp. 18–27, 2017.
- [17] H. Zhao, H. Jiang, M. Cheng, Q. Lin, Y. Iv, Y. Xu, J. Xie, J. Liu, Z. Men, D. Ma, "Boron adsorption and its effect on stability and CO activation of χ -Fe₅C₂ catalyst: An ab initio DFT study," *Applied Catalysis A General*, vol. 627, no. August, pp. 118382–118391, 2021.
- [18] J. Li N. J. Coville, "Effect of boron on the sulfur poisoning of Co/TiO₂ Fischer-Tropsch catalysts," *Applied Catalysis A General*, vol. 208, no. 1–2, pp. 177–184, 2001.
- [19] A. Almofleh H. A. Aljama, "Boron Doping to Limit Sulfur Poisoning on Metal Catalysts," *ChemCatChem*, vol. 202201545, pp. 1–8, 2023.
- [20] G. Kresse J. Hafner, "Ab initio molecular dynamics for liquid metals," *Physical Review B*, vol. 47, no. 1, pp. 558–561, Jan. 1993.
- [21] G. Kresse J. Furthmuller, "Efficient iterative schemes for ab initio total-energy calculations using a plane-wave basis set," *Physical Review B*, vol. 54, no. 16, pp. 11169–11186, 1996.
- [22] J. P. Perdew, K. Burke, M. Ernzerhof, "Generalized gradient approximation made simple," *Physical Review Letters*, vol. 77, no. 18, pp. 3865–3868, 1996.
- [23] M. Dion, H. Rydberg, E. Schroder, D. C. Langreth, B. I. Lundqvist, "Van der Waals density functional for general geometries," *Physical Review Letters*, vol. 92, no. 24, pp. 246401–246412, 2004.
- [24] G. Roman-Perez J. M. Soler, "Efficient Implementation of a van der Waals Density Functional: Application to Double-Wall Carbon Nanotubes," *Physical Review Letters*, vol. 103, no. 9, pp. 096102–096109, 2009.
- [25] J. Klimes, D. R. Bowler, A. Michaelides, "Chemical accuracy for the van der Waals density functional," *Journal of Physics-Condensed Matter*, vol. 22, no. 2, pp. 022201–022209, 2010.
- [26] J. Klimes, D. R. Bowler, A. Michaelides, "Van der Waals density functionals applied to solids," *Physical Review B*, vol. 83, no. 19, pp. 195131–195138, 2011.
- [27] C. Chen, Q. Wang, G. Wang, B. Hou, L. Jia, D. Li, "Mechanistic insight into the C₂ hydrocarbons formation from Syngas on fcc-Co(111) surface: A DFT study," *Journal of Physical Chemistry C*, vol. 120, no. 17, pp. 9132–9147, 2016.
- [28] P. E. Blochl, "Projector Augmented-Wave Method," *Physical Review B*, vol. 50, no. 24, pp. 17953–17979, 1994.

- [29] H. J. Monkhorst J. D. Pack, “Special Points For Brillouin-Zone Integrations,” *Physical Review B*, vol. 13, no. 12, pp. 5188–5192, 1976.
- [30] G. Henkelman, B. P. Uberuaga, H. Jonsson, “A climbing image nudged elastic band method for finding saddle points and minimum energy paths,” *Journal of Chemical Physics*, vol. 113, no. 22, pp. 9901–9904, 2000.
- [31] Y. Daga A. C. Kizilkaya, “Mechanistic Insights into the Effect of Sulfur on the Selectivity of Cobalt-Catalyzed Fischer–Tropsch Synthesis: A DFT Study,” *Catalysts*, vol. 12, no. 4, pp. 425–441, 2022.
- [32] D. R. Alfonso, “First-principles studies of H₂S adsorption and dissociation on metal surfaces,” *Surface Science*, vol. 602, no. 16, pp. 2758–2768, 2008.
- [33] R. Zhang, H. Liu, Q. Li, B. Wang, L. Ling, D. Li, “Insight into the role of the promoters Pt, Ru and B in inhibiting the deactivation of Co catalysts in Fischer–Tropsch synthesis,” *Applied Surface Science*, vol. 453, pp. 309–319, 2018.

Theoretical Analysis and Simulation of SiO₂ and ZrO₂ Based Antireflective Coatings to Improve Crystalline Silicon Solar Cell Efficiency

İmran Kanmaz 

Karadeniz Technical University, Faculty of Sciences, Department of Physics, Trabzon, Türkiye,
imrankanmaz@ktu.edu.tr

ARTICLE INFO

ABSTRACT

Keywords:

Antireflection coating
ZrO₂
SiO₂
SCAPS

Article History:

Received: 11.09.2023

Accepted: 08.05.2024

Online Available: 06.06.2024

The Solar cell efficiency is crucial, and optical losses can hinder it significantly. Anti-reflective coatings are effective in minimizing these losses. In our study, we used Fresnel equations to calculate reflectance values for single-layer SiO₂, ZrO₂, a SiO₂-ZrO₂ mixture, and a double-layer SiO₂/ZrO₂ configuration. We then assessed their impact on crystalline silicon solar cells using the SCAPS program. The reflectance values of single-layer SiO₂, ZrO₂ and 10%SiO₂-90%ZrO₂ mixture were calculated as 19.17%, 13.09% and 13.01%, respectively. Notably, the double-layer SiO₂/ZrO₂ coating showed a low reflectance of 7.58%, a significant improvement compared to uncoated silicon at 37.45%. Efficiency values for crystalline silicon solar cells were calculated for single layer as 18,95% (SiO₂), 20,39% (ZrO₂), 20,40% (mixed coating) respectively and 21.68% for the double-layer SiO₂/ZrO₂ configuration.

1. Introduction

Zirconium dioxide (ZrO₂) thin films are widely used in science, technology and industry, with various applications such as optical filters, photocatalysts, and transistors [1-3]. ZrO₂ is found in three different phases: monoclinic (1443K), tetragonal (1443-2643K) and cubic (2643-2953K) at different annealing temperatures and has a stable structure in these temperature ranges [4]. When the cubic phase of the ZrO₂ thin films is considered, it has a band gap of 6.1 eV and a refractive index of around 2 [5, 6]. Because of these properties of ZrO₂ thin films can be used as an anti-reflective coating for crystalline silicon solar cells. Anti-reflective coatings can be applied to the top surface of crystalline silicon solar cells as one or more layers of thin films. The minimum reflection condition of anti-reflective thin films is related to the thickness and refractive index of the thin films.

These conditions can be expressed as [7],

$$n_1 = \sqrt{n_0 n_2} \quad (1)$$

$$d_1 = \frac{\lambda_0}{4n_1} \quad (2)$$

ZrO₂ thin films can be easily produced by methods such as vacuum evaporation, sputtering, pulsed laser deposition, ion-assisted deposition, ion beam sputtering, and Sol-gel [8-10]. However, it is important both in terms of time and cost to calculate the film thickness for the appropriate reflectance value of the film to be coated and to carry out the experiments in this direction. Therefore, the thickness value of the materials to be coated can be easily calculated with Fresnel equations to obtain the ideal reflectance value of the single-layer and double-layer films. While some of the sun rays coming to the surface of the solar cell are reflected back from the surface, some of them may pass through the surface and cause current formation in the solar cell. By using anti-reflective coatings, light reflection can be reduced, and transmittance can be increased. In this way, higher efficiency solar cells can be produced. The Fresnel equations in which the reflection value is measured for anti-

reflective coatings are given in eq (3) and eq (4) for single layer and double layer, respectively.

$$R_{SL} = |r^2| = \frac{r_1^2 + r_2^2 + 2r_1r_2\cos 2\theta}{1 + r_1^2r_2^2 + 2r_1r_2\cos 2\theta} \quad (3)$$

where; $r_1 = \frac{n_0 - n_1}{n_0 + n_1}$, $r_2 = \frac{n_1 - n_2}{n_1 + n_2}$, $\theta = \frac{2\pi n_1 d_1}{\lambda}$

$$R_{DL} = \frac{A+B+C+D+E+F}{1+(r_1^2r_2^2)+(r_1^2r_3^2)+(r_2^2r_3^2)+C+D+E+F} \quad (4)$$

where;

$$r_1 = \frac{n_0 - n_1}{n_0 + n_1}, r_2 = \frac{n_1 - n_2}{n_1 + n_2}, r_3 = \frac{n_2 - n_3}{n_2 + n_3},$$

$$\theta_1 = \frac{2\pi n_1 t_1}{\lambda}, \theta_2 = \frac{2\pi n_2 t_2}{\lambda} \text{ and}$$

$$A = r_1^2 + r_2^2 + r_3^2, B = r_1^2 r_2^2 r_3^2,$$

$$C = 2r_1 r_2 (1 + r_3^2) \cos 2\theta_1,$$

$$D = 2r_2 r_3 (1 + r_1^2) \cos 2\theta_2,$$

$$E = 2r_1 r_3 \cos 2(\theta_1 + \theta_2),$$

$$F = 2r_1 r_2 r_3 \cos 2(\theta_1 - \theta_2)$$

In this study, reflectance calculations were made for the first layer of anti-reflective layer ZrO₂ thin film and for the second layer, SiO₂ thin films with good optical transmittance and passivation effect in solar cells [11], and average reflectance values were obtained. In order to investigate the anti-reflective effect of SiO₂ and ZrO₂ mixtures, the refractive index of the mixture at various ratios was calculated with the Arago-Biot (A-B) equation and the reflectance values were calculated. In addition, the different equations for calculating the refractive index of mixtures are expressed as;

$$\text{Arago-Biot (A-B) : } n = n_1 \phi_1 + n_2 \phi_2 \quad (5)$$

n =Refractive index of mixture, n_1 =Refractive index of pure component-1, n_2 =Refractive index of pure component-2, ϕ_1 =Volume fraction of pure component-1 and ϕ_2 =Volume fraction of pure component-2 Where, also $\phi_1 = x_1 V_1 / \sum x_i V_i$ and $\phi_2 = x_2 V_2 / \sum x_i V_i$ here x is the mole fraction V_i is the molar volume of component i [12-14].

2. Methodology and Simulation

In our research, we conducted an analysis of the average reflectivity values for single-layer Zirconium Dioxide (ZrO₂), Silicon Dioxide (SiO₂), and double-layer SiO₂/ZrO₂ thin films, as well as the average reflectivity values of SiO₂-ZrO₂ mixtures at varying ratios. These calculations were performed using eq (3) and eq (4). Furthermore, we determined the refractive indices of SiO₂-ZrO₂ mixtures with different composition ratios employing the Arago-Biot (A-B) formula presented in eq (5). Additionally, to explore the impact of average reflectivity values on crystalline silicon solar cell parameters, we employed the numerical simulation program SCAPS.

SCAPS is a versatile software tool capable of simulating various thin-film solar cell types, including solar cells, Copper Indium Gallium Selenide (CIGS) cells, Cadmium Telluride (CdTe) cells, Gallium Arsenide (GaAs) cells, crystalline silicon (c-Si) cells, and amorphous Silicon (a-Si:H) cells, as described in references [15, 16]. The SCAPS program performs calculations involving steady-state band diagrams, recombination profiles, and carrier transport in one dimension, based on Poisson's equation and the continuity equations for both holes and electrons [17].

3. Result and Discussion

This study was conducted in three sequential stages. In the initial stage, we computed the reflectance values of single-layer ZrO₂, SiO₂, and double-layer SiO₂/ZrO₂ thin films using Fresnel equations. Subsequently, in the second stage, we determined the refractive indices of SiO₂, ZrO₂, mixtures across various ratios and calculated reflectance values dependent on film thickness. Finally, in the third stage, we applied the average reflectance values of single-layer SiO₂, ZrO₂, SiO₂-ZrO₂ mixtures, and double-layer SiO₂/ZrO₂ thin films as anti-reflective coatings to crystalline silicon (c-Si) solar cells using the SCAPS solar cell program. To calculate the reflectance values of SiO₂ and ZrO₂ thin films at different thicknesses, we systematically varied the thicknesses from 30nm to 100nm and summarized the obtained reflectance values in Figure 1.

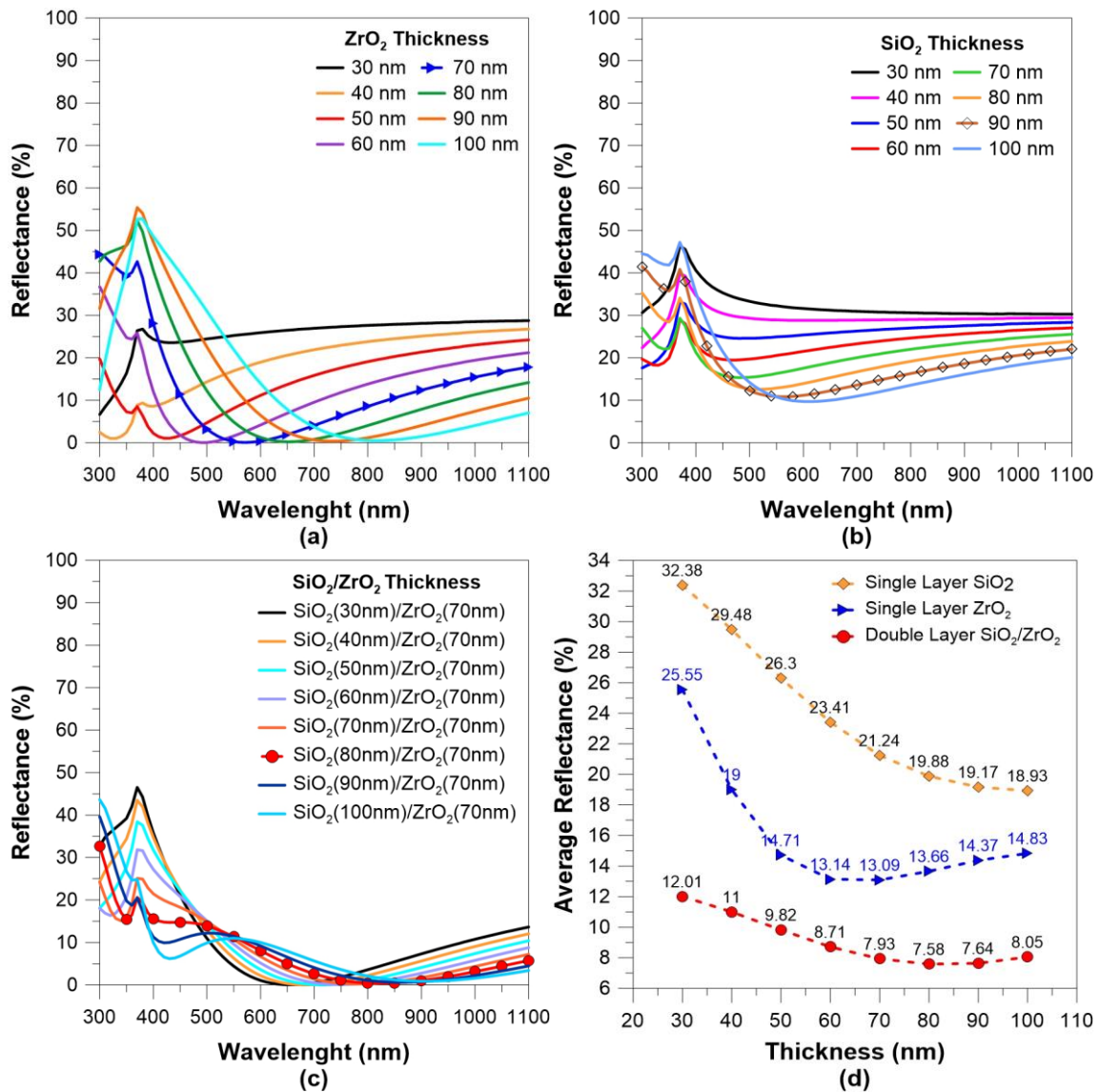


Figure 1. Reflective values of single-layer ZrO₂ (a) single-layer SiO₂ (b), double layer SiO₂/ZrO₂ (c) and average reflectance values (d)

As depicted in Figure 1(a), for ZrO₂ thin films with low thicknesses, high reflectance values were observed. With increasing thickness, both the reflectance values significantly decreased, and the minimum reflectance point shifted towards longer wavelengths. Figure 1(d) illustrates that the lowest average reflectance value for ZrO₂ thin films, 13.09%, was achieved at a thickness of 70nm. Additionally, as the thickness of the single-layer SiO₂ thin film increased, the average reflectance values decreased, reaching a minimum of 19.17% for a thickness of 90nm.

By employing multiple anti-reflective layers in solar cells, the reflective properties can be further reduced, thereby enhancing solar cell efficiency [18]. The reflectance values of double-layer anti-reflective coatings can be readily calculated

using Eq (4). The thickness of the ZrO₂ thin film, previously determined as the optimal thickness, was held constant at 70nm, while the thickness of the SiO₂ thin film was varied between 30nm and 100nm. In order to achieve the lowest reflectance value. The reflectivity of the SiO₂/ZrO₂ double-layer thin film decreased from 12.01% to its lowest point of 7.58% when the SiO₂ thin film reached a thickness of 80nm. When the thickness of the SiO₂ thin film was increased from 80nm to 100nm, the average reflectivity value increased from 7.58% to 8.05%. In the literature, it is commonly observed that double-layer thin films offer advantages in terms of anti-reflective properties, leading to lower levels of reflection compared to single-layer thin films [19, 20]. When two materials with different refractive indices are mixed at different rates, the refractive

index of the mixture is expected to be a value between the refractive indices of both materials included in the mixture ($n_{Low} < n_{Mix} < n_{High}$).

Based on the refractive indices of SiO₂ and ZrO₂ materials, the refractive indices of SiO₂-ZrO₂ mixtures at different ratios were calculated using eq (5) at nine different ratios

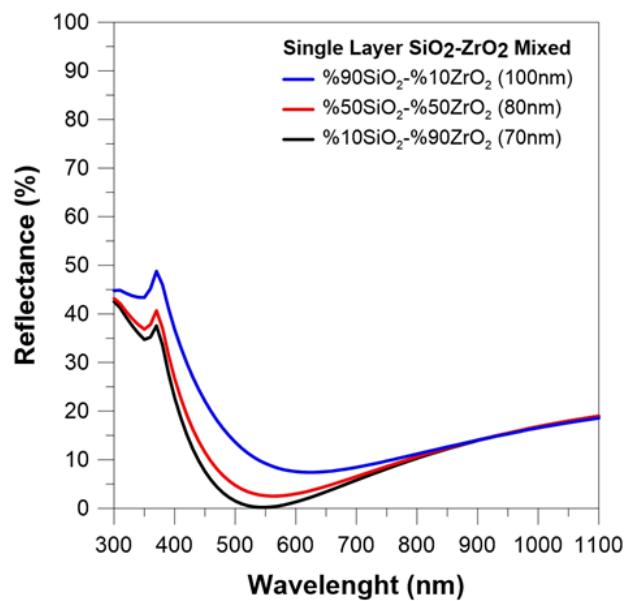


Figure 2. Graph of the reflectance of three different ratios of SiO₂-ZrO₂ mixed

Table 1. Refractive index of SiO₂-ZrO₂ mixtures at different ratios and reflectance values depending on different thickness values

Mixed Ratio	n(mixed)	Average Reflectance (%)							
		30nm	40nm	50nm	60nm	70nm	80nm	90nm	100nm
%90SiO ₂ -%10ZrO ₂	1.49	31.79	28.47	24.91	21.81	19.62	18.36	17.78	17.66
%80SiO ₂ -%20ZrO ₂	1.55	31.19	27.45	23.53	20.29	18.16	17.03	16.61	16.62
%70SiO ₂ -%30ZrO ₂	1.60	30.58	26.42	22.19	18.88	16.87	15.92	15.65	15.80
%60SiO ₂ -%40ZrO ₂	1.66	29.96	25.40	20.91	17.61	15.76	15.01	14.91	15.17
%50SiO ₂ -%50ZrO ₂	1.71	29.33	24.38	19.69	16.48	14.85	14.30	14.36	14.73
%40SiO ₂ -%60ZrO ₂	1.77	28.70	23.38	18.57	15.51	14.12	13.78	13.99	14.46
%30SiO ₂ -%70ZrO ₂	1.82	28.06	22.41	17.55	14.71	13.58	13.44	13.80	14.33
%20SiO ₂ -%80ZrO ₂	1.88	27.43	21.48	16.65	14.07	13.21	13.27	13.75	14.31
%10SiO ₂ -%90ZrO ₂	1.93	26.81	20.61	15.88	13.61	13.01	13.26	13.84	14.40

Considering the refractive index of SiO₂ as 1.44 [21] and of ZrO₂ as 2.05 [22], it is clearly seen from table 1 that the refractive index of SiO₂-ZrO₂ mixture varies between 1.49 and 1.93. Eq (5) was used for the refractive index of each SiO₂-ZrO₂ ratios, and the reflectance values were calculated with the eq (3) by changing the thin film thicknesses from 30nm to 100nm. Calculations were made by taking molarity of SiO₂ and ZrO₂ as equal. It was seen that the mole fractions of SiO₂ and ZrO₂ changed in direct proportion to $V_{SiO_2}/(V_{SiO_2}+V_{ZrO_2})$ and $V_{ZrO_2}/(V_{SiO_2}+V_{ZrO_2})$, respectively.

50%ZrO₂, 90%SiO₂-10%ZrO₂) is given in figure 2. It can be clearly seen from table 1 that the lowest average reflectance value of 10%SiO₂-90%ZrO₂ mixture was calculated as 13.01% for the 70nm thickness. It was also noted that as the SiO₂ ratio in the mixture increased, the refractive index of the mixture decreased and therefore the average reflectance values decreased. In addition, as the SiO₂ ratio increases, the thin film thickness required to be coated in order to obtain low reflectance values also increases.

The reflection-wavelength graph for three different ratios (10%SiO₂-90%ZrO₂, 50%SiO₂-

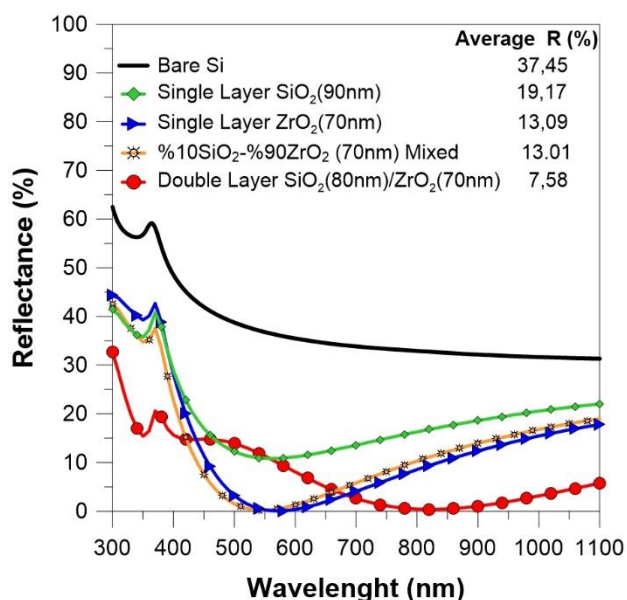


Figure 3. Reflection-wavelength graphs of different thin films

When the refractive indices of $\text{SiO}_2\text{-ZrO}_2$ mixtures at different ratios were examined, it was seen that the average reflectance value decreased as the refractive index approached 2. Unfortunately, the desired reflection values cannot be achieved even if ideal refractive index materials are produced for anti-reflective coatings with the mixture of two different materials in different ratios. From the reflectance wavelength graphs given in figure 3, it is clearly seen that the reflectance values of double layer $\text{SiO}_2/\text{ZrO}_2$ thin films give better results compared to the single layer reflectance values. While the best reflectance value in single layer layers was 13.01% for 10% $\text{SiO}_2\text{-90}\%$ ZrO_2 thin film, this value decreased to 7.58% for double layer $\text{SiO}_2/\text{ZrO}_2$ thin film. Therefore, multi-layer anti-reflective coatings are highly preferred for high-efficiency solar cells due to their low reflectance values [23].

The average reflectance values of single layer SiO_2 , single layer ZrO_2 , single layer %10 $\text{SiO}_2\text{-}$

%90 ZrO_2 mixed and double layer $\text{SiO}_2(80\text{nm})/\text{ZrO}_2(70\text{nm})$ thin films and the initial parameters of the crystalline silicon solar cell given in table 2 were used together in the SCAPS program to investigate the effect of anti-reflective coatings on the crystalline silicon solar cell. Figure 4 shows a schematic representation of conventional crystalline silicon solar cells.

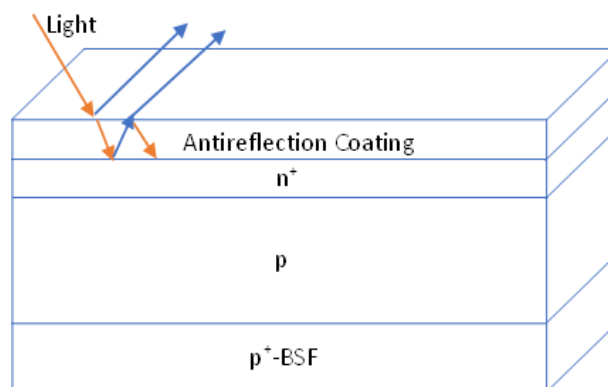


Figure 4. Schematic representation of Crystalline silicon solar cell

The current-voltage graph of this solar cell is given in figure 5 and the parameters of the solar cell are summarized in table 3. As can be seen from table 3, anti-reflective coatings have a great effect on solar cell parameters. For the uncoated c-Si solar cell, the V_{oc} , J_{cs} , FF and efficiency values were calculated as 752.20V, 25.48mA/cm², 82.80% and 14.63%, respectively, and serious improvements were achieved on the solar cell parameters by applying anti-reflective coating to the solar cells. For example, the efficiency values for single layer SiO_2 increased from 14.63% to 18.95% compared to the uncoated solar cell. In addition, the efficiency values for single layer ZrO_2 , single layer 10% $\text{SiO}_2\text{-90}\%$ ZrO_2 mixed and double layer $\text{SiO}_2\text{-ZrO}_2$ were recorded as 20.39%, 20.40% and 21.68%, respectively

Table 2. Some initially parameters of c-Si solar cell for SCAPS [24]

	n ⁺	p-Si	p ⁺ -Si-Bsf
Thickness (μm)	0.3	200	7
Bandgap (eV)	1.12	1.12	1.12
Electron affinity (eV)	4.05	4.05	4.05
Dielectric permittivity	11.90	11.90	11.90
CB effective density of states (cm ⁻³)	4.79x10 ¹⁸	2.80x10 ¹⁹	2.80x10 ¹⁹
VB effective density of states (cm ⁻³)	4.52x10 ¹⁸	1.04x10 ¹⁹	1.04x10 ¹⁹
Electron mobility (cm ² /Vs)	73.36	1041	202
Hole mobility (cm ² /Vs)	155.6	412	77
Shallow uniform donor density N _D (cm ⁻³)	1x10 ²⁰	1x10 ¹⁶	-
Shallow uniform acceptor density N _A (cm ⁻³)	-	1x10 ¹⁶	1x10 ¹⁹

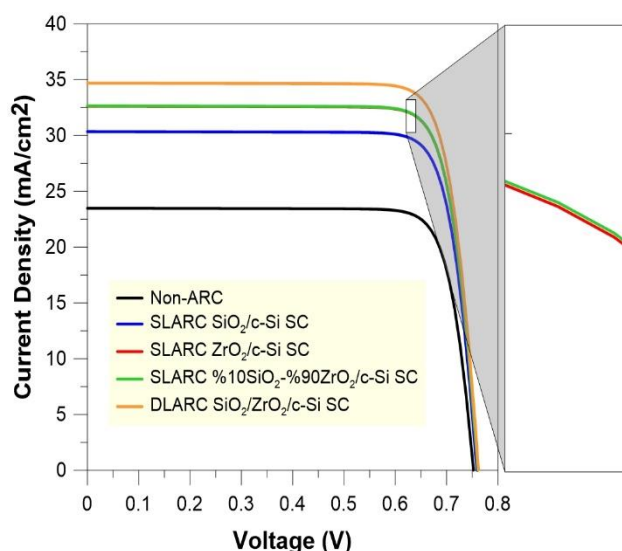


Figure 5. I-V graphics of crystalline silicon solar cell of uncoated and different anti-reflective coating

Table 3. The effect of different anti-reflective coatings on crystalline silicon solar cells

	$V_{oc}(mV)$	$J_{sc}(mA/cm^2)$	FF(%)	Eff.(%)
Non-ARC/c-Si SC	752.2	23.48	82.80	14.63
SLARC SiO ₂ /c-Si SC	758.9	30.34	82.30	18.95
SLARC ZrO ₂ /c-Si SC	760.8	32.62	82.12	20.39
SLARC %10SiO ₂ /%90ZrO ₂ Mixed/c-Si SC	760.8	32.66	82.12	20.40
DLARC SiO ₂ /ZrO ₂ /c-Si SC	762.4	34.69	81.95	21.68

4. Conclusions

This study investigated the potential of anti-reflective coatings, specifically single-layer SiO₂, ZrO₂, SiO₂-ZrO₂ mixtures, and double-layer SiO₂/ZrO₂ thin films, to enhance the performance of crystalline silicon solar cells. Reflectance calculations and refractive index assessments were conducted for various coating configurations, and their impact on solar cell efficiency was investigated using the SCAPS program. The results demonstrated significant improvements in solar cell parameters with the application of anti-reflective coatings. Single-layer SiO₂, ZrO₂, and SiO₂-ZrO₂ mixtures all showed enhanced efficiency compared to uncoated solar cells. Furthermore, the double-layer SiO₂/ZrO₂ configuration exhibited the highest efficiency among the coatings studied.

These findings emphasize the critical role of anti-reflective coatings in increasing the efficiency of crystalline silicon solar cells, paving the way for more efficient and sustainable solar energy conversion technologies. The utilization of multi-layer anti-reflective coatings, such as double-layer SiO₂/ZrO₂, is particularly

promising for achieving low reflectance values and maximizing solar cell performance.

Article Information Form

Funding

The author (s) has no received any financial support for the research, authorship or publication of this study.

The Declaration of Conflict of Interest/ Common Interest

No conflict of interest or common interest has been declared by the authors.

The Declaration of Ethics Committee Approval

This study does not require ethics committee permission or any special permission.

The Declaration of Research and Publication Ethics

The authors of the paper declare that they comply with the scientific, ethical and quotation rules of SAUJS in all processes of the paper and that they do not make any falsification on the data collected. In addition, they declare that Sakarya University Journal of Science and its editorial board have no responsibility for any ethical

violations that may be encountered, and that this study has not been evaluated in any academic publication environment other than Sakarya University Journal of Science.

Copyright Statement

Authors own the copyright of their work published in the journal and their work is published under the CC BY-NC 4.0 license.

References

- [1] T. Yamaguchi, "Application of ZrO₂ as a catalyst and a catalyst support", *Catalysis today*, vol. 20, pp. 199-217, 1994.
- [2] Q. Zhang, X. Li, J. Shen, G. Wu, J. Wang, L. Chen, "ZrO₂ thin films and ZrO₂/SiO₂ optical reflection filters deposited by sol-gel method", *Materials Letters*, vol. 45 pp. 311-314, 2000.
- [3] J. H. Park, Y. B. Yoo, K. H. Lee, W. S. Jang, J. Y. Oh, S. S. Chae, H. W. Lee, S. W. Han, H. K. Baik, "Boron-doped peroxo-zirconium oxide dielectric for high-performance, low-temperature, solution-processed indium oxide thin-film transistor", *ACS applied materials & interfaces*, vol. 5 pp. 8067-8075, 2013.
- [4] G. Balakrishnan, P. Kuppasami, S. Murugesan, C. Ghosh, R. Divakar, E. Mohandas, D. Sastikumar, "Characterization of Al₂O₃/ZrO₂ nano multilayer thin films prepared by pulsed laser deposition", *Materials Chemistry and Physics*, vol. 133 pp. 299-303, 2012
- [5] W. J. Shin, W.-H. Huang, M. Tao, "Low-cost spray-deposited ZrO₂ for antireflection in Si solar cells", *Materials Chemistry and Physics*, vol. 230, pp. 37-43, 2019.
- [6] U. Sikder, M. A. Zaman, "Optimization of multilayer antireflection coating for photovoltaic applications", *Optics & Laser Technology*, vol.79, pp. 88-94, 2016.
- [7] A. J. Thosar, M. Thosar, R. Khanna, "Optimization of anti-reflection coating for improving the performance of GaAs solar cell", *Indian Journal of Science and Technology*, vol. 7 pp. 637-641, 2014.
- [8] M. Epifani, C. Giannini, L. Tapfer, L. Vasanelli, "Sol-gel synthesis and characterization of Ag and Au nanoparticles in SiO₂, TiO₂, and ZrO₂ thin films", *Journal of the American Ceramic Society*, vol. 83 pp. 2385-2393, 2000.
- [9] J. Čyviienė, M. Laurikaitis, J. Dudonis, "Deposition of nanocomposite Zr-ZrO₂ films by reactive cathodic vacuum arc evaporation", *Materials Science and Engineering: B*, vol. 118, pp. 238-241, 2005.
- [10] D. Panda, T.-Y. Tseng, "Growth, dielectric properties, and memory device applications of ZrO₂ thin films", *Thin Solid Films*, vol. 531 pp. 1-20, 2013.
- [11] A. Uzum, I. Kanmaz, "Passivation properties of HfO₂-SiO₂ mixed metal oxide thin films with low reflectivity on silicon substrates for semiconductor devices", *Thin Solid Films*, vol. 738 pp. 138965, 2021.
- [12] M. A. Khan, M. Sohel, M.A. Islam, F. I. Chowdhury, S. Akhtar, "Refractive Indices of Aqueous Solutions of Isomeric Butylamines at 303.15 K: Experimental and Correlative Approach", *Journal of Applied Science & Process Engineering*, vol. 8 pp. 1020-1030, 2021.
- [13] S. Sharma, P. B. Patel, R. S. Patel, J. Vora, "Density and comparative refractive index study on mixing properties of binary liquid mixtures of eucalyptol with hydrocarbons at 303.15, 308.15 and 313.15 K", *E-Journal of Chemistry*, vol. 4 pp. 343-349, 2007.
- [14] F. Pretorius, W. W. Focke, R. Androsch, E. du Toit, "Estimating binary liquid composition from density and refractive index measurements: A comprehensive review of mixing rules", *Journal of Molecular Liquids*, vol. 332 pp. 115893, 2021.

- [15] A. Kowsar, M. Billah, S. Dey, S. C. Debnath, S. Yeakin, S. F. U. Farhad, "Comparative Study on Solar Cell Simulators, in: 2019" 2nd International Conference on Innovation in Engineering and Technology (ICIET), IEEE, 2019, pp. 1-6.
- [16] S. M. Seck, E. N. Ndiaye, M. Fall, S. p. Charvet, "Study of efficiencies CdTe/CdS photovoltaic solar cell according to electrical properties by scaps simulation", *Natural Resources*, vol. 11 pp. 147-155, 2020.
- [17] A. Teyou Ngoupo, S. Ouédraogo, J. Ndjaka, "Numerical analysis of interface properties effects in CdTe/CdS: O thin film solar cell by SCAPS-1D", *Indian Journal of Physics*, vol. 93 pp. 869-881, 2019.
- [18] W. Zhang, K. Hu, J. Tu, A. Aierken, D. Xu, G. Song, X. Sun, L. Li, K. Chen, D. Zhang, "Broadband graded refractive index $\text{TiO}_2/\text{Al}_2\text{O}_3/\text{MgF}_2$ multilayer antireflection coating for high efficiency multi-junction solar cell", *Solar Energy*, vol. 217 pp. 271-279, 2021.
- [19] K. Ali, S. A. Khan, M. M. Jafri, "Effect of double layer ($\text{SiO}_2/\text{TiO}_2$) anti-reflective coating on silicon solar cells", *Int. J. Electrochem. Sci*, vol. 9 pp. 7865-7874, 2014
- [20] M. A. Zahid, M. Q. Khokhar, S. Park, S. Q. Hussain, Y. Kim, J. Yi, "Influence of $\text{Al}_2\text{O}_3/\text{IZO}$ double-layer antireflective coating on the front side of rear emitter silicon heterojunction solar cell", *Vacuum*, vol. 200, pp. 110967, 2022.
- [21] S.-Y. Lien, D.-S. Wu, W.-C. Yeh, J.-C. Liu, "Tri-layer antireflection coatings ($\text{SiO}_2/\text{SiO}_2\text{-TiO}_2/\text{TiO}_2$) for silicon solar cells using a sol-gel technique", *Solar Energy Materials and Solar Cells*, vol. 90, pp. 2710-2719, 2006.
- [22] F. Karaömerlioğlu, E. Mehmetov, "Optical Properties and Technological Applications of Multilayer Antireflection Coatings", vol. 19 pp. 1-6, 2008.
- [23] X. Xiao, H. Z. Liu, J. Tu, "Multilayer antireflection coatings design for SiO_2 -passivated silicon solar cells", *Materialwissenschaft und Werkstofftechnik*, vol. 53 pp. 80-88, 2022.
- [24] İ. Kanmaz, "Simulation of CdS/p-Si/p+-Si and ZnO/CdS/p-Si/p+-Si Heterojunction Solar Cells", *Results in Optics*, pp. 100353, 2023.

Investigation of the Effect of High-Frequency Induction Sintering on Phase Structure and Microstructure of SiC Reinforced Aluminum Matrix Composites

Muhterem Koç^{1*} , Mehmet Sadrettin Zeybek² 

¹ Kütahya Dumlupınar University, Faculty of Architecture, Department of Industrial Design, Kütahya, Türkiye, muhterem.koc@dpu.edu.tr

² Manisa Celal Bayar University, Turgutlu Vocational School, Department of Material and Material Processing Technologies, Manisa, Türkiye, sadrettin.zeybek@cbu.edu.tr

*Corresponding Author

ARTICLE INFO

ABSTRACT

Keywords:
HFIS
Aluminum
SiC
Al₄C₃
Sintering



Article History:
Received: 19.09.2023
Accepted: 04.03.2024
Online Available: 06.06.2024

In this study, SiC-reinforced aluminum matrix composites were powder metallurgically (PM) prepared and sintered using high-frequency induction system (HFIS). The samples with different ratios of SiC (wt.% 10, 20 and 40) added to the aluminum matrix were sintered at 660, 800, and 1000 °C. In addition, Al/SiC composites were compared by sintering with the conventional sintering (CS) method under similar sintering conditions. The heating rate for the sintering process using HFIS was 500 °C/min, while the CS method used a heating rate of 10 °C/min. The effect of the temperature and SiC ratio on the density, hardness, phase structure, and microstructure of composites was investigated. The optimum sintering temperature was determined according to the SiC additive amount. When 10%, 20%, and 40% SiC by weight were added to the aluminum matrix in the sintering process with HFIS, the required sintering temperatures were determined as 660, 800, and 1000 °C, respectively. While new phases were not formed as a result of short-term HFIS sintering, a high-temperature Al₄C₃ phase was detected in CS sintering. HFIS sintered Al/SiC composite samples were obtained in Al and SiC phases with high density and hardness ranging from 43-118 HV. In the high-temperature sintering process with HFIS, the formation of Al₄C₃ was prevented and its physical and mechanical properties were improved.

1. Introduction

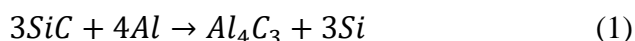
Aluminum matrix composite materials are extensively utilized in aerospace, automotive, and electronic industries as they form the primary constituent of engineering products that possess favorable properties such as high strength, low density, high elastic modulus, hardness, and wear resistance. Silicon Carbide (SiC), Titanium Carbide (TiC), Boron Carbide (B₄C) and Alumina (Al₂O₃) are the most widely used inter-metallic compounds in the aluminum matrix composites. SiC is the most widely used reinforcement phase in aluminum matrix composites due to its superior properties such as high elastic modulus, strength, wear resistance and hardness [1, 2]. Evaluation of SiC particles

as a reinforcement element in the aluminum matrix composites has some restrictions. High production cost, non-homogenous distribution of reinforcement phase, grain growth in the matrix, and undesired phases occurrence such as Al₄C₃ in the matrix are the most popular restrictive factors of the Al/SiC composites [3, 4].

Previous studies have shown that liquid-phase or solid-phase production is effective in determining the properties of aluminum matrix composites. Pressure infiltration, laser melting, and mold casting methods are the techniques used in the liquid-phase production [5-7]. In production processes involving liquids, production inherently occurs within a liquid medium, and obtaining the proper distribution of

the reinforcement phase becomes a great difficulty. In addition, agglomeration of the grains leads to a decrease in the mechanical properties of the composite materials. Hot press sintering, hot isostatic press, spark-plasma, and sintering in the argon medium are alternative solid phase methods for production of the net shaped materials. This powder metallurgy method generally needs long operation periods and temperatures, so some of the restricts and obstacles must be controlled and even eliminated during the process [8-10].

High temperature sintering causes to the occurrence of inter metallic compounds which significantly decrease the performances of composites and their ductility properties. In the production of Al-SiC composites, aluminum does not react with SiC particles until the melting temperature of 660 °C, but different products can be formed depending on the temperature by reacting with SiC above the Al melting temperature. Needle shaped, very brittle and hydrophobic Al_4C_3 compound formation occurs in between 650 °C and 920 °C temperature interval. However, under the 650 °C operation conditions, the occurrence of Al_4C_3 phase has a very low possibility in the composite structure. When the composites are obtained at short operation periods and used low amount of SiC compositions, there is not much considerable formation of Al_4C_3 phase. However, when the sintering temperature is high, the Al_4C_3 phase is rapidly formed [11, 12]. For that reason, when Al/SiC system was considered, there is a potential of the development of Al_4C_3 phase as a reaction product because of the dissolution of SiC in the liquid aluminum on the interface of Al/SiC depending on the reaction at the equation 1 [13].



Long term sintering process is required to produce Al/SiC composites in the conventional methods which causes some unfavorable effects such as particle growth and occurrence of undesired phases, so new manufacturing techniques are needed. Moreover, the conventional sintering methods causes disadvantages for commercial productions because of long operation periods needed.

To eliminate these problems, HFIS is a promising sintering technique that provides rapid heating at the desired sintering temperature. HFIS reaches high temperatures with a heating rate of over 500 °C, providing the opportunity to reach the desired temperature in a short time. Heating is obtained from the induction coil by using alternating current. To induce the metal object itself, heating is derived by creating an electromagnetic field around the coil. HFIS is very effective in sintering the composite materials in a few minutes to prevent thermal deformation and undesired grain growth and as a result, it was shown that various properties of composites were improved [14].

In this study, sintering conditions of Al/SiC composites in HFIS were investigated according to the SiC ratio. Densities, microstructures, and phase formations of Al/SiC composites were investigated. Similar conditions were used in the conventional sintering methods and compared with high frequency induction system.

2. Materials and Methods

In this work, aluminum (99%) and SiC (99.5%) were used in the production of aluminum composites reinforced with different ratios SiC. In Figure 1, when the SEM analysis of aluminum and SiC powders is observed, aluminum grains are elliptical sphere shape and SiC particles have sharp corners. It was seen that powders particle size was under the 100 µm. The average grain size of Al and SiC powders was determined to be 58 and 64 µm, respectively (Malvern/Mastersizer 3000). Aluminum powders to which 10, 20, and 40 wt.% SiC were added were mixed for one hour using a V-type mixer. Prepared compositions were shaped in a cylindrical metallic mold under 40 MPa pressure by means of a uniaxial hydraulic press.

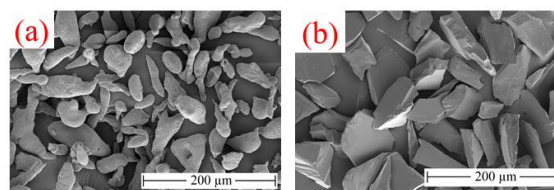


Figure 1. Aluminum (a) and SiC (b) powders microstructure analysis

Samples were sintered in argon atmosphere using HFIS and CS methods. Tube furnace was used in

CS method. The sintering operation was performed at 660, 800, and 1000 °C with the heating rates of 500 °C/min and 10 °C/min in the HFIS and the CS method, respectively. In Figure 2, a time and temperature graph were given for HFIS and CS methods. The sintering process performed with HFIS at a temperature of 1000 °C was completed in 3 minutes, and with CS sintering in approximately 141 minutes.

Sintered sample characterization was made by using density, phase analysis, hardness, and microstructure. Experimental density was measured with the Archimedes method. Theoretical calculation of the densities of Al/SiC composites was made using the mixture rules. Phase components were determined with XRD (PANalytical Empyrean High-resolution X-ray diffractometer) analysis. XRD analyses were performed by 0.026° and the interval was of 10°–70° (2 θ). Microstructure analyses of the composites were measured using scanning electron microscopy (SEM, SUPRA 40VP). Before the microstructure analysis, the samples were sanded with 600, 1000, and 2000 sanding and finally, a smooth surface was obtained using diamond solution. Sintered Al/SiC composite hardness was measured using a Vickers hardness testing machine (HBRV-187.5 Digital Universal Hardness Tester) 30 gf load applied for 10 seconds). Five measurements were taken from each composite and their average was determined.

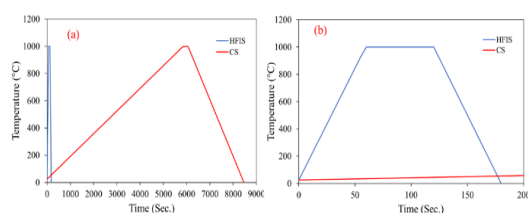


Figure 2. The time and temperature graph for HFIS and CS methods: (a) general graphic, (b) detail graphic.

3. Result and Discussion

In this study, HFIS was used in the sintering of aluminum composites prepared by adding SiC at different rates (10, 20 and 40 wt.%). The optimum sintering temperature was determined according to the amount of SiC additive. The Experimental density values of samples prepared with different SiC ratios are given in Table 1. The

experimental densities of the samples increased with sintering temperature. As the SiC ratio increased, the sintering temperature required to increase the experimental density also increased. When 10 wt. % SiC was added to aluminum, a similar density value was obtained at all sintering temperatures. Therefore, the sintering temperature of the composition with 10% SiC was determined to be 660 °C. When the SiC ratio was 20% and 40%, the sintering temperatures were 800 and 1000 °C, respectively. Because the sintering process took place quickly, higher temperatures were needed to achieve the desired density. Liu et al. determined the sintering temperature as 770 °C for the addition of 15% SiC in the microwave sintering process [15].

Table 1. Density analysis of Al/SiC composites produced with HFIS

SiC ratio (wt.%)	Theoretical density (gr/cm ³)	Experimental density (gr/cm ³)		
		660 °C	800 °C	1000 °C
10	2.75	2.70	2.72	2.72
20	2.80	2.67	2.74	2.76
40	2.90	2.71	2.75	2.79

SEM images of the sintered samples are given in Figure 3a-i. The interface formed between aluminum particles and SiC particles is effective on the properties of Al-SiC composites. The SiC ratio and sintering temperature are the determining parameters in forming a good interface. The melting temperature of aluminum metal is known to be 660 °C. In conventional sintering processes, it has been observed that dense materials are obtained with long sintering time, such as 1-2 hours, below the melting temperature. [16]. At high SiC ratios the sintering process was carried out above the melting temperature of aluminum [4, 17]. In this study, the required sintering temperature was determined according to the SiC ratio in the sintering process with HFIS. SEM analysis in Figure 3 showed that a homogeneous microstructure was obtained at all SiC ratios.

Additionally, in Figures 3d, g and j, no fracture occurred in the SiC grains despite the high sintering temperature. Partial aggregation is observed when the SiC ratio is 40%, but it is at a low level. In Figure 3g, it was determined that partially pores were more in the sintering made at 660 °C at 40% SiC ratio. It was observed that

these pores decreased as the sintering temperature increased. When the microstructure and density values of the samples sintered by HFIS were examined, it was determined that the sintering temperature increased depending on the SiC ratio. In the sintering process with HFIS, 10, 20 and 40 wt. % SiC was added and the required sintering temperatures were determined to be 660, 800 and 1000 °C, respectively.

Photographs of composites produced under optimum conditions are given in Figure 4. The samples were produced at different temperatures without deformation. It was observed that the samples became darker as the sintering temperature increased. This darkening was caused by a small amount of oxide layer formed due to the sintering process at high temperatures.

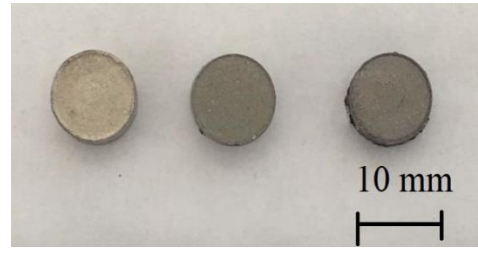
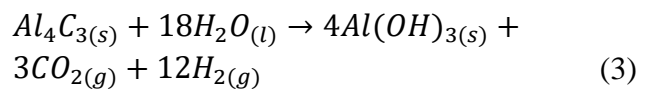
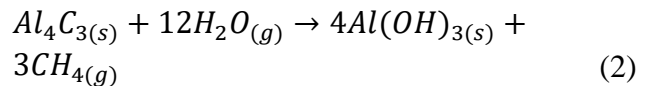


Figure 4. Photograph of Al/SiC composites produced with HFIS at optimum temperatures (from left to right; Al composites with 10, 20, 40% SiC addition)

The microstructure images obtained as a result of sintering the optimum compositions with the CS method were given in Figure 5. It was determined that the Al/SiC composite produced with the addition of 10 wt% SiC at low temperature (660 °C) had a homogeneous microstructure. As the sintering temperature and SiC ratio increased, fractures began to occur in the SiC grains. In addition, short dimensional lath Al_4C_3 structures in white color were formed (Figure 5b). It was stated that Al_4C_3 structures were formed in sintering above the melting temperature.

The formation of a harmful aluminum carbide (Al_4C_3) phase has been detected in long-term contact of SiC grains with the liquid aluminum outer surface [18, 19]. It was observed that when sintering time and SiC amount increased, more Al_4C_3 structures were formed. When the microstructure formed as a result of sintering the Al40 composition at 1000°C was examined, it was observed that the SiC grains were more broken. Al_4C_3 structures also began to form longer. Figure 5d, lath Al_4C_3 length was determined to be around 50 microns. When samples containing Al_4C_3 phase are kept under atmospheric conditions, they slowly hydrolyze and form an Al-hydroxide structure [18]. Moisture-induced decomposition of the Al_4C_3 phase occurs in the reactions given in equations 2 and 3.



Al_4C_3 phase is an undesirable phase because it causes deterioration of the mechanical and

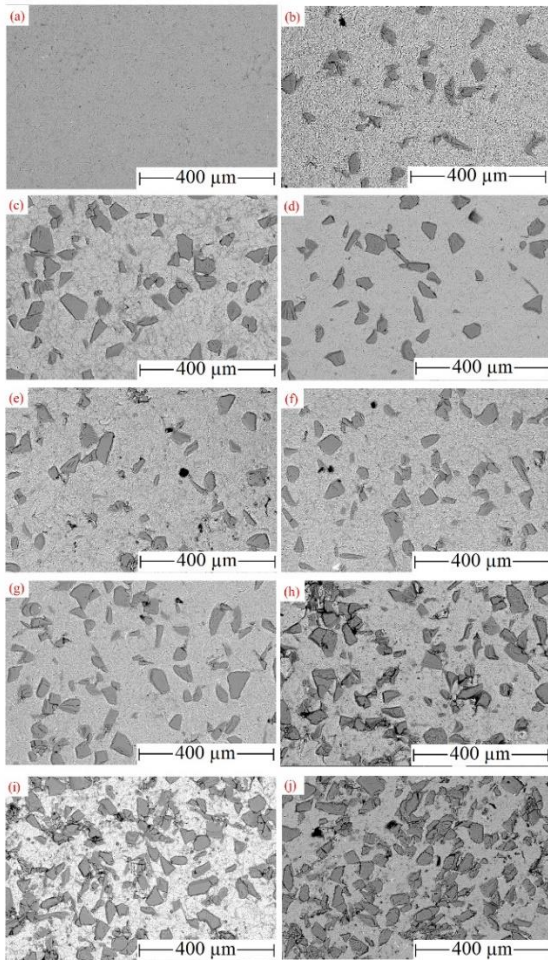


Figure 3. Microstructure images of samples sintered with HFIS at different SiC ratios and different temperatures; (a)Al-660 °C (b) Al10-660 °C, (c) Al10-800 °C, (d) Al10-1000 °C, (e) Al20-660 °C, (f) Al20-800 °C, (g) Al20-1000 °C, (h) Al40-660 °C, (i) Al40-800 °C, (j) Al40-1000 °C

physical properties of the material. Figure 6 shows the microstructure of a sample containing Al_4C_3 phase, which is formed as a result of keeping it under room conditions for 1 year. As a result of the reaction of the unstable Al_4C_3 phase with water, cracks occurred in the sample due to the formation of $\text{Al}(\text{OH})_3$ structure. However, Al_4C_3 structure is not formed in samples exposed to high temperatures for a short time during sintering with HFIS (Figure 3e-j).

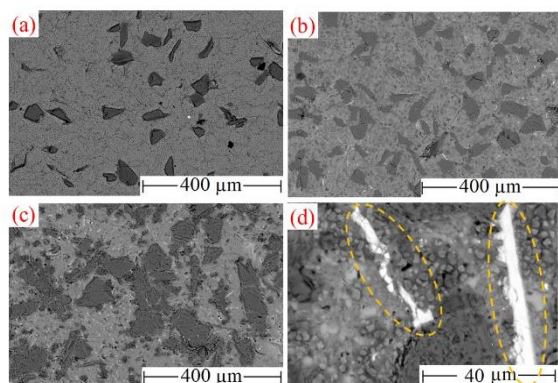


Figure 5. Microstructure images of samples sintered with CS at different SiC ratio and temperatures: (a) Al10-660 °C, (b) Al20-800 °C, (c) Al40-1000 °C, (d) Al40-1000 °C (high resolution)

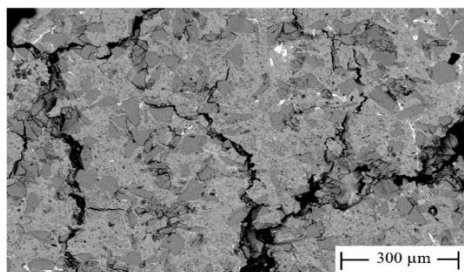


Figure 6. Microstructure image of 40% SiC doped aluminum composite, which is sintered by CS method at 1000 °C and kept for one year at room conditions

In Figure 7, XRD analyzes of samples sintered with HFIS at different temperatures and SiC ratios are given. Al (PDF# 98-007-7363) and SiC (PDF# 00-027-1402) peaks were detected in the samples produced under different conditions. In the XRD analysis, it is clearly seen that the Al_4C_3 phase is not formed. According to the diffraction peaks of Al_4C_3 between 30° and 33° as shown in Figure 8a, the presence of an Al_4C_3 phase could not be detected after the HFIS sintering process at all temperatures. The characteristic peaks of Al_4C_3 were observed when the composite of Al/SiC (wt.%40) was sintered in the convectional

system at 1000 °C (Figure 8b). It is stated that the Al_4C_3 phase, which generally occurs at high temperatures, is formed even below 660 °C [18, 20]. Therefore, short-term sintering with HFIS is an advantageous process in preventing the Al_4C_3 phase.

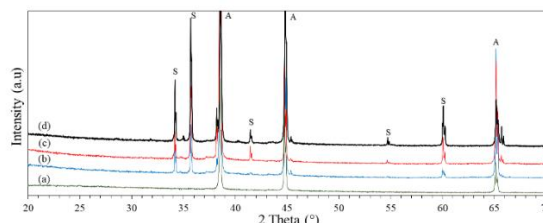


Figure 7. X-ray diffraction patterns of Al/SiC composites sintered with HFIS; (a) Al-660 °C, (b) Al10-660 °C (c) Al20-800 °C, (d) Al40-1000 °C (A: Aluminium, S: SiC)

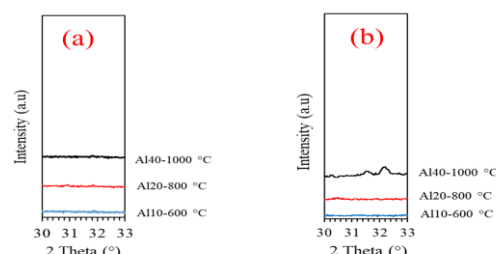


Figure 8. X-ray diffraction patterns of Al/SiC composites after sintering; (a) HFIS, (b) CS

Figure 9 shows the relationship between the hardness of the composites and the SiC content for both sintering methods. Hardness increases with increasing SiC addition [21]. When the SiC ratio was wt.% 10, 20 and 40, the hardness values were found to be 43, 69 and 118 HV, respectively. In the literature, the hardness values of Al/SiC composites vary between 25 and 90 HV depending on the SiC ratio [16, 22-25].

It was determined that the hardness values obtained in this study were compatible with the literature. When the SiC ratio was wt.% 40, a very high hardness value was obtained (118 HV). In the sintering process with CS, the hardness value of the composite with wt% 40 SiC addition was determined as 91 HV. This difference in hardness value may result from the breaking of SiC grains during conventional sintering (Figure 5c). HFIS is an advantageous process for sintering Al/SiC composites without degradation.

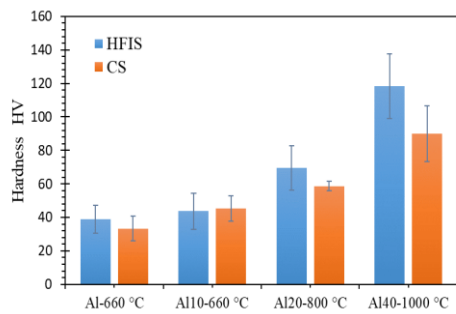


Figure 9. Hardness value of Al/SiC composites

4. Conclusion

In this study, aluminum matrix composites containing different ratios of SiC were successfully produced with HFIS. The required sintering temperature was determined according to the SiC ratio used. When the SiC ratio is 10, 20 and 40%, the required sintering temperature was determined to be 660, 800 and 1000 °C, respectively. Al/SiC composites were produced successfully without the formation of harmful Al_4C_3 phase in sintering with HFIS. Composite samples were obtained in Al and SiC phases, with hardness values of 43-118 HV, at high experimental density above the melting temperature of aluminum.

When the composites were sintered with the CS method with a heating rate of 10 °/min and compared with HFIS, it was determined that the Al_4C_3 phase was formed (wt.%40 SiC added composition). This composition decomposes under long-term atmospheric conditions. Al/SiC composites were successfully produced by HFIS sintering process without new phases forming above the melting temperature.

Article Information Form

Funding

This study was supported by the Scientific Research Projects Coordination Unit of Manisa Celal Bayar University within the scope of the project numbered 2014-087.

Authors' Contribution

The authors contributed equally to the study.

The Declaration of Conflict of Interest/ Common Interest

No conflict of interest or common interest has been declared by the authors.

The Declaration of Ethics Committee Approval

This study does not require ethics committee permission or any special permission.

The Declaration of Research and Publication Ethics

The authors of the paper declare that they comply with the scientific, ethical and quotation rules of SAUJS in all processes of the paper and that they do not make any falsification on the data collected. In addition, they declare that Sakarya University Journal of Science and its editorial board have no responsibility for any ethical violations that may be encountered, and that this study has not been evaluated in any academic publication environment other than Sakarya University Journal of Science.

Copyright Statement

Authors own the copyright of their work published in the journal and their work is published under the CC BY-NC 4.0 license.

References

- [1] S. Sursha, B. K. Sridhara, Wear characteristics of hybrid aluminium matrix composites reinforced with graphite and silicon carbide particulates. *Composites science and Technology*, vol 70, pp, 1652-1659, 2010.
- [2] Y. Xie, Y. Huang, F. Wang, X. Meng, J. Li, Z. Dong, J. Cao, Deformation-driven metallurgy of SiC nanoparticle reinforced aluminum matrix nanocomposites, *Journal of Alloys and Compounds*, vol. 823, pp, 153741 2020.
- [3] L. Zhang, X. Hanqing, Z. Wang, Q. Li, J. Wu, Mechanical properties and corrosion behavior of Al/SiC composites, *Journal of Alloys and Compounds*, vol. 678 pp, 23-30, 2016.
- [4] Z. Xiu, W. Yang, R. Dong, M. Hussain, L. Jiang, Y. Liu, G. Wu, Microstructure and mechanical properties of 45 vol.% SiCp/7075Al composite, *Journal of Materials Science & Technology*, vol. 31, pp, 930-934, 2015.

- [5] K. M. Sree Manu, L. Ajay Raag, T. P. D. Rajan, B. C. Pai, V. Petley, S. N. Verma, Self-lubricating bidirectional carbon fiber reinforced smart aluminum composites by squeeze infiltration process, *Journal of Materials Science & Technology*, vol. 35, pp, 2559-2569, 2019.
- [6] Y. S. Yi, Y. Meng, D. Q. Li, S. Sugiyama, J. Yanagimoto, Partial melting behavior and thixoforming properties of extruded magnesium alloy AZ91 with and without addition of SiC particles with a volume fraction of 15%, *Journal of Materials Science & Technology*, vol. 34, pp, 1149-1161, 2018.
- [7] Z. Hu, F. Chen, J. Xu, Q. Nian, D. Lin, C. Chen, X. Zhu, Y. Chen, M. Zhang, 3D printing graphene-aluminum nanocomposites, *Journal of Alloys and Compounds*, vol. 746, pp, 269-276, 2018.
- [8] P. Jin, B. Xiao, Q. Wang, Z. Ma, Y. Liu, S. Li, Effect of hot extrusion on interfacial microstructure and tensile properties of SiCp/2009Al composites fabricated at different hot-pressing temperatures, *Journal of Materials Science & Technology*, vol. 27 pp, 518-524, 2011.
- [9] Z. M. Xu, N. L. Loh, W. Zhou, Hot isostatic pressing of cast SiCp-reinforced aluminium-based composites, *Journal of Materials Processing Technology*, vol. 67, pp, 131-136, 1997.
- [10] X. P. Li, C. Y. Liu, M. Z. Ma, R. P. Liu, Microstructures and mechanical properties of AA6061-SiC composites prepared through spark plasma sintering and hotrolling, *Materials Science and Engineering: A*, vol. 650, pp, 139-144, 2016.
- [11] A. M. Samuel, H. Liu, F. H. Samuel, Effect of melt, solidification and heat treatment processing parameters on the properties of Al-Si-Mg/SiC(p) composites, *Journal of Materials Science*, vol. 28, pp, 6785-6798, 1993.
- [12] V. K. Singh, S. Chauhan, P. C. Gope. A. K. Chaudhary. Enhancement of Wettability of Aluminum Based Silicon Carbide Reinforced Particulate Metal Matrix Composite. *High Temperature Materials and Processes*. vol. 34, no 2, pp, 163-170, 2015.
- [13] A. Riquelme, P. Rodrigo, M. D. Escalera-Rodríguez, J. Rams. Characterisation and mechanical properties of Al/SiC metal matrix composite coatings formed on ZE41 magnesium alloys by laser cladding, *Results in Physics*, vol. 13 pp, 102, 2019.
- [14] C. Hsieh, Y. Ho, H. Wang, S. Sugiyama, J. Yanagimoto, Mechanical and tribological characterization of nanostructured graphene sheets/A6061 composites fabricated by induction sintering and hot extrusion, *Materials Science and Engineering: A*, vol. 786, pp, 1-8, 2020.
- [15] J. Liu, B. Zhou, L. Xu, Z. Han, J. Zhou, Fabrication of SiC reinforced aluminium metal matrix composites through microwave sintering, *Materials Research Express* vol. 7 pp, 125101, 2020.
- [16] M. Dhanashekar, P. Loganathan, S. Ayyanar, S. R. Mohan, T. Sathish, Mechanical and wear behaviour of AA6061/SiC composites fabricated by powder metallurgy method, *Materials Today: roceedings*, vol. 21, pp, 1008-1012, 2020.
- [17] H. Wanga, R. Zhanga, X. Hua, C. Wangb, Y. Huang, Characterization of a powder metallurgy SiC/Cu-Al composite, *Journal of Materials Processing Technology*, vol.197 pp, 43-48, 2008.
- [18] M. Rodri'guez-Reyes, M. I. Pech-Canul, J. C. Rendo'n-Angeles, J. Lo'pez-Cuevas, Limiting the development of Al₄C₃ to prevent degradation of Al/SiCp composites processed by pressureless infiltration, *Composites Science and Technology*, vol. 66 pp, 1056-1062, 2006.

- [19] M. Hoseini, M. Meratian, Fabrication of in situ aluminum–alumina composite with glass powder, *Journal of Alloys and Compounds*, vol. 471 pp, 378–382, 2009.
- [20] P. Wang, G. Chen, L. Jiang, D. Li, G. Wu, Effect of thermal exposure on the microstructure of the interface in a Grf/Al composite, *Science and Engineering of Composite Materials*, vol. 23, no 6, pp, 751–757, 2016.
- [21] Sumarji, N. F. Albajil, M. Darsin, R. R. Sakura, A. Sanata, Effect of Variation of SiC and Mg Mass Fraction on Mechanical Properties of Al-SiC Composite Using Stir Casting Method, *Journal of Mechanical Engineering Science and Technology* vol. 6, pp. 23-33, 2022.
- [22] A. Canakci, T. Varol, Microstructure and properties of AA7075/Al–SiC composites fabricated using powder metallurgy and hot pressing, *Powder Technology*, vol. 268, no 72–79, 2014.
- [23] K. Bravilin Jiju, G. Selvakumar, S. Ram Prakash, Study on preparation of Al – SiC metal matrix composites using powder metallurgy technique and its mechanical properties, *Materials Today: Proceedings*, vol. 27 pp, 1843–1847, 2020.
- [24] A. Wąsik, B. Leszczyńska-Madej, M. Madej, the influence of SiC particle size on mechanical properties of aluminium matrix composites, *Metallurgy and Foundry Engineering*, vol. 43, pp, 41–49, 2017.
- [25] P. Ajagol, A. B. N, R. N. Marigoudar, P. K. G. V., Effect of SiC Reinforcement on Microstructure and Mechanical Properties of Aluminum Metal Matrix Composite, *IOP Conf. Series: Materials Science and Engineering* vol. 376 pp. 012057, 2018.



First-principles Calculations of TlCdF_3 Compound under Pressure

Belgin Koçak^{1*}, Yasemin Öztekin Çiftci²

¹Ostım Technical University, Vocational School of Higher Education, Department of Electronics and Automation, Ankara, Türkiye, belgin.kocak@ostimteknik.edu.tr

²Gazi University, Faculty of Science, Department of Physics, Ankara, Türkiye, yasemin@gazi.edu.tr

*Corresponding Author

ARTICLE INFO

ABSTRACT

Keywords:

DFT

Fluoro-perovskite

Elastic properties

Electronic properties

Article History:

Received: 29.09.2023

Accepted: 30.04.2024

Online Available: 06.06.2024

The present study focused on investigating various properties including structural, elastic, electronic, and optical of TlCdF_3 compound under hydrostatic pressure using Density Functional Theory (DFT). The estimated results were consistent with previous investigations. The analysis of the electronic band structures between 0 and 50 GPa revealed that this compound possesses an indirect band gap. The stress-strain method was used to explain elastic properties, and the findings revealed that this compound is ductile, anisotropic and mechanically stable between 0 and 50 GPa. Investigations were done on significant optical features such as refractive index $n(\omega)$, extinction coefficient $k(\omega)$, absorption coefficient $\alpha(\omega)$ and reflectivity $R(\omega)$ at various pressures between 0 and 50 eV. Our results imply that TlCdF_3 compound has the potential for a broad range of technological applications under hydrostatic pressure.

1. Introduction

The technical and scientific significance of fluoride-type perovskite materials (XYF_3) has been probed due to their various applications in optoelectronic, medical field, magnetism, semi-conductivity, transistors, memory storages devices, light-emitting devices, catalysis [1-5]. Researchers are becoming more and more interested in these kinds of ternary compounds owing to their electronic, optical, thermodynamical, elastic, and vibrational properties [1-8].

XYF_3 , where X (X = alkali metal) and Y (Y = transition metal or alkaline metal) elements represent cations and F (fluorine) elements express an anion, is the standard chemical formula for the well-known alloys as fluoro-perovskites [1]. Herein, we selected TlCdF_3 fluoro-perovskite compound as they can be potential candidates for technological applications due to their wide band gap value.

This compound has been studied both theoretically [7-9] and experimentally [10-13] so far. Zaman et al. [14] also theoretically reported physical properties of TlCdCl_3 and TlCaCl_3 compounds within WIEN2k code in the space group Pm-3m. They found that these compounds exhibit wide and indirect band gap characteristics. Using DFT within GGA+U approximations, the electronic, optical, and elastic characteristics of TlCaF_3 , TlCdF_3 , TlHgF_3 and TlMgF_3 compounds were evaluated by Khan et al. [7]. They stated that these compounds show a ductile nature. By employing WIEN2k code for first principles calculation, Cheriet et al. [8] conducts a theoretical analysis of the physical properties of the title compound. Their research indicates that the band gap value for TlCdF_3 compound was determined as 3.66 eV for WC approach and 5.70 eV for TB-mBJ method. First-principles calculation utilizing TB-mBJ approximation of TlCaF_3 and TlCdF_3 compounds were predicted by Sohail et al. [9].

Chabin et al. [10] experimentally reported the thermal properties of TlCdF_3 compound. Rousseau et al. [11] experimentally investigated the phase transition of the title compound using Raman Scattering. The third and fourth elastic constants of TlCdF_3 compound were experimentally researched by Ref. [12]. The elastic constants of TlCdF_3 compound were studied by Berger et al. [13] via Brillouin scattering. Fujimoto et al. [6] were experimentally exploring the luminescence as well as scintillation properties of TlMgCl_3 compound using the Bridgman–Stockbarger method. They indicate that TlMgCl_3 compound have a great potential for Gamma-ray and X-ray application due to this compound's high atomic number and medium density.

In spite of all the effort, the research on how pressure dependence of physical properties of TlCdF_3 compound is quite restricted. Hence, this study has been attempted to be clarified to serve as a guide for future research. The study is structured as follows: Following the introduction, the second section elaborates on our computational method. The examined structural, elastic, electronic and optical results are given in the third section. Finally, the conclusion part presents a summary of the findings.

2. Computational Methods

In the present study, VASP [15-17] (Vienna Ab initio Simulation Package) code was employed for performing the calculations. VASP is a widely used computational tool that operates within the framework of density functional theory (DFT) and employs the projector augmented wave (PAW) method [18] for treating electron-ion interactions. The Perdew-Burke-Ernzerhof (PBE) [19] functional, which is a generalized gradient approximation (GGA) for the exchange-correlation energy, was utilized to handle the electronic interactions. The PBE functional has been proven to provide reliable results for a variety of materials and properties. To ensure convergence of the calculations, a convergence test was conducted. Following the convergence test, the number of k-points was fixed to $16 \times 16 \times 16$ in the Monkhorst-Pack [20] scheme, with a 700 eV cut-off energy. For the electronic band calculations, which require

higher precision, the number of k-points was increased to $32 \times 32 \times 32$. This increased density of k-points allows for a more accurate determination of the electronic band structure. By employing these computational parameters and methods, the study aimed to predict reliable and accurate results for investigating properties of the TlCdF_3 compound under hydrostatic pressure.

3. Results and Discussion

3.1. Structural properties under pressure

TlCdF_3 compound lattice parameters are obtained with the use of fully geometrical relaxation. In the equilibrium structure, Tl atom (0.00, 0.00, 0.00), Cd atom (0.50, 0.50, 0.50) and F atoms (0.00, 0.50, 0.50), (0.50, 0.00, 0.50) and (0.50, 0.50, 0.00) are placed in Wyckoff positions. Table 1 displays the lattice constant (a_0) values calculated within GGA-PBE. The computed lattice constant of this compound is found as 4.477 Å at zero pressure. It agrees well with the experimental lattice constant of 4.395 Å stated in Ref [11]. Table 1 also indicates how lattice constant changes as pressure rises. It is obvious that it gets smaller with increasing pressure.

Table 1. Lattice constant values a_0 (Å) at different pressures for TlCdF_3 compound

Pressure	Present a_0 (Å)	Exp. a_0 (Å)	Theory a_0 (Å)
0 GPa	4.477	4.395 [11]	4.49 [7]
			4.492 ^{PBE} [8]
			4.402 ^{WC} [8]
			4.325 ^{LDA} [8]
			4.33 [9]
10 GPa	4.296		
20 GPa	4.183		
30 GPa	4.099		
40 GPa	4.035		
50 GPa	3.981		

3.2. Elastic properties under pressure

Investigation of pressure-induced elastic properties provides a powerful tool to describe atomic bonding, mechanical stability, phase transformation, hardness and intrinsic characteristics of the material which helps in the understanding and attraction of their future applications. Herein, the elastic constants (C_{ij}) of TlCdF_3 compound were computed by the "stress-

strain" method [21] in the pressure range of 0-50 GPa. The obtained results are tabulated in Table 2 at 0 GPa and 0 K. It is worth noting that our results are quite consistent with the experimental values [11, 13] of $C_{11}=102.8$ (103.6) GPa, $C_{12}=38.5$ (39.6) GPa and $C_{44}=17.7$ (18.08) GPa, respectively. These results also agree generally with earlier theoretical reports [7-9].

At the analyzed pressures, the elastic constants of TlCdF_3 compound are positive. With the following conditions, we can say that this compound satisfies the requirements for mechanical stability [22]: $C_{11}>0$; $C_{44}>0$; $(C_{11}+2C_{12})>0$; $(C_{11}-C_{12})>0$. As shown in Fig. 1a, the elastic constants C_{11} and C_{12} climb linearly with increasing pressure, whereas C_{44} decreases.

The Voigt-Reuss-Hill approximation [23-25] was used to clarify the important elastic parameters including bulk modulus (B), Young's modulus (E), shear modulus (G), and Poisson's ratio (ν) of TlCdF_3 compound. The equations used in the calculations are given below [26-28]:

$$B_V = B_R = B_H = \frac{C_{11}+2C_{12}}{3} \quad (1)$$

$$G_H = \frac{G_V+G_R}{2} \quad (2)$$

$$G_V = \frac{C_{11}-C_{12}+3C_{44}}{5} \quad (3)$$

$$G_R = \frac{5(C_{11}-C_{12})C_{44}}{3C_{11}-3C_{12}+4C_{44}} \quad (4)$$

$$E = \frac{9B_H G_H}{3B_H+G_H} \quad (5)$$

$$\nu = \frac{3B_H-2G_H}{6B_H+2G_H} \quad (6)$$

Table 2 contains a list of these findings, and Figs. 1(b-d) show the pressure dependence graphs. According to Fig. 1b, the bulk modulus increases with pressure more than Young's and Shear modulus. Cauchy pressure ($C_{12}-C_{44}$), B/G ratio and Poisson's ratios (ν) are three important markers for predicting a material's ductility or brittleness. The material is classified ductile if the B/G ratio [27, 29] is more than 1.75, the Poisson's ratio is bigger than 0.26 [14, 30], and the Cauchy pressure [27, 31] is positive; otherwise, it is considered brittle. The title

compound is ductile, as shown by our findings. These results corroborate with those of other studies [7-9]. Furthermore, as shown in Fig. 1c, the increase in B/G ratio with pressure demonstrates that the ductility of the material increases.

Table 2. Calculated elastic properties of TlCdF_3 compound at 0 GPa with other results

TlCdF_3	Present	Other	Exp.
C_{11} (GPa)	110.556	106.62 [7] 124.7 [8] 114.34 [9]	102.8 [11] 103.6 [13]
C_{12} (GPa)	35.761	46.89 [7] 39.59 [8] 32.57 [9]	38.5 [11] 39.6 [13]
C_{44} (GPa)	13.352	18.09 [7] 11.53 [8] 15.08 [9]	17.7 [11] 18.08 [13]
Cauchy Pressure (GPa)	22.409		
B (GPa)	60.693	66.80 [7] 67.99 [8] 172.03 [9]	
G (GPa)	20.473	22.13 [7] 20.109 [8] 22.78 [9]	
E (GPa)	55.210	59.81 [7] 54.912 [8] 72.631 [9]	
B/G	2.965	3.01 [7] 3.380 [8] 7.549 [9]	
ν	0.348	0.50 [7] 0.365 [8] 0.43 [9]	
A	0.357	0.60 [7] 0.8629 [8] 0.369 [9]	

The degree of elastic anisotropy in materials is calculated using the Zener anisotropy factor [26-28]:

$$A = \frac{2C_{44}}{C_{11}-C_{12}} \quad (7)$$

The anisotropy factor has a value of 1 for entirely isotropic materials [9, 14]. It was found to be 0.357 at 0 GPa for this compound. According to our obtained values, the title compound shows anisotropic behavior in the 0-50 GPa pressure range. As shown in Fig. 1d, Zener anisotropy factor diminishes linearly as pressure rises.

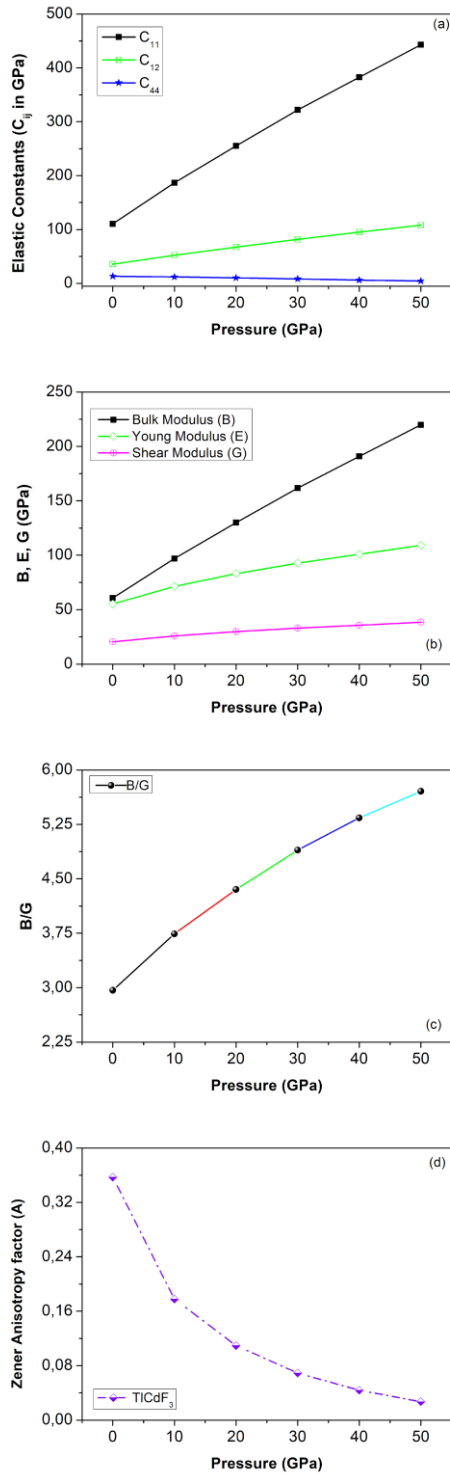


Figure 1. a) Elastic constants (C_{ij}), b) Bulk, Shear, and Young's moduli, c) B/G ratio, and d) Zener anisotropy factor variations with pressure for TICdF₃ compound

3.3. Electronic properties under pressure

Using the equilibrium lattice constants of TICdF₃ compound, the electronic band structures and partial density state (PDOS) corresponding to

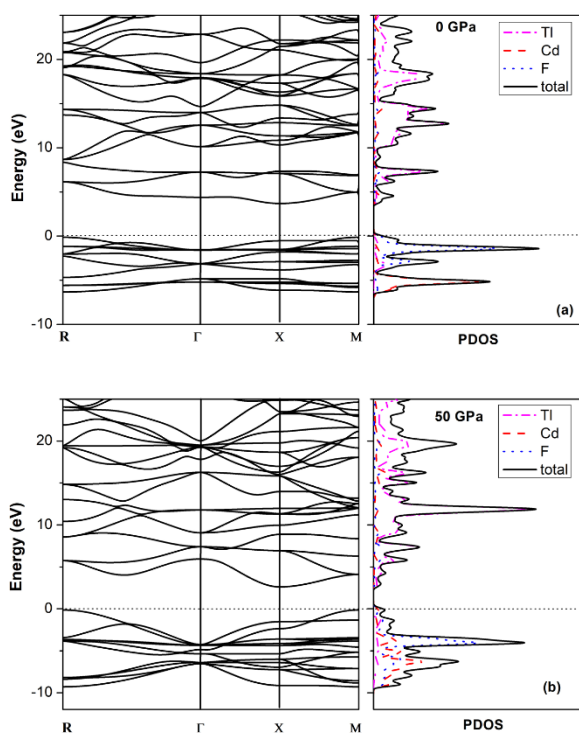
high symmetry directions were calculated under pressure. Since the electronic band gap characteristic of TICdF₃ compound is the same at all pressure levels (0-50 GPa), Figs. 2 (a-b) displays graphs for 0 GPa and 50 GPa pressure. The conduction band minimum is situated at the X high symmetry point, while the valence band maximum is located at the R high symmetry point, as shown in Figs. 2. As a result, the indirect band gap of this compound at 0 GPa is 3.817 eV. TICdF₃ compound indirect band gap values at 10 GPa, 20 GPa, 30 GPa, 40 GPa, and 50 GPa are 3.577 eV, 3.345 eV, 3.122 eV, 2.927 eV, and 2.749 eV, respectively.

Khan et al. [7] is reported that TICdF₃ compound has an indirect band gap because the valence band maximum is at M symmetry point and the conduction band minimum occurs at Γ symmetry point. Their calculated energy band gap is 3.46 eV at 0 GPa using the GGA+U. According to Cheriet et al. [8], the top of the valence band is at the M-point, while the bottom of the conduction band is at the X-point, with an indirect band gap of 5.70 eV for TB-mBJ and 3.66 eV for WC approximation. Sohail et al. [9] found that title compound has a direct band gap at X symmetry point with 5.7 eV using the TB-mBJ potential method. Unfortunately, no experimental studies on the electronic band structure of TICdF₃ compound are currently available to analyze and debate the findings. The obtained results at various pressures present in Table 3 and contrasted with findings from earlier theoretical investigations [7, 9]. As can be seen in Table 3, very consistent results were achieved at 0 GPa.

The electronic partial density of states (PDOS) is the energy levels occupied by the electrons of each atom or group of atoms in a material. In Fig. 2a, on the right side, it is shown that the F atom contributes most to the valence band between 0 and -5 eV. The Cd atom primarily contributes to the valence band between -5 and -10 eV. Additionally, the Tl atom makes a larger contribution to the total density of states in the conduction band. This information can be used to gain insights into the electronic properties of the material and to design materials with specific electronic properties for various applications

Table 3. Energy band gap values (E_g , in eV) of TlCdF_3 compound at various pressures

	Theory		Present				
	0 GPa	0 GPa	10 GPa	20 GPa	30 GPa	40 GPa	50 GPa
$E_g^{\text{M-M}}$	5.21 [7] 5.24 [9]	5.18	4.98	4.48	4.41	5.85	4.18
$E_g^{\text{X-X}}$	3.67[7] 5.7 [9]	4.27	4.28	4.14	4.19	4.10	4.12
$E_g^{\Gamma-\Gamma}$	3.46 [7] 6.94 [9]	5.92	7.23	9.04	8.95	9.50	10.18
$E_g^{\text{R-}\Gamma}$	6.19 [7] 5.82 [9]	4.44	4.98	5.67	5.72	6.02	6.00
$E_g^{\Gamma-\text{X}}$	3.23[7] 6.69[9]	5.26	5.82	6.44	6.45	6.62	6.87

**Figure 2.** Computed electronic band structure and partial density of states (PDOS) of TlCdF_3 compound at a) 0 GPa and b) 50 GPa

3.4. Optical properties under pressure

The complex dielectric function, represented by $\epsilon(\omega) = \epsilon_1(\omega) + i\epsilon_2(\omega)$, provides detailed information about the linear optical characteristics of a material [9, 32-34]. The optical features of TlCdF_3 compound have been investigated under various pressures and energies (0–50 eV). The curves of real $\epsilon_1(\omega)$ and imaginary $\epsilon_2(\omega)$ parts of dielectric function of our investigated compound are shown in Figs.

3(a-b). The pressures are shown in steps of 10 GPa from 0–50 GPa.

The static dielectric constant represents the value of $\epsilon_1(\omega)$ at zero energy ($\omega = 0$). For TlCdF_3 at 0 GPa, $\epsilon_1(0)$ is found to be approximately 2.94, while at 50 GPa, it increases to around 3.52. This indicates that an increase in pressure leads to a higher static dielectric constant. The imaginary part of the dielectric function, $\epsilon_2(\omega)$, exhibits peaks at specific energy values. For TlCdF_3 , the largest peaks of $\epsilon_2(\omega)$ are detected at 5.27 eV at 0 GPa and 7.9 eV at 50 GPa in the ultraviolet (UV) region (3.1-124 eV). The imaginary $\epsilon_2(\omega)$ parts of the dielectric function show that the maximum peak values rise with pressure.

With the use of the Kramer-Kronig relations [7, 9, 14, 33], the refractive index $n(\omega)$, extinction coefficient $k(\omega)$, absorption coefficient $\alpha(\omega)$, and reflectivity $R(\omega)$ of TlCdF_3 compound are calculated and depicted in Figs. 4 (a-d). The curves shapes for refractive index $n(\omega)$ and extinction coefficient $k(\omega)$ follow the same pattern as the real $\epsilon_1(\omega)$ and imaginary $\epsilon_2(\omega)$ parts of the complex dielectric function, respectively. The static refractive index of TlCdF_3 compound at 0 GPa is found to be 1.71. As the pressure increases to 50 GPa, the static refractive index also increases and becomes 1.88. The main peak value of the extinction coefficient increases with pressure. The static reflectivity $R(0)$ also rises as the pressure increases. This indicates that the material becomes more reflective with increasing pressure.

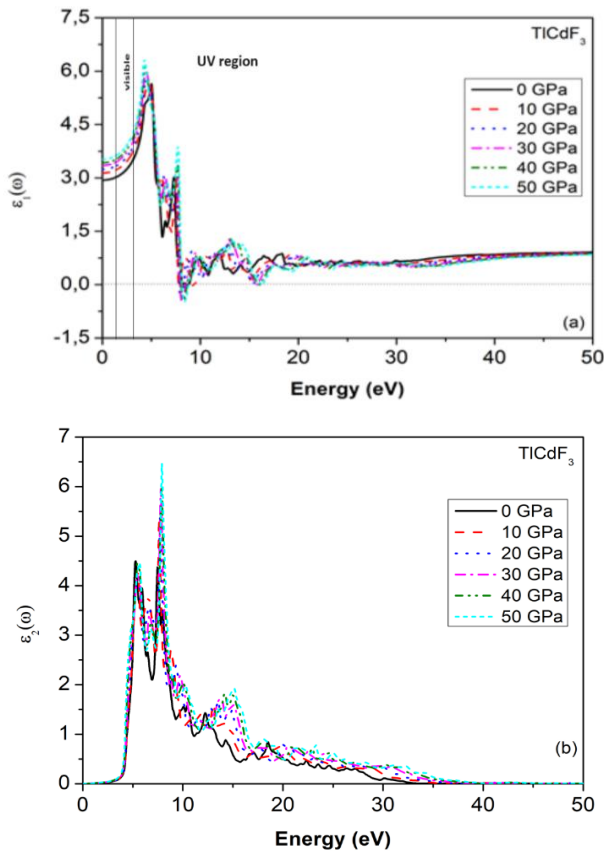


Figure 3. a) Real part of dielectric function $\varepsilon_1(\omega)$, b) imaginary part of dielectric function $\varepsilon_2(\omega)$ of TICdF₃ compound

The absorption coefficient denotes the quantity of energy lost by the wave as it goes across the material. The incident photons in the ultraviolet region have energies ranging from 3.1 eV to 124 eV [9, 34]. As shown in Figure 4c, the absorption spectra show the peak starting UV region. It is noticeable that the absorption coefficient curves shift to higher energies with the increase in pressure. This implies that the optical features of TICdF₃ compound become more pronounced and enhanced under higher pressures. As a result, this material has the potential to be used in optoelectronic devices operating in the ultraviolet region under pressure (0-50 GPa). The current optical results of TICdF₃ compound are consistent with previous research [7, 9]. This agreement adds confidence to the accuracy and reliability of the investigation.

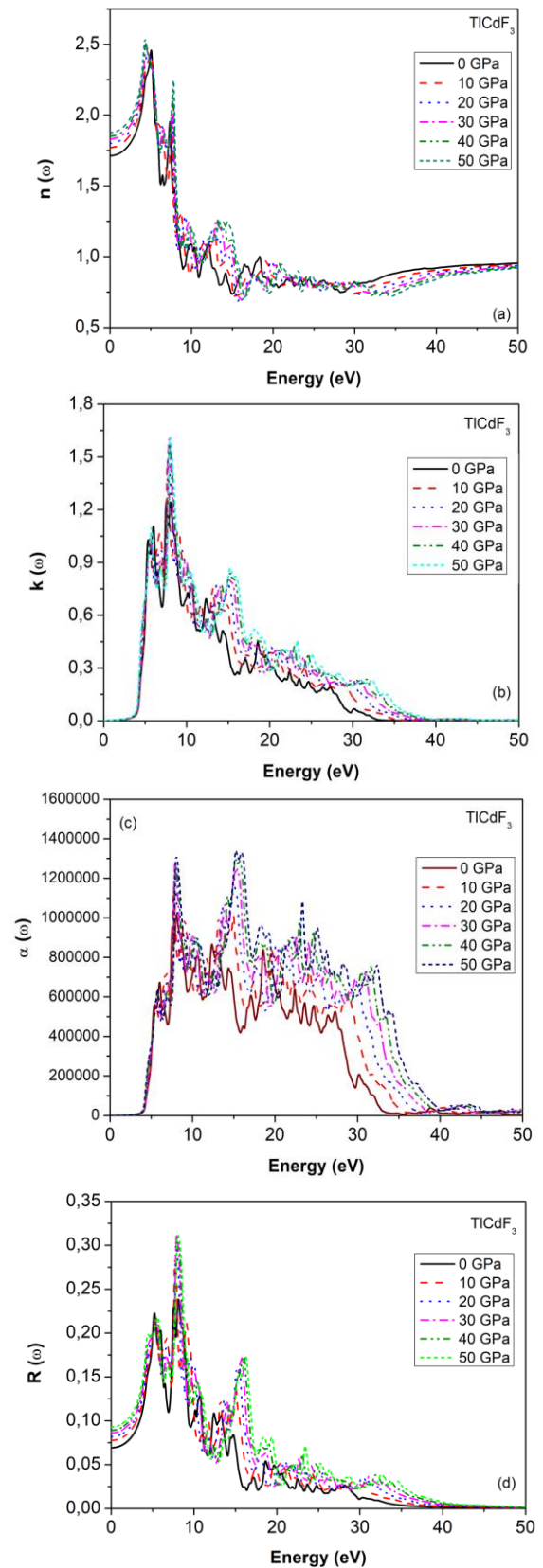


Figure 4. The optical properties of TICdF₃ compound under pressure

4. Conclusion

GGA-PBE approximation is used to evaluate the first principles calculation of the TICdF₃ fluoroperovskites compound at various pressures. Our

calculated ground state properties, electronic band structure, optic, elastic constants and related properties agree with literature. TlCdF_3 compound exhibits an indirect band gap under investigated pressures, in accordance with the electronic band structure. This compound is ductile and mechanically stable up to 50 GPa, as evidenced by its elastic characteristics. The various optical properties are also investigated across a broad energy range of 0 eV to 50 eV. It is found that TlCdF_3 exhibits absorption in the UV energy range. Due to these properties, TlCdF_3 compound can be suitable for technological application for the fluoroperovskite family. These results can also give valuable information for researchers exploring new materials in the fields of semiconductors, optics, and engineering materials.

Article Information Form

Acknowledgments

The numerical calculations reported in this paper were performed at TUBITAK ULAKBIM, High Performance and Grid Computing Center (TRUBA resources).

Funding

The author (s) has no received any financial support for the research, authorship or publication of this study.

Authors' Contribution

B.K.: Writing-original draft, Investigation, Calculations, Visualization, Conceptualization, Review & editing. **Y.O.C:** Calculations, Conceptualization, Writing – review & editing.

The Declaration of Conflict of Interest/ Common Interest

No conflict of interest or common interest has been declared by the authors.

The Declaration of Ethics Committee Approval

This study does not require ethics committee permission or any special permission.

The Declaration of Research and Publication Ethics

The authors of the paper declare that they comply with the scientific, ethical and quotation rules of SAUJS in all processes of the paper and that they

do not make any falsification on the data collected. In addition, they declare that Sakarya University Journal of Science and its editorial board have no responsibility for any ethical violations that may be encountered, and that this study has not been evaluated in any academic publication environment other than Sakarya University Journal of Science.

Copyright Statement

Authors own the copyright of their work published in the journal and their work is published under the CC BY-NC 4.0 license.






References

- [1] M. K. Shahzad, S. Hussain, M. U. Farooq, R. A. Laghari, M. H. Bilal, S. A. Khan, M. Tahir, A. Khalil, J. U. Rehman, M. M. Ali, "First-principles calculations to investigate structural, electronic, elastic and optical properties of radium based cubic fluoroperovskite materials," *Heliyon*, vol. 9, pp. E13687, (2023).
- [2] Shakeel, A. H. Reshak, S. Khan, A. Laref, G. Murtaza, J. Bila, "Pressure induced physical variations in the lead free fluoroperovskites XYF_3 (X=K, Rb, Ag; Y=Zn, Sr, Mg): Optical materials," *Optical Materials*, vol. 109, pp. 110325, 2020.
- [3] T. Tianyu, Y. Tang, "First-Principles Calculations to Investigate Direct-Band Novel Cobalt-Based Double Perovskite Materials for Optoelectronic Applications," *Energy & Fuels*, vol. 37, pp. 1266–1274, 2022.
- [4] J. Saddique, M. Husain, N. Rahman, R. Khan, Zulfiqar, A. Iqbal, M. Sohail, S. A. Khattak, S. N. Khan, A. A. Khan, A.H. Reshak, A. Khan, "Modeling structural, elastic, electronic and optical properties of ternary cubic barium based fluoroperovskites MBaF_3 (M = Ga and In) compounds based on DFT," *Materials Science in Semiconductor Processing*, vol. 139, pp. 106345, 2022.
- [5] T. Nishimatsu, N. Terakubo, H. Mizuseki, Y. Kawazoe, D. A. Pawlak, K. Shimamura,

- T. Fukuda, "Band Structures of Perovskite-Like Fluorides for Vacuum-Ultraviolet-Transparent Lens Materials," *Japanese Journal of Applied Physics*, vol. 41, pp. 090301, 2002.
- [6] Y. Fujimoto, M. Koshimizu, T. Yanagida, G. Okada, K. Saeki, K. Asai, "Thallium magnesium chloride: A high light yield, large effective atomic number, intrinsically activated crystalline scintillator for X-ray and gamma-ray detection," *Japanese Journal of Applied Physics*, vol. 55, pp. 090301, 2016.
- [7] S. Khan, S. U. Zaman, R. Ahmad, N. Mehmood, M. Arif, H. J. Kim, "Ab Initio Investigations of Structural, Elastic, Electronic and Optical Properties of the Fluoroperovskite $TiXF_3$ ($X = Ca, Cd, Hg,$ and Mg) Compounds," *Materials Research Express*, vol. 6, no.12, pp. 125923, 2020.
- [8] A. Cheriet, B. Lagoun, M. Halit, M. Zaabat, C. Abdelhakim, H. Lidjici, "First-principles study of structural, electronic, optical and elastic properties of cadmium based Fluoro-Perovskite $MCdF_3$ ($M= Rb,$ Tl)," *Solid State Phenomena*, vol. 297, pp. 173-186, 2019.
- [9] M. Sohail, M. Husain, N. Rahman, K. Althubeiti, M. Algethami, A. A. Khan, A. Iqbal, A. Ullah, A. Khanfg, R. Khan "First-principal investigations of electronic, structural, elastic and optical properties of the fluoroperovskite $TiLF_3$ ($L= Ca, Cd$) compounds for optoelectronic applications," *RSC Advances*, vol. 12, no.12, pp. 7002-7008, 2022.
- [10] M. Chabin, F. Gilletta, C. Ridou, "Thermal properties of $TlCdF_3$ and $RbCaF_3$ near their phase transitions," *Physica status solidi (a)*, vol. 48(1), pp. 67-70, 1978.
- [11] M. Rousseau, J. Y. Gesland, J. Julliard, J. Nouet, J. Zarembowitch, A. Zarembowitch, "Crystallographic, elastic, and Raman scattering investigations of structural phase transitions in $RbCdF_3$ and $TlCdF_3$," *Physical Review B*, vol. 12, no.4, pp.1579, 1975.
- [12] M. Fischer, "Third and fourth order elastic constants of fluoperovskites $CsCdF_3,$ $TlCdF_3,$ $RbCdF_3,$ $RbCaF_3,$ " *Journal of Physics and Chemistry of Solids*, vol. 43, no.8, pp. 673-682, 1982.
- [13] J. Berger, G. Hauret, M. Rousseau, "Brillouin scattering investigation of the structural phase transition of $TlCdF_3$ and $RbCaF_3$," *Solid State Communications*, vol. 25, no.8, pp. 569-571, 1978.
- [14] S. U. Zaman, N. Rahman, M. Arif, M. Saqib, M. Husain, E. Bonyah, Z. Shah, S. Zulfiqar, A. Khan, "Ab initio investigation of the physical properties of Tl based chloroperovskites $TlXCl_3$ ($X= Ca$ and Cd)," *AIP Advances*, vol. 11(1), pp. 015204, 2021.
- [15] J. Hafner, "Ab-initio simulations of materials using VASP: Density-functional theory and beyond," *Journal of Computational Chemistry*, vol. 29, pp. 2044-2078, 2008.
- [16] G. Kresse, J. Hafner, "Ab initio molecular-dynamics simulation of the liquid-metal-amorphous semiconductor transition in germanium," *Physical Review B*, 49: pp.14251, 1994.
- [17] G. Kresse, J. Hafner, "Ab initio molecular dynamics for liquid metals," *Physical Review B*, vol.47, pp. 558-561, 1993.
- [18] G. Kresse, J. Furthmuller, "Efficiency of ab-initio total energy calculations for metals and semiconductors using a plane-wave basis set," *Computational Materials Science*, vol. 6, pp. 15-50, 1996.
- [19] J. P. Perdew, K. Burke, M. Ernzerhof, "Generalized gradient approximation made simple," *Physical Review Letters*, vol. 77, pp. 3865-3868, 1996.
- [20] H. J. Monkhorst, J. D. Pack, "Special points for Brillouin-zone integrations,"

- Physical Review B, vol. 13, no. 12, pp. 5188-5192, 1976.
- [21] Y. Le Page, P. Saxe, "Symmetry-general least-squares extraction of elastic data for strained materials from ab initio calculations of stress," *Physical Review B*, vol. 65 10, pp. 104104, 2002.
- [22] F. Mouhat, F. X. Coudert, "Necessary and sufficient elastic stability conditions in various crystal systems," *Physical Review B*, vol. 90, pp 224104, 2014.
- [23] A. Reuss, "Berechnung der Fließgrenze von Mischkristallen auf Grund der Plastizitätsbedingung für Einkristalle", *Zeitschrift für Angewandte Mathematik und Mechanik*, vol. 9, pp. 49. 1929.
- [24] W. Voigt, "Lehrbuch der Kristallphysik", vol. 34, Teubner, Leipzig, Germany, 1928.
- [25] R. Hill, "The Elastic Behaviour of a Crystalline Aggregate," *Proceedings of the Physical Society, Section A*, vol. 65, pp. 349, 1952.
- [26] V. V. Bannikov, I. R., Shein, A. L. Ivanovskii, "Elastic properties of antiperovskite-type Ni-rich nitrides MNi_3 (M= Zn, Cd, Mg, Al, Ga, In, Sn, Sb, Pd, Cu, Ag and Pt) as predicted from first-principles calculations," *Physica B: Condensed Matter*, vol. 405 (22), pp.4615-4619, 2010.
- [27] T. Seddik, R. Khenata, O. Merabiha, A. Bouhemadou, S. Bin-Omran, D. Rached, "Elastic, electronic and thermodynamic properties of fluoro-perovskite $KZnF_3$ via first-principles calculations," *Applied Physics A*, vol. 106, pp. 645-653, 2012.
- [28] B. Mayer, H. Anton, E. Bott, M. Methfessel, J. Sticht, J. Harris, P. C. Schmidt, "Ab-initio calculation of the elastic constants and thermal expansion coefficients of Laves phases," *Intermetallics*, vol. 11(1), pp. 23-32, 2003.
- [29] S. F. Pugh, "XCII. Relations between the elastic moduli and the plastic properties of polycrystalline pure metals," *The London, Edinburgh, and Dublin Philosophical Magazine and Journal of Science*, vol. 45 (367), pp. 823-843, 1954.
- [30] I. N. Frantsevich, F. F. Voronov, S. A. Bokuta, "Elastic Constants and Elastic Moduli of Metals and Insulators Handbook", edited by I. N. Frantsevich Naukuva Dumka, Kiev, 1982.
- [31] D. G. Pettifor, "Theoretical predictions of structure and related properties of intermetallics," *Materials science and technology*, vol. 8, pp. 345-349, 1992.
- [32] M. Fox, "Optical Properties of Solids", Oxford University Press, New York, 2001.
- [33] W. Belkilali, F. Belkharroubi, M. Ameri, N. Ramdani, F. Boudahri, F. Khelfaoui, A. Amara, S. Azzi, L. Drici, I. Ameri, Y. Douri, "Theoretical investigations of structural, mechanical, electronic and optical properties of NaScSi alloy," *Emergent Materials*, vol. 4, pp. 1465-1477, 2021.
- [34] M. A. Iqbal, N. Erum, "Opto-Electronic Investigation of Rubidium Based Fluoro-Perovskite for Low Birefringent Lens Materials," *Scientific Inquiry and Review*, vol. 1(1), pp. 37-48, 2017.

The Role of Water on the Oxidation Process of Graphene Oxide Structures

Kürşat Kanbur^{1,2} , Işıl Birlik^{3,4*} , Fatih Sargın^{1,2} , N. Funda Ak Azem^{3,4} , Ahmet Türk² 

¹Dokuz Eylül University, The Graduate School of Natural and Applied Sciences, Department of Metallurgical and Materials Engineering, İzmir, Türkiye, kursat.kanbur@cbu.edu.tr, fatih.sargin@cbu.edu.tr

²Manisa Celal Bayar University, Faculty of Engineering and Natural Sciences, Department of Metallurgical and Materials Engineering, Manisa, Türkiye, kursat.kanbur@cbu.edu.tr, fatih.sargin@cbu.edu.tr, ahmet.turk@cbu.edu.tr

³Dokuz Eylül University, Faculty of Engineering, Department of Metallurgical and Materials Engineering, İzmir, Türkiye, isil.kayatekin@deu.edu.tr, funda.ak@deu.edu.tr

⁴Dokuz Eylül University, The Graduate School of Natural and Applied Sciences, Department of Nanoscience and Nanoengineering, İzmir, Türkiye, isil.kayatekin@deu.edu.tr, funda.ak@deu.edu.tr

*Corresponding Author

ARTICLE INFO

ABSTRACT

Keywords:

Graphene oxide
Hummers method
Oxidation process
Characterization



Article History:

Received: 04.08.2023

Accepted: 11.02.2024

Online Available: 14.06.2024

Graphene oxide (GO) has recently attracted attention with its unique chemical and physical properties and serves as a raw material for graphene-based materials. GO has been produced for decades by the Hummers Method with the oxidation process of graphite. The properties and structure of GO are significantly affected by the production parameters of Hummers Method. In this study, the effect of the water content on the oxidation level of GO structure was investigated. GO was produced with different amounts of water in the oxidation stage of Hummers Method. The structural characterizations of produced GO were carried out by X-ray Diffraction Technique (XRD), Fourier Transform Infrared Spectroscopy (FTIR), X-ray Photoelectron Spectroscopy (XPS), Energy Dispersive X-ray Spectroscopy (EDS), UV-Visible Spectroscopy (UV-Vis) and Raman Spectroscopy. Additionally, morphological and thermal characterization of the produced GO samples were performed by Scanning Electron Microscopy (SEM) and Thermogravimetric Analysis (TGA)/Differential Thermal Analysis (DTA), respectively. According to XRD, FTIR, XPS, and EDS results, it was determined that the oxidation degree of GO decreased with increasing amount of water. Besides, it was revealed that the post-oxidation step generated more defects in the basal plane of graphene according to the results of the Raman Analysis. Also, it was observed that GO had a smoother surface and was found to have higher thermal stability with increasing amounts of water. The results show that the post-oxidation step reduces the oxidation degree of GO, increases the amount of the defect, provides a less wrinkled structure, and improves the thermal stability of GO.

1. Introduction

Graphene is a two-dimensional honeycomb lattice structure consisting of sp^2 hybridized carbon atoms [1, 2]. Graphene is one of the most important candidates for high-tech applications due to its advanced mechanical, electrical, optical, and thermal properties [3, 4]. However, various functional groups are required for some special applications such as sensors [5], filters

[6], and biomaterials [7]. GO, a single layer of graphene nanosheets functionalized by several oxygen-containing groups has been synthesized via oxidation of graphite into graphitic oxide followed by exfoliation [8, 9]. It has remarkable physical and chemical properties which makes it a sought-after material for applications in areas that include electronics, biomedicine, energy, and the environment.

GO stands out in the production of chemically modified graphene because it is easy to functionalize with a wide variety of functional groups [10-12]. The functional groups are placed on the graphene planes by oxidation of the graphite basal planes during GO production. As these functional groups are bonded to the basal plane, the carbon atoms perform sp^3 hybridization at the location of the functional groups [13]. Thus, the conductivity of the GO structure decreases as the oxidation degree increases, since the excess electrons are used to bond with the functional groups.

Under extreme oxidation conditions, these functional groups can bind to the carbon basal plane and the carbon basal plane is distorted. However, these functional groups provide hydrophilic properties for GO structures and GO structures are dissolved in a variety of organic and water-based solutions. Thus, GO structures are easily used as reinforcement or matrix material in nanocomposite production for various applications by forming stable colloids [2]. Also, the properties of GO structures can be changed by adjusting the oxidation degree or various modifications [14].

GO production with the chemical oxidation of graphite provides large-scale productivity and efficiency [15]. The production of GO begins with the intercalation between graphite layers and proceeds with the oxidation of graphite layers in the chemical oxidation procedure. The first known work on the oxidation of graphite was made by Benjamin Brodie [16]. The Brodie method was evolved by Staudenmaier in 1898 by reducing the amount of HNO_3 (oxidizing agent) and adding sulfuric acid (H_2SO_4) instead of HNO_3 [10].

In the Staudenmaier method, the release of toxic gases has decreased compared to the Brodie method thanks to the lower amount of HNO_3 . However, the Staudenmaier method was still a dangerous process due to the release of toxic gases. Therefore, a safer chemical oxidation method was found by Hummers and Offeman in 1958 [17] and it became the most widely used method for GO production. Hummers method has advantages in terms of reaction time than previous methods. However, there are emissions

of nitrogen-based toxic gases (NO_2 and N_2O_4) due to $NaNO_3$. The Hummers Method was developed by Marcano et al [18] in 2010 and named as Improved Hummers Method. This method has a higher degree of oxidation and a better-quality structure with fewer defects for GO compared to previous methods. Various modifications have been made to Hummers method in the literature for optimization and adjusting controllable structure for GO production [14, 19].

According to the literature, the first oxidation stage is started by adding $KMnO_4$ after graphite is mixed with a mixture of H_2SO_4 and H_3PO_4 acid. After the solution is mixed at a certain time and temperature, the post-oxidation stage is initiated by adding water. However, many studies apply different processes in the post-oxidation stage. Hummers and Offeman used 4.6 liters of water for 100 g graphite and mixed it to the graphite-acid solution at $98^\circ C$ for only 15 minutes [17]. Eigler et al. [11], 60 ml water was mixed with 1 g graphite for 2 hours at $10^\circ C$.

Cote et al. [20], mixed 80 ml water for 2 g graphite at $90^\circ C$ for 1 hour. In 2015, Kang J. H. et al. [21] examined different times and temperatures in the post-oxidation stage. Accordingly, as the temperature increases, the hydroxyl, carbonyl, and carboxyl functional groups ratios of GO are increased. Also, conversion of epoxy groups to hydroxyl-containing groups in GO structure has been found. However, no study has been found in the literature on the effect of the amount of water in the post-oxidation stage on the GO structure.

In this study, GO structures were successfully synthesized by carefully controlling the amount of water in the post-oxidation stage and the effect of the water content during the production stage on the oxidation level of GO has been systematically investigated.

2. Materials and Method

Graphite powder (average powder size $<20 \mu m$) was purchased from Sigma Aldrich. H_2SO_4 (95-97%), H_3PO_4 (85%), $KMnO_4$ (99%), and H_2O_2 (35%) were obtained from Isolab Chemicals. All chemicals were used as received without further

purification. GO was produced by using Improved Hummers Method from pure graphite powder. Briefly, 1 g graphite was stirred in 100 ml H₂SO₄:H₃PO₄ acid solution at a ratio of 9:1 to provide pre-oxidation. The first oxidation step was initiated by adding 6 g KMnO₄ as the oxidizing agent. (H₂SO₄:H₃PO₄)/Distilled water volume ratio was then determined as 1:0.5, 1:1 and 1:1.5 ml to determine the effect of water content in the forthcoming oxidation step, and the samples were designated as W1, W2, and W3, respectively. Sample without water content was also prepared as W0 for comparison the effect of water content in the post-oxidation stage. H₂O₂ was used to stop oxidation reaction.

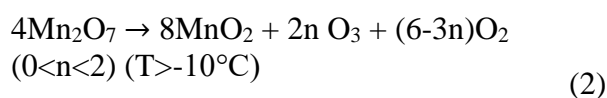
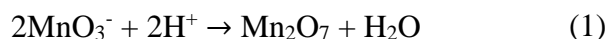
The resulting product was left to precipitate overnight, and the supernatant was discarded. The obtained product was washed three times with HCl solution to remove impurities. The GO was then washed with distilled water until the pH of the solution was neutral. Centrifugation was performed to separate the supernatant at each wash step (NF1200R, Nuve). Finally, the remaining product was dried overnight to obtain GO sample. Structural, morphological, and thermal characterizations were performed to determine the structure and the effect of different water contents during oxidation stages on the properties of GO. For this purpose, X-ray diffraction (XRD) analysis with Cu-K_α radiation (λ=0.154 nm) was performed to determine the oxidation degree and interlayer distance of the GO.

Fourier Transform Infrared Spectroscopy (FTIR) analysis was performed using the Thermo Scientific FTIR Spectrometer with an attenuated total reflection (ATR) module to identify functional groups on the GO basal planes. Also, absorbance of functional groups was determined according to water amount to define the effect of oxidation stage. Thermo Scientific K-Alpha XPS was performed to determine the types and amounts of elemental bonds of the GO structure. In XPS analysis, Al-K_α radiation was measured with 0.1 eV energy step size. The obtained peaks were deconvoluted with Gaussian fitting after Shirley background subtraction. SEM analysis (Zeiss GeminiSem 500) was performed to determine the effect of oxidation step on the morphological structure of GO. UV-Vis analysis

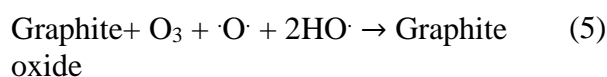
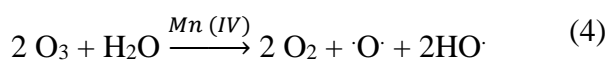
(Thermo Scientific Evolution 260 BIO UV Spectrophotometer) was carried out to specify the sp²-conjugation on the GO basal plane. DTA/TGA analysis was carried out to determine the thermal properties of the produced GO structures. Analysis was carried out in a Shimadzu DTG 60-H instrument up to 900°C with a heating rate of 2°C/min under nitrogen atmosphere. Micro-Raman analysis was performed with Renishaw In Via Confocal Raman Microscope to investigate defects in the GO samples (532 nm laser and 2400 l/mm).

3. Results and Discussion

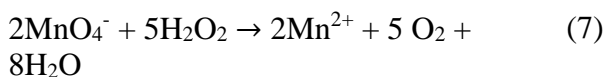
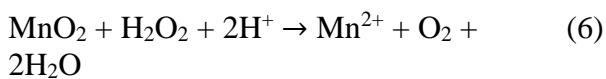
The oxidation stage begins with the addition of KMnO₄ to graphite-acid solutions. Dimanganese heptoxide (Mn₂O₇) and permanganate cation (MnO₃⁺) are formed with H⁺ ions in the solution (Equation 1) [22]. With the decomposition of Mn₂O₇, O₃ is produced as a by-product (Equation 2). O₃ also oxidizes graphite like Mn₂O₇. This stage is the first oxidation stage in Hummers method. Since the oxidation process is exothermic, homogenous mixing is necessary to avoid local overheating in the container. After this stage, post-oxidation stage begins with addition of water.



It is generally recommended to keep the temperature below 60°C to control the temperature and prevent foaming [23]. Adding water to the medium quenches Mn₂O₇ and permanganate acid is formed (HMnO₄) (Equation 3) [23]. During this step, oxidation is carried out by permanganate (MnO₄⁻) in acidic aqueous solution with various manganese (VII) containing oxo-species. The proposed mechanism was shown in equations 4 and 5 [24].



However, when H_2O_2 is added without any water addition, second oxidation step is skipped. [21]. In the last step, manganese compounds present in the solution converted to manganese ions by H_2O_2 (Equation 6 and 7) [23]:



The XRD results of graphite and GO samples are given in Figure 1. According to the XRD analysis of graphite, the characteristic peak belonging to the (002) plane was detected at 26.60° [25]. The peak belonging to the (004) plane of graphite was also found at 54.40° . Besides, the other peaks (42.3 , 44.4 , 54.4 , 77.5 and 83.5) are generally located in the graphite phase. The whole structure was determined to consist of graphite phase with high crystallinity [26]. The 2θ values of W0, W1, W2 and W3 samples are 10.2° , 11.56° , 11.96° and 12.24° , respectively. The peak around $2\theta=11^\circ$ is the characteristic peak of the GO structure associated with (001) plane [25].

According to the results, the 2θ angle of the characteristic (001) plane shifts to a higher angle with the increasing water content. The interlayer distance values (d) of GO was calculated according to the Bragg's Law [27] and listed in Table 1. The interlayer distance of graphite, W0, W1, W2 and W3 samples are 3.348 , 8.665 , 7.648 , 7.393 and 7.225 Å, respectively. The functional groups are formed during oxidation process and so it increases the interlayer distance of graphite layers. All samples produced with different water content has higher interlayer distance than the graphite interlayer distance (3.34 Å), which demonstrates the successful oxidation process. In addition, it was found that the oxidation degree decreases with the increasing water amount due to the increase in the interlayer distances. In a study, it was noted that adding more than 4 ml of water reduces the interlayer distance of GO layers [24].

Tour M. et. al. [28] specified that too much dilute acid solution reduces oxidation of graphite. In another study [10], it was stated that with the addition of water in the second oxidation step,

Mn_2O_7 is quenched and transformed into MnO_4^- . It was pointed out that the Mn_2O_7 was more oxidizing than MnO_4^- . Therefore, as the oxidation degree reduced with the increasing amount of water, functional groups were decreased at interlayer distances of GO. Accordingly, the characteristic peak of GO was shifted to the higher angle. Also, it was interpreted that the characteristic peak of the graphite (002) plane, which is around 26.6° , is observed in the XRD result of the W3 sample [29]. It was determined that the unexfoliated graphite structure was still present in the W3 sample and the oxidation conditions were not sufficient to oxidize all the graphite for W3 sample. Therefore, it was figured out that there was not enough oxidizing condition in W3.

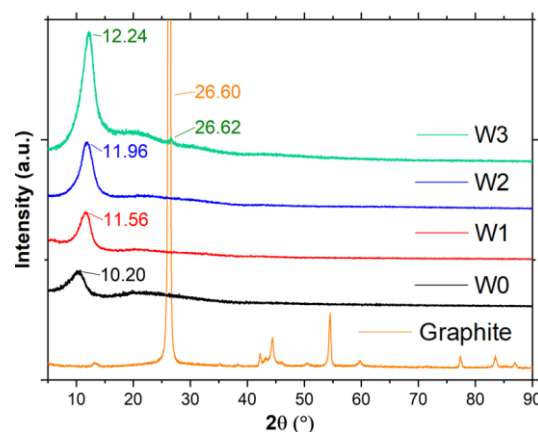


Figure 1. XRD analysis of GO samples produced with different water content

Table 1. Interlayer distance of produced GO with different water content

Sample	2θ ($^\circ$)	d (Å)
Graphite	26.60	3.348
W0	10.2	8.665
W1	11.56	7.648
W2	11.96	7.393
W3	12.24	7.225

FTIR analysis was performed to evaluate the functional groups of GO samples. The FTIR results of GO samples with different water content were given in Figure 2. All samples have characteristic absorbance bands indicating functional groups of GO structure [15]. FTIR results indicated that there were hydroxyl groups (OH) between $3600\text{--}2400\text{ cm}^{-1}$, carbonyl (C=O)

group at 1720 cm^{-1} , stretch mode of C-C bond and absorbed OH groups at 1620 cm^{-1} [30]. Also, 1417 cm^{-1} and 1260 cm^{-1} show symmetrical O-H bending and C-OH stretching in carboxylic acid [31], respectively while 1221 cm^{-1} , 1047 cm^{-1} and 971 cm^{-1} demonstrate O-H bending vibrations in carboxylic acid, C-O-C stretching and axial C-O stretching vibrations, respectively [2, 32, 33].

Also, the absorbance band around 1160 cm^{-1} demonstrates the carboxyl or carbonyl groups in the graphene oxide structures [34]. According to the results, the absorbance of 1620 cm^{-1} and 1260 cm^{-1} absorbance bands slightly increased in the W1, W2 and W3 samples due to the formation of hydroxyl groups originating from the post-oxidation stage (indicated by the arrow) [21]. Therefore, it was determined that the absorbance band associated with the OH functional groups increased with increasing amount of water. In addition, the absorbance of the 1047 cm^{-1} and 1160 cm^{-1} bands increased in the W0 sample and indicates the high oxidation degree of GO (indicated by the arrow) [35].

Moreover, the intensity of $1720\text{ cm}^{-1}/1620\text{ cm}^{-1}$ absorbance bands show an increase of oxidation degree for graphene oxide structures [24]. Accordingly, the intensity of $1720\text{ cm}^{-1}/1620\text{ cm}^{-1}$ was found highest in the W0 sample by the FTIR results and so these results are consistent with the XRD results.

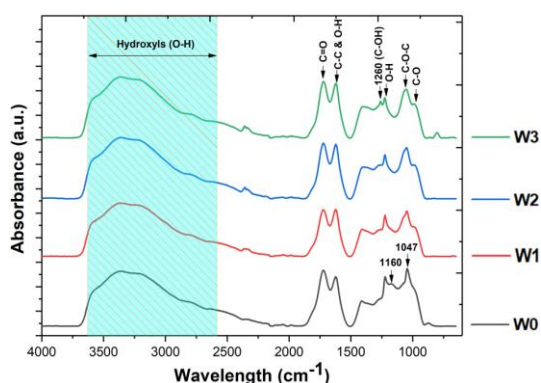


Figure 2. FTIR analysis of GO produced with different water content

XPS is an important analysis method to examine the elemental bonds and chemical states of functional groups in the GO structure. W0 and W3 samples were selected for XPS analysis in order to compare the effect of the water on post-

oxidation process. C1s and O1s spectrum results of W0 and W3 samples were shown in Figures 3(a) and 3(b) in XPS analysis. According to the obtained results, it is obvious that the carbon bond depicted by C1s intensity of the W0 decreased compared to the W3. In addition, the intensity of the O1s spectrum is dominant for W0 compared to W3 sample. The ratios of C1s and O1s spectra from survey analysis were given in Table 2 for W0 and W3 samples. The C/O ratio was calculated to determine the oxidation degree of GO [29].

According to the results, the C/O ratio is 1.45 for W0 sample and 1.59 for W3 sample, respectively. Therefore, it was observed that the W0 sample had a higher oxidation degree due to its low C/O ratio [29]. Besides, C1s spectrum was deconvoluted to examine in detail for W0 and W3 samples and the results were shown in Figures 3c and 3d. In the deconvolution process, three different functional groups peaks around 284.8, 286.6, 287.8 and 289 indicate C-C/C=C, C-O-C, C=O and O-C=O functional groups, respectively [12, 14, 18]. The ratio of C-C/C=C spectra obtained from deconvolution is 51.98% for the W3 sample and 50.32% for the W0 sample.

Besides, the ratio of spectrums associated with oxygenated functional groups were 49.68% and 48.02% for samples W0 and W3, respectively. The C-C/C=C regions of the W0 sample decreased due to more oxidation [36]. Therefore, the areas of functional groups in the W0 sample increased even more. Moreover, the intensity of the C-O-C epoxy bond is higher in the W0 sample. As the amount of epoxy group increases, the distance between the layers also increases. This situation explains the fact that the interlayer distance is the highest in the W0 sample as a result of XRD. As the temperature of the first oxidation stage is raised, the degree of oxidation increases.

The Mn (VII) compound shows extreme oxidizing properties at high temperatures [24], and so it is understood that the carbon basal plane of the W0 sample is more oxidized. The obtained results are compatible with XRD results due to the lower 2θ values. At the same time, XPS analysis supports the results of FTIR analysis,

since the absorbance of the 1047 cm^{-1} peak is higher for the W0 sample in the FTIR analysis.

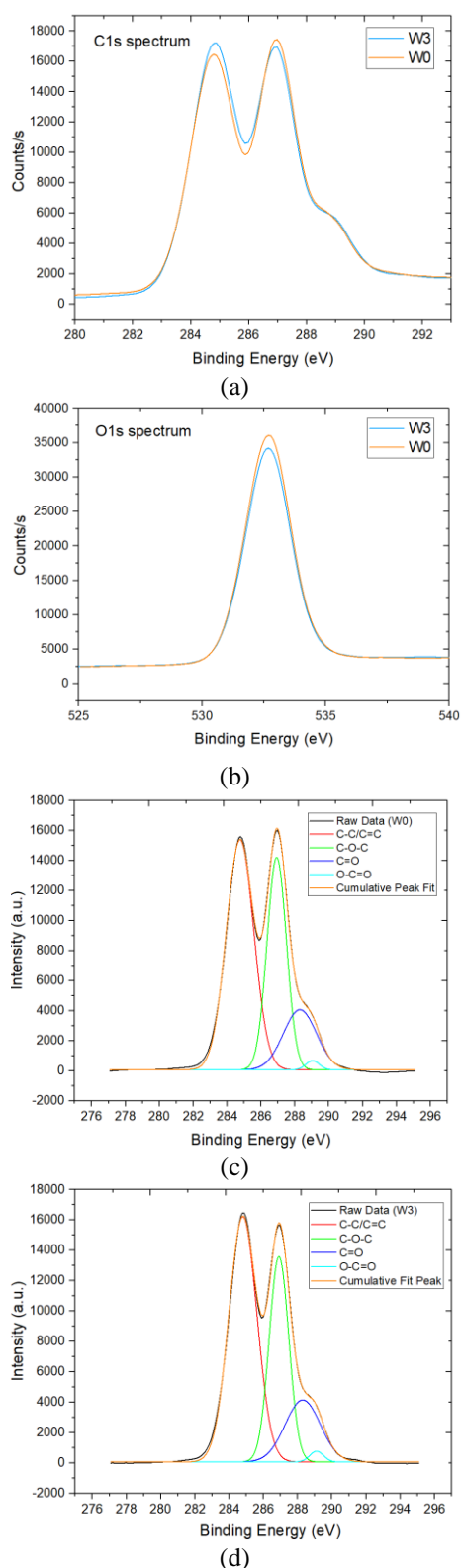


Figure 3. XPS analysis of GO produced with different water ratios. (a) C1s and (b) O1s spectrum of W0 and W3 samples. Deconvoluted C1s XPS spectrum of (c) W0 and (d) W3 samples

Table 2. Ratio of C1s and O1s results from XPS analyses

Samples	C 1s	O 1s	S 2p	C1s/O1s
W0	57.41	39.49	3.1	1.45
W3	61.40	38.60	-	1.59

SEM analysis is performed to determine the effect of water on the morphology of the samples in the second oxidation step. EDS analysis was carried out to determine the elemental distribution in the produced GO structure. The results of SEM and EDS analysis are shown in Figure 4. According to the results of SEM analysis, all GO structures have folded and crumpled structures. The wrinkled GO surface is due to the addition of functional groups to the graphene basal plane during oxidation [25].

However, a smoother surface is formed as the amount of water increases. As the oxidation conditions increase, the formation of a wrinkled structure is expected. The fluctuation of the GO structure increases with the increasing number of functional groups in the GO structure [37]. Therefore, the W0 sample was observed to undergo high oxidation due to its wrinkled surface structure. In the EDS results, the carbon (C), oxygen (O) and sulfur (S) elements were detected. Graphene oxide structures consist of the C, O, and hydrogen (H) elements. However, H element cannot be detected in the EDS analysis. The element S is included in the structure due to the use of H_2SO_4 in production [38].

Therefore, C and O elements are seen in the EDS analysis. The atomic C/O ratio was calculated to compare the oxidation degree of the GO samples and is shown in the Figure 4. Accordingly, the C/O ratios reached 1.29, 1.48, 1.54 and 1.55 for W0, W1, W2 and W3 samples, respectively. The C/O ratio increased from the W0 sample to the W3 sample. It is known that the C/O ratio in EDX analysis decreases with the increasing oxidation degree of GO [12]. As a result, it was determined that the W0 sample had the highest oxidation degree in the EDX analysis. It is also supported by the EDS analysis result that the degree of oxidation increases with the decreasing amount of water. These results are also compatible with XRD and XPS results.

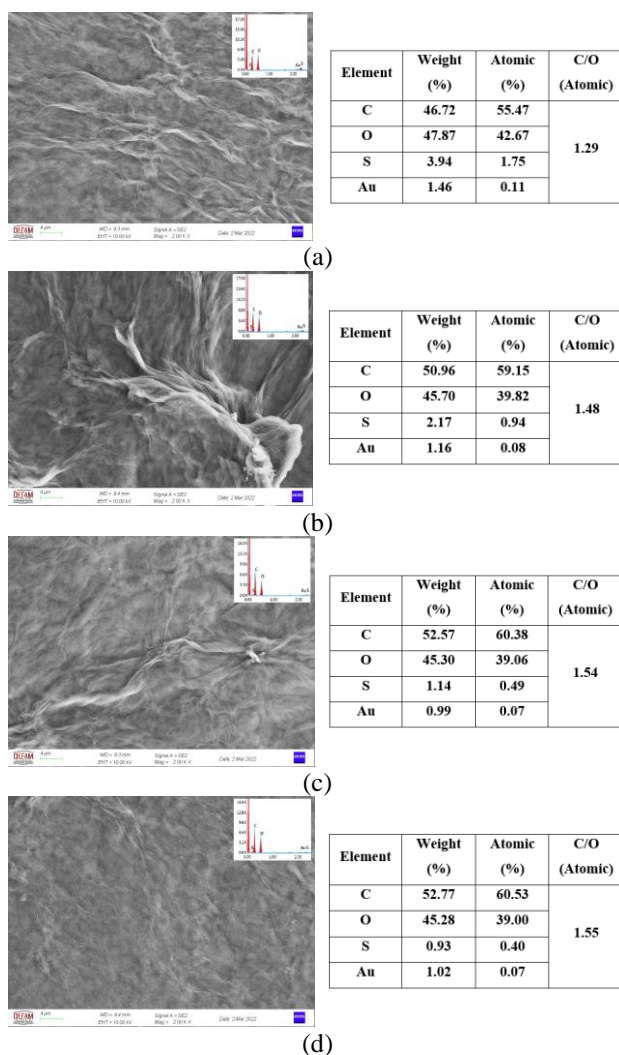


Figure 4. SEM and EDS analysis of GO produced with different water ratios. SEM and EDS analysis of (a) W0, (b) W1, (c) W2 and (d) W3 samples

TGA/DTA analysis was performed to determine the thermal decomposition behavior of the produced GO and the results were shown in the Figure 5. According to the result of TGA analysis, a continuous weight loss occurred with increasing temperature in all samples. Weight loss up to 100°C is due to the release of trapped water between the GO layers. At this stage, the W0 sample appears to have the highest moisture content due to the greatest weight loss. The sudden weight loss between about 160-220°C is due to the degradation of unstable oxygen functional groups [12, 39]. For decomposition to occur, the strong interlayer hydrogen bond must be overcome.

Therefore, decomposition is more difficult in samples with more hydrogen bonds. The presence of the newly-OH functional group in the FTIR results of samples with the second

oxidation stage indicates that hydrogen bonding is more in these samples [40]. Therefore, the decomposition temperature also increases with the increasing water amount in the second oxidation stage. In the DTA analysis, an exothermic peak is observed for GO samples between approximately 160 and 200 °C due to the combustion of functional groups [41]. According to the DTA results, the highest decomposition temperature was observed in the W3 sample with 202.86 °C. A gradual loss of mass between about 230 °C and 900 °C is due to the removal of more stable functional groups [24]. At the end of 900 °C, the highest weight loss occurred in the W0 sample, since it has lower hydrogen bonds and more functional groups. Since TGA analysis evaluates in terms of weight loss, it is thought that the structures with the highest weight loss have more functional groups [13].

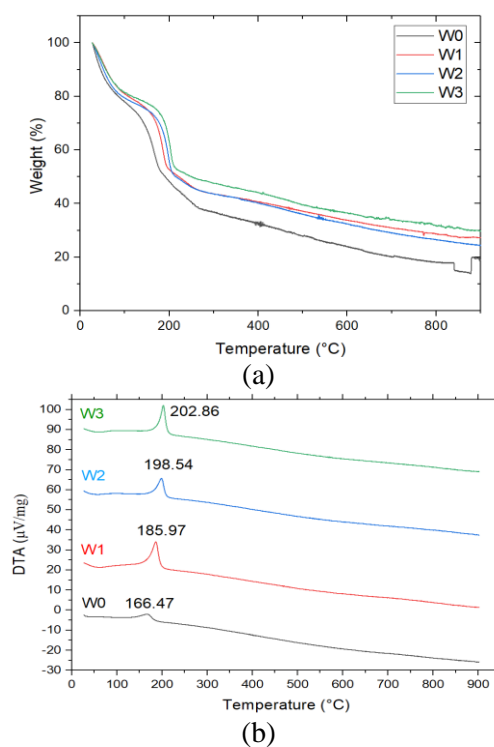


Figure 5. (a) TGA and (b) DTA analysis of produced GO with different water ratios

The results of the UV-Vis analysis performed to determine the effect of the post-oxidation step are shown in Figure 6. The UV-Vis spectrum of GO has two characteristic absorbance bands that are used to determine the degree of oxidation of graphene oxide and the amount of sp² conjugate structure. The absorbance band around 229 nm indicates the $\pi \rightarrow \pi^*$ electron transition of carbon

aromatic bonds (sp^2). The second characteristic peak is around 300 nm and was seen as the shoulder. This shoulder indicates the $n \rightarrow \pi^*$ electron transition of the C=O bond. According to the results, the maximum point of the carbon aromatic bond electron transition of the W0 sample was 226 nm and it was determined that it shifted to the left compared to other samples. This is due to the exfoliation of GO in the post-oxidation step with the increasing oxidation degree [15]. XRD and XPS results also support this situation. As can be seen in the XRD, FTIR and XPS results, the C-C and C=C bond decreased in the W0 sample. Therefore, the W0 sample showed absorbance at the lowest wavelength, since its sp^2 conjugate structure also decreased.

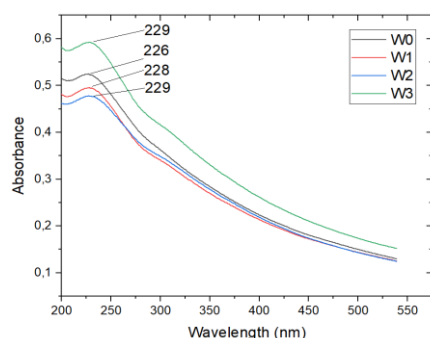


Figure 6. UV-Vis analysis of produced GO with different water ratios

Raman analysis was performed to examine the defects in the structure of GO samples. The Raman analysis results of the samples are shown in the Figure 7. There are two characteristic bands as D and G in Raman Analysis for GO. The D band shows the breathing mode of A_{1g} symmetry in sp^2 systems and is around 1350 cm^{-1} band [15, 32]. The G band indicates the E_{2g} phonons at the Brillouin zone center and is around 1590 cm^{-1} band. D and G bands were obtained around 1350 cm^{-1} and 1600 cm^{-1} bands. The shift of the G band may be due to the isolated double bonds after oxidation [29].

To compare the defect rate of GO materials, it is determined by the I_D/I_G ratio using the intensity of the D and G peaks [40, 42]. The I_D/I_G ratios for W0 and W3 samples were 0.82 and 0.84, respectively. In Raman analysis, the D peak increases with the rate of defect or disorder in the graphene plane [40]. Accordingly, more defects

were formed in the GO structure with the post-oxidation process.

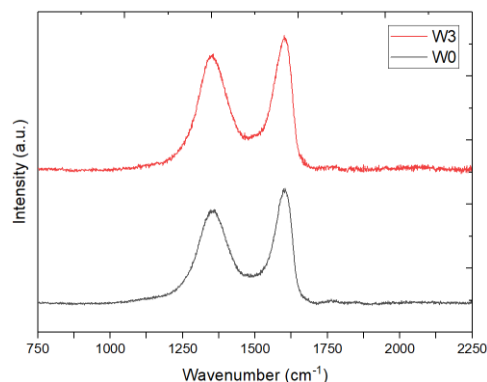


Figure 7. Raman analysis for W0 and W3 samples

4. Conclusion

GO was successfully produced with the Improved Hummers Method. Effect of water content on the post-oxidation level of GO structure was investigated. The interlayer distance was reduced with the post-oxidation step, and so W0 sample had the highest oxidation degree. The hydroxyl functional group increased in the produced samples with the post-oxidation step. In XPS analysis, the C/O ratio increased from the W0 sample to the W3 sample. In addition, the intensity of the oxygen-containing functional groups is higher for the W0 sample. In the UV-Vis analysis, the W0 sample was detected to have a lower sp^2 conjugate structure.

This indicates that the GO basal plane is excessively oxidized under the W0 sample conditions. According to thermal analysis, the W3 sample was more stable in terms of thermal properties due to lower thermal decomposition temperature. Besides, it was revealed that the highest weight loss occurred in the W0 sample due to the excess of functional groups. Overall results show that the post-oxidation step with increasing water content reduces the oxidation degree of GO, increases defects amount, provides a less wrinkled structure, and improves the thermal stability of GO.

Article Information Form

Acknowledgments

Authors would like to thank Dokuz Eylul University (DEU) Department of Metallurgical and Materials Engineering and Center for

Fabrication and Application of Electronic Materials for their valuable supports. They would also like to thank Arifmert Cen, Ceyda Otlu, Yunus Emre Demir and Cem İnci for their support in laboratory studies.

Funding

This research was financially supported by Scientific Research Projects Coordination Unit of Manisa Celal Bayar University (MCBU-BAP Project No: 2020-038).

Authors' Contribution

The authors contributed equally to the study.

The Declaration of Conflict of Interest/ Common Interest

No conflict of interest or common interest has been declared by the authors.

The Declaration of Ethics Committee Approval

This study does not require ethics committee permission or any special permission.

The Declaration of Research and Publication Ethics

The authors of the paper declare that they comply with the scientific, ethical and quotation rules of SAUJS in all processes of the paper and that they do not make any falsification on the data collected. In addition, they declare that Sakarya University Journal of Science and its editorial board have no responsibility for any ethical violations that may be encountered, and that this study has not been evaluated in any academic publication environment other than Sakarya University Journal of Science.

Copyright Statement

Authors own the copyright of their work published in the journal and their work is published under the CC BY-NC 4.0 license.

References

- [1] M. P. Araújo, O. S. G. P. Soares, A. J. S. Fernandes, M. F. R. Pereira, C. Freire, "Tuning the surface chemistry of graphene flakes: new strategies for selective oxidation," *RSC Advances*, vol. 7, no. 23, pp. 14290–14301, 2017.
- [2] J. Guerrero-Contreras, F. Caballero-Briones, "Graphene oxide powders with different oxidation degree, prepared by synthesis variations of the Hummers method," *Materials Chemistry and Physics*, vol. 153, pp. 209–220, 2015.
- [3] J. Chen, B. Yao, C. Li, G. Shi, "An improved Hummers method for eco-friendly synthesis of graphene oxide," *Carbon*, vol. 64, no. 1, pp. 225–229, 2013.
- [4] W. S. Koe, J. W. Lee, W. C. Chong, Y. L. Pang, L. C. Sim, "An overview of photocatalytic degradation: photocatalysts, mechanisms, and development of photocatalytic membrane," *Environmental Science and Pollution Research*, vol. 27, no. 3, pp. 2522–2565, 2020.
- [5] T. A. Saleh, G. Fadillah, "Recent trends in the design of chemical sensors based on graphene–metal oxide nanocomposites for the analysis of toxic species and biomolecules," *Trends in Analytical Chemistry*, vol. 120, 2019.
- [6] R. K. Joshi, S. Alwarappan, M. Yoshimura, V. Sahajwalla, Y. Nishina, "Graphene oxide: the new membrane material," *Applied Materials Today*, vol. 1, no. 1, pp. 1–12, 2015.
- [7] D. Ege, A. R. Kamali, A. R. Boccaccini, "Graphene Oxide/Polymer-Based Biomaterials," *Advanced Engineering Materials*, vol. 19, no. 12, p. 1700627, 2017.
- [8] S. Thangavel, G. Venugopal, "Understanding the adsorption property of graphene-oxide with different degrees of oxidation levels," *Powder Technology*, vol. 257, pp. 141–148, 2014.
- [9] Y. Wei, X. Hu, Q. Jiang, Z. Sun, P. Wang, Y. Qiu, W. Liu, "Influence of graphene oxide with different oxidation levels on the properties of epoxy composites," *Composites Science and Technology*, vol. 161, no. April, pp. 74–84, 2018.

- [10] D. R. Dreyer, S. Park, C. W. Bielawski, R. S. Ruoff, "The chemistry of graphene oxide," *Chem. Soc. Rev.*, vol. 39, no. 1, pp. 228–240, 2010.
- [11] S. Eigler, S. Grimm, F. Hof, A. Hirsch, "Graphene oxide: a stable carbon framework for functionalization," *Journal of Materials Chemistry A*, vol. 1, no. 38, p. 11559, 2013.
- [12] V. Panwar, A. Chattree, K. Pal, "A new facile route for synthesizing of graphene oxide using mixture of sulfuric-nitric-phosphoric acids as intercalating agent," *Physica E: Low-Dimensional Systems and Nanostructures*, vol. 73, pp. 235–241, 2015.
- [13] M. D. P. Lavin-Lopez, A. Romero, J. Garrido, L. Sanchez-Silva, J. L. Valverde, "Influence of Different Improved Hummers Method Modifications on the Characteristics of Graphite Oxide in Order to Make a More Easily Scalable Method," *Industrial & Engineering Chemistry Research*, vol. 55, no. 50, pp. 12836–12847, 2016.
- [14] D. Yang, A. Velamakanni, G. Bozoklu, S. Park, M. Stoller, R. D. Piner, S. Stankovich, I. Jung, D. A. Field, C. A. Ventrice, R. S. Ruoff, "Chemical analysis of graphene oxide films after heat and chemical treatments by X-ray photoelectron and Micro-Raman spectroscopy," *Carbon*, vol. 47, no. 1, pp. 145–152, 2009.
- [15] S. Eigler, A. M. Dimiev, "Characterization Techniques," in *Graphene Oxide: Fundamentals and Applications*, A. M. Dimiev and S. Eigler, Eds., United Kingdom: John Wiley & Sons, 2016, pp. 85–118.
- [16] B. C. Brodie, "XIII. On the atomic weight of graphite," *Philosophical Transactions of the Royal Society of London*, vol. 149, no. 1, pp. 249–259, 1859.
- [17] W. S. Hummers, R. E. Offeman, "Preparation of Graphitic Oxide," *Journal of the American Chemical Society*, vol. 80, no. 6, pp. 1339–1339, 1958.
- [18] D. C. Marcano, D. V. Kosynkin, J. M. Berlin, A. Sinitskii, Z. Sun, A. Slesarev, L. B. Alemany, W. Lu, J. M. Tour, "Improved synthesis of graphene oxide," *ACS Nano*, vol. 4, no. 8, pp. 4806–4814, 2010.
- [19] F. Boran, S. Çetinkaya Güner, "The effect of starting material types on the structure of graphene oxide and graphene," *Turkish Journal of Chemistry*, vol. 43, no. 5, pp. 1322–1335, 2019.
- [20] L. J. Cote, J. Kim, Z. Zhang, C. Sun, J. Huang, "Tunable assembly of graphene oxide surfactant sheets: wrinkles, overlaps and impacts on thin film properties," *Soft Matter*, vol. 6, no. 24, p. 6096, 2010.
- [21] J. H. Kang, T. Kim, J. Choi, J. Park, Y. S. Kim, M. S. Chang, H. Jung, K. T. Park, S. J. Yang, C. R. Park, "Hidden Second Oxidation Step of Hummers Method," *Chemistry of Materials*, vol. 28, no. 3, pp. 756–764, 2016.
- [22] A. M. Dimiev, J. M. Tour, "Mechanism of graphene oxide formation," *ACS Nano*, vol. 8, no. 3, pp. 3060–3068, 2014.
- [23] F. J. Tölle, K. Gamp, R. Mülhaupt, "Scale-up and purification of graphite oxide as intermediate for functionalized graphene," *Carbon*, vol. 75, no. April, pp. 432–442, 2014.
- [24] J. Chen, Y. Zhang, M. Zhang, B. Yao, Y. Li, L. Huang, C. Li, G. Shi, "Water-enhanced oxidation of graphite to graphene oxide with controlled species of oxygenated groups," *Chemical Science*, vol. 7, no. 3, pp. 1874–1881, 2016.
- [25] R. Muzyka, M. Kwoka, Ł. Smędowski, N. Díez, G. Gryglewicz, "Oxidation of graphite by different modified Hummers methods," *New Carbon Materials*, vol. 32, no. 1, pp. 15–20, 2017.

- [26] A. A. Muhsan, K. Lafdi, "Numerical study of the electrochemical exfoliation of graphite," *SN Applied Sciences*, vol. 1, no. 3, p. 276, 2019.
- [27] J. Epp, "X-ray diffraction (XRD) techniques for materials characterization," in *Materials Characterization Using Nondestructive Evaluation (NDE) Methods*, G. Huebschen, I. Altpeter, R. Tschuncky, and H.-G. Herrmann, Eds., Elsevier Inc., 2016, pp. 81–124.
- [28] A. L. Higginbotham, D. V. Kosynkin, A. Sinitskii, Z. Sun, J. M. Tour, "Lower-Defect Graphene Oxide Nanotubes Nanoribbons from Multiwalled Carbon Nanotubes," *ACS nano*, vol. 4, no. 4, p. 2059, 2010.
- [29] M. F. R. Hanifah, J. Jaafar, M. H. D. Othman, A. F. Ismail, M. A. Rahman, N. Yusof, W. N. W. Salleh, F. Aziz, "Facile synthesis of highly favorable graphene oxide: Effect of oxidation degree on the structural, morphological, thermal and electrochemical properties," *Materialia*, vol. 6, no. May, p. 100344, 2019.
- [30] K. Krishnamoorthy, M. Veerapandian, K. Yun, S.-J. Kim, "The chemical and structural analysis of graphene oxide with different degrees of oxidation," *Carbon*, vol. 53, pp. 38–49, 2013.
- [31] M. Wojtoniszak, D. Rogińska, B. Machaliński, M. Drozdziak, E. Mijowska, "Graphene oxide functionalized with methylene blue and its performance in singlet oxygen generation," *Materials Research Bulletin*, vol. 48, no. 7, pp. 2636–2639, 2013.
- [32] M. J. Yoo, H. B. Park, "Effect of hydrogen peroxide on properties of graphene oxide in Hummers method," *Carbon*, vol. 141, pp. 515–522, 2019.
- [33] S. Thakur, N. Karak, "Green reduction of graphene oxide by aqueous phytoextracts," *Carbon*, vol. 50, no. 14, pp. 5331–5339, 2012.
- [34] V. Țucureanu, A. Matei, A. M. Avram, "FTIR Spectroscopy for Carbon Family Study," *Critical Reviews in Analytical Chemistry*, vol. 46, no. 6, pp. 502–520, 2016.
- [35] Y. Hou, S. Lv, L. Liu, X. Liu, "High-quality preparation of graphene oxide via the Hummers' method: Understanding the roles of the intercalator, oxidant, and graphite particle size," *Ceramics International*, vol. 46, no. 2, pp. 2392–2402, 2020.
- [36] R. Al-Gaashani, A. Najjar, Y. Zakaria, S. Mansour, M. A. Atieh, "XPS and structural studies of high quality graphene oxide and reduced graphene oxide prepared by different chemical oxidation methods," *Ceramics International*, vol. 45, no. 11, pp. 14439–14448, 2019.
- [37] A. Allahbakhsh, F. Sharif, S. Mazirani, "The Influence of Oxygen-Containing Functional Groups on The Surface Behavior and Roughness Characteristics of Graphene Oxide," *Nano*, vol. 08, no. 04, p. 1350045, 2013.
- [38] S. Eigler, C. Dotzer, F. Hof, W. Bauer, A. Hirsch, "Sulfur Species in Graphene Oxide," *Chemistry - A European Journal*, vol. 19, no. 29, pp. 9490–9496, 2013.
- [39] R. Ikram, B. M. Jan, W. Ahmad, "An overview of industrial scalable production of graphene oxide and analytical approaches for synthesis and characterization," *Journal of Materials Research and Technology*, vol. 9, no. 5, pp. 11587–11610, 2020.
- [40] Q. Zhang, Y. Yang, H. Fan, L. Feng, G. Wen, L. Qin, "Roles of water in the formation and preparation of graphene oxide," *RSC Advances*, vol. 11, pp. 15808–15816, 2021.
- [41] P. S. Narayan, N. L. Teradal, S. Jaldappagari, A. K. Satpati, "Eco-friendly reduced graphene oxide for the determination of mycophenolate mofetil in

pharmaceutical formulations,” *Journal of Pharmaceutical Analysis*, vol. 8, no. 2, pp. 131–137, 2018.

- [42] N. Yadav, B. Lochab, “A comparative study of graphene oxide: Hummers, intermediate and improved method,” *FlatChem*, vol. 13, no. February, pp. 40–49, 2019.

Vancomycin-Loaded Gel Ocular Drug Delivery System for Treatment of Endophthalmitis

Ebru Erdal 

Faculty of Medicine, Advanced Technologies Application and Research Center, Ankara Yıldırım Beyazıt University, Ankara, Türkiye, ebuerdalbio@gmail.com

ARTICLE INFO

ABSTRACT

Keywords:

Endophthalmitis
Vancomycin
Hydrogel
Alginate
Antibacterial



Article History:

Received: 04.09.2023

Accepted: 09.04.2024

Online Available: 14.06.2024

In case of endophthalmitis, which develops as a result of microbial infection of the intraocular tissues, is not treated, it can lead to anatomical or functional losses in the eye. Intravitreal injections are the most preferred method in the treatment of endophthalmitis, which can be exogenous or endogenous. The combination of antibiotics effective against bacteria has disadvantages such as re-injection, unresponsiveness to treatment, and drug toxicity. Treatment in which antibiotics effective against both gram (+) and gram (-) bacteria are used in combination has disadvantages such as re-injection, unresponsiveness to treatment, and drug toxicity. In order to overcome these disadvantages, studies are carried out to develop injectable forms of active substances that provide long-term release. In this study, the antibiotic Vancomycin (Van), which is frequently used in the treatment of endophthalmitis, was loaded into alginate hydrogels; characterization, in vitro release and toxicity were determined. Its morphology was visualized by environmental scanning electron microscopy (ESEM) and Fourier transform infrared (FTIR) spectroscopy was used to characterize changes in chemical structure. The release of Van from the hydrogels continued for more than 2 weeks. It was determined that the toxicity of free Van decreased with loading of hydrogels. Its antibacterial activity was evaluated with the disc diffusion test and it was determined that it was more effective against *Staphylococcus aureus*.

1. Introduction

Endophthalmitis is an inflammatory condition caused by bacterial, fungal or parasitic microorganisms infecting the humor vitreous and humor aquosus (intraocular cavity) of the eye. The spread of infection to all tissues of the eye, such as the sclera, tenon capsule and orbital soft tissues, is called panophthalmitis. It can be of exogenous origin after eye surgery, trauma or endogenous origin such as systemic diseases or immune disorders [1]. When endophthalmitis is left untreated, it can result in anatomical and functional loss of the eye [2].

Intravitreal antibiotic injection is the most common treatment method used in the clinic [1]. However, the need for repeat injections in case of prolonged treatment is considered unfavorable both in terms of patient welfare and new

complications [3]. Preventive treatment protocols are primarily used for exogenous endophthalmitis. The use of topical antiseptics or antibiotics before a surgical operation, and topical, subconjunctival and systemic administration of an effective antibiotic to ocular tissues during and after surgery reduce the incidence of endophthalmitis. However, in case of bacterial infection, intravitreal, systemic antibiotics and corticosteroids are used in combination with intravitreal drug injection or pars plana vitrectomy [4].

Due to the low and limited permeability of the blood retinal barrier, intravitreal antibiotic administration is frequently preferred in clinical practice for the treatment of endophthalmitis [1]. Antibiotics with broad spectrum and low retinal toxicity are used for treatment. Dual antibiotic

combinations effective against gram (+) and gram (-) anaerobic bacteria increase treatment efficacy. In clinical practice, Vancomycin and Amikacin/Seftazidime combination is most commonly preferred for this purpose [5]. The use of vancomycin, which is used for Gram (+) microorganisms, at a concentration of 1 mg/0.1 ml has been found to be non-toxic to the retina. There are situations that should be considered in combined use. Since vancomycin has a low pH, it can cause chemical and physical instability when mixed with other antibiotics. Precipitation has been reported after intravitreal injection of vancomycin and ceftazidime combination. This was resolved by complete clearance of the precipitates from the vitreous cavity for 2 months. However, visual acuity decreases during this period [6, 7].

Studies have shown that the administration of toxic, poorly water soluble or short half-life active substances with a carrier increases treatment efficacy. The use of structures such as nanoparticles, nanogels, hydrogels or inclusion complexes eliminates these disadvantages of active ingredients [8, 9]. The vitreous structure of the eye is transparent and heterogeneous, containing 98% water, 2% collagen and hyaluronic acid [10]. Therefore, it is important to choose gel forms that are suitable for the structure of the vitreous, since the non-transparent form of the materials to be applied intravitreal affect the visual field. The use of nanogels or injectable hydrogels as carriers in ocular applications has the advantage of both not affecting the visual function and having different hydrogel structures.

Hydrogels are 3-dimensional structures cross-linked by physical or chemical bonds and swell by absorbing water and biological fluids. Hydrogels are preferred for eye applications due to their high water content and their ability to release by responding to pH, temperature and ionic strength changes in the organism according to the material they are prepared. Hydrogels are soft, flexible and some forms have an injectable structure owing to the high amount of water in their structure. The most important areas of use are controlled drug release systems, wound dressing materials, soft tissue substitution and contact lenses [11-13]. The use of hydrogels for

controlled release systems aims to prolong the residence time of the drug in the environment and accordingly extending the application interval, reduce toxic effects and deliver the drug to the target tissue [14].

Hydrogels can be obtained from natural polymers such as cellulose, pectin, starch, dextran, alginate, chitosan, collagen, gelatin or synthetic polymers such as polyesters (lactic acid-glycolic acid copolymers, poly (ε-caprolactone), poly (trimethylene carbonate), poly (trimethylene carbonate), poly (orthoesters), etc.), polyamides, poly (glutamic acid), poly (orthoesters) [15, 16]. In this study, hydrogel was prepared from alginate for controlled release of vancomycin. Sodium alginate is a linear polysaccharide (heteropolymer of 1,4-bonded-D mannuronic acid and 1,4-bonded-L-guluronic acid) typically derived from brown seaweed or *Azotobacter* and *Pseudomonas* bacteria.

Alginate has different and intensive usage areas in biomedical applications (drug release, implantation and cell encapsulation studies) with its biocompatible, hydrophilic, mucoadhesive, low cost and gelation with divalent cations such as Ca^{+2} (Kuo and Ma, 2001). Homogeneous gel structures are obtained by replacing sodium ions in the structure of sodium alginate with divalent cations such as calcium. While it allows diffusion of the loaded drug due to its large pore size, the pore size can also be adjusted with various modifications [17, 18].

In the study, vancomycin-loaded alginate hydrogels (Van-Alg Gel) were prepared to ensure the controlled and prolonged release of the active ingredient vancomycin in the vitreous. In this way, it is aimed to reduce the frequency of intravitreal injection of vancomycin. After the characterization of Van-Alg Gels, the release profile and toxicity were determined. Since vancomycin is used for the treatment of endophthalmitis, its antibacterial effect was determined by disc diffusion method.

2. Material and Methods

2.1. Materials

Vancomycin loaded into gels and Alginat were purchased from Sigma-Aldrich (St. Louis, Missouri, USA). In vitro cytotoxicity tests were performed with the human retinal microvascular endothelial (HRMEC) (ACBRI 181) cell line. The media and supplementary materials used for the culture of HRMEC cells were obtained from Cell System.

2.2. Preparation of Alg and Van-Alg hydrogel

An alginate-based in situ gelling system has been developed for the controlled release of vancomycin antibiotic [19]. In the in situ gelling system, hydrogel network formation and encapsulation of the active substance into the gel occur simultaneously. 25 mg of Van was added to 5 ml of 1% alginate solution, and the solution was stirred until clear (1 hour). Then, 1% CaCl₂ was added dropwise to the solution and centrifuged at 3000 rpm for 5 minutes to remove the Van that was not trapped in the gel after gel formation. The same procedure was followed for the preparation of blank alginate gels, except that PBS was added to the solution instead of vancomycin.

2.3. Characterization of the hydrogels

2.3.1. Morphology

The morphology of the Alg and Van-Alg Gels was determined by using environmental scanning electron microscopy (ESEM) (FEI QUANTA 200 FEG ESEM). Unlike the scanning electron microscope, ESEM is used for imaging uncoated or wet samples. After the gels were placed in the sample holder, surface imaging was performed under low vacuum.

2.3.2. FTIR analysis

Fourier transform infrared (FTIR) (Thermo Fisher, Nicolet is50) spectroscopy was used to characterize changes in chemical structure as a result of vancomycin loading into hydrogels. The spectra of alginate, vancomycin, Alg and Van-

Alg Gels were scanned between 500 and 4000 cm⁻¹.

2.3.3. Rheological properties

The rheological properties of the hydrogels were determined using a Malvern Kinexus Pro+ rheometer (Malvern, UK) at 4 and 37°C. In order to evaluate the flow properties and viscoelastic behavior of the hydrogels, shear rate $\dot{\gamma}$ =0.1–1000 s⁻¹ and frequency scanning tests were determined as 0.1500 Hz. The samples were placed on the plate and measurements were made at a distance of 1 mm between the two plates.

2.4. Vancomycin loading and release

In order to determine the amount of Van loaded on the gels and released depending on time, first of all, spectrum scanning of Van was performed and the wavelength at which it gave maximum absorbance was determined as 280 nm. The amount of vancomycin loaded on the gels (Entrapment Efficiency-EE) was determined by the indirect method. The indirect method is based on the determination of vancomycin remaining in the supernatant after gel formation is complete. The percentage encapsulation efficiency was calculated by subtracting the vancomycin that was not entrapped in the gel from the vancomycin initially added. For release studies, 6 mg of Van-Alg Gel (average of 50±3,5%) was placed on the dialysis membrane (cut-off 14-12 kDa; Sigma, USA) and both ends of the membrane were sealed. The delivery system placed in 10 ml of BSS (Balanced Salt Solution) was incubated at 37±1°C and 100 rpm shaking speed. At certain time intervals, 1 ml of BSS was taken and replaced with the same volume of BSS. Time-dependent release of Van from the gels was determined by using a UV spectrophotometer at 280 nm and all experiments were repeated three times.

2.5. Cytotoxicity

In vitro cytotoxic effects of Van, Alg and Alg-Van Gels were determined by MTT assay on HRMEC cells. MTT (3-[4,5-Dimethylthiazol-2-yl]-2,5-diphenyltetrazolium bromide; Thiazolyl blue) or XTT (2,3-bis-(2-methoxy-4-nitro-5-sulfophenyl)-2H-tetrazolium-5-carboxanilide)

assays are performed to determine the cytotoxic effect of materials designed to interact directly or indirectly with living tissue on cells. Metabolically active cells reduce the tetrazolium salt to purple colored formazan crystals. The density of formazan crystals is used as an indicator of cell viability, proliferation, and cytotoxicity [20]. For the MTT assay, HRMEC cells were seeded in a 96-well plate at 5×10^4 cells/well in 200 μ l of medium and incubated overnight in an incubator. Hydrogels prepared at different weights were sterilized by exposing to UV light for 1 hour [21]. Hydrogels (25, 50, 100, 200 μ g/ml) were incubated with cells at 5% CO₂ and 37°C for 24 hours. After incubation, the hydrogels were removed and MTT solution (1 mg/ml) was added to the cells. After incubation for 4 hours in the dark and at 37°C, the MTT solution was removed and the plate was read at 570 nm after incubating with pure isopropanol containing 0.04 M HCl for 30 minutes. The cells in the first column were incubated with the medium alone and the average of absorbance values obtained from these wells was accepted as 100% and the cytotoxicity rate was determined by comparing the average of absorbances obtained from the test wells.

2.6. Antibacterial efficacy

The antibacterial effect of Van, Alg and Alg-Van Gels was determined by disk diffusion method. *Escherichia coli* (*E. coli*) (ATCC 35218) (gram-negative) and *Staphylococcus aureus* (*S. aureus*) (ATCC 29213) (gram-positive) strains were used for the antibacterial activity of the gels [22]. First of all, bacterial solutions were prepared by suspension method. For bacterial suspensions, colonies of *E. coli* and *S. aureus* were taken from agar plates with inoculating loops and suspended in Todd Hewitt broth. After 24 hours of incubation at 37°C and a shaking speed of 100 rpm, the bacterial solution was diluted with sterile buffer (0.5 McFarland). After inoculating bacteria on agar, discs with a diameter of 6 mm were placed and gels of different formulations and free Van were absorbed into the discs. The dry weights of the Alg and Van-Alg hydrogels were determined. The hydrogels were placed on disks with the weight written on the petri dishes (25, 50, 100 and 200 μ g/ml). After 24 hours of incubation of the agar plates at 37°C, the

diameters of the zones formed around the discs were measured (n=3).

3. Results and Discussion

3.1. Characterization of hydrogels

3.1.1. Morphology of hydrogels

The change in the morphology of Alg hydrogels caused by vancomycin encapsulation was visualized by ESEM. Hydrogel images taken without drying and coating are given in Figure 1. It is seen that Alg hydrogels have a rough and homogeneous surface, while the pore structure is very low (Figure 1A). However, interconnected micro and macropores are observed in Van-Alg Gel (Figure 1B).

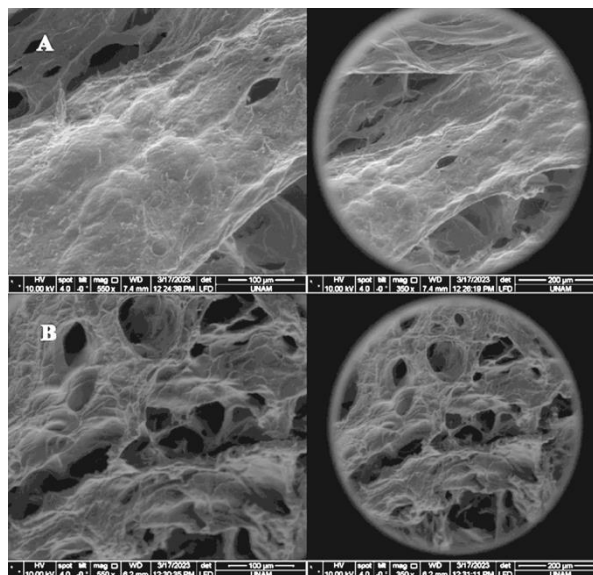


Figure 1. ESEM image of Alg hydrogels (A) and Van-Alg hydrogels (B)

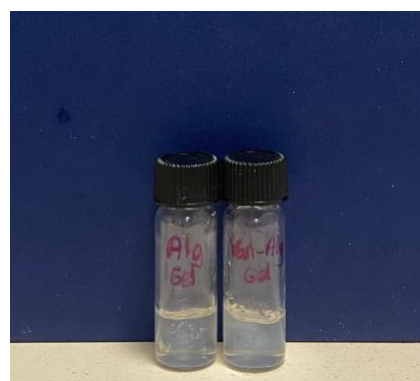


Figure 2. Alg and Van-Alg hydrogels

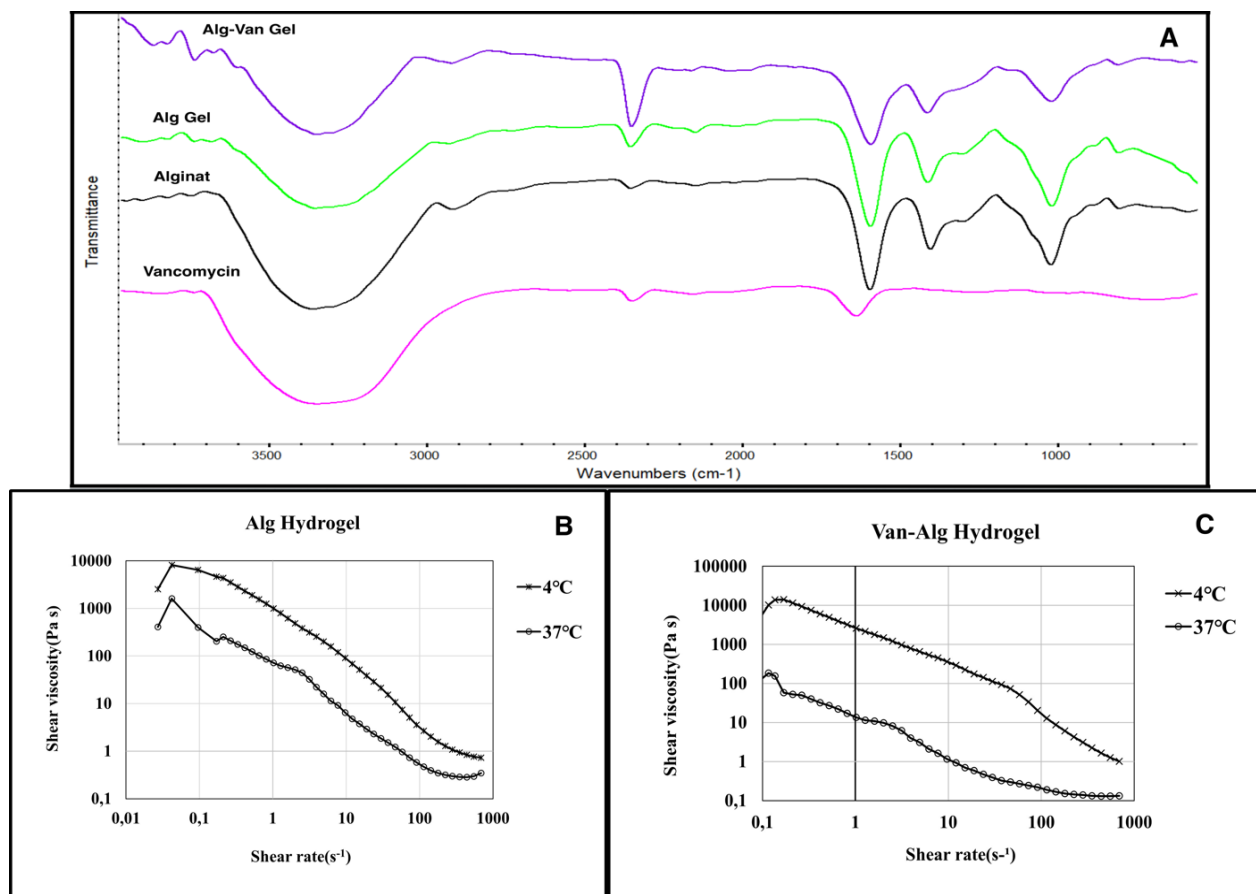


Figure 3. FTIR spectra of Alg and Alg-Van Gels, Alginate Polymer and Vancomycin (A). Viscosity measurement of Alg Gel (B) and Van-Alg Gel (C) at 4°C and 37°C.

This indicates that the active ingredient loading accelerates the formation of the porous structure in the gel structure. When the drug is loaded into hydrogels, their pore structure becomes larger and heterogeneous. The varying microstructure and swelling behavior of hydrogels depending on the polymer or crosslinker concentration have a significant effect on the controlled drug release and drug kinetics [23]. The gel form of the structures to be used in intravitreal applications has the advantages of being compatible with the vitreous structure and minimally affecting the visual field (Figure 2).

3.1.2. FTIR analysis

The peaks obtained from the FTIR spectrum of Alg, Alg Gel, Alg-Van Gel and Van are shown in Figure 3A. The bands at 1591 cm⁻¹ and 1415 cm⁻¹ are attributed to asymmetric and symmetric stretching vibrations of the carboxylate groups (COO⁻) found in Alg and Alg Gel. Saccharide ring structure peaked in 1022 and 1295 cm⁻¹ bands. C-O and CO-C vibrations of groups in guluronic and mannuronic units peak at 1022

cm⁻¹ and 1295 cm⁻¹. The peak in the 814 cm⁻¹ (C-O vibration) band is due to the α -configuration of the guluronic units [24-26]. The peaks seen at 3340, 2353, 1642 and 691 cm⁻¹ in Van's FTIR spectrum are due to the OH group of H₂O, alkinene, C=O group of amides and amines [27, 28]. These characteristic peaks were also seen in the FTIR spectrum of Alg-Van Gel.

3.1.3. Rheological properties

The viscosity of Alg and Van-Alg Gels was measured using a rheometer equipped with a parallel plate (Malvern Kinexus, Japan). The measurements were conducted at temperatures of 4 and 37°C with a gap of 5mm between the plates and a shear rate ranging from 0.01 to 1000 s⁻¹ (Figure 3B-3C). Figure 3 shows that increasing the temperature resulted in a decrease in viscosity for both gels. However, the viscosity of Van-Alg gels decreased more compared to Alg gels 37°C. This suggests that Van penetrated the alginate polymer chains, and no molecular interaction occurred between the Van and the polymer chains. The lack of interaction between Van and

the polymer chains affects the drug release profile and explains the initial rapid release of Van.

3.2. Vancomycin loading and release

In the treatment of endophthalmitis, administration of antibiotics with a carrier to reduce the frequency of repetitive injections may increase treatment efficacy. Therefore, the determination of the time-dependent release of vancomycin loaded into alginate hydrogels is necessary to determine the application dose and re-injection time. The following formulation was used to determine entrapment efficiency and loading efficiency. EE was determined that an average of $30 \pm 8\%$ of the initially added drug was loaded into the gels. The Van loaded to the unit weight of the hydrogels is an average of $50 \pm 3,5\%$ (LE). Van release showed a burst effect at the beginning and an average of 70% of the Van was released in the first 24 hours. After 48 hours, the release slowed and remained at a constant concentration (Figure 4A). Van release continued for an average of 2 weeks (average of $80 \pm 2,6\%$).

Entrapment Efficiency = $\frac{\text{Total Drug conc.} - \text{Supernatant Drug conc.}}{\text{Total Drug conc.}} \times 100$

Loading Efficiency (%LE) = $\frac{\text{Amount of Van in Gel}}{\text{Amount of Gel}} \times 100$.

There is no standard number of injections for an infected eye in clinical practice. Vancomycin and Ceftazidime combination is used in the treatment of endophthalmitis. Imamura et al. studied the pharmacokinetics of intravitreal vancomycin and ceftazidime in Macaque eyes and determined that the half-life of vancomycin in the aqueous humor of normal, vitrectomized, and silicone oil-filled eyes was 29.4, 21.1, and 6.8 hours, respectively [6]. The half-life of vancomycin is 30 hours in average healthy aqueous humor. This period becomes shorter in treated eyes. The patient's need for re-injection is determined by clinical examination and the injection is repeated if the infection remains untreated. However, repeat injections have disadvantages. In long-term release forms, treating the infection with the effect of the first burst effect and continuing the

release for at least 1 week ensures treatment effectiveness and thus aims to reduce the number of injections.

3.3. Cytotoxicity

The cytotoxicity of different concentrations of Alg, Van-Alg Gels and free Van on HRMEC cells was determined by MTT assay (Figure 4 B). HRMEC cell viability decreases due to increased concentration of gel and free Van. It has been determined that the toxicity of the empty and Van-Alg Gels is on average over 80% at 200 $\mu\text{g/ml}$ and lower concentrations. Van has higher toxicity on cells. The viability of cells exposed to 100 $\mu\text{g/ml}$ Van and 200 $\mu\text{g/ml}$ Alg-Van Gels were $74.93 \pm 4.7\%$ and $82.39 \pm 4.37\%$, respectively ($P < 0.05$).

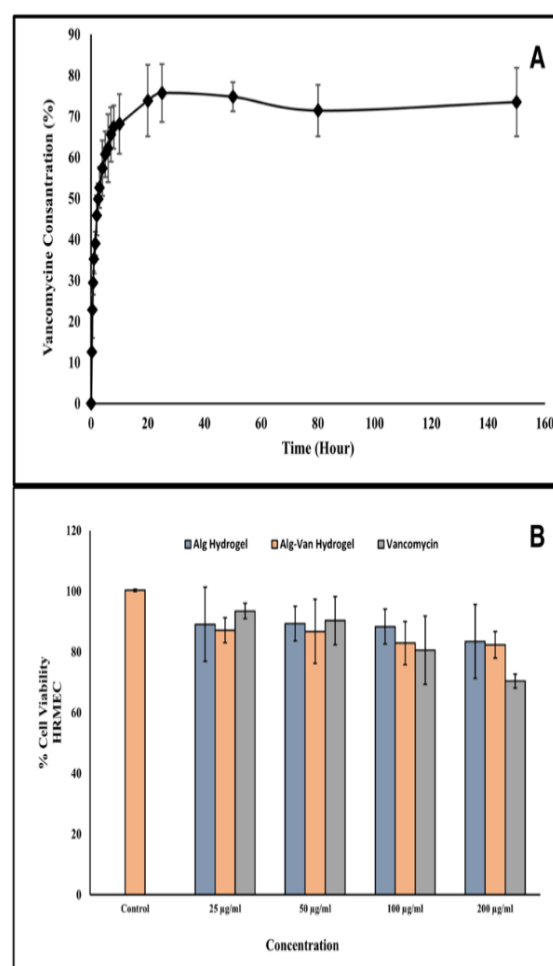


Figure 4. Cytotoxicity of different concentrations of alginate, Van-Alg hydrogel and free Van on HRMEC cells (A). *Van was used at the concentration loaded on gels (50%). Cumulative Van release from Alg Hydrogel (B)

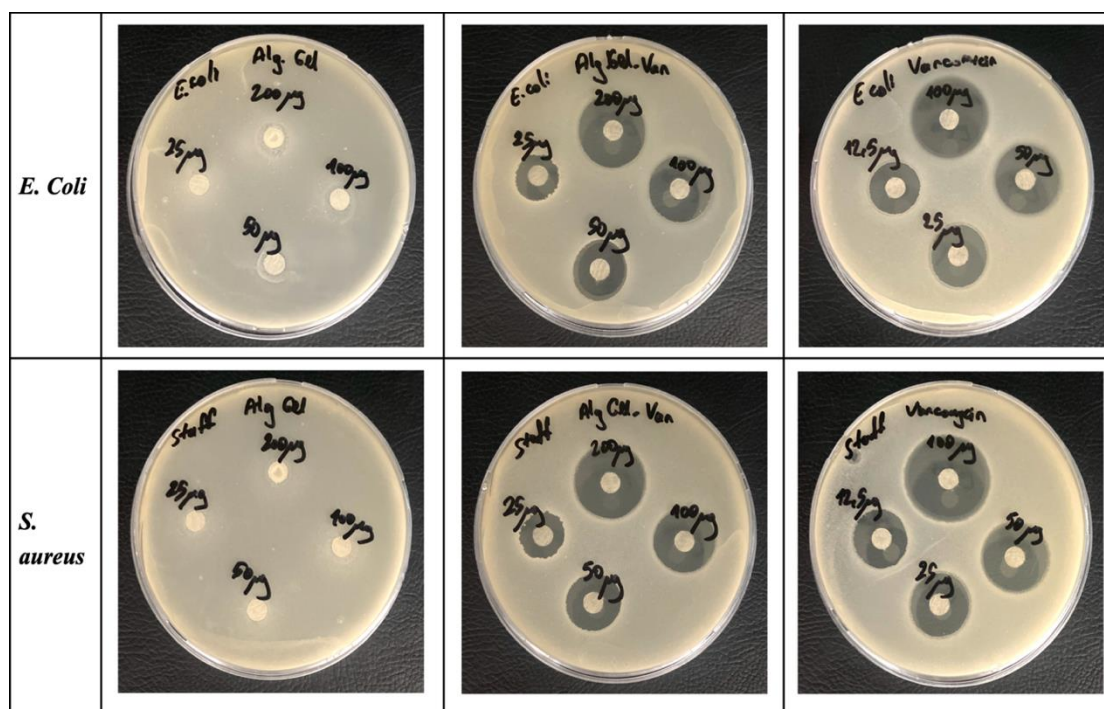


Figure 5. Antibacterial effect of different concentrations of Alg, Van-Alg Gels and Van on *E. coli* (gram-negative) and *S. aureus* (gram-positive) strains.

Van causes a decrease in cell viability more than the hydrogel-loaded form. Similarly, in the study conducted in 2019, van's liposome van. In a study conducted in 2019, it was also stated that vancomycin is more toxic than liposome-loaded vancomycin [29]. Cell viability incubated with 25 µg/ml Alg-Van Gels was 87.15 ± 4.14 , while it was 82.39 ± 4.37 at 200 µg/ml ($P > 0.05$). In the study of Miyake et al in 2019, the toxic and inflammatory effects of moxifloxacin, cefuroxime and vancomycin on human retinal vascular cells (RVEC) were determined. In the study, in which both in vitro and in vivo evaluations were made, retinal toxicity caused by intravitreal injection was evaluated. It has been determined that intravitreal injections of cefuroxime and vancomycin in mice cause retinal and vascular toxicity extending to the inner nuclear layers [30].

3.4. Antibacterial efficiency

The antibacterial effect of Van, empty and Van-Alg Gels was determined by disk diffusion method. Vancomycin is an antibiotic that is widely used in the treatment of endophthalmitis,

especially against gram (+) bacteria. Therefore, determination of its antibacterial activity is important in terms of administration and dosage determination. Vancomycin loaded on alginate hydrogels acts by binding to the D-Alanyl-D-alanine terminal in the cell wall of bacteria and inhibiting cell wall synthesis. The glycopeptide antibiotic also disrupts RNA synthesis and bacterial cell wall permeability [31].

Due to this principle, its effectiveness on gram-positive bacteria is higher [32]. It is used in the clinic especially for the treatment of endophthalmitis caused by gram-positive bacteria such as *S. aureus* [33]. Disk diffusion method was used to determine its antibacterial activity. Zone diameters formed by Van and hydrogels at different concentrations against 2 different bacterial species were determined (Table 1 and Figure 5). Alg hydrogels did not form zones in either bacterial species. Van was applied to the gels at the concentration at which it was loaded. Zone diameter formed by Van is higher than Alg-Van Gels ($p > 0.05$). In *S. aureus* culture, 200 µg Alg-Van hydrogel and Van has a zone diameter of 2.4 ± 0.2 cm and 2.7 ± 0.3 cm. Vancomycin is more active against gram (+) bacteria. However, this is more evident at higher concentrations.

Table 1. Antibacterial effect of different concentrations of Alg, Van-Alg Gels and Van on *E. coli* (gram-negative) and *S. aureus* (gram-positive) strains.

		<i>E. Coli</i>	<i>S. aureus</i>
Vancomycin	12,5 µg	1.6±0.3cm	1.6±0.2 cm
	25 µg	1.8±0.2cm	1.9±0.1 cm
	50 µg	2.0±0.3cm	2.2±0.2 cm
	100 µg	2.5±0.2 cm	2.7±0.3 cm
Van-Alg Gels	25 µg	1.1±0.2 cm	1.2±0.4 cm
	50 µg	1.4±0.2 cm	1.8±0.1 cm
	100 µg	1.8±0.1 cm	2.1±0.2 cm
	200 µg	1.9±0.2 cm	2.4±0.2 cm

4. Conclusion

Endophthalmitis is an infectious disease that develops when the intraocular cavity becomes infected as a result of surgery, trauma or a systemic disorder and can cause blindness. Although the incidence decreases with preventive measures, it can lead to serious and irreversible indications in the eye. The biggest problems of the combined antibiotic treatments applied are that they require frequent injections and retinal toxicity. Infection can occur weeks after the operation. Therefore, controlled release forms that allow antibiotics to remain in the vitreous for a long time are being investigated. Loading the vancomycin into the hydrogel both prolonged the release time and reduced the toxicity. In addition, its gel form is similar to the vitreous structure. Hydrogel-based controlled release systems show promise as carriers for intravitreal drug administration. The controlled release of 2 antibiotics by loading the hydrogels will increase the effectiveness of the treatment.

Article Information Form

Funding

This study was financially supported by Ankara Yıldırım Beyazıt University with the project number THD-2023-2475.

The Declaration of Conflict of Interest/ Common Interest

Financial interests: Author Ebru ERDAL declare that they have no financial interests.

The Declaration of Ethics Committee Approval

This study does not require ethics committee permission or any special permission.

The Declaration of Research and Publication Ethics

During the writing process of our study, the information of which is given above, international scientific, ethical and citation rules have been followed, no falsification has been made on the data collected, and Sakarya University Journal of Science and its editorial board have no responsibility for any ethical violations that may be encountered. I undertake that I have full responsibility and that this study has not been evaluated in any academic environment other than Sakarya University Journal of Science.

Copyright Statement

Authors own the copyright of their work published in the journal and their work is published under the CC BY-NC 4.0 license.



References

- [1] M. L. Durand, "Endophthalmitis," *Clinical Microbiology and Infection*, vol. 19, no. 3, pp. 227-234, 2013.
- [2] S.-J. Sheu, "Endophthalmitis," *Korean Journal of Ophthalmology*, vol. 31, no. 4, pp. 283-289, 2017.
- [3] M. Kernt, A. Kampik, "Endophthalmitis: Pathogenesis, clinical presentation, management, and perspectives," (in English), *Clinical Ophthalmology*, vol. 4, pp. 121-135, 2010.
- [4] C. Fabiani, M. Agarwal, M. Dogra, G. M. Tosi, J. L. Davis, "Exogenous Endophthalmitis," *Ocular immunology and inflammation*, pp. 1-10, 2022.
- [5] K. Vaziri, S. G. Schwartz, K. Kishor, H. W. Flynn, "Endophthalmitis: state of the art," (in English), *Clinical Ophthalmology*, vol. 9, pp. 95-108, 2015.
- [6] T. Imamura, M. Kakinoki, D. Hira, T. Kitagawa, S. Ueshima, M. Kakumoto, T. Terada, I. Kawamoto, M. Murase, M. Ohji,

- "Pharmacokinetics of Intravitreal Vancomycin and Ceftazidime in Silicone Oil-Filled Macaque Eyes," (in English), *Translational Vision Science and Technology*, vol. 10, no. 3, Mar 2021.
- [7] D. B. Roth, H. W. Flynn, "Antibiotic selection in the treatment of endophthalmitis: The significance of drug combinations and synergy," (in English), *Survey of Ophthalmology*, vol. 41, no. 5, pp. 395-401, Mar-Apr 1997.
- [8] A. Fahr, X. Liu, "Drug delivery strategies for poorly water-soluble drugs," (in English), *Expert Opinion on Drug Delivery*, vol. 4, no. 4, pp. 403-416, Jul 2007.
- [9] P. van Hoogevest, X. L. Liu, A. Fahr, "Drug delivery strategies for poorly water-soluble drugs: the industrial perspective," (in English), *Expert Opinion on Drug Delivery*, vol. 8, no. 11, pp. 1481-1500, Nov 2011.
- [10] C. L. Schepens, A. Neetens, *The vitreous and vitreoretinal interface*. Springer Science & Business Media, 2012.
- [11] J. Kopeček, "Hydrogel biomaterials: a smart future?" *Biomaterials*, vol. 28, no. 34, pp. 5185-5192, 2007.
- [12] E. M. Ahmed, "Hydrogel: Preparation, characterization, and applications: A review," (in English), *Journal of Advanced Research*, vol. 6, no. 2, pp. 105-121, Mar 2015.
- [13] K. Deligkaris, T. S. Tadele, W. Olthuis, A. van den Berg, "Hydrogel-based devices for biomedical applications," (in English), *Sensor Actuat B-Chemical*, vol. 147, no. 2, pp. 765-774, Jun 3 2010.
- [14] A. Gürsoy, "Kontrollü salım sistemleri," *Kontrollü Salım Sistemleri Derneği, İstanbul*, pp. 3-6, 2002.
- [15] D. A. Gyles, L. D. Castro, J. O. C. Silva, R. M. Ribeiro-Costa, "A review of the designs and prominent biomedical advances of natural and synthetic hydrogel formulations," (in English), *European Polymer Journal*, vol. 88, pp. 373-392, Mar 2017.
- [16] S. Garg, A. Garg, R. Vishwavidyalaya, "Hydrogel: Classification, properties, preparation and technical features," *Asian Journal of Biomaterial Research*, vol. 2, no. 6, pp. 163-170, 2016.
- [17] M. Zhang, X. Zhao, "Alginate hydrogel dressings for advanced wound management," (in English), *International Journal of Biological Macromolecules*, vol. 162, pp. 1414-1428, Nov 1 2020.
- [18] A. D. Augst, H. J. Kong, D. J. Mooney, "Alginate hydrogels as biomaterials," *Macromolecular bioscience*, vol. 6, no. 8, pp. 623-633, 2006.
- [19] Y. A. Khan, K. Ozaltin, A. Bernal-Ballen, A. Di Martino, "Chitosan-alginate hydrogels for simultaneous and sustained releases of ciprofloxacin, amoxicillin and vancomycin for combination therapy," (in English), *Journal of Drug Delivery Science and Technology*, vol. 61, Feb 2021.
- [20] R. Supino, "MTT assays," *In vitro toxicity testing protocols*, pp. 137-149, 1995.
- [21] C. J. Maxwell, A. M. Soltisz, W. W. Rich, A. Choi, M. A. Reilly, K. E. Swindle-Reilly, "Tunable alginate hydrogels as injectable drug delivery vehicles for optic neuropathy," (in English), *Journal of Biomedical Materials Research Part A*, vol. 110, no. 10, pp. 1621-1635, Oct 2022.
- [22] B. Sadeghi, M. Jamali, S. Kia, N. A. AMINI, S. Ghafari, "Synthesis and characterization of silver nanoparticles for antibacterial activity," *International Journal of Nano Dimension*, Vol. 1 no. 2, pp. 119-124, 2010.
- [23] L. Y. Xue, T. Deng, R. Guo, L. Peng, J. Guo, F. Tang, J. Lin, S. Jiang, H. Lu, X. Liu, L. A. Deng, "A Composite Hydrogel

- Containing Mesoporous Silica Nanoparticles Loaded with Artemisia argyi Extract for Improving Chronic Wound Healing" (in English), *Frontiers in Bioengineering and Biotechnology*, vol. 10, Mar 25 2022.
- [24] S. Najafi-Soulari, H. Shekarchizadeh, M. Kadivar, "Encapsulation optimization of lemon balm antioxidants in calcium alginate hydrogels," *Journal of Biomaterials science, Polymer edition*, vol. 27, no. 16, pp. 1631-1644, 2016.
- [25] S. Jabeen, M. Maswal, O. A. Chat, G. M. Rather, A. A. Dar, "Rheological behavior and Ibuprofen delivery applications of pH responsive composite alginate hydrogels," *Colloids and Surfaces B: Biointerfaces*, vol. 139, pp. 211-218, 2016.
- [26] G. Lawrie, I. Keen, B. Drew, A. Chandler-Temple, L. Rintoul, P. Fredericks, L. Grøndahl, "Interactions between alginate and chitosan biopolymers characterized using FTIR and XPS," *Biomacromolecules*, vol. 8, no. 8, pp. 2533-2541, 2007.
- [27] Q. Yao, P. Nooeaid, J. A. Roether, Y. Dong, Q. Zhang, A. R. Boccaccini, "Bioglass®-based scaffolds incorporating polycaprolactone and chitosan coatings for controlled vancomycin delivery," *Ceramics International*, vol. 39, no. 7, pp. 7517-7522, 2013.
- [28] A. Kaur, D. Goyal, R. Kumar, "Surfactant mediated interaction of vancomycin with silver nanoparticles," *Applied Surface Science*, vol. 449, pp. 23-30, 2018.
- [29] F. Hajiahmadi, M. Y. Alikhani, H. Shariatifar, M. R. Arabestani, D. Ahmadvand, "The bactericidal effect of liposomal vancomycin as a topical combating system against Methicillin-resistant Staphylococcus aureus skin wound infection in mice," *Medical Journal of the Islamic Republic of Iran*, vol. 33, p. 153, 2019.
- [30] H. Miyake, D. Miyazaki, Y. Shimizu, S.I. Sasaki, T. Baba, Y. Inoue, K. Matsuura, "Toxicities of and inflammatory responses to moxifloxacin, cefuroxime, and vancomycin on retinal vascular cells" (in English), *Scientific Reports*, vol. 9, Jul 5 2019.
- [31] R. G. Finch, D. Greenwood, R. J. Whitley, S. R. Norrby, *Antibiotic and chemotherapy e-book*. Elsevier Health Sciences, 2010.
- [32] J. Pauwels I. Spriet, X. Fu, S. Von Winkelmann, L. Willems, J. Hoogmartens, A. V. Schepdael, "Chemical Stability and Compatibility Study of Vancomycin for Administration by Continuous Infusion in Intensive Care Units," *Journal of liquid chromatography & related technologies*, vol. 34, no. 17, pp. 1965-1975, 2011.
- [33] M. Schafer, T. R. Schneider, G. M. Sheldrick, "Crystal structure of vancomycin," (in English), *Structure*, vol. 4, no. 12, pp. 1509-1515, Dec 15 1996.

Beta Vulgaris L. Extract: pH Effect on Total Phenolic Content and Antioxidant Properties

Rama Alkayarı¹ , Zuhâl Şahin^{2*} , Fatih Sönmez² , Mustafa Küçükislamoğlu³ 

¹Sakarya University, Institute of Natural Sciences, Department of Chemistry, Sakarya, Türkiye, rama.alkayari@ogr.sakarya.edu.tr

²Sakarya University of Applied Sciences, Pamukova Vocational School, Sakarya, Türkiye, fsonmez@subu.edu.tr

³Sakarya University, Faculty of Sciences, Department of Chemistry, Sakarya, Türkiye, mustafak@sakarya.edu.tr

*Corresponding authors

ARTICLE INFO

ABSTRACT

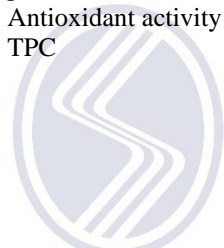
Keywords:

Beta vulgaris L

pH effect

Antioxidant activity

TPC



Article History:

Received: 25.10.2023

Accepted: 07.03.2024

Online Available: 14.06.2024

Red beet (*Beta vulgaris* L.) is a rich source of phenolic content including colour pigments and have also high antioxidant capacities. The amounts of their phenolic substances and antioxidant activities change depending on the extraction conditions (pH, time, solvent, etc.). In this work, the coloured water extracts were obtained from red beet at different pH values (pH 4-10) for both an hour and 24 hours. The extracts were evaluated regarding antioxidant activities and total phenolic contents (TPC). The results showed that the total phenolic content of red beet extract in all extraction conditions ranged from 0.55±0.02 to 2.30±0.19 mg GAE/g FW. The highest total phenolic contents (2.30±0.19 mg GAE/g FW) were obtained from red beet at 24 h and pH=4. On the other hand, while the IC₅₀ values for DPPH activity of red beet extracts at all pH values and times are between 0.84±0.04 and 5.44±0.75 mg/mL, the IC₅₀ values for ABTS activity are between 1.46±0.42 and 3.65± 0.28 mg/mL. The extract obtained from red beet at 24 h and pH=4 exhibited the strongest DPPH activity with the IC₅₀ values of 0.84±0.04 mg/mL, it showed the best ABTS activity with the IC₅₀ values of 1.46±0.42 mg/mL at 24 h and pH=4.

1. Introduction

Naturally occurring colour pigments are important determinants of quality attributes in fresh fruits and vegetables [1]. Colourful fruits and vegetables have become very popular today due to the vitamins, minerals and bioactive substances they contain, and they are recommended to be consumed daily [2]. Consumption of fruits and vegetables, as well as nutrition, should be stored in a value that should be taken into account due to the evaluation of their importance in human health [3].

Many types of vegetables are grown in Türkiye, and red beet (*Beta vulgaris* L.) has an important place among these vegetables [4]. Red beet is grown and widely consumed all over the world [5]. All types of beet leaves can be eaten raw or cooked. It is rich in nutrients such as vitamins A,

K, C, protein, fibre, calcium, manganese, magnesium, potassium, copper, iron, zinc, phosphorus [6]. Red beet helps to lower high blood pressure, cardiovascular diseases, raises haemoglobin. In addition, it reduces obesity, lowers blood sugar, improves skin, hair, eye, bone and muscle health, and is also a powerful antioxidant [7]. Red beet contains many bioactive compounds (flavonoids, carotenoids, betalain, ascorbic acid, polyphenols) that are effective on health [8].

In nature, betalains are commonly found in roots, fruits, and flowers [9]. They are used to add nutritional value to food, change colour or give colour to food. The most common source of betalain is beetroot [10]. Betalains are water-soluble and nitrogen-containing-coloured pigments known as betalaminic acid derivatives [11].

The molecular structures of the compounds that give colour to the red beet is given in Figure 1.

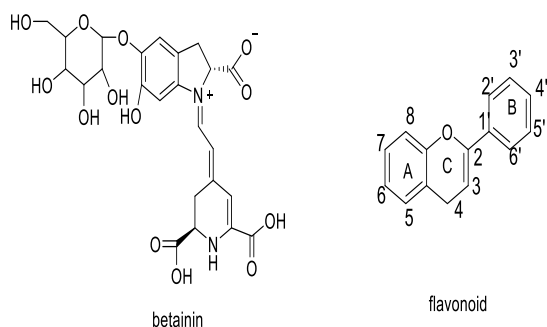


Figure 1. Molecular structure of some colour pigments

In this study, total phenolic compounds were extracted from red beet at different pH/different time intervals. The extraction time and pH effects on total phenolic content and ABTS and DPPH activities as antioxidant properties were investigated.

2. Materials and Methods

2.1. Materials

All used chemicals were purchased from Sigma Aldrich and Merck. Red beet, grown in Türkiye, were sourced from the local market.

2.2. Extraction

Red beet sample was dissected after cleaning. 10 g sample was extracted with distilled water. The extraction conditions of the samples were adjusted to different pH values (pH 4-10). pH treatment was carried out with citric acid and sodium carbonate (Na_2CO_3). The extracts were stored in jars in dark until their analysis.

2.3. Total Phenolic Content (TPC)

Folin-Ciocalteu reagent was used when determining total phenolic content [12]. Stock extracts were mixed with diluted Folin-Ciocalteu reagent. This solution was incubated at 25°C for 3 min. and mixed with 1 mL of Na_2CO_3 . The absorbance value was measured at 765 nm after 60 min. of incubation in the dark. Drawing a standard curve with gallic acid. The total amount of phenolic compounds was calculated and

expressed as mg GAE (Gallic Acid Equivalent) /g FW (fresh weight).

2.4. DPPH Radical Scavenging Activity

DPPH activity of the extract was determined using Sönmez et al. as a reference [13]. Samples at different concentrations were prepared from extracts with different pH values. 3 mL of DPPH solution was mixed with these different concentrations of the extracts. This thoroughly mixed solution was incubated for 30 minutes. After the absorbance of these solutions was measured at 517 nm. IC_{50} values were determined by calculating DPPH activity.

$$\% \text{ DPPH inhibition} = \frac{[(\text{Abs}_c - \text{Abs}_s) / \text{Abs}_c] * 100}{1} \quad (1)$$

2.5. ABTS Radical scavenging activity

ABTS scavenging activities of the extract was measured according to the method described by Sonmez et al. [14]. ABTS radical solution was generated by mixing 19.2 mg of ABTS and $\text{K}_2\text{S}_2\text{O}_8$. This solution was kept at 25°C and in the dark for one day. The absorbance of this prepared solution was adjusted to be 0.70 ± 0.01 at 734 nm. It was mixed with ABTS prepared with samples of different concentrations. The absorbance of the samples was measured at baseline and after 6 minutes. The measurement was made at a wavelength of 734 nm. The absorbance-concentration graph was drawn. IC_{50} value was calculated as mg/mL.

3. Results and Discussion

The graphical representations of total phenolic contents, DPPH and ABTS activity results are presented in Figures 2-4.

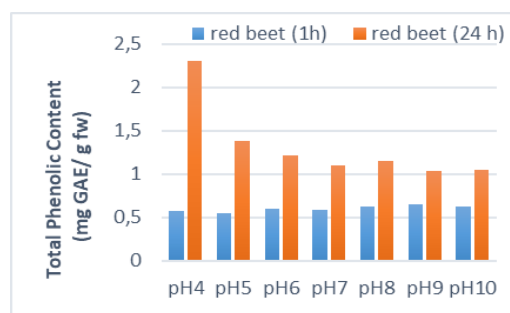


Figure 2. Graphical representation of TPC results for red beet.

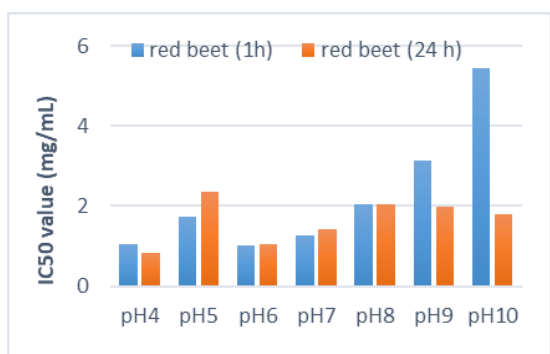


Figure 3. Graphical representation of IC₅₀ values of red beet extracts for DPPH activity.

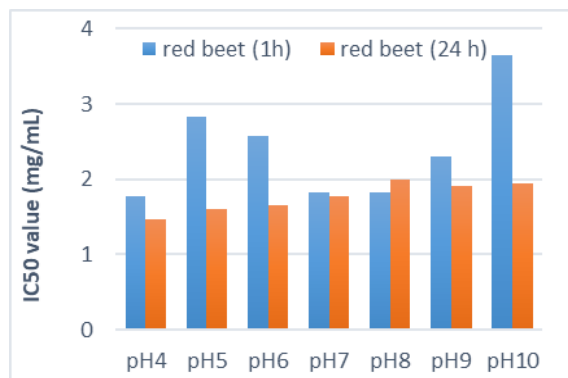


Figure 4. Graphical representation of IC₅₀ values of red beet extracts for ABTS activity.

Total phenolic content and antioxidant activity values of red beet is presented in Table 1-2.

The results showed that total phenolic contents (TPC) of red beet extract is between 0.55±0.02 and 0.65±0.06 mg GAE/g FW at pH=4-10 and 1h. The total phenolic content of red beet extract is between 1.03±0.09 and 2.30±0.19 mg GAE/g FW at pH=4-10 and 24h. Red beet extract had the high total phenolic content at 24h and pH=4.

Red beet extracts showed DPPH activity with an IC₅₀ value of 1.01± 0.28 - 5.44± 0.75 mg/mL at 1h and with an IC₅₀ value of 0.84± 0.28 - 2.37± 0.39 mg/mL at 24h. Among them, red beet extract exhibited the strongest DPPH activity at 24h and pH=4.

Table 1. TPC and DPPH, ABTS activity (IC₅₀ values) of red beet extracts obtained for 1h.

pH	Sample	TPC (mg GAE/ g FW)	DPPH	ABTS
			(IC ₅₀ , mg/mL)	(IC ₅₀ , mg/mL)
			Extraction time	
			1h	1h
4	red beet	0.57± 0.02	1.06± 0.03	1.78± 0.23
5	red beet	0.55± 0.02	1.73± 0.49	2.83± 0.53
6	red beet	0.60± 0.06	1.01± 0.28	2.57± 0.67
7	red beet	0.59± 0.07	1.25± 0.43	1.82± 0.18
8	red beet	0.63± 0.01	2.05± 0.47	1.82± 0.45
9	red beet	0.65± 0.06	3.13± 1.06	2.30± 0.50
10	red beet	0.62± 0.1	5.44± 0.75	3.65± 0.28

Results are expressed as means ± SD (standard deviation) (n=3).

Table 2. TPC and DPPH, ABTS activity (IC₅₀ values) of red beet extracts obtained for 24h.

pH	Sample	TPC (mg GAE/ g FW)	DPPH	ABTS
			(IC ₅₀ , mg/mL)	(IC ₅₀ , mg/mL)
			Extraction time	
			24 h	24 h
4	red beet	2.30± 0.19	0.84± 0.04	1.46± 0.42
5	red beet	1.38± 0.16	2.37± 0.39	1.61± 0.12
6	red beet	1.21± 0.12	1.04± 0.05	1.66± 0.26
7	red beet	1.10± 0.07	1.41± 0.01	1.78± 0.18
8	red beet	1.15± 0.07	2.04± 0.97	1.99± 0.04
9	red beet	1.03± 0.04	1.97± 0.24	1.91± 0.07
10	red beet	1.05± 0.06	1.78± 0.01	1.95± 0.38

Results are expressed as means ± SD (standard deviation) (n=3).

Red beet extracts showed ABTS activity with an IC₅₀ value of 1.78± 0.23 - 3.65± 0.28 mg/mL at 1h, and with an IC₅₀ value of 1.46± 0.42 - 1.99± 0.04 mg/mL at 24h. Among them, red beet extract exhibited the highest ABTS activity at 24h and pH=4.

4. Conclusion

In conclusion, red beet extracts, obtained different pH values and extraction time, were compared in terms of total phenolic content and antioxidant properties. The results show that the phenolic content of red beet is between 0.55 ± 0.02 and 2.30 ± 0.19 mg GAE/g FW. Moreover, the red beet extracts showed strong antioxidant activity. It was determined that the extraction time is 24h and pH value is 4 for the highest TPC of red beet extract. On the other hand, it was observed that extraction time is 24h, pH values are 4 as the best conditions for DPPH and ABTS activity. According to all these results, it is considered that red beet extracts may be preferred to use for natural colorant additive for various nutrition.

Article Information Form

Funding

This work was supported by Research Fund of the Sakarya University of Applied Sciences (Project Number: 107-2022)

Authors' Contribution

The authors who have made substantial contributions to the work reported in the manuscript are:

R.A. and Z.S.: Term, Conception and design of study, Visualization, Writing - Original Draft, Data Curation, Investigation, Formal analysis, Validation. F.S. and M.K.: Supervision, Project administration, Conceptualization, Writing-Original Draft, Data Curation, Investigation, Formal analysis, Validation, Methodology.

The Declaration of Conflict of Interest/ Common Interest

No conflict of interest.

The Declaration of Ethics Committee Approval

This study does not require ethics committee permission or any special permission.

The Declaration of Research and Publication Ethics

The authors of the paper declare that they comply with the scientific, ethical and quotation rules of SAUJS in all processes of the paper and that they

do not make any falsification on the data collected. In addition, they declare that Sakarya University Journal of Science and its editorial board have no responsibility for any ethical violations that may be encountered, and that this study has not been evaluated in any academic publication environment other than Sakarya University Journal of Science.

Copyright Statement

Authors own the copyright of their work published in the journal and their work is published under the CC BY-NC 4.0 license.


References

- [1] F.C. Stintzing, R. Carle, "Functional properties of anthocyanins and betalains in plants, food, and in human nutrition," Trends in food science & technology, vol. 15, no. 1, pp. 19–38, 2004.
- [2] I. Amao, "Health benefits of fruits and vegetables: Review from Sub-Saharan Africa" Vegetables: importance of quality vegetables to human health, vol. 22, pp. 33-53, 2018.
- [3] T.G. Ulger, A.N. Songur, O. Cırak, "Role of Vegetables in Human Nutrition and Disease Prevention," Intechopen, pp. 7-32, 2018.
- [4] R. Karl, M.A. Koch, "A world-wide perspective on crucifer speciation and evolution: phylogeny, biogeography and trait evolution in tribe Arabideae," Annals of Botany, vol. 112, no. 6, pp. 983–1001, 2013.
- [5] I. Sadowska-Bartosz, G. Bartosz, "Biological properties and applications of betalains," Molecules, vol. 26, no. 9, pp. 2520, 2021.
- [6] N. Chhikara, K. Kushwaha, P. Sharma, Y. Gat, A. Panghal, "Bioactive compounds of beetroot and utilization in food processing industry: A critical review," Food chemistry, vol. 272, pp. 192–200, 2019.

- [7] L. Sharma, M. Sardana, “Organoleptic properties of a standardised food product (cookies) developed from beet root extract and bengal gram flour,” *International Journal of Food, Nutrition and Dietetics*, vol. 5, no. 2, pp. 51-57, 2017.
- [8] T. Clifford, G. Howatson, D.J. West, E.J. Stevenson, “The potential benefits of red beetroot supplementation in health and disease,” *Nutrients*, vol. 7, no. 4, pp. 2801-2822, 2015.
- [9] D. Strack, T. Vogt, W. Schliemann, “Recent advances in betalain research” *Phytochem*, vol. 62, no. 3, pp. 247-269, 2003.
- [10] K. Ozcan, S.E. Bilek, “Production and stability of food colorant from red beetroot,” *Akademik Gıda*, vol. 16, no. 4, pp. 439-449, 2018.
- [11] V.H. Ozyurt, H. Saralı, S. Otles, “Usage of betalain extracts in food,” *Pamukkale University Journal of Engineering Sciences*, vol. 25, no. 7, pp. 864-870, 2019.
- [12] F. Sonmez, Z. Sahin, “Comparative study of total phenolic content, antioxidant activities, and polyphenol oxidase enzyme inhibition of quince leaf, peel, and seed extracts” *Erwerbs-Obstbau*, vol. 65, no. 4, pp. 745-750, 2023.
- [13] F. Sonmez, Z. Gunesli, B.Z. Kurt, I. Gazioglu, D. Avci & M. Kucukislamoglu “Synthesis, antioxidant activity and SAR study of novel spiro-isatin-based Schiff bases” *Molecular Diversity*, vol. 23, pp. 829–844, 2019.
- [14] F. Sonmez, Z. Gunesli, T. Demir, K. Cıkrıkçı, A. Ergun, N. Gencer, O. Arslan, “The effect of total anthocyanins extracted from sweet cherry cultivars on carbonic anhydrases and antioxidant activity,” *Erwerbs-Obstbau*, vol. 64, pp. 145-153, 2022.



Preparation of Hybrid Films Containing Chitosan, Starch, Ascorbic Acid, and Different Metal Ions for Release of Doxorubicin

Umran Duru Kamacı 

Yildiz Technical University, Faculty of Science and Letters, Department of Chemistry, İstanbul, Türkiye, umranduru@gmail.com

ARTICLE INFO

ABSTRACT

Keywords:

Drug release
Composite
Biofilm
Biopolymer

Article History:

Received: 25.11.2023

Accepted: 25.04.2024

Online Available: 14.06.2024

As known, composite films containing different metal ions provide improvement in the properties of drug release systems. In this study, it was aimed to prepare composite films containing different metal ions for DOX release, and the effect of metal ions on drug release, swelling, and thermal properties were investigated. The structural characterization of the composite films was carried out using FT-IR, SEM, and TG analysis techniques. SEM images showed that the metal-free film was composed of a homogeneous structure while the calcium composite films consisted of a non-homogenous surface. Also, thermal analysis results showed that the thermal stability increased with the addition of metal ions to the composite film matrix. The swelling and drug-release behavior of the composite films were also studied, and metal ions-containing films exhibited a higher swelling performance and drug-release behavior than the metal-free composite.

1. Introduction

Biopolymers, which are also known as natural polymers, such as chitosan, starch, alginate, etc. are highly demanded in biomedical applications due to their biodegradability, biocompatibility, and non-toxic characteristics [1, 2]. Among these polymers, starch has attracted considerable attention due to its low cost, easy availability, and suitability for use as food [3]. Starch is also preferred in the production of large-scale biopolymer films and is used in food packaging, agriculture, and pharmaceutical distribution systems [4, 5].

On the other hand, starch-based films have shown poor thermal stability, low mechanical strength, and decomposition temperature [6]. Cao et al. stated that mixing starch with chitosan overcomes these disadvantages and improves some properties of starch such as easy film forming and antibacterial properties [7].

Chitosan is a biopolymer composed of linear polycationic polysaccharide units with inelastic behavior, and it has an excellent film-forming property [8, 9]. Chitosan, which also contains abundant amine (-NH₂) and hydroxyl (-OH) groups as its characteristic structural feature, is used as a biosorbent in dyes and organic pollutants [10]. It is also used in drug release applications due to its physical, chemical, and biological properties [11]. In addition, chitosan can easily chelate with metal ions due to its polycationic structure [12]. Although chitosan films have been shown good mechanical properties, they have poor flexibility and stress resistance [13]. Therefore, these features need to be developed.

Adding metal ions into a biocompatible material not only facilitates cross-linking and provides durability to the material, but also provides many benefits for the body's biological functions. As known, metal ions play an active role in many biological metabolisms such as protein, bone, and nucleic acid structure, electron transfer,

charge balance, DNA signaling, redox, and acid-base catalysis. The use of metal ions in biomaterials positively affects cells in different aspects [14].

In the present paper, a series of ascorbic acid-based composite films were prepared by using chitosan, starch, L-ascorbic acid, and various cations such as Ag^+ , Ca^{2+} , or Mg^{2+} . Metal ions were used as chelating agents. The usability of the fabricated films as drug delivery applications was also investigated. The structural characterization was carried out by using FT-IR, SEM, and TG analysis techniques. The swelling and doxorubicin release behavior of the composite films were also investigated.

2. Materials and Method

2.1 Reagents

Medium molecular weight chitosan (CS), starch (from potato, S), L-ascorbic acid (AA), calcium chloride dihydrate ($\text{CaCl}_2 \cdot 2\text{H}_2\text{O}$), magnesium chloride hexahydrate ($\text{MgCl}_2 \cdot 6\text{H}_2\text{O}$), silver chloride (AgCl), acetic acid (CH_3COOH), and doxorubicin (DOX) were obtained as

commercially from Sigma Aldrich. All other chemicals were commercially supplied and they were used without any purification processes.

2.2. Preparation of the composite films

Composite films were fabricated by using chitosan, starch, ascorbic acid, and different metal cations (Ag, Ca, and Mg) as follows, and they were called the metal-free film, Ag, Ca, and Mg composite films according to containing cations (Table 1):

2.5 g of chitosan solution was prepared in distilled water containing 2.0% (v:v) acetic acid solution to prepare 2.5% (w:v) stock solution. Then, 2.0% starch (w:v), 1% L-ascorbic acid (w:v), and 5 mM of the cation (Ca, Mg, and Ag) solutions were prepared in distilled water and added into the chitosan solution as summarized in Table 1. Then, the solution was homogenized using a homogenizer for 3 minutes, and it was mixed for 4 hours at room temperature. The composite films were poured into the petri dish, and the solvent was completely evaporated under ambient conditions. Finally, the fabricated films were stored at $+4\text{ }^\circ\text{C}$ for further experiments [15, 16].

Table 1. Composition of the composite films

Composite film	CS (v:v)	S (v:v)	AA (v:v)	Ca (v:v)	Mg (v:v)	Ag (v:v)
Metal-free	80	5	10	-	-	-
Ca composite	80	5	10	5	-	-
Mg composite	80	5	10	-	5	-
Ag composite	80	5	10	-	-	5

2.3.Characterization

Fourier Transform-Infrared spectroscopy (FT-IR, Perkin-Elmer Spectrum Two FT-IR spectrometer) with an ATR unit was used to confirm functional groups in the starting materials and composite films. These measurements were carried out in the range from 500 to 4000 cm^{-1} under ambient conditions. The thermal degradation behavior of the composite films was also investigated using a Perkin-Elmer Diamond Thermogravimetric Analysis (TGA) with a heating rate of $10\text{ }^\circ\text{C min}^{-1}$ in the range from 20 to $700\text{ }^\circ\text{C}$ under a nitrogen atmosphere.

The surface morphology of the composite films was determined using a Zeiss EVO LS 10 Scanning Electron Microscopy (SEM) under the high electron voltage (10 kV).

2.4. Swelling behavior of the composite films

A certain amount (20-25 mg) of the fabricated composite films was weighed and immersed into the freshly prepared phosphate buffer solution (PBS, pH 7.4, 25 mL) to investigate the swelling performance at room temperature. The composite films were removed from the solution at predetermined times, and their weights were

recorded. The swelling percentage was calculated using the following equation (Eq.1) [17, 18]:

$$\% \text{Swelling} = \frac{m_2 - m_1}{m_1} \times 100 \quad (1)$$

where m_1 and m_2 are the weights of the dry and wet films, respectively.

2.5. Drug delivery behavior

Doxorubicin (DOX), which is one of the most effective chemotherapy drugs used in various cancer treatments such as breast, and prostate, etc., was used as a model drug for drug release experiments in the present paper [19, 20]. The drug release performance of the composite films was determined in 20 mL PBS (pH 7.4) as the following equation (Eq. 2) [21]:

$$\% \text{Released drug} = \frac{\text{Cumulative DOX weight}}{\text{Total weight of DOX}} \times 100 \quad (2)$$

About 10 mg of the composite film was added to the 20 mL 0.01 M PBS containing DOX and placed in a shaking incubator at 37 °C. At certain time intervals, 3 mL of DOX-containing PBS was removed from the solution medium, and the same amounts of the freshly prepared buffer solution were also added. The drug release amount was measured with the help of an UV-Vis spectrophotometer at 480 nm, and the released drug % was found.

3. Results and Discussion

3.1. Characterization of the composite films

FT-IR spectra of chitosan (CS), starch, L-ascorbic acid (AA), magnesium chloride hexahydrate (Mg), and Mg composite film were represented in Figure 1, and all FT-IR data were given in Table 2. In the FT-IR spectrum of CS, the characteristic peaks at 3279, 2864, 1646, 1414, 1372, and 1025 cm^{-1} were associated with the stretching vibrations of the hydroxyl (-OH), aliphatic -CH (Al-CH), -NH, -C-O, aromatic -CH (Ar-CH), and -C-O-C, respectively [22]. In the FT-IR spectrum of the starch, -OH, Al-CH, -C-O, and Ar-CH stretching, and -C-O-H bending vibrations were seen at 3280, 2920, 1418, 1329, and 991 cm^{-1} , respectively [23].

In the spectra of the Ca, and Mg, the stretching and bending vibration of H_2O were seen at 3322-3356 and 1608-1610 cm^{-1} , respectively [24]. According to the FT-IR spectrum of L-ascorbic acid, -OH, Al-CH, -C-O, enol hydroxide (-C=C-OH), and -C-O-C stretching vibrations were recorded at 3205, 2916, 1429, 1317, and 1023 cm^{-1} , respectively [25]. Also, the mentioned stretching vibrations were observed in the range from 3245 to 3267 cm^{-1} , 2885 to 2936 cm^{-1} , 1588 to 1639 cm^{-1} , 1386 to 1410 cm^{-1} , 1328 to 1305 cm^{-1} , and 1012 to 1018 cm^{-1} in the structure of composite films. These findings showed that the most of stretching vibrations of the composite films were shifted to the lower values compared to the chitosan and starch. This tendency was evidenced by the successful preparation of composite films [18]

Table 2. FT-IR data of the using materials and composite films

Materials	1	2	3	4	5	6
Chitosan	3279	2864	1646	1414	1372	1025
Starch	3280	2920	-	1418	1329	991
L-Ascorbic acid	3205	2916	-	1429	1317	1023
Metal-free	3228	2874	1638	1407	1306	1017
Ag composite	3245	2917	1589	1386	1328	1012
Ca composite	3250	2936	1588	1410	1305	1014
Mg composite	3267	2885	1639	1408	1305	1018

1: Hydroxy (-OH)
2: Aliphatic -CH (Al-CH)
3: -NH

4: -C-O
5: Enol hydroxy (-C=C-OH) or aromatic -CH (Ar-CH)
6: -C-O-C or -C-O-H

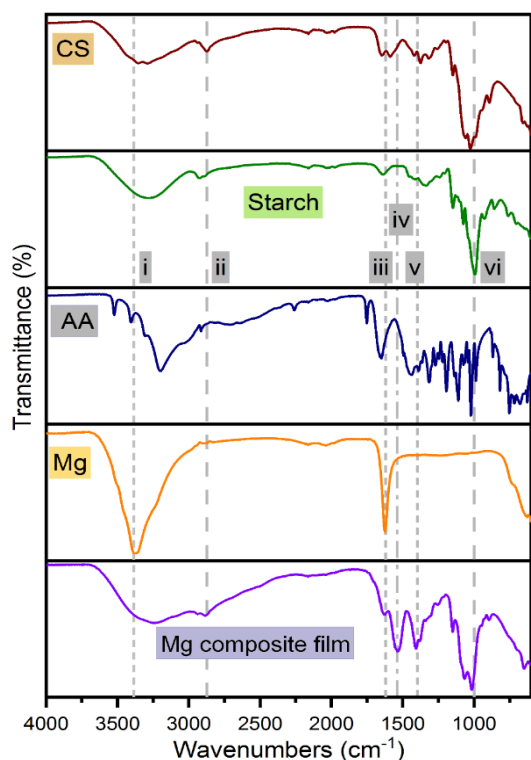


Figure 1. FT-IR spectra of chitosan (CS), starch, L-ascorbic acid (AA), Mg and Mg composite film

The surface of the fabricated metal-free composite and Ca composite film was investigated by using Scanning Electron Microscopy (SEM), and SEM images were shown in Figure 2. As can be seen in Figure 2, the metal-free film has a homogeneous and smooth surface whereas Ca composite film has been composed of a non-homogenous surface. Also, the surface roughness of the Ca composite film was increased after the addition of Ca^{2+} ions into the starch, chitosan, and L-ascorbic acid-containing composite matrix.

The thermal degradation behavior of the metal-free and composite films was clarified by using Thermogravimetric Analysis (TGA). Thermograms of the films were represented in Figure 3 and the results were summarized in Table 3. According to the degradation behavior of the composite films, they exhibited the two-step decomposition behavior.

The first degradation step, which takes place between room temperature and about 200 °C, is due to the evaporation of water, and acetic acid used in the fabrication of the composite films. The second degradation step, in which the main mass loss step was performed in the range from 200 to 350 °C, was due to the degradation of the

saccharide rings in the structure of the composite films, the degradation of acetylated units or the decomposition of the biopolymer chains [26].

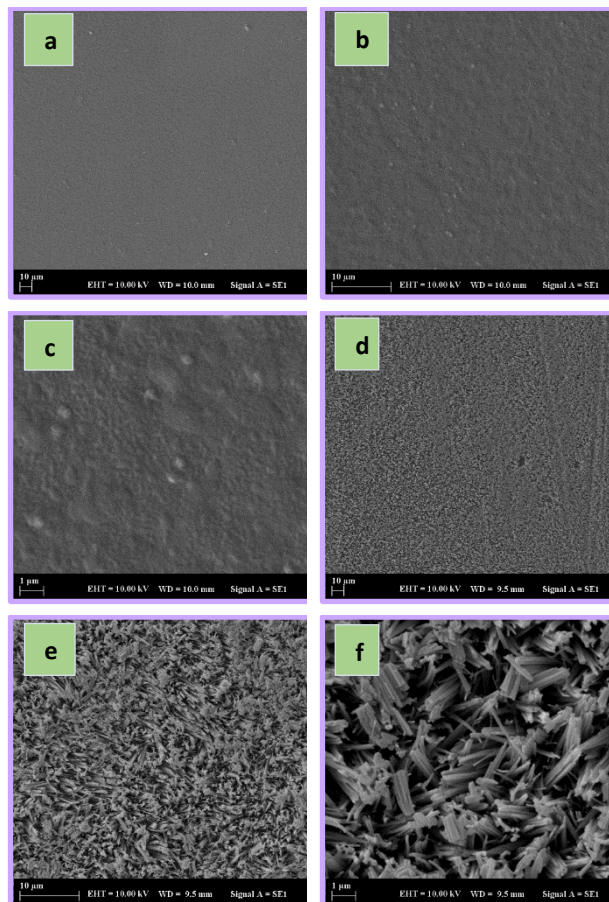


Figure 2. SEM image of metal-free film (a, b, c) and Ca composite film (d, e, f) at different magnitudes at 1, 5, and 20 kX

Also, T_{\max} , T_{20} , T_{50} , and char residual at 700 °C (char) of metal-free film, Ag, Ca, and Mg composite films were found in the range from 233 to 262 °C, 208 to 219 °C, 287 to 325 °C, and 30.77 to 35.99%, respectively. As can be seen in the char value of the films, the addition of cations into the composite film matrix, it was slightly increased.

Table 3. TG data of the composite films

Composite film	T_{\max} (°C)	T_{20} (°C)	T_{50} (°C)	%Char (at 700 °C)
Metal-free	262	208	307	30.77
Ag composite	235	215	325	35.99
Ca composite	233	219	307	35.96
Mg composite	237	208	287	33.63

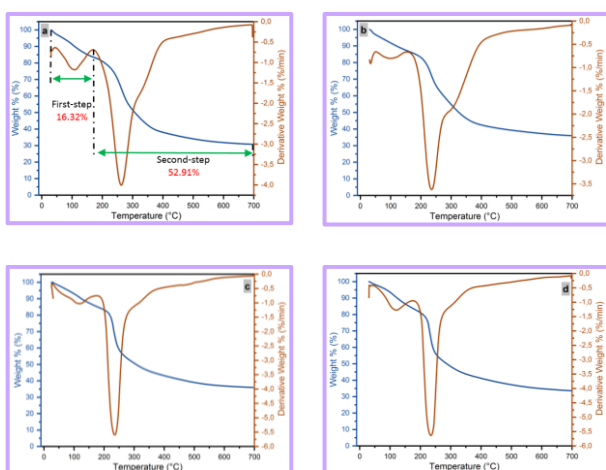


Figure 3. TG curves of metal-free film (a), Ag (b), Ca (c), and Mg (d) composite films

3.2. Swelling performance

The water uptake performance of the fabricated composite films was studied for 240 minutes, and the results were given in Figure 4. %Swelling capacity of metal-free film, Ag, Ca, and Mg composite films were determined as 58, 65, 79, and 94% after the 240 minutes. These results indicated that the % swelling performance of the composite films was increased after the addition of cations into the film matrix. The prepared chitosan, starch, and L-ascorbic acid matrix interact strongly with metal ions such as Ag^+ , Ca^{2+} , and Mg^{2+} , and as a result, the swelling capacity of the composite films was increased due to the formation of a tight structure compared to the metal-free film [27].

3.3. Drug release behavior

Drug release behavior of the metal-free film and composite films was also studied, and doxorubicin was used as a model drug in these studies. DOX release performance of the films gradually increased within the first 90 minutes and it reached a constant value after the mentioned times (Figure 5).

%DOX release amounts of the metal-free film and composite films were calculated as 80.5, 55.0, 37.2, and 20.2% for Mg, Ca, Ag composite films, and metal-free films. Niazvand and coworkers stated that the desired properties of a drug release system can be achieved by the development of metal-containing composites. In addition, with the development of composite-

containing cations for drug release systems, long-term controlled drug release can be achieved, the stability of the drug delivery system can be increased, and the preservation of drug bioactivity in the polymer-based composite system can be improved [28].

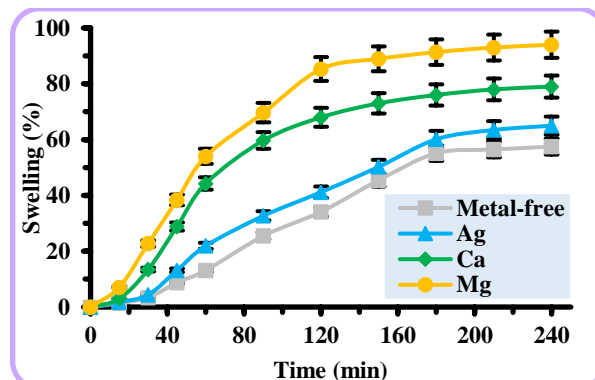


Figure 4. Swelling performance of the composite films

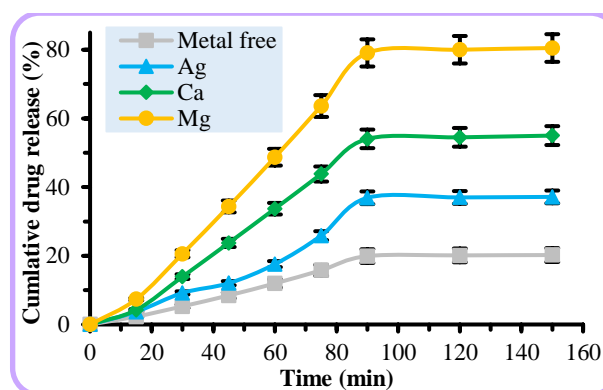


Figure 5. Drug release behavior of the composite films

4. Conclusion

In this paper, composite films based on chitosan, starch, L-ascorbic acid, and different metal ions such as Ag^+ , Ca^{2+} , or Mg^{2+} were successfully fabricated to study the release of doxorubicin. The structural confirmation of the composite films was performed by FT-IR, SEM, and TG analysis techniques to clarify the structure, and chemical interactions, morphological and thermal properties. The swelling and drug release behavior of the composite films were also studied in 0.1 M PBS (pH 7.4). The results demonstrated that the addition of the metal ions into the composite film matrix increased the swelling, drug release, and thermal properties, and the developed composite films have the potential to be used for doxorubicin release.

Article Information Form

Funding

The author(s) has no received any financial support for the research, authorship, or publication of this study.

The Declaration of Conflict of Interest/ Common Interest

No conflict of interest or common interest has been declared by the authors.

The Declaration of Ethics Committee Approval

This study does not require ethics committee permission or any special permission.

The Declaration of Research and Publication Ethics

The authors of the paper declare that they comply with the scientific, ethical, and quotation rules of SAUJS in all processes of the paper and that they do not make any falsification on the data collected. In addition, they declare that Sakarya University Journal of Science and its editorial board have no responsibility for any ethical violations that may be encountered and that this study has not been evaluated in any academic publication environment other than Sakarya University Journal of Science.

Copyright Statement

Authors own the copyright of their work published in the journal and their work is published under the CC BY-NC 4.0 license.

References

- [1] G. A. Martau, M. Mihai, D. C. Vodnar, “The use of chitosan, alginate, and pectin in the biomedical and food sector—biocompatibility, bioadhesiveness, and biodegradability”, *Polymers* vol. 11, pp. 1837, 2019.
- [2] E. B. Yahya, F. Jummaat, A. A. Amirul, A. S. Adnan, N. G. Olaiya, C. K. Abdullah, S. Rizal, M. K. M. Haafiz, H. P. S. A. Khalil, “A review on revolutionary natural biopolymer-based aerogels for antibacterial delivery”, *Antibiotics*, vol. 9, pp. 648, 2020.
- [3] W. Zhu, D. Zhang, X. Liu, T. Ma, J. He, Q. Dong, Z. Din, J. Zhou, L. Chen, Z. Hu, J. Cai, “Improving the hydrophobicity and mechanical properties of starch nanofibrous films by electrospinning and cross-linking for food packaging applications”, *LWT- Food Science and Technology*, vol. 169, pp. 114005, 2022.
- [4] L. Wu, S. Lv, D. Wei, S. Zhang, S. Zhang, Z. Li, L. Liu, T. He, “Structure and properties of starch/chitosan food packaging film containing ultra-low dosage GO with barrier and antibacterial”, *Food Hydrocolloids*, vol. 137, pp. 108329, 2023.
- [5] L. Tuovinen, S. Peltonen, K. Jarvinen, “Drug release from starch-acetate films”, *Journal of Controlled Release*, vol. 91, pp. 345–354, 2003.
- [6] A. Guo, X. Tao, H. Kong, X. Zhou, H. Wang, J. Li, F. Li, Y. Hu, “Effects of aluminum hydroxide on mechanical, water resistance, and thermal properties of starch-based fiber-reinforced composites with foam structures”, *Journal of Materials Research and Technology*, vol. 23, pp. 1570-1583, 2023.
- [7] Y. Cao, J. Yin, Y. Shi, J. Cheng, Y. Fang, C. Huang, W. Yu, M. Liu, Z. Yang, H. Zhou, H. Liu, J. Wang, G. Zhao, “Starch and chitosan-based antibacterial dressing for infected wound treatment via self-activated NO release strategy”, *International Journal of Biological Macromolecules*, vol. 220, pp. 1177–1187, 2022.
- [8] O. M. Khubiev, A. R. Egorov, A. A. Kirichuk, V. N. Khrustalev, A. G. Tskhovrebov, A. S. Kritchenkov, “Chitosan-based antibacterial films for biomedical and food applications”, *International Journal of Molecular Sciences*, vol. 24, pp. 10738, 2023.
- [9] Z. Jiang, J. Wang, D. Xiang, Z. Zhang, “Functional properties and preservative effect of p-hydroxybenzoic acid grafted

- chitosan films on fresh-cut jackfruit”, *Foods*, vol. 11, pp. 1360, 2022.
- [10] S. S. Vedula, G. D. Yadav, “Chitosan-based membranes preparation and applications: Challenges and opportunities”, *Journal of the Indian Chemical Society*, vol. 98, pp. 100017, 2021.
- [11] D. Radha, J. S. Lal, K. S. Devaky, “Chitosan-based films in drug delivery applications”, *Starch*, vol. 74, pp. 2100237, 2022.
- [12] P. S. Bakshi, D. Selvakumar, K. Kadirvelu, N. S. Kumar, “Chitosan as an environment friendly biomaterial – a review on recent modifications and applications”, *International Journal of Biological Macromolecules*, vol. 150, pp. 1072–1083, 2020.
- [13] A. A. Abd-Elghany, E. A. Mohamad, M. A. El-Sakhawy, S. Mansouri, S. H. Ismail, M. S. Elneklawi, “Enhancement of mechanical properties of chitosan film by doping with sage extract-loaded niosomes”, *Materials Research Express*, vol. 9, pp. 035006, 2022.
- [14] G. Janarthanan, I. Noh, “Recent trends in metal ion based hydrogel biomaterials for tissue engineering and other biomedical applications”, *Journal of Materials Science and Technology*, vol. 63, pp. 3553, 2021.
- [15] I. K. Sani, S. Pirsas, S. Tag, “Preparation of chitosan/zinc oxide/*Melissa officinalis* essential oil nanocomposite film and evaluation of physical, mechanical and antimicrobial properties by response surface method”, *Polymer Testing*, vol. 79, pp. 106004, 2019.
- [16] S. Li, J. Yi, X. Yu, Z. Wang, L. Wang, “Preparation and characterization of pullulan derivative/chitosan composite film for potential antimicrobial applications”, *International Journal of Biological Macromolecules*, vol. 148, pp. 258–264, 2020.
- [17] S. Ediyilyam, B. George, S. S. Shankar, T. T. Dennis, S. Waclawek, M. Cernik, V. V. T. Padil, “Chitosan/gelatin/silver nanoparticles composites films for biodegradable food packaging applications”, *Polymers*, vol. 13, pp. 1680, 2021.
- [18] U. Duru Kamaci, M. Kamaci, “Preparation of polyvinyl alcohol, chitosan and polyurethane-based pH-sensitive and biodegradable hydrogels for controlled drug release applications”, *International Journal of Polymeric Materials and Polymeric Biomaterials*, vol. 69, pp. 1167–1177, 2020.
- [19] M. Kciuk, A. Gielecinska, S. Mujwar, D. Kolat, Z. K. Kolat, I. Celik, R. Kontek, “Doxorubicin—an agent with multiple mechanisms of anticancer activity”, *Cells*, vol. 12, pp. 659, 2023.
- [20] R. Sawpari, S. Samanta, J. Banerjee, S. Das, S. S. Dash, R. Ahmed, B. Giri, S. K. Dash, “Recent advances and futuristic potentials of nano-tailored doxorubicin for prostate cancer therapy”, *Journal of Drug Delivery Science and Technology*, vol. 81, pp. 104212, 2023.
- [21] S. Karimi, H. Rasuli, R. Mohammadi, “Facile preparation of pH-sensitive biocompatible alginate beads having layered double hydroxide supported metal-organic framework for controlled release from doxorubicin to breast cancer cells”, *International Journal of Biological Macromolecules*, vol. 234, pp. 123538, 2023.
- [22] M. Kamaci, “Polyurethane-based hydrogels for controlled drug delivery applications”, *European Polymer Journal*, vol. 123, pp. 109444, 2020.
- [23] F. J. Warren, M. J. Gidley, B. M. Flanagan, “Infrared spectroscopy as a tool to characterise starch ordered structure—a joint FTIR–ATR, NMR, XRD and DSC study”, *Carbohydrate Polymers*, vol. 139, pp. 35–42, 2016.

- [24] H. Zhou, D. Zhang, “Effect of graphene oxide aerogel on dehydration temperature of graphene oxide aerogel stabilized $\text{MgCl}_2 \cdot 6\text{H}_2\text{O}$ composites”, *Solar Energy*, vol. 184, pp. 202–208, 2019.
- [25] A. Umer, S. Naveed, N. Ramzan, M. S. Rafique, M. Imran, “A green method for the synthesis of copper nanoparticles using L-ascorbic acid”, *Revista Materia*, vol. 19, pp. 197-203, 2014.
- [26] L. Balau, G. Lisa, M. I. Popa, V. Tura, V. Melnig, “Physico–chemical properties of chitosan films”, *Central European Journal of Chemistry*, vol. 2, pp. 638–647, 2004.
- [27] F. Doustdar, A. Olad, Marjan Ghorbani, “Effect of glutaraldehyde and calcium chloride as different crosslinking agents on the characteristics of chitosan/cellulose nanocrystals scaffold”, *International Journal of Biological Macromolecules*, vol. 208, pp. 912-924, 2022.
- [28] F. Niazvand, A. Cheshmi, M. Zand, R. N. Azadani, B. Kumari, A. Raza, S. Nasibi, “An overview of the development of composites containing Mg and Zn for drug delivery”, *Journal of Composites and Compounds*, vol. 2, pp. 193-204, 2020.

Pigment Production From Bacteria Isolated From Whey

Sude Çardak^{1*}, İlke Karakaş², Nurcihan Hacıoğlu Dođru¹

¹Çanakkale Onsekiz Mart University, Faculty of Science, Department of Biology, Çanakkale, Türkiye, sudecardak6666@gmail.com, nurcihan.n@gmail.com

²Çanakkale Onsekiz Mart University, Vocational School of Health Services, Pharmacy Services Program, Çanakkale, Türkiye, ilke.karakas@comu.edu.tr

*Corresponding Author

ARTICLE INFO

ABSTRACT

Keywords:
Microbial pigment
Carotenoid
Industrial raw material
Whey

Environmental pollution and population growth necessitate more efficient production processes. Organic whey, which is a low-cost substrate for the food industry, constitutes a promising raw material with its low cost and chemical content for biotechnological processes. This study investigated the pigment production capabilities of bacteria isolated from whey, an industrial waste. Among the isolated bacteria, 4 were determined to be effective pigment producing bacteria. The pigment was extracted from 4 isolates. Pigment characterization was performed by UV spectrophotometer (OD470-OD580) and Fourier Transform Infrared Spectroscopy (FTIR). As a result of the spectrum scanning, it was determined that all pigments gave the maximum absorbance value in the range of 500 nm to 505 nm. In FTIR analysis, all extracted pigments showed characteristic absorption bands of carotenoids between 400 nm and 520 nm. The FTIR peaks obtained from 1469 cm⁻¹ and 1726 cm⁻¹ regions are known as the fingerprint regions of microbial pigments for biorecolorants. When the results obtained in our study are compared with the literature data, the absorbance values obtained show that the pigment produced is carotenoid and its derivative.

Article History:

Received: 29.11.2023

Accepted: 12.03.2024

Online Available: 14.06.2024

1. Introduction

Pigments are defined as intensely colored chemical covering compounds that are insoluble in water, can absorb light in the visible region, and are used to color various materials. In recent years, producers have focused on the production of natural pigments produced from “plants” and “microorganisms” instead of synthetic pigments, which are potentially harmful to the environment and especially to human health [1]. Since plant-derived pigments have limited water solubility and are not stable against heat and light, microbial pigments attract more attention in the fields of food, textiles, and cosmetics [2, 3].

Bacteria are a good source of pigments. They produce mostly carotenoids, especially β -

carotene. *Streptomyces chrestomycetius rubescens* produces lycopene, while *Flavobacterium* sp. has gained importance for its production of zeaxanthin and lutein [2-4]. A mutant strain of *Flavobacterium* can produce zeaxanthin at low temperatures in a base medium with the addition of glucose, corn syrup, and palmitic acid. *Corynebacterium* sp. and *Rhodococcus maris* are also microorganisms adapted for canthaxanthin production [4]. Microbial pigments are preferred due to their features such as reliability in use, medical benefits, being a source of nutrients such as vitamins, production being independent of seasonal and geographical conditions, controllability, wide color range, and efficiency [5].

In industrial scale, cheap carbon, trace elements, and nitrogen sources are used as substrates. It is important to select sustainable substrates in large-scale microbial production. The use of industrial waste in production is important for both cost reduction and in reducing damage to environmental protection [2-6]. In studies on alternative sources, many different food industrial wastes have been used in pigment production. In this context, paddy straw [7], waste beer [8], beer wort waste [9], orange peels [10], sugarcane [11, 12], rice water [13], sweet potato [14] were used in pigment production.

Whey, which is released at high rates during cheese production, is an important waste for the dairy industry. It is defined as the greenish-yellow liquid by-product that separates from the curd after cutting the curd and remains outside the curd. Nowadays, various whey products such as whey protein concentrates, whey protein isolates, low lactose whey, demineralized whey, and hydrolyzed whey are obtained thanks to technologies such as ultrafiltration, microfiltration, etc. [15].

Whey is a very valuable by-product when processed and turned into powder due to its significant protein, fat, and lactose content, but when released directly into nature, organic substances that can be biodegraded by microorganisms easily cause environmental pollution [16]. Dissolved oxygen in water is used to break down these substances. Since the nitrogen contained in whey dissolves in water, it can mix with groundwater and threaten human and animal health [15, 16]. Approximately 180-190 million tons of whey produced annually poses a major threat to the environment due to its high organic load. In this study, it was aimed to produce and characterize pigments from bacteria isolated from whey.

2. Materials and Methods

2.1. Isolation of bacteria from whey

The whey used in the study was obtained from the cheese factory in Çanakkale province. Bacterial isolation from whey samples transported to the laboratory under appropriate conditions was performed using Tryptic Soy

Agar (TSA) (Biolife, 4021502) and Tryptic Soy Broth (TSB) (Biolife, 4021552) media. Isolation and plantings were made in a sterile inoculation (Heal Force, HFsafe 1200LC). After appropriate dilutions, whey samples were taken from 0.1 mL sample tubes and transferred to petri dishes containing the medium, and they were cultivated according to the spread plate method. Petri dishes were incubated at 37°C for 24 hours and bacterial growth was monitored throughout the incubation period. Bacterial samples that showed growth in petri dishes were taken with a sterile loop, and they were inoculated again in petri dishes containing TSA and isolated. Isolated cultures were planted on horizontal agar and short-term stocks were stored at +4°C and long-term stocks were stored at -20°C.

2.2. Determination of active pigment producing isolate

Microorganisms with morphologically colorful colonies among the isolated and purified bacterial isolates were planted in Nutrient Agar (NA) (Lab M, 129472) and incubated for 7 days to be evaluated in terms of pigment production. Pigmented microorganisms were detected among the developing microorganisms. At the end of the incubation period, pigmented colony-forming organisms were transferred to Nutrient Broth (NB) (Lab M, 129491) and incubated at 37°C for 24 hours. Color material production studies were continued with Mineral Salt Medium (MSM) Broth [17].

2.3. Extraction of color matter

Isolates in NB were adjusted to 0.5 McFarland level with 0.9% physiological saline and inoculated into 100 ml MSM Broth. The samples were kept in a shaking incubator at 35°C for 10 days, and at the end of the incubation period, they were transferred to 50 ml sterile centrifuge tubes and centrifuged at 6000 rpm for 15 minutes. The supernatant was discarded and 20 ml of ethyl alcohol solvent was added to the colored cell section at the bottom and kept for 1 night. At the end of one night, the solvent supernatant was cleared of cells by centrifugation at 6000 rpm for 10 minutes and transferred to sterile falcons for spectrum scanning (OD470-580) (Thermo Scientific Genesys 10S).

To obtain dry biomass, colorants were poured into petri dishes in thick layers and left to dry in an oven at 60°C. At the end of 5 days, the dried materials were scraped from the petri dishes and placed in eppendorfs. This obtained dry material was used in all characterization steps [18].

2.4. Microbial pigment spectrum scans

The dried colorants were redissolved in ethyl alcohol and solutions (50, 100, 250, 500, and 1000 µg/ml) were prepared. For the isolates, the spectrum value corresponding to µg/ml of the pigment substance was obtained by measuring the absorbance of the colors given by the pigments at different wavelengths [18].

2.5. Fourier transform infrared spectroscopy (FTIR) analysis

In this study, FTIR analyses were performed to determine the possible groups in the chemical structures of the substances used as pigments. KBr discs prepared with dry pigments were used for FTIR analyses. Powdered pigment samples were mixed with 1% potassium bromide (KBr) and pressed into discs [17]. The FTIR spectrum of the disk is expected to be taken in the region of 400 cm⁻¹ - 4000 cm⁻¹.

3. Results and Discussion

3.1. Isolation of bacteria

In the study, 10 Gram (+) and catalase negative isolates that formed colored colonies in whey medium were selected and purified. Microorganisms with morphologically colorful colonies among the purified bacterial isolates were planted in NA and incubated for 7 days to be evaluated in terms of pigment production. Pigmented microorganisms were detected and purified among the incubated microorganisms.

3.2. Identification of active pigment producing isolate and extraction of color substance

Isolates selected according to the colony colors on the NA were inoculated into MSM broth and the color differences in the medium were observed. According to these differences, the

isolates with the most prominent pigmentation were selected for microbial pigment production and coded as P1, P2, P3, and P4. To extract pigment-producing bacteria, various methods such as centrifugation (Figure 1), filtration, and ethanol were used to disrupt the cell, and the intracellular pigment was extracted and dried in the oven.

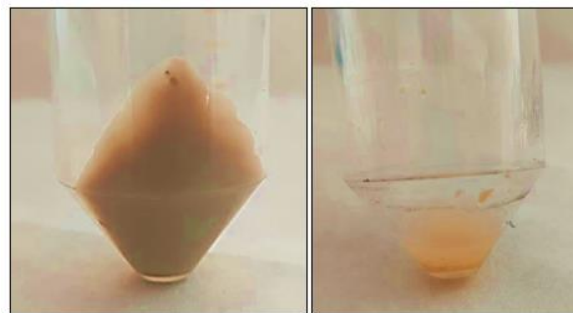


Figure 1. Pigment images obtained from isolates

3.3. Microbial pigment spectrum scans

It was determined that the pigments produced from P1 and P4 isolates were light orange, and the pigments produced from P2 and P3 isolates were yellow. For spectrum scanning, dry microbial pigments prepared from isolates coded P1, P2, P3, and P4 were dissolved in the appropriate solvent, and solutions were prepared at concentrations of 50, 100, 250, 500, and 1000 ppm. Readings were made in the appropriate spectrum on the spectrophotometer (OD470-OD580) with the prepared solutions. The most efficient result was obtained at an amount of 500 ppm. The resulting graphs are shown in Figure 2 to 5.

The dry pigments were dissolved in ethanol and spectra were scanned. In the analysis of the samples, especially in the measurements in the UV region, high absorption regions were detected due to compound proteins. As a result of the spectrum scanning, it was determined that all pigments gave their maximum absorbance values between 500 nm and 505 nm. In some studies, it has been determined that quinone molecules have high absorbance points, especially in regions starting from 280 nm wavelengths to 550 nm wavelengths [18]. Different studies have been carried out in the literature for the characterization of pigments. Indra et al., [19] investigated bacterial species that produce high carotenoid pigments on 41 soil samples.

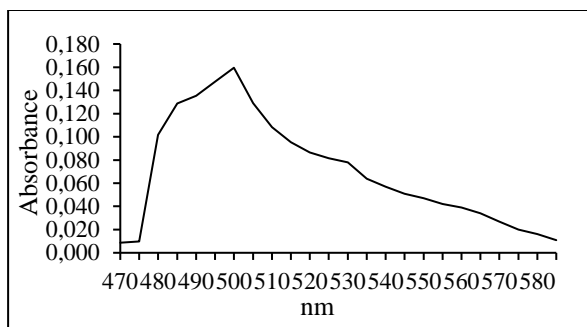


Figure 2. Spectrum scan of P1 coded isolate pigment

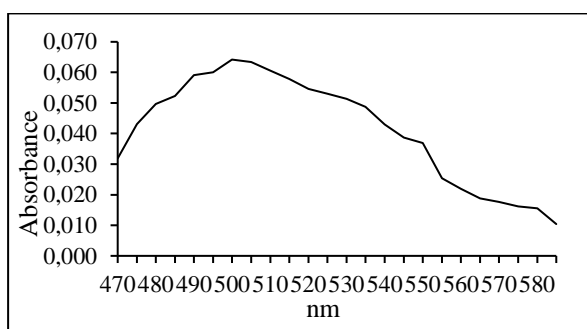


Figure 3. Spectrum scan of P2 coded isolate pigment

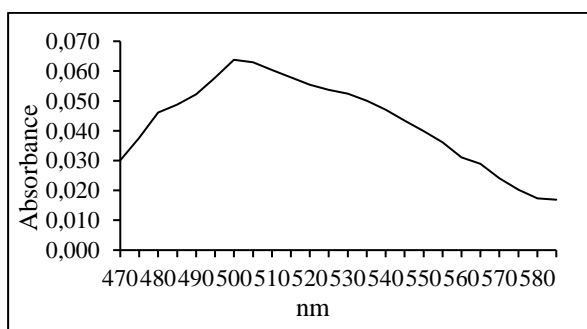


Figure 4. Spectrum scan of P3 coded isolate pigment

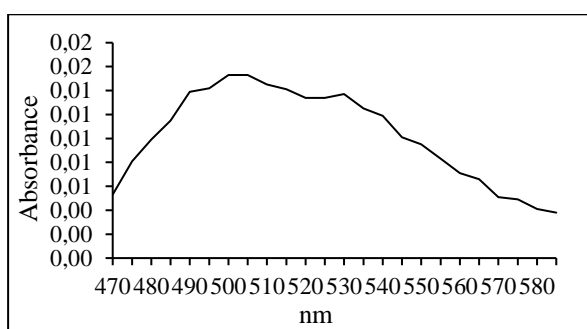


Figure 5. Spectrum scan of P4 coded isolate pigment

As a result of research and bacterial isolation, they obtained 24 bacterial isolates that appeared to produce yellow pigment. These pigments were prepared for spectrophotometric measurements

using methanol extract. Evaluations were made as a result of spectrophotometric analysis and the peaks occurring at 450 nm showed the presence of carotenoid pigment. Trivedi et al., [20] isolated bacteria from soil samples. They used methanol, ethanol, and ethyl acetate solvents to isolate pigments from bacteria and performed spectrophotometric analysis and FTIR to characterize the pigments they isolated. As a result of FTIR analysis, it was determined that the pigment obtained was similar to the beta carotene used as standard and that the pigment was a carotenoid derivative. Different spectrophotometric studies have been conducted in the literature. When the results obtained in our study are compared with the literature data, the absorbance values obtained show that the pigment produced is a carotenoid and its derivative [2, 9, 17].

3.4. FTIR analysis

FTIR absorption spectra were determined to characterize the pigment extracts produced by isolates purified from whey. The obtained data are shown in Figure 6 to 9.

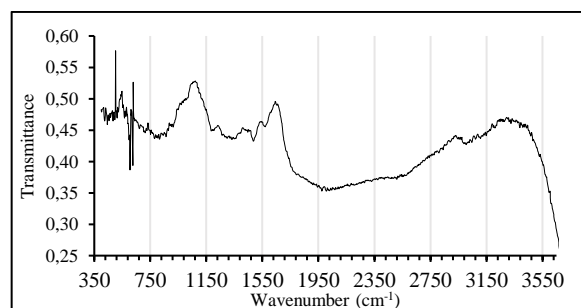


Figure 6. FTIR spectroscopy results of isolate pigment number P1

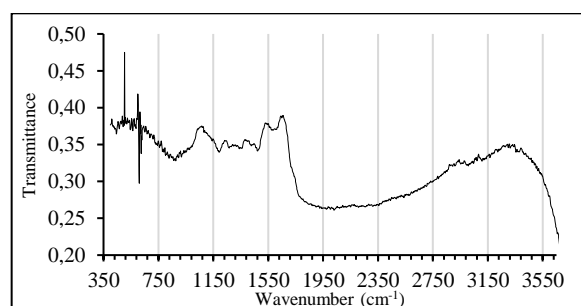


Figure 7. FTIR spectroscopy results of isolate pigment number P2

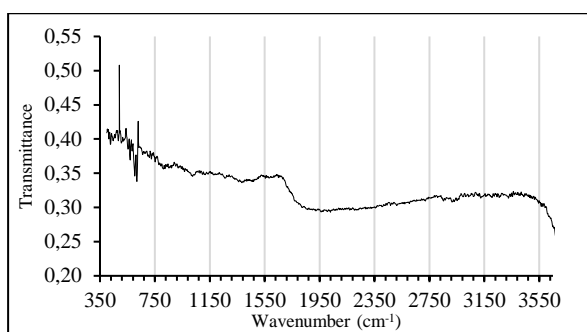


Figure 8. FTIR spectroscopy results of isolate pigment number P3

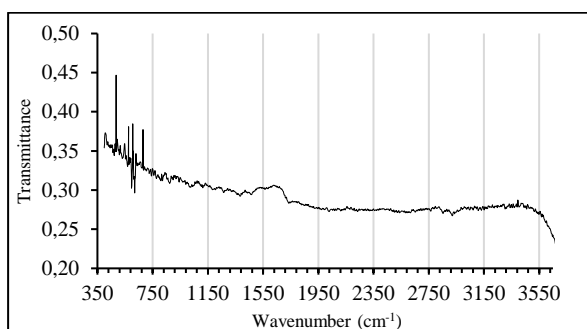


Figure 9. FTIR spectroscopy results of isolate pigment number P4

All extracted pigments showed 400 to 520 nm absorption bands characteristic of carotenoids. The measured spectra correspond to the absorbance of chromophore groups present in the chemical structures of carotenes. β -carotene and zeaxanthin have maximum absorption between 482 nm and 511 nm, depending on the chemical property of the solvent. In addition, the maximum absorbance values determined for lutein are between 440 nm and 503.8 nm. It is thought that the peaks in the range of 1500 cm^{-1} – 1620 cm^{-1} seen in the FTIR graph of pigments P1 and P2 indicate stretching vibrations between aromatic $\text{C} = \text{C}$ or $\text{C} = \text{O}$ groups.

The bands in the range of 1320 cm^{-1} – 1390 cm^{-1} of all pigments indicate that the pigment contains pyrrole or indole in its structure. In FTIR spectroscopy of microbial pigments, moderate peaks at 1469 cm^{-1} and 1726 cm^{-1} are known as fingerprint regions for biocolorants. The peaks at 1460 cm^{-1} and 1450 cm^{-1} regions indicate the presence of aliphatic groups, which are organic compounds containing a skeleton in the form of straight or branched chains, formed by covalent bonding of various atoms to each other, in the molecular structures of the pigment material. It is known that the small and continuous peaks seen

in the range of 3350 cm^{-1} – 3440 cm^{-1} are formed as a result of OH and NH_2 stretching.

In this study, the pigment producing ability of bacteria isolated from whey was investigated and the basic characterization of the produced pigment was carried out [4-6, 15].

Ahmad et al., [21] pigment-producing bacteria *Serratia marcescens*, *Streptomyces coelicolor* and *Thiobacillus versutus* were isolated and their prodigiosin production abilities were investigated. The characterization of the obtained pigment was evaluated in terms of physical and chemical properties by various methods such as FTIR and UV-vis Spectroscopy.

Órdenes-Aenishanslins et al., [22] pigment production abilities of psychrotolerant bacteria isolated from soil were investigated using UV-Vis spectrophotometry and FTIR methods. Red and yellow pigments were produced from bacteria identified as *Hymenobacter* sp. and *Chryseobacterium* sp.

Atalay, [23] produced red pigment with bacteria isolated from waste beer and carried out optimization studies. A comparison of the results obtained in our study with literature data shows that the pigment produced is a carotenoid and its derivative. It is envisaged that, with more detailed studies, a raw material with commercial potential and use will be revealed.

4. Conclusion

Although natural pigments were previously produced from plants, microbial pigments have begun to replace vegetable pigments rapidly, as they are not affected by weather conditions and grow quickly and easily. The interest in microbial pigments, which were not preferred at first due to their effects on human health and being more expensive than synthetic ones, increased as it was revealed that they did not have any toxic properties and their prices became competitive with synthetics thanks to the use of cheap raw materials in developing biological processes. Microbial pigments not only grow rapidly and are not affected by environmental conditions, but also the fact that industrial and chemical wastes can be used to grow the

microorganisms used is an extra advantage due to their contribution to environmental pollution. Microbial biotechnology, which is developing day by day around the world, will continue to play a role in reducing environmental pollution by transforming waste into usable products due to the increasing need for cheap raw materials in the future. An increase in microbial diversity due to the research of new microorganisms that can be used in these areas, and biological processes developed for the naturalization of many products will lead to progress in the field of biotechnology and the production of healthier products.

This study examines the presence of Gram (+) microorganisms capable of producing pigments in whey, a by-product of cheese production. With increasing demand across all industries, the use of pigments derived from natural sources is gaining importance. Therefore, the discovery of potential pigment-producing microorganisms in by-products such as whey, which are considered waste, could be a significant step towards meeting the demand for natural colorants across various industries.

Microorganisms are valuable resources used in the production of various industrial products in biotechnological applications. In this context, the discovery of pigment-producing microorganisms in waste products such as whey could contribute to sustainable production processes. Using pigments derived from natural sources offers a more environmentally friendly and sustainable option than synthetic alternatives.

Furthermore, the biodiversity and adaptation capabilities of microorganisms provide a wide potential for synthesizing different pigments in industrial applications. Therefore, the identification and characterization of pigment-producing microorganisms in waste products like whey represent a crucial step in the discovery and development of new and diverse natural colorant sources.

In conclusion, this study not only identifies the presence of Gram (+) microorganisms capable of producing pigments in whey but also emphasizes their significance as valuable resources to meet the demand for natural colorants across all

industries. These findings could contribute to further understanding the use of natural pigment-producing microorganisms in future research and the development of more sustainable colorant options in industrial applications.

Article Information Form

Funding

This study TÜBİTAK-2209 A Project which is supported with the frame of an Undergraduate Students Grant in Biological Science.

Authors' Contribution

The authors contributed equally to the study.

The Declaration of Conflict of Interest/ Common Interest

No conflict of interest or common interest has been declared by the authors.

The Declaration of Ethics Committee Approval

This study does not require ethics committee permission or any special permission.

The Declaration of Research and Publication Ethics

The authors of the paper declare that they comply with the scientific, ethical and quotation rules of SAUJS in all processes of the paper and that they do not make any falsification on the data collected. In addition, they declare that Sakarya University Journal of Science and its editorial board have no responsibility for any ethical violations that may be encountered, and that this study has not been evaluated in any academic publication environment other than Sakarya University Journal of Science.

Copyright Statement

Authors own the copyright of their work published in the journal and their work is published under the CC BY-NC 4.0 license.

References

- [1] F. M. Said, N. F. B. Hamid, "Optimization of Red Pigment Production by *Monascus purpureus* FTC 5356 Using Response Surface Methodology," IJUM Engineering Journal, vol. 19, no. 1, pp. 34-47, 2018.

- [2] G. Sharmila, B. Nidhi, C. Muthukumar, "Sequential Statistical Optimization of Red Pigment Production by *Monascus purpureus* (MTCC 369) Using Potato Powder," *Industrial Crops and Products*, vol. 44, pp. 158-164, 2013.
- [3] A. Kumar, H. S. Vishwakarma, J. Singh, S. Dwivedi, M. Kumar, "Microbial Pigments: Production and Their Applications in Various Industries," *International Journal of Pharmaceutical and Chemical Sciences*, vol. 5, no. 1, pp. 203-212, 2015.
- [4] C. K. Venil, P. Lakshmanaperumalsamy, "An Insightful Overview on Microbial Pigment, Prodigiosin," *Electronic Journal of Biology*, vol. 5, no. 3, pp. 49-61, 2009.
- [5] G. Y. Liu, V. Nizet, "Color Me Bad: Microbial Pigments as Virulence Factors," *Trends in Microbiology*, vol. 17 no.9, pp. 842-966, 2009.
- [6] D. Pleissner, Q. Qi, C. Gao, C. P. Rivero, C. Webb, C. S. K. Lin, J. "Venus, Valorization of Organic Residues for The Production of Added Value Chemicals: A Contribution to The Bio-Based Economy," *Biochemical Engineering Journal*, vol. 116, pp. 3-16, 2016.
- [7] J. Liu, Y. Luo, T. Guo, C. Tang, X. Chai, W. Zhao, Q. Lin, "Costeffective Pigment Production by *Monascus Purpureus* Using Rice Straw Hydrolysate as Substrate in Submerged Fermentation", *Journal of Bioscience and Bioengineering*, vol. 129, no. 2, pp. 229-236, 2020.
- [8] P. Atalay, "Microbial Production of Color Pigment from Waste Beer," Master Thesis, Ege University, İzmir, Türkiye, 2020.
- [9] M. S. Şilbir, "Production of *Monascus* Color Pigments from Beer Waste and Determination of Their Stability," Ege University, İzmir, Türkiye, 2019.
- [10] A. Kantifedaki, V. Kachrimanidou, A. Mallouchos, S. Papanikolaou, A. A. Koutinas, "Orange Processing Waste Valorisation for the Production of Bio-Based Pigments Using the Fungal Strains *Monascus Purpureus* and *Penicillium Purpurogenum*," *Journal of Cleaner Production*, vol. 185, pp. 882-890, 2018.
- [11] S. T. Silveira, D. J. Daroit, V. Sant'Anna, A. Brandelli, "Stability Modeling of Red Pigments Produced by *Monascus purpureus* In Submerged Cultivations with Sugarcane Bagasse," *Food and Bioprocess Technology*, vol. 6, no. 4, pp. 1007-1014, 2013.
- [12] R. T. Hilares, R. A. de Souza, P. F. Marcelino, S. S. da Silva, G. Dragone, S. I. Mussatto, J. C. Santos, "Sugarcane Bagasse Hydrolysate as A Potential Feedstock for Red Pigment Production by *Monascus ruber*," *Food Chemistry*, vol. 245, pp. 786-791, 2018.
- [13] N. Singh, G. Goel, N. Singh, K. Pathak, D. Kaushik, "Modeling the Red Pigment Production by *Monascus purpureus* MTCC 369 by Artificial Neural Network Using Rice Water Based Medium," *Food Bioscience*, vol. 11, pp. 17-22, 2015.
- [14] P. Srivastav, V. K. Yadav, S. Govindasamy, M. Chandrasekaran, "Red Pigment Production by *Monascus purpureus* Using Sweet Potato-Based Medium in Submerged Fermentation," *Nutrafoods*, vol. 14, no. 3, pp. 159-167, 2015.
- [15] O. Yerlikaya, Ö. Kınık, N. Akbulut, "Functional Properties of Whey and Milk Beverages Produced Using Whey," *Gıda*, vol. 35, no. 4, pp. 289-296, 2010.
- [16] J. Hausjell, M. Miltner, C. Herzig, A. Limbeck, Z. Saracevic, E. Saracevic, O. Spadiut, "Valorisation of Cheese Whey As Substrate and Inducer for Recombinant Protein Production in *E. coli* HMS174 (DE3)," *Bioresource Technology Reports*, vol. 8, pp. 100340, 2019.
- [17] S. Yıldırım, "Production of Pigment by Isolated Microorganisms from

Hydrocarbon Pollution of Soil,” Master Thesis, Eskişehir Osmangazi University, Eskişehir, Türkiye, 2014.

- [18] B. Zhou, J. Wang, Y. Pu, M. Zhu, S. Liu, S. Liang, “Optimization of Culture Medium for Yellow Pigments Production with *Monascusanka* Mutant Using Response Surface Methodology,” *European Food Research Technology*, vol. 228, pp. 895–901, 2008.
- [19] P. Indra Arulselvi, S. Umamaheswari, G. Ranandkumar Sharma, C. Karthik, C. Jayakrishna, “Screening of Yellow Pigment Producing Bacterial Isolates from Various Eco-Climatic Areas and Analysis of the Carotenoid Produced by the Isolate,” *Journal of Food Processing Technology*, vol. 5, pp. 292, 2014.
- [20] N. Trivedi, S. Tandon, A. Dubey, “Fourier Transform Infrared Spectroscopy (FTIR) Profiling of Red Pigment Produced by *Bacillus subtilis* PD5,” *African Journal of Biotechnology*, vol. 16, no. 27, pp. 1507-1512, 2017.
- [21] W. A. Ahmad, W. Y. W. Ahmad, Z. A. Zakaria, N. Z. Yusof, “Isolation of Pigment-Producing Bacteria and Characterization of the Extracted Pigments,” *Application of Bacterial Pigments as Colorant*, pp. 25–44, 2011.
- [22] N. Órdenes-Aenishanslins, G. Anziani-Ostuni, M. Vargas-Reyes, J. Alarcón, A. Tello, J. Pérez-Donoso, “Pigments from UV-Resistant Antarctic Bacteria as Photosensitizers in Dye Sensitized Solar Cells,” *Journal of Photochemistry and Photobiology B: Biology*, vol. 162, pp. 707-714, 2016.
- [23] P. Atalay, S. Sargın, Y. Goksungur, Y., “Utilization of Residual Beer for Red Pigment Production by *Monascus purpureus* in Submerged Fermentation,” *Fresenius Environmental Bulletin*, vol. 29, pp. 1025-1034, 2020.

A Detailed Comparison of Two New Heuristic Algorithms Based on Gazelles Behavior

Emine Baş Konya Technical University, Faculty of Engineering and Nature Sciences, Department of Software Engineering, Konya, Türkiye, ebas@ktun.edu.tr

ARTICLE INFO

ABSTRACT

Keywords:
Gazelle
Exploration
Exploitation
Benchmarks



Article History:
Received: 03.12.2023
Accepted: 29.04.2024
Online Available: 15.06.2024

In this study, Mountain Gazelle Optimization (MGO) and Gazelle Optimization Algorithm (GOA) algorithms, which have been newly proposed in recent years, were examined. Although MGO and GOA are different heuristic algorithms, they are often considered the same algorithms by researchers. This study was conducted to resolve this confusion and demonstrate the discovery and exploitation success of both algorithms. While MGO developed the exploration and exploitation ability by being inspired by the behavior of gazelles living in different groups, GOA model was developed by being inspired by the behavior of gazelles in escaping from predators, reaching safe environments and grazing in safe environments. MGO and GOA were tested on 13 classical benchmark functions in seven different dimensions and their success was compared. According to the results, MGO is more successful than GOA in all dimensions. GOA, on the other hand, works faster than MGO. Additionally, MGO and GOA were tested on three different engineering design problems. While MGO was more successful in the tension/compression spring design problem and welded beam design problems, GOA achieved better results in the pressure vessel design problem. The results show that MGO improves the ability to explore and avoid local traps better than GOA. MGO and GOA are also compared with three different heuristic algorithms selected from the literature (GSO, COA, and ZOA). According to the results, MGO has shown that it can compete with new algorithms in the literature. GOA, on the other hand, lags behind comparison algorithms.

1. Introduction

While an optimization problem describes a problem that has more than one feasible solution, optimization is the process of finding the best solution among all available solutions [1]. Optimization problems consist of decision variables, constraints and objective function [2]. Various methods, such as gradient-based methods and numerical calculations, have been proposed to solve optimization problems [1]. In an optimization problem, simply finding a solution is not enough. The cost and time involved in reaching this solution are important. Real-world problems often have multiple decision variables and complex nonlinear relationships. The inability of analytical methods to solve optimization problems has led to the

emergence of meta-heuristic algorithms. Meta-heuristic algorithms are stochastic methods inspired by nature and its mechanisms, which try to send the initial population to the global optimum and provide appropriate solutions close to the global optimum in a reasonable time [3].

Many new metaheuristic algorithms have been proposed in recent years due to their success in solving many real-world problems. The most important of these are Mountain Gazelle Optimization (MGO) [4], Gazelle Optimization Algorithm (GOA) [5], Aquila Optimizer (AO) [1], Harris Hawks Optimization (HHO) [6], Slime Mould Algorithm (SMA) [7], Tunicate Swarm Algorithm (TSA) [8], Equilibrium Optimizer (EO) [9], SCA, Arithmetic Optimization Algorithm (AOA) [10], Marine

Predators Algorithm (MPA) [11], Zebra Optimization Algorithm (ZOA) [12], Crayfish Optimization Algorithm (COA) [13], Golden Search Optimization Algorithm (GSO) [14], etc.

In recent years, many heuristic algorithms have been proposed for continuous optimization in the literature. This may also cause the similarities in the names of these algorithms. Similarities in the names of algorithms often cause confusion among researchers. Sometimes they are used interchangeably and sometimes cause pronunciation errors. For this reason, heuristic algorithms, which are often confused, are compared one to one in the literature. For example, Baş and Ülker proposed a comparison between SSA and SSO algorithm inspired in the behavior of the social spider for constrained optimization in 2021 [15]. SSA and SSO heuristic optimization algorithms are two different algorithms inspired by spider behavior.

The frequent use of SSO instead of SSA in the literature has pushed the SSA algorithm into the background and delayed its discovery by researchers. At the same time, in many studies, SSA was often abbreviated as SSO and sometimes SSO was abbreviated as SSA. This situation has caused even more complexity among algorithms with similar names. Baş and Ülker noticed this situation and introduced this study to the literature. Baş and Ihsan compared the Gray wolf and Kirill herd algorithms, which are two herd-based heuristic algorithms that have been widely preferred in recent years [16]. Their aim is to compare the success of both algorithms on CEC-C06 2019 functions in small and large sizes. In addition, they compared their success on big data optimization problems and drew attention to their success in large size problems.

In this study, two newly proposed heuristic algorithms, MGO and GOA, were examined in recent years. The reason why these heuristic algorithms were chosen is that the living groups inspired by both algorithms are similar. Both heuristic algorithms were inspired by the imitation of the social lifestyles of gazelle groups existing in nature. Although MGO and GOA are often considered the same heuristic algorithms in the literature, the discovery and exploitation capabilities of both algorithms differ. Four main

factors in the life of mountain gazelles are used in the MGO mathematical model. These are single male herds, natal herds, solitary, territorial males and migrate in search of food [4]. MGO realizes its exploration and exploitation abilities with these four groups of mountain gazelles. The GOA model was inspired by the behavior of gazelles to escape from predators, reach safe environments and graze in safe environments. While the grazing behavior of gazelles in safe environments was used for the exploitation ability of the GOA, the behavior of escaping from predators was used for the exploration ability of the GOA.

When the literature was examined, it was noticed that a one-to-one comparison of these two similar algorithms was not given. In this study, these two algorithms are examined in detail and their success is shown in 13 classical benchmark functions in sizes 10, 20, 30, 50, 100, 500, and 1000. Both algorithms were compared according to best, worst, average, standard deviation, and time. The discovery and exploitation abilities of the algorithms are compared with each other. Wilcoxon signed rank test was performed on the results to determine whether there were semantic differences between MGO and GOA results. MGO and GOA were then compared on three different engineering design problems. According to the results, MGO explores the search space better than GOA and is less likely to get caught in local traps. MGO and GOA were compared with three different heuristic algorithms in recent years (GSO, COA, and ZOA) and it was examined whether they fell behind the literature.

The rest of the paper follows: In Section 2, MGO and GOA are explained in detail. Additionally, classical benchmarks used in comparisons are shown. In Section 3, MGO and GOA are compared on classical benchmarks in three low dimensions and four high dimensions. Statistical tests were performed on the results. In Section 4, MGO and GOA comparison results are interpreted and discussed.

2. General Methods

2.1. Mountain gazelle optimization algorithm (MGO)

Mountain gazelle is one of the gazelle species. It was a source of inspiration in the mathematical formation of MGO. Mountain gazelles are social creatures that live territorially and run very fast. Mountain gazelle territories consist of three groups. These are the mother-offspring herds, young male herds, and single males' territory [17]. Young male gazelles are in a constant struggle over the environment.

Mathematical model of MGO:

MGO is an optimization algorithm based on the social behavior and lifestyle of mountain gazelles. While modeling the MGO algorithm mathematically, basic concepts related to the social and group life of mountain gazelles are used. Four main factors in the life of mountain gazelles are used in the MGO mathematical model. These are single male herds, natal herds, solitary, territorial males, and migrate in search of food [4]. In MGO, each gazelle must be a member of one of the maternity herds, bachelor male herds, or solitary, territorial males. A new gazelle may also be born from these herds. In MGO, the best individuals are adult male gazelles. In MGO, candidate solutions added to the population are considered as gazelles in natal herds. In order to maintain the population number in each repetition, strong gazelles, that is, gazelles with quality solutions, remain in the population, while sick and old gazelles, that is, gazelles with poor quality solutions, are removed from the population. Thus, the herd population number is maintained [4].

In MGO, exploration and exploitation are carried out in four parallel mechanisms.

a- Territorial Solitary Males (TSM):

Male mountain gazelles are highly territorial. When they reach adulthood, that is, when they become strong enough, they create a territory. Regions are separated by large distances. Adult male gazelles fight for territory or possession of females. While young male gazelles try to

occupy the territory or the female, adult males try to protect their environment. Adult male individuals are shown in Equations 1-5 [4].

$$TSM = male_{gazelle} - |(ri_1 \times BH - ri_2 \times X(t)) \times F| \times Cof_r \tag{1}$$

$$BH = X_{ra} \times [r_1] + M_{pr} \times [r_2], \quad ra = \left\{ \left[\frac{N}{3} \right] \dots N \right\} \tag{2}$$

$$F = N_1(D) \times \exp \left(2 - Iter \times \left(\frac{2}{Iter_{max}} \right) \right) \tag{3}$$

$$Cof_i = \begin{cases} (a + 1) + r_3, \\ a \times N_2(D), \\ r_4(D), \\ N_3(D) \times N_4(D)^2 \times \cos((r_4 \times 2) \times N_3(D)), \end{cases} \tag{4}$$

$$a = -1 + Iter \times \left(\frac{-1}{Iter_{max}} \right) \tag{5}$$

where $male_{gazelle}$ is the position of the best global gazelle (adult male). ri_1 and ri_2 are random integers 1 or 2. BH is the young male herd coefficient vector. Cof_r is a randomly selected coefficient vector updated in each iteration. $X(t)$ is the position of the gazelle in the t^{th} iteration. X_{ra} is a random gazelle (young male). M_{pr} is the average number of search gazelles. They are chosen randomly. N is population size and $r_1, r_2, r_3,$ and r_4 are random values between 0 and 1. D is the problem dimension. exp is exponential function. $Iter_{max}$ is the number of the maximum iteration and $Iter$ is the number of the current iteration. N_1 is a random number from the standard distribution. $N_2(D), N_3(D),$ and $N_4(D)$ are random numbers in the normal range and the dimensions of the problem [4].

a- Maternity Herds (MH):

Maternity herds have a significant impact on the life of mountain gazelles. Maternity herds can give birth to male gazelles. The formation of maternal herds is shown in Equation 6 [4].

$$MH = (BH + Cof_{2,r}) + (ri_3 \times male_{gazelle} - ri_4 \times X_{rand}) \times Cof_{3,r} \quad (6)$$

where BH is the young male herd coefficient vector. $Cof_{2,r}$ and $Cof_{3,r}$ are a randomly selected coefficient vectors. ri_3 and ri_4 are random integers 1 or 2. $male_{gazelle}$ is the position of the best global gazelle (adult male). X_{rand} is the vector position of a random gazelle in the gazelle population [4].

b- Bachelor Male Herds (BMH):

As male gazelles mature, they tend to establish territories. They also want to capture female gazelles. This situation is shown in Equations 7-8.

$$BMH = (X(t) - D) + (ri_5 \times male_{gazelle} - ri_6 \times BH) \times Cof_r \quad (7)$$

$$D = (|X(t)| + |male_{gazelle}|) \times (2 \times r_6 - 1) \quad (8)$$

where $X(t)$ is the position of the gazelle in the t^{th} iteration. ri_5 and ri_6 are random integers 1 or 2. $male_{gazelle}$ is the position of the best global gazelle (adult male). BH is the young male herd coefficient vector. Cof_r are a randomly selected coefficient vectors. r_6 is also a random number between 0 and 1[4].

c- Migration to Search for Food (MSF):

Mountain gazelles constantly search for food sources in the search space, this situation is formulated by Equation 9 [4].

$$MSF = (Boundary_{upper} - Boundary_{lower}) \times r_7 + Boundary_{lower} \quad (9)$$

where $Boundary_{upper}$ and $Boundary_{lower}$ are the upper and lower bounds of the problem. r_7 is a random number between 0 and 1. Figure 1 shows the pseudo-code of MGO and Figure 2 shows the flowchart of MGO [4].

Algorithm 1: Pseudo-code of MGO

Start:

Set MGO's Parameters (N =population size, $Iter_{max}$ = maximum iteration, D =problem dimension)

Create a random gazelle population (X_i) ($i=1, 2, 3, \dots, N$)

Calculate objective values of the gazelle population

While ($t \leq Iter_{max}$) **do**

For ($int\ i=1; i \leq N; i++$)

 Calculate TSM using Equation 1.

 Calculate MH using Equation 6.

 Calculate BMH using Equation 7.

 Calculate MSF using Equation 9.

 Calculate objective values of the MSF , BMH , MH , and TSM .

 Add MSF , BMH , MH , and TSM in gazelle population.

For end

Gazelle population sorting in ascending order.

Update best gazelle.

Remove the four worst gazelles from the gazelle population.

End while

Return Global Gazelle

Stop.

Figure 1. The pseudo-code of MGO [4].

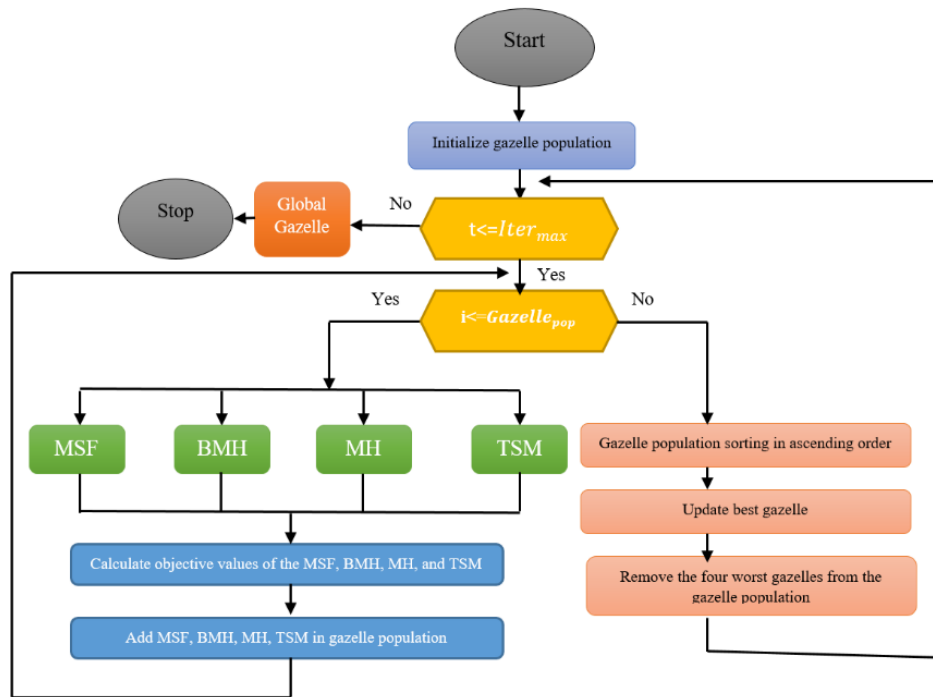


Figure 2. The flowchart of MGO [4]

2.2. Gazelle optimization algorithm (GOA)

Gazelles are creatures that can live in many areas, including arid areas and deserts. There are approximately 19 different species of gazelles worldwide [18]. They are mostly prey for other predators. Gazelles are light and fast and have a strong sense of hearing, sight and smell. These distinctive features are what allow them to escape predators. Gazelles are herbivores. They mostly socialize by living in groups. This situation is usually due to security. The more members there are in the group, the more secure the herd is. Sometimes groups of gazelles can group together depending on gender. Gazelles give birth once or twice a year. Reproduction generally occurs in seasons when water and food resources are abundant [5]. GOA was modeled on some characteristics of gazelles. These features can be listed as follows:

- The most notable aspects are grazing and escaping from predators.
- The grazing feature of gazelles can be used for exploitation. This should occur when there are no predators around.
- The situation of gazelles escaping from predators and reaching a safe environment has been used for exploration.

In GOA, initially all gazelles are randomly positioned in the search space. This situation is shown in Equations 10-11. Here D indicates the problem size ($D=1, 2, \dots, d$) and N indicates the population size ($N=1, 2, \dots, n$). X represents the gazelle population ($X=1, 2, \dots, N$). The X matrix is created at the lower and upper limits where the problem is defined. $Boundary_{upper}$ and $Boundary_{lower}$ are the upper and lower bounds of the problem. $rand$ is a random number [5].

$$X = \begin{bmatrix} x_{1,1} & x_{1,2} & \dots & x_{1,d-1} & x_{1,d} \\ x_{2,1} & x_{2,2} & \dots & x_{2,d-1} & x_{2,d} \\ \vdots & \vdots & \vdots & \vdots & \vdots \\ \vdots & \vdots & x_{i,j} & \vdots & \vdots \\ \vdots & \vdots & \vdots & \vdots & \vdots \\ x_{n,1} & x_{n,2} & \dots & x_{n,d-1} & x_{n,d} \end{bmatrix} \quad (10)$$

$$x_{i,j} = rand \times (Boundary_{upper,j} - Boundary_{lower,j}) + Boundary_{lower,j} \quad (11)$$

In each iteration, search agents produce a solution in a candidate. The *Elite* matrix is formed as best solution so far. This matrix is used in the displacement equations of gazelles in later stages. The *Elite* matrix is shown in Equation 12 [5]. The elite will be updated at the end of each iteration if a better gazelle replaces the best gazelle. $x'_{i,j}$ represents the position vector of the top gazelle [5].

$$Elite = \begin{bmatrix} x'_{1,1} & x'_{1,2} & \dots & x'_{1,d-1} & x'_{1,d} \\ x'_{2,1} & x'_{2,2} & \dots & x'_{2,d-1} & x'_{2,d} \\ \vdots & \vdots & \ddots & \vdots & \vdots \\ \vdots & \vdots & x'_{i,j} & \vdots & \vdots \\ \vdots & \vdots & \vdots & \vdots & \vdots \\ x'_{n,1} & x'_{n,2} & \dots & x'_{n,d-1} & x'_{n,d} \end{bmatrix} \quad (12)$$

The Brownian motion:

Equation 13 shows the standard brownian motion at point x ($\mu = 0$ and $\sigma^2 = 1$) [19].

$$fB(x; \mu, \sigma) = \frac{1}{\sqrt{2\pi\sigma^2}} \exp\left(-\frac{(x-\mu)^2}{2\sigma^2}\right) = \frac{1}{\sqrt{2\pi}} \exp\left(-\frac{x^2}{2}\right) \quad (13)$$

The Le'vy flight:

A random walk is performed using le'vy flight. Le'vy flight is shown in Equations 14-17 [20].

$$L(x_j) \approx |x_j|^{1-\alpha} \quad (14)$$

where α represents power-law exponent ($\alpha=(1,2)$). x_j represents the flight distance [20].

$$fL(x; \alpha, \gamma) = \frac{1}{\pi} \int_0^\infty \exp(-\gamma q^\alpha) \cos(qx) \delta q \quad (15)$$

where γ represents the scale unit [20].

$$Levy(\alpha) = 0.05 \times \frac{x}{|y|^\alpha} \quad (16)$$

where $x = Normal(0, \sigma_x^2)$ and $y = Normal(0, \sigma_y^2)$ [20].

$$\sigma_x = \left[\frac{\Gamma(1+\alpha) \sin(\frac{\pi\alpha}{2})}{\Gamma(\frac{(1+\alpha)}{2}) \alpha 2^{\frac{(\alpha-1)}{2}}} \right]^{1/\alpha}, \sigma_y = 1, \text{ and } \alpha = 1 \quad (17)$$

Exploitation:

In the exploitation phase of GOA, it is assumed that gazelles graze without predators or that the hunter follows the gazelles. At this stage, brownian motion was used in gazelle walks. This movement is shown in Equation 18 [5].

$$X_{i+1} = X_i + s.R * R_B * (Elite_i - R_B * X_i) \quad (18)$$

where X_{i+1} shows the position of the gazelle at the next iteration. X_i shows the position of the gazelle at the current iteration. s shows grazing speed of the gazelles. R is a vector of uniform random numbers [0,1]. R_B shows a vector containing random numbers representing the Brownian motion [5].

Exploration:

The exploration phase begins when gazelles see a predator. Gazelles start running and hunters chase them. Levy flight was used at this stage. Gazelles can make sudden changes in direction. With each iteration, a direction change was made in the GOA. The mathematical model of the gazelle's behavior when it detects the predator is as shown in Equation 19 [5].

$$X_{i+1} = X_i + S.\mu.R * R_L * (Elite_i - R_L * X_i) \quad (19)$$

where S shows the top speed. R_L shows a vector of random numbers based on Le'vy distributions. The movement of a gazelle being chased by a predator is shown in Equations 20-21 [5].

$$X_{i+1} = X_i + S.\mu.R * CF * R_B * (Elite_i - R_L * X_i) \quad (20)$$

$$CF = \left(1 - \frac{iter}{iter_{max}}\right)^{\left(2 \times \frac{iter}{iter_{max}}\right)} \quad (21)$$

where CF shows the cumulative effect of the predator [5].

The PSR value expresses the success rate of the predator. It affects the gazelle's ability to escape, which means the algorithm avoids getting stuck in the local minimum. The PSR effect on the algorithm is shown in Equations 22-23 [5]. Figure 3 shows the pseudo-code of GOA and Figure 4 shows the flowchart of GOA [5].

$$X_{i+1} = \begin{cases} X_i + CF[B_{lower} + R * (B_{upper} - B_{lower})] * U & \text{if } r \leq PSR \\ X_i + [PSR(1-r) + r](X_{r1} - X_{r2}) & \text{else} \end{cases} \quad (22)$$

$$U = \begin{cases} 0, & \text{if } r < 0.34 \\ 1, & \text{otherwise} \end{cases} \quad (23)$$

Algorithm 1: Pseudo-code of GOA

Start:
Set GOA's Parameters (N =population size, $Iter_{max}$ = maximum iteration, D =problem dimension)
Set GOA's Parameters ($s=[0,1]$; $\mu = [-1,1]$; $S=88\text{kmph}$; $PRS=0.34$)
Set GOA's Parameters (R and r random numbers $[0,1]$)
 Create a random gazelle population (X_i) ($i=1, 2, 3, \dots, N$)
While ($t \leq Iter_{max}$) **do**
 Calculate objective values of the gazelle population.
 Create *Elite gazelle* matrix using Equation 12.
 If $r < 0.5$ **then**
 Update gazelle using Equation 18.
 Else
 If $\text{mod}(\text{iter}, 2) = 0$ **then**
 $\mu = -1$;
 Else
 $\mu = 1$;
 If end
 If $\text{iter} < \text{size}(\text{gazelle}, 1) / 2$ **then**
 Update gazelle using Equation 19.
 Else
 Update gazelle using Equation 20.
 If end
 End If
 Update fitness values
 Update *Elite gazelle*
 Update best gazelle matrix
 Applying PRS effect using Equation 22.
 End while
Return Global Gazelle
Stop.

Figure 3. The pseudo-code of GOA

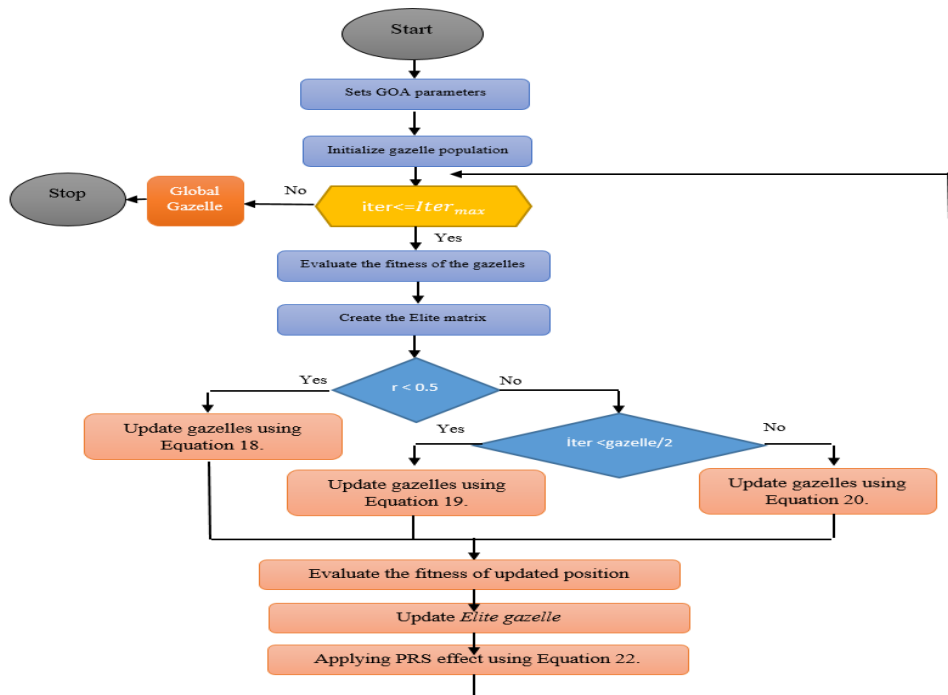


Figure 4. The flowchart of GOA

2.3. Classical benchmark functions

In this study, comparisons of MGO and GOA algorithms were compared on 13 classical test functions. These test functions are taken from <https://www.sfu.ca/~ssurjano/optimization.html> [1]. The classic test function consists of 7 unimodal and 6 multimodal test functions. Table 1 and Table 2 shows unimodal and multimodal test functions, respectively. Two different groups of benchmark functions were selected in this study. The reason for choosing these function

groups is to test the performance of MGO and GOA from different aspects.

The first group of functions, single-mode benchmark functions, has a single minimum and thus the utilization and convergence rates of MGO and GOA are tested. The second group of functions, multimodal benchmark functions, have multiple minima, making them more challenging than single-mode benchmarks. Thus, the exploration and exploitation capabilities of MGO and GOA can be tested by multimodal

benchmark functions. Figures 5-7 show 3D plots of F1 function, F9 function, and F11 function ([1, 21, 22]).

Table 1. The unimodal benchmark test functions of the mathematical formulations [1]

No	Range	F _{min}	Formulation
F1	[-100,100]	0	$f1(\vec{x}) = \sum_{i=1}^D x_i^2$
F2	[-10, 10]	0	$f2(\vec{x}) = \sum_{i=1}^D x_i + \prod_{i=1}^D x_i $
F3	[-100,100]	0	$f3(\vec{x}) = \sum_{i=1}^D ([x_i + 0.5])^2$
F4	[-100,100]	0	$f4(\vec{x}) = \max_i \{ x_i , 1 \leq i \leq D \}$
F5	[-30,30]	0	$f5(\vec{x}) = \sum_{i=1}^{D-1} [100(x_{i+1} - x_i^2)^2 + (x_i - 1)^2]$
F6	[-100,100]	0	$f6(\vec{x}) = \sum_{i=1}^D ([x_i + 0.5])^2$
F7	[-1.28,1.28]	0	$f7(\vec{x}) = \sum_{i=1}^D ix_i^4 + \text{random}[0,1]$

Table 2. The multimodal benchmark test functions of the mathematical formulations [1]

No.	Range	F _{min}	Formulation
F8	[-500, 500]	418,9829×5	$f8(\vec{x}) = \sum_{i=1}^n -x_i \sin(\sqrt{ x_i })$
F9	[-5.12, 5.12]	0	$f9(\vec{x}) = \sum_{i=1}^D [x_i^2 - 10 \cos(2\pi x_i) + 10]$
F10	[-32,32]	0	$f10(\vec{x}) = -20 \exp\left\{-0.2 \sqrt{\frac{1}{n} \sum_{i=1}^D x_i^2}\right\} - \exp\left\{\frac{1}{D} \sum_{i=1}^D \cos(2\pi x_i)\right\} + 20 + e$
F11	[-600, 600]	0	$f11(\vec{x}) = \frac{1}{4000} \sum_{i=1}^D x_i^2 - \prod_{i=1}^D \cos\left(\frac{x_i}{\sqrt{i}}\right) + 1$
F12	[-50,50]	0	$f12(\vec{x}) = \frac{\pi}{D} \left\{ 10 \sin^2(\pi y_1) + \sum_{i=1}^{D-1} (y_i - 1)^2 [1 + 10 \sin^2(\pi y_{i+1})] + (y_D - 1)^2 \right\} + \sum_{i=1}^D u(x_i, 10, 100, 4)$ $y_i = 1 + \frac{1}{4} (x_i + 1) u_{x_i, a, k, m}$ $= \begin{cases} k(x_i - a)^m & x_i > a \\ 0 & -a \leq x_i \leq a \\ k(x_i - a)^m & x_i < -a \end{cases}$
F13	[-50,50]	0	$f13(\vec{x}) = \frac{1}{10} \left\{ \sin^2(\pi x_1) + \sum_{i=1}^{D-1} (x_i - 1)^2 [1 + \sin^2(3\pi x_{i+1})] + (x_n - 1)^2 [1 + \sin^2(2\pi x_{i+1})] \right\} + \sum_{i=1}^D u(x_i, 5, 100, 4)$

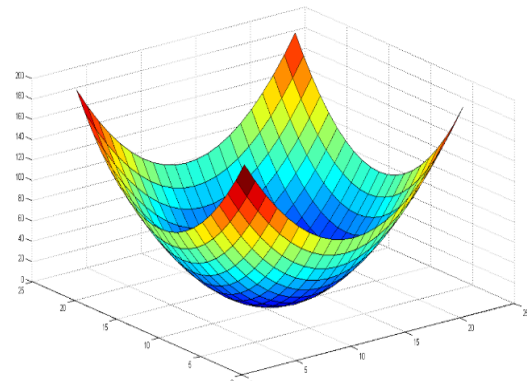


Figure 5. 3D plots of F1 function ([1], [21], [22])

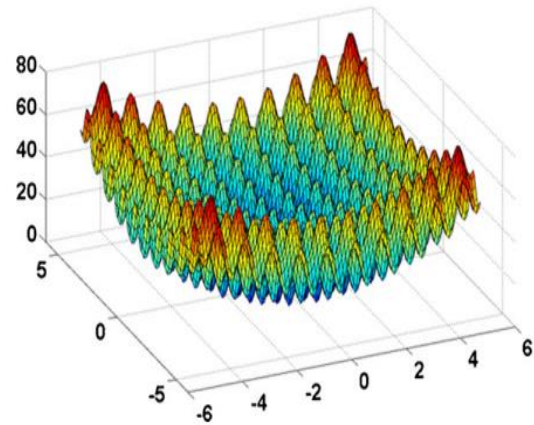


Figure 6. 3D plots of F9 function ([1], [21], [22])

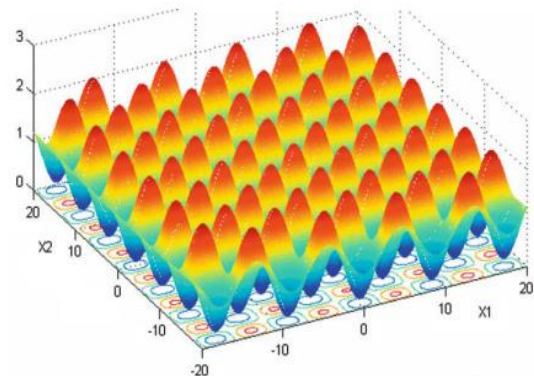


Figure 7. 3D plots of F11 function ([1], [21], [22])

3. Results and Discussion

3.1. The comparison of MGO and GOA on 13 classical benchmark functions

In this section, the results of MGO and GOA algorithms on 13 classical benchmarks in seven different dimensions are compared. The codes of the MGO and GOA algorithms were obtained from the mathworks library (<https://ww2.mathworks.cn/en/>). MGO and

GOA algorithms were run on a PC with Windows 10 Home with 64 bits operating system, Intel(R) Core(TM) i5 1.19 GHz CPU, and 12 GB RAM. Comparisons were made under equal conditions to ensure fairness. Parameter settings for both algorithms are shown in Table 3.

Table 3. The parameter settings for MGO and GOA

Parameters	Values
Population size (N)	30
Maximum iterations	200 ($Iter_{max}$)
Dimension (D)	10, 30, 50, 100, 500, 1000
GOA	PSRs = 0.34; S=0.88

There is no need for special fixed parameter tuning for MGO. The *PSRs* and *S* parameter settings used in GOA are determined as 0.34 and 0.88, respectively. These parameter settings were determined by the authors who proposed the GOA algorithm in the literature [5]. In this paper,

PSRs and *S* parameters are used at similar values. Both algorithms were run independently 20 times on 13 classical benchmarks. Best, worst, average (Mean), standard deviation (Std), and average time (Time) statistical evaluations were made on the results obtained. The results are shown for seven different sizes in Tables 4-10. Wilcoxon signed rank test was performed on the results to determine whether there were semantic differences between the MGO and GOA results. *p* and *h* values are shown in Table 11. The Wilcoxon signed rank test is a statistical test used to compare two samples of data to detect significant differences between them [23]. In this test, *p* value or *h* value are the criteria that determine the superiority of one algorithm over another. If the *p* value is equal to or above 0.05, there is no semantic difference and the *h* value is 0. If the *p* value is below 0.05, there is a semantic difference and the *h* value is 1.

Table 4. The results of the MGO and GOA on classical benchmark functions (D=10)

F_ID	MGO					GOA				
	Best	Worst	Mean	Std	Time	Best	Worst	Mean	Std	Time
F1	2.88e-52	6.80e-46	7.01e-47	1.70e-46	0.727	2.0e-38	1.76e-17	8.85e-19	3.83e-18	0.511
F2	8.65e-30	1.29e-25	2.27e-26	3.98e-26	0.751	6.93e-23	2.81e-11	1.42e-12	6.12e-12	0.721
F3	2.25e-17	5.99e-09	3.46e-10	1.30e-09	1.365	7.870e-16	1.55E-04	8.03e-06	3.38e-05	0.950
F4	1.01e-20	1.36e-15	6.96e-17	2.97e-16	1.069	1.90e-14	1.05E-03	6.06e-05	2.29E-04	0.722
F5	1.75e-12	1.68e-04	8.44e-06	3.66e-05	1.292	4.00E+00	5.85 e+00	5.19 e+00	0.48 e+00	0.712
F6	7.01e-19	7.56e-14	9.51e-15	2.04e-14	1.335	8.84e-05	1.70 E-03	5.98E-04	3.89E-04	0.724
F7	2.64e-05	1.18e-03	5.09e-04	3.39e-04	1.281	6.01E-04	6.24E-03	2.52e-03	1.26 e-03	0.758
F8	-4.19e+03	-4.19e+03	-4.19e+03	7.37e-12	1.401	-4.00E+03	-3.14E+03	-3.60E+03	2.42E+02	0.751
F9	0.00e+00	0.00e+00	0.00e+00	0.00e+00	1.378	0.00e+00	2.02e+00	0.15e+00	0.48e+00	0.712
F10	8.88e-16	4.44e-15	1.78e-15	1.54e-15	1.384	4.44e-15	5.02e-09	2.53e-10	1.09e-09	0.750
F11	0.00e+00	0.00e+00	0.00e+00	0.00e+00	1.178	0.00e+00	8.45E-02	1.04E-02	2.27E-02	0.784
F12	6.14e-24	1.53e-18	1.51e-19	3.40e-19	1.530	5.84e-06	3.52E-04	1.26E-04	9.14E-05	0.955
F13	7.72e-26	2.45e-20	1.41e-21	5.30e-21	1.529	1.71E-04	3.20E-03	1.03E-03	7.89E-04	0.980

Table 5. The results of the MGO and GOA on classical benchmark functions (D=20)

F_ID	MGO					GOA				
	Best	Worst	Mean	Std	Time	Best	Worst	Mean	Std	Time
F1	1.93E-36	7.18E-29	4.62E-30	1.60E-29	0.760	1.40E-25	8.46E-10	4.84E-11	1.85E-10	0.481
F2	4.45E-22	2.95E-18	3.79E-19	7.41E-19	1.054	2.05E-16	1.45E-05	7.27E-07	3.16E-06	0.455
F3	1.78E-11	2.08E-04	4.76E-05	6.99E-05	2.097	1.26E-05	1.16E+02	6.49E+00	2.53E+01	0.720
F4	1.31E-13	1.11E-10	1.43E-11	2.76E-11	1.082	1.03E-08	3.35E-02	3.18E+03	9.38E-03	0.468
F5	2.27E-14	3.75E-09	2.33E-10	8.21E-10	1.178	1.54E+01	1.86E+01	1.67E+01	6.37E-01	0.474
F6	1.46E-08	3.21E-06	7.31E-07	1.03E-06	1.342	8.62E-03	2.24E-01	9.06E-02	6.09E-02	0.467
F7	7.41E-05	3.12E-03	8.36E-04	7.02E-04	1.363	8.68E-04	2.69E-02	6.76E-03	5.86E-03	0.562
F8	-8.38E+03	-8.38E+03	-8.38E+03	1.18E-06	1.271	-6.02E+03	-4.64E+03	-5.23E+03	3.94E+02	0.477
F9	0.00E+00	0.00E+00	0.00E+00	0.00E+00	1.333	0.00E+00	1.52E+01	3.08E+00	5.23E+00	0.489
F10	8.88E-16	4.44E-15	3.73E-15	1.42E-15	1.515	1.15E-14	6.46E-03	3.37E-04	1.41E-03	0.480
F11	0.00E+00	0.00E+00	0.00E+00	0.00E+00	1.435	0.00E+00	7.65E-02	8.14E-03	2.00E-02	0.495
F12	1.01E-18	2.60E-13	4.25E-14	6.03E-14	1.769	1.73E-03	1.54E-02	5.59E-03	3.22E-03	0.614
F13	8.01E-19	1.56E-15	1.65E-16	3.42E-16	1.622	1.18E-02	1.97E-01	7.63E-02	4.62E-02	0.642

Table 6. The results of the MGO and GOA on classical benchmark functions (D=30)

F_ID	MGO					GOA				
	Best	Worst	Mean	Std	Time	Best	Worst	Mean	Std	Time
F1	3.99e-37	1.52e-27	8.630e-29	3.31e-28	1.089	1.02E-22	2.94E-04	2.40E-05	7.4E-05	0.508
F2	5.43e-19	1.57e-16	2.38e-17	4.04e-17	1.424	5.49E-14	4.30E-07	2.17E-08	9.36E-08	0.713
F3	5.27e-07	2.84E-02	2.87E-03	6.64E-03	2.816	3.85E-02	7.13E+02	4.93E+01	1.55E+02	1.336
F4	3.25e-13	3.85e-10	9.14e-11	1.05e-10	1.290	8.45E-07	6.10E-01	5.02E-02	1.38E-01	0.750
F5	3.60e-16	8.37e-10	7.48e-11	1.94e-10	1.530	2.65E+01	2.91E+01	2.73E+01	6.35E-01	0.907
F6	6.10e-08	8.42e-05	2.03e-05	2.43e-05	1.372	3.29E-01	1.42E+00	7.91E-01	2.92E-01	0.822
F7	7.77e-05	2.10E-03	8.18E-04	5.89E-04	1.491	3.75E-03	1.95E-02	7.68E-03	3.96E-03	0.867
F8	-1.26E+04	-1.26E+04	-1.26E+04	2.32E-04	1.431	-8.64E+03	-5.23E+03	-6.84E+03	7.55E+02	0.814
F9	0.00E+00	0.00E+00	0.00E+00	0.00E+00	1.542	0.00E+00	3.25E+01	2.66E+00	7.33E+00	0.827
F10	8.88e-16	4.71e-14	6.22e-15	9.50e-15	1.559	6.07E-12	5.12E-04	2.56E-05	1.11E-04	0.798
F11	0.00E+00	0.00E+00	0.00E+00	0.00E+00	1.514	0.00E+00	2.65E-02	2.08E-03	6.50E-03	0.842
F12	3.52e-15	4.47E-12	6.00e-13	1.09e-12	2.017	1.24E-02	5.70E-02	3.51E-02	1.30E-02	1.082
F13	7.53e-17	4.6e-14	7.93e-15	1.20e-14	2.045	2.70E-01	9.37E-01	5.48E-01	1.68E-01	1.054

Table 7. The results of the MGO and GOA on classical benchmark functions (D=50)

F_ID	MGO					GOA				
	Best	Worst	Mean	Std	Time	Best	Worst	Mean	Std	Time
F1	1.11E-30	2.55E-23	1.35E-24	5.55E-24	1.212	1.54E-17	4.24E-10	3.91E-11	1.12E-10	0.560
F2	1.58E-18	3.13E-14	2.76E-15	6.75E-15	1.476	6.92E-12	2.57E-03	1.31E-04	5.59E-04	0.793
F3	2.17E-06	1.62E+00	8.25E-02	3.53E-01	3.603	3.37E+01	3.32E+03	8.27E+02	8.84E+02	1.755
F4	4.76E-13	4.27E-09	4.50E-10	9.97E-10	1.341	2.77E-05	6.47E-01	5.05E-02	1.55E-01	0.72
F5	1.17E-12	1.09E-08	1.04E-09	2.48E-09	1.390	4.66E+01	4.87E+01	4.81E+01	6.37E-01	0.938
F6	3.83E-07	5.49E-03	6.81E-04	1.21E-03	1.325	2.30E+00	4.88E+00	3.57E+00	6.65E-01	0.812
F7	7.99E-05	3.43E-03	1.10E-03	8.33E-04	1.608	3.02E-03	8.15E-02	1.55E-02	1.77E-02	0.998
F8	-2.09E+04	-2.09E+04	-2.09E+04	3.85E-03	1.38	-1.04E+04	-7.54E+03	-8.47E+03	8.69E+02	0.836
F9	0.00E+00	0.00E+00	0.00E+00	0.00E+00	1.364	0.00E+00	8.82E+01	1.09E+01	2.63E+01	0.878
F10	8.88E-16	1.15E-13	1.40E-14	2.55E-14	1.381	2.47E-10	2.05E-02	1.11E-03	4.46E-03	0.888
F11	0.00E+00	0.00E+00	0.00E+00	0.00E+00	1.387	0.00E+00	6.53E-01	3.56E-02	1.42E-01	0.928
F12	6.32E-14	3.19E-11	4.15E-12	7.80E-12	2.458	7.24E-02	2.07E-01	1.24E-01	3.15E-02	1.219
F13	1.52E-15	5.08E-13	9.82E-14	1.24E-13	2.316	1.69E+00	5.03E+00	2.61E+00	6.91E-01	1.229

Table 8. The results of the MGO and GOA on classical benchmark functions (D=100)

F_ID	MGO					GOA				
	Best	Worst	Mean	Std	Time	Best	Worst	Mean	Std	Time
F1	3.43E-31	1.98E-24	2.73E-25	5.13E-25	1.021	6.53E-14	8.38E+01	4.20E+00	1.83E+01	0.849
F2	7.48E-17	6.56E-14	9.33E-15	1.71E-14	0.961	7.11E-10	2.13E-01	1.06E-02	4.64E-02	1.085
F3	1.89E-05	5.07E+00	9.08E-01	1.58E+00	6.223	7.51E+02	2.17E+04	8.43E+03	6.36E+03	3.278
F4	1.71E-12	2.22E-08	2.49E-09	5.03E-09	1.761	6.17E-04	5.55E-01	6.17E-02	1.22E-01	0.657
F5	2.47E-12	2.56E-08	2.48E-09	5.89E-09	1.831	9.78E+01	6.09E+04	3.14E+03	1.32E+04	0.986
F6	1.13E-05	2.83E-02	3.67E-03	7.58E-03	1.651	1.10E+01	1.70E+01	1.39E+01	1.31E+00	1.281
F7	2.42E-04	4.25E-03	1.56E-03	1.08E-03	2.331	4.67E-03	6.14E-02	1.59E-02	1.54E-02	1.649
F8	-4.19E+04	-4.19E+04	-4.19E+04	1.83E-02	1.778	-2.28E+04	-1.02E+04	-1.22E+04	2.77E+03	1.365
F9	0.00E+00	0.00E+00	0.00E+00	0.00E+00	1.591	2.50E-12	2.94E+01	1.72E+00	6.44E+00	1.338
F10	4.44E-15	7.61E-13	1.32E-13	2.18E-13	1.416	3.77E-08	4.27E+00	3.35E-01	1.05E+00	1.383
F11	0.00E+00	0.00E+00	0.00E+00	0.00E+00	1.715	4.77E-14	1.37E+00	7.61E-02	2.98E-01	1.439
F12	2.60E-14	2.61E-11	3.51E-12	7.04E-12	2.764	2.54E-01	4.42E-01	3.37E-01	5.86E-02	2.230
F13	1.86E-14	2.31E-12	6.56E-13	6.61E-13	2.82	7.88E+00	1.03E+02	1.70E+01	2.27E+01	2.267

Table 9. The results of the MGO and GOA on classical benchmark functions (D=500)

F_ID	MGO					GOA				
	Best	Worst	Mean	Std	Time	Best	Worst	Mean	Std	Time
F1	1.88e-27	1.19e-19	7.00e-21	2.59e-20	2.892	1.79E-09	1.81E+00	9.09E-02	3.94E-01	1.737
F2	7.12e-17	2.80e-11	1.68e-12	6.06e-12	3.147	5.85E-07	5.70E+80	2.85E+79	1.24E+80	2.597
F3	5.54E-01	1.23E+04	1.56E+03	2.90E+03	33.232	6.04E+04	5.56E+05	3.10E+05	1.55E+05	18.250
F4	2.20e-11	9.30e-08	8.12e-09	2.01e-08	2.718	1.04E-01	4.08E+01	1.19E+01	1.40E+01	2.585
F5	5.75e-12	3.78e-07	4.70e-08	8.35e-08	2.555	4.98E+02	5.39E+05	3.05E+04	1.17E+05	2.605
F6	2.16e-05	3.18E-01	5.26E-02	8.94E-02	2.791	1.04E+02	5.78E+02	1.33E+02	1.02E+02	2.502
F7	9.76e-05	9.15E-03	2.35E-03	2.09E-03	5.476	5.87E-03	1.31E-01	3.37E-02	3.17E-02	4.294
F8	-2.09E+05	-2.09E+05	-2.09E+05	6.13E-01	3.149	-3.76E+04	-2.26E+04	-2.72E+04	3.91E+03	2.431
F9	0.00E+00	0.00E+00	0.00E+00	0.00E+00	2.573	3.52E-10	3.95E+03	2.18E+02	8.62E+02	2.706
F10	1.87E-14	2.26E-11	2.75E-12	5.88E-12	2.887	3.65E-06	1.06E+01	1.13E+00	2.99E+00	2.795
F11	0.00E+00	0.00E+00	0.00E+00	0.00E+00	2.767	8.25E-10	3.51E+02	1.75E+01	7.64E+01	2.805
F12	2.54E-15	3.18E-11	4.16E-12	9.29E-12	8.111	7.85E-01	3.36E+01	2.82E+00	7.16E+00	6.266
F13	9.36E-14	5.53E-10	4.74E-11	1.21E-10	9.073	4.91E+01	2.05E+02	5.84E+01	3.39E+01	5.880

Table 10. The results of the MGO and GOA on classical benchmark functions (D=1000)

F_ID	MGO					GOA				
	Best	Worst	Mean	Std	Time	Best	Worst	Mean	Std	Time
F1	4.04e-26	8.78e-17	4.42e-18	1.91e-17	4.525	1.40E-07	1.51E+05	1.24E+04	3.81E+04	1.860
F2	5.20e-14	1.09e-11	2.32e-12	2.820e-12	5.260	5.27E+02	2.30E+163	1.15E+162	null	1.925
F3	2.43E+00	6.37E+04	1.41E+04	1.83E+04	82.032	3.87E+05	3.54E+06	1.58E+06	8.21E+05	26.34
F4	2.82e-12	2.98e-08	5.11e-09	9.04e-09	4.585	6.67E-01	9.97E+01	3.18E+01	3.00E+01	1.858
F5	1.99e-09	2.90e-06	2.54e-07	6.18e-07	4.778	9.98E+02	8.80E+07	4.44E+06	1.92E+07	1.947
F6	3.70e-06	1.04E+00	1.89E-01	2.91E-01	4.669	2.28E+02	4.94E+02	2.47E+02	5.67E+01	1.885
F7	1.12E-04	8.41E-03	2.14E-03	2.29E-03	9.406	1.00E-02	2.05E+00	1.63E-01	4.42E-01	3.577
F8	-4.19E+05	-4.19E+05	-4.19E+05	3.70E-01	5.281	-4.12E+04	-3.23E+04	-3.61E+04	2.28E+03	2.181
F9	0.00E+00	0.00E+00	0.00E+00	0.00E+00	4.977	6.52E-09	4.68E+02	2.80E+01	1.02E+02	2.029
F10	7.99E-15	2.72E-11	3.58E-12	6.75E-12	5.136	1.15E-05	8.73E+00	4.40E-01	1.90E+00	2.099
F11	0.00E+00	0.00E+00	0.00E+00	0.00E+00	5.125	1.20E-08	4.90E+02	2.45E+01	1.07E+02	2.121
F12	1.03E-16	2.19E-11	4.24E-12	6.16E-12	14.966	8.99E-01	2.28E+01	2.11E+00	4.74E+00	5.634
F13	1.77E-12	2.01E-09	1.91E-10	4.41E-10	15.096	9.90E+01	2.26E+03	2.24E+02	4.69E+02	5.605

Table 11. The wilcoxon signed rank test results of the MGO and GOA on classical benchmark functions (D={10, 20, 30, 50, 100, 500, 1000}) (p-value) (h-value)

F_ID	MGO-GOA													
	D=10		D=20		D=30		D=50		D=100		D=500		D=1000	
	p	h	p	h	p	h	p	h	p	h	p	h	p	h
F1	0.0002	1	0.00049	1	0.00049	1	0.00024	1	0.000244	1	0.000244	1	0.000244	1
F2	0.0049	1	0.00049	1	0.00049	1	0.00024	1	0.000244	1	0.000244	1	0.000244	1
F3	0.00097	1	0.00024	1	0.00024	1	0.00049	1	0.000244	1	0.000244	1	0.000244	1
F4	0.0048	1	0.00024	1	0.00024	1	0.00024	1	0.000244	1	0.000244	1	0.000244	1
F5	0.00098	1	0.00024	1	0.00024	1	0.00098	1	0.000244	1	0.000244	1	0.000244	1
F6	0.00024	1	0.00049	1	0.00049	1	0.00024	1	0.000244	1	0.000244	1	0.000244	1
F7	0.0068	1	0.00024	1	0.00024	1	0.00024	1	0.000244	1	0.000244	1	0.000244	1
F8	0.00049	1	0.00049	1	0.00049	1	0.00024	1	0.000244	1	0.000244	1	0.000244	1
F9	0.00049	1	0.00049	1	0.00049	1	0.00049	1	0.000244	1	0.000244	1	0.000244	1
F10	0.00049	1	0.00024	1	0.00024	1	0.00049	1	0.000244	1	0.000244	1	0.000244	1
F11	0.00098	1	0.00049	1	0.00049	1	0.00049	1	0.000244	1	0.000244	1	0.000244	1
F12	0.00489	1	0.00024	1	0.00024	1	0.00024	1	0.000244	1	0.000244	1	0.000244	1
F13	0.00342	1	0.00098	1	0.00098	1	0.00024	1	0.000244	1	0.000244	1	0.000244	1

Figures 8-13 show the convergence graphs of MGO and GOA on classical benchmark functions for dimension=30. Figures 14-17 show the boxplot graphs of MGO and GOA for D={10, 20, 30, 50, 100, 500, and 1000}, respectively. Boxplots show five features of a data set: minimum value, first (25%) quartile, median, third (75%) quartile, and maximum value. Minimum value is the lowest value, excluding outliers (shown at the end of the left). First quarter (25%) shows the twenty-five percent of the scores.

Median is the median marks the midpoint of the data and is represented by the line dividing the box into two parts. Third quarter (75%) is shows the seventy-five percent of the scores. Hence, 25% of the data is above this value. Maximum value shows the highest value excluding outliers. Box plots allow one to quickly identify mean values, distribution of the data set, and signs of variability (https://yalin-dunya.com/2020/06/19/kutu-grafigi-boxplot/).

According to Table 4, MGO achieved superior results than GOA in all classical functions in the best, Mean, and Std comparison criteria. When the time results are examined, it is seen that GOA works in a shorter time than MGO. Worst results are given for informational purposes only and do not mean anything when comparing MGO and GOA. The results obtained in Table 4 are similar in different dimensions (in Tables 5-10). When Table 11 is examined, it is seen that there is a semantic difference between MGO and GOA results in all classical benchmark functions and in all different dimensions. According to Figures 8-13, MGO converged much faster than GOA in all classical benchmark functions.

When Figures 14 - 17 are examined, it is seen that the data distributions are generally not symmetrical. Additionally, the five values (minimum value, first quartile, median, third quartile, maximum value) shown by the box plots are very close to each other. Outliers are observed in some dimension datasets.

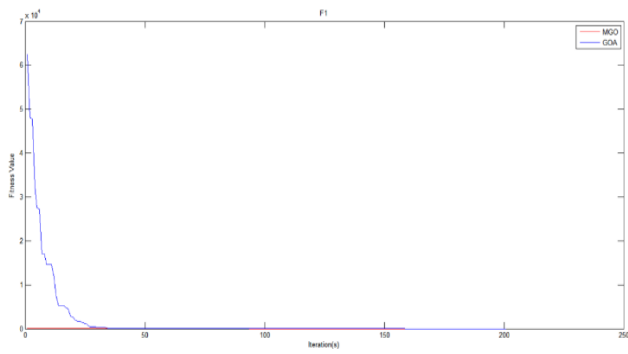


Figure 8. The convergence graphs of MGO and GOA for dimension=30 (F1)

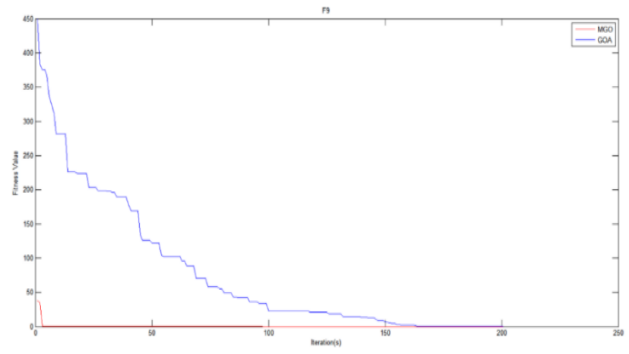


Figure 11. The convergence graphs of MGO and GOA for dimension=30 (F9)

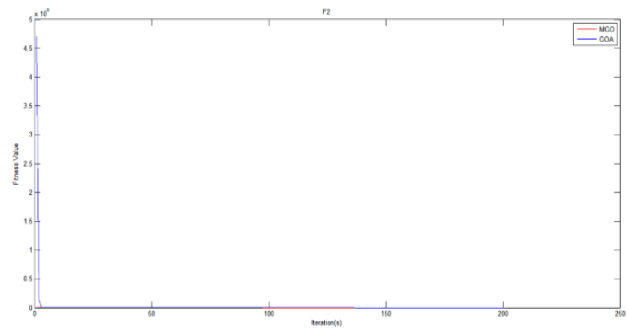


Figure 9. The convergence graphs of MGO and GOA for dimension=30 (F2)

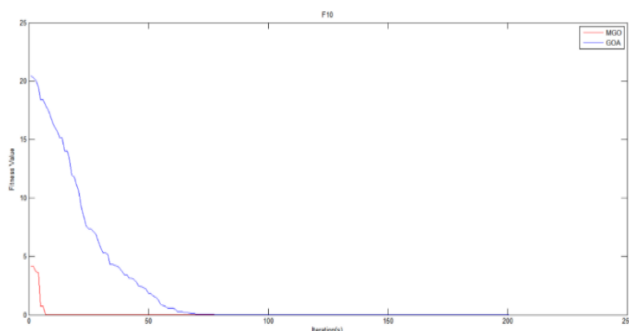


Figure 12. The convergence graphs of MGO and GOA for dimension=30 (F10)

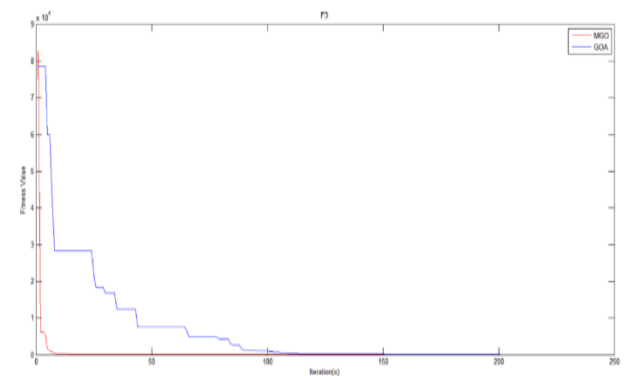


Figure 10. The convergence graphs of MGO and GOA for dimension=30 (F3)

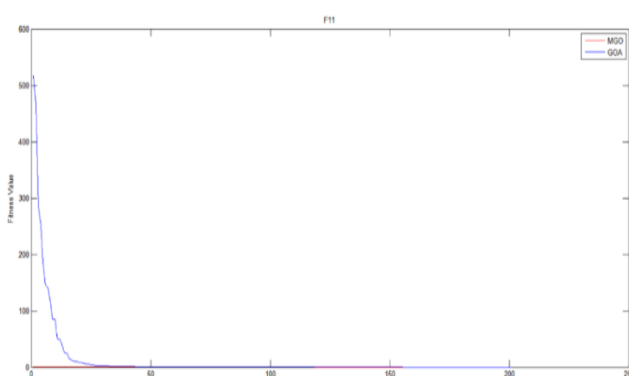
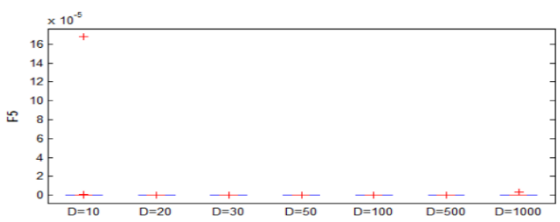
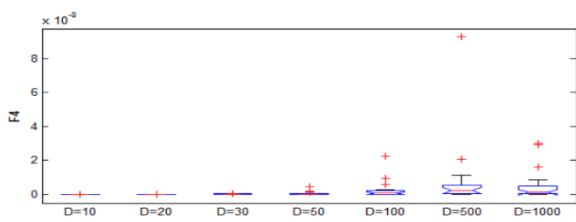
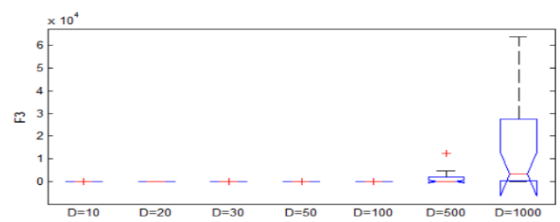
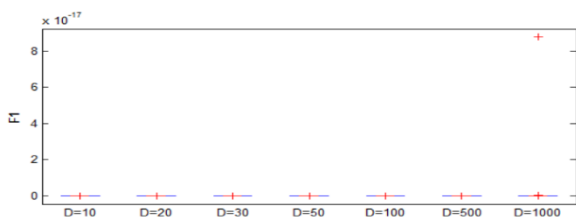


Figure 13. The convergence graphs of MGO and GOA for dimension=30 (F11)



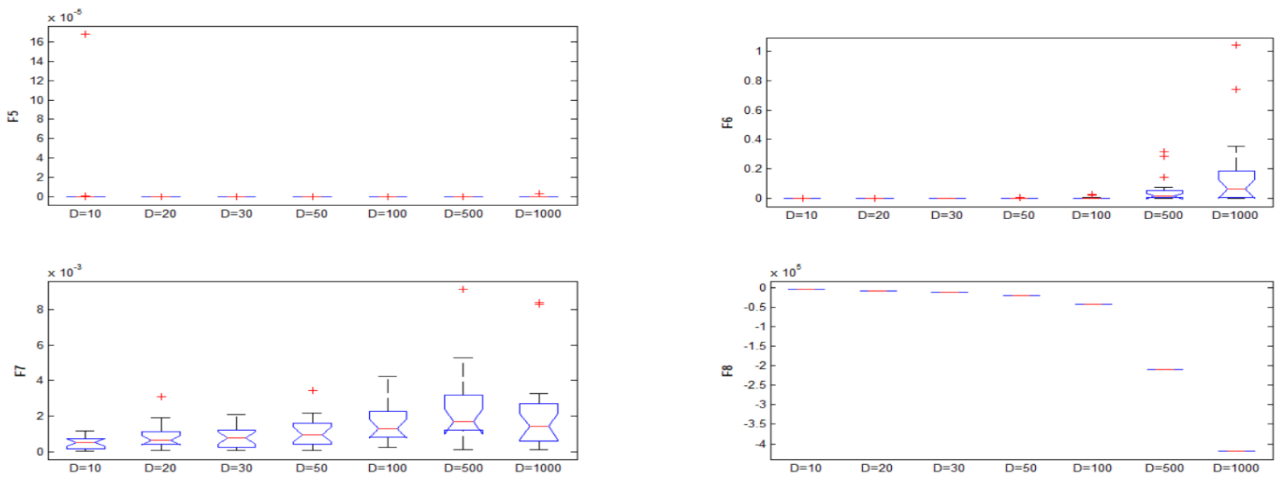


Figure 14. Boxplot graph of MGO for $D=\{10, 20, 30, 50, 100, 500, \text{ and } 1000\}$

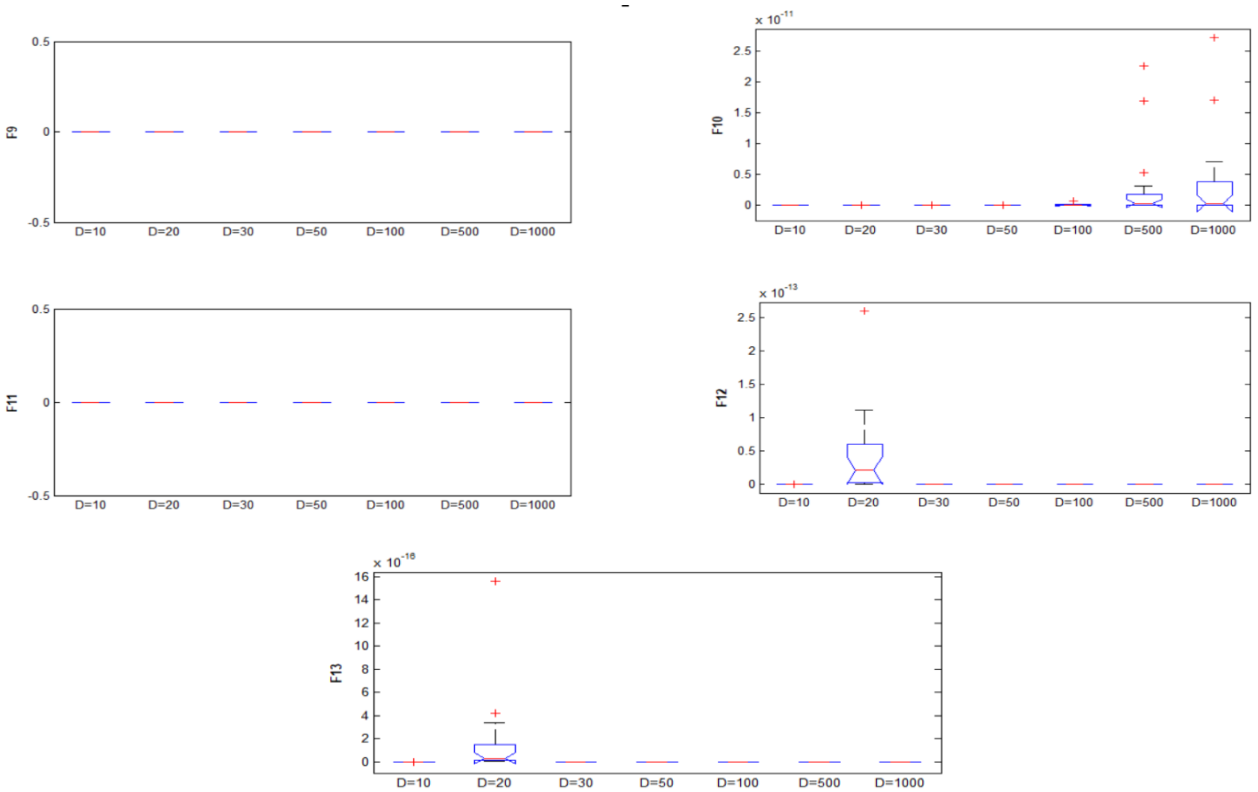
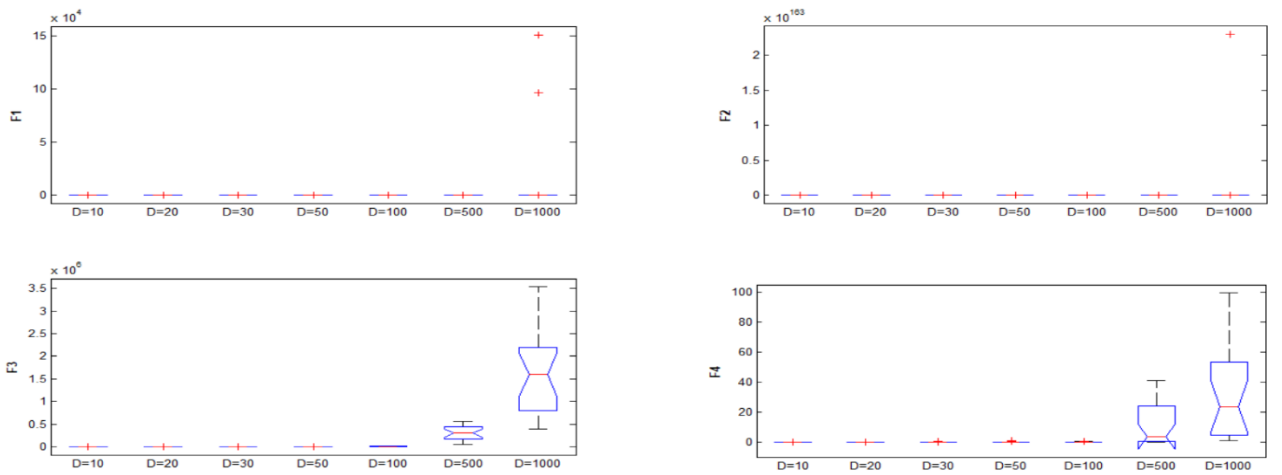


Figure 15. Boxplot graph of MGO for $D=\{10, 20, 30, 50, 100, 500, \text{ and } 1000\}$



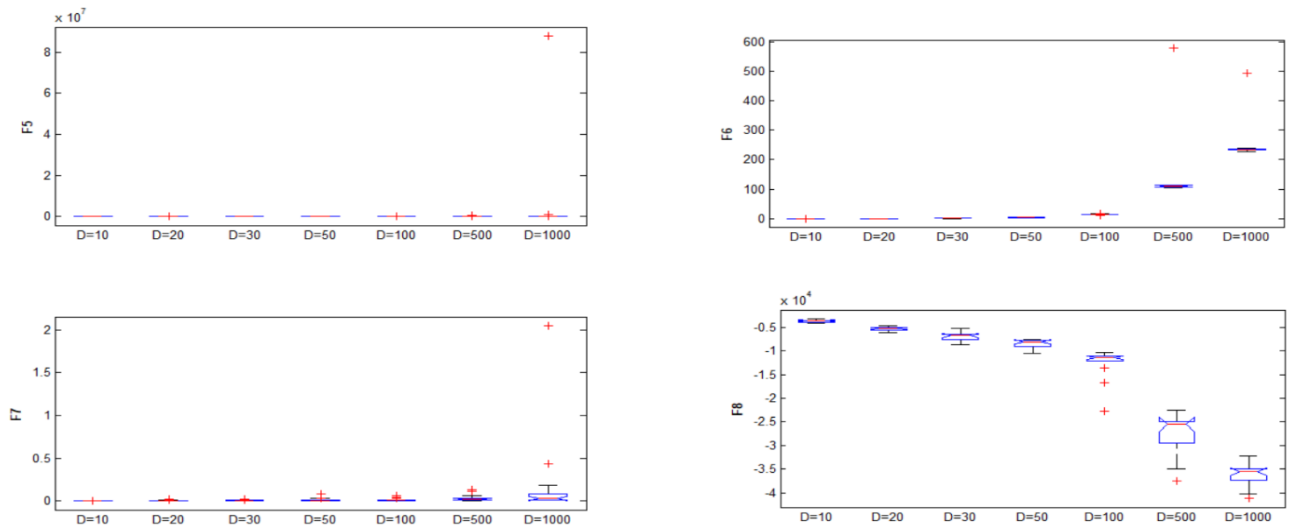


Figure 16. Boxplot graph of GOA for $D=\{10, 20, 30, 50, 100, 500, \text{ and } 1000\}$

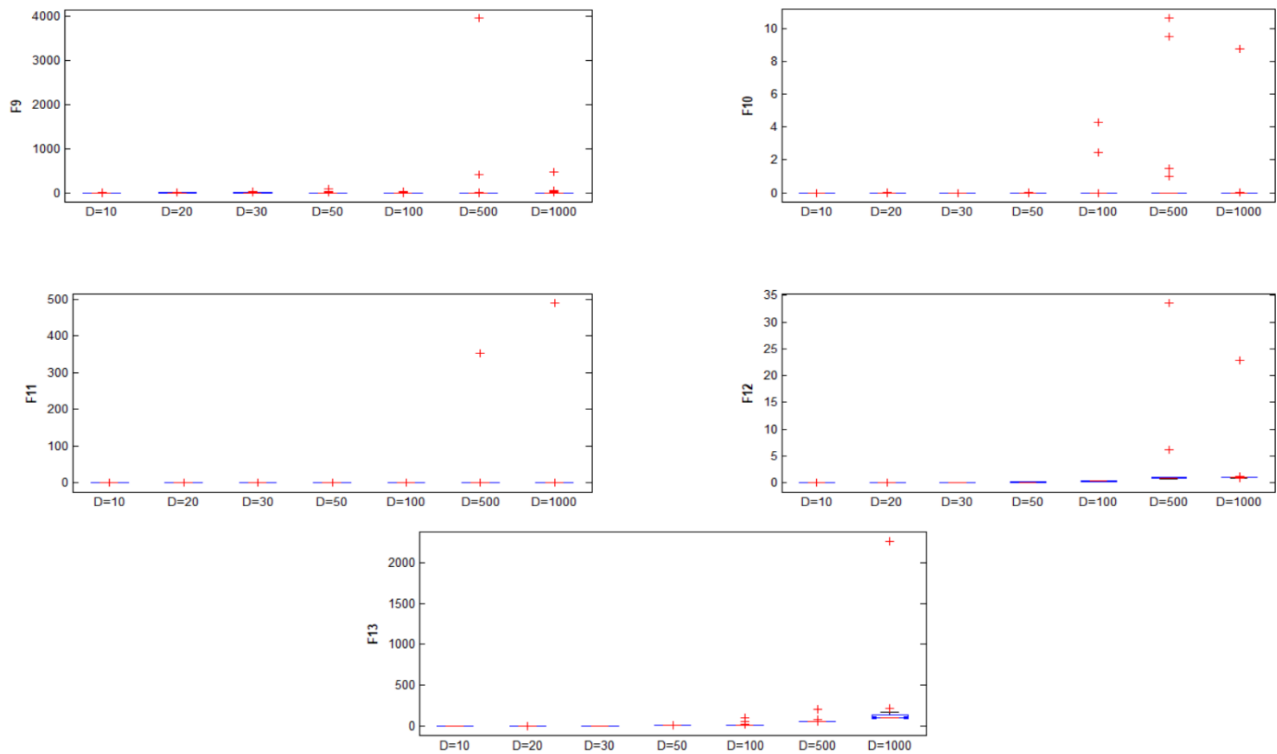


Figure 17. Boxplot graph of GOA for $D=\{10, 20, 30, 50, 100, 500, \text{ and } 1000\}$

3.2. The comparison of MGO and GOA on engineering design problems

Algorithms that are successful in classical benchmark functions can often fail to solve real-world problems. That's why MGO and GOA have been shown to be successful in three different engineering problems. The range of all variables in these problems is known and can be controlled [12, 13]. Every problem can be created as a mathematical model [12, 13]. These problems are often difficult to solve due to a lot of calculations and many variables that need to

be processed [12, 13]. Three engineering problems are selected in this subsection to measure the success of MGO and GOA algorithms in solving engineering problems.

3.2.1. The comparison of MGO and GOA on pressure vessel design problem

The aim of the pressure vessel design problem is to minimize the total cost of cylindrical pressure vessels [12, 13]. Problem variables: shell thickness (T_s), head thickness (Th), inner radius (R), and container length (L) [12, 13]. The

mathematical equations of the problem are shown in Equations 24-30 [12, 13]. MGO and GOA were run independently 20 times under equal conditions. The population size was determined as 30 and the maximum number of iterations was determined as 200. Best, worst, average (Mean), standard deviation (Std), and average time (Time) statistical evaluations were made on the results obtained. The statistical results are shown in Table 12. The values of the variable values (T_s , T_h , R , and L) in the case of the best cost result are shown in Table 13. Figure 18 shows the schematic view of the the pressure vessel design problem [12, 13]. Figure 19 shows the convergence graphs of MGO and GOA for the pressure vessel design problem.

According to Table 12, while MGO achieved the best results, GOA also achieved the best results in terms of mean and standard deviation. Additionally, GOA worked in a shorter time. According to Table 13, in 20 independent studies, MGO achieved a better result than GOA and obtained the corresponding problem

variables. Thus, MGO ranked first in the rank order. According to Figure 19, although MGO achieved a worse fitness at first, it converged to the best result with a faster convergence than GOA. GOA, on the other hand, achieved slower convergence in each iteration.

Variables:

$$\vec{x} = [x_1 \ x_2 \ x_3 \ x_4] = [T_s, T_h \ R \ L] \tag{24}$$

$$\text{Minimize } f(\vec{x}) = 0.6224x_1x_2x_3 + 1.7781x_2x_3^2 + 3.1661x_1^2x_4 + 19.84x_1^2x_3 \tag{25}$$

Subject to:

$$g_1(\vec{x}) = -x_1 + 0.0193x_3 \leq 0, \tag{26}$$

$$g_2(\vec{x}) = -x_2 + 0.00954x_3 \leq 0, \tag{27}$$

$$g_3(\vec{x}) = -\pi x_3^2 x_4 - \frac{4}{3}\pi x_3^3 + 1296000 \leq 0 \tag{28}$$

$$g_4(\vec{x}) = x_4 - 240 \leq 0. \tag{29}$$

Variable range:

$$0 \leq x_1, x_2 \leq 99, \ 10 \leq x_3, x_4 \leq 200 \tag{30}$$

Table 12. The statistical results of MGO and GOA for the pressure vessel design problem

Algorithm	Best	Worst	Mean	Std	Time
MGO	5888.0874	7318.982	6422.1588	506.88686	2.765137
GOA	5901.282591	6226.880046	5966.696622	73.00917999	0.699607

Table 13. The comparison results of MGO and GOA for the pressure vessel design problem

Algorithm	T_s	T_h	R	L	Best cost	Rank
MGO	0.77977687	0.38544411	40.4029465	198.8433	5888.0874	1
GOA	0.778731	0.389645	40.34135	199.7133	5901.282591	2

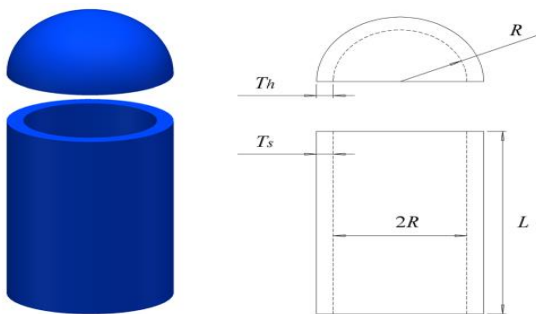


Figure 18. The The schematic view of the pressure vessel design problem [12, 13]

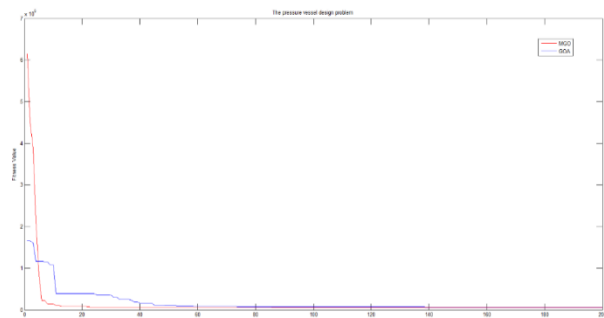


Figure 19. The convergence graphs of MGO and GOA for the pressure vessel design problem

3.2.2. The comparison of MGO and GOA on welded beam design problem

The goal of this problem is to obtain the minimum weight under four constraint conditions [12, 13]. Problem variables: weld

width h , connecting beam length l , beam height t , and connecting beam thickness b [12, 13]. The mathematical equations of the problem are shown in Equations 31-46 [12, 13]. MGO and GOA were run independently 20 times under equal conditions. The population size was

determined as 30 and the maximum number of iterations was determined as 200.

Best, worst, average (Mean), standard deviation (Std), and average time (Time) statistical evaluations were made on the results obtained. The statistical results are shown in Table 14. The values of the variable values (h , l , t , and b) in the case of the best cost result are shown in Table 15. Figure 20 shows the schematic view of the the welded beam design problem [12, 13]. Figure 21 shows the convergence graphs of MGO and GOA for the welded beam design problem.

According to Table 14, while GOA achieved the best results, MGO also achieved the best results in terms of mean and standard deviation. GOA worked in a shorter time than MGO. According to Table 15, in 20 independent studies, GOA achieved a better result than MGO and obtained the corresponding problem variables. Thus, GOA ranked first in the rank order. According to Figure 21, GOA converged to the best result with a faster convergence than MGO.

Variables:

$$\vec{x} = [x_1 \ x_2 \ x_3 \ x_4] = [h \ l \ t \ b] \tag{31}$$

$$\text{Minimize } f(\vec{x}) = 1.10471x_1^2x_2 + 0.04811x_3x_4 + (14.0 + x_2) \tag{32}$$

Subject to:

$$g_1(\vec{x}) = \tau(\vec{x}) - \tau_{max} \leq 0, \tag{33}$$

$$g_2(\vec{x}) = \sigma(\vec{x}) - \sigma_{max} \leq 0, \tag{34}$$

$$g_3(\vec{x}) = \delta(\vec{x}) - \delta_{max} \leq 0, \tag{35}$$

$$g_4(\vec{x}) = x_1 - x_4 \leq 0, \tag{36}$$

$$g_5(\vec{x}) = P - P_c(\vec{x}) \leq 0, \tag{37}$$

$$g_6(\vec{x}) = 0.125 - x_1 \leq 0, \tag{38}$$

$$g_7(\vec{x}) = 1.10471x_1^2 + 0.04811x_3x_4(14.0 + x_2) - 0.5 \leq 0, \tag{39}$$

where:

$$\tau(\vec{x}) = \sqrt{(\tau')^2 + 2\tau'\tau''\frac{x_2}{2R} + (\tau'')^2}, \tau' = \frac{P}{\sqrt{2x_1x_2}}, \tau'' = \frac{MR}{J}, \tag{40}$$

$$M = P\left(L + \frac{x_2}{2}\right), R = \sqrt{\frac{x_2^2}{4} + \left(\frac{x_1+x_3}{2}\right)^2}, \sigma(\vec{x}) = \frac{6PL}{x_4x_3^2}, \tag{41}$$

$$J = 2\left\{\sqrt{2x_1x_2}\left[\frac{x_2^2}{4}\left(\frac{x_1+x_3}{2}\right)^2\right]\right\}, \delta(\vec{x}) = \frac{6PL^3}{Ex_4x_3^2}, \tag{42}$$

$$P_c(\vec{x}) = \frac{4.01E\sqrt{\frac{x_2^2x_4^6}{0}}}{L^2}, \left(1 - \frac{x_3}{2L}\sqrt{\frac{E}{4G}}\right), \left(1 - \frac{x_3}{2L}\sqrt{\frac{E}{4G}}\right), \tag{43}$$

$$P = 6000lb, L = 14 \text{ in}, \delta_{max} = 0.25 \text{ in}, E = 30 \times 10^6 \text{ psi}, \tag{44}$$

$$\tau_{max} = 13600 \text{ psi}, \text{ and } \sigma_{max} = 30000 \text{ psi} \tag{45}$$

Variable range:

$$0.1 \leq x_1 \leq 2, \ 0.1 \leq x_4 \leq 2, \ 0.1 \leq x_1 \leq 10, \ 0.1 \leq x_1 \leq 10 \tag{46}$$

Table 14. The statistical results of MGO and GOA for the welded beam design problem

Algorithm	Best	Worst	Mean	Std	Time
MGO	2.397591	2.903343	2.507813	0.141959	1.97952
GOA	2.386234	3.334676	2.569828	0.255182	0.754791

Table 15. The comparison results of MGO and GOA for the welded beam design problem

Algorithm	h	l	t	b	Best cost	Rank
MGO	0.243847	6.026648	8.517861	0.243909	2.397591	2
GOA	0.243791	6.216256	8.324413	0.244319	2.386234	1

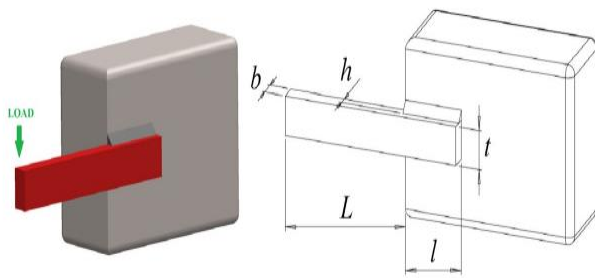


Figure 20. The schematic view of the welded beam design problem [12, 13]

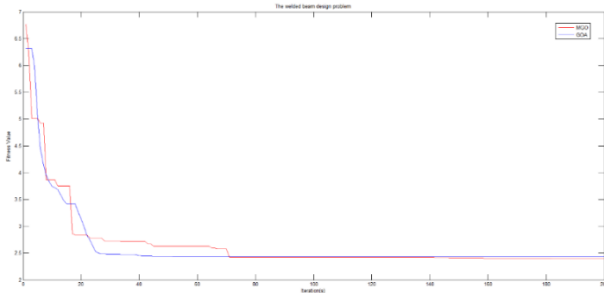


Figure 21. The convergence graphs of MGO and GOA for the welded beam design problem

3.2.3. The comparison of MGO and GOA on tension/compression spring design problem

The aim of the problem is to obtain the minimum spring mass with the existing variables and constraints [12, 13]. Problem variables: coil diameter d , average coil diameter D , and effective coil number N [12, 13]. The mathematical equations of the problem are shown in Equations 47-53 [12, 13]. MGO and GOA were run independently 20 times under equal conditions. The population size was determined as 30 and the maximum number of iterations was determined as 200. Best, worst, average (Mean), standard deviation (Std), and average time (Time) statistical evaluations were made on the results obtained.

The statistical results are shown in Table 16. The values of the variable values (d , D , and N) in the case of the best cost result are shown in Table 17. Figure 22 shows schematic view the tension/compression spring design problem [12, 13]. Figure 23 shows the convergence graphs of MGO and GOA for the tension/compression spring design problem.

According to Table 16, MGO achieved the best results in terms of best, mean, and standard deviation. GOA worked in a shorter time than MGO. According to Table 17, in 20 independent studies, MGO achieved a better result than GOA and obtained the corresponding problem variables. Thus, MGO ranked first in the rank order. According to Figure 23, MGO converged to the best result with a faster convergence than GOA.

Variables:

$$\vec{x} = [x_1 \ x_2 \ x_3] = [d \ D \ N] \tag{47}$$

$$\text{Minimize } f(\vec{x}) = (x_3 + 2) \times x_2 \times x_1^2 \tag{48}$$

Subject to:

$$g_1(\vec{x}) = 1 - \frac{x_3 \times x_2^3}{71785 \times x_1^4} \leq 0, \tag{49}$$

$$g_2(\vec{x}) = \frac{4 \times x_2^2 - x_1 \times x_2}{12566 \times x_1^4} + \frac{1}{5108 \times x_1^2} - 1 \leq 0, \tag{50}$$

$$g_3(\vec{x}) = 1 - \frac{140.45 \times x_1}{x_2^2 \times x_3} \leq 0, \tag{51}$$

$$g_4(\vec{x}) = \frac{x_1 + x_2}{1.5} - 1 \leq 0, \tag{52}$$

Variable range:

$$0.05 \leq x_1 \leq 2.0, \ 0.25 \leq x_2 \leq 1.3, \ 2.0 \leq x_3 \leq 15.0 \tag{53}$$

Table 16. The statistical results of MGO and GOA for the tension/compression spring design problem

Algorithm	Best	Worst	Mean	Std	Time
MGO	0.012682	0.017774	0.013348	0.001234	1.290039
GOA	0.01269	0.017423	0.013678	0.001482	0.617529

Table 17. The comparison results of MGO and GOA for the tension/compression spring design problem

Algorithm	d	D	N	Best cost	Rank
MGO	0.051513	0.352257	11.56701	0.012682	1
GOA	0.052776	0.383432	9.882135	0.01269	2

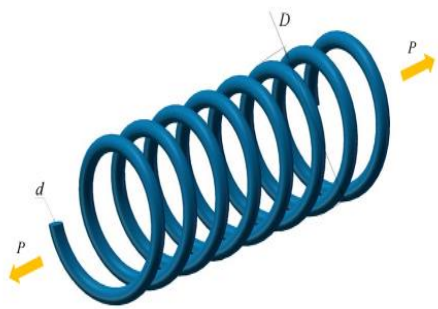


Figure 22. The schematic view of the tension/compression spring design problem [12, 13]

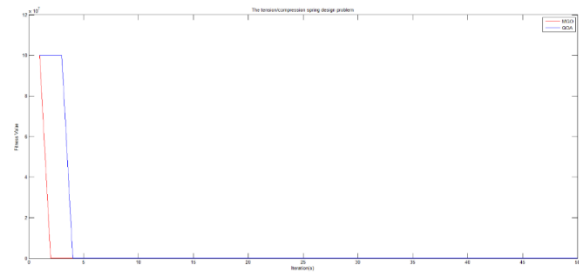


Figure 23. The convergence graphs of MGO and GOA for the tension/compression spring design problem

3.3.The comparisons of the MGO, GOA, and other algorithms on classical test Functions

In this subsection, three different heuristic algorithms newly proposed in recent years, MGO and GOA, are compared. Thus, the success of MGO and GOA was compared with the literature. Algorithms selected from the literature are as follows: Golden Search Optimization algorithm (GSO) [14], Crayfish Optimization Algorithm (COA) [13], and Zebra Optimization Algorithm (ZOA) [12]. The codes of the MGO, GOA, GSO, COA, and ZOA algorithms were obtained from the mathworks library (<https://ww2.mathworks.cn/en/>).

All algorithms were compared under equal conditions on 13 classical benchmarks. The population size was determined as 30, the maximum iteration was determined as 200, and the dimension was determined as 30. Each algorithm was run independently 20 times. Best, mean, standard deviation (Std), and average time (Time) calculations were made on the results.

The results are shown in Tables 18-19. Convergence graphs of the algorithms are shown in Figures 24-31.

When the average results are examined according to Table 18, the most successful algorithms are MGO and COA. Both algorithms showed superior success in 7 out of 13 functions. MGO and COA are followed by ZOA and GSO, respectively. The most unsuccessful algorithm was GOA. When Table 19 is examined, a similar situation can be seen. While MGO was especially successful in the F5, F6, F8, F9, F10, F11, F12, and F13 functions, COA was especially successful in the F1, F2, F3, F4, F9, F10, and F11 functions. Total average time results are listed in Table 19.

In this case, the fastest running algorithm was ZOA. It was followed by GSO and COA. The longest running algorithm was MGO. When the convergence graphs are examined, it is observed that GOA and GSO converge slowly, while MGO and COA converge faster.

Table 18. The comparisons results of the MGO, GOA, and other algorithms (D=30)

F_ID	MGO		GOA		GSO		COA		ZOA	
	Mean	Std	Mean	Std	Mean	Std	Mean	Std	Mean	Std
F1	8.630e-29	3.31e-28	2.40E-05	7.4E-05	3.00E-111	9.86E-111	0.00E+00	0.00E+00	4.10E-95	1.53E-94
F2	2.38e-17	4.04e-17	2.17E-08	9.36E-08	4.40E-57	1.33E-56	8.51E-156	0.00E+00	1.50E-51	4.10E-51
F3	2.87E-03	6.64E-03	4.93E+01	1.55E+02	8.21E-108	3.56E-107	0.00E+00	0.00E+00	1.06E-58	3.12E-58
F4	9.14e-11	1.05e-10	5.02E-02	1.38E-01	5.23E-46	2.27E-45	1.34E-160	0.00E+00	5.29E-44	1.33E-43
F5	7.48e-11	1.94e-10	2.73E+01	6.35E-01	2.42E+01	1.92E+01	2.84E+01	4.43E-01	2.87E+01	1.65E-01
F6	2.03e-05	2.43e-05	7.91E-01	2.92E-01	2.07E+00	1.94E+00	1.94E+00	6.55E-01	3.63E+00	5.29E-01
F7	8.18E-04	5.89E-04	7.68E-03	3.96E-03	4.11E-04	4.82E-04	2.41E-04	2.46E-04	2.19E-04	1.57E-04
F8	-1.26E+04	2.32E-04	-6.84E+03	7.55E+02	-1.03E+04	5.58E+02	-6.96E+03	9.87E+02	-6.26E+03	5.98E+02
F9	0.00E+00	0.00E+00	2.66E+00	7.33E+00	0.00E+00	0.00E+00	0.00E+00	0.00E+00	0.00E+00	0.00E+00
F10	6.22e-15	9.50e-15	2.56E-05	1.11E-04	8.88E-16	0.00E+00	8.88E-16	0.00E+00	8.88E-16	0.00E+00
F11	0.00E+00	0.00E+00	2.08E-03	6.50E-03	0.00E+00	0.00E+00	0.00E+00	0.00E+00	0.00E+00	0.00E+00
F12	6.00e-13	1.09e-12	3.51E-02	1.30E-02	5.93E-02	8.34E-02	1.24E-01	1.16E-01	2.44E-01	9.99E-02
F13	7.93e-15	1.20e-14	5.48E-01	1.68E-01	2.52E-01	2.82E-01	2.56E+00	2.32E-01	2.26E+00	3.08E-01

Table 19. The comparisons results of the MGO, GOA, and other algorithms (D=30)

F_ID	MGO		GOA		GSO		COA		ZOA	
	Best	Time	Best	Time	Best	Time	Best	Time	Best	Time
F1	3.99e-37	1.089	1.02E-22	0.508	5.43E-170	0.094	0.00E+00	0.454	3.72E-102	0.053
F2	5.43e-19	1.424	5.49E-14	0.713	2.91E-86	0.096	2.04E-236	0.512	9.39E-55	0.061
F3	5.27e-07	2.816	3.85E-02	1.336	1.59E-158	0.311	0.00E+00	1.189	5.22E-68	0.568
F4	3.25e-13	1.290	8.45E-07	0.750	3.93E-69	0.122	1.26E-211	0.767	2.14E-46	0.115
F5	3.60e-16	1.530	2.65E+01	0.907	1.37E+00	0.323	2.73E+01	0.711	2.84E+01	0.133
F6	6.10e-08	1.372	3.29E-01	0.822	4.69E-04	0.422	5.00E-01	0.497	2.30E+00	0.104
F7	7.77e-05	1.491	3.75E-03	0.867	6.19E-06	0.471	1.17E-05	0.518	1.96E-05	0.182
F8	-1.26E+04	1.431	-8.64E+03	0.814	-1.10E+04	0.207	-8.36E+03	0.574	-7.39E+03	0.107
F9	0.00E+00	1.542	0.00E+00	0.827	0.00E+00	0.198	0.00E+00	0.748	0.00E+00	0.125
F10	8.88e-16	1.559	6.07E-12	0.798	8.88E-16	0.186	8.88E-16	0.860	8.88E-16	0.160
F11	0.00E+00	1.514	0.00E+00	0.842	0.00E+00	0.193	0.00E+00	0.576	0.00E+00	0.159
F12	3.52e-15	2.017	1.24E-02	1.082	2.99E-04	0.300	3.30E-02	0.777	7.26E-02	0.400
F13	7.53e-17	2.045	2.70E-01	1.054	7.44E-03	0.306	2.06E+00	0.860	1.62E+00	0.411
Total Time:		2.11E+01		1.13E+01		3.23E+00		9.04E+00		2.58E+00
Rank:		5		4		2		3		1

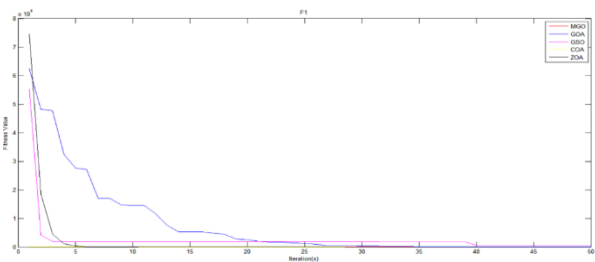


Figure 24. The convergence graphs of MGO, GOA, GSO, COA, and ZOA for dimension=30 (F1)

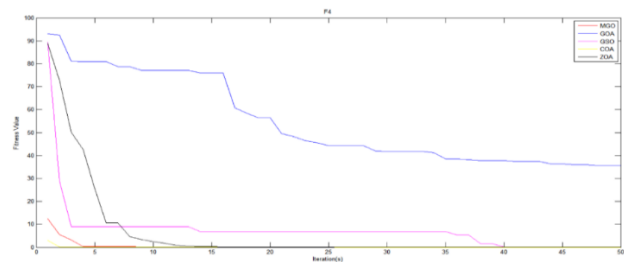


Figure 27. The convergence graphs of MGO, GOA, GSO, COA, and ZOA for dimension=30 (F4)

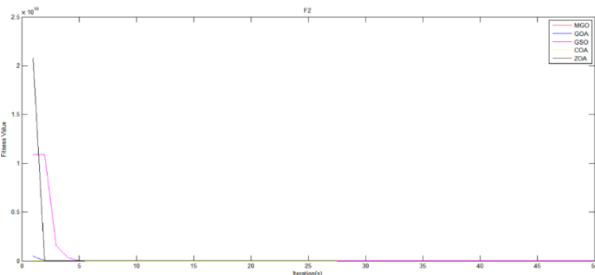


Figure 25. The convergence graphs of MGO, GOA, GSO, COA, and ZOA for dimension=30 (F2)

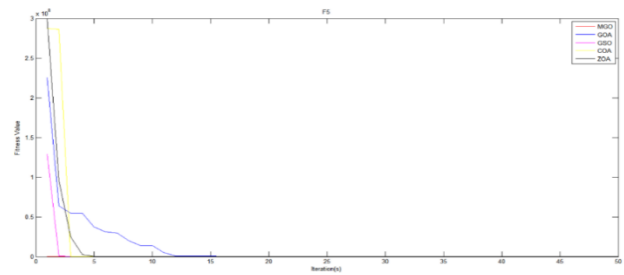


Figure 28. The convergence graphs of MGO, GOA, GSO, COA, and ZOA for dimension=30 (F5)

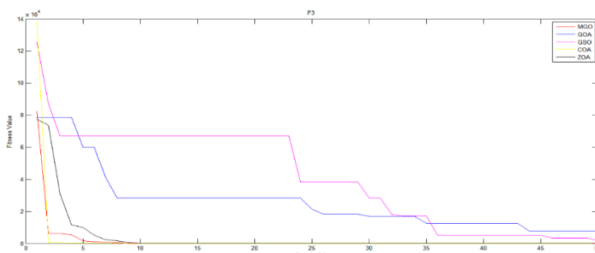


Figure 26. The convergence graphs of MGO, GOA, GSO, COA, and ZOA for dimension=30 (F3)

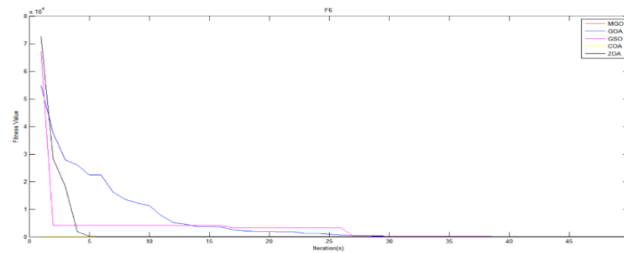


Figure 29. The convergence graphs of MGO, GOA, GSO, COA, and ZOA for dimension=30 (F6)

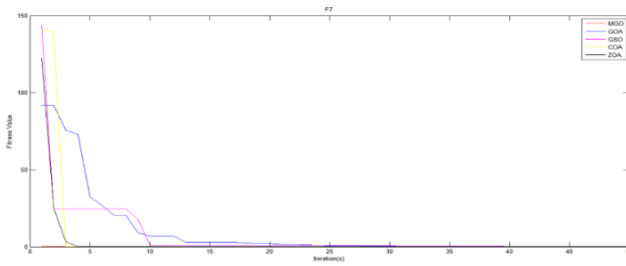


Figure 30. The convergence graphs of MGO, GOA, GSO, COA, and ZOA for dimension=30 (F7)

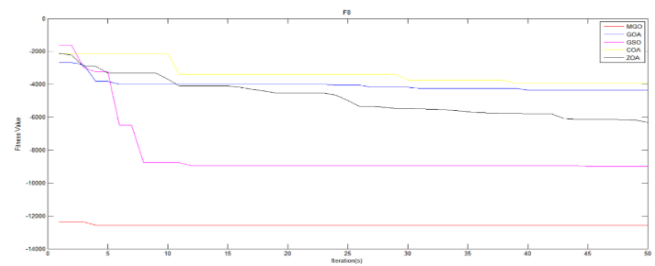


Figure 31. The convergence graphs of MGO, GOA, GSO, COA, and ZOA for dimension=30 (F8)

3.4. The parameter analysis for GOA and MGO algorithm

In this subsection, a population analysis was performed for MGO and GOA algorithms. In addition, $PSRs$ and S parameters, which are fixed parameters of GOA, were analyzed. There are no special fixed parameters for MGO. The discovery and exploitation abilities of these parameters on the algorithms are discussed.

To analyze the effect of population size on MGO and GOA, ten different values were examined ($N=\{10, 20, 30, 40, 50, 60, 70, 80, 90, \text{ and } 100\}$) on the classic benchmarks. MGO and GOA were run independently 20 times, with a dimension of 30 and a maximum iteration of 200. Average calculations were made on the results obtained. The results are shown in Tables 20-21. According to the results, as the population size increased, the performance of MGO and GOA increased. Inversely proportional to this, working time has also increased.

In this subsection, two fixed parameter analyzes that affect GOA's exploration and exploitation capabilities have been carried out. The first of these is the $PSRs$ parameter setting. The effect of nine different values on GOA ($PSRs=\{0.10, 0.15, 0.20, 0.25, 0.30, 0.35, 0.40, 0.45, \text{ and } 0.50\}$) for the $PSRs$ parameter was examined. GOA was run independently 20 times, with a dimension of 1000, a maximum iteration of 200, and a population size of 30. The mean of the results obtained are calculated and the results are shown in Table 22. According to Table 22, the most successful results were obtained when the $PSRs$ value was 0.50. It was later followed by 0.35. The $PSRs$ value was taken as 0.34 by Agushaka et al. in their original paper [5]. The findings obtained are parallel to the original paper. In this study, the $PSRs$ parameter value

was taken as 0.34 in the experimental part of the study.

The second parameter analysis performed on GOA is the S parameter value. the effects of nine different values for the S parameter on GOA were examined. The mean of the results obtained are calculated and the results are shown in Table 23. According to Table 23, the most successful results were obtained when the S value was 0.10. It was later followed by 0.90. The S value was taken as 0.88 by Agushaka et al. in their original paper. It has been observed that there is no full agreement between the value suggested in the original paper and the value found for the S value. In this study, in order to remain faithful to the original structure of GOA, the S parameter value was taken as 0.88 in the experimental part of the study.

4. Conclusion

In this study, two newly proposed heuristic algorithms in recent years were examined. These algorithms are mountain gazelle optimization (MGO) and gazelle optimization algorithm (GOA). both algorithms were inspired by the social lifestyle of gazelles. Due to this similarity, they are often confused in the literature and seen as the same algorithms. This study was carried out to eliminate this confusion. Four main factors in the life of mountain gazelles are used in the MGO mathematical model.

These are single male herds, natal herds, solitary, territorial males and migrate in search of food. MGO realizes its exploration and exploitation abilities with these four groups of mountain gazelles. The GOA model was inspired by the behavior of gazelles to escape from predators, reach safe environments and graze in safe environments. While the grazing behavior of gazelles in safe environments was used for the

exploitation ability of the GOA, the behavior of escaping from predators was used for the exploration ability of the GOA. MGO and GOA were run on 13 classical unimodal and multimodal benchmark functions in seven different dimensions (10, 20, 30, 50, 100, 500, 1000) and their success was compared. According to the results, MGO is more successful than GOA in all dimensions. GOA, on the other hand, works faster than MGO. Then, MGO and GOA were tested on 3 different engineering design problems. While MGO was more successful in the tension/compression spring design problem and welded beam design problems, GOA achieved

better results in the pressure vessel design problem. The success of MGO and GOA has been compared with 3 different algorithms (GSO, COA, and ZOA) that have been proposed in the literature in recent years. While MGO competes with literature algorithms, GOA lags behind the literature.

In future studies, it is planned to hybridize MGO and GOA (modified MGO-GOA) to obtain a more successful heuristic algorithm. It is planned to combine the superior aspects of both heuristic algorithms and eliminate the negative aspects.

Table 20. The population size analysis for MGO on classical benchmark functions (D=30, $Iter_{max}=200$, $PSRs = 0.34$, and $S=0.88$) (Mean)

F_ID	MGO									
	N=10	N=20	N=30	N=40	N=50	N=60	N=70	N=80	N=90	N=100
	Mean	Mean	Mean	Mean	Mean	Mean	Mean	Mean	Mean	Mean
F1	3.68E-20	5.76E-26	8.630e-29	2.46E-32	3.09E-34	1.96E-34	1.15E-36	1.14E-38	3.07E-39	7.36E-41
F2	4.15E-14	2.36E-15	2.38e-17	6.38E-19	1.17E-19	3.70E-21	1.74E-21	4.47E-22	3.82E-23	1.11E-23
F3	6.90E-01	2.36E-02	2.87E-03	1.57E-04	3.30E-04	1.71E-03	3.28E-05	3.15E-05	6.76E-06	1.75E-06
F4	4.45E-07	3.84E-10	9.14e-11	1.57E-11	3.95E-12	3.76E-13	1.19E-13	1.15E-13	1.12E-14	1.65E-14
F5	2.46E-06	2.02E-08	7.48e-11	4.91E-11	6.80E-12	1.38E-11	3.50E-11	1.95E-13	1.92E-12	8.12E-14
F6	3.16E-03	2.36E-04	2.03e-05	5.45E-06	3.18E-07	3.72E-08	2.19E-07	1.22E-08	5.13E-09	1.31E-09
F7	2.17E-03	1.37E-03	8.18E-04	7.43E-04	5.26E-04	6.18E-04	6.02E-04	3.76E-04	3.31E-04	3.06E-04
F8	-1.26E+04	-1.26E+04	-1.26E+04	-1.26E+04	-1.26E+04	-1.26E+04	-1.26E+04	-1.26E+04	-1.26E+04	-1.26E+04
F9	0.00E+00	0.00E+00	0.00E+00	0.00E+00	0.00E+00	0.00E+00	0.00E+00	0.00E+00	0.00E+00	0.00E+00
F10	2.13E-11	4.85E-14	6.22e-15	2.84E-15	2.31E-15	2.31E-15	1.60E-15	1.60E-15	1.60E-15	8.88E-16
F11	0.00E+00	0.00E+00	0.00E+00	0.00E+00	0.00E+00	0.00E+00	0.00E+00	0.00E+00	0.00E+00	0.00E+00
F12	5.75E-09	9.54E-12	6.00e-13	8.76E-14	6.01E-15	1.34E-15	7.88E-16	2.32E-16	8.11E-17	4.37E-17
F13	1.26E-10	2.17E-13	7.93e-15	2.75E-16	1.35E-16	3.73E-18	2.00E-18	2.61E-19	1.21E-19	1.60E-19
Total:	-12599.30	-12599.97	-12600.00	-12600.00	-12600.00	-12600.00	-12600.00	-12600.00	-12600.00	-12600.00
Rank:	10	9	7	8	5	6	4	3	2	1

Table 21. The population size analysis for GOA on classical benchmark functions (D=30, $Iter_{max} = 200$, $PSRs = 0.34$, and $S=0.88$) (Mean)

F_ID	GOA									
	N=10	N=20	N=30	N=40	N=50	N=60	N=70	N=80	N=90	N=100
	Mean	Mean	Mean	Mean	Mean	Mean	Mean	Mean	Mean	Mean
F1	1.19E-03	8.25E-07	2.40E-05	6.64E-06	1.36E-06	1.24E-14	9.35E-10	2.80E-08	6.63E-08	4.95E-08
F2	1.97E-04	1.55E-05	2.17E-08	1.13E-08	5.37E-06	3.57E-06	1.03E-06	2.91E-06	3.24E-06	2.02E-06
F3	4.07E+01	5.13E+01	4.93E+01	5.87E+01	8.86E+01	6.49E+01	5.86E+01	5.40E+01	5.08E+01	1.35E+01
F4	3.77E-01	4.37E-01	5.02E-02	2.80E-02	3.83E-02	1.02E-01	2.05E-04	1.36E-04	9.45E-04	7.32E-02
F5	2.92E+01	2.73E+01	2.73E+01	2.68E+01	2.66E+01	2.68E+01	2.62E+01	2.64E+01	2.61E+01	3.01E+01
F6	2.03E+00	8.48E-01	7.91E-01	4.58E-01	4.82E-01	4.03E-01	4.83E-01	3.64E-01	3.38E-01	2.72E-01
F7	2.25E-02	7.53E-03	7.68E-03	4.88E-03	5.81E-03	5.62E-03	3.82E-03	5.26E-03	2.91E-03	3.93E-03
F8	-6.04E+03	-6.42E+03	-6.84E+03	-7.04E+03	-6.85E+03	-6.96E+03	-7.12E+03	-7.30E+03	-7.57E+03	-7.17E+03
F9	1.09E+01	4.92E+00	2.66E+00	4.09E+00	4.32E+00	2.62E+00	4.57E+00	1.57E+00	2.94E+00	6.09E+00
F10	2.99E-05	2.01E-06	2.56E-05	5.33E-05	1.36E-04	8.64E-06	8.27E-07	2.11E-04	9.00E-06	7.29E-06
F11	1.01E-02	1.25E-03	2.08E-03	5.52E-04	7.29E-05	9.40E-04	1.19E-03	7.17E-04	5.02E-04	3.25E-03
F12	8.57E-02	4.01E-02	3.51E-02	2.81E-02	2.96E-02	2.50E-02	2.12E-02	2.20E-02	1.99E-02	1.40E-02
F13	1.36E+00	8.68E-01	5.48E-01	4.49E-01	4.08E-01	3.78E-01	3.24E-01	2.58E-01	3.27E-01	2.74E-01
Total:	-5.96E+03	-6.33E+03	-6.76E+03	-6.95E+03	-6.73E+03	-6.86E+03	-7.03E+03	-7.22E+03	-7.49E+03	-7.12E+03
Rank:	5	10	8	6	9	7	4	2	1	3

Table 22. The *PSRs* parameter analysis for GOA algorithm on classical benchmark functions (N=30, D=1000, $Iter_{max} = 200$, and $S = 0.88$)

F_ID	GOA								
	<i>PSRs</i> =0.10	<i>PSRs</i> =0.15	<i>PSRs</i> =0.20	<i>PSRs</i> =0.25	<i>PSRs</i> =0.30	<i>PSRs</i> =0.35	<i>PSRs</i> =0.40	<i>PSRs</i> =0.45	<i>PSRs</i> =0.50
	Mean	Mean	Mean	Mean	Mean	Mean	Mean	Mean	Mean
F1	2.66E+03	3.70E+02	1.12E-01	5.98E-01	1.38E+01	1.09E+02	3.48E+01	2.55E+01	4.58E+01
F2	2.07E+88	2.94E+166	1.57E+122	1.26E+110	6.10E+225	8.54E+02	4.49E+142	4.50E+202	5.73E+02
F3	9.46E+05	9.47E+05	1.03E+06	1.18E+06	8.81E+05	1.47E+06	1.50E+06	1.64E+06	2.42E+06
F4	9.47E+00	1.98E+01	2.14E+01	2.00E+01	2.59E+01	2.05E+01	2.83E+01	2.71E+01	3.92E+01
F5	6.95E+05	2.20E+03	8.46E+05	3.29E+05	7.45E+03	5.89E+05	3.83E+04	1.08E+03	6.10E+04
F6	6.55E+03	2.34E+02	3.15E+03	6.34E+03	2.72E+02	2.88E+02	2.36E+02	2.37E+02	1.80E+03
F7	2.68E+01	2.64E-01	1.68E+01	7.21E-02	6.57E-02	1.18E-01	1.41E+01	9.14E+00	8.06E+01
F8	-3.47E+04	-3.67E+04	-3.86E+04	-3.98E+04	-4.06E+04	-3.62E+04	-4.07E+04	-3.69E+04	-3.92E+04
F9	1.70E+00	5.16E+01	1.60E+02	1.94E+01	1.86E+01	1.58E+02	1.58E+01	1.67E+02	3.19E+02
F10	2.66E-01	7.02E-01	1.71E-01	2.70E-03	2.12E-01	7.21E-01	3.67E-01	3.50E-02	1.50E-01
F11	2.05E+00	9.27E-01	3.90E+01	2.78E+01	2.19E+01	2.40E+01	5.37E+01	6.14E+01	2.17E+00
F12	1.50E+00	1.01E+00	5.31E+04	2.94E+03	1.33E+00	1.49E+00	2.99E+04	2.15E+00	7.79E+01
F13	1.19E+02	1.13E+05	1.07E+02	1.15E+02	1.07E+02	8.50E+05	3.09E+06	4.98E+05	1.35E+02
Total:	2.07E+88	2.94E+166	1.57E+122	1.26E+110	6.10E+225	2.87E+06	4.49E+142	4.50E+202	2.44E+06
Rank:	3	7	5	4	9	2	6	8	1

Table 23. The *S* parameter analysis for GOA algorithm on classical benchmark functions (N=30, D=1000, $Iter_{max} = 200$, and $PSRs = 0.34$)

F_ID	GOA								
	<i>S</i> =0.10	<i>S</i> =0.20	<i>S</i> =0.30	<i>S</i> =0.40	<i>S</i> =0.50	<i>S</i> =0.60	<i>S</i> =0.70	<i>S</i> =0.80	<i>S</i> =0.90
	Mean	Mean	Mean	Mean	Mean	Mean	Mean	Mean	Mean
F1	3.32E+03	1.98E+02	4.11E+03	3.25E+03	3.04E-04	9.38E+03	1.05E+03	1.62E+02	4.25E-02
F2	8.90E+02	1.09E+29	1.14E+79	6.50E+142	3.41E+131	1.79E+161	1.58E+10	3.99E+67	8.15E+02
F3	1.14E+06	9.67E+05	9.64E+05	1.16E+06	1.16E+06	1.24E+06	1.47E+06	1.35E+06	1.29E+06
F4	6.40E+00	2.25E+01	1.59E+01	1.92E+01	1.53E+01	2.62E+01	1.90E+01	3.30E+01	3.54E+01
F5	2.37E+03	9.98E+02	1.33E+03	1.11E+04	6.83E+06	1.29E+03	1.05E+03	1.17E+03	3.36E+05
F6	2.52E+02	2.32E+02	2.51E+02	3.19E+03	1.62E+03	5.16E+02	2.34E+02	1.91E+03	5.63E+03
F7	2.06E-02	4.41E-01	7.11E-02	7.66E-02	1.23E-01	1.19E+01	8.69E-02	4.21E+01	3.24E+01
F8	-3.89E+04	-4.12E+04	-3.86E+04	-3.89E+04	-4.09E+04	-3.78E+04	-3.88E+04	-3.78E+04	-3.95E+04
F9	4.67E+00	4.88E+02	2.88E+02	4.66E+01	2.26E+02	5.46E+00	1.68E+02	7.81E+01	5.52E+00
F10	2.48E-01	4.00E-01	1.77E-01	7.17E-01	4.55E-01	3.22E-01	1.73E-01	8.70E-03	1.06E+00
F11	5.46E-02	1.14E-01	5.40E+01	1.92E+00	2.79E+01	9.49E-02	7.72E+01	2.88E+00	1.89E+00
F12	1.22E+00	5.38E+04	2.67E+00	1.08E+00	1.04E+00	1.68E+00	1.06E+00	1.61E+05	1.23E+00
F13	1.68E+02	4.96E+02	1.71E+02	1.15E+02	4.80E+02	1.06E+02	2.15E+03	3.07E+06	1.14E+04
Total:	1.11E+06	1.09E+29	1.14E+79	6.50E+142	3.41E+131	1.79E+161	1.58E+10	3.99E+67	1.60E+06
Rank:	1	4	6	8	7	9	3	5	2

Article Information Form

Funding

The author (s) has no received any financial support for the research, authorship or publication of this study.

The Declaration of Conflict of Interest/ Common Interest

No conflict of interest or common interest has been declared by the authors.

The Declaration of Ethics Committee Approval

This study does not require ethics committee permission or any special permission.

The Declaration of Research and Publication Ethics

The authors of the paper declare that they comply with the scientific, ethical and quotation rules of SAUJS in all processes of the paper and that they do not make any falsification on the data collected. In addition, they declare that Sakarya University Journal of Science and its editorial board have no responsibility for any ethical violations that may be encountered, and that this study has not been evaluated in any academic publication environment other than Sakarya University Journal of Science.

Copyright Statement

Authors own the copyright of their work published in the journal and their work is published under the CC BY-NC 4.0 license.

References

- [1] L. Abualigah, D. Yousri, M. Abd Elaziz, A. A. Ewees, M. A. Al-Qaness, A. H. Gandomi, "Aquila optimizer: a novel metaheuristic optimization algorithm," *Computers & Industrial Engineering*, vol. 157, pp. 1-37, 2021.
- [2] C. L. Hwang, A. S. M. Masud, "Multiple Objective Decision Making— Methods and Applications: A State-of-the-Art Survey," Berlin, Germany, Springer, 2012.
- [3] P. Agrawal, H. F. Abutarboush, T. Ganesh, A. W. Mohamed, "Metaheuristic algorithms on feature selection: A survey of one decade of research (2009–2019)," *IEEE Access*, vol. 9, pp. 26766–26791, 2021.
- [4] B. Abdollahzadeh, F. S. Gharehchopogh, N. Khodadadi, S. Mirjalili, "Mountain gazelle optimizer: A new nature-inspired metaheuristic algorithm for global optimization problems," *Advances in Engineering Software*, vol. 174, no. 103282, 2022.
- [5] J. O. Agushaka, A. E. Ezugwu, L. Abualigah, "Gazelle optimization algorithm: a novel nature-inspired metaheuristic optimizer," *Neural Computing and Applications*, vol. 35(5), pp. 4099-4131, 2023.
- [6] A. A., Heidari, S. Mirjalili, H. Faris, I. Aljarah, M. Mafarja, H. Chen, "Harris hawks optimization: Algorithm and applications," *Future Generation Computer Systems*, vol. 97, pp. 849–872, 2019.
- [7] S. Li, H. Chen, M. Wang, A. A. Heidari, S. Mirjalili, "Slime mould algorithm: A new method for stochastic optimization," *Future Generation Computer Systems*, vol. 111, pp. 300–323, 2020.
- [8] S. Kaur, L. K. Awasthi, A. L. Sangal, G. Dhiman, "Tunicate swarm algorithm: A new bio-inspired based metaheuristic paradigm for global optimization," *Engineering Applications of Artificial Intelligence*, vol. 90, pp. 103541, 2020.
- [9] A. Faramarzi, M. Heidarnejad, B. Stephens, S. Mirjalili, "Equilibrium optimizer: A novel optimization algorithm," *Knowledge-Based Systems*, Vol. 191, pp. 105190, 2020.
- [10] L. Abualigah, A. Diabat, S. Mirjalili, M. A. Elaziz, A. H. Gandomi, "The arithmetic optimization algorithm," *Computer Methods Applied Mechanics and Engineering*, vol. 376, pp. 113609, 2021.
- [11] A. Faramarzi, M. Heidarnejad, S. Mirjalili, A. H. Gandomi, "Marine predators algorithm: A nature-inspired metaheuristic," *Expert Systems with Applications*, vol. 152, pp. 113377, 2020.
- [12] E. Trojovská, M. Dehghani, P. Trojovský, "Zebra optimization algorithm: A new bio-inspired optimization algorithm for solving optimization algorithm," *IEEE Access*, vol. 10, pp. 49445-49473, 2022.
- [13] H. Jia, H. Rao, C. Wen, S. Mirjalili, "Crayfish optimization algorithm," *Artificial Intelligence Review*, pp. 1-61, 2023.
- [14] M. Noroozi, H. Mohammadi, E. Efatinasab, A. Lashgari, M. Eslami, B. Khan, "Golden search optimization algorithm," *IEEE Access*, vol. 10, pp. 37515-37532, 2022.
- [15] E. Baş, E. Ülker, "Comparison between SSA and SSO algorithm inspired in the behavior of the social spider for constrained optimization," *Artificial Intelligence Review*, vol. 54(7), pp. 5583-5631, 2021.

- [16] E. Baş, A. İhsan, “Performance analysis and comparison of gray wolf optimization and Krill herd optimization algorithm,” Pamukkale University Journal of Engineering Sciences, vol. 1000(1000), pp. 0-0, 2023.
- [17] G. A. Grau, F. R. Walther, “Mountain gazelle agonistic behaviour,” *Animal Behavior*, vol. 24 (3), pp. 626–36, 1976.
- [18] S. Omondi, “Gazelle Facts - Animals of the World. Retrieved from WorldAtlas / Environment, (2017, August 1). [Online]. Available: <https://www.worldatlas.com/articles/gazelle-facts-animals-of-the-world.html>.
- [19] A. Einstein, “Investigations on the Theory of the Brownian Movement Courier Corporation,” US, 1956.
- [20] R. N. Mantegna, “Fast, accurate algorithm for numerical simulation of Levy stable stochastic processes,” *Physical Review E*, vol. 49(5), pp. 4677, 1994.
- [21] R. Rajabioun, “Cuckoo optimization algorithm,” *Applied soft computing*, vol. 11(8), pp. 5508-5518, 2011.
- [22] A. Ahrari, M. R. Saadatmand, M. Shariat-Panahi, A. A. Atai, “On the limitations of classical benchmark functions for evaluating robustness of evolutionary algorithms,” *Applied Mathematics and Computation*, vol. 215(9), pp. 3222-3229, 2010.
- [23] F. Wilcoxon, “Individual comparisons by ranking methods,” in *Break throughs in Statistics*, New York, NY, USA: Springer, 1992, pp. 196–202.

Solid Waste Analysis and Improvement Studies in Local Governments (Çayırova Municipality Example)

Kader Duran¹ , Berna Kırıl Mert^{1*} 

¹Department of Environmental Engineering, Sakarya University, Sakarya, Türkiye, kaderonal@yahoo.com, bkiril@sakarya.edu.tr

*Corresponding Author

ARTICLE INFO

ABSTRACT

Keywords:
Solid waste
Characterization
Waste management
in municipalities
Integrated waste management



Article History:
Received: 04.12.2023
Accepted: 05.03.2024
Online Available: 14.06.2024

Solid wastes have become one of the most critical problems in urban areas because of the increase in the amount and the environmental problems caused by the variety of these wastes. In the same local governments where waste management is mismanaged, much money is wasted, and landfills are unnecessarily occupied. Making a profit out of solid wastes, seen as a heavy burden to the world and our country, aims firstly to collect these wastes apart from their sources by characterizing them. Recycling of both household and industrial wastes should be planned and done at the source. Collection is the most laborious and costly element of solid waste management. The study area was divided into four groups according to income levels, and the waste generated there was evaluated. The study showed that for 2022, kitchen waste ranks first with 67.25%. Kitchen waste is followed by packaging waste at 21.03%; flammable wastes (textile etc.) at 21.04%; ash waste at 44%, While hazardous wastes have a share of 0.55%; lastly, park and garden wastes and electronic wastes were not detected at all. It is seen that waste management activities are carried out in the Çayırova region, but the integration of citizens into waste management activities needs to be increased. In this regard, improvement efforts have been made to increase efficiency in separating collection from the source and reduce the amount of final waste.

1. Introduction

In Environmental Law No. 2872, solid waste is defined as "solid waste materials that are generated as a result of domestic, commercial and/or industrial activities, which are intended to be disposed of by the producer on the grounds that they are no longer useful, and which must be disposed of regularly in order to protect the peace of the society and especially the environment" [1].

The two most essential parameters in solid waste generation are population and unit solid waste production amount. The amount of unit solid waste production varies depending on factors such as socio-economic status, living standards, living habits, geographical location, climate characteristics, and the size of the settlement. In

general, as people's economic status increases, the amount of waste they create also increases. There is a continuous increase for waste produced per person due to reasons such as rapid urbanization and increasing consumption trends in parallel with changes in living conditions [2].

Solid wastes have become one of the most critical problems in urban areas due to the increase in their amount and the serious environmental problems caused by the diversity in their content. It is possible to classify the methods used to eliminate the solid waste problem caused by human activities as irregular (wild) storage, regular storage, composting, reuse, recycling, recovery, and incineration [3, 4].

Landfill is the most common way to reduce the amount of solid waste. However, any waste not

separated at its source will unnecessarily occupy the sanitary landfills and adversely affect public health by increasing the formation of flies and mice in provinces and/or towns without sanitary landfill facilities [5]. In addition, considering our rapidly developing cities and increasing population, it has become challenging to meet the criteria in the Regulation on the Landfill of Wastes, which came into force after being published in the Official Gazette dated 26.03.2010 and numbered 27533 for sanitary landfills [6].

Domestic solid wastes pose a biological, physical, and chemical hazard to human and environmental health. If solid wastes are not disposed of in accordance with the technique, leachate generated in landfills can cause pollution of soil, surface, and underground waters, while landfill gas can cause air pollution due to its high methane content, causing chemical and biological problems [7]. According to the European Union Waste Framework Directive, the first goal of any waste policy should be to reduce the harmful effects of waste production and management on human health and the environment [2]. On the other hand, solid waste management aims to use scarce natural resources such as energy and raw materials with maximum efficiency, support low-waste production, recover and reuse wastes, and dispose of them without harming air, water, soil, and living things in all disposal processes. The daily increase in solid waste with industrialization and the development of environmental awareness in global market economy conditions necessitate effectively managing these solid wastes [8]. The first step of waste management begins with separating waste at its source. Solid wastes It is divided into various branches as domestic wastes, packaging wastes, domestic, commercial wastes, coarse bulky wastes, rubbish wastes, treatment sludge, marketplace wastes, hazardous and medical wastes, construction wastes, accumulators and waste batteries, and end-of-life tires [9, 10]. The National Waste Management and Action Plan (NWMAP) covering 2016-2023 has been prepared. National Waste Management and Action Plan (2016-2023), in order to achieve the goals of an integrated waste management system in all 81 provinces, to reduce and limit the

amount of waste going to landfills within the framework of the circular economy, and to determine the targets for the needed waste recovery, recycling and energy production. It was published in 2017 for this purpose. According to the National Waste Management and Action Plan, it aims to recover 35% of the waste generated in 2023 and dispose of 65% by landfill. NWMAP revision studies have been initiated for the years 2023-2035 in order to harmonize existing management plans with the zerowaste management plan, increase and disseminate separate collection efficiency at the source, and determine recovery and disposal methods. According to the Ministry of Environment, Urbanization and Climate Change data, this figure is currently 22.4% in Türkiye [11].

The collection, removal, and disposal of solid wastes fall under the responsibility of local governments. The provision of these services requires a holistic approach, which is achieved through solid waste management [12].

Our Constitution has made local governments responsible for waste collection, transportation, and disposal following Municipality Law No. 5393 [13] and Metropolitan Municipality Law No. 5216 [14-15]. In our country, there are two different types of local government units as villages and municipalities in the local government system [16]. In addition, according to these laws, the task of disposing of solid wastes is assigned to metropolitan municipalities in places with a metropolitan organization and to provincial, district, and town municipalities without a metropolitan organization [17].

For the protection and improvement of the environment, municipalities' implementation of a transparent management model and their openness to public participation, and therefore acting in cooperation and communication with the public, will ensure the integration of the municipality and the local people. As the "Local Environmental Manager" and the self-organization of society, municipalities should realize this natural necessity—environmental management at different growing scales and including each other. Local governments, especially municipalities, have a particular

importance in these structures. Because municipalities are institutions that both affect the environment with the other public services they carry out and can directly assume functions in environmental management [18].

It is seen that consumption culture in the world is shaped according to income level. The income level is efficient for waste generated. Countries in the upper-income group produce more waste, while countries in the lower-income group produce the least waste. It is observed that a person living in high-income countries, that is, in developed countries, produces waste between at least 0.70 kg and at most 14 kg per day [19]. On average, a high-income person generates nearly three times more waste than a low-income person. The waste produced by the upper-income group constitutes approximately 46% of the total produced globally. In other words, about half of the waste produced in the world is produced by the upper-income group. People in wealthy, developed, and underdeveloped or developing countries can be low-income, lower middle income, upper-middle-income, or high-income. Considering the composition of the wastes produced in developed countries, the organic wastes produced are at a lower rate than those in developing countries. In addition, it is noteworthy that metal, paper, and glass wastes are high. Today, countries in Africa and South Asia produce the least amount of waste globally, while developed countries such as the USA, Canada, Germany, England, etc. OECD countries, which are formed by countries, produce about half of the waste produced in the world [20].

In the study conducted by Pires et al. in 2011, models and tools that will eliminate the uncertainties in waste management studies in European countries as much as possible were carried out comprehensively. They covered the pros and cons of waste management practices in each European Union member country. On the other hand, while Southern European Union countries need to develop more measures and reach EU directives to implement integrated solid waste management, the middle/central European Union needs models and tools to make technological preference management strategies efficient. However, it is also stated that system

analysis models and tools, taken together, will provide opportunities to develop better solid waste management strategies that will ensure compliance with current standards and help develop future perspectives of both the waste management industry and government agencies in the EU [21]. Within the scope of solid waste management in Türkiye, different studies have been carried out for the evaluation of solid waste management based on provinces and districts such as Eskişehir, Malatya, Bitlis, Konya, İstanbul, Bursa [7, 20, 22-25]. In the study of Güvenç (2016), they stated that electricity generation from solid waste and solid waste characterization are the most critical factors affecting environmental sustainability, and they stated that municipal solid waste characterization depends on social status and income level. The characterization study, carried out by conducting a seasonal analysis of the amount of municipal solid waste generated in the Kartal District of Istanbul, depending on the income level, aimed to determine the diversity in the waste components [24]. In another study, because of the analysis made throughout Türkiye, it was thought that it would be beneficial for municipalities to organize waste collection activities effectively because of determining the optimum population sizes for the municipalities to perform waste management activities effectively and estimating the marginal and average costs of the waste management system [8].

In this study, based on 2022, the processes of reducing the waste at the source and evaluating the wastes, from the generation of domestic waste to the disposal process, were evaluated according to the income levels in the borders of Çayırova District. In addition, how waste characterization has changed with the last ten years' data was examined and compared.

2. Material and Method

The rapidly increasing population and urbanization process have become one of the current problems of solid waste treatment, which is a part of local governments. In order to protect environmental health in urban areas, a planned solid waste management is needed to eliminate solid wastes that need to be regularly collected,

transported, stored and disposed of without causing major problems [26].

2.1. General information about Çayırova District

Çayırova, one of the most important industrial districts of Kocaeli, which is considered in the study, is Gebze in the east and south. The Şifa District of Tuzla, which is located within the borders of Istanbul in the west, is also located in the Akfırat District of Tuzla District in the north, and the area of the district is 27.391,221m². Çayırova Municipality 2022 population is 150.792.

As it is known, the essential condition for the proper execution of waste management is the excellent management of waste characterization. Among the factors affecting the character of waste are seasons, the economic situation of the people in the region, and the cultural structure.

In the Çayırova District of Kocaeli Province, located in the Marmara Region of Türkiye, a degraded Black Sea climate (hotter summers and colder winters) prevails. In determining the waste characterization, the neighborhoods within the boundaries of Çayırova Municipality, where the application will be made, are divided according to their income levels. The cultural structure of the district is cosmopolitan, and the income levels of the district quarters are;

- Low: İnönü District
- Medium: Freedom District, Yeni Mahalle, Çayırova District
- High: Cumhuriyet District
- Bazaar: Fatih Street is registered as Çobanoğlu Street.

Waste samples were taken to the waste dump site or intermediate storage area by taking representative samples on Monday, the weekend, and Tuesday, the weekday.

2.2. Waste characterization and analysis

During characterization, weighing scale, plastic cover (5m*10m), plastic container, fixed volume container (1m*1m*1m or 1m*1m*0.5m), material (mask, etc.) equipment were used. In

addition, disposable gloves and disposable overalls were supplied and used by the personnel in accordance with hygiene and safety rules. The wastes brought by separating them according to their income levels on the cover laid on the floor are emptied in 4 heaps. Then, they are taken from the wastes created according to the income level in order (in the form of a separate process for each), and the waste is placed in the container with the dimensions of 1m×1m×1m, with an open top. The container filled with waste is lifted by holding its handles, and a substance group analysis is performed on the waste remaining on the plastic cover. Afterward, the wastes for which the substance group analysis is made are placed in a previously tared plastic bucket with labels. The entire container is weighed, and the difference between gross and tare is recorded as net weight.

The characterization study of the district has been carried out twice a year, in summer and winter, and improvement studies are still being carried out in the region according to the characterization results. The photograph of the waste characterization study of Çayırova Municipality is given in Figure 1 below.



Figure1. Example of characterization study

As improvement works, the "Mobile Waste Collection Vehicle" for the separate collection of waste at the source was put into service, and the issue of including street collectors in waste management, which came into force with the Circular No. 2022/6 published by the Ministry of Environment, Urbanization and Climate Change, was discussed. In this study, street collectors give the recyclable materials they sort to licensed facilities. Trainings on "Zero Waste" were organized in all schools and it was planned to include students in the system with these trainings.

3. Results and Discussion

3.1. Solid waste characterization assessment for 2022

In a city with an average population, garbage varies between 0.7-1 kg per person [19]. In Kocaeli, the daily waste amount of a person was determined as 1.2 kg in 2002, 0.8 kg in 2014 and 0.82 kg in 2018. It is seen that the amount of waste per person in Kocaeli was always below the Türkiye average during the examined period [27]. In Türkiye, 1.03 kg of waste per person per day was reported in 2022, and 0.82 kg in Kocaeli. When these rates are compared, the amount per person in Kocaeli remains below the Türkiye average [28]. For Çayırova Municipality, for the year 2022, the average amount of solid waste produced per person(kg/person-day) was reported as 0.91 and 0.67 (kg/person-day) for summer and winter seasons. In Figure 2, the waste characterization graph of Çayırova Municipality in (a) and Kocaeli province in (b) can be seen.

The general characterization for Çayırova for 2022 results of the municipality are given in Table 1 by dividing them for each waste type according to their income.

Considering the general characterization results for 2022 in Table 1, although wastes were collected from different regions with different income levels, it is seen that kitchen wastes constitute the most significant proportion, with 67.25%. Similarly, in the solid waste composition of Malatya in general, with a rate of 43%, kitchen waste constitutes a large part of the composition. When we compare the solid waste composition of Çayırova and Türkiye, it is seen that there is a parallelism between the two compositions in general [20]. For example, while kitchen waste has the highest rate with 67.25% in Çayırova, it still has the highest rate with 34% in Türkiye. While the paper rate in Çayırova is 4.39%, it is 11% in Türkiye. While the rate of other non-flammable solid waste was not detected at all in Çayırova, it was 22% in Türkiye, and the rate of other flammable solid waste was 9.88% in Çayırova and 19% in Türkiye.

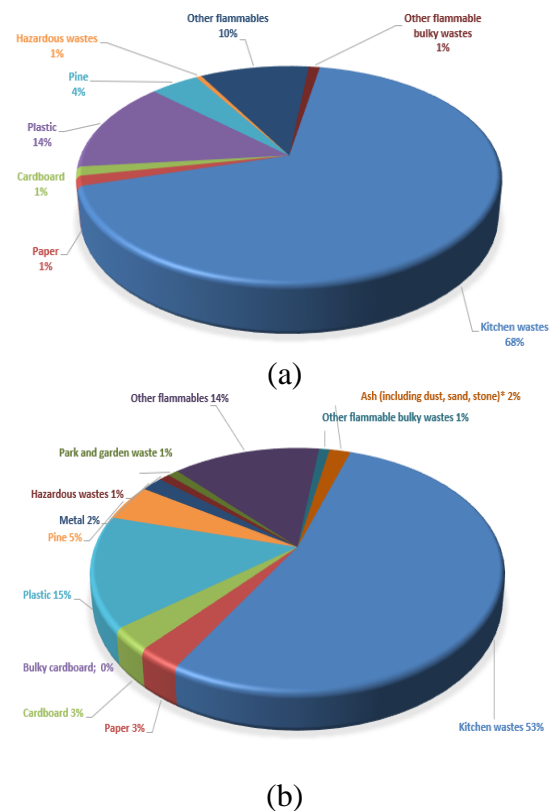


Figure 2. Waste characterization graph for Çayırova municipality (a) and Kocaeli city [29]. (b).

In addition, 21.03% of these wastes are packaging wastes, 9.88% are flammable wastes (textiles, etc.) and 0.44% are ash wastes. This is followed by hazardous waste with 0.37% and finally electronic waste with 0.07%. In a similar study; As result of studies carried out in the Municipality of Kano, Northern Nigeria, A high amount of garbage in the world is created (30.97% - 21.67%), plastics (29.22% - 27.88%), agricultural waste in the waste composition (21.785% - 15.54%), textile wastes (11.48% - 5.13%), papers (9.8%) 12.68 - 4.70%), food waste and residues (7.49 - 0.67%), while glass (3.63% - 1.57%) and metals (0.19 - .000%) were found to be the least [30].

In Ankara, Türkiye's second-largest city, 43.80% of the waste generated in 2018 was kitchen waste, 40.40% was excavation waste, 10.10% was park and garden waste, 2.40% was textile waste, 2.40% was wasted. 1.50% comprises plastic waste, 1.40% comprises paper waste, and 0.30% comprises metal waste [31].

Table1. Çayırova municipality characterization study average data for 2022

Solid Waste Components	Income Levels												AVERAGE													
	LOW			MIDDLE			HIGH			BAZAAR			Net													
	Gross	Tare	Ratio (%)	Gross	Tare	Ratio (%)	Gross	Tare	Ratio (%)	Gross	Tare	Ratio (%)	Net	Ratio (%)												
Kitchen wastes	94.50	5.90	88.60	65.36	5.10	51.15	53.36	74.55	6.30	68.25	158.25	8.90	149.35	76.43	89.34	67.25										
Paper	0.00	0.00	0.00	0.00	2.45	1.15	1.20	5.80	2.60	3.20	5.35	1.90	3.45	1.77	1.95	1.47										
Cardboard	3.30	0.70	2.60	1.92	2.35	0.70	1.72	0.00	0.00	0.00	4.20	1.30	2.90	1.48	1.79	1.35										
Bulky cardboard	0.00	0.00	0.00	0.00	0.00	0.00	0.00	0.00	0.00	0.00	0.00	0.00	0.00	0.00	0.00	0.00										
Plastic	30.35	9.05	21.30	15.71	25.55	6.80	18.75	19.56	26.45	8.10	18.35	11.30	13.45	6.88	17.96	13.52										
Pine	8.80	2.55	6.25	4.61	6.30	1.40	4.90	5.11	5.40	1.40	4.00	3.83	11.00	2.95	8.05	4.12										
Metal	2.55	2.00	0.55	0.41	1.70	1.30	0.40	0.42	1.25	1.15	0.10	1.40	0.70	0.36	0.44	0.33										
Bulky metal	0.00	0.00	0.00	0.00	0.00	0.00	0.00	0.00	0.00	0.00	0.00	0.00	0.00	0.00	0.00	0.00										
Waste electrical and electronic equipment	0.00	0.00	0.00	0.00	0.00	0.00	0.00	0.00	0.00	0.00	0.00	0.00	0.00	0.00	0.00	0.00										
Hazardous wastes	2.10	0.70	1.40	1.03	1.60	1.15	0.45	0.47	1.40	0.70	0.70	1.05	0.70	0.35	0.18	0.73										
Park and garden waste	0.00	0.00	0.00	0.00	0.00	0.00	0.00	0.00	0.00	0.00	0.00	0.00	0.00	0.00	0.00	0.00										
Other un-flammables	0.00	0.00	0.00	0.00	0.00	0.00	0.00	0.00	0.00	0.00	0.00	0.00	0.00	0.00	0.00	0.00										
Other flammables	19.35	6.85	12.50	9.22	17.75	2.55	15.20	15.86	11.95	2.00	9.95	17.95	3.10	14.85	7.60	13.13										
Other flammable bulky wastes	0.00	0.00	0.00	0.00	3.50	1.30	2.20	2.30	0.00	0.00	0.00	3.45	1.15	2.30	1.18	0.85										
Other un-flammable bulky wastes	0.00	0.00	0.00	0.00	0.00	0.00	0.00	0.00	0.00	0.00	0.00	0.00	0.00	0.00	0.00	0.00										
Others	0.00	0.00	0.00	0.00	0.00	0.00	0.00	0.00	0.00	0.00	0.00	0.00	0.00	0.00	0.00	0.00										
Ash (including dust, sand, stone)*	3.05	0.70	2.35	1.73	0.00	0.00	0.00	0.00	0.00	0.00	0.00	0.00	0.00	0.00	0.00	0.00										
TOTAL	135.55			100.00			95.85			100.00			104.55			100.00			195.40		100.00		132.84		100.00	

While characterizing the wastes, the content of the hazardous wastes recorded at the rate of 0,55% is recorded as the packaging of cleaning materials, and fluorescent, battery, etc., are recorded in the wastes. In this situation, it is understood that the waste batteries and fluorescents are not thrown into the domestic waste containers by the public and that the district municipality carries out the necessary studies to collect such waste.

3.2. Solid waste characterization assessment for 2022-2013

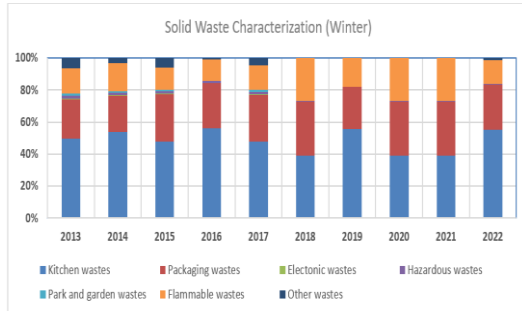
Solid waste characterization was also evaluated on a seasonal basis. Winter waste characterization studies were carried out by analyzing the waste group as of February, and summer waste characterization studies were carried out covering the six-month period in August. Seasonal percentages are given in Figure 3.

The seasonal solid waste characterization for 2022 shows that kitchen waste in the summer season (74.48%) increases compared to the winter season (55.37%). It has been observed that flammable and packaging wastes are more prevalent in winter than in summer. The amount of flammable waste in winter and summer was determined as 15.10% and 8.07%, and packaging waste was 28.18% and 16.68%, respectively.

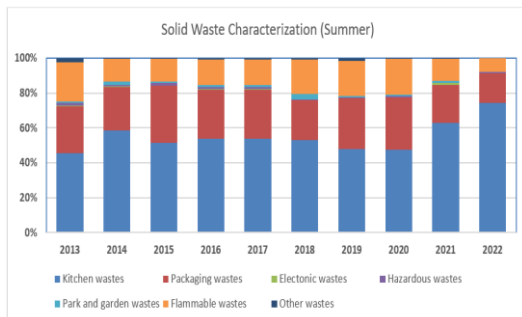
If an evaluation is made for the last ten years, except for 2013 and 2019, kitchen waste has always been analyzed higher in summer than winter. Considering the winter season, the highest value in packaging waste is seen as 56.35% in 2016. In 2022, waste close to this value was generated at 55.37%. In the summer season, the highest packaging waste was seen in 2015, with 32.77%, while the lowest value was determined to be 16.68% in 2022. While electronic waste could not be detected after 2018, it was seen as 1.23% in the winter of 2021. While park and garden waste were not detected in the winter season after 2017, in the summer season, these wastes were detected in other years except 2022.

Flammable wastes were found to be higher than the summer season, especially in the winter season, 26.69%, 26.69%, and 15.10%,

respectively, in 2020-21-22. In 2022, flammable waste in the summer was determined to be 8.07%, the lowest value in the last ten years. In winter, it was found to be very similar to 2013. Hazardous waste was found to be higher in winter than in summer in all years except 2017.



(a)



(b)

Figure 3. 2022 winter (a) and summer (b) season characterization results

When the data in Figure 3 are examined, it is seen that the kitchen waste, which has the largest share in the waste content, increases in the summer months, and it is thought that the reason for this increase is the rapid deterioration of the food with the warming of the weather.

68.87% of domestic solid wastes in Türkiye are organic and wet solid wastes, 14.09% are recyclable solid wastes, and 17.04% are ash and slag wastes. In Kocaeli province, when the solid waste characterization results are evaluated, approximately 46.2% are organic wastes, 23.7% are packaging wastes, and 30.01% are other waste groups. In the years 2010-11-12, there is not much difference in these categorization distinctions [19]. In Mustafakemalpaşa district, 65% of domestic solid wastes are vegetables and decomposable materials, 22% are recyclable solid wastes, and 13% are ash and slag wastes. Waste characterization of the district is higher than the average of Türkiye in terms of recovery rate [25].

In the study of Zhang et al. 2010, the formation and waste composition of municipal solid wastes in China were examined, and it was revealed that the waste composition in China contains a high percentage of organic waste and moisture from kitchen waste has the highest proportion (about 60%) of municipal solid waste has been placed [32]. In the study of Güvenç (2016), organic waste was determined to be the highest amount, with 57.69% [24]. In another study, 40-85% of total solid waste is food waste, 5-60% is recyclable solid waste and 0-10% is ash, dust, etc. It has been stated that [33].

While the amount of packaging waste was 28.18% in winter, it decreased to 16.68% in summer. Since Çayirova district, an industrial area, is not a tourist center, the population of the region's people decreases significantly following the school holidays in summer, which causes a decrease in the rate of packaging waste collected from schools and residences. Contrary to packaging waste, the increase in glass waste in summer is undoubtedly caused by the rapid consumption of cold drinks in glass bottles in hot weather.

Considering the composition of wastes produced in developed countries, organic wastes are at a lower rate than those in developing countries. In addition, it is noteworthy that metal, paper, and glass wastes are high [34]. A one-year study was conducted by Gidaracos et al. (2006) in a large area of Crete to describe waste composition (including physical and chemical characterization) and seasonal variations. Metals such as lead, cadmium, and mercury were also investigated by classifying the collected wastes into plastics, paper, metal, aluminum, leather-wood-textile-rubbers, organic wastes, non-flammable and mixed categories [35]. Three main categories of waste have been identified, representing 76% of the total mixed waste in Crete: organic waste, paper, and plastics. In addition, the high percentage of glass waste and seasonal aluminum detection in the waste composition is explained as the result of some human activities such as tourism.

Although there is no significant difference in other waste types, there was an increase in the amount of ash in winter due to the presence of houses using stoves in the region and an increase

in summer characterization study for this type of waste due to the construction and maintenance of parks and gardens in summer.

Waste characterization percentages show that although the Municipality carries out studies on the separate collection of wastes at the source, the public's indifference is an obstacle to the healthy execution of the project. The raw materials of some packaging wastes are imported, and the recyclable wastes that go to landfills are not evaluated, causing high economic losses. This situation causes the project life to decrease and air and water pollution to increase by filling the regular landfills, which are designed for storing domestic waste, with other wastes. The comparison of waste characterization data for 2013-2022 is given in Figure 4.



Figure 4. Characterization data for the last ten years

According to the data in Figure 4, while organic waste distribution is expected to decrease, it is seen that the lowest organic waste distribution was in 2013, with 43.23%. The distribution of organic waste, which is expected to increase depending on the population, is expected to decrease in line with the studies carried out within the framework of the legislation and the information activities covered by these studies. The amount of organic waste increased to 50.3 percent in 2014, 49.73 percent in 2015, 58.18 percent in 2016, and decreased to 48.07 percent in 2017. While the amount of organic waste was close to each other between 2017 and 2019, it was observed that it increased by 60.28% in 2021 and 67.25% in 2022.

When looking at the percentages of packaging waste in these distributions, the fact that the highest rate was 30.68% in 2015 and the lowest rate was 20.6% in 2022 shows that there are some

disruptions in the functioning of the system. In the study, electrical and electronic equipment wastes, hazardous wastes, park and garden wastes, other flammable materials, other non-flammable wastes, other flammable wastes, bulky wastes, other non-flammable bulky wastes, ash, etc. The distribution of waste is named "Other". The highest two-year "Other" rate in the last ten years was 30.67% in 2013 and then 24.86% in 2017. In the last two years, it can be seen that the category waste amounts are characterized by the lowest value of 11.17% in 2022 when it decreased significantly.

Although it is seen that the amount of packaging waste collected in Çayirova Municipality varies constantly over the years, when the data of the last decade is examined, the high rate of packaging waste among the wastes to be directed to final disposal shows that the collection activities carried out by the Municipality are inefficient. In the Regulation on the Control of Packaging Wastes, issued with reference to the Environmental Law No. 2872, published in the Official Gazette No. 18132 dated 11.08.1983, it is seen that the variability of the free phase is the biggest reason for the instability in waste collection [36].

The fact that the rate of glass waste was 3% in the 2022 characterization results shows that the public is more sensitive about glass waste, and the municipality is more efficient in collecting glass waste. In addition, education and awareness-raising activities of the people of the district should be accelerated, and citizens should be encouraged to use returnable products.

The fact that the percentage of textile waste comes right after organic waste in the waste characterization data that will go to landfill in 2022 has revealed the need for Çayirova to carry out studies to collect textile wastes separately at the source. In this regard, as of 2018, the district municipality has started to recycle textile waste, and textile waste collection boxes have been placed on suitable streets in the region.

4. Conclusion

In this study, a characterization study was carried out by grouping the domestic wastes of Kocaeli

Çayırova Municipality according to their income levels. This study was conducted primarily for the year 2022 and evaluated how the waste content changed with the data of the last ten years. In the study, for 2022, kitchen waste was 67.25%, packaging waste was 21.03%, flammable wastes (textile, etc.) with 21.04%, ash waste at 44%, and Hazardous wastes were detected at a rate of 0.55%. Considering the last ten years, it has been determined that 2022 will have the highest percentage of organic waste and the lowest percentage of packaging waste. When evaluated based on summer and winter seasons, it was observed that kitchen waste was generally higher in summer for all years. "In this study, it was seen that waste management activities are carried out in the Çayırova region, but the integration of citizens into waste management activities should be increased. In a process where the implementation is continued in terms of legislation, the fact that there is already waste going to the landfill in the characterization data shows that incentive efforts should be increased to direct citizens to separate collection activities at the source.

Domestic organic wastes, packaging wastes, textile wastes (as of 2018), glass wastes, construction and demolition wastes, hazardous domestic wastes (used batteries, fluorescent lamps, etc.), and bulky wastes are collected separately at the source by the Municipality. "Mobile Waste Collection Vehicle" has been put into service, and it is planned to include students in the system by organizing training on "Zero Waste" in all schools. If the public does not show interest in the subject, the rates targeted by local governments cannot be reached, and an inefficient collection will develop.

The conscious and concerned segment of the public is negatively affected by the lack of continuity in collections and the occurrence of disruptions. In this regard, the Municipality's posters and billboards should be used periodically to train the public. The Ministry and its provincial and central organizations are obliged to impose administrative sanctions on natural or legal persons who directly or indirectly dump their wastes into nature within the framework of the provisions of Mer legislation. A practical result cannot be achieved. For this

reason, the institutional capacity of the competent authorities needs to be increased.

Article Information Form

Acknowledgement

We would like to thank Çayırova Municipality and Kocaeli Environmental Protection and Control De-partment for their support, which shared their data throughout this study.

Funding

The author (s) has no received any financial support for the research, authorship or publication of this study.

Author Contributions

Berna KIRIL MERT; Supervisor: Conception / Design, Data Collection, Data Analysis / Interpretation, Writing, Technical Support / Material Support, Critical Review of Content, Literature Review.

Kader DURAN; Graduate Student: Data Collection Data Analysis / Interpretation, Literature Review.

The Declaration of Conflict of Interest/ Common Interest

There is no conflict of interest between the authors. All authors have read, understood, and have complied as applicable with the statement on "Ethical responsibilities of Authors" as found in the Instructions for Authors.

The Declaration of Ethics Committee Approval

This study does not require ethics committee permission or any special permission.

The Declaration of Research and Publication Ethics

The authors of the paper declare that they comply with the scientific, ethical and quotation rules of SAUJS in all processes of the paper and that they do not make any falsification on the data collected. In addition, they declare that Sakarya University Journal of Science and its editorial board have no responsibility for any ethical violations that may be encountered, and that this study has not been evaluated in any academic publication environment other than Sakarya University Journal of Science.

Copyright Statement

Authors own the copyright of their work published in the journal and their work is published under the CC BY-NC 4.0 license.

References

- [1] H. Palabıyık, D. Altunbaş, “Kentsel katı atıklar ve yönetimi”, Çevre Sorunlarına Çağdaş Yaklaşımlar, Beta, İstanbul, 2004.
- [2] Y. Soysal, “Yerel yönetimler için evsel katı atık tarifelerinin belirlenmesi üzerine geliştirilen bir hesap yöntemi”, Yüksek Lisans Tezi, İstanbul Teknik Üniversitesi, İstanbul, 2015.
- [3] M. Topal, B. Karagözoğlu, E. Öbek, “Sızıntı sularının doğal arıtımı”, AKU J SCI 11, 025401, 1-16, 2011.
- [4] B. Şahin, Türkiye’de depo gazından enerji eldesi ve adana ili örneği, Yüksek Lisans Tezi, Nevşehir Hacı Bektaş Veli Üniversitesi, Nevşehir, 2021.
- [5] M. Çekim, S. Yıldız, T. Dere, “Güneydoğu anadolu bölgesi katı atık sorunları ve çevresel etkileri: Adıyaman örneği”. 2nd International Sustainable Buildings Symposium, 28-30 Mayıs, Ankara, Türkiye, 2015.
- [6] Anonim, (2010). Çevre ve orman bakanlığından: atıkların düzenli depolanmasına dair yönetmelik Guide to citing internet sources [Online]. Available: <https://www.resmigazete.gov.tr/eskiler/2010/03/20100326-13.html>
- [7] H. Durmaz Bekmezci, H. Çetin, “Kentsel katı atıklar ve geri kazanımlarının faydaları; Eskişehir örneği”, BEÜ Fen Bilimleri Dergisi BEU Journal of Science, 9 (3), 1415-1424, 2020.
- [8] P. Kaya, “Yerel yönetimlerde katı atık yönetiminin maliyet analizi: türkiye geneli ve istanbul ili örneği”, Yüksek Lisans Tezi, İstanbul Teknik Üniversitesi, İstanbul, 2013.
- [9] A. A. Gündüzalp, S. Güven, “Atık, çeşitleri, atık yönetimi, geri dönüşüm ve tüketicisi: Çankaya belediyesi ve semt tüketicileri örneği”. Hacettepe Üniversitesi Sosyolojik Araştırmalar E-Dergisi, 9, 1-19, 2016.
- [10] F. Ukşal, “Üsküdar ilçesi ambalaj atıklarının yönetimi ve yaşam döngüsü analizi ile değerlendirilmesi”. Yüksek Lisans Tezi, Yıldız Teknik Üniversitesi, İstanbul, 2019.
- [11] Anonim, 2021, Guide to citing internet sources [Online]. T.C. Çevre, Şehircilik İklim Değişikliği Bakanlığı, Çevresel Etki Değerlendirmesi, İzin Ve Denetim Genel Müdürlüğü, Çevre Envanteri Ve Bilgi Yönetimi Dairesi Başkanlığı, Çevresel Göstergeler, Ankara.
- [12] S. Güleç Solak, Ş. Pekküçükşen, “Türkiye’de kentsel katı atık yönetimi: karşılaştırmalı bir analiz”, MANAS Journal of Social Studies Vol.: 7 No: 3, 2018.
- [13] Anonim, (2005). 5393 sayılı belediye kanunu 13.07.2005 tarihli ve 25874 sayılı resmi gazete, Guide to citing internet sources [Online]. Available: <http://www.mevzuat.gov.tr/MevzuatMetin/1.5.5393.pdf>.
- [14] Anonim, (2004). 5216 Law on Metropolitan Municipalities Law No: 5216 Date of Enactment: 10/7/2004 Published in the Official Gazette: Date: 23/7/2004 Issue: 25531 Publication Series: Edition: 5 Volume: 43 P:1-21 <http://www.lawsturkey.com/law/law-on-metropolitan-municipalities-5216>
- [15] N.T. Arslan, “İdari ve mali paylaşım açısından merkezi yönetim yerel yönetim ilişkileri”, No:33, 2005.
- [16] Anonim, (2011). Türkiye mülki idare bölümleri. Retrieved from: <https://www.e-icisleri.gov.tr/Anasayfa/MulkiIdariBolumleri>. Guide to citing internet sources [Online]. Available: 21.02.2019.

- [17] K. Duran, “Yerel yönetimlerde katı atık analizi ve iyileştirme çalışmaları: çayırova belediyesi örneği”, Yüksek Lisans Tezi, Sakarya Üniversitesi, Sakarya, 2019.
- [18] C. Öztaş, E. Zengin, “Yerel yönetimler ve çevre”, Sosyal Siyaset Konferansları Dergisi Yıl, Cilt 0, Sayı 54, 181 - 200, 2008.
- [19] K.O. Demirarslan, D. Demirarslan, “Kentlerde yeni yerleşim alanlarının gelişimi ve katı atık sorunu: izmit-yahyakaptan mahallesi örneği”, Artvin Çoruh Üniversitesi Doğal Afetler Uygulama ve Araştırma Merkezi Doğal Afetler ve Çevre Dergisi, Cilt:2, Sayı:2, Sayfa:108-120, 2016.
- [20] Ü.Z. Kolukısa, “Belediyelerde katı atık yönetimi: Malatya belediyesi örneği”, Yüksek Lisans Tezi, İ.Ü. Sosyal Bilimler Enstitüsü, Malatya, 2013.
- [21] A. Pires, G. Martinho, N., Chang, “Solid Waste Management in European countries: A review of systems analysis techniques”, Journal of environmental management 92(4),1033-1050, 2011.
- [22] A. D. Yetiş, L. Gazigil, Z. Şapçı, O.T. Can, M. M. Tütün, C., Gözetten, H., Durmaz Bekmezci, Z. Yücesoy, Bitlis ili katı atık yönetiminin değerlendirilmesi, UKAY 2013, 5. Ulusal Katı Atık Yönetimi Kongresi, Kocaeli, 2013.
- [23] A. Çoban, S. Kiliç, “Türkiye’de yerel yönetimlerin çevreye yönelik politikaları: konya selçuklu belediyesi selkap örneği”, Selçuk Üniversitesi Sosyal Bilimler Enstitüsü Dergisi, 22, 2009.
- [24] L. Güvenç, “Kartal belediyesi sınırları içerisinde oluşan ambalaj atıklarının karakterizasyonu ve ekonomik analizi”, İstanbul Üniversitesi, Fen Bilimleri Enstitüsü Çevre Mühendisliği Bölümü, Yüksek Lisans Tezi, İstanbul, 2016.
- [25] M. Şen, K. Kestioğlu, “Kırsal belediyelerde evsel katı atıkların geri kazanımı ve ekonomik analizi: mustafakemalpaşa ilçesi/bursa örneği”, Ekoloji, 17, 65, 45-51, 2007.
- [26] A. Yılmaz, Y. Bozkurt, “Türkiye’de kentsel katı atık yönetimi uygulamaları ve kütahya katı atık birliği (KÜKAB) örneği”. Süleyman Demirel Üniversitesi İktisadi ve İdari Bilimler Fakültesi Dergisi, 15(1): 11-28, 2010.
- [27] S. Menteşe, G. Kızılcım, “Türkiye’de katı atık yönetim uygulamaları ile İzaydaş (Kocaeli) örneğinin karşılaştırılması”, Doğu Coğrafya Dergisi, 26 (46), 109-128, 2021, DOI: <https://doi.org/10.17295/ataunidcd.1035958>.
- [28] Anonim, (2023), Guide to citing internet sources [Online]. Available: <https://biruni.tuik.gov.tr/medas/?kn=119&locale=tr>.
- [29] Anonim, (2023). “Kocaeli ili 2022 yılı çevre durum raporu”, Türkiye Cumhuriyeti Kocaeli Valiliği Çevre, Şehircilik Ve İklim Değişikliği İl Müdürlüğü.
- [30] A. B. Nabegu,” An analysis of municipal solid waste in kano metropolis”, Nigeria, , Journal of Human Ecology, 31(2), 111-119.31:2, 111-119, 2010.
- [31] M. Gül, K. Yaman, Türkiye’de atık yönetimi ve sıfır atık projesinin değerlendirilmesi: Ankara örneği”, Atatürk Üniversitesi İktisadi ve İdari Bilimler Dergisi, 35(4): Sayfa: 1267-1296, 2021, <https://doi.org/10.16951/atauniiibd.870434>.
- [32] Q. D. Zhang, K. S. Tan, R. M. Gersberg, Municipal solid waste management in china: status, problems and challenges”, Journal of Environmental Management, vol. 91,p. 1623-1633, 2010.
- [33] G. Tchobanoglous, H. Theisen, S. A. Vigil, “Integrated solid waste management: engineering principles and management issues”, Cilt 2, McGraw-Hill Higher Education 1993.

- [34] D. Hoornweg, P. Bhada-Tata, “What a waste; a global review of solid waste management”, Washington: World Bank. <http://www-wds.worldbank.org/external/default/WDSContentServer/WDSP/IB>, 2012.
- [35] E. Gidakos, G. Havas, P. Ntzomilis, “Municipal solid waste composition determination supporting the integrated solid waste management system in the island of Crete”, Waste management, 26(6), 668-679, 2006.
- [36] Anonim, (1983). 2872 sayılı çevre kanunu, Guide to citing internet sources [Online]. Available: 11/8/1983, Sayı: 18132, <http://www.mevzuat.gov.tr/MevzuatMetin/1.5.2872.pdf>.

Experimental Study on Springback Properties of 6061 Aluminum in V-Bending

Ahmed Ozan Örnekcı¹ , Seçil Ekşi^{2*} 

¹Milli Savunma Bakanlığı, 41 inci Bakım Fabrika Müdürlüğü, İstanbul, Türkiye, a.ozanornekci@gmail.com

²Sakarya University, Faculty of Engineering, Department of Mechanical Engineering, Sakarya, Türkiye, eksi@sakarya.edu.tr

*Corresponding Author

ARTICLE INFO

ABSTRACT

Keywords:

Aluminum
Sheet metal forming
V-bending
Springback



Article History:

Received: 03.01.2024

Accepted: 28.02.2024

Online Available: 14.06.2024

Sheet metal bending is one of the most commonly applied methods among sheet metal forming operations. In this study, the springback behavior of aluminum alloys of different thicknesses was examined by performing v-bending processes at different die angles and widths. The experiments were carried out on 1 and 1.5 mm thick plates at die angles of 140°, 150° and 160° and three different die widths: 10 mm, 16 mm and 20 mm. In this experimental study, it was observed that springback decreased as the die width increased. As the die angle increased, springback values also increased. It has been observed that sheet thickness has little effect on springback. As the sheet thickness increased, the amount of springback decreased. The lowest springback value of 0.1° was obtained in the 1.5 mm thick specimen with a die width of 10 mm and a die angle of 140°. The highest spring-go value of -2.7° was obtained in the 1 mm thick specimen with a die width of 20 mm and a die angle of 140°. As a result of the variance (ANOVA) analysis, it was seen that the die width had a more significant effect (78.42%) on springback than the die angle. The effect of die angle on springback is 10.73%. As a result of the experiments and statistical analysis, it was seen that the parameter that most affects springback is die width.

1. Introduction

Aluminum alloys are widely preferred due to their low density, high strength properties and good corrosion resistance. 6XXX alloy is used in various non-aerospace components such as buildings, rolling stock, boat hulls, ship superstructures, and, increasingly, automotive components. Al 6061-T6 aluminum alloy is strengthened by heat treatment and is widely used especially in the automotive and aircraft manufacturing industries [1, 2].

Bending is one of the commonly applied methods in shaping aluminum sheet metals. The usage areas of shaped sheet metal sheets are pretty high. Sheet metal forming applications are widely encountered at many different technological levels, from high-tech industries such as automotive, aircraft, and defense to the white goods industry. Bending forming is one of the

most basic and widely used sheet metal forming methods [3-5]. Bending operations also vary depending on various variables such as the shape of the sheet metal part, material properties, and production quantity. Different methods shape the sheet metal into the desired final forms. These methods are basically based on shaping the sheet material with the help of more rigid objects with the desired form. The most used of these is shaping made by placing sheet metal between molds made of cast iron or steel materials, which complement each other and are generally called male and female, and applying force [6-8].

Springback is significantly influenced by many factors. Umur et al. investigated DP steels' spring back/spring forward behavior with the v-bending process. Effects of material thickness, die/punch radius, bending angle, and rolling direction were investigated systematically [9]. The sheet material undergoes plastic deformation above the

elastic deformation limit with the force applied in these forming processes. Therefore, there is still some elastic deformation within the total deformation. Elastic deformation forming process parameters: It causes backward or forward springing behavior depending on the mold or forming geometry, part geometry, and material properties [9-11]. Since spring back or spring-go means deviation from the desired final shaping geometry, predictability and minimizing this variability before forming becomes essential in terms of time and cost savings.

The most fundamental problem in bending operations is springback. Springback behavior in sheet materials is a forming problem in which multiple interactions of many elements, such as mechanical and dimensional properties of the material and forming variables, are involved. The springback during the bending process cannot be eliminated entirely, but some predictable and compensatory work can be done. The phenomenon of the part returning its elastic deformation due to a shaping process is called spring-back. Springback is affected by many process variables [12-16].

Researchers examined these variables in two groups. The first is the material properties that affect the formability, and the second is the process parameters. Material properties are modulus of elasticity, yield, and tensile strength, elongation, strain hardening exponent, plastic anisotropy, and strain rate sensitivity exponent. Process parameters can be listed as deformation rate, temperature, friction and lubrication, sheet pressing force, tool geometry and size, and material thickness [17-21].

Wei-pink et al. investigated springback behavior of 6016 aluminum alloy in hot stamping under different conditions using V-shape dies. Researchers reported that springback decreased significantly when the initial blank temperature increased to 500 °C. As the die holding pressure increased, springback decreased. As the die corner radius decreased, the springback

decreased [21]. Material properties have a great impact on springback. Guan et al. examined the effect of artificial aging time on the bending and springback behavior of 6061 aluminum through the bending process. They reported that springback and cross-sectional deformation increased as the artificial aging time increased [22].

Choi et al. studied the mechanical properties, springback, and formability of W-temper and peak aged 7075 aluminum alloy sheets. The formability and springback of the W-tempered sheet are analyzed by simulations.

The researchers revealed that the WT process could potentially be used to produce high-strength aluminum sheets at room temperature as an alternative to hot and hot forming processes [23].

In this study, the v-bending behavior of aluminum sheets was investigated experimentally. The aim of this study is to investigate the effects of parameters such as sheet metal thickness (t), die angle (DA), and die width (DW) on the v-bending process. The effect of process parameters from the experimental results will also be examined by variance and regression analyses. In addition, the results obtained are aimed to be a guide that can be used for studies in the industrial field.

2. Experimental Study

2.1. Material

In this study, Al 6061-T6 Alloy was used. Aluminum 6061-T6 Alloy has high hardness and corrosion resistance. It is used in many areas, such as the defense industry, aircraft industry, railway industry, shipbuilding industry, bridges, pipes, transportation, and space applications. The chemical composition and mechanical properties of Al 6061-T6 Alloy are given in Table 1 and Table 2. The thicknesses of aluminum sheet metal are 1 mm and 1.5 mm. The dimensions of the v-bending test specimens are 70x70 mm.

Table 1. Chemical composition of 6061aluminium alloy

Element	Si	Fe	Cu	Mn	Mg	Cr	Zn	Ti	Al
Al 6061	0.4-0.8	0.7	0.15-0.4	0.15	0.8-1.2	0.04-0.35	0.25	0.15	Balance

Table 2. Mechanical properties of Al 6061-T6

Material	Tensile Strength (MPa)	Yield Strength (MPa)	Elongation at break %	Brinell Hardness (500 g load, 10 mm ball)	Shear Strength (MPa)
Al 6061-T6	310	276	12	95	207

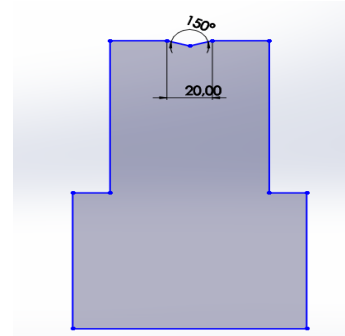
2.2. Method

The effects of sheet thickness, die angle, and die width on the springback behavior of aluminum 6061 alloys were examined by v-bending experiments. V-bending experiments were carried out on 1 mm and 1.5 mm thick aluminum plates using 140°, 150°, and 160° dies. Experiments were carried out with three different die widths of 10, 16, and 20 mm. The experiments were carried out on a DENER brand press machine with a capacity of 135 tons. The press force applied for a 1 mm thick aluminum sheet is 3.1 tons, and for 1.5 mm, it is 4.6 tons. A view of the press machine is given in Figure 1. Experiments were carried out at constant speed. The parameters and their levels determined in the V-bending experiments are given in Table 3.

**Figure 1.** Press machine**Table 3.** Experiments parameters and levels

Parameters	Level 1	Level 2	Level 3
Thickness (mm)	1	1.5	-
Die angle (°)	140	150	160
Die width (mm)	10	16	20

Schematic view of die and specimen in v-bending process is given in Figure 2.

**Figure 2.** Schematic view of die in v-bending process (for die angle 150° and die width 20 mm)

The bending angle was measured in the specimens with a digital protractor. A view of the measurement of the spring back is given in Figure 3.

**Figure 3.** The view of digital protractor

3. Experimental Results

V-bending test results are given in this section. Experimental springback results are given in Table 4.

When Table 4 is examined, springback is noted in the experiments performed with a 10 mm wide die on samples with 1 mm sheet thickness, and springing-go is noted in the bending processes performed in 16 and 20 mm wide dies. As the die angle increased, the springback angle increased for 10, 16, and 20 mm die widths. Similar results on aluminum A1100-O material were seen in the study conducted by Thipprakmas et al. Springback was observed at low bending angles such as 30° and 45°, and spring-go was observed at high bending angles such as 120° and 135°.

Similarly, in the same study, it was observed that springback decreased as the thickness increased [24]. Similar results were obtained in this study when the sheet thickness was 1.5 mm and the springback or spring-go behavior did not change. As the thickness increased, the spring back and spring-go values decreased. The variation of spring back depending on die angle and die width for two different sheet thicknesses is given in Figure 4.

When Figure 4 was examined, for 1 mm thickness and 10 mm die width, when the die angle was 140°, the springback was 0.2°, while at 160°, it increased by 4 times to 0.8°. With a die width of 16 mm, while the spring-go was -2° at 140°, it increased by 60% to -0.8° at 160°. With a die width of 20 mm, the spring-go increased by 44% to -1.5° at 160°, while it was -2.7° at 140°. When experiments were performed with different thicknesses using the same die angle, it was observed that the springback angle decreased as the thickness increased [25]. For 1.5 mm thickness and 10 mm die width, when the die angle was 140°, the spring-go was 0.1°, while at 160°, it increased by 7 times to 0.7°. With a die width of 16 mm, while the spring-go was -1.1° at

140°, it increased by 54% to -0.5° at 160°. With a die width of 20 mm, the spring-go increased by 44% to -0.9° at 160°, while it was -1.6° at 140°.

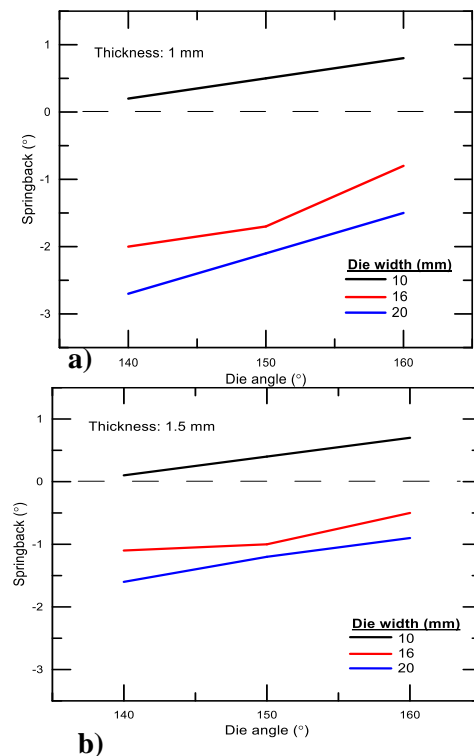


Figure 4. The variation of springback depending on die angle for a) 1 mm and b) 1.5 thickness

Table 4. Experimental results

Thickness (mm)	Die angle (°)	Springback angle (°) (Die width: 10 mm)	Spring-go angle (°) (Die width: 16 mm)	Spring-go angle (°) (Die width: 20 mm)
1	140	0.2	-2	-2.7
1	150	0.5	-1.7	-2.1
1	160	0.8	-0.8	-1.5
1.5	140	0.1	-1.1	-1.6
1.5	150	0.4	-1	-1.2
1.5	160	0.7	-0.5	-0.9

In Figure 4, it is clearly seen that the springback or spring-go decreases as the die width increases. As a result, when the plate thickness increases at any bending angle, springback values decrease. However, springback values were increased for sheets with the same thickness as the bending angle increased [26]. Similar results were found in the study conducted by Heng et al. on the 6061-T4 Al alloy. As the bending angle increased, springback values increased [27].

Springback or springback values decrease with increasing die width. In another study, springback behavior was examined by performing v-bending experiments on 6061 Al alloy. The effects of length, thickness and bending angle on springback were investigated. They reported that springback is more important in terms of thickness and bending angle, while length provides less effect [28]. View of the bent specimens is given in Figure 5-6.

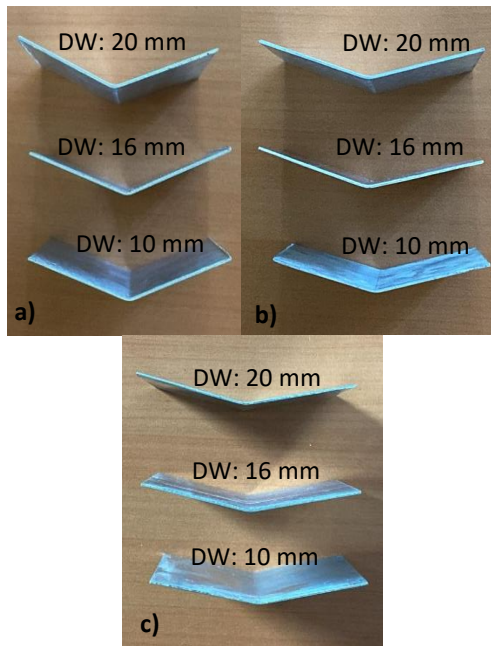


Figure 5. View of the bent specimens for 1 mm thickness, a) 140°, b) 150°, c) 160°

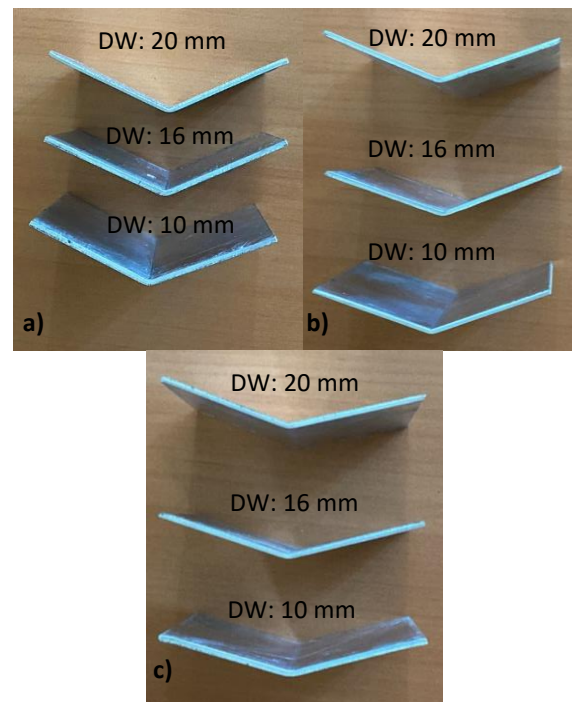


Figure 6. View of the bent specimens for 1.5 mm thickness, a) 140°, b) 150°, c) 160°

4. Variance (ANOVA) and Regression Analysis

Variance (ANOVA) and regression analyses were carried out using the Minitab 18 program.

4.1. Variance (ANOVA) analysis

Analysis of variance is used to determine the effect of different values of the independent variable or variables on the dependent variable. In Table 5, ANOVA results based on measured springback values are given. The parameters' contribution percentages are given in the table's last column.

Accordingly, the die width is the determining factor for springback.

Table 5. ANOVA results

Source	Df	Adj SS	Adj MS	F-value	P-value	Contribution %
Thickness (t)	1	0.9800	0.98000	11.16	0.006	5.20
Die angle (DA)	2	2.0233	1.01167	11.53	0.002	10.73
Die width (DW)	2	14.7633	7.38167	84.09	0.000	78.42
Error	12	1.0533	0.08778			5.65
Total	17	18.8200				100.00

4.2. Regression analysis

Regression analysis is a method used to determine the relationship between two or more variables. In this study, the dependent variable is springback, and the independent variables are die width (DW), die angle (DA) and sheet thickness

In ANOVA, the importance of parameters is determined by comparing the F ratio of each parameter. The correlation coefficient (R^2) value of the analysis is 94.40%. The effect of sheet thickness on the springback value was determined as 5.20%, and the effect of the die angle on the springback value was determined as 10.73%. The most influential parameter on springback is the die width (78.42%).

(t). The prediction equation for springback given in Equation (1) was obtained by regression analysis. The correlation coefficient (R^2) of the equation obtained with the linear regression model for the springback value was 91.51%.
Regression equation:

$$\text{Springback} = -4.77 + 0.933 t + 0.04083 \text{ DA} - 0.2164 \text{ DW} \quad (1)$$

5. Conclusions

In this study, the springback and spring-go behavior of 6061 Aluminum alloy was investigated experimentally by the v-bending process. Plates with 1 mm and 1.5 mm thickness were examined at 140, 150, and 160 die angles and 10, 16, and 20 mm die width. It was seen that the die width and the die angle significantly affected the springback behavior. Springback was observed at 10 mm die width and spring-go was observed at 16 and 20 mm die widths. As the die width increases, spring back or spring-go decreases. It was seen that the springback or spring-go increased as the die angle increased. It has been observed that sheet thickness has little effect on springback. As the sheet thickness increased, the amount of springback decreased. As a result of variance (ANOVA) analysis, it was seen that die width (78.42%) has a more significant effect on springback than die angle (10.73%) and sheet thickness (5.20%). As a result of the regression analysis, an equation giving the springback angle depending on the sheet thickness, die width and die angle was suggested.

Article Information Form

Funding

The author (s) has no received any financial support for the research, authorship or publication of this study.

Authors' Contribution

The authors contributed equally to the study.

The Declaration of Conflict of Interest/ Common Interest

No conflict of interest or common interest has been declared by the authors.

The Declaration of Ethics Committee Approval

This study does not require ethics committee permission or any special permission.

The Declaration of Research and Publication Ethics

The authors of the paper declare that they comply with the scientific, ethical and quotation rules of SAUJS in all processes of the paper and that they do not make any falsification on the data collected. In addition, they declare that Sakarya University Journal of Science and its editorial board have no responsibility for any ethical violations that may be encountered, and that this study has not been evaluated in any academic publication environment other than Sakarya University Journal of Science

Copyright Statement

Authors own the copyright of their work published in the journal and their work is published under the CC BY-NC 4.0 license.

References

- [1] H. Li, K. P. Shi, H. Yang, Y. L. Tian, "Springback law of thin-walled 6061-T4 Al-alloy tube upon bending," Transactions of Nonferrous Metals Society of China, vol. 22, no. 2, pp. 357–363, 2012.
- [2] G. Wang, G. Zhu, T. Li, L. Kou, "Effect of heat treatment conditions on mechanical properties and springback of 6061 Aluminum alloy sheets," IOP Conf Ser Mater Sci Eng, vol. 788, no. 1, pp.1-9, 2020.
- [3] C. Chen, C. Chen, "Experimental Study on Punch Radius and Grain Size Effects in V-Bending Process Experimental Study on Punch Radius and Grain Size Effects in V-Bending Process," Materials and Manufacturing Processes, vol. 29, no. 4, pp. 461-465,2014.
- [4] H. Seok, M. Koc, "Numerical investigations on springback characteristics of aluminum sheet metal alloys in warm forming conditions," Journal of Materials Processing Technology, vol. 204, no. 1-3, pp. 370–383, 2008.
- [5] Y. Chen, X. Li, L. Lang, "Various elastic moduli of AA6016 and their application on

- accurate prediction of springback,” *Journal of the Chinese Institute of Engineers*, vol. 42, no. 4, pp. 319–326, 2019.
- [6] K. Yilamu, R. Hino, H. Hamasaki, F. Yoshida, “Air bending and springback of stainless steel clad aluminum sheet,” *Journal of Materials Processing Technology*, vol. 210, no. 2 pp. 272–278, 2010.
- [7] Y. Zong, P. Liu, B. Guo, D. Shan, “Springback evaluation in hot v-bending of Ti-6Al-4V alloy sheets,” *The International Journal of Advanced Manufacturing Technology*, vol.76, pp. 577-585, 2015.
- [8] X. Li, Y. Yang, Y. Wang, J. Bao, S. Li, “Effect of the material-hardening mode on the springback simulation accuracy of V-free bending,” *Journal of Materials Processing Technology*, vol. 123, no. 2 pp. 209-211, 2002.
- [9] Y. Umur, H. Aydin, K. Yigit, A. Bayram, “Springback/springforward behaviour of DP steels used in the automotive industry,” *Tehnicki Vjesnik*, vol. 27, no. 1, pp. 243-250, 2020.
- [10] D. Fei, P. Hodgson, “Experimental numerical studies of springback in air v-bending process for cold rolled TRIP steels,” *Nuclear Engineering and Design*, vol. 236, no. 18, pp. 1847-1851, 2006.
- [11] D. Sargeant, Z. Sarkar, R. Sharma, M. Knezevic, D. T. Fullwood, M. P. Miles, “Effect of pre-strain on springback behavior after bending in AA 6016-T4: Experiments and crystal plasticity modeling,” *International Journal of Solids and Structures*, vol. 283, no. 9, p. 112485, 2023.
- [12] A. R. Park, J. H. Nam, M. Kim, I. S. Jang, Y. K. Lee, “Evaluations of tensile properties as a function of austenitizing temperature and springback by V-bending testing in medium-Mn steels,” *Materials Science and Engineering: A*, vol. 787, no. 4, p. 139534, 2020.
- [13] L. Wang, G. Huang, H. Zhang, Y. Wang, L. Yin, “Evolution of springback and neutral layer of AZ31B magnesium alloy V-bending under warm forming conditions,” *Journal of Materials Processing Technology*, vol. 213, no. 6, pp. 844-850, 2013.
- [14] N. Asnafi, “Springback and fracture in v-die air bending of thick stainless steel sheets,” *Materials and Design*, vol. 21, no. 3, pp. 217-236, 2000.
- [15] H. Xie, Q. Wang, K. Liu, F. Peng, X. Dong, J. Wang, “Investigation of influence of direct-current pulses on springback during V-bending of AZ31B magnesium alloy sheet,” *Journal of Materials Processing Technology*, vol. 219, pp. 321-327, 2015.
- [16] D. Lepadatu, R. Hambli, A. Kobi, A. Barreau, “Optimisation of springback in bending processes using FEM simulation and response surface method,” *International Journal of Advanced Manufacturing Technology*, vol. 27, no. 1-2, pp. 40-47, 2005.
- [17] G. Béres, Z. Lukács, M. Tisza, “Springback evaluation of tailor welded blanks at V-die bending made of DP steels,” *Procedia Manufacturing*, vol. 47, pp. 1366-1373, 2020.
- [18] Q. Meng, R. Zhai, Y. Zhang, P. Fu, J. Zhao, “Analysis of springback for multiple bending considering nonlinear unloading-reloading behavior, stress inheritance and Bauschinger effect,” *Journal of Materials Processing Technology*, vol. 307, no. 6, p. 117657, 2022.
- [19] P. Kumar Sharma, V. Gautam, A. Kumar Agrawal, “Investigations on effect of bending radius on springback behaviour of three-ply clad sheet,” *Materials Today: Proceedings*, vol. 62, no. 3 pp. 1651-1657, 2022.

- [20] A. Polat, M. Avsar, F. Ozturk, "Effects of the artificial-aging temperature and time on the mechanical properties and springback behavior of AA6061," *Materiali in Tehnologije*, vol. 49, no. 4, pp. 487-493, 2015.
- [21] W. ping Ma, B. yu Wang, W. chao Xiao, X. ming Yang, Y. Kang, "Springback analysis of 6016 aluminum alloy sheet in hot V-shape stamping," *Journal of Central South University*, vol. 26, no. 3, pp. 524-535, 2019.
- [22] W. Guan, L. Ting, K. Linyuan, Z. Guangxu, Z. Xuejun, S. Xin, L. Zhiwen, "Influence of artificial aging time on bending characteristics of 6061 aluminum sheet," *Materwiss Werksttech*, vol. 51, no. 11, pp. 1533-1542, 2020.
- [23] Y. Choi, J. Lee, S. S. Panicker, H. K. Jin, S. K. Panda, M. G. Lee, "Mechanical properties, springback, and formability of W-temper and peak aged 7075 aluminum alloy sheets: Experiments and modeling," *International Journal of Mechanical Sciences*, vol. 170, no. 9, p. 105344, 2020.
- [24] S. Thipprakmas, W. Phanitwong, "Process parameter design of spring-back and spring-go in V-bending process using Taguchi technique," *Materials and Design*, vol. 32, pp. 4430-4436, 2011.
- [25] M.L. Garcia-Romeu, J. Ciurana, I. Ferrer, "Springback determination of sheet metals in an air bending process based on an experimental work," *Journal of Materials Processing Technology*, vol. 191, pp. 174-177, 2007.
- [26] Z. Tekiner, "An experimental study on the examination of springback of sheet metals with several thicknesses and properties in bending dies," *Journal of Materials Processing Technology*, vol. 145, pp. 109-117, 2004.
- [27] L. Heng, S. Kai-peng, Y. He, T. Yu-li, "Springback law of thin-walled 6061-T4 Al-alloy tube upon bending," *Transactions of Nonferrous Metal Society of China*, vol. 22, pp. 357-363, 2012.
- [28] A. B. Abdullah, Z. Samad, "An experimental investigation of springback of AA6061 aluminum alloy strip via V-bending process," 2013 IOP IOP Conference Series: Materials Science and Engineering Volume 50, Malaysia, 2013, pp. 513-518.

Investigation of Alkali Activated Ferrochromium Slag Composites Including Waste Marble Powder

Merve Koç Keskinçilince^{1*}, Servet Yıldız¹, Şule Sekin Eronat¹, Mehmet Emiroğlu²

¹Firat University, Technology Faculty, Department of Civil Engineering, Elazığ, Türkiye, mervekoçkeskinkilince@gmail.com, syildiz@firat.edu.tr, sulesekin23@gmail.com

²Sakarya University, Faculty of Engineering, Department of Civil Engineering, Sakarya, Türkiye, mehmetemiroglu@sakarya.edu.tr

* Corresponding Author

ARTICLE INFO

ABSTRACT

Ferrochromium slag
Alkali-activated composites
Marble powder
Alternative construction materials



Article History:

Received: 20.12.2023

Accepted: 18.04.2024

Online Available: 14.06.2024

This study investigates the potential of alkali-activated ferrochrome slag (AAFS) as a sustainable building material in combination with waste marble powder. Na_2SiO_3 and various molarity levels of NaOH, were evaluated to create AAFS. The study encompasses a comprehensive analysis, including SEM, XRD, and XRF, to understand the microstructure and chemical composition of the resulting composites. Consistency tests showed that an increase in molarity of the alkali activator decreased setting times, indicating that higher NaOH concentrations led to the earlier setting of the samples. XRD analysis revealed the presence of forsterite, spinel, and other crystal phases in the alkali-activated dough samples, suggesting incomplete activation of the ferrochrome slag. Higher molarity values improved compressive strength, while the inclusion of more waste marble powder reduced due to increased porosity. Additional tests, such as density measurements, capillarity experiments, and ultrasonic pulse velocity tests, provided valuable insights into the material's physical and mechanical properties. The results showed that temperature, molarity, and presence of waste marble influenced these properties. The compressive strength achievement of approximately 15 MPa at a modest temperature of 60°C during alkaline activation expresses the exceptional performance of the mixture, with marble powder utilized at the highest proportion (30%). This not only represents an energy-efficient solution but also showcases a sustainable approach that efficiently repurposes waste materials. As a result, this study demonstrates that AAFS, when properly activated and blended with waste marble powder, can yield alkali-activated composites with promising compressive strength and potential as a sustainable building material.

1. Introduction

Blast furnace slag is produced as a by-product during the manufacture of iron in a blast furnace. It results from the fusion of a limestone flux with ash from coke and the siliceous and aluminous residue remaining after the reduction and separation of the iron from the ore [1]. Blast furnace slag is a waste product that basically contains silica, calcium aluminates silica, and some of the basic compounds obtained during the production of iron [2]. The crystal structure of the slag is as important as its chemical compounds

consisting of $\text{CaO-SiO}_2\text{-Al}_2\text{O}_3$ [3]. Conversely, slag typically has specific surface properties similar to ordinary Portland cement; their variability and more comprehensive composition range make their reactivity less intense, particularly at early ages [4].

Ferro-alloys are commonly used as master alloys in the iron and steel industry because they are the most economical way to introduce an alloying element into the steel melt. Ferrochromium is a master alloy of iron and chromium, containing 45–80% Cr and various amounts of Fe, C, and

other elements. The ferrochromium slag consists mainly of SiO_2 , Al_2O_3 , and MgO in different phases such as spinel, $\text{MgO}\cdot\text{Al}_2\text{O}_3$, and forsterite, $\text{MgO}\cdot\text{SiO}_2$, but also smaller amounts of CaO , chromium and iron oxides and metal fragments. This slag is chemically very stable and has better mechanical properties than many rock types used in road building, paving, landfills, etc. Especially in areas where suitable rocks for these purposes are in short supply, ferrochrome slag is in great demand. Comprehensive studies have been carried out on recycling Elazığ ferrochromium slag in a certain period, either as aggregate in concrete or asphalt pavement or by replacing it with cement as supplementary cementitious materials. Some recent studies have paid attention to the potential use of ferrochromium slag as pozzolans in cement clinker and as an aggregate in concrete or asphalt mixes [5].

Zelic (2004) investigated the properties of the ferrochromium slag and the standard physical and mechanical properties of Portland cement concrete pavements made with the slag as aggregate. Zelic indicates that better concrete pavement having higher compressive strength, wear resistance, and specific weight than those from natural (limestone) aggregate in commercial Portland cement, type CEM II/B-S 42.5 (EN 197) can be made with a proper selection of slag as an artificial aggregate [5]. Yazıcıoğlu et al. (2005) investigated the effects of ferrochromium slag on compressive strength and impact energy of the concrete. They demonstrate that ferrochromium slug can be used as a cementitious material for up to 5 % to decrease the cost of concrete [6]. Yılmaz and Süttaş (2008) have investigated the usage of ferrochromium slag in the base layer material of road pavements, and they indicated that using the ferrochromium slag is a good alternative for stabilization of base layers of pavements with high traffic volume highways in terms of its satisfying strength [7].

One of the prerequisites for ensuring sustainable industrial production is the contribution of science to environmental material technologies. Although concrete is the most widely used building material today, its processes that consume the most natural resources and energy and cause environmental pollution in building

technology during cement and concrete production are not environmentally friendly [8]. During cement production, an average of 125 liters of fossil fuel and 118 kWh of electricity are consumed. Thus, it is a building material that releases greenhouse gases at a high rate [9]. For this reason, many studies have been carried out to obtain environmentally friendly alternative products for cement and concrete production. These are mainly the preference of pozzolans in concrete production, evaluation of geopolymer, and alkali-activated composites. Although these materials are generally more environmentally friendly than conventional concrete, it is known that they have disadvantages compared to concrete in terms of physical and mechanical properties [8-13]. Researchers have studied composites containing alkali-activated slag (AAC) since the 1940s. Intensive studies have been conducted on these composites' production, tests, and standardization in the last two decades. AAC stands out with its many positive features as a clinker-free composite that can be an alternative to conventional concrete production [13].

Waste marble dust, another environmental problem of industrial production, comes out after cutting and surface treatments of marble production. This waste, which has a high limestone content, has been evaluated as a filling material in cement composites in recent years, and positive results have been reported [14-17]. Alyamaç and İnce (2007) evaluated the marble sludge as a powder material in self-compacting concrete. As a result, they stated that waste marble dust could be used as a powder material to produce self-compacting concrete [18]. Demirel (2010) evaluated waste marble dust as fine aggregate in concrete production [19].

Kelestemur et al. (2014) investigated the possibility of producing fiber reinforced concrete with waste marble dust and determined the freeze-thaw resistance of the composites [20]. Alyamaç and Aydın (2015) evaluated marble dust as fine aggregate in the concretes produced with waste marble dust [21]. When the studies on ferrochrome slag are examined, it is observed that most of the studies carried out to date have focused on replacing this waste with cement by volume or weight or evaluating it as aggregate in

conventional concrete or asphalt concrete [16, 22-26]. Studies involving the evaluation of Elazığ ferrochrome slag and its use in the production of alkali-activated concrete/mortar can be listed as follows. Kantarcı (2013) and Türkmen et al. (2013) investigated the behavior of the alkali-activated composite produced with Elazığ ferrochrome slag under the influence of fire [27, 28]. Maraş (2013) examined the performance of the composite obtained with Elazığ ferrochrome slag under the influence of sulfate [29]. Mahmut and Emiroğlu (2016) investigated composites' physical and mechanical properties produced with Elazığ ferrochrome slag [30]. Elibol and Şengül (2016) investigated the possibility of using slag to produce alkali-activated mortar in their study [31]. When the studies are examined, evaluating both wastes as building materials makes it possible to produce new composites, and the environmental effects of these wastes are reduced.

When examining studies on alkali-activated slag composites and geopolymers, it becomes evident that researchers usually concentrate on critical issues such as curing conditions [32-34], strength (primarily compressive strength) [35, 36] durability [37], and hydration [38, 39]. Moreover, researchers conduct extensive studies on how to reuse various natural and artificial waste materials [40-42] in these composites.

The primary goal of this study is to explore the potential of activated composites incorporating two industrial wastes, namely Ferrochromium slag and waste marble dust, both of which are local issues. Sustainable production methods such as alkali activation have gained significant

attention in both practical applications and academic research. The study aims to develop novel composites with sufficient strength and durability for diverse applications, promoting energy efficiency and effective waste management practices.

2. Materials and Method

2.1. Determination of concrete mixture ratios

In this study, slag stored in the stocks of Etikrom A.Ş.'s Elazığ Ferrochrome plant, marble powder, sodium silicate, sodium hydroxide, and fine and coarse aggregates were used as raw materials in the production of alkaline-activated ferrochrome slag (AAFC). The specific gravity of ferrochrome slag and marble dust is 2.62. Ferrochrome slag contains 30.95% SiO₂, 20.13% Al₂O₃, and 34.83% MgO. Marble dust primarily comprises a high percentage (98.49%) of CaO. The ferrochrome slag was obtained and ground using a Los Angeles device and subsequently sieved through a 125-micron sieve. After grinding, marble powder was sieved through a 2 mm sieve and utilized in the ACC. The maximum grain diameter of the aggregate used is 12 mm. Na₂SiO₃ aqueous and NaOH solutions were used as alkaline activators in the mixtures prepared at 16, 18, and 20 mole ratios. When adding these aqueous solutions to the mixture, the ratio of NaOH to Na₂SiO₃ by weight was maintained at 1:1.50. In the study, the alkali activator (NaOH+Na₂SiO₃) to binder (slag+marble powder) ratio, as detailed in Table 1, was kept constant at 0.40. In Table 1, the ratios of EFC (Elazığ Ferrochrome Slag) to other materials were separately calculated for each molarity value.

Table 1. Geopolymer mortar mixture ratios

Alkaline Activator (NaOH+Na ₂ SiO ₃) / binder (slag+marble powder)	NaOH molarity	The rate of Waste Marble Powder (%)	EFC (g)	EFC/ Waste Marble Powder (g)	EFC/ Fine Aggregate (g)	EFC/ Coarse Aggregate (g)	EFC/NaOH (g)	EFC/Na ₂ SiO ₃ (g)
0.40	16	10	253.6	0.112	0.889	1.333	0.178	0.267
	18	20	225.4	0.250	1.000	1.500	0.200	0.300
	20	30	197.23	0.429	1.143	1.714	0.229	0.343

In addition to fine aggregate, coarse aggregate, blast furnace slag ground to a size smaller than 0.125 mm, and waste marble, sodium hydroxide,

and sodium silicate were added as activators. The prepared specimens were created by mixing fine aggregate, coarse aggregate, blast furnace slag,

and waste marble powder according to the specified mixing ratios. The alkaline activators were mixed and quickly added to the binder mixture. Each prepared specimen was placed into lubricated molds in three layers, each tamped 25 times. As a final step, the sample surfaces were leveled with the assistance of a trowel, completing the casting process.

Samples with molarity values of 16, 18, and 20 were placed in an oven for 24 hours each at activation temperatures of 25°C, 60°C, and 90°C. Once removed from the oven, the samples were kept in the molds under laboratory conditions for three days. To determine the consistency, tests were conducted on freshly prepared samples following TS EN 196-3/2017 guidelines. A spreading table test was also performed for consistency determination, following TS EN 1015-3 (2000). The samples' initial and final setting times were determined per TS EN 196-3/2017. The fresh mortar specimens samples were then subjected to SEM and XRD analysis following the relevant temperature curing. Finally, three 70x70x70 mm cube specimens were produced for each temperature and molarity value. Compressive strength tests were conducted on these cube specimens in accordance with TS EN 12390-3/2010. Additionally, ultrasound transmission rate tests, following TS EN 12504-4/2004, capillarity tests, following TS EN 3526, and unit weight tests, following TS 706 EN 12620 standard, were performed on cube samples of the same size.

2.2. Experiments on geopolymer paste

2.2.1. Consistency

The required amounts of Elazığ ferrochrome slag and waste marble powder for a 500-gram sample were accurately calculated and weighed using a precision scale with a 1-gram precision. The alkaline activator content to be added to the mixture was determined to be 25%, 30%, 35%, and 40% of the total weight and measured in graduated containers. Furthermore, a flow table experiment was performed to evaluate the consistency.

2.2.2. Determination of the setting times of samples

The sample was prepared by weighing 500 grams of Elazığ ferrochrome slag and waste marble powder. A mixture was created by measuring approximately 35% of the powder material, which amounted to 175 grams. The initial setting time, also known as the socket start time, was recorded in minutes when the socket reached an insertion depth of 3-5 mm. The specimens placed in the Vicat ring were inverted to determine the final setting time, and a needle was inserted into the instrument. The final setting time was recorded in minutes when the needle reached an insertion depth of 0.05 mm.

2.2.3. SEM analysis

Electron microscopes use data obtained from the interaction of electrons emitted from an electron source with the sample to generate images. SEM analysis, commonly used to evaluate the surface morphology of various products, including concrete, ceramics, and alkali-activated composites, was also employed to examine the microstructure of the composites produced in this study. Specifically, scanning electron microscope (SEM) analyses, a type of electron microscope, were conducted at the Inonu University Scientific and Technological Research Centre. The schematic is shown in Figure 1.

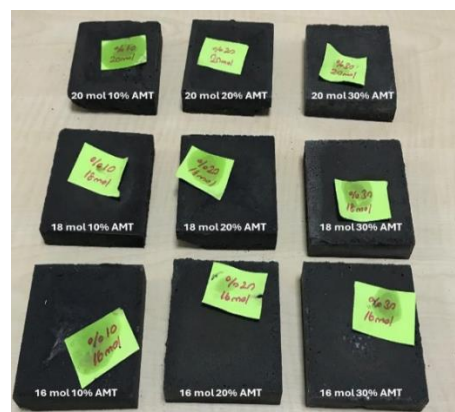


Figure 1. SEM working principle and samples prepared for analysis

2.2.4. XRD analysis

The X-ray diffraction method (XRD) is grounded on the principle that X-rays are characteristically refracted by each crystalline phase, depending on

its distinctive atomic arrangement. These diffraction profiles serve as a unique "fingerprint" for each crystal. The alkali-activated slag composites underwent XRD analyses in this study at the Central Research Laboratory of Eskisehir Osmangazi University. The shape is shown in Figure 2.

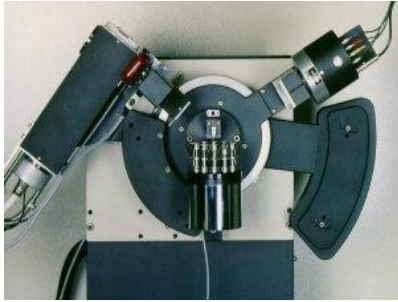


Figure 2. XRD device and samples prepared for analysis

2.2.5. XRF analysis

X-ray fluorescence (XRF) analysis can be used to analyze the composition of many materials. The fact that this method can be done quickly and a large number of elements can be analyzed non-destructively in a few minutes is one of the reasons why it is mainly preferred [43]. The chemical compositions of Elazığ ferrochrome slag and waste marble dust used in the study were analyzed by Elazığ Seza Cement with an XRF device.

2.2.6. Unit weight test

The unit weight test was conducted on 70x70x70 mm cubic samples for each temperature and molar condition in accordance with TS EN 12390-7 standards. Subsequently, calculations were performed based on the obtained measurements (Figure 3).

2.2.7. Capillarity

The capillarity test determines the capillarity coefficients (k) of concrete specimens [44]. Cubic specimens measuring 70x70x70 mm are prepared and exposed to temperatures of 60 °C and 90 °C in an oven for 24 hours. Before the experiment, the dry weights of the specimens were measured.



Figure 3. Unit weight measurements of the specimens

These specimens are then placed in a container to contact the water's surface, and weight measurements are taken at specific intervals between the first and last measurements. The amount of water absorbed through capillary action is recorded during these intervals. Capillarity coefficients are calculated using the Eq.1.

$$q^2 = \left(\frac{Q}{A}\right)^2 = k \times t \quad (1)$$

Where Q represents the absorbed water amount (g), A is the surface area (cm²), q is the water absorbed per unit area (g/cm²), and k is the capillarity coefficient (cm/sec^{0.5}). This method provides valuable information about the capillary water absorption properties of concrete [45], which is essential for assessing its durability and performance in different environmental conditions.

2.2.8. Ultrasonic pulse velocity test

The Ultrasonic Pulse Velocity (UPV), a non-destructive test, is conducted to measure the ultrasonic wave propagation velocity in the specimens, and it is performed per TS EN 12504-4 standards. 70x70x70 mm cubic samples were used, and three samples were prepared for each temperature and molar condition. Measurements are taken from the smooth surfaces of these cubic samples. During measurements, the sensors are positioned opposite each other to ensure accurate readings and a rigid platform countertop is used to facilitate sensor alignment. The UPV testing apparatus transmits ultrasound waves into the specimen, and the time it takes to pass through the specimen between its two surfaces is measured. This allows the calculation of the wave velocity within the composite. This method

provides essential data for assessing composite specimens' structural integrity and quality under varying conditions [30].

$$UPV = \frac{l}{V}(\text{km/sec}) \quad (2)$$

In this context, the variables used to calculate the speed of sound waves (V) in alkali-activated slag composite are V (speed in km/s), S (L) (distance in meters), and t (transit time in μs). The resulting UPV values estimate the composite's quality, allowing for quick assessments of its structural characteristics and suitability for various applications [30].

2.2.9. Compressive strength

The compressive strength test involved 70x70x70 mm cubic samples for various temperatures and molar conditions, following TS EN 12390-3 standards. A constant loading rate of 0.4 MPa/s was applied until the maximum load was reached. The results were obtained by averaging data from three samples for each condition. The shape is shown in Figure 4.

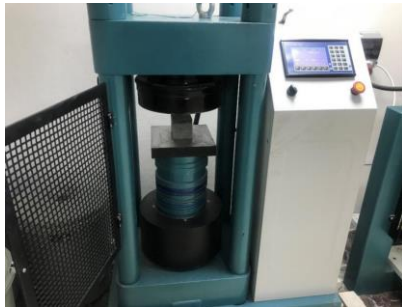


Figure 4. Picture of compressive strength test

3. Findings and Discussion

3.1. Consistency determination and setting time results

Flow diameter test and setting time determination tests were performed on the prepared blast furnace slag alkali-activated composite mortar, and the results are presented in Figure 5 and Figure 6.

The flow diameter values of the specimens decreased with an increase in MP content in all series. These results suggest that the consistency of the composites decreases as the percentage of

marble powder increases, regardless of the molarity of the alkaline activator (NaOH).

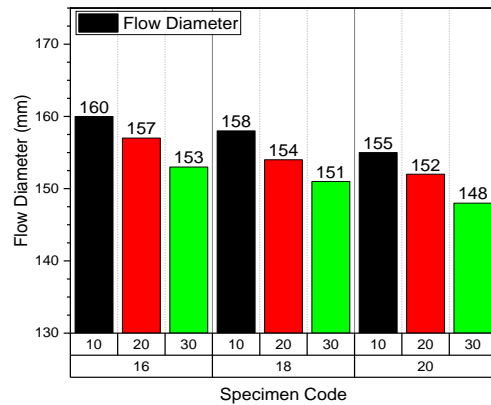


Figure 5. Flow table test result

Based on the results obtained from the setting time experiments, it is evident that an increase in the molarity of the NaOH solution leads to a decrease in the initial setting time of the samples (Figure 5). In other words, using a higher concentration of NaOH allows the samples to be set earlier. The experimental results indicate that AAFC composites typically initiated the setting process within an average time of 60 minutes.

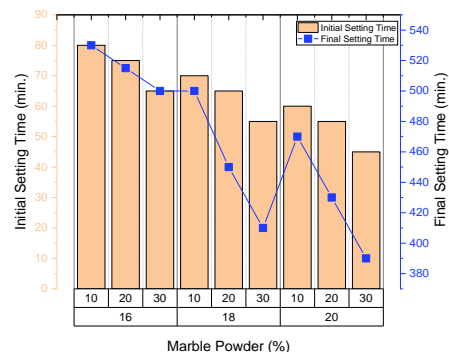
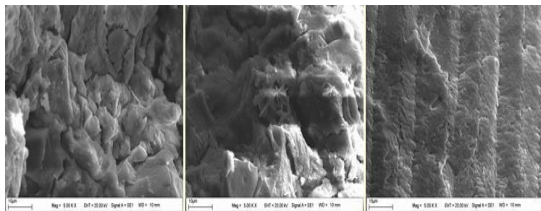


Figure 6. Setting time test result

Moving on to Figure 6, a similar relationship is observed between NaOH molarity and the setting times, specifically regarding the final setting time. It was observed that the samples' final setting times ranged between 390 minutes and 530 minutes (approximately 6-9 hours). Notably, the inclusion of marble powder instead of ferrochrome slag resulted in a reduction in both the initial and final setting times of the samples. Including marble powder instead of ferrochrome slag resulted in an earlier setting of the samples, indicating a decrease in the setting time as the molarity value of the mixture increased.

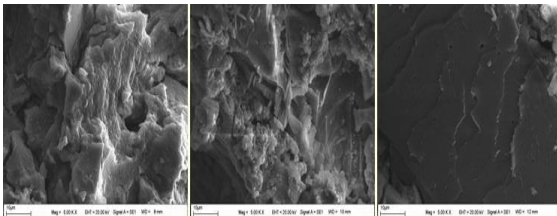
3.2. Results of SEM analysis

Specimens were prepared by incorporating 10%, 20%, and 30% waste marble dust in the alkali-activated composites, followed by curing at an activation temperature of 60°C. SEM images of these specimens are presented in Figure 7., Figure8., Figure 9. Upon examining the figures, it is evident that the specimens exhibit a dense and smooth structure of sodium aluminosilicate hydrate (NASH) gels. The cracks in the samples observed in the SEM images are likely attributed to two factors. Firstly, it is believed to result from incomplete NASH (sodium aluminosilicate hydrate) gelation, which can lead to structural weaknesses and crack formation. Secondly, the crumbling of the samples during the preparation for analysis may have contributed to the appearance of cracks.



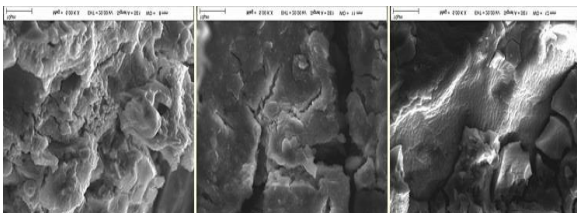
a) % 10 AMT, b) % 20 AMT, c) % 30 AMT

Figure 7. SEM images of samples containing 16 mol NaOH cured at 60°C activation temperature



a) % 10 AMT, b) % 20 AMT, c) % 30 AMT

Figure 8. SEM images of samples containing 18 mol NaOH cured at 60°C activation temperature

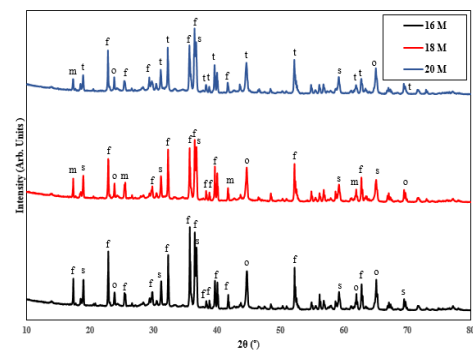


a) % 10 AMT, b) % 20 AMT, c) % 30 AMT

Figure 9. SEM images of samples containing 20 mol NaOH cured at 60°C activation temperature

3.3. Results of XRD analysis

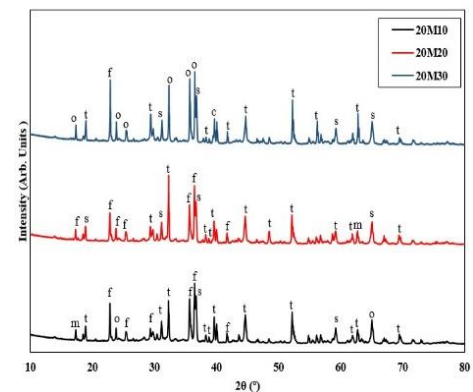
XRD experiments were conducted on alkali-activated dough samples, which were subsequently ground into powder for analysis. The XRD diffractograms of the samples are depicted in Figure 10. and Figure 11. Upon examining the diffractograms, distinct peaks corresponding to crystal phases of forsterite (Mg_2SiO_4), spinel ($MgAl_2O_4$), olivine ($(Mg,Fe)_2SiO_4$), and magnesium iron silicate ($Fe_{0.2}Mg_{1.8}SiO_4$) were observed in relation to the alkali-activated dough samples.



f: forsterite, s: spinel, o: olivine,

m: magnesium iron silicate, t: tobermorite

Figure 10. XRD diffractograms of samples containing 16M, 18M, and 20M NaOH



f: forsterite, s: spinel, o: olivine,

m: magnesium iron silicate, t: tobermorite

Figure 11. XRD diffractograms of samples containing 20M NaOH

In their study, Yazıcı and Kaya (2003) examined the XRD analyses of samples taken from ferrochrome slag. Since the elemental analysis results in the fractions were closely matched, the phases containing chromium elements could not be observed in the diffractograms. Instead, forsterite (Mg_2SiO_4) and spinel ($MgAl_2O_4$) crystal phases were prominently detected [46]. This suggests that ferrochrome slag did not

undergo sufficient reaction, especially at 16 and 18 mol NaOH molarities. However, at 20 mol NaOH molarity, the presence of CSH peaks in the XRD analysis indicates that the slag requires a higher NaOH molarity for activation. In another study by Türkmen et al. (2019), they reported the presence of spinel and forsterite crystals in the XRD analysis of ferrochrome slag-based geopolymer samples. These peaks were attributed to the ferrochrome slag, suggesting incomplete activation [28].

Additionally, in the samples prepared with a 20 mol activator, formations of tobermorite (C-S-H) were also observed. This observation suggests that at higher molarity values, such as 20 mol, the hydration of CaO in the marble powder occurs. As a result, CSH (calcium silicate hydrate) gels are formed in a manner similar to those found in cement-based samples.

3.4. XRF analysis results

XRF analysis results on ferrochrome slag and marble powder used in the study are depicted in Table 2.

Table 2. shows that the chemical composition of Elazig ferrochrome slag is dominated by MgO (34.83%), SiO₂ (30.95%), Al₂O₃ (20.13%), and Cr₂O₃ (6.22%). It is understood that these results agree with the information presented by Vapur et al. (2013) and Yazıcıođlu et al. (2003) [47, 48]. Yılmaz and Süttaş (2008) observed that silicon, magnesium, aluminum, and calcium elements dominate in the chemical content of ferrochrome slag. It was stated that the elements in oxides constitute 95% of the slag on average. Small amounts of iron and chromium were also observed [7]. In light of the XRF results of the waste marble powder, it is understood that the waste marble dust used in the study consists of a high proportion (98.49%) of CaO when the loss of superheat is not considered. The chemical composition results obtained in this study were analyzed and are consistent with the data [49].

Table 2. XRF results of ferrochromium slag and marble powder used in the study

Materials/Oxides (%)	SiO ₂	Al ₂ O ₃	Fe ₂ O ₃	CaO	MgO	Cr ₂ O ₃	L.O.I.
Slag	30.95	20.13	2.72	2.58	34.83	6.22	1.61
Marble Powder	0.18	0.32	0.01	56.05	0.47	--	43.09

3.5. Tests applied to hardened concrete specimens

3.5.1. Density test

Based on the experimental results, the density values were generally found to be 2.49 g/cm³. In the 18-mole samples, the highest density value of 2.49 g/cm³ was obtained in the samples containing 10% waste marble powder and cured at 25°C. A decrease in unit weight values was observed with increasing temperature.

Density measurements for AAFC specimens were performed after a 28-day curing period at 60°C and 90°C. It is observed that the density values of specimens cured at both 60°C and 90°C are positively affected as the molarity of the NaOH alkali solution increases.

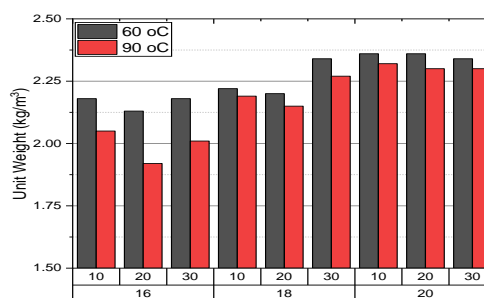


Figure 12. Unit weight of the specimens

Figure 12 shows how density values change when marble powder is used in the mixtures. It is believed that the lower density values in some samples, despite the filling effect of marble powder, may be attributed to insufficient chemical reactions during activation when marble powder is substituted.

3.5.2. The results of the capillarity experiment

When the results of the capillarity experiments were observed, the capillarity coefficients decreased with the increase in molarity. In contrast to this situation, it was observed that capillarity increased with the rise in marble dust. The highest capillarity coefficient value was obtained from the samples at 16 molarity, while the lowest capillarity coefficient results were obtained from the samples at 20 molarity. The shape is shown in figure 13.

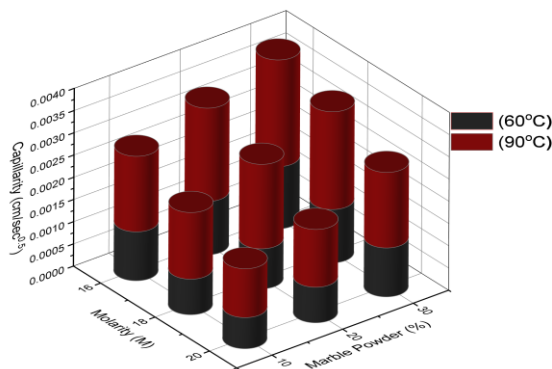


Figure 13. Capillarity test result

3.5.3. The results of the ultrasonic pulse velocity test

As a result of the experimental findings, the ultrasonic pulse velocity values of the samples decreased with the increase in the amount of waste marble dust; the increase in the molarity ratio increased the ultrasonic pulse velocity of the samples (Figure 14).

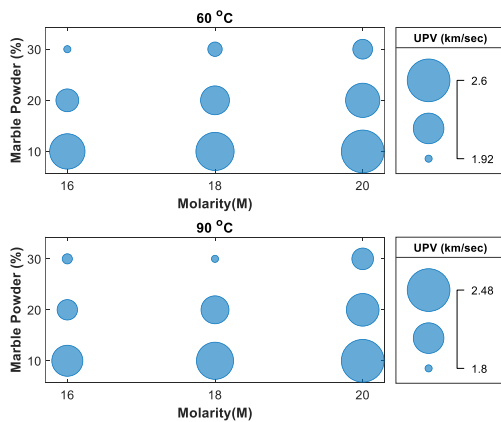


Figure 14 Ultrasonic pulse velocity (UPV) values of the specimens

3.5.4. Compressive strength

Compression tests were performed on the specimens in accordance with TS EN 12390-3/2010 with a constant loading rate of 0.4 MPa/s. The results obtained were calculated by taking the average of these three samples.

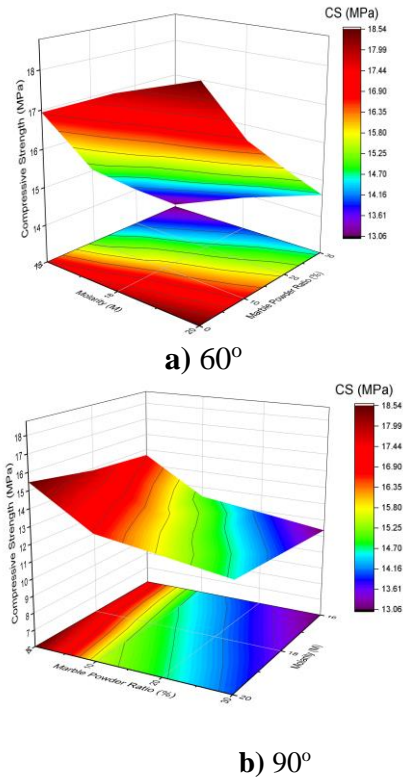


Figure 15. Compressive strength (CS) of the specimens (under 60° and 90° degrees)

When the test results obtained from the specimens, cast in groups of three for each mixture ratio (10%, 20%, 30%), and cured separately at 25°C, 60°C, and 90°C, were analyzed, the highest strengths were achieved in the specimens cured at 60°C activation temperature. According to the data obtained, the highest strength of 16.85 MPa was recorded for the mixture prepared with a 20 mol activator and 10% marble powder. With an increase in activation temperature, some decrease in strength was observed, especially in the samples cured at 90°C.

The increase in compressive strengths was observed to have a strong positive correlation with the rise in molarity values, indicating a high linear relationship. However, when considering the specimens containing 100% ferrochrome slag used for control purposes, a decrease in

compressive strength was observed as the amount of waste marble dust substitution increased. The ratios of marble dust substitution inversely affected the compressive values. The shape is shown in figure 15.

4. Conclusion

In conclusion, the critical findings of this study can be summarized as follows:

- Sodium silicate and sodium hydroxide as alkaline activators contribute to forming alkali-activated concrete, demonstrating binding properties.
- SEM analyses revealed a dense and smooth structure in the samples, but crack formations were observed, potentially occurring during sample reduction for analysis.
- Diffractograms showed the presence of crystal phases such as forsterite, spinel, olivine, magnesium iron silicate, and tobermorite in the alkali-activated dough samples.
- The molarity value of alkaline activators and the ratio of waste marble powder influenced the spreading diameters and receptacle durations of the samples.
- Compressive strength increased with higher molarity values, while the inclusion of more waste marble powder led to a decrease in compressive strength due to an increased clearance rate in the internal structure.
- Temperature had an impact on unit weight values, with an increase resulting in a decrease, and water absorption decreased with increasing molarity.
- Ultrasound passage rates were influenced by the molarity ratio and the presence of waste marble powder, with higher ratios and less marble powder resulting in increased passage rates.
- During capillarity experiments, stains were observed on sample surfaces due to sodium hydroxide accumulation.

- Alkaline-activated mixtures containing Elazığ ferrochrome slag and waste marble powder demonstrated compressive strengths above 16 MPa, increasing with higher molarity values.

- Elazığ ferrochrome slag used in the study was observed to be finer-grained than waste marble dust. The specific surface area of ferrochrome slag was 2375.1 cm²/g, while the specific surface area of waste marble dust was 1187.8 cm²/g. The chemical composition of Elazığ ferrochrome slag was mainly composed of MgO, SiO₂, Al₂O₃, and Cr₂O₃, while the composition of waste marble dust was 98.49% CaO.

- Based on the analysis of strength and durability, it was observed that the mixtures containing 20M NaOH and reference (0%) activated at 60°C, combined with 10% waste marble powder, exhibited the best results. In terms of sustainability, it can be concluded that the series with 20M NaOH molarity and 30% waste marble dust activated at 60°C is the most suitable option, as it has the necessary strength and durability properties.

Article Information Form

Funding

The author received no financial support for this paper's research, authorship, and/or publication.

Authors' Contribution

Merve Koç Keskinçin: Resources, Conceptualization, Investigation, Methodology, Visualization, Formal analysis, Writing – original draft. Servet Yıldız: Resources, Supervision, Methodology, Conceptualization, Şule Sekin Eronat: Formal analysis, Investigation, Visualization, Formal analysis, Conceptualization, Writing – original draft, Writing – review & editing. Mehmet Emiroğlu: Conceptualization, Methodology, Formal analysis, Visualization, Writing – original draft, Writing – review & editing.

The Declaration of Conflict of Interest / Common Interest

No conflict of interest or common interest has been declared by the author.

The Declaration of Ethics Committee Approval

The author declares that this document does not require an ethics committee approval or any special permission.

The Declaration of Research and Publication Ethics

The author of the paper declares that he complies with the scientific, ethical, and quotation rules of SAUJS in all processes of the paper and that he does not make any falsification on the data collected. In addition, he declares that Sakarya University Journal of Science and its editorial board have no responsibility for any ethical violations that may be encountered and that this study has not been evaluated in any academic publication environment other than Sakarya University Journal of Science.

Copyright Statement

Authors own the copyright of their work published in the journal and their work is published under the CC BY-NC 4.0 license.

References

- [1] J. Newman, B. S. Choo, "Advanced Concrete Technology: Constituent Materials" Butterworth-Heinemann, 2003.
- [2] Ş. Erdoğan, Ş. Kurbetçi, "Betonun performansına sağladıkları etkinlik açısından kimyasal ve mineral katkı maddeleri", Türkiye Mühendislik Haberleri, 426, 115-120, 2003.
- [3] A. Dorum, Y. Koçak, B. Yılmaz, A. Uçar, "Yüksek Fırın Cürufunun Çimento Yüzey Özelliklerine ve Hidratasyona Etkileri", DPÜ Fen Bilimleri Enstitüsü Dergisi, Sayı 19, pp., 47-58, 2009.
- [4] M. Riekkola., Vanhanen, "Finnish expert report on best available techniques in ferrochromium production", Environmental Institute Helsinki, pp. 1-50, 1999.

- [5] J. Zelic, "Properties of concrete pavements prepared with ferrochromium slag as concrete aggregate", Cement and Concrete Research 35, 2340-2349, 2005.
- [6] S. Yazıcıoğlu, T. Gönen, Ö. C. Çobanoğlu, "Elazığ Ferrokrom Cürufunun Betonun Basınç Dayanımı ve Çarpma Enerjisi Üzerine Etkisi", Fırat Üniv. Fen ve Müh. Bil. Der. 17 (4), 681-686, 2005.
- [7] A. Yılmaz, İ. Süttaş, "Ferrokrom Cürufunun Yol Temel Malzemesi Olarak Kullanımı." Teknik Dergi, 19(93), 4455-4470, 2008.
- [8] N. R. Rakhimova, R. Z. Rakhimov, "Toward clean cement technologies: a review on alkali-activated fly-ash cements incorporated with supplementary materials." Journal of Non-Crystalline Solids, 509, 31-41, 2019.
- [9] M. Saedi, K. Behfarnia, H. Soltanian, "The effect of the blaine fineness on the mechanical properties of the alkali-activated slag cement". Journal of Building Engineering, 26, 100897, 2019.
- [10] A. Fernández-Jiménez, A. Palomo, "Composition and microstructure of alkali activated fly ash binder: Effect of the activator". Cement and concrete research, 35(10), 1984-1992, 2005.
- [11] F. Pacheco-Torgal, J. Labrincha, C. Leonelli, A. Palomo, P. Chindaprasit, "Handbook of alkali-activated cements, mortars and concretes", Elsevier, 2014.
- [12] Y. Kocak, S. Nas, "The effect of using fly ash on the strength and hydration characteristics of blended cements". Construction and Building Materials, 73, 25-32, 2014.
- [13] P. Rovnaník, I. Kusák, P. Bayer, P. Schmid, L. Fiala, "Comparison of electrical and self-sensing properties of Portland cement and alkali-activated slag mortars". Cement and Concrete Research, 118, 84-91, 2019.

- [14] M. Keskinlınç Koç, “Alkali aktive edilmiş harç üretiminde krom cürufu ve atık mermer tozunun değerlendirilmesi”, Yüksek Lisans Tezi, Fırat Üniversitesi, Fen Bilimleri Enstitüsü, Elazığ, 2019.
- [15] A. Yılmaz, “Antalya Ferrokrom İşletmesinin Elektrik-Ark Fırını Cüruflarının ve Baca Tozu Atıklarının Asfalt Betonunda Kullanılabilirliğinin Araştırılması”, Yüksek Lisans Tezi, Akdeniz Üniversitesi, Antalya, 2002.
- [16] M. M. Yadollahi, S. Varolgüneş, F. İşsever, “Na₂O, silika modülü, su/bağlayıcı oranı ve yaşlanmanın cüruf tabanlı geopolimerlerin basınç mukavemetinde olan etkileri”. *Türk Doğa ve Fen Dergisi*, 6(2), 26-31, 2017.
- [17] A. Şentürk, L. Gündüz, Y. İ. Tosun, A. Sarıışık, “Mermer teknolojisi”. Süleyman Demirel Üniversitesi Mühendislik Mimarlık Fakültesi Maden Mühendisliği, Isparta, 1996.
- [18] K. E. Alyamaç, R. İnce, “Study on the usability of waste marble mud in self-compacting concrete as a powder material”. In *Proceedings of TÇMB 3rd International Symposium*, Istanbul, Turkey, pp. 821-832, 2007.
- [19] B. Demirel, “The effect of the using waste marble dust as fine sand on the mechanical properties of the concrete”. *Int. J. Phys. Sci.* 5, 1372-1380, 2010.
- [20] O. Keleştemur, S. Yıldız, B. Gökçer, E. Arıcı, “Statistical analysis for freeze-thaw resistance of cement mortars containing marble dust and glass fiber”. *Materials & Design*, 60, 548-555, 2014.
- [21] K. E. Alyamac, A. B. Aydın, “Concrete properties containing fine aggregate marble powder”. *KSCE Journal of Civil Engineering*, 19, 2208-2216, 2015.
- [22] Ö. Can, “Ferrokrom cürufunun kerpicing mühendislik özelliklerine etkisi”, Selçuk-Teknik Dergisi, [S.1.], Cilt 7, Sayı:2 pp. 175-185, 2008.
- [23] M. Yılmaz, B. V. Kök, “Ferrokrom cürufu kullanımının bitümlü sıcak karışımların mekanik özelliklerine etkisi”, Süleyman Demirel Üniversitesi Fen Bilimleri Enstitüsü Dergisi, 12(3), 186-194, 2008.
- [24] A. Yılmaz, M. Kardeşahin, “Mechanical properties of ferrochromium slag in granular layers of flexible pavements”. *Materials and structures*, 43(3), 309-317, 2010.
- [25] O. Gencil, F. Koksal, C. Özel, W. Brostow, “Combined effects of fly ash and waste ferrochromium on properties of concrete”. *Construction and Building Materials*, 29, 633-640, 2012.
- [26] O. Gencil, M. Sutcu, E. Erdogmus, V. Koc, V. V. Cay, M. S. Gok, “Properties of bricks with waste ferrochromium slag and zeolite”. *Journal of Cleaner Production*, 59, 111-119, 2013.
- [27] F. Kantarcı, “Elazığ ferrokrom cürufundan alkali aktivasyon metoduyla üretilen geopolimer çimentolu betonların yangın dayanımının araştırılması”, Yüksek Lisans Tezi, İnönü Üniversitesi, Malatya, 2013.
- [28] İ. Türkmen, M. M. Maraş, M. B. Karakoç, R. Demirboğa, F. Kantarcı, “Fire resistance of geopolymer concrete produced from Ferrochrome slag by alkali activation method”. In *2013 International Conference on Renewable Energy Research and Applications (ICRERA)*, IEEE, pp. 58-63, 2013.
- [29] M. M. Maraş, “Elazığ Ferrokrom cürufundan üretilen geopolimer çimentolu betonların sülfat direncinin araştırılması”, Yüksek Lisans Tezi, İnönü Üniversitesi, Malatya, 2013.
- [30] O. Mahmut, M. Emiroğlu, “Elazığ Ferrokrom Cürufunun Alkali Aktive Edilmiş Harç Üretiminde Kullanım Potansiyelinin Araştırılması”. Fırat

- Üniversitesi Mühendislik Bilimleri Dergisi, 28(1), 23-34, 2016.
- [31] C. Elibol, O. Sengul, "Effects of Activator Properties and Ferrochrome Slag Aggregates on the Properties of alkali-activated Blast Furnace Slag Mortars", *Arabian Journal for Science and Engineering*, 41(4), pp. 1561–1571, 2016.
- [32] S. Shin, G. Goh, C. Lee, "Predictions of compressive strength of GPC blended with GGBFS developed at varying temperatures". *Construction and Building Materials*, 206, 1-9, 2019.
- [33] Y. D. Adufu, S. O. Sore, P. Nshimiyimana, "Effect of curing conditions on physico-mechanical properties of metakaolin-based geopolymer concrete containing calcium carbide residue". *MRS Advances* 8, 591–595, 2023.
- [34] R. G. Sertbakan, İ. İ. Atabey, U. Durak, S. İlkentapar, O. Karahan, C. D. Atış, "Alkali ile Aktive Edilmiş Cüruf ve Uçucu Kül Harçlarına Yüksek Sıcaklık Sonrası Hava Kürünün Etkisi", *Düzce Üniversitesi Bilim ve Teknoloji Dergisi*, 10 (2022) 114-126.
- [35] Z. B. Öztürk, İ. İ. "Atabey, Mechanical and microstructural characteristics of geopolymer mortars at high temperatures produced with ceramic sanitaryware waste". *Ceramics International*, 48(9), 12932-12944, 2022.
- [36] X. Liu, C. Shi, Y. Yao, "Strengthening Mechanism of Geopolymer Lightweight Cellular Concrete Reinforced with Glass Fibers". *Arab J Sci Eng*, 2024.
- [37] İ. İ. Atabey, O. Karahan, C. Bilim, C. D. Atış, "The influence of activator type and quantity on the transport properties of class F fly ash geopolymer". *Construction and Building Materials*, 264, 120268, 2020.
- [38] S. Song, D. Sohn, Jennings, H.M. et al. "Hydration of alkali-activated ground granulated blast furnace slag". *Journal of Materials Science* 35, 249–257, 2000.
- [39] S. Pu, Z. Zhu, W. Song, W. Huo, J. Zhang, "Mechanical and microscopic properties of fly ash phosphoric acid-based geopolymer paste: A comprehensive study". *Construction and Building Materials*, 299, 123947, 2021.
- [40] X. Jiang, R. Xiao, Y. Ma, M. Zhang, Y. Bai, B. Huang, "Influence of waste glass powder on the physico-mechanical properties and microstructures of fly ash-based geopolymer paste after exposure to high temperatures". *Construction and Building Materials*, 262, 120579, 2020.
- [41] N. Bheel, P. Awoyera, I. A. Shar, S. A. Abbasi, S. H. Khahro, A. K. Prakash, "Synergic effect of millet husk ash and wheat straw ash on the fresh and hardened properties of Metakaolin-based self-compacting geopolymer concrete". *Case Studies in Construction Materials*, 15, e00729, 2021.
- [42] S. Çelikten, İ. İ. Atabey, "Farklı Silis ve Alümin Kaynaklarının Atık Mermer Tozu Esaslı Alkali ile Aktive Edilmiş Harçların Özelliklerine Etkisi". *Mühendislik Bilimleri ve Tasarım Dergisi*, 9(2), 396-405, 2021.
- [43] İ. Küçük, "X-Işını Floresans Spektroskopisi (XRF) Deney Föyü", *Bursa Teknik Üniversitesi* 2017.
- [44] Ü. Yurt, F. Bekar, "Comparative study of hazelnut-shell biomass ash and metakaolin to improve the performance of alkali-activated concrete: A sustainable greener alternative", *Construction and Building Materials*, 320, 126230, 2022.
- [45] M. Şahmaran, V.C. Li, "Influence of microcracking on water absorption and sorptivity of ECC." *Materials and structures*, 42, 593-603, 2009.
- [46] A. Yazıcı, M. Kaya, "Ferrokrom Curufunun Karakterizasyonu", *F.Ü. Fen ve Mühendislik Bilimleri Dergisi*, 15(4), 539-548, 2003.

- [47] H. Vapur, T. O. P. Soner, A. Teymen, M. Trkmenođlu, “Elazıđ Ferrokrom Tesisi Crflarının Agrega zelliklerinin Arastırılması”. ukurova niversitesi Mhendislik- Mimarlık Fakltesi Dergisi, 28(1), 77-88, 2013.
- [48] S. Yazıcıođlu, E. Arıcı, T. Gnen, “Elazig errokrom Crfunun Betonda Karbonatlamaya Etkisi”, 5. Ulusal Beton Kongresi Betonun Dayanıklılığı (Durabilite), Insaat Mhendisleri Odasi Istanbul Subesi, 2003.
- [49] B. Demirel, K. E. Alyama, “Waste marble powder/dust”. In Waste and Supplementary Cementitious Materials in Concrete, pp.181-197, Woodhead Publishing, 2018.

Investigation of Modifying Alloying Elements in High-Pressure Injection Casting Eutectic Al-Si Alloys

Alparslan Kılıçarslan^{1*} , Hatem Akbulut² 

¹ Ayhan Metal Pressure Casting A.S., Kocaeli, Türkiye, alparslankilicarslan@gmail.com

² Sakarya University, Faculty of Engineering, Department of Metallurgy and Materials Engineering, Sakarya, Türkiye
² NESSTEC Energy & Surface Technologies A.S., Technology Development Zones, Sakarya, Türkiye, akbulut@sakarya.edu.tr

*Corresponding Author

ARTICLE INFO

ABSTRACT

Keywords:
AlSi12(Fe) alloy
High-Pressure casting
Ti and Sr modification
Microstructure
Mechanical properties



Article History:
Received: 23.12.2023
Accepted: 13.05.2024
Online Available: 24.06.2024

In the study, the mechanical properties of aluminum alloys produced by the injection molding method, especially using Strontium and Titanium metals, were optimized without being subjected to cold forming. Mechanical tests were applied to the alloys produced by the high-pressure casting technique, and their strength, hardness, and microstructure were examined. Optical and SEM microscopy examinations investigated grain structures. Within the scope of the study, AlTi5B1 master alloy and AlSr10 master alloy were added to the pure AlSi10 (Fe) alloy in 5 different compositions. AlTi5B1 master alloy added to pure AlSi10(Fe) alloy significantly increased the hardness by reducing the grain size. Si modification took place with the addition of AlSr10 master alloy, and it was observed that the obtained weight ratios of 150ppm, 300ppm, and 450ppm Sr increased the hardness proportionally by 2.5 HB each. With the increase in Ti and Sr master alloys added, a significant increase was observed in tensile and yield strengths and % elongation rates. In the compression test, the percentage (%) deformation elongation, the reduction of the grain structure of the material by the added Ti and Sr elements, and the transformation of the eutectic silicon into a spherical structure absorbed the applied Fm force. This led to an increase in strength, and while the permanent deformation elongation decreased as the weight of Ti increased, it was observed that the permanent deformation elongation decreased proportionally with each added amount of 150 ppm Sr. The addition of the Ti element reduced the grain size by shrinking the α -Al dendrites, but it did not affect the eutectic Si.

1. Introduction

Ti and Sr elements are widely used as grain refiners and modifiers in aluminum alloys to increase the durability of the material by improving its mechanical properties. In aluminum alloys, the strength is increased by low-temperature pressing (dislocation formation) to obtain the required strength under a certain load. The structure after the deformation process applied to Al and its alloy in the rolling manufacturing method elongation of equiaxed grains in the direction of rolling and with the elongation allowing shape change within the

structure in direct proportion to the refinement of the force. The strengthening of the material occurs as a result of the increase in the number of dislocations at the grain boundaries. It restricts and creates stress hardening within the structure. With stress hardening, An increase in the strength properties of the material is observed [1].

It has been expected that the mechanical properties of aluminum alloys produced by injection molding, especially those using Sr and Ti metals, will be improved without the need for cold forming. A unique aluminum alloy with

high strength and low permanent deformation was developed by adding some alloying elements to aluminum alloys in different proportions as grain refiners and modifiers. To improve the formability, reduction efficiency, and mechanical properties of Al-Mg-Si alloy, 6063 aluminum alloy. It has been found that melting the homogeneous billet in the second stage and cooling it in the furnace not only produced brittle cracks during the extrusion process but also refined the grain size. Online quenching of 6063 aluminum alloy profiles with complex cross-sections can prevent abnormal grain growth during the offline solid solution process and improve production efficiency. The strength of profiles extruded from cast billets and air-cooled homogeneous billets was found to be comparable. Therefore, most 6063 aluminum alloy profiles are extruded directly from molten billets without the need for homogenization, improving production efficiency. It was found that homogeneous billets cooled in the furnace had the lowest flow stress. This shows that the breaking force that can cause extrusion is lower. It is recommended to use oven-cooled homogeneous blanks for profiles with complex cross-sections or requiring high performance. In the Al-Mg-Si AA 6068 alloy, including Cu and Zr, microstructure, mechanical properties, and fatigue properties were studied. The alloy was characterized in its original form after homogenization, extrusion, and T6 heating. The microstructure and fracture morphology of the fractured samples were analyzed using optical microscopy, scanning electron microscopy, transmission electron microscopy, and energy dispersive spectrometry. The quasi-static strength of the AA 6086 aluminum alloy was significantly higher than some other AA 6xxx alloys, but the ductility remains almost the same. Extensive fatigue test results under low-cycle fatigue (LCF) and high-cycle fatigue (HCF) conditions demonstrated good fatigue resistance. The new AA 6086 aluminum alloy has provided a reasonable basis for engineering design applications [2].

Controlling the microstructure and mechanical properties with additively produced aluminum-silicon alloys has been reported to be an important part of the automotive and aerospace industries. This is a popular choice that has

proven to be cost-effective, with good defect tolerance and static properties. However, these alloys have unique properties when processed via laser powder bed fusion (LPBF). Although finely dispersed silicon precipitates can produce fine-grained microstructures with superior static properties than their cast counterparts, they cause weak directional connections through layered deposition. This reduces shear and crack resistance, weakening and strengthening the structure. Therefore, these effects must be taken into account in the design of parts produced using LPBF. Heat treatments can complement machining procedures and improve critical properties such as ductility and fatigue strength, but often reduce the static strength of the material. In general, a more comprehensive range of achievable properties, including tensile, compressive, and torsional behavior, fracture toughness, and fatigue resistance, are achieved [3]. The nanostructured Al-9%Si-3%Cu alloy obtained by direct metal laser sintering (DMLS) was then processed using the high-pressure torsion (HPT) process. This results in significant grain refinement down to 60 nm, as well as significant dislocation density. These results demonstrate that controllable ultra-fine-grained microstructures can be achieved through coating fabrication and efficient severe plastic deformation processes [4].

Controlling microstructure and, therefore, mechanical and physical properties have been widely used for aluminum alloys, including age hardenable aluminum alloy materials [5]. In general, the researchers demonstrated that grain refinement can not only refine the grain size but also achieve partially modified microstructure from coarse silicon particles broken up into smaller pieces [6].

Since the excellent casting behavior and mechanical and corrosion properties of Al-Si-based alloys for the manufacture of lightweight components with complex geometries, grain refinement to improve the properties further needs to use different alloying elements and modifiers. The addition of Sr and Ti alone as solutes has little effect on grain size. Because of this, together with the Sr addition to the Al-Si

alloys, Ti addition is also aimed at using the Al-5Ti-1B refiner [7]. It has been reported by Bogdanoff et al., that the addition of 0.12–0.13% Ti and 100–150 ppm Sr modification elements into the Al-Si alloys results in a continuous increase of Si content with an apparent strength increase up to an amount of 11.4% [8]. It has been reported that the combined addition of Ti and Sr resulted in a considerable improvement in tensile properties for the extruded and T6-heat-treated Al 6070 alloys [9].

In the Al-Si-Cu-Ni alloy, Dong et al. found that the combined effect of Ti and Sr on the microstructure and mechanical properties of the alloy was positive. They have shown that the addition of 0.1% Ti and 0.02% Sr significantly reduced grain size and changed the morphology of eutectic Si. The strength and plasticity were increased considerably with ultimate tensile strength, yield strength, and elongation [10]. Similarly, Lee et al. studied the effect of Sr modifier and Ti in the form of an Al-Ti-B grain refiner in the Al-7Si-0.35Mg cast alloy, and they investigated the interaction between Sr and Al-5Ti-1B. They reported that the combined additions of Sr and Ti produced both eutectic Si modification and α -Al grain refinement while increasing the nucleation frequency of Al-Si eutectic grains compared to an alloy with the addition of Sr alone [11].

In this study, in the commercial AlSi12 alloy, the systematic research on the microstructural and mechanical properties is aimed to perform. The double addition effect of Ti and Sr on the primary a-grain and eutectic silicon crystals is targeted to optimize.

2. Experimental Studies

2.1. Method

Within the scope of this study, the modification of aluminum and silicon was achieved by adding Ti and Sr to the AlSi12 (Fe) alloy cast under high pressure. At the same time, the addition of Ti modified Al, the addition of Sr modified Si. Ti addition affects grain refinement. The mechanical effects of Ti addition and Sr addition on the eutectic Si alloy were investigated. To examine the impact of Ti modification and Sr

modification on Al-Si alloy parts produced by the high-pressure casting method, Sr alloys were tried at 0.08% Ti and 0 ppm (without Sr addition), 150ppm, 300ppm, and 450ppm rates. A Radiographic (Digital RT) examination of the parts produced in the casting was carried out. The method applied in the experimental study, and the alloys used are shown in Figure 1.

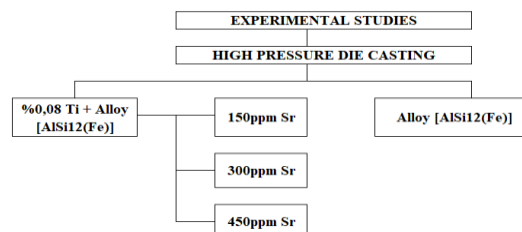


Figure 1. Methods and alloys applied in the experimental study schematic (representation)

Casting was made from AlSi10(Fe) ingot in accordance with EN AC 44300 standard, without adding Ti and Sr to pure AlSi10(Fe). Casting was carried out by adding AlTi5B1 master alloy with 0.08% Ti alloy by weight. Casting parts were produced by adding AlSr10 master alloy for 150ppm Sr, 300ppm Sr, and 450ppm Sr alloys by weight. A total of 20 prints were obtained from a single charge in approximately 30 minutes, with a cycle time of 90 sec/print. The tests carried out within the scope of the experimental studies applied to the obtained sprue parts are shown in Figure 2.

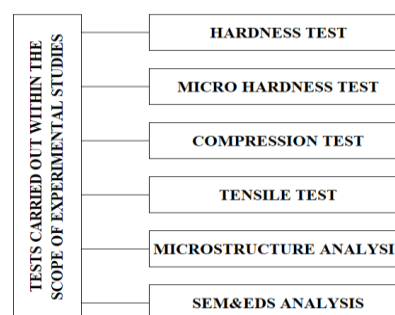


Figure 2. Tests to be applied in experimental studies schematic (representation)

2.2. Alloys and materials used in the research

AlSi12(Fe) alloy was used in the experimental study. The alloy's equivalent in international standards is EN AC 44300 (EN), ISO AlSi12(Fe) (DIN EN 1676), ETİAL140 (Eti Alüminyum), LM6(UK), A-S13(FR), UNI 4514, AC3A(JPN).

and in AA, it is known as ASTM-A413(USA). For pure AlSi10(Fe), the percentage (%) chemical composition of the alloy without adding Ti and Sr is given in Table 1.

Table 1. Percentage of chemical composition of pure AlSi12(Fe) alloy used in experimental studies

Si%	Fe %	Cu %	Mn %	Mg%	Cr %	Zn %
Avr. 12,0842	0.81	0.08 57	0.09 27	0.2879	0.01 42	0.08 04
Min. 10,5	0.45	0	0	-	-	0
Max. 13,5	1	0.1	0.55	-	-	0.15
Ni%	B%	Be %	Co %	Ca%	Cd %	Pb %
Avr. 0,0168	0.00 44	<0.0 03	0.00 65	0.0062	<0.0 01	0.00 97
Min.	0	0	0	0	0	0
Max. 0.15	0.05	0.05	0.05	0.15	0.01	0.1
Sn%	Ti%	V%	Sr%	Al%		
Avr. 0,0047	0.04 77	0.01 47	0.00 2	86.430 9		
Min. 0	0	0	0	0		
Max. 0.05	0.15	0.05	0.05	remain der		

2.3. Modification materials

AlTi5B1 master alloy was used for aluminum modification. AlTi5B1 master alloy was used in the form of bars with a diameter of 10 mm and a length of 500 mm. The percentage (%) chemical composition of the master alloy used in the experimental study is shown in Table 2.

Table 2. Weight % chemical composition of the AlTi5B1 master alloy used in the experimental study

Master Alloy	Al	Ti	B	Si	Fe	Mg
AlTi5B1	Remainder	5 1	1 1	<0.1 5	<0.2 0	<0.1 0

AlSr10 master alloy was used for silicon modification. AlSr10 master alloy was used in the form of rods with a diameter of 10 mm and a length of 750 mm. The percentage (%) chemical composition of the master alloy used in the experimental study is shown in Table 3.

Table 3. Weight percent chemical composition of the AlSr10 master alloy used in the experimental study

Master Alloy	Al	Sr	Fe	Si	Ca	Mg
AlSr10	Remainder	9- 11	<0.3 0	<0.3 0	<0.1 0	<0.1 0

2.4. Hardness test

12mmx12mm analysis sample pieces were taken from 5 different samples. Each sample piece was sanded using papers of 240, 400, 800, 1000, and 1200 grid degrees, respectively. 10 measurements were taken from each sample by applying a load of 62.5 kg. The results obtained were calculated by subtracting the lowest and highest values and taking their average.

2.5. Microhardness test

Microhardness tests were conducted, and measurements were made on a-Al matrix and eutectic silicon. 10 measurements were taken from each sample. During the microhardness test process, a load of 25 kg was reached in 10 seconds. The results obtained were calculated by subtracting the lowest and highest values and taking their average.

2.6. Tensile test

Tensile tests for cylindrical tensile bars obtained from 5 different alloy samples were carried out according to ISO 6892-1 standard. The pulling speed is set as a standard of 1 mm/ min. To calculate the actual percentage (%) extension, an extensometer was used in the 25mm-40mm size range. Preload is applied as 5kg and 0.5mm/ min. 5 tensile tests were performed for each parameter. In the analysis, tensile strength, yield strength, and percentage (%) elongation values of the samples were taken.

2.7. Compression test

Non-runner samples obtained from 5 different samples were carried out according to BIS 452 and ISO 7500-1 annex 1 standard. The standard pressing speed was 2 mm/min. An extensometer with a 25mm-40mm range was used to calculate the actual percentage (%) of Deformation Elongation.

The application was made at max FP, and the preloading application was completed at FM(1/2FP). After removing the FP load, the compression process was reversed, and the difference in deformation in FM was calculated. The samples are placed between two plates with a strength of 65 HRC. It is subject to a preload of 65 kN (half the load to be applied). The load was increased to 130 kN. Development of % deformation: It is calculated as the change between the first applied 65kN load and the last applied 65kN load. For each alloy, 5 compression tests were performed, and the average was taken.

2.8. Microstructure analysis

12mmX12mm analysis sample pieces were taken from 5 different samples. Each sample piece was sanded using 240, 400, 800, 1000, and 1200 grid-grade papers, respectively. Samples are dried after filing intervals to prevent oxidation. Then, the samples were polished. Colloidal silica baize (iron-free polishing material) was used in the polishing process. After polishing, images were taken and subjected to engraving. After cauterization, optical images were viewed. Etching was done by preparing Keller's solution. The Keller Composition Table is given in 4 Morphological structures, and grain sizes were examined in microstructural imaging.

Table 4. Composition of Keller's solution

Etchant	Composition
Keller Solution	Pure Water 190 ml
	Nitric Acid (conc .) 5 ml
	Hydrochloric Acid (conc .) 10 ml
	Hydrofluoric Acid (48%) 2ml

2.9. SEM & EDS analysis

Microstructure of the samples after Ti and Sr modification were analyzed at $\times 1000$ magnification. A Backscatter electron detector (BSED) was used in the SEM analysis. From the images obtained, Point and regional EDS analysis graphs and visuals were created. Percentage (%) of chemical combinations were obtained from the graphs. Intermetallic phases were examined in SEM image and EDS analysis.

3. Results and Discussion

3.1. Hardness test results

The test was prepared by cross-sectioning 5 different alloy pieces, each cast in different compositions. The average hardness values of the samples are given in Table 3. It was observed that the hardness value of pure AlSi10(Fe) increased by 5 HB by increasing the Ti ratio to 0.08%. A significant increase in the hardness value of the alloys was observed with every 150ppm Sr increase added while keeping the Ti ratio at 0.08%. The alloy with the highest hardness is AlSi10(Fe) alloy containing 450ppm Sr.

Table 5. Average Brinell hardness values

Alloys	Hardness Value (HB)
Alloy [AlSi12(Fe)]	65,3
Alloy + %0.08 Ti	70
Alloy + %0.08 Ti + 150ppm Sr	72.7
Alloy + %0.08 Ti + 300ppm Sr	74.8
Alloy + %0.08 Ti + 450ppm Sr	77.3

In high-pressure casting, the hardness of the AlSi12(Fe) alloy with a 0.08% Ti ratio increased with the addition of Sr after the grain refinement increased. The increase in hardness value increased proportionally with the addition rate. It was observed that the hardness of the 150ppm Sr added AlSi10(Fe) alloy increased by 2.5 HB, with 300ppm Sr increase, the hardness of the added AlSi10(Fe) alloy increased by 5 HB, and the hardness of the 450ppm Sr added AlSi10(Fe) alloy increased by 7.5 HB. The curve and standard deviation in hardness changes are shown in Figure 3.

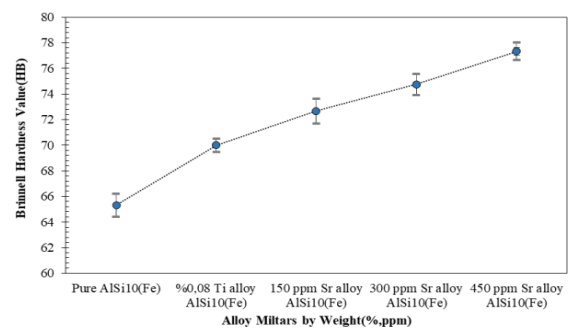


Figure 3. Alloys with 5 different weight compositions, standard deviation, and average hardness values obtained depending on additions.

3.2. Microhardness results

The average microhardness values of α -Al dendrite and eutectic silicon phases formed after Ti and Sr modification are given in Table 5. In α -Al Dendrite microhardness values, the microhardness value showed a significant increase by increasing the Ti ratio to 0.08% in the pure AlSi10 (Fe) alloy. It was observed that the microhardness value of the alloys continued to increase significantly with each 150ppm Sr increase while keeping the Ti ratio at 0.08%. In Eutectic Silicon microhardness values, the microhardness value did not show a significant increase by increasing the Ti ratio to 0.08% in the pure AlSi10 (Fe) alloy. It was observed that the microhardness value of the alloys continued to increase significantly with each 150ppm Sr increase while keeping the Ti ratio at 0.08%, are shown in Table 6.

Table 6. Average Vickers microhardness values

Alloys	α -Al Dendrit (HV/25/10)	Eutectic Silicon (HV/25/10)
Alloy [AlSi12(Fe)]	77	113
Alloy + %0.08 Ti	109	117
Alloy + %0.08 Ti + 150ppm Sr	138	162
Alloy + %0.08 Ti + 300ppm Sr	175	198
Alloy + %0.08 Ti + 450ppm Sr	216	256

In α -Al Dendrite microhardness values, after the significant increase in the microhardness of the AlSi12 (Fe) alloy with 0.08% Ti content due to grain refinement, the increase with each 150ppm Sr addition was observed to be approximately 35 HV. When we look at the microhardness of Eutectic Silicon, it is seen that the addition of Ti does not have a significant effect on the hardness of Silicon. Still, the increase in microhardness as a result of Si modification with the addition of Sr increases by approximately 40 HV for each 150ppm increase. The curves of the changes in α -Al Dendrite microhardness are shown in Figure 4. The curves of the changes in eutectic Silicon microhardness and standard deviation are shown in Figure 5.

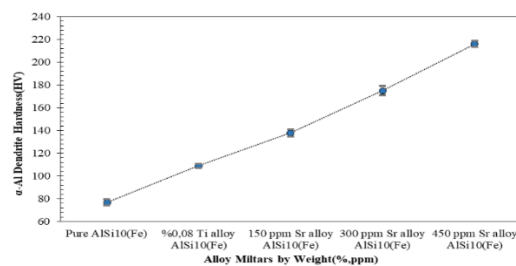


Figure 4. Alloys with 5 different weight compositions standard deviation and α -Al dendrite microhardness values obtained depending on additions.

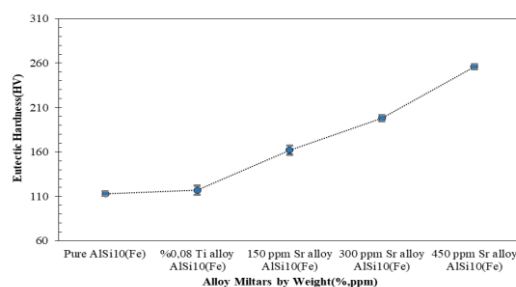


Figure 5. Alloys with 5 different weight compositions, standard deviations, and eutectic silicon microhardness values obtained depending on additions.

3.3. Tensile test results

The tensile strength (σ_t) values obtained from the tensile test results performed on 5 different alloy parts, each cast with different compositions, are shown in Table 7.

Table 7. Tensile strength values

Alloy by Weight	Tensile Strength σ_t (N/mm ²)
Pure AlSi10(Fe)	123
%0,08 Ti alloy AlSi10(Fe)	138
150 ppm Sr alloy AlSi10(Fe)	148
300 ppm Sr alloy AlSi10(Fe)	155
450 ppm Sr alloy AlSi10(Fe)	161

By increasing the Ti ratio to 0.08% in the pure AlSi10(Fe) alloy, a 15 MPa increase in tensile strength was observed. An increase of approximately 10 MPa in the tensile strength value of the alloy was contributed with a rise of 150 ppm Sr while keeping the Ti ratio at 0.08%. A 7 MPa increment was observed in the tensile strength value of the alloy with an increase of 300 ppm Sr and a 6 MPa increase in the tensile strength value of the alloy was observed with an increase of 450 ppm Sr. The curves of tensile strength changes are given in Figure 6.

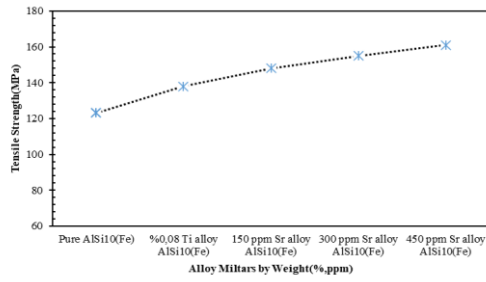


Figure 6. Tensile strength (σ_t) values obtained depending on alloys with 5 different weight compositions

Yield strength (σ_y) values obtained from the tensile test results are shown in Table 8.

Table 8. Yield Strength values

Alloy by Weight	Yield Strength σ_y (N/mm ²)
Pure AlSi10(Fe)	108
%0,08 Ti alloy AlSi10(Fe)	116
150 ppm Sr alloy AlSi10(Fe)	113
300 ppm Sr alloy AlSi10(Fe)	121
450 ppm Sr alloy AlSi10(Fe)	131

An 8 MPa increase in yield strength was observed by increasing the Ti ratio to 0.08% in the pure AlSi10(Fe) alloy. No significant increase in the yield strength of the alloy was observed with the rise of 150ppm Sr added while keeping the Ti ratio at 0.08%. Approximately 10 MPa increase in the yield strength value of the alloy was observed with the rise of 300ppm and 450ppm Sr. The curves of yield strength changes are given in Figure 7.

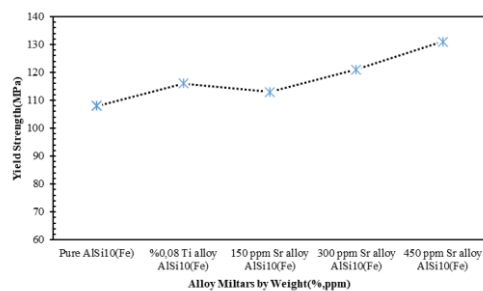


Figure 7. Alloys with 5 different weight compositions

Yield Strength (σ_t) values are obtained depending on the additions.

The percentage (%) elongation values obtained from the tensile test results are shown in Table 9.

Table 9. Percent (%) elongation values

Alloy by Weight	% Elongation
Pure AlSi10(Fe)	0.83
%0,08 Ti alloy AlSi10(Fe)	0.91
150 ppm Sr alloy AlSi10(Fe)	0.99
300 ppm Sr alloy AlSi10(Fe)	1.17
450 ppm Sr alloy AlSi10(Fe)	1.4

By increasing the Ti ratio to 0.08% in the pure AlSi10(Fe) alloy, a 0.08% increase in the percent (%) elongation value was observed. By keeping the Ti ratio at 0.08% and adding 150ppm Sr, the percentage (%) elongation value of the alloy is approximately 0.07%, with an increase of 300ppm Sr, the tensile strength value of the alloy is 0.18%, and with an increase of 450 ppm Sr, the alloy's percentage (%) elongation value is approximately 0.07%. An increase of 23 was observed. Curves of percentage (%) elongation changes are given in Figure 8.

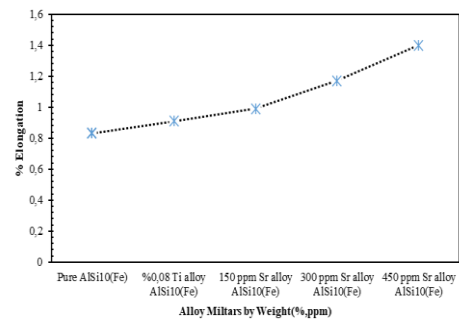


Figure 8. Percent elongation values obtained depending on alloys with 5 different compositions by weight

It has been found that the effect of Ti and Sr on the microstructure and mechanical properties of the Al-Si-Cu-Ni alloy is similar. It was observed that the addition of Sr and Ti together had a more distinct microstructure compared to the addition of Sr or Ti alone. They stated that the precipitates contained Al₂Cu, Al₃CuNi, and Al₇Cu₄Ni in the Al-12Si-4.5Cu-2Ni alloy. They concluded that strength and flexibility increased simultaneously with the combined effect of deposition defects and nano-Al₂Cu, and the alloy transitioned from fracture to ductility. This result supports our study [12].

3.4. Compression test results

The permanent deformation values as % elongation under 130 kN load in the compression test performed for 5 different alloy parts, each

cast with different compositions, are shown in Table 10. A significant increase in the elongation was observed by increasing the Ti ratio to 0.08% in the pure AlSi10(Fe) alloy. Percentage elongation of the alloys with each 150ppm Sr increase added while keeping the Ti ratio at 0.08%. No significant increase was observed, but it was observed that it reduced permanent deformation by 1%.

Table 10. Average of % Deformation Elongation values as a result of compression test

Alloys	Deformation (% elongation) under 130 kN load
Alloy [AlSi12(Fe)]	0.335
Alloy + %0.08 Ti	0.282
Alloy + %0.08 Ti + 150ppm Sr	0.271
Alloy + %0.08 Ti + 300ppm Sr	0.265
Alloy + %0.08 Ti + 450ppm Sr	0.247

Permanent % deformation elongation values of compressive strength results are shown in Figure 9.

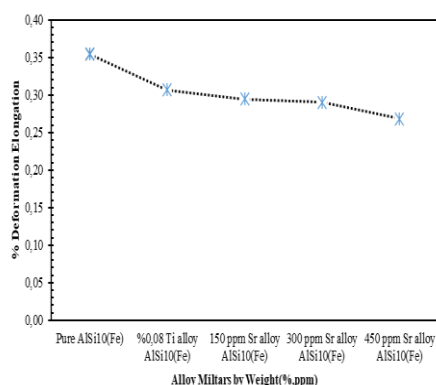


Figure 9. Average percent deformation elongation values obtained under 130 kN load depending on alloys with 5 different compositions by weight

3.5. Microstructure analysis results

It consists of 5 different alloy parts, each cast, polished, and engraved with a different composition. Optical microscopy results show that the microstructure image of α -Al dendrites and silicon eutectic phases formed after Ti and Sr modification during the growth process is shown in Figure 9. In a study investigating the microstructure and mechanical properties of phosphorus and Al-Ti-B on sub-eutectic silicon aluminum AlSi7Mg alloy, Ti/B was selected considering the optimal ratio of 5:1. Modifiers containing different contents of titanium, boron, and phosphorus were added to the AlTiBP master alloys; Phosphorus was added in amounts of

0.1%, 0.2%, and 0.3% by weight of the modified casting. The test results confirmed the modification effect of adding the parent alloy. Modifiers with different chemical compositions can achieve different microstructure morphologies. It was observed that the modifier containing 0.25% Ti + 0.03% B + 0.2% P had the most positive effect, and its measurable parameters (among the obtained parameters) had the highest mechanical properties. It was also concluded that titanium and boron affect the microstructure and mechanical properties of sub-eutectic silicon AlSi7Mg in the presence of phosphorus [13].

Microstructural images of pure AlSi10(Fe) samples are provided. When we examine the unmodified microstructure, it can be seen that the large eutectic silicon phase of α -Al dendrites is in the form of large plate-like and needle-like particles.

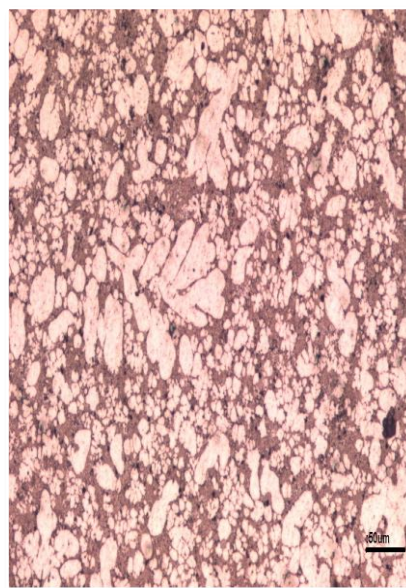


Figure 10. Microstructure images of pure AlSi10(Fe) sample

When we examined the microstructure images of the 0.08% Ti alloyed AlSi10(Fe) sample, it was observed that the α -Al dendrites became smaller. If the α -Al dendrites are in their state, they grow in the opposite direction of the heat, and long lateral arms are seen to increase. Since reducing the dendrites is the same as reducing the grain size, it has been observed that the grain size decreases. However, it was observed that the addition of Ti did not change the microstructure of eutectic Si Figure 10.

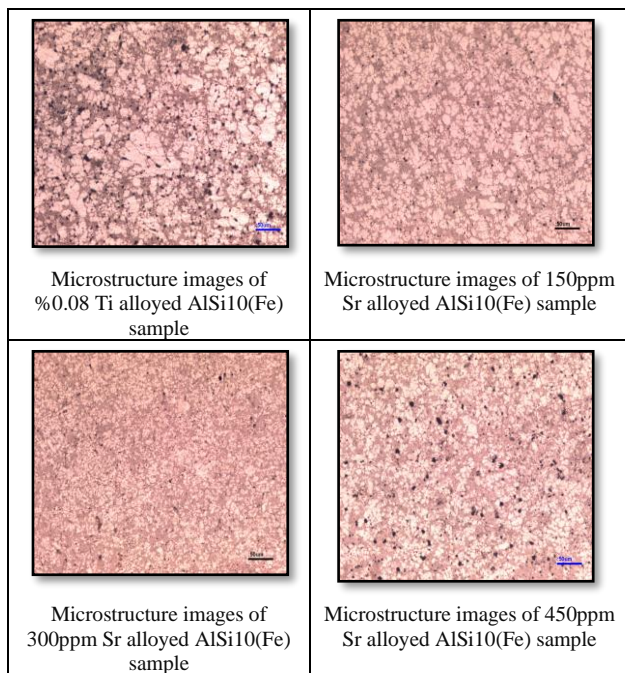


Figure 11. Microstructure of eutectic Si by Ti addition

When we examined the microstructure images of the 150ppm Sr alloyed AlSi10(Fe) sample, a needle-like structure in which large lamellae were fragmented in the eutectic silicon phase was observed. α -Al dendrites were small in size and tended to be spherical Figure 11.

It was observed that very little needle-like structure remained in the eutectic silicon phase. The α -Al dendrites reached a smaller size compared to the 150ppm Sr alloyed AlSi10(Fe) sample, and the spheroidization increased further.

When the microstructure images of the 450ppm Sr alloyed AlSi10(Fe) sample were examined, it was observed that the structure with the maximum increase in the eutectic silicon phase was fibrosis and spherical fibrous structure, as shown in.

In an A356 alloy, the addition of Ti and B significantly increases the toughness of the alloy, but only if the alloy is completely modified. Also, note that you must use the correct alloy type and addition amount. The highest total absorbed energy values recorded for tempered T6 alloys were obtained using Al-5%Ti-1%B and Al-10%Ti. There was an exception of 0.04% where impact properties were significantly degraded due to impact. It was concluded that the

increase in strength can be attributed to Sr-B interactions (in some cases), changes in Si particle morphology, and dissolution and decomposition of some intermetallic compounds at T6 temperatures [14]. According to the morphology of silicon dioxide, the eutectic modification was upgraded and modified from the American Foundry Society (AFS) modification grade to AFS grade 5 [15].

The degradation degree of eutectic silicon according to silicon dioxide morphology is shown in Table 11. The degree of distortion, according to the American Foundry Association, is shown in Figure 12.

Table 11. Eutectic modification classification according to silica morphology

No	Classification	Silicon morphology
AFS 1	No modification	Large lamellar/acicular particles
AFS 2	Lamellar/acicular form structure	Fine lamellar/acicular particles
AFS 3	Partial modification	Needle-like structure in which the lamellae are disintegrated
AFS 4	Reduced acicular structure	Structure in which tiny acicular phase remains
AFS 5	modified	Fibrosis/spheroidized structure

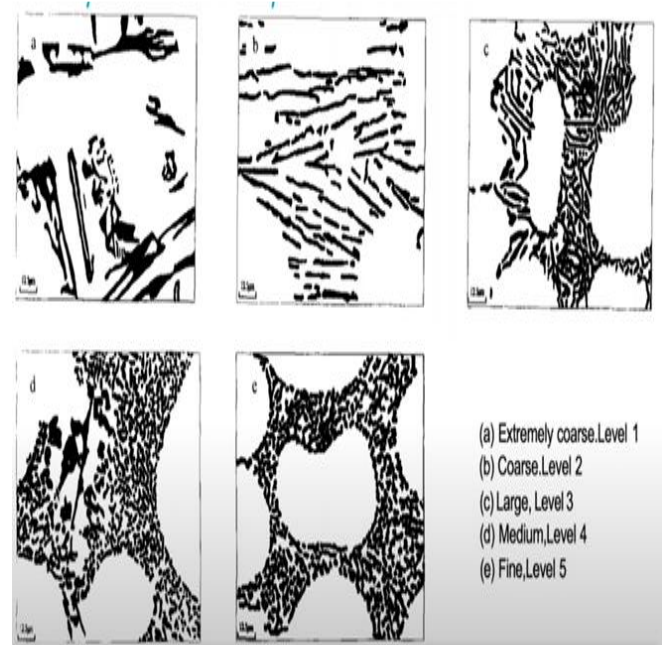


Figure 12. American Foundry Association modification levels [15]

Microstructure images of α -Al dendrite and eutectic silicon phases formed after Ti and Sr modification are shown in Figure 13.

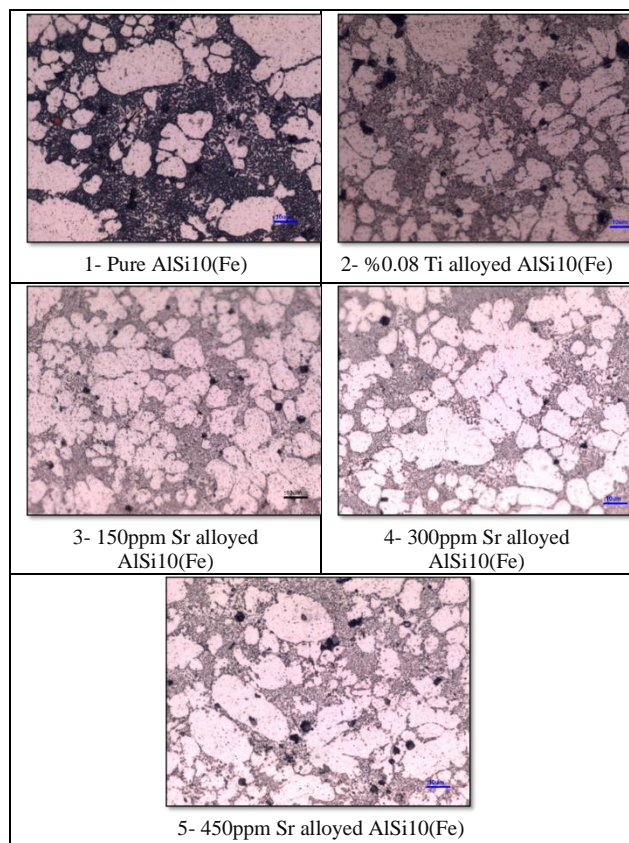


Figure 13. Microstructure images of samples obtained from alloys with 5 different weight compositions 1) Undoped AlSi10(Fe), 2) 0.08% Ti alloyed AlSi10(Fe), 3) 150ppm Sr alloyed AlSi10(Fe), 4) 300ppm Sr alloyed AlSi10(Fe) 5) 300ppm Sr alloyed AlSi10(Fe)

3.6. SEM analysis results

SEM images and EDS analyses were performed on the samples examined with an optical microscope. Microstructure images of α -Al dendrite and eutectic silicon phases formed after Ti and Sr modification are shown in Figure 14.

SEM images of the pure AlSi10(Fe) sample are given. When we examined the unmodified image, it was observed that the α -Al dendrites were very large, and the eutectic silicon phases were large lamellar and needle-like particles. However, no change was observed in the microstructure of eutectic Si.

In the literature study, high Fe-containing AlSi12 alloy was processed by laser powder bed fusion (LPBF) additive manufacturing to understand the properties of microstructures and mechanical properties in the fabricated state. Fe impurity was found to be beneficial for improving mechanical properties in LPBFed samples. Parameters including the combination of 200 W laser power,

1110 mm/s scanning speed, 0.15 mm cover gap, 0.03 mm layer thickness, and 40 J/mm³ laser volumetric energy density were optimized to achieve a high relative intensity of 99%. 7 As-LPBFed AlSi12FeMn alloy is found to have a high density, significantly refined spherical α -Al(Fe, Mn) Si phase (10-50 nm), consistent with the Al matrix. Meanwhile, the as-LPBFed AlSi12FeMn alloy can offer superior mechanical properties, including a yield strength of 305 MPa, ultimate tensile strength of 485 MPa, and fracture strain of 6.1%. The improved mechanical properties are attributed to synergistic strengthening mechanisms, including solid solution strengthening, grain boundary strengthening, and precipitation strengthening. Moreover, the formation of high-density deposition defects (SFs) and Lomer-Cottrell locks (LCs) in local regions has also resulted in the as-LPBFed AlSi12FeMn alloy, which can provide strengthening [16].

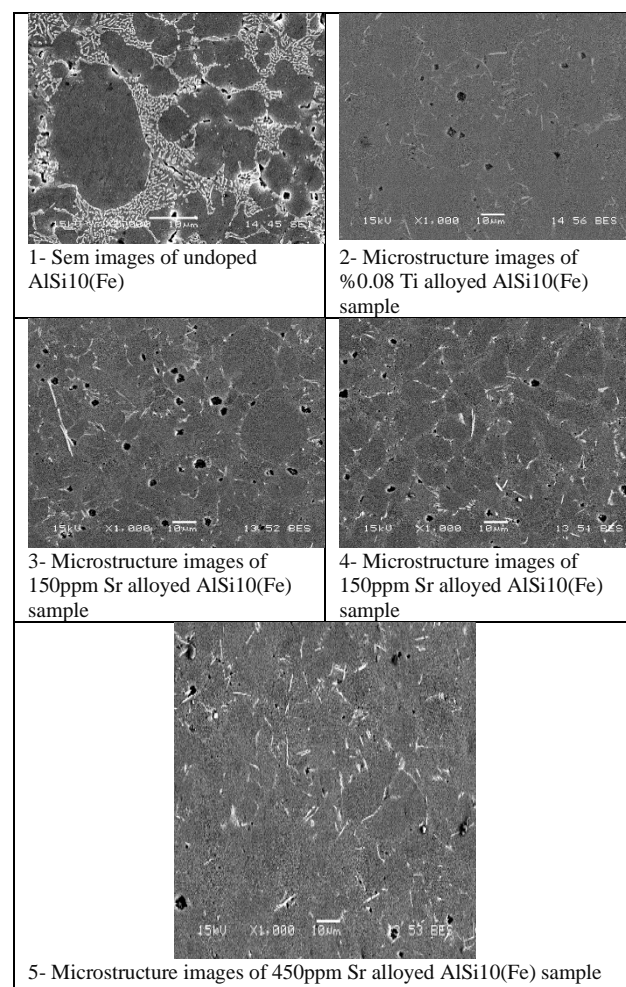


Figure 14. SEM images of samples obtained from alloys with 5 different weight compositions

- 1- SEM images of undoped AlSi10(Fe) sample,
- 2- Microstructure images of 0.08% Ti alloyed AlSi10(Fe) sample,
- 3- Microstructure images of 150ppm Sr alloyed AlSi10(Fe) sample,
- 4- Microstructure images of 300ppm Sr alloyed AlSi10(Fe) sample,
- 5- Microstructure images of 450ppm Sr alloyed AlSi10(Fe) sample.

When we examined the microstructure images of the 0.08% Ti alloyed AlSi10(Fe) sample, it was observed that the α -Al dendrites had become significantly smaller. For the microstructure images of the 150ppm Sr alloyed AlSi10(Fe) sample, it was observed that the large lamellae in the eutectic silicon crystals became smaller. When the microstructure images of the 300ppm Sr alloyed AlSi10(Fe) sample were examined, more refined silicon was observed in the eutectic silicon crystals compared to the 150ppm Sr alloyed AlSi10(Fe) alloy. For the microstructure images of the 450ppm Sr alloyed AlSi10(Fe) sample, the most prominent thin silicones in the eutectic silicon crystals were observed. The black dots clearly observed in SEM images are residues from bakelite.

Point and regional EDS and analysis results of SEM images taken from pure AlSi10(Fe) alloy are given in Figure 15.

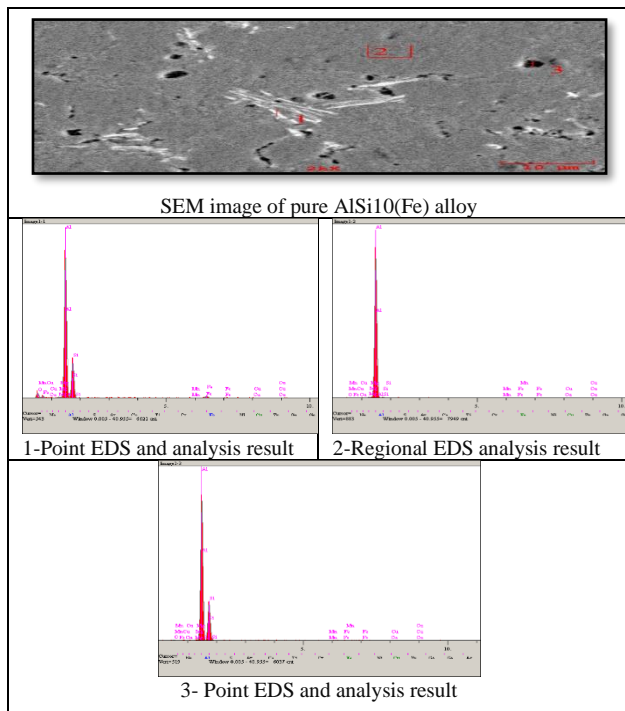


Figure 15. SEM image taken for the pure AlSi10(Fe) alloy sample and regional and point EDS analysis results obtained from this image

The chemical analysis compositions of the EDS results obtained are given below as point analysis, regional analysis, and point analysis results in Table 12.

Table 12. 1)Point analysis, 2)Regional analysis, 3)Point analysis, Results marked in the SEM image obtained for the pure AlSi10(Fe) alloy sample

Elt.	1. Point Analysis	2. Regional Analysis	3. Point Analysis	Units
O	6.247	0.687	1.249	wt.%
Mg	0.305	0.349	0.187	wt.%
Al	60.133	96.132	64.177	wt.%
Si	26.475	1.176	30.954	wt.%
Mn	0.325	0.984	0.434	wt.%
Fe	4.278	0.652	1.238	wt.%
Cu	2.238	0.000	1.762	wt.%
	100	100	100	wt% Total

When we examined the EDS analyses, when we looked at the point analysis and regional analysis results, it was observed that the main components by weight of the elements in the intermetallic phases were Al, Si, Fe, Cu, O. There were trace amounts of Mg and Mn elements.

Point and regional EDS and analysis results of SEM images taken from 0.08% Ti alloyed AlSi10(Fe) alloy are given in Figure 16.

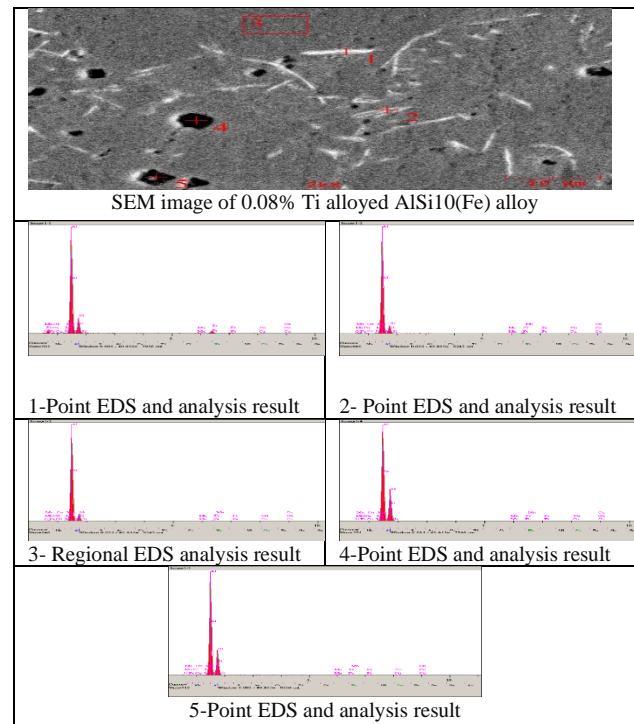


Figure 16. SEM image taken for the 0.08% Ti alloyed AlSi10(Fe) alloy sample and regional and point EDS analysis results obtained from this image.

The chemical analysis compositions of the EDS results obtained locally and regionally are given in Table 13.

Table 13. 1)Point analysis, 2)Point analysis, 3)Regional analysis, 4)Point analysis, 5)Point Analysis. Results marked in the SEM image obtained for the pure AlSi10(Fe) alloy sample

Elt.	1. Point Analysis	2. Point Analysis	2. Regional Analysis	4. Point Analysis	5. Point Analysis	Units
O	0.000	0.022	0.409	0.917	0.531	wt. %
Mg	0.516	0.369	0.120	0.206	0.060	wt. %
Al	69.352	82.022	96.139	60.756	66.865	wt. %
Si	18.712	12.555	1.148	34.770	31.691	wt. %
Mn	0.914	0.148	0.092	0.468	0.106	wt. %
Fe	8.388	3.559	0.730	1.347	0.692	wt. %
Cu	2.118	1.323	1.362	1.536	0.055	wt. %
	100	100	100	100	100	Total wt%

When we examine the EDS analyses, when we look at the point analysis and regional analysis results, it is observed that the main components by weight percent (%) of the elements in the intermetallic phases are Al, Si, Fe, and Cu. There are trace amounts of Mg, Mn, and O elements. Point and regional EDS and analysis results of SEM images taken from 150ppm Sr alloyed AlSi10(Fe) alloy are given in Figure 17.

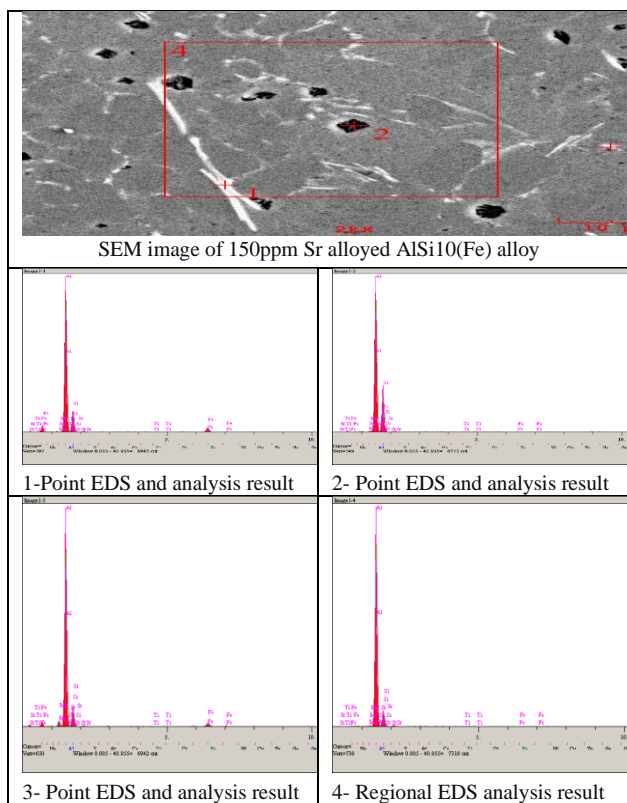


Figure 17. SEM image taken for 150ppm Sr alloyed AlSi10(Fe) alloy sample and regional and point EDS analysis results obtained from this image

The chemical analysis compositions of the EDS results obtained are given pointwise and regionally in Table 14.

Table 14. 1)Point analysis, 2)Point analysis, 3)Regional analysis, 4)Point analysis. Results marked in the SEM image obtained for the pure AlSi10(Fe) alloy sample

Elt.	1. Point Analysis	2. Point Analysis	3. Regional Analysis	4. Point Analysis	Units
Mg	0.183	0.193	2.064	0.380	wt. %
Al	71.198	64.567	74.768	84.407	wt. %
Si	17.053	33.181	13.890	13.869	wt. %
Ti	0.000	0.323	0.556	0.452	wt. %
Fe	11.566	1.019	8.722	0.892	wt. %
Sr	0.000	0.717	0.000	0.000	wt. %
	100	100	100	100	Total wt%

When we examined the EDS analyses, when we looked at the point analysis and regional analysis results, it was observed that the main components by weight of the elements in the intermetallic phases were Al, Si, and Fe. There were trace amounts of Mg, Ti, Sr elements. Point and regional EDS and analysis results of SEM images taken from 300ppm Sr alloyed AlSi10(Fe) alloy are given in Figure 18.

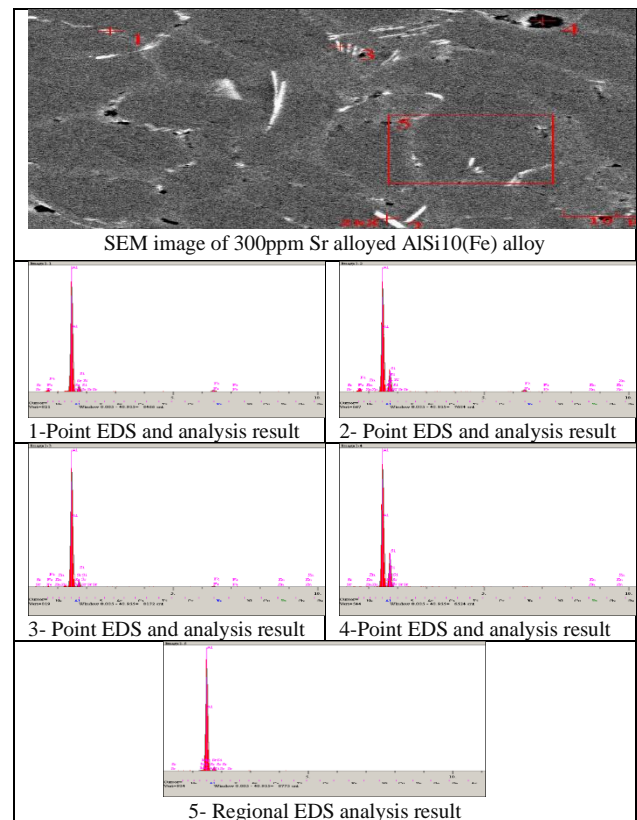


Figure 18. SEM image taken for 300ppm Sr alloyed AlSi10(Fe) alloy sample and regional and point EDS analysis results obtained from this image

The chemical analysis compositions of the EDS results obtained are given pointwise and regionally in Table 15.

Table 15. 1)Point analysis, 2)Point analysis, 3)Point analysis, 4)Regional analysis, 5)Regional analysis. Results marked in the SEM image obtained for the pure AlSi10(Fe) alloy sample

Elt.	1. Point Analysis	2. Point Analysis	2. Point Analysis	4. Regional Analysis	5. Regional Analysis	Units
Mg	-	-	-	-	0.488	wt.%
Al	82.322	67.313	84.776	67.142	92.514	wt.%
Si	9.108	21.771	8.202	30.580	6.998	wt.%
Fe	8.570	8.077	4.536	-	-	wt.%
Zn	-	2.838	2.486	0.685	-	wt.%
Sr	0.000	0.000	0.000	0.000	0.000	wt.%
	100	100	100	100	100	Total wt%

When we examined the EDS analyses, when we looked at the point analysis and regional analysis results, it was observed that the main components by weight percent (%) of the elements in the intermetallic phases were Al, Si, Fe, and Zn elements. Point and regional EDS and analysis results of SEM images taken from 450ppm Sr alloyed AlSi10(Fe) alloy are given in Figure 19.

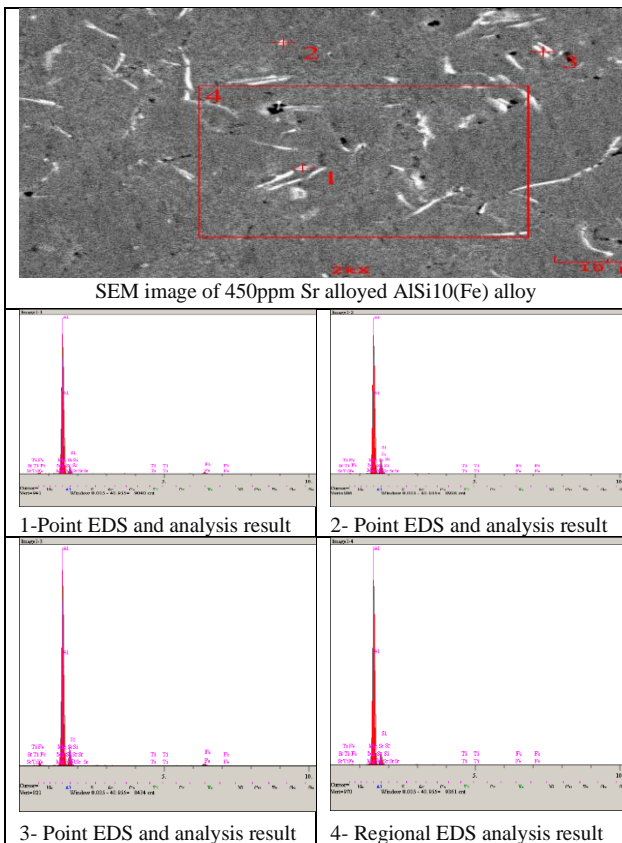


Figure 19. SEM image taken for the 450ppm Sr alloyed AlSi10(Fe) alloy sample and regional and point EDS analysis results obtained from this image

The chemical analysis compositions of the EDS results obtained as point and regional analysis are given in Table 16.

Table 16. 1)Point analysis, 2)Point analysis, 3)Point analysis, 4)Regional analysis. Results marked in the SEM image obtained for the pure AlSi10(Fe) alloy sample

Elt.	1. Point Analysis	2. Point Analysis	3. Point Analysis	4. Regional Analysis	Units
Mg	0.407	0.362	0.212	0.216	wt.%
Al	85.761	81.573	79.483	87.248	wt.%
Si	8.217	16.465	13.287	11.715	wt.%
Ti	0.306	0.183	0.330	0.132	wt.%
Fe	5.309	1.000	6.687	0.178	wt.%
Sr	0.000	0.416	0.000	0.511	wt.%
	100	100	100	100	Total wt%

When we examine the EDS analyses, when we look at the point analysis and regional analysis results, it is observed that the main components by weight percent (%) of the elements in the intermetallic phases are Al, Si, Fe, and there are trace amounts of Mg, Ti, Sr elements.

4. Conclusions and Discussion

4.1. Results

In this study, samples were produced by high-pressure casting method from alloys formed in 5 different compositions by adding Al5Ti1B master alloy and AlSr10 master alloy to pure AlSi10(Fe) alloy. The hardness, microhardness, mechanical properties, microstructure, and SEM analyses of the obtained alloys were examined comparatively.

1- In our study, the addition of Ti significantly increased the hardness by reducing the grain size. It is seen that the addition of 150ppm, 300ppm, and 450ppm Sr increases the hardness proportionally by 2.5 HB.

In the study, samples with different cross-sectional areas between 0° and 1° with an increment of 0.1° were produced from AA2024, AA6061, and AA7075 Al alloy sheets with a thickness of 2 mm by cutting them with the water jet method. The heat treatment process was applied to the test samples with different cross-sectional areas produced under two other

conditions. The first heat treatment process was used in the study. The heat treatment was applied by dissolving at 510°C for 2 hours + quenching + aging at 160°C. In the second heat treatment process, test samples were obtained by performing the heat treatment stages of 2 hours of dissolution at 510°C + quenching + 168 hours of shallow-cryogenic cooling at $\approx -75^\circ\text{C}$ + aging at 160°C. At the end of each applied processing step, the hardness properties and natural frequency values of Al alloys were analyzed. When the hardness data of AA2024, AA6061, and AA7075 Al alloys were examined, it was determined that the applied heat treatment stages affected the hardness values of the materials. The supersaturated solid structure formed in the internal structure was obtained by quenching heat treatment after dissolving for 2 hours at 510°C applied to the Al alloy series, and it was determined that the time and temperature values during the used heat treatment stage were suitable for the AA2024, AA6061 and AA7075 Al alloy series. For the AA2024 Al alloy series, the maximum hardness value due to aging heat treatment was measured as 131HV after 7 hours. It was observed that the material hardness value started to decrease with the aging process continued after 7 hours. The maximum hardness value for AA6061 series Al alloy was measured as 93HV at the 12th hour. After this value was obtained, the aging process continued, and during the 13-15 hour aging process, it was observed that the hardness value decreased from 93HV to 74HV, and the aging process was completed for AA6061 Al alloy.

The data obtained in the hardness analysis taken after dissolution for AA7075 series Al alloy was measured as 31HV. The changes in the hardness properties of the material were examined with the aging heat treatment applied in 1-hour periods after the dissolution process. Accordingly, the maximum hardness value for the AA7075 Al alloy series was measured as 143HV at the 13th hour. After 13 hours, the aging heat treatment continued. Gradual decreases in hardness values were observed at 14 and 15 hours. In the clock problem, the measured hardness value decreased from 143HV to 120HV [17].

2- In our study, Ti addition reduced the size of α -Al dendrites. The addition of Si changed the

eutectic silicon phase. These two modified phases appear to increase the HV hardness significantly.

In the study, a new Al-11Si-3Cu alloy with high strength, flexibility, and low cost was developed by adding a small amount of Sr + Sc mixed substituent content. The effects of minor Sr and Sc contents on the microstructure and mechanical properties of the alloys were also investigated. In the study, a new high-strength, ductile, and low-cost Al-11Si-3Cu alloy microalloyed with little Sr + Sc was developed and shown to improve ultimate tensile strength and elongation over most developed Al-Si-3Cu alloys [18].

3- In our study, the addition of Ti and Sr elements showed a significant increase in tensile strength.

4- In our study, yield strength increased with the addition of Ti. Percentage (%) While there was no increase in 150 ppm Sr by weight, an increase was observed in 300 ppm and 450 ppm Sr.

In a different study, we investigated the effect of Ti and Sr addition on the microstructure and mechanical properties of Al-Si-Cu-Ni alloy and revealed the impact mechanism. The effect of Ti and Sr on the microstructure and mechanical properties of Al-Si-Cu-Ni alloy was investigated. Studies showed that the addition of 0.1% Ti and 0.02% Sr significantly reduced the grain size and changed the morphology of eutectic Si. Sr promoted the formation of stacking defects and nano-Al₂Cu. The strength and plasticity increased significantly, with the ultimate tensile strength, yield strength, and elongation being 239.6 MPa, 140.6 MPa, and 2.11%, respectively. Our research showed that adding Sr and Ti together had a more distinct microstructure compared to adding Sr or Ti alone. The precipitates included Al₂Cu, Al₃CuNi and Al₇Cu₄Ni in the Al-12Si-4.5Cu-2Ni alloy. Strength and flexibility were simultaneously increased by the combined effect of stacking defects and nano-Al₂Cu, and it was observed that the alloy transitioned from a brittle structure to a more ductile fracture [10].

5- In our study, a significant increase in % elongation values was observed with the addition of Ti and Sr.

In this thesis study, by making Sr modifications to the AlSi12(Fe) alloy produced using the high-pressure casting method, the effect of the amount of Sr on the mechanical and microstructural characteristics of the alloy was examined. As a result, it has been observed that both the microstructural and mechanical properties of the AlSi12 (Fe) alloy produced by the high-pressure casting method are positively affected depending on the increasing amount of Sr. A significant improvement was detected in the yield strength, tensile strength, and % elongation value of the AlSi12(Fe) alloy with increasing Sr amount. According to the results of the notch impact test, the energy absorption ability of the alloy was improved by increasing the amount of Sr. It was concluded that the ductility property of AlSi12(Fe) alloy was significantly enhanced with the use of 160 ppm Sr [19].

6- In our study, while the permanent deformation elongation decreased with the addition of Ti, it was observed that the permanent deformation elongation decreased proportionally with every additional 150 ppm Sr amount.

In the study, the effect of grain refinement (Al–5Ti–1B) and modification (Al–10Sr) on the microstructure, the morphology of the iron-containing needle-shaped beta phase, and the mechanical properties of the cast Al–12Si alloy were examined. Grain refinement of the alloy with the optimum amount of Al-Ti-B master alloy (0.00125 wt% Ti) in Al-12Si-based alloy reduces the size of Al-Fe-Si intermetallic compounds and transforms the needle-like β -morphology. Phase intermetallic compound into block form, similarly, modification of the alloy with the optimum amount of Al-Sr master alloys (0.06 wt% Sr) in the base metal Al-12Si alloy has been observed to refine eutectic Si [20].

7- In our study, it was observed that the addition of the Ti element reduced the grain size by shrinking the α -Al dendrites but did not affect the eutectic Si. It has been observed that the addition of the Sr element changes Si. When we reached 450ppm Sr, it was observed that it changed from a rough lamellar and needle-like structure to a fibrous/spherical structure.

8- In our study, it was determined that α -Al dendrites and Si crystals shrank in the images in SEM-EDS analyses, and this supports the optical image results. It has also been observed that there are intermetallic phases consisting of Al, Si, and Fe elements as the main components.

4.2. Suggestions

Based on the findings obtained as a result of experimental studies, the following suggestions can be made for future studies.

The effect of phosphorus on the same study can be investigated by using phosphorus along with strontium.

The effect of Ti and Sr over a certain period can be examined by taking samples from pressures at different times.

Except for the high-pressure casting method, the same experimental study can be carried out with the low-pressure casting method with the same parameters, and its effects on mechanical properties and microstructure can be examined.

Experiments can be made with different etchants to examine SEM images in detail.

Article Information Form

Funding

The author has not received any financial support for the research, authorship, or publication of this study.

Authors' Contribution

Alpaslan KILIÇARSLAN contributed conception / dizayn, data collection, data analysis/interpretation, writing, technical support / material support.

Prof.Dr. Hatem AKBULUT contributed data analysis/interpretation, technical support / material support, critical review of content, and literature review.

The Declaration of Conflict of Interest/ Common Interest

The authors have declared no conflict of interest or common interest.

The Declaration of Ethics Committee Approval

This study does not require an ethics committee permission or any special permission.

The Declaration of Research and Publication Ethics

The authors of the article declare they will respect the scientific, ethical, and rating rules of the SAUJS in all processes of the article and not carry out any falsification of the data collected. Furthermore, they state that the Sakarya University Journal of Science and its editorial board take no responsibility for any ethical violations that may be encountered and that this study has not been evaluated in any academic publishing environment other than the Sakarya University Journal of Science.

Copyright Statement

Authors own the copyright of their work published in the journal and their work is published under the CC BY-NC 4.0 license.

References

- [1] X. Wang, G. Zhao, L. Sun, Y. Wang, H. Li, "A strategy to promote formability, production efficiency and mechanical properties of al-mg-si alloy," *Journal of Materials Research and Technology*, vol. 24, pp. 3853-3869, 2023.
- [2] F. Zupanič, M. Steinacher, S. Žist, T. Bončina, "Microstructure, mechanical properties and fatigue behavior of a new high-strength aluminum alloy aa 6086", Contents lists available at ScienceDirect, *Journal of Alloys and Compounds*, vol. 941, pp. 168-976, 2023.
- [3] J. Kadkhodapour, S. Schmauder, F. Sajadi, "Quality analysis of additively manufactured," *Metals, Simulation Approaches, Processes, and Microstructure Properties*, Chapter Nine, 1st Edition – November, vol. 30, pp. 886-9789, 2022.
- [4] A. S. J. Al-Zubaydi, N. Gao, S. Wang, P. A. S. Reed, "Microstructural and hardness evolution of additively manufactured Al-Si-Cu alloy processed by highpressure torsion", *Metals & Corrosion, Journal of Materials Science*, vol. 57, pp. 8956–8977, 2022.
- [5] O. Altuntaş, "Enhancement of impact toughness properties of Al 7075 alloy via double aging heat treatment", *Gazi University Journal of Science Part C: Design and Technology*, vol. 10, pp. 195-202, 2022.
- [6] B. A. E. Haj, A. Hamadellah, A. Bouayad, C. E. Akili, "Review of grain refinement performance of aluminium cast alloys", *Journal of Metallurgy and Materials Engineering*, vol. 29-2, pp. 1-15, 2023.
- [7] B. Callegari, T. N. Lima, R. S. Coelho, "The influence of alloying elements on the microstructure and properties of al-si-based casting alloys: a review", *Metals*, vol. 13, pp. 1174, 2023.
- [8] T. Bogdanoff, S. Seifeddine, A. K. Dahle, "The effect of si content on microstructure and mechanical properties of al-si alloy", *Metall. Ital.*, vol. 108, pp. 65–68, 2016.
- [9] M. Emamy, B. Pourbahari, M. Mostafapour, "Significant grain refinement and enhanced mechanical properties of 6070 Al alloy via Ti/Sr addition and hot extrusion", *J. Ultrafine Grained Nanostruct Mater*, vol. 53-2, pp. 190-203, 2020.
- [10] J. Dong, J. Jiang, Y. Wang, M. Huang, Y. Liu, Y. Zhang, "Effect of Ti and Sr on the microstructure and mechanical properties of Al-12Si-4.5Cu-2Ni alloy", *Materials Letters*, vol. 352, pp. 135129, 2023.
- [11] J. Y. Lee, J. M. Lee, K. S. Son, J. I. Jang, Y. H. Cho, "A study on the interaction between a Sr modifier and an Al-5Ti-1B grain refiner in an Al-7Si-0.35Mg casting alloy", *Journal of Alloys and Compounds*, vol. 938, pp. 168598, 2023.
- [12] A. P. Hekimoğlu, M. Hacıosmanoğlu, M. Baki, "Effect of zinc additives at different rates on the structural, mechanical and

- tribological properties of EN AC-48100 (Al-17Si-4Cu-Mg) alloy”, Journal of the Faculty of Engineering and Architecture of Gazi University, vol. 35, pp. 1799-1814, 2020.
- [13] B. Yalçın, R. Varol, “Determination of wear performance and some mechanical properties of sintered titanium alloys”, Journal of the Faculty of Engineering and Architecture of Gazi University, vol: 24, pp. 63-72, 2009.
- [14] J. M. Yu, N. Wanderka, A. Rack, R. Daudin, E. Boller, H. Markötter, J. Banhart, “Influence of impurities, strontium addition and cooling rate on microstructure evolution in Al-10Si-0.3Fe casting alloys”, Journal of Alloys and Compounds, vol. 766, pp. 818–827, 2018.
- [15] Y. S. Lerner, N. R. Posinasetti, “Metal casting principles and techniques”, Editor: American Foundry Society, pp. 274, 2013.
- [16] A. M. Samuel, H. W. Doty, S. F. H. Valtierra, F. H. Samuel, “Effect of grain refining and sr-modification interactions on the impact toughness of Al–Si–Mg cast alloys”, Materials and Design, vol. 56, pp. 264–273, 2014.
- [17] R. Arslan, “Investigation of the effects of shallow-cryogenic and aging heat treatments applied to AA2024, AA6061, AA7075 Al alloys on microstructure, hardness and natural frequency properties”, Pamukkale University, Institute of Science, Department of Metallurgical and Materials Engineering, pp. 1-110, 2023.
- [18] Z. Shi, R. He, Y. Chen, H. Yan, H. Song, C. Luo, Q. Nie, Z. Hu, “Microstructural evolution and strengthening mechanisms of a novel Al–11Si–3Cu alloy microalloyed with minor contents of Sr and Sc”, Contents lists available at ScienceDirect, Materials Science & Engineering A, Materials Science & Engineering A, vol. 853 pp. 143738, 2022.
- [19] İ. Sapmaz, “Investigation of the effect of Sr additions in AlSi12(Fe) high pressure casting alloy on the microstructure and mechanical properties of the alloy”, Bursa Technical University, Institute of Science and Technology, pp. 1-99, 2021.
- [20] S. H. Rodríguez, R. E. Goytia-Reyes, D. K. Dwivedi, V. H. Baltazar-Hernández, H. Flores-Zúñiga, M. J. Pérez-López, “On influence of Ti and Sr on microstructure, mechanical properties and quality, index of cast eutectic Al–Si–Mg alloy”, Contents lists available at ScienceDirect, Materials and Design, Materials and Design, vol. 32, pp. 1865–1871, 2011.